UNIVERSITÉ DE MONTRÉAL

THE HYDRAULIC BEHAVIOR OF INTERCONNECTED SUBCHANNELS IN NUCLEAR FUEL ROD BUNDLES

Siamak KAVEH-KHORIE

DÉPARTEMENT DE GÉNIE MÉCANIQUE

ÉCOLE POLYTECHNIQUE DE MONTRÉAL

MÉMOIRE PRÉSENTÉ EN VUE DE L'OBTENTION

DU DIPLÔME DE MAÎTRISE ÈS SCIENCES APPLIQUÉES (M.Sc.A.)

(GÉNIE ÉNERGÉTIQUE)

Avril 1995

© Siamak KAVEH-KHORIE, 1995.

National Library of Canada
Acquisitions and Bibliographic Services Branch
395 Wellington Street
Ottawa, Ontario
K1A 0N4

Bibliothèque nationale du Canada
Direction des acquisitions et des services bibliographiques
395, rue Wellington
Ottawa (Ontario)
K1A 0N4

Your file *Votre référence*

Our file *Notre référence*

THE AUTHOR HAS GRANTED AN IRREVOCABLE NON-EXCLUSIVE LICENCE ALLOWING THE NATIONAL LIBRARY OF CANADA TO REPRODUCE, LOAN, DISTRIBUTE OR SELL COPIES OF HIS/HER THESIS BY ANY MEANS AND IN ANY FORM OR FORMAT, MAKING THIS THESIS AVAILABLE TO INTERESTED PERSONS.

L'AUTEUR A ACCORDE UNE LICENCE IRREVOCABLE ET NON EXCLUSIVE PERMETTANT A LA BIBLIOTHEQUE NATIONALE DU CANADA DE REPRODUIRE, PRETER, DISTRIBUER OU VENDRE DES COPIES DE SA THESE DE QUELQUE MANIERE ET SOUS QUELQUE FORME QUE CE SOIT POUR METTRE DES EXEMPLAIRES DE CETTE THESE A LA DISPOSITION DES PERSONNE INTERESSEES.

THE AUTHOR RETAINS OWNERSHIP OF THE COPYRIGHT IN HIS/HER THESIS. NEITHER THE THESIS NOR SUBSTANTIAL EXTRACTS FROM IT MAY BE PRINTED OR OTHERWISE REPRODUCED WITHOUT HIS/HER PERMISSION.

L'AUTEUR CONSERVE LA PROPRIETE DU DROIT D'AUTEUR QUI PROTEGE SA THESE. NI LA THESE NI DES EXTRAITS SUBSTANTIELS DE CELLE-CI NE DOIVENT ETRE IMPRIMES OU AUTREMENT REPRODUITS SANS SON AUTORISATION.

ISBN 0-612-03662-6

Canada

UNIVERSITÉ DE MONTRÉAL

ÉCOLE POLYTECHNIQUE DE MONTRÉAL

Ce mémoire intitulé:

THE HYDRAULIC BEHAVIOR OF INTERCONNECTED SUBCHANNELS IN NUCLEAR FUEL ROD BUNDLES

présenté par: KAVEH-KHORIE Siamak

en vue de l'obtention du diplôme de: Maîtrise ès sciences appliquées

a été dûment accepté par le jury d'examen constitué:

M. ZIKOVSKY Lubomir, Ph.D., président

M. TEYSSEDOU Alberto, Ph.D., membre et directeur de recherche

M. TAPUCU Altan, D.Sc.A., membre et codirecteur

Mme TROCHE Nadia, M.Sc.A., membre

To my parents and sisters,

whom I love the most.

ACKNOWLEDGMENTS

I would like to thank my thesis directors Dr. Altan Tapucu and Dr. Alberto Teyssedou for the invaluable help and guidance they have given to me throughout the course of this work. I am sure they know how much I appreciate the help they have given me during the last 2 years.

I would like to extend my special thanks to Dr. L. Zikovsky for his invaluable help during the admission process. Without his help, I simply would not have been able to begin my studies at IGN.

This work would not have been possible without the help of N. Troche (M.Sc.A.) and A. Bellil (Ph.D. candidate) during the experimental work. Also, I would like to thank J. Lambert (M.Sc.A. candidate) who corrected the French section of this text.

Finally, my special gratitude goes to P. Tye (Ph.D. candidate) who kindly accepted to read and correct the last version of this text in a short period of time.

RÉSUMÉ

L'analyse thermohydraulique des grappes de combustible utilisées dans le coeur des réacteurs de puissance est exécutée en utilisant "le code de sous-canaux COBRA-IV". Dans ce code la géométrie compliquée des grappes de combustible est divisée en petites cellules appelées "sous-canaux". Les équations unidimensionnelles de conservation de masse, énergie et quantité de mouvement sont développées pour chacun des sous canaux et résolues numériquement, en considérant toutes les interactions possibles avec les sous canaux voisins. Les interactions naturelles entre deux sous canaux peuvent être modélisées à partir de deux approches: l'égalité des échanges de masse, et l'égalité des échanges de volume. Le code de sous-canaux interconnectés COBRA-IV utilise un modèle basé sur l'égalité des échanges de masse entre deux sous canaux voisin. Dans ce modèle, les phénomènes de mélanges naturels sont modélisés en utilisant un simple coefficient de mélange, appelé (β). Le succès du code de sous canaux interconnectés COBRA-IV, dépend en partie de la précision avec laquelle ce coefficient est déterminé. Cette étude est décomposée en trois parties:

En utilisant une section de test représentant deux sous canaux interconnectés dans une grappe de combustible et une boucle air-eau adiabatique, le comportement hydraulique de deux sous canaux latéralement interconnectés est étudié expérimentalement lorsque les débits de liquide à l'entrée de chaque sous canal sont, soit égaux, soit essentiellement différents. Les paramètres mesurés de l'écoulement sont:

- la distribution axiale de taux de vide (en utilisant la méthode de conductivité), et
- la perte de pression le long de la région interconnectée (en utilisant des "capteurs" de pression).

Les données obtenues à partir des expériences ont été utilisées pour évaluer les performances du code COBRA-IV. Une analyse de sensibilité a été effectuée pour déterminer l'effet du coefficient de mélange (β) sur les prédictions du code. La valeur optimale de β a été déterminée pour chacune des expériences. Cependant les tentatives de corrélation des valeurs optimales de β avec les conditions moyennes d'entrée (flux massique, taux de vide et titre) n'ont pas réussis.

Finalement, les prédictions de COBRA-IV sont comparées avec les données obtenues pour deux sous canaux latéralement interconnectés dont l'un d'eux est partiellement obstrué. Les données expérimentales sélectionnées incluent des obstructions abruptes ou graduelles allant jusqu'à une obstruction de 60% de la section de passage pour des écoulements monophasiques et diphasiques. Une analyse de sensibilité est réalisée pour les paramètres clefs utilisés par COBRA-IV, i.e., le facteur de résistance à l'écoulement latéral (K_{ij}), le coefficient de pertes de pression irréversible (k) et le coefficient du mélange (β). On observe que la valeur du facteur de résistance à l'écoulement latéral (K_{ij}) n'a pratiquement aucun effet sur les prédictions du code, cependant, dans certains cas, la convergence de la procédure numérique dépend essentiellement de ce paramètre. Les résultats de l'analyse de sensibilité montrent aussi que les valeurs expérimentales du coefficient de pertes de pression irréversible (k) peuvent être adéquatement utilisées dans COBRA-IV. De plus, il a été observé que les prédictions de pertes de pression totale et de débits de liquides sont fortement affectées par une variation de ce paramètre. L'analyse de sensibilité a permis de suggérer les valeurs optimales pour le coefficient de mélange (β) et d'observer que ce paramètre affecte les prédictions de COBRA-IV pour les taux de vide et les débits de liquide. Finalement les comparaisons des prédictions de COBRA-IV avec des données expérimentales confirment que celui-ci est capable de simuler des écoulements

monophasiques et diphasiques dont la section de passage est obstruée jusqu' a 60%. Cependant les prédictions par le code du débit de liquide quand 60% de la section de passage est obstrué de manière abrupte ne sont pas satisfaisantes.

ABSTRACT

The thermalhydraulic analysis of the nuclear fuel assemblies used in power reactors is carried out by using the "COBRA-IV subchannel code." In this code the complex geometry of the fuel assemblies is divided into small cells called "subchannels." The one dimensional conservation equations of mass momentum and energy are written for each subchannel and solved numerically while considering the possible interactions with adjacent ones. The natural turbulent interactions between two subchannels can be modeled based on two approaches, equal mass exchange, and equal volume exchange. The COBRA-IV subchannel code uses an equal mass model which is based on a fluctuating equal mass exchange between adjacent subchannels. In this model, the natural mixing phenomena are modeled by using a simple mixing coefficient, the so-called (β). The success of the COBRA-IV subchannel code, to some extent, depends on how well this coefficient is determined. The present research consists of three parts:

Using a test section representing two interconnected subchannels in a rod bundle array and an adiabatic air-water loop, the experiments have been conducted to study the hydraulic behavior of two laterally interconnected subchannels where mass flow rates and void fractions in the subchannels at the beginning of the interconnected region were equal or substantially different. The measured flow parameters are:

- axial distribution of the void fraction (by using conductivity method), and
- pressure drop along the interconnected region (by using pressure transducers).

The data obtained from the experiments have been used to evaluate the performance of the COBRA-IV subchannel code. A sensitivity analysis has been carried out to determine the effect of the mixing coefficient (β) on the predictions of the COBRA-IV subchannel code. The best value of β for each experiment has been determined. However, the attempts to correlate the best values of β to the average inlet conditions, i.e., the average inlet mass flux, the average inlet void fraction, and the average inlet dryness fraction have failed.

Finally, the prediction of the COBRA-IV is compared with the data obtained on two laterally interconnected subchannel when one of them is partially blocked. The selected experimental data include plate and smooth blockage, up to 60% of flow area reduction for both single- and two-phase flows. The sensitivity analysis for the values of key parameters used in the COBRA-IV subchannel code, i.e., the cross-flow resistance factor (K_{ij}), the irreversible pressure drop coefficient (k), and the mixing coefficient (β) have been carried out. It has been observed that the values of cross-flow resistance factor (K_{ij}) has no major effect on the code's predictions while the convergence of the numerical scheme in some cases, depends on the values of this parameter. The results of the sensitivity analysis show that experimental values for the irreversible pressure drop coefficient (k) can be safely used in the COBRA-IV subchannel code. It has also been observed that the predictions of the total pressure drops and the liquid flow rates are strongly affected by the changes in the values of this parameter. Based on the results obtained from the sensitivity analysis, the best values for the mixing coefficient (β) have been suggested and it has been observed that this parameter affects the predictions of the COBRA-IV subchannel code for the void fractions and liquid flow rates. Furthermore, it has been observed that the COBRA-IV subchannel code can be used safely, for the blockage cases up to 60% of flow area reduction. However, the liquid

flow rates for the plate blockage cases with 60% of area reduction, are not well predicted by the code.

CONDENSÉ EN FRANÇAIS

I. Problème posée

Le comportement thermohydraulique du caloporteur des réacteurs nucléaires à eau pressurisée fait l'objet de nombreux programmes de recherche. Les résultats de ces recherches sont essentiels pour l'évaluation des performances et les études de sûreté des centrales électronucléaires. L'objectif ultime visé est de prédire correctement l'évolution du caloporteur au sein du circuit primaire de refroidissement. L'endroit le plus critique de ce circuit est le coeur du réacteur où le caloporteur a pour rôle d'évacuer adéquatement et en toutes situations l'énergie thermique dégagée par la fission nucléaire dans les grappes de combustible.

La complexité des écoulement dans les réacteurs nucléaires est due essentiellement à trois facteurs:

- La géométrie des grappes de combustible formées de plusieurs dizaines de crayons permettant d'augmenter la surface d'échange avec le caloporteur; la frontière fluide-solide est donc très compliquée et l'écoulement obtenu est turbulent et tridimensionnel.
- La nature diphasique eau-vapeur de l'écoulement; on envisage comme possible ébullition du caloporteur soit en fonctionnement normal à pleine puissance, soit en cas d'accident (dépressurisation, par exemple). L'écoulement est donc formé d'un mélange liquide et d'eau vapeur.
- Le phénomène d'ébullition qui met en jeu des échanges complexes entre les parois chauffantes, le liquide et la vapeur.

II. Méthode utilisée

a) Définition de la méthode des sous-canaux interconnectés

Pour traiter ce type de problèmes, une méthode fréquemment utilisée pour l'analyse thermohydraulique des grappes de combustible, consiste à diviser la section de passage complexe en petites cellules élémentaires, appelées "sous-canaux". Pour obtenir les paramètres d'écoulement, on utilise la méthode des sous-canaux pour écrire les équations de masse, de quantité de mouvement et d'énergie qui permettent de décrire l'écoulement axial pour chaque sous canal. Toutefois, pour tenir compte des interactions qui existent entre les sous-canaux adjacents, on utilise une équation constitutive de quantité de mouvement transversal. Ces équations sont par la suite résolues en utilisant un schéma numérique adéquat. Un choix judicieux du modèle d'échanges de masse, de quantité de mouvement et d'énergie entre les sous-canaux est nécessaire pour permettre la prédiction de la redistribution de l'écoulement entre les sous-canaux interconnectés latéralement, dans des conditions d'écoulement vertical ou horizontal. Par conséquent, ces modèles doivent être capables de modéliser adéquatement les phénomènes physiques gouvernant l'écoulement en général et les mécanismes d'échanges en particulier.

Dans ce travail, la contribution au développement des modèles et des codes de sous-canaux repose sur la comparaison entre les simulations produites par le code de sous-canaux "COBRA-IV" et les résultats d'expériences effectuées à l'institut de génie nucléaire précédemment ou spécialement pour cette étude. En effet, une large gamme d'expériences qui permet de couvrir différentes conditions d'opération des sous-canaux a été réalisée afin de valider ce code et d'apprécier ses performances.

b) Approche analytique

Dans le code COBRA-IV, l'écriture d'un modèle unidimensionnel pour les écoulements diphasiques nécessite un certain nombre d'approximations. Ces approximations sont étroitement liées aux moyennes effectuées sur les variables du système. Ainsi, les moyennes dans le temps et dans le espace effectuées permettent d'éliminer le caractère aléatoire et discontinue de l'écoulement diphasique. Les équations de masse, de quantité de mouvement et d'énergie sont d'abord développées sur un volume de contrôle Eulerien (fixé dans le temps et l'espace) pour un écoulement diphasique homogène. Les équations simplifiées ainsi obtenues sont appliquées sur un volume de contrôle adapté à la géométries des sous-canaux. En introduisant toutes les interactions possibles avec les sous canaux voisins, les équations utilisée dans le code de sous-canaux COBRA-IV sont alors établies. Pour faire cette dérivation, un certain nombre d'hypothèses simplificatrices ont été utilisées. Les implications physiques qui découlent de ces hypothèses sont analysées en détails. Ensuite, le schéma numérique servant à solutionner cette série d'équations est développé à partir de deux approches: implicite ou explicite. Les interactions naturelles entre deux sous canaux peuvent être modélisées par les équation constitutive à partir de deux approches: l'égalité des échanges de masse, et l'égalité des échanges de volume. Le code de sous-canaux interconnectés COBRA-IV utilise un modèle basé sur l'égalité des échanges de masse entre deux sous canaux voisin. Dans ce modèle, les phénomènes de mélanges naturels sont modélisés en utilisant un simple coefficient de mélange, appelé (β). Le succès du code de sous canaux interconnectés COBRA-IV, dépend en partie de la précision avec laquelle ce coefficient est déterminé.

c) Approche expérimentale

Pour l'étude expérimentale, une section de test représentant deux sous canaux interconnectés dans une grappe de combustible et une boucle air-eau adiabatique est utilisée. Le comportement hydraulique de deux sous canaux latéralement interconnectés est alors étudié expérimentalement lorsque les débits de liquide à l'entrée de chaque sous canal sont, soit égaux, soit essentiellement différents. La mise en oeuvre de l'installation et son instrumentation restent donc relativement simples et permettent d'obtenir une information abondante et précise sur les caractéristiques des écoulements. Le choix de ces fluides de travail (eau-air) est adéquat lorsqu'on s'intéresse au comportement purement hydrodynamique et en particulier aux mécanismes d'échanges entre sous-canaux voisins, ceci explique son utilisation par de nombreux laboratoires. L'ensemble des expériences de cette étude a été réalisé en deux étapes distinctes. La première étape comporte uniquement des expériences avec un seul sous-canal. Cette étape a permis la calibration des électrodes de mesure du taux de vide ainsi que la détermination de lois caractéristiques des écoulements diphasiques en géométrie de sous-canal vertical telles que les pertes de pression par frottement ou la loi de dépendances du titre volumique en fonction du taux de vide. Les informations ainsi obtenues sont essentielles pour les expériences avec deux sous-canaux ainsi que pour les simulations par un code de calcul tel COBRA-IV. Dans la seconde partie expérimentale, des expériences sur deux sous-canaux interconnectés sont effectuées pour des débits de liquide à l'entrée de chaque sous canal qui sont, soit égaux, soit essentiellement différents. L'ensemble des mesures effectuées dans les expériences à deux sous-canaux interconnectés a permis de déterminer pour l'ensemble de la section instrumentée, la variation des grandeurs suivantes le long de l'interconnexion:

- la distribution axiale de taux de vide (en utilisant la méthode de conductivité), et

- la perte de pression le long de la région interconnectée (en utilisant des capteurs de pression).

Les données obtenues à partir des expériences ont été utilisées pour évaluer les performances du code COBRA-IV. Une analyse de sensibilité a été effectuée pour déterminer l'effet du coefficient de mélange (β) sur les prédictions du code. La valeur optimale de β a été déterminée pour chacune des expériences.

III. Résultats et Analyses

a) Flux massiques égaux a l'entrée

Les figures 5.4 à 5.57 montrent les pertes de pression, les variation du taux de vide et les transferts de débit de liquide entre les sous-canaux pour des débits liquides égaux à l'entrée du sous-canal A et B. Les taux de vide à l'entrée des sous-canaux sont différents ou sont égaux. On peut observer que les prédictions du taux de vide des canaux receveurs suivent assez bien les donnés expérimentales. Pour les canaux receveurs, on observe qu'à partir du début de l'interconnexion, la prédiction du taux de vide suit très bien les tendances des données expérimentales. Cependant, il faut noter que le modèle utilisé par COBRA-IV n'arrive pas à suivre l'augmentation du taux de vide observée expérimentalement dans la région proche de la fin de l'interconnexion. Ce phénomène observé expérimentalement, peut être expliqué par l'effet de la dilation de l'air. Lorsque les débits de liquides entre sous canaux sont égaux, au tout début de l'interconnections, les mécanismes dominants de mélanges entre les sous-canaux sont l'écoulement latéral forcée et le mélange turbulent du vide. Le mécanisme de l'écoulement latéral forcé est causé par la différence de pression imposée par les conditions à l'entrées des sous-canaux telles que montré aux figures 5.4 à 5.57. Ce mécanisme est très présent au

tout début de l'interconnexion, ce qui explique l'augmentation rapide du taux de vide dans le canal receveur. Au fur et à mesure qu'on s'éloigne de l'interconnexion ce mécanisme s'attenu, vue que la différence de pression entre les deux sous-canaux décroît rapidement. D'autre part, le mécanisme de mélange turbulent du vide continue à s'imposer comme mécanisme dominant qui gouverne le transfert grâce à la présence d'un mélange naturel de vide entre les sous-canaux. Dans cette région, les prédictions de code COBRA-IV sont satisfaisantes mais il manque un peu de précision. Les valeur suggérées pour le coefficient de mélange sont données dans les tableaux 5.4 et 5.7 .

b) Flux massiques non-égaux à l'entrée

Les figures 5.58 à 5.129 montrent les pertes de pression, les distributions axiales du taux de vide ainsi que les débits de liquide le long des sous-canaux. On peut observer que les prédictions de l'écoulement dans le canal donneur suivent assez bien les tendances des donnés expérimentales. Il faut noter que le modèle n'arrive pas à suivre la diminution puis l'augmentation observées expérimentalement pour les taux vide élevés. Une attention particulière devrait être allouée aux cas de ce genre afin d'améliorer les prédictions. Pour le canal receveur, on remarque que les prédictions suivent assez bien les tendances des données expérimentales. Dans ces cas, les mécanismes dominants au début de l'interconnections sont l'écoulement latéral forcé et le mélange turbulent de vide. Le mécanismes de l'écoulement latéral forcé semble être plus intense dans ce cas que lorsque les débits de liquides sont égaux. Ceci s'explique par l'existence d'une forte différence de pression entre les deux sous-canaux due à la différence de flux massiques imposés à l'entrée des sous canaux. Par conséquent, au début de l'interconnexion un échange important s'établit du canal au taux de vide élevé vers le canal au taux de vide faible. Ceci est bien reflété par l'augmentation très rapide du taux de vide dans le canal

receveur au début de l'interconnections. Par la suite, l'écoulement sera gouverné essentiellement par le mélange turbulent du vide. Pour ces cas, les valeur suggérées de β sont disponible dans les tableaux 5.5 et 5.6. Cependant les corrélations des valeurs optimales de β avec les conditions moyennes d'entrée (flux massique, taux de vide et titre) sont impossibles.

c) Les sous-canaux partiellement obstrués

Les prédictions de COBRA-IV sont comparées avec les données obtenues pour deux sous canaux latéralement interconnectés dont l'un d'eux est partiellement obstrué. Les données expérimentales sélectionnées incluent des obstructions abruptes ou graduelles allant jusqu'à une obstruction de 60% de la section de passage pour des écoulements monophasiques et diphasiques. Une analyse de sensibilité est réalisée pour les paramètres clefs utilisés par COBRA-IV, i.e., le facteur de résistance à l'écoulement latéral (K_{ij}), le coefficient de pertes de pression irréversible (k) et le coefficient du mélange (β). On observe que la valeur du facteur de résistance à l'écoulement latéral (K_{ij}) n'a pratiquement aucun effet sur les prédictions du code, cependant, dans certains cas, la convergence de la procédure numérique dépend essentiellement de ce paramètre. Les résultats de l'analyse de sensibilité montrent aussi que les valeurs expérimentales du coefficient de pertes de pression irréversible (k) peuvent être adéquatement utilisées dans COBRA-IV. De plus, il a été observé que les prédictions de pertes de pression totale et de débits de liquides sont fortement affectées par une variation de ce paramètre. L'analyse de sensibilité a permis de suggérer les valeurs optimales pour le coefficient de mélange (β) et d'observer que ce paramètre affecte les prédictions de COBRA-IV pour les taux de vide et les débits de liquide. Finalement les comparaisons des prédictions de COBRA-IV avec des données expérimentales confirment que celui-ci

est capable de simuler des écoulements monophasiques et diphasiques dont la section de passage est obstruée jusqu' a 60%. Cependant les prédictions par le code du débit de liquide quand 60% de la section de passage est obstrué de manière abrupte ne sont pas satisfaisantes. En plus, l'expérience d'utilisation et la comparaison des prédictions du code COBRA-IV avec les mesures expérimentales a permis de tirer les conclusion importantes résumées ci-dessous.

- Le modèle implanté dans COBRA-IV est un outil bien adapté pour les simulation des expériences, qui incluent des obstructions abruptes ou graduelle allant jusqu'à une obstruction de 60% de la section de passage pour des écoulements monophasiques et diphasiques.
- L'utilisation dans COBRA-IV de corrélations déduites des expériences de calibration a démontré l'utilité des efforts à porter sur l'établissement de bonnes corrélations afin d'améliorer les prédictions du code.
- Les difficultés observées dans les prédictions apparaissent surtout dans le voisinage de l'obstruction. Ces difficultés sont attribuées aux faiblesses de l'approche monodimensionnelle appliquée à des phénomènes tridimensionnels.
- La modélisation d'une obstruction abrupte nécessite de grandes précaution. L'utilisation d'une section de passage réduite n'est ici qu'un artifice à la disposition de l'utilisateur pour reproduire les effets réversibles d'accélération sur le fluide. Ceci peut être utilisé au même titre que la perte de charge singulière qui représente les effets irréversibles associés à l'obstruction.
- Une étude complémentaire peut être envisagée afin d'identifier l'influence possible de la présence d'une obstruction sur les convergence de schéma implicite utilisée par COBRA-IV.

TABLE OF CONTENTS

DEDICATION ..... **iv**

ACKNOWLEDGMENTS ..... **v**

RÉSUMÉ ..... **vi**

ABSTRACT ..... **ix**

CONDENSÉ EN FRANÇAIS ..... **xii**

TABLE OF CONTENTS ..... **xx**

LIST OF FIGURES ..... **xxiv**

LIST OF TABLES ..... **xxxvi**

NOMENCLATURE ..... **xxxvii**

1 INTRODUCTION **1**

1.1 Purpose and Organization of Present Work 3

2 LITURATURE SURVEY **6**

2.1 Models and Methods for Two-Phase Flow 6

2.2 The Subchannel Method 9

2.2.1 Basic Definitions and Methods 9

2.2.2 Intersubchannel Mixing Mechanisms 12

2.2.3 Development of mixing models 14

2.2.4 Solution Techniques : Numerical Methods 18

3 COBRA-IV: MODEL AND METHOD 20

3.1 General Balance Equations 20

3.2 Subchannel Equations 25

3.2.1 Subchannel Mass Balance Equation 26

3.2.2 Subchannel Energy Balance equation 27

3.2.3 Subchannel Axial Momentum Balance Equation 30

3.2.4 Subchannel Lateral momentum Balance Equation 31

3.3 Numerical Solution 34

3.3.1 Numerical schemes 38

3.3.2 Implicit Solution 39

3.3.3 Explicit Solution 44

3.4 Constitutive Equations 48

3.4.1 Turbulent Mixing Modeling 48

4 EXPERIMENTAL APPARATUS AND PROCEDURES 56

4.1 Experimental Apparatus 56

4.2 Instrumentation 58

4.2.1 Liquid and Gas Flow Rates 58

4.2.2 Void Fraction Measurement 58

4.2.3 Pressures 61

4.2.4 Liquid Mass Exchange Between Subchannels 62

4.3 Data Acquisition System 63

4.4 Experimental Procedures 64

4.4.1 Single Subchannel Calibration Experiments 64

4.4.1.1 Calibration of the impedance void Gauges 65

4.4.1.2 Frictional Pressure Losses 66

4.4.1.3 Volumetric Flow Quality and Flux of the Gas, and Dryness Fraction 68

4.4.2 Interconnected Subchannels 69

4.4.2.1 Void Fraction 69

4.4.2.2 Liquid Phase Mass Exchange 72

4.4.2.3 Net Gas Mass Transfer 75

5 COMPARSION OF MEASURED AND PREDICTED RESULTS-NO BLOCKAGE CASES 104

5.1 Constitutive Equations and Input Data for COBRA-IV 104

5.1.1 Constitutive Equations 105

5.1.2 Configuration of the Input Data 107

5.2 Results of the Comparison 109

5.2.1 Equal inlet mass Fluxes 110

5.2.2 Unequal Inlet mass Fluxes 112

5.3 General Conclusions 115

5.3.1 Equal Inlet Mass Fluxes 116

5.3.2 Unequal Inlet Mass Fluxes 116

6 COMPARISON OF MEASURED AND PREDICTED RESULTS-BLOCKAGE CASES 189

6.1 Basic Definitions and Considerations 190

6.2 Basic relations 191

6.3 Comparison of COBRA-IV Predictions with the Experimental Results 193

6.3.1 Input Data Configuration 193

6.3.2 Comparison of COBRA Predictions with Single-Phase Data 195

6.3.3 Conclusions for Single-Phase Flow Cases 198

6.3.4 Comparison of COBRA Predictions With Two-Phase Flow Data 198

6.3.5 Conclusions for Two-Phase Flow Cases 206

7 CONCLUSIONS AND RECOMMENDATIONS 256

BIBLIOGRAPHY 262

LIST OF FIGURES

Figure 3.1 Relation of Subchannel Control Volume to Reactor Core 51

Figure 3.2 Subchannel Control Volume 52

Figure 3.3 Rod and Wall Surface Heat Transfer Geometry 53

Figure 3.4 Lateral Heat Conduction Geometry 53

Figure 3.5 Control Volume for Lateral Momentum 54

Figure 3.6 Placement of the Variables for Implicit Solution 55

Figure 3.7 Placement of Major Variables on the Computation Mesh 55

Figure 4.1 Two-Phase Flow Experimental Apparatus 78

Figure 4.2 Cross-Sectional View of the Test Section 79

Figure 4.3 Air-Water Mixer 80

Figure 4.4 Impedence Gauge 81

Figure 4.5 Location of the Void Gauges and Pressure Taps 82

Figure 4.6 Block Diagram of the Void Fraction Measurment System 83

Figure 4.7 Electronic Circuit Associated with the Void Gauges 84

Figure 4.8 Gas Phase Separation Pots. 85

Figure 4.9 Typical Calibration Curve of a Void Gauge 86

Figure 4.10 Typical Calibration Curve of Void Fraction 87

Figure 4.11 Set-up for Frictional Pressure Loss 88

Figure 4.12 Variation of the Two-Phase Multiplier, Φ_L^2, with void fraction, Channel A 89

Figure 4.13 Variation of the Two-Phase Multiplier, Φ_L^2, with Void Fraction, Channel B 90

Figure 4.14 Relationship between Volumetric Flow Quality and Void Fraction Channel A 91

Figure 4.15 Relationship between Volumetric Flow Quality and Void Fraction Channel B 92

Figure 4.16 Relationship between Volumetric Flux of the Gas and Void Fraction, Channel A ... 93

Figure 4.17 Relationship between Volumetric Flux of the Gas and Void Fraction, Channel B ... 94

Figure 4.18 Relationship between the Void Fraction and theDryness Fraction, Channel A 95

Figure 4.19 Relationship between the Void Fraction and theDryness Fraction, Channel B 96

Figure 4.20 Relationship between the Volumetric flux of liquid and void Fraction, Channel A .. 97

Figure 4.21 Relationship between the Volumetric flux of liquid and void Fraction, Channel B .. 98

Figure 4.22 Void Fraction Correction Curve, 1000 kg/m²s 99

Figure 4.23 Void Fraction Correction Curve, 2000 kg/m²s 100

Figure 4.24 Void Fraction Correction Curve, 2500 kg/m²s 101

Figure 4.25 Void Fraction Correction Curve, 3000 kg/m²s 102

Figure 4.26 Mass Conservation Liquid and Tracer 103

Figure 5.1 Friction factor vs. Reynolds number valid for both channel A, B 123

Figure 5.2 Two-phase Multiplier vs. Dryness Fraction Valid for both channel 124

Figure 5.3 Void Fraction vs. Dryness Fraction Valid for both channel 125

Figure 5.4 Total Pressure Drop Profile, Run SV94-01, Channel A 126

Figure 5.5 Total Pressure Drop Profile, Run SV94-01, Channel B 126

Figure 5.6 Void Fraction Profile, Run SV94-01, Channel A 127

Figure 5.7 Void Fraction Profile, Run SV94-01, Channel B 127

Figure 5.8 Mass Flow Rate Profile, Run SV94-01, Channel A 128

Figure 5.9 Mass Flow Rate Profile, Run SV94-01, Channel B 128

Figure 5.10 Total Pressure Drop Profile, Run SV94-03, Channel A 129

Figure 5.11 Total Pressure Drop Profile, Run SV94-03, Channel B 129

Figure 5.12 Void Fraction Profile, Run SV94-03, Channel A 130

Figure 5.13 Void Fraction Profile, Run SV94-03, Channel B 130

Figure 5.14 Mass Flow Rate Profile, Run SV94-03, Channel A 131

Figure 5.15 Mass Flow Rate Profile, Run SV94-03, Channel B 131

Figure 5.16 Total Pressure Drop Profile, Run SV94-18, Channel A 132

Figure 5.17 Total Pressure Drop Profile, Run SV94-18, Channel B 132

Figure 5.18 Void Fraction Profile, Run SV94-18, Channel A 133

Figure 5.19 Void Fraction Profile, Run SV94-18, Channel B 133

Figure 5.20 Mass Flow Rate Profile, Run SV94-18, Channel A 134

Figure 5.21 Mass Flow Rate Profile, Run SV94-18, Channel B 134

Figure 5.22 Total Pressure Drop Profile, Run SV94-20, Channel A 135

Figure 5.23 Total Pressure Drop Profile, Run SV94-20, Channel B 135

Figure 5.24 Void Fraction Profile, Run SV94-20, Channel A 136

Figure 5.25 Void Fraction Profile, Run SV94-20, Channel B 136

Figure 5.26 Mass Flow Rate Profile, Run SV94-20, Channel A 137

Figure 5.27 Mass Flow Rate Profile, Run SV94-20, Channel B 137

Figure 5.28 Total Pressure Drop Profile, Run SV94-02, Channel A 138

Figure 5.29 Total Pressure Drop Profile, Run SV94-02, Channel B 138

Figure 5.30 Void Fraction Profile, Run SV94-02, Channel A 139

Figure 5.31 Void Fraction Profile, Run SV94-02, Channel B 139

Figure 5.32 Mass Flow Rate Profile, Run SV94-02, Channel A 140

Figure 5.33 Mass Flow Rate Profile, Run SV94-02, Channel B 140

Figure 5.34 Total Pressure Drop Profile, Run SV94-04, Channel A 141

Figure 5.35 Total Pressure Drop Profile, Run SV94-04, Channel B 141

Figure 5.36 Void Fraction Profile, Run SV94-04, Channel A 142

Figure 5.37 Void Fraction Profile, Run SV94-04, Channel B 142

Figure 5.38 Mass Flow Rate Profile, Run SV94-04, Channel A 143

Figure 5.39 Mass Flow Rate Profile, Run SV94-04, Channel B 143

Figure 5.40 Total Pressure Drop Profile, Run SV94-19, Channel A 144

Figure 5.41 Total Pressure Drop Profile, Run SV94-19, Channel B 144

Figure 5.42 Void Fraction Profile, Run SV94-19, Channel A 145

Figure 5.43 Void Fraction Profile, Run SV94-19, Channel B 145

Figure 5.44 Mass Flow Rate Profile, Run SV94-19, Channel A 146

Figure 5.45 Mass Flow Rate Profile, Run SV94-19, Channel B 146

Figure 5.46 Total Pressure Drop Profile, Run SV94-21, Channel A 147

Figure 5.47 Total Pressure Drop Profile, Run SV94-21, Channel B 147

Figure 5.48 Void Fraction Profile, Run SV94-21, Channel A 148

Figure 5.49 Void Fraction Profile, Run SV94-21, Channel B 148

Figure 5.50 Mass Flow Rate Profile, Run SV94-21, Channel A 149

Figure 5.51 Mass Flow Rate Profile, Run SV94-21, Channel B 149

Figure 5.52 Total Pressure Drop Profile, Run SV94-05, Channel A 150

Figure 5.53 Total Pressure Drop Profile, Run SV94-05, Channel B 150

Figure 5.54 Void Fraction Profile, Run SV94-05, Channel A 151

Figure 5.55 Void Fraction Profile, Run SV94-05, Channel B 151

Figure 5.56 Mass Flow Rate Profile, Run SV94-05, Channel A 152

Figure 5.57 Mass Flow Rate Profile, Run SV94-05, Channel B 152

Figure 5.58 Total Pressure Drop Profile, Run SV94-06, Channel A 153

Figure 5.59 Total Pressure Drop Profile, Run SV94-06, Channel B 153

Figure 5.60 Void Fraction Profile, Run SV94-06, Channel A 154

Figure 5.61 Void Fraction Profile, Run SV94-06, Channel B 154

Figure 5.62 Mass Flow Rate Profile, Run SV94-06, Channel A 155

Figure 5.63 Mass Flow Rate Profile, Run SV94-06, Channel B 155

Figure 5.64 Total Pressure Drop Profile, Run SV94-08, Channel A 156

Figure 5.65 Total Pressure Drop Profile, Run SV94-08, Channel B 156

Figure 5.66 Void Fraction Profile, Run SV94-08, Channel A 157

Figure 5.67 Void Fraction Profile, Run SV94-08, Channel B 157

Figure 5.68 Mass Flow Rate Profile, Run SV94-08, Channel A 158

Figure 5.69 Mass Flow Rate Profile, Run SV94-08, Channel B 158

Figure 5.70 Total Pressure Drop Profile, Run SV94-07, Channel A 159

Figure 5.71 Total Pressure Drop Profile, Run SV94-07, Channel B 159

Figure 5.72 Void Fraction Profile, Run SV94-07, Channel A 160

Figure 5.73 Void Fraction Profile, Run SV94-07, Channel B 160

Figure 5.74 Mass Flow Rate Profile, Run SV94-07, Channel A 161

Figure 5.75 Mass Flow Rate Profile, Run SV94-07, Channel B 161

Figure 5.76 Total Pressure Drop Profile, Run SV94-09, Channel A 162

Figure 5.77 Total Pressure Drop Profile, Run SV94-09, Channel B 162

Figure 5.78 Void Fraction Profile, Run SV94-09, Channel A 163

Figure 5.79 Void Fraction Profile, Run SV94-09, Channel B 163

Figure 5.80 Mass Flow Rate Profile, Run SV94-09, Channel A 164

Figure 5.81 Mass Flow Rate Profile, Run SV94-09, Channel B 164

Figure 5.82 Total Pressure Drop Profile, Run SV94-10, Channel A 165

Figure 5.83 Total Pressure Drop Profile, Run SV94-10, Channel B 165

Figure 5.84 Void Fraction Profile, Run SV94-10, Channel A 166

Figure 5.85 Void Fraction Profile, Run SV94-10, Channel B 166

Figure 5.86 Mass Flow Rate Profile, Run SV94-10, Channel A 167

Figure 5.87 Mass Flow Rate Profile, Run SV94-10, Channel B 167

Figure 5.88 Total Pressure Drop Profile, Run SV94-11, Channel A 168

Figure 5.89 Total Pressure Drop Profile, Run SV94-11, Channel B 168

Figure 5.90 Void Fraction Profile, Run SV94-11, Channel A 169

Figure 5.91 Void Fraction Profile, Run SV94-11, Channel B 169

Figure 5.92 Mass Flow Rate Profile, Run SV94-11, Channel A 170

Figure 5.93 Mass Flow Rate Profile, Run SV94-11, Channel B 170

Figure 5.94 Total Pressure Drop Profile, Run SV94-12, Channel A 171

Figure 5.95 Total Pressure Drop Profile, Run SV94-12, Channel B 171

Figure 5.96 Void Fraction Profile, Run SV94-12, Channel A 172

Figure 5.97 Void Fraction Profile, Run SV94-12, Channel B 172

Figure 5.98 Mass Flow Rate Profile, Run SV94-12, Channel A 173

Figure 5.99 Mass Flow Rate Profile, Run SV94-12, Channel B 173

Figure 5.100 Total Pressure Drop Profile, Run SV94-14, Channel A 174

Figure 5.101 Total Pressure Drop Profile, Run SV94-14, Channel B 174

Figure 5.102 Void Fraction Profile, Run SV94-14, Channel A 175

Figure 5.103 Void Fraction Profile, Run SV94-14, Channel B 175

Figure 5.104 Mass Flow Rate Profile, Run SV94-14, Channel A 176

Figure 5.105 Mass Flow Rate Profile, Run SV94-14, Channel B 176

Figure 5.106 Total Pressure Drop Profile, Run SV94-13, Channel A 177

Figure 5.107 Total Pressure Drop Profile, Run SV94-13, Channel B 177

Figure 5.108 Void Fraction Profile, Run SV94-13, Channel A 178

Figure 5.109 Void Fraction Profile, Run SV94-13, Channel B 178

Figure 5.110 Mass Flow Rate Profile, Run SV94-13, Channel A 179

Figure 5.111 Mass Flow Rate Profile, Run SV94-13, Channel B 179

Figure 5.112 Total Pressure Drop Profile, Run SV94-15, Channel A 180

Figure 5.113 Total Pressure Drop Profile, Run SV94-15, Channel B 180

Figure 5.114 Void Fraction Profile, Run SV94-15, Channel A 181

Figure 5.115 Void Fraction Profile, Run SV94-15, Channel B 181

Figure 5.116 Mass Flow Rate Profile, Run SV94-15, Channel A 182

Figure 5.117 Mass Flow Rate Profile, Run SV94-15, Channel B 182

Figure 5.118 Total Pressure Drop Profile, Run SV94-16, Channel A 183

Figure 5.119 Total Pressure Drop Profile, Run SV94-16, Channel B 183

Figure 5.120 Void Fraction Profile, Run SV94-16, Channel A 184

Figure 5.121 Void Fraction Profile, Run SV94-16, Channel B 184

Figure 5.122 Mass Flow Rate Profile, Run SV94-16, Channel A 185

Figure 5.123 Mass Flow Rate Profile, Run SV94-16, Channel B 185

Figure 5.124 Total Pressure Drop Profile, Run SV94-17, Channel A 186

Figure 5.125 Total Pressure Drop Profile, Run SV94-17, Channel B 186

Figure 5.126 Void Fraction Profile, Run SV94-17, Channel A 187

Figure 5.127 Void Fraction Profile, Run SV94-17, Channel B 187

Figure 5.128 Mass Flow Rate Profile, Run SV94-17, Channel A 188

Figure 5.129 Mass Flow Rate Profile, Run SV94-17, Channel B 188

Figure 6-1 Simulation of a Plate Blockage 211

Figure 6-2 Simulation of a Smooth Blockage 212

Figure 6.3 Pressure Drop profile, Single-Phase, Blocked Channel, RUN #08 213

Figure 6.4 Pressure Drop profile, Single-Phase, Unblocked Channel, RUN #08 213

Figure 6.5 Liquid Flow Rate Profile, Single-Phase, Blocked Channel, RUN #08 214

Figure 6.6 Liquid Flow Rate Profile, Single-Phase, Unblocked Channel, RUN #08 214

Figure 6.7 Pressure Drop profile, Single-Phase, Blocked Channel, RUN #10 215

Figure 6.8 Pressure Drop profile, Single-Phase, Unblocked Channel, RUN #10 215

Figure 6.9 Liquid Flow Rate Profile, Single-Phase, Blocked Channel, RUN #10 216

Figure 6.10 Liquid Flow Rate Profile, Single-Phase, Unblocked Channel, RUN #10 216

Figure 6.11 Pressure Drop profile, Single-Phase, Blocked Channel, RUN #11 217

Figure 6.12 Pressure Drop profile, Single-Phase, Unblocked Channel, RUN #11 217

Figure 6.13 Liquid Flow Rate Profile, Single-Phase, Blocked Channel, RUN #11 218

Figure 6.14 Liquid Flow Rate Profile, Single-Phase, Unblocked Channel, RUN #11 218

Figure 6.15 Pressure Drop profile, Single-Phase, Blocked Channel, RUN #18 219

Figure 6.16 Pressure Drop profile, Single-Phase, Unblocked Channel, RUN #18 219

Figure 6.17 Liquid Flow Rate Profile, Single-Phase, Blocked Channel, RUN #18 220

Figure 6.18 Liquid Flow Rate Profile, Single-Phase, Unblocked Channel, RUN #18 220

Figure 6.19 Pressure Drop profile, Single-Phase, Blocked Channel, RUN #19 221

Figure 6.20 Pressure Drop profile, Single-Phase, Unblocked Channel, RUN #19 221

Figure 6.21 Liquid Flow Rate Profile, Single-Phase, Blocked Channel, RUN #19 222

Figure 6.22 Liquid Flow Rate Profile, Single-Phase, Unblocked Channel, RUN #19 222

Figure 6.23 Pressure Drop profile, Two-Phase Case, Blocked Channel, RUN #01 223

Figure 6.24 Pressure Drop profile, Two-Phase Case, Unblocked Channel, RUN #01 223

Figure 6.25 Void Fraction profile, Two-Phase Case, Blocked Channel, RUN #01 224

Figure 6.26 Void Fraction profile, Two-Phase Case, Unblocked Channel, RUN #01 224

Figure 6.27 Liquid Flow Rate, Two-phase Case, Blocked Channel, RUN #01 225

Figure 6.28 Liquid Flow Rate, Two-Phase Case, Unblocked Channel, RUN #01 225

Figure 6.29 Pressure Drop profile, Two-Phase Case, Blocked Channel, RUN #04 226

Figure 6.30 Pressure Drop profile, Two-Phase Case, Unblocked Channel, RUN #04 226

Figure 6.31 Void Fraction profile, Two-Phase Case, Blocked Channel, RUN #04 227

Figure 6.32 Void Fraction profile, Two-Phase Case, Unblocked Channel, RUN #04 227

Figure 6.33 Liquid Flow Rate, Two-phase Case, Blocked Channel, RUN #04 228

Figure 6.34 Liquid Flow Rate, Two-Phase Case, Unblocked Channel, RUN #04 228

Figure 6.35 Pressure Drop profile, Two-Phase Case, Blocked Channel, RUN #10 229

Figure 6.36 Pressure Drop profile, Two-Phase Case, Unblocked Channel, RUN #10 229

Figure 6.37 Void Fraction profile, Two-Phase Case, Blocked Channel, RUN #10 230

Figure 6.38 Void Fraction profile, Two-Phase Case, Unblocked Channel, RUN #10 230

Figure 6.39 Liquid Flow Rate, Two-phase Case, Blocked Channel, RUN #10 231

Figure 6.40 Liquid Flow Rate, Two-Phase Case, Unblocked Channel, RUN #10 231

Figure 6.41 Pressure Drop profile, Two-Phase Case, Blocked Channel, RUN #13 232

Figure 6.42 Pressure Drop profile, Two-Phase Case, Unblocked Channel, RUN #13 232

Figure 6.43 Void Fraction profile, Two-Phase Case, Blocked Channel, RUN #13 233

Figure 6.44 Void Fraction profile, Two-Phase Case, Unblocked Channel, RUN #13 233

Figure 6.45 Liquid Flow Rate, Two-phase Case, Blocked Channel, RUN #13 234

Figure 6.46 Liquid Flow Rate, Two-Phase Case, Unblocked Channel, RUN #13 234

Figure 6.47 Pressure Drop profile, Two-Phase Case, Blocked Channel, RUN #02 235

Figure 6.48 Pressure Drop profile, Two-Phase Case, Unblocked Channel, RUN #02 235

Figure 6.49 Void Fraction profile, Two-Phase Case, Blocked Channel, RUN #02 236

Figure 6.50 Void Fraction profile, Two-Phase Case, Unblocked Channel, RUN #02 236

Figure 6.51 Liquid Flow Rate, Two-phase Case, Blocked Channel, RUN #02 237

Figure 6.52 Liquid Flow Rate, Two-Phase Case, Unblocked Channel, RUN #02 237

Figure 6.53 Pressure Drop profile, Two-Phase Case, Blocked Channel, RUN #02 238

Figure 6.54 Pressure Drop profile, Two-Phase Case, Unblocked Channel, RUN #02 238

Figure 6.55 Void Fraction profile, Two-Phase Case, Blocked Channel, RUN #02 239

Figure 6.56 Void Fraction profile, Two-Phase Case, Unblocked Channel, RUN #02 239

Figure 6.57 Liquid Flow Rate, Two-phase Case, Blocked Channel, RUN #02 240

Figure 6.58 Liquid Flow Rate, Two-Phase Case, Unblocked Channel, RUN #02 240

Figure 6.59 Pressure Drop profile, Two-Phase Case, Blocked Channel, RUN #05 241

Figure 6.60 Pressure Drop profile, Two-Phase Case, Unblocked Channel, RUN #05 241

Figure 6.61 Void Fraction profile, Two-Phase Case, Blocked Channel, RUN #05 242

Figure 6.62 Void Fraction profile, Two-Phase Case, Unblocked Channel, RUN #05 242

Figure 6.63 Liquid Flow Rate, Two-phase Case, Blocked Channel, RUN #05 243

Figure 6.64 Liquid Flow Rate, Two-Phase Case, Unblocked Channel, RUN #05 243

Figure 6.65 Pressure Drop profile, Two-Phase Case, Blocked Channel, RUN #11 244

Figure 6.66 Pressure Drop profile, Two-Phase Case, Unblocked Channel, RUN #11 244

Figure 6.67 Void Fraction profile, Two-Phase Case, Blocked Channel, RUN #11 245

Figure 6.68 Void Fraction profile, Two-Phase Case, Unblocked Channel, RUN #11 245

Figure 6.69 Liquid Flow Rate, Two-phase Case, Blocked Channel, RUN #11 246

Figure 6.70 Liquid Flow Rate, Two-Phase Case, Unblocked Channel, RUN #11 246

Figure 6.71 Pressure Drop profile, Two-Phase Case, Blocked Channel, RUN #03 247

Figure 6.72 Pressure Drop profile, Two-Phase Case, Unblocked Channel, RUN #03 247

Figure 6.73 Void Fraction profile, Two-Phase Case, Blocked Channel, RUN #03 248

Figure 6.74 Void Fraction profile, Two-Phase Case, Unblocked Channel, RUN #03 248

Figure 6.75 Liquid Flow Rate, Two-phase Case, Blocked Channel, RUN #03 249

Figure 6.76 Liquid Flow Rate, Two-Phase Case, Unblocked Channel, RUN #03 249

Figure 6.77 Pressure Drop profile, Two-Phase Case, Blocked Channel, RUN #06 250

Figure 6.78 Pressure Drop profile, Two-Phase Case, Unblocked Channel, RUN #06 250

Figure 6.79 Void Fraction profile, Two-Phase Case, Blocked Channel, RUN #06 251

Figure 6.80 Void Fraction profile, Two-Phase Case, Unblocked Channel, RUN #06 251

Figure 6.81 Liquid Flow Rate, Two-phase Case, Blocked Channel, RUN #06 252

Figure 6.82 Liquid Flow Rate, Two-Phase Case, Unblocked Channel, RUN #06 252

Figure 6.83 Pressure Drop profile, Two-Phase Case, Blocked Channel, RUN #12 253

Figure 6.84 Pressure Drop profile, Two-Phase Case, Unblocked Channel, RUN #12 253

Figure 6.85 Void Fraction profile, Two-Phase Case, Blocked Channel, RUN #12 254

Figure 6.86 Void Fraction profile, Two-Phase Case, Unblocked Channel, RUN #12 254

Figure 6.87 Liquid Flow Rate, Two-phase Case, Blocked Channel, RUN #12 255

Figure 6.88 Liquid Flow Rate, Two-Phase Case, Unblocked Channel, RUN #12 255

LIST OF TABLES

Table 4.1 Geometric Parameters of the Test Section 57

Table 4.2 Location of the Pressure Taps During the Calibration and Experiments 61

Table 4.3 Configuration of Data Accquisition System 64

Table 5.1 Inlet Flow Conditions Used for the Experiments 118

Table 5.2 Pseudo-property Table for Air-Water Mixture 119

Table 5.3 General Results Obtained for the Experiments SV94-01 to SV94-21 120

Table 5.4 Result Obtained for the Case with G_A=G_B=3000 (kg/m^2s) 121

Table 5.5 Result Obtained for the Case with G_A=3000 and G_B=1000 (kg/m^2s) 121

Table 5.6 Result Obtained for the Case with G_A=3000 and G_B=2000 (kg/m^2s) 122

Table 5.7 Result Obtained for the Case with G_A= G_B=2000 and G_A=G_B=1000 (kg/m^2s) 122

Table 6.1 Inlet Flow Conditions for Single-Phase flow Experiments 208

Table 6.2 Summary of the Comparsion of the code predictions with Experimental Data (Single-Phase) 208

Table 6.3 Inlet Flow Conditions for Two-Phase Flow Experiments 209

Table 6.4 Summary of the Comparsion of the code predictions with Experimental Data (Two-Phase) 136

NOMENCLATURE

A	Flow area	$[m^2]$
c	Correction factor	[-]
$C_{i,j}$	Cross sectional average concentration	$[kg/l]$
C_o	Void distribution parameter	[-]
C_s	Coupling factor for transverse momentum	[-]
C_T	Correction factor for turbulent transport of momentum	[-]
D_h	Hydraulic diameter	$[m]$
$[D_c]$	Channel-to-channel connection matrix	[-]
$[D_c]^T$	Transpose of the channel-to-channel connection matrix	[-]
$[D_r]$	Rod-to-channel connection matrix	[-]
$[D_w]$	Wall-to-channel connection matrix	[-]
$\vec{f}$	Body forces	$[N]$
f', f	Friction factor	[-]
F_D	Axial drag force	$[N]$
F_m	Turbulent momentum mixing	$[Nm/s]$
F_p	Total force due to pressure	$[N]$
g	Gravitational field constant	$[m/s^2]$
G	Mass flux	$[kg/m^2s]$
G'	Transverse mass flux	$[kg/m^2s]$
G_s	Transverse momentum convected by transverse flow	$[Nm/s]$
h	Enthalpy	$[J/kg]$
h'	Enthalpy transferred by cross-flow	$[J/kg]$
h^*	Flowing enthalpy	$[J/kg]$

H	Surface heat transfer coefficient	$[J/m^2{}^oC]$
H_r	Heat transfer coefficient between fuel rod and flow	$[J/m^2{}^oC]$
H_w	Heat transfer coefficient between conducting wall and flow	$[J/m^2{}^oC]$
i	Internal thermal energy	$[J]$
$\tilde{I}$	Identity tensor	[-]
$\vec{j}$	Volumetric flux	$[m/s]$
j_g	Volumetric flux of the gas	$[m/s]$
k, K'_{TP}	Irreversible pressure drop factor	[-]
K_f	Fluid thermal conductivity	$[J/m^2{}^oC]$
K	Effective turbulent diffusion coefficient,	[-]
K_{ij}	Cross-flow resistance factor	[-]
l	Prandtl's mixing length (centroid-to-centroid)	$[m]$
L_w	Longitude of conducting wall	$[m]$
m	Axial mass flow rate	$[kg/s]$
$\vec{n}$	Unit vector	[-]
N	Binary factor for cross-flow direction	[-]
p	Pressure	$[N]$
p^*	Reference pressure	$[N/m^2]$
P_r	Total perimeter of the rod	$[m]$
Q_c	Lateral fluid heat conduction	$[J]$
Q_g	Gas flow rate	$[m^3/s]$
Q_r	Total heat input from fuel rods	$[J]$
Q_w	Total heat exchange with the walls	$[J]$
q'''	Internal heat rate	$[J/kg]$
$\vec{q}'$	Heat flux vector	$[J/m^2]$
Re	Reynolds number	[-]
s	Gap clearance	$[m]$

S	Source term	[-]
t	Time	$[s]$
T	Temperature	$[^oC]$
$\tilde{T}$	Shear surface tensor	$[N/m^2]$
$\vec{u}$	Flow velocity field	$[m/s]$
u'	Axial velocity transported by the turbulence cross-flow	$[m/s]$
u^*	Momentum velocity	$[m/s]$
v	Lateral velocity	$[m/s]$
v^*	Momentum specific volume	$[m^3/kg]$
V	Volume	$[m^3]$
V'	Volume of modified control volume	$[m^3]$
$\vec{V}_{gi}$	Drift velocity	$[m/s]$
$\vec{V}_r$	Relative velocity vector	$[m/s]$
W'	Fluctuating cross-flow per unit length	$[kg/ms]$
x	Coordinate axis	$[m]$
x^*	Flowing quality	[-]
z	Coordinate axis	$[m]$

α	Void fraction	[-]
β	Turbulent mixing factor	[-]
$\Delta p_{accelaration}$	Acceleration pressure drop	$[N/m^2]$
$\Delta p_{form,TP}$	Irreversible pressure loss	$[N/m^2]$
$\Delta p_{friction}$	Friction pressure loss	$[N/m^2]$
$\Delta p_{gravity}$	Gravity pressure loss	$[N/m^2]$
Δp_T	Total pressure drop	$[N/m^2]$
ε	Eddy diffusivity,	$[m^2/s]$

ε_n	Correction factor for the void fraction	[-]
ε_t	Thermal eddy diffusivity	$[m^2/s]$
θ	Subchannel axis orientation angle	$[rad]$
μ	Viscosity	$[Ns/m^2]$
ρ	Density	$[kg/m^3]$
ρ'	Momentum density	$[kg/m^3]$
ρ_H	Homogeneous two-phase density	$[kg/m^3]$
Φ_L^2	Two-phase flow multiplier	[-]
$\tilde{\Pi}$	Viscous stress tensor	$[N/m^2]$
Ψ	Function defining relationship between h and h^*	$[kg/m^3]$

SUBSCRIPTS

1, *l*	Refers to liquid phase	[-]
2, *g*	Refers to gas phase	[-]
D	Drag	[-]
EQ	Equilibrium	[-]
f	Refers to fluid part of the control volume	[-]
i	Refers to subchannel i	[-]
j	Refers to subchannel j	[-]
ij	Between subchannel i and j	[-]
MIX	Refers to turbulent mixing	[-]
s	Refers to gap clearance	[-]
TP	Two-phase	[-]
VD	Refers to void drift	[-]
w	Refers to solid wall part of the control volume	[-]

SUPERSCRIPTS

*	Refers to flowing quantities	[-]
n	Identify previous time step	[-]
′	Refers to cross-flow	[-]

SPECIAL NOTATION

∇	Gradient space	[-]
~	Identify actual time but previous iteration	[-]
<< >>	Average over volume	[-]
< >	Average over surface	[-]

CHAPTER 1

INTRODUCTION

The fuel assemblies employed in most of the nuclear reactors used in the power industry are in the form of rod bundles. Fluid flow and heat transfer in such rod bundles are very complicated processes. The basic understanding of these phenomena is essential to achieve the optimum performance of the reactor during normal operating conditions and in determining the behavior of the systems under hypothetical accident conditions. In particular for nuclear power reactors there are two fundamental questions to be answered:

1. What is the average and local density distribution of the coolant in the various parts of the core? (The answer to this question is needed for the reactor physics calculations and for the planing of the fuel management.)

2. What is the maximum safe operation limit of power generation for a given rod bundle configuration before the rate of steam generation on the heated walls blocks the coolant contact with fuel rods and causes damages due to overheating? (Prediction of critical heat flux or burnout.)

Experiments on large scale models of the assemblies with electrical heating is the most traditional way of providing answers to such questions. On the basis of physical measurements, correlations for heat transfer coefficients, pressure drop and critical heat flux as a function of geometry and non-dimensional physical parameters, i.e., Reynolds number, Prandtl number, etc., can be developed. This approach can be used on only a

limited number of cases and at a very great cost. For each new fuel assembly geometry, a new model must be manufactured and new experiments performed. Furthermore, scaling from the model to design size causes a great deal of uncertainty in the design process, due to the fact that the performance of instruments and measuring techniques usually limit data to just global heat transfer and flow rates while detailed temperature and velocity distributions are needed for an optimal design. Evidently, the correlations whose development is based on such measurements are valid only in the range of the measured parameters.

An *alternative* approach is to develop direct numerical solutions of the conservation equations of mass, momentum and energy with appropriate initial and boundary conditions of the physical system under consideration. This allows the costly and complicated experimental simulations to be replaced by computational models. There are four main approaches for analyzing and predicting detailed thermal-hydraulic behavior of reactor fuel assembly [Van Doormal, 1980, Sha, 1980], these are:

I. the finite element method,
II. the boundary fitted curvilinear co-ordinate method,
III. the porosity and distributed resistance method, and
IV. subchannel analysis.

Over the last three decades a great deal of effort has been put into the development of subchannel analysis in the form of *subchannel codes* which allow the mass, momentum and enthalpy distribution in the rod bundles of nuclear power rectors to be predicted. Primarily these codes are used in connection with appropriate CHF (Critical Heat Flux) correlations to demonstrate the adequacy of the thermal-hydraulic

design limit, i.e., critical power ratio under steady-state and transient conditions. Besides the verification of the various correlations used, the application of subchannel computer codes to the design of nuclear power reactor fuel rod bundles requires information on the mass, momentum and energy transport processes between the different subchannels (known as *intersubchannel mixing effects*) and between the two phases in each individual subchannel. The parameters in the models simulating such transport processes can only be obtained experimentally in full scale bundle geometries under realistic operational conditions. However, due to experimental difficulties very limited detailed data including local void fraction profiles, liquid and gas mass flow rates and pressures throughout the rod bundles are available. Furthermore, most of the data that is available is for adiabatic cases only.

1.1 Purpose and Organization of Present Work

The objectives of the present work are divided into three parts. First to experimentally investigate the hydraulic behavior of two laterally interconnected subchannels where the inlet mass flow rates and void fractions are substantially different. The hydraulic behavior of the two interconnected subchannel where the inlet mass flow rates are equal will also be investigated. Following these investigations, detailed data on the pressure drop and the void fraction will be available. The second objective consists of an evaluation of the ability of the COBRA-IV subchannel code to predict the flow distribution in the subchannels by using the data obtained from the experiments. The third objective is to compare the predictions of the COBRA-IV subchannel code against the experimental data on two laterally interconnected subchannels when one of them is partially blocked, in both single- and two-phase flow conditions. To meet these objectives, the following steps will be carried out:

1. A literature survey on two-phase flow modeling, on subchannel analysis and on the intersubchannel mixing phenomena will be done.

2. A detailed description of the COBRA-IV subchannel code including all governing equations will be presented. The starting point is the general transient balance laws for mass, energy and linear momentum for a single component two-phase flow in the form of the phase integral balance equations on an arbitrary fixed (Eulerian) co-ordinate system. Later, a survey of the numerical techniques used in the COBRA-IV code will be presented. Finally, the intersubchannel mixing model used in COBRA-IV will be presented.

3. Since experimental work was done as a main part of the research, a detailed description of the experimental air-water facility at the Institute de Génie Nucléaire as well as the experimental procedure used in the present work will be given.

4. All the experimental data obtained in the course of this work will be compared with COBRA-IV predictions. The performance of the mixing model (equal mass exchange) used by COBRA-IV will be verified. A sensitivity analysis will be carried out to determine the effect of the mixing coefficient used in COBRA-IV on its predictions. As the experimental results cover cases of both equal inlet mass flux and unequal inlet mass fluxes, it should be possible to suggest the best values for the mixing coefficient under a wide range of applications.

5. Using the data from experiments on two interconnected subchannels with the blockage conducted by Tapucu et. al. [1984, 1988] and Teyssedou [1987], the predictive capability of COBRA-IV in blockage cases will be studied.

Recommendations will be made for the values of key parameters used in the COBRA-IV subchannel code, i.e., the irreversible pressure drop coefficient, cross-flow resistance factor, and the mixing coefficient.

CHAPTER 2

LITERATURE SURVEY

2.1 Models and Methods for Two-Phase Flow

Since two-phase flow phenomena are of extreme importance in nuclear fuel rod-bundles and many other industrial process, one needs a set of basic equations which describes the conservation of mass, momentum and energy for such flows. For single-phase flow, these basic equations are rigorously provided in the form of mass, momentum and energy balances in an infinitesimal volume dv, and an infinitesimal time interval dt. These equations form the local instant equations for density, velocity and energy which can be integrated in all volume and time domains. For example, such derivations are given by Schlichting [1979] and Whitaker [1982].

For two-phase flow, such local instant field equations are not available without using appropriate averaging techniques. To obtain field equations for two-phase media valid in all volume and time domains, one inevitably forces the differentiation of the discontinuous functions which represent the density, velocity and energy at the interfaces between two phases. Such differentiation can not be executed in the ordinary notion of a function. Furthermore, interfaces are of large importance in mass, momentum and energy transfer. Therefore, source terms must be defined at the interface which is practically not possible in ordinary notion of a function. Such difficulties in mathematical treatment are considered to be main reason why the local instant field equations of two-phase flow have not been obtained so far.

For two-phase flow the most traditional model is the homogeneous mixture model, in which, both phases are assumed to be completely mixed and to move with the same velocity. Considering these assumption the density, velocity and energy of the two-phase mixture are defined and local instant conservation field equations for mass, momentum and energy are obtained. Zuber and Findlay [1965], Wallis [1969], Ishii [1977] and Ishii & Zuber [1979] considered the diffusion effects of each phase. This permits the two phases to move with different velocities which are defined relative to the center of the mass of the mixture. This model is called "drift flux model" and has become very popular in subchannel analysis.

Another direction of two-phase flow formulation has been developed by Ishii [1975], Delhaye [1968], Delhaye et al. [1981], Bourè [1973], Wallis [1969], Kocamustafaogullari [1971], Banerjee [1980], Banerjee and Chan [1980]. They have developed two-fluid model formulations of two-phase flow. In this model, each phase is treated separately and the interface is considered as a moving boundary which causes discontinuities in the continuous media of each phase. For each phase, the local instant generalized conservation equation for single-phase flow is written and at the interface, local instant balances of mass, momentum and energy are formulated as boundary conditions. After this, the aforementioned equation will be averaged over time and space. Using different integral theorems (Leibniz's, Gauss's theorems), the average field equations can be derived for each phase. This formulation accurately reflects the physical aspects of two-phase flow. However, the field equations obtained are given in averaged forms in a certain volume or over a certain time period. Local instant formulations used in the two-fluid model are valid only in each phase or at the interface and they are not local instant field equations which are valid for all the space and time domain.

It is desirable that the local instant conservation field equations of mass, momentum, and energy be formulated without any averaging techniques. Recent developments in measurement techniques for two-phase flow (laser Doppler anemometry, etc.) have provided detailed knowledge of microscopic structure of two-phase flow which permit various averaging procedures of the basic equations without using complicated integral theorems. Some statistical treatment have been applied to the local interfacial area concentration by Kataoka et al. [1984]. Such a formulation will be particularly useful in analyzing the microscopic structure of two-phase flow (turbulence, void diffusion, etc.).

The idea of "distribution" which has been developed by Schwartz [1950], [1961] and has been widely applied in neutronics, is used by researchers to formulate local instant field equations. Only by using distribution functions, is the differentiation at the discontinuities possible. Furthermore, the source term can be represented in terms of this distribution. One of the most widely applied distribution was proposed by Dirac and it has been used in physics and engineering. In two-phase flow the Dirac distribution function has been used by Gray & Lee [1977] for modeling of the two-phase flow. Later, Kataoka et al. [1984] derived the local instant formulation of the interfacial area concentration for two-phase flow in terms of this distribution functions. This local instant interfacial area concentration is essential when considering the local instant balances of mass, momentum, and energy in two-phase flow. Later Kataoka et al. [1986] used the local instant interfacial area concentration and derivatives of discontinuous functions to develop the local instant field equations of mass, momentum, and energy. Recently, Guido-Lavalle et al. [1994] presented a statistical formulation to describe gas-liquid two-phase flows. They introduced a transport equation for bubbly flow which explicitly accounts for bubble break up and coalescence

phenomena. The excellent agreement of the predictions of their model compared to experimental data has shown the ability of this kind of modeling for predicting the axial void fraction distribution.

2.2 The Subchannel Method

2.2.1 Basic Definitions and Methods

The term subchannel is used to denote the flow passage that is formed between a number of rods or between some rods and adjacent the walls of the shroud tube or box or pressure tube. Each subchannel is surrounded by some solid walls and a few boundary lines. The boundary lines between subchannels are, as a rule, drawn at the position of minimum distance (gaps) between the solid walls. However, the selection of the minimum gap is not a requirement if a boundary concides with a symmetry line. Each subchannel will be specified by its geometrical characteristics and topography [Rouhani, 1978]. The geometrical data include flow cross sectional area as well as the heated and wetted perimeters. The topography gives information on the surrounding walls, the heat flux on the heated walls, the open boundaries, their width, and, finally, the neighboring subchannels. The entering flow distributes itself between different bundles or subchannels and the fractional flow areas or subchannels of each bundle and the heat input from the surface of the fuel rods changes the properties of the coolant. Within each subchannel the flow is considered as one dimensional, exchange mechanisms between adjacent subchannels are also taken into consideration.

The principle of subchannel analysis is the application of field equations (conservation equations of mass, momentum, and energy) to the flow through and

between the individual subchannels. By dividing the axial dimension into a number of increments with a length of Δx, one establishes a kind of nodal division of the total flow passage. The conservation equations which are used in difference form, relate the local variations of velocity, enthalpy and density of each node to those of neighboring nodes. The coupling of the subchannels in the transverse directions is done by means of the concept of diversion cross-flow and the help of the so-called transverse momentum equation. Using proper numerical processes and complementary equations allow the local values of densities, mass fluxes, the total pressure drop and in the case of water-cooled reactors an estimation of the parameters that indicate a safety margin against critical heat flux to be evaluated.

To develop field equations for subchannel analysis two approaches could be followed. The first approach is to simplify the general conservation equations of mass, momentum and energy for a one-dimensional control volume as if the subchannel where a simple pipe having the same hydraulic diameter as the subchannel. The second approach which is a more *rational* approach for obtaining the set of equations used in subchannel modeling, consist of applying the one-dimensional elementary transport theorem combined with appropriated averaging techniques [Ishii, 1978]. Such a theoretical approach provides a better identification of the exchange mechanisms between adjacent subchannels. In both approaches additional terms are added to describe, in a simplified manner, the mechanisms that produce the cross-flow between adjacent subchannels. In all cases the cross-flow is assumed to be much smaller than the axial flow, which in most cases, it is completely justified and reasonable assumption. A typical example for obtaining the conservation equations of subchannels directly from the general field equation (first approach) is given by Tye [1991].

As has already been mentioned, in subchannel analysis, the coupling of the one-dimensional conservation equations of mass, momentum and energy between the subchannels is done by the so-called transverse momentum equation. A historical approach to development of subchannel codes shows how the transverse momentum equation formulation has been improved. The first subchannel models, such as THINC-I [Zernick et al. 1962], considered a number of isolated subchannels which were connected only at the top and bottom. These subchannels were analyzed separately and the inlet flow adjusted to give the same pressure drop as a previously selected flow model. In some other codes, the flow distribution was attributed to the radial pressure gradient without considering any transverse flow resistance allowing the solution of the subchannel interchanges with the same axial pressure drop for each subchannel. As proposed to the previous cases the first generation of subchannel codes such as COBRA-I [Rowe, 1967], HAMBO [Bowring, 1968] and COBRA-II [Rowe, 1970] used some simplified form of transverse momentum balance due to mixing effects that considered only a friction resistance against cross-flow between two adjacent subchannels. Later, in the model of COBRA-III, Rowe [1973] suggested the use of a differential formulation for the lateral momentum equation. This idea permitted the temporal and spatial acceleration of cross-flow between adjacent subchannels to be considered.

Using the differential formulation of the lateral momentum equation, several second generation subchannel codes, such as, THERMIT II [Kelly et al., 1981], COBRA-TF [Turgood et al., 1983], and FIDAS [Sugawara et al., 1991] have been developed during the last 15 years. Two-phase fluid models, i.e., one-dimensional conservation equations of mass, energy, axial momentum and lateral momentum for each phase have been used in these codes. It should be mentioned that considerable

uncertainties in the proper analytical, semi-empirical or empirical formulations of the interfacial transport phenomena are the most important problems in the second generation codes.

2.2.2 Intersubchannel Mixing Mechanisms

The interactions between adjacent subchannels are quite complex and difficult to decompose into more elementary terms but they could be decomposed arbitrarily into five independent mechanisms:

I. Diversion cross-flow,
II. Turbulent mixing,
III. Turbulent void diffusion,
IV. Void drift,
V. Buoyancy drift.

Diversion cross-flow can be defined as the transverse directed flow due to pressure gradients between subchannels. These gradients may be induced by differences in subchannel geometries, the variation of heat flux from one subchannel to the other, initial boiling in one subchannel or by flow section variations caused by blockages.

Turbulent mixing occurs due to stochastic pressure and flow fluctuations. These random fluctuations enhance the mass, momentum and energy exchange between the subchannels. It should be mentioned that intersubchannel mixing due to turbulence of the fluid occurs in both equilibrium and non equilibrium two-phase flow (equilibrium two-phase flow is a flow without net mass and volume changes for each phase).

Fluctuations of velocity and pressure in a fixed point cause the diffusion of scalar and vectorial quantities in continuous media without net mass or volume exchanges between the adjacent subchannels for each phase in a period of time. Interpretation of turbulent mixing between subchannels depends directly on how the turbulent effects in each individual subchannel are evaluated. In subchannel analysis all the effects of turbulence on the fine structure of the flow have been neglected.

Turbulent void diffusion occurs due to void fraction gradients between different neighboring subchannels. Because of the void drift effect, data on the two-phase flow redistribution approaching an equilibrium two-phase flow, i.e., equal void fraction in adjacent subchannels, due to turbulent void diffusion have never been reported.

Void drift is the mechanism used to account for the tendency of the gas phase to shift to higher velocity zones and/or subchannels. In other words, void drift accounts for the tendency of the two-phase flow to exhibit a non-uniform void distribution in an equilibrium two-phase flow. This effect is one of the most important and yet least understood aspects of two-phase flow in both an individual channel and in laterally interconnected subchannels. It is believed that the measured flow and enthalpy distributions in the subchannels of nuclear fuel rod bundles which differ from the prediction of subchannels codes such as COBRA is strongly due to lack of information on transverse phase distribution. Despite numerous experimental and analytical studies of two-phase flow during the past 30 years, no one has been able to satisfactorily predict lateral phase distribution either in an individual channel or in laterally interconnected subchannels.

Experimentally, the void drift phenomenon has been observed by a number of

different researches such as Bergles [1969], Lahey [1969] in rod bundle experiments and more clearly by Van Der Ros [1970], Gonzalez-Santalo [1972], Tsuge [1979], Shoukri et al. [1984], Lahey [1986], Sato [1988], Tapucu et al. [1988], and Sadatomi et al. [1994] in experiments on two laterally interconnected subchannels. These experiments have been performed to give flow distribution data for air-water flow in the absence of diversion cross-flow. The experiments of Shoukri et al. [1984] were concentrated on gravity separation, which is important in horizontal two-phase flow.

Buoyancy drift occurs in horizontal channels where the void is pushed upwardly normal to the major flow direction due to the difference in specific mass between the two phases. The significance of this mechanism should diminish at high mass fluxes.

The performance of a practical subchannel code strongly depends on how the aforementioned mixing mechanisms are modeled. Furthermore, in rod bundles the effects of mechanical components, i.e., grid spacers, wire wraps spacers, end plates, etc. should be considered. These components normally promote the mixing effect, which requires new theoretical and experimental data to validate the models.

2.2.3 Development of Mixing Models

In order to the subchannel code to be able to accurately predict the flow in interconnected subchannels, accurate modeling of the mixing mechanisms is essential. Different mixing models have been developed by Du Bousquet [1969], Van Der Rose [1970], Gonzalez-Santalo [1972], Gosman [1973], Rowe [1973], Chiu et al. [1979], Chiu [1981], Shoukri [1984] among others. The common goal of these methods is the development of a phenomenological model with the help of some empirical parameters

which correctly represent the intersubchannel mixing. Basically, these models can be distinguished by which one of two fundamental approaches that they use. These are:

- *equal mass exchange* between subchannels, and
- *equal volume exchange* between subchannels.

The *equal mass model* is based on a fluctuating equal mass exchange between adjacent subchannels. This model is an extension of the single-phase flow mixing model. In single-phase mixing, there is usually no net mass transfer due to the mixing process since the densities in adjacent subchannels are equal. This model has been used in the COBRA-IV subchannel computer code and will be discussed in detail in the next chapter.

The *equal volume exchange model* is based on a volume-for-volume exchange between adjacent subchannels. Since, in two-phase flow, substantial mass transfer between the subchannels has been observed, Gonzalez-Santalo [1972] proposed an exchange of globes of equal volume but of different densities. He interpreted the mixing process as a diffusion phenomenon of the gas phase as a discrete media in the liquid phase as continuum media. Based on experimental observations, he concluded that under equilibrium conditions between two subchannels, the transverse gas flow rate is zero, however, the void fractions of two adjacent subchannels are different. The formulation of Gonzalez-Santalo's model is:

$$\frac{\Delta Q_g}{\Delta z} = -K[(\alpha_1 - \alpha_2) - (\alpha_1 - \alpha_2)_{EQ}] \quad , \qquad (2\text{-}1)$$

where Q_g is the transverse gas flow rate, α is the void fraction, EQ stands for

equilibrium conditions and K is the effective turbulent diffusion coefficient. By using this model, the effect of a non uniform void fraction distribution at equilibrium conditions can be taken into account in the mixing equations. Later, Lahey and Moody [1977] proposed a volume-for-volume mixing exchange between adjacent subchannels based on the hypothesis that the transverse fluctuating velocities for the gas and liquid phases are equal. This assumption is a direct result of considering equal volumetric flow exchanges between two subchannels. The hypothesis that the two-phase mixing is proportional to the non-equilibrium void fraction gradient implies that the net exchange due to mixing ceases when the equilibrium is achieved. Hence, they proposed:

$$G' = G'_{MIX} + G'_{VD}\ , \tag{2-2}$$

where G' is the total intersubchannel mixing mass flux, G'_{MIX} is the turbulent mixing mass flux and G'_{VD} is void drift based on equilibrium void fractions. At equilibrium conditions $G' = 0$ and this means $G'_{MIX} = -G'_{VD}$. This model can be written in the following form:

$$G' = \frac{\varepsilon}{l}(\rho_l - \rho_g)\left\{(<\alpha_j> - <\alpha_i>) - (<\alpha_j> - <\alpha_i>)_{EQ}\right\}, \tag{2-3}$$

where EQ denotes the mixture equilibrium conditions, ε is the eddy diffusivity, l is mixing length usually taken to be the centroid-to-centroid distance between adjacent subchannels, $<\alpha_i>$ and $<\alpha_j>$ are the average of void fractions over the flow areas in subchannels i and j respectively, ρ_l is the density of the liquid phase and ρ_g is the density of the gas phase. When an equilibrium distribution is achieved, net mass exchange vanishes. This model allows us to predict the correct data trends. However, equilibrium conditions are never achieved in the adiabatic case under consideration. Equation (2-3) indicates that while turbulent mixing causes a net flow of liquid from subchannel i to

subchannel j and a net flow of vapor from subchannel j to subchannel i, void drift and turbulent mixing oppose each other. One is trying to pump vapor out of subchannel i, while the other is trying to pump it in. While not perfect the Lahey model is, to date, the best mechanistic model for void drift and turbulent void diffusion. This model is used by Sugenerana et al. [1991] in a typical second generation subchannel code (FIDAS).

Shoukri et al. [1984] studied the redistribution of two-phase flow in horizontal interconnected subchannels. Based on the drift flux model, they developed a model for taking into account the diversion cross-flow, gravity phase separation and void diffusion. But the Shoukri model did not account for the void drift effect. In ASSERT-4 Carver et al. [1987] used an equal volume exchange model to allow net fluctuating transverse mass flux from one subchannel to the other. This model is based on the drift flux model, Constitutive relationships for the lateral relative velocity V_r, are expressed as follows:

$$\vec{V}_r = \underbrace{\frac{(C_0 - 1)\langle \vec{j} \rangle}{< 1 - \alpha >}}_{1} + \underbrace{\frac{\vec{V}_{gi}}{\langle 1 - \alpha \rangle}}_{2} - \underbrace{\frac{\varepsilon}{\langle \alpha \rangle \langle 1 - \alpha \rangle} \nabla(\alpha - \alpha_{EQ})}_{3}, \qquad (2\text{-}4)$$

where C_0 is the distribution parameter, $\vec{j}$ is the volumetric flux of the mixture, $\vec{V}_{gi}$ is the drift velocity, α is the void fraction, ε is the diffusion coefficient and $< >$ represents an average over cross sectional flow. In the above equation, term (1) expresses the relative velocity due to cross-sectional averaging, term (2) denotes the relative velocity due to gravitational effects and term (3) is related to turbulent void diffusion and void drift. Since equation (2-4) is a vectorial equation, for vertical flows in the axial direction only the first two terms are important and the term (3) is negligible. Tapucu et al. [1994] concluded that this model predicts the experimental trends better than the equal mass

exchange model used in COBRA-IV.

2.2.4 Solution Techniques : Numerical Methods

Once, the conservation equations of mass, momentum, energy for each subchannel are developed, the next step is choosing an appropriate numerical solution. The total number of dependent variables, depends on the flow models, and usually determines the total number of complementary/constitutive relations needed to close the set of equations.

In COBRA-III [Rowe, 1973], the coupling of the subchannels in the transverse directions is done by means of the concept of diversion cross-flow and the help of the so-called transverse momentum equation. The solution strategy is related to the determination of the forced diversion cross-flow which results from the existing pressure difference in the transverse directions for each axial calculational plane. The solution advances in space by marching from a known inlet flow boundary condition towards the exit of the geometry under consideration, where given system pressure there is specified as a boundary condition. A pseudo-boundary value problem is solved by successively looping from bottom to top thus propagating a disturbance by one spatial node per loop. This method, the so-called cross-flow solution technique is the basis for a whole generation of computer codes. The major defiency for this method is that, there is no guaranty that decreasing the spatial and/or temporal step sizes would result in one unique solution Wolf [1987], moreover, even decreasing the mass flow convergence criteria for the iterative looping scheme does not necessarily lead to an improved answer. Rather this may introduce spurious fluctuations with a resulting divergence of the solution Wolf [1987]. It should be mentioned that the original coding

of COBRA was extremely inefficient in not taking advantage of the extreme sparseness of the resulting connectivity matrices, thus prohibiting the code's use for large problems and for transient conditions. The modified versions of COBRA-IIIC such as COBRA-IV-I [Stewart et al. 1977] employ an iterative solution scheme for the set of linear equations for its implicit marching scheme, however, despite this improvement in numerical efficiency, the solution strategy still relies upon the cross-flow concept and thus still suffers from the disadvantage of nodal sensitivities. An effort to improve the efficiency of COBRA-IIIC was made by Masterson and Wolf [1978]. The result, COBRA-IIIP, is faster and is able to solve larger and more complex problems, such as full-core PWR transients. The numerical solution in COBRA-IIIP is based on a type of pressure-velocity method called the MAT method (Modified and Advanced Theta Method).

CHAPTER 3

COBRA-IV : MODEL AND METHOD

The objective of this chapter is to present an overall review of the COBRA-IV subchannel code. The description of the model and the numerical procedure presented in this chapter have been reproduced in large part from Stewart et al. [1977].

3.1 General Balance Equations

To write governing equations in the rod bundles, the balance equations for mass, energy and linear momentum for a single component two-phase mixture are considered. These equations are written in an integral form using an Eulerian control volume. It is assumed that the mixture variables are *sufficiently space and time averaged* to provide continuous derivatives inside the fixed volume and over its surface.

The integral balances are written for the Eulerian control volume, V, which is bounded by a fixed surface, A. This surface may consist of both a solid boundary, such as a fuel rod or structural wall, and a fluid boundary, i.e., the interconnecting regions. Solid materials are considered to be outside of V. The local composition of the flow mixture is described by the space-time averaged vapor volume fraction, α, thus, any mixture variable can be expressed as the volume weighted sum of individual phases variables Ω_l , Ω_v as:

$$\Omega = \alpha\, \Omega_v + (1 - \alpha)\, \Omega_l,$$

where Ω, can be a scalar or a vector variable. For mass, energy, and momentum

respectively, the above equation becomes:

$$\rho = \alpha\rho_v + (1-\alpha)\rho_l,$$

$$\rho e = \alpha\rho_v e_v + (1-\alpha)\rho_l e_l, \text{ and}$$

$$\rho\vec{u} = \alpha\rho_v\vec{u}_v + (1-\alpha)\rho_l\vec{u}_l. \qquad (3\text{-}1)$$

Where v and l stand for vapor and liquid phases, respectively and e, is the sum of the internal thermal energy, i, and total kinetic energy: $e = i + \frac{|\vec{u}|^2}{2}$. If Ω is defined as a given quantity per unit of volume, the integral balance equation for that quantity can be written as:

$$\underbrace{\frac{\partial}{\partial t}\int_V \Omega\, dV}_{\text{rate of the change of } \Omega \text{ in control volume}} + \underbrace{\int_A \Omega(\vec{u}.\vec{n})\, dA}_{\text{convected } \Omega \text{ through the surfaces of the control volume}} = \underbrace{\int_V S.dV}_{\text{source of } \Omega \text{ inside control volume}}, \qquad (3\text{-}2)$$

where $\vec{u}$, is the fluid velocity, $\vec{n}$ is the outward directed normal unit vector and S represents the net volumetric source of Ω in V.

Considering equations (3-2) and (3-1), the associated integral equations for the mass, energy and linear momentum, are respectively written as:

a) mass:

$$\frac{\partial}{\partial t}\int_V \rho dV + \int_A \rho(\vec{u}\cdot\vec{n})\, dA = 0, \qquad (3\text{-}3)$$

b) energy:

$$\frac{\partial}{\partial t}\int_V \rho e dV + \int_A \rho e(\vec{u}\cdot\vec{n})dA = \int_V \left[\rho\left(\vec{f}\cdot\vec{u}\right) + \rho q'''\right]dV + \int_A \left[\left(\bar{T}.\vec{u}\right) - \vec{q}'\right]\cdot\vec{n}\,dA, \quad (3\text{-}4)$$

c) linear momentum:

$$\frac{\partial}{\partial t}\int_V \rho\vec{u}\,dV + \int_A \rho\vec{u}\,(\vec{u}\cdot\vec{n})dA = \int_V \rho\vec{f}\,dV + \int_A (\bar{T}\cdot\vec{n})\,dA. \quad (3\text{-}5)$$

Where $\vec{f}$ is the sum of body forces acting on the fluid, q''' is the rate of internal heat generation per unit volume, $\bar{T}$ is shear stress tensor and $\vec{q}$ is the heat flux vector.

Each of the three equations (3-3 through 3-5) represents the sum of two similar equations for the individual phases. If the equations 3-3 through 3-5 are written for each phase separately, then, by considering the six separate equations and adding *an equation of state for each phase*, then theoretically, it is possible to calculate the velocity, density and energy of each phase as well as the local mixture composition and the pressure field. However, this would require detailed knowledge about transport of mass, momentum and energy at the interfaces. Furthermore, constitutive equations for the heat flux at the surfaces of the control volume, $\vec{q}$ and shear stress tensor, $\bar{T}$ would be necessary.

With some loss of generality, COBRA-IV introduced some simplifications to the governing equations. Stewart et al. [1977] considered the motion of one of the phases with respect to the other or to the mixture is known and assumed that the phases are under conditions of the thermal equilibrium. These assumptions allow the field equations to be written by only *as three mixture balance equation and one state equation*. Further, the relative velocity between the two phases can be specified via a correlation

for the slip ratio. An additional equation is required for each phase to account for departure from saturation. This permits the mixture equations not necessarily be limited to homogeneous equilibrium flows. Since, COBRA-IV is written for low speed cross-flows with substantial surface heat transfer the following additional assumptions are considered:

I. The changes in kinetic energy are small.
II. The work done by the body forces and the shear stress are negligible in the energy equation as compared to the surface heat flux.
III. There is no internal heat generation in the fluid.
IV. Gravity is the only significant body force considered in the momentum equation.

For a better comprehension of surface transport phenomena represented by surface integrals in the general balance equations (3-2), it is appropriate to split the surface integrals into two components. Considering $\vec{\Phi}$ as an arbitrary surface flux at the surfaces of the control volume, we can write:

$$\int_A (\vec{\Phi} \cdot \vec{n}) dA = \int_w (\vec{\Phi}_w \cdot \vec{n}) dA + \int_f (\vec{\Phi}_f \cdot \vec{n}) dA \qquad (3\text{-}6)$$

where w represents the solid wall portion and f represents the fluid part of *the surface A of the control volume V.*

The only surface integrals of interest over the solid wall are the heat flux and surface forces. Using Fourier's law and an empirical surface heat transfer coefficient H, the total heat transfer becomes:

$$\underbrace{\int_A (\vec{q}' \cdot \vec{n}) dA}_{\text{total heat transfer through surfaces}} = \underbrace{-\int_f K_f \left(\vec{\nabla} T \cdot \vec{n}\right) dA}_{\text{heat transfer through the fluid surface}} + \underbrace{\int_w H(T_w - T_f) dA}_{\text{heat transfer through the solid surface}} \qquad (3\text{-}7)$$

where K_f is the fluid thermal conductivity, T_f is an appropriate local fluid temperature and T_w is the temperature of the solid boundary.

The stress tensor, $\tilde{T}$, can be written as the sum of a hydrostatic component, $p\tilde{I}$, and a viscous stress tensor $\tilde{\Pi}$, as follows:

$$\int_A \left(\tilde{T} \cdot \vec{n}\right) dA = -\int_A \left(p\tilde{I} \cdot \vec{n}\right) dA + \int_A (\tilde{\Pi} \cdot \vec{n})\, dA \ , \qquad (3\text{-}8)$$

consequently, the fluid and solid components of the surface stress integral, equation (3-8) could be split as :

$$\underbrace{\int_A \left(\tilde{T} \cdot \vec{n}\right) dA}_{\text{total surface force}} = \underbrace{-\int_f \left(p\tilde{I} \cdot \vec{n}\right) dA + \int_f (\tilde{\Pi} \cdot \vec{n})\, dA}_{\text{surface force acting on fluid surface}} + \underbrace{\left[-\int_w \left(p\tilde{I} \cdot \vec{n}\right) dA + \int_w (\tilde{\Pi} \cdot \vec{n}) dA\right]}_{\text{surface force acting on solid surface}} \qquad (3\text{-}9)$$

The solid component in this equation is modeled by empirical friction factor in the momentum equation. Also, since the work done by shear stresses on the surface of the control volume has been assumed to be negligible, the last term of energy equation (3-4) can be simplified as:

$$\int_A \tilde{T} \cdot (\vec{u} \cdot \vec{n}) dA = -\int_f p\tilde{I} \cdot (\vec{u} \cdot \vec{n}) dA = 0 \qquad (3\text{-}10)$$

Applying equations (3-7), (3-9) and (3-10) to the general conservation

equations for mass, energy and momentum (3-3 through 3-5) can be rewritten in the following forms:

Mass:

$$\frac{\partial}{\partial t}\int_V \rho dV + \int_f \rho(\vec{u}\cdot\vec{n})dA = 0\ , \tag{3-11}$$

Energy:

$$\frac{\partial}{\partial t}\int_V (\rho h)dV + \int_f \rho h(\vec{u}\cdot\vec{n})dA = -\int_f K_f\left(\vec{\nabla}T\cdot\vec{n}\right)dA + \int_w H(T_w - T_f)dA, \tag{3-12}$$

Momentum:

$$\frac{\partial}{\partial t}\int_V \rho\vec{u}\,dV + \int_f \rho\,\vec{u}\,(\vec{u}.\vec{n})\,dA = \int_V (\rho\vec{g})dV - \int_f \left(\tilde{pI}\,.\,\vec{n}\right)dA + \int_f (\tilde{\Pi}\cdot\vec{n})dA$$

$$-\int_w \left(\tilde{pI}\,.\,\vec{n}\right)dA + \int_w (\tilde{\Pi}\,.\,\vec{n})\,dA. \tag{3-13}$$

These integral balance equations will be use to write the subchannel model as used in the rod-bundle geometry, in the next section.

3.2 Subchannel Equations

The relation of the subchannel control volume to the reactor core can be observed in Figure (3.1). In COBRA-IV, it is assumed that any lateral flow is directed by the gap through which it flows and loses its sense of direction after leaving the gap

region. This assumption allows the vectorial sense of the lateral flow to be neglected. Since the spatial orientation of each cross-flow is determined by its associated gap, The following conventions used to take into account the direction of the cross-flow: for two adjacent subchannel i and j, separated by gap k, the cross-flow W_k is positive if the flow is from i to j and negative if from j to i when j is greater than i. These sign conventions can be conveniently incorporated in the following matrix operators $[D_c]$, which performs the *difference operation* across each connection and $[D_c]^T$ which performs the directed *summing operation* (Σ) on gap connections around each subchannel. Similar conventions are applied to connections between fuel rods and subchannels and to connections between thermally conducting walls and subchannels by defining the matrixes $[D_r]$ and $[D_w]$. The volume and surface averages are defined as:

$$\langle\langle \rho \rangle\rangle \equiv \frac{1}{V} \int_V \rho \cdot \, dV, \text{ and} \tag{3-14}$$

$$\langle \rho u \rangle \equiv \frac{1}{A} \int_A \rho(\vec{u} \cdot \vec{n}) \, dA. \tag{3-15}$$

The Figure (3.2) shows the control volume used in COBRA-IV. The centroid of the control volume is located at x and the lower and upper surfaces are at $x - \frac{\Delta x}{2}$ and $x + \frac{\Delta x}{2}$, respectively. The volume of the control volume can be written as $A.\Delta x$, where A is the axial flow area in volume V. The gap width is s and the lateral velocity is v. The gap clearance s may vary from gap to gap but the area of each lateral surface is $s.\ \Delta x$.

3.2.1 Subchannel Mass Balance Equation

Equation (3-11) can be applied directly to the subchannel control volume Figure (3.2). It should be mentioned that this control volume is one-dimensional.

$$V\frac{\partial}{\partial t}\langle\langle\rho\rangle\rangle_V+\langle\rho u\rangle_A(A)_{x+\frac{\Delta x}{2}}-\langle\rho u\rangle_A(A)_{x-\frac{\Delta x}{2}}+\sum_k\langle\rho v\rangle_s s\cdot\Delta x=0,$$

The transpose of the connection matrix $[D_c]$, forms the lateral component of the mass flux integral and is used to replace Σ, thus:

$$V\frac{\partial}{\partial t}\langle\langle\rho\rangle\rangle_V+\langle\rho u\rangle_A(A)_{x+\frac{\Delta x}{2}}-\langle\rho u\rangle_A(A)_{x-\frac{\Delta x}{2}}+[D_c]^T\langle\rho v\rangle_s s\cdot\Delta x=0, \qquad (3\text{-}16)$$

where:

$$\langle\rho v\rangle_s=\frac{1}{s.\Delta x}\int_{A=s\cdot\Delta x}\rho(\vec{u}\cdot\vec{n})\,dA \qquad (3\text{-}17)$$

Dividing equation (3.16) by Δx and taking limit as Δx approaches zero, the equation on conservation of the mass can be re-written as:

$$A\frac{\partial}{\partial t}\langle\langle\rho\rangle\rangle_V+\frac{\partial}{\partial x}\langle\rho u\rangle_A A+[D_c]^T\langle\rho v\rangle_s s=0 \qquad (3\text{-}18)$$

The first term represents the rate of change of mass per unit axial length, the second term is the spatial variation of the axial mass flow rate per unit length and the last term is the sum of all gap connections of lateral mass flow rate per unit length which is generally identified as "cross-flow".

3.2.2 Subchannel Energy Balance equation

In order to apply equation (3-12) to a subchannel, additional definitions should be made to describe the surface heat transfer and lateral fluid heat conduction. Considering Figure (3.3) the total heat input to control volume from the fuel rods is:

$$Q_r = \Delta x [D_c]^T \{P_r \Phi H_r\} [D_r] \{T\} , \tag{3-19}$$

where: Δx is the length of the subchannel control volume, $[D_r]$ rod-to-channel connection matrix, H_r is heat transfer coefficient between fuel rod and flow, P_r is the total perimeter of rod, Φ is the fraction of the fuel rod in contact with a given subchannel and $\{T\}$ is the appropriate bulk temperature matrix. It should be mentioned that $[D_r]\{T\}$ forms the difference between the rod surface temperature and bulk fluid temperature.

For the control volumes in contact with the conducting walls, heat exchange with the wall can be written as:

$$Q_w = \Delta x [D_w]^T \{L_w H_w\} [D_w] \{T\}, \tag{3-20}$$

where : $[D_w]$ is the wall-to-channel connection matrix, H_w is the heat transfer coefficient between wall and flow, L_w is the length of the conducting wall for the control volume and $[D_w]\{T\}$ forms the difference between wall and bulk fluid temperature.

The lateral heat transfer across the interconnection due to the heat conduction of the fluid (Figure 3.4), can be written as:

$$Q_c = -s \Delta x \left\langle K_f \frac{\partial T}{\partial y} \right\rangle_s , \tag{3-21}$$

where Q_c is the lateral fluid heat conduction through gap and K_f is the fluid thermal conductivity and y is the direction of the cross-flow. Since the lateral temperature gradient in a complex geometry like a rod-bundle is not available, the heat conduction must be related to the bulk fluid temperature. Thus the lateral heat conduction could be

reformulate as :

$$Q_c = -\Delta x [D_c]^T \left[\frac{sc\langle K_f \rangle}{L_c} \right] [D_c]\{T\}, \qquad (3\text{-}22)$$

where : L_c is the centroid to centroid distance between two subchannels and c is an empirical correction factor to take into account the effect of replacing a gradient by a discrete difference referred to the bulk temperatures and to the centroid-to-centroid distances.

For lateral exchange of energy due to turbulence, an equal mass exchange between adjacent subchannels is considered. The total transfer of energy due to turbulence in the control volume V, Q_T can be expressed as:

$$Q_T = -\Delta x [D_c]^T [W'] [D_c] \{h'\}. \qquad (3\text{-}23)$$

$[W']$ is a fluctuating cross-flow per unit length and h' is the enthalpy transported by the turbulent cross-flow.

Applying equation (3-12) to the subchannel control volume (one-dimensional), considering the relations (3-19) through (3-23), dividing by Δx and taking the limit when Δx approaches zero, the final form of the energy equation for a subchannel geometry becomes:

$$\underbrace{A\frac{\partial}{\partial t}\langle\langle \rho h \rangle\rangle_V}_{\substack{\text{rate change} \\ \text{of enthalpy}}} + \underbrace{\frac{\partial}{\partial x}\langle \rho u h \rangle_A A}_{\substack{\text{transport of enthalpy} \\ \text{by axial convection}}} + \underbrace{[D_c]^T \{\langle \rho v h \rangle_s s\}}_{\substack{\text{lateral energy transfer} \\ \text{due to cross flow}}} = \underbrace{[D_c]^T \{P_r \Phi H_r\} [D_r]\{T\}}_{\substack{\text{heat transfer from} \\ \text{the rods}}} +$$

$$\underbrace{[D_w]^T\{L_wH_w\}[D_w]\{T\}}_{\substack{\text{heat conduction}\\ \text{over unheated walls}}} + \underbrace{\frac{\partial}{\partial x}A\left\langle K_f\frac{\partial T}{\partial x}\right\rangle_A}_{\text{Axial heat conduction}} \underbrace{-[D_c]^T\left[\frac{sc\langle K_f\rangle}{L_c}\right][D_c]\{T\}}_{\substack{\text{transverse heat}\\ \text{conduction}}} - \underbrace{[D_c]^T[W'][D_c]\{h'\}}_{\substack{\text{heat transport due to}\\ \text{turbulent exchange}}}$$

(3-24)

The heat transfer coefficients as well as the geometric factors and turbulent mixing coefficients have to be evaluated by using empirical relationships.

3.2.3 Subchannel Axial Momentum Balance Equation

In order to write axial momentum balance equation following definitions have to used. In the equation (3-13) the solid surface integral is approximated by an empirical wall friction coefficient and a form loss coefficient. An axial drag force F_D proportional to the axial momentum flux is defined as:

$$F_D = \frac{1}{2}\left[\frac{f'\Delta x}{D_h} + K\right]\langle \rho u^2\rangle_A \cdot A \ , \tag{3-25}$$

where f' is the friction factor, D_h is the hydraulic diameter and K is the total loss coefficient.

In code COBRA-IV, the fluid-to-fluid viscous shear stress (turbulent momentum diffusion) is neglected since it is small compared to the wall shear forces. The turbulent momentum mixing is modeled in the same way as in the thermal energy mixing model, hence:

$$F_m = -C_T\Delta x[D_c]^T[W'][D_c]\{u'\}, \tag{3-26}$$

where u' is the axial velocity transported by the turbulent cross-flow, and C_T is a constant for compensating the imperfect analogy between turbulent transport of energy and momentum.

Other forces should be considered in the axial momentum equation: F_p, the net force due to pressure acting on the ends of control volume. The total force due to pressure on the control volume, F_P can be written as:

$$F_p = -A\frac{\partial}{\partial x}\langle P\rangle \,. \tag{3-27}$$

Applying equation (3-13) in to subchannel control volume (one-dimensional), employing the definitions given by (3-25), (3-26) and (3-27), dividing by Δx and taking limit when Δx approaches zero, the axial momentum balance can be written as:

$$\frac{\partial}{\partial t}\langle\langle \rho u\rangle\rangle_V A + \frac{\partial}{\partial x}\langle \rho u^2\rangle_A A + [D_c]^T\langle \rho uv\rangle_s s = -A\frac{\partial}{\partial x}\langle p\rangle_A - \frac{1}{2}\left(\frac{f'}{D_h} + \frac{K}{\Delta x}\right)\langle \rho u^2\rangle$$

$$-A\langle\langle \rho\rangle\rangle_V \cos\theta - C_T[D_c]^T[W'][D_c]\{u'\}, \tag{3-28}$$

θ is the subchannel axis orientation angle with respect to the vertical line. Since the fluid-to-fluid friction is negligible the third term in R.H.S. of the equation (3-13) considered equal to zero.

3.2.4 Subchannel Lateral Momentum Balance Equation

For the lateral momentum component, it has been assumed that the flow direction is determined by the gap orientation and that the cross-flow loses its identity

away from the gap. Therefore, equation (3-13) needs to be integrated only in the region of the influence of each gap. This is done by a modified control volume centered in the gap as it is shown in Figure (3-5). This control volume is surrounded by the fuel rods surfaces and by planes, g', joining the adjacent subchannel centroids and the fuel rod centerlines. The upper and lower surfaces of control volume, V' are closed by the flow area, A'. It should be mentioned that:

$$\int_{V'} dV' = \int_{V} dV \,,$$

and it is useful to define a pseudo length, l, such as $sl = A'$ with s the gap width and l approximately the distance between the centroids of the adjacent subchannels. The pressure loss through the gap is modeled by a global loss coefficient, k_G or (K_{ij}), which accounts for friction and drag caused by the flow area change. The total drag force F_d acting in the control volume is modeled as:

$$F_d = \frac{1}{2} k_G \langle \rho v^2 \rangle_s s \cdot \Delta x \quad . \tag{3-29}$$

In COBRA-IV neither fluid shear stress nor turbulent momentum diffusion is explicitly considered in the lateral direction.

The main driving force for cross-flow is the pressure imbalance between adjacent subchannels. It is modeled in the following manner:

$$F_P = s \cdot \Delta x [D_c] \{ \langle p \rangle_A \} \,. \tag{3-30}$$

The average pressure over the lateral surfaces, g', is approximated by the subchannel

area averaged pressure, $\langle p \rangle_A$.

The lateral momentum balance is formed by adding the momentum fluxes to the summation of forces. Then dividing by $\Delta x \cdot l$ and taking the limit when Δx approaches zero. This yields the subchannel differential equation for cross-flow as:

$$\frac{\partial}{\partial t}\langle\langle \rho v \rangle\rangle_{V'} + \frac{\partial}{\partial x}\langle \rho uv \rangle_{A'} s = \frac{s}{l}[D_c]\{\langle p \rangle_A\} - \frac{1}{2}\frac{s}{l}k_G \langle \rho v^2 \rangle_s . \qquad (3\text{-}31)$$

The *first term on the L.H.S.* of equation (3-31) is rate of change of lateral momentum, the *second term in the L.H.S* is the transverse momentum convected by the axial flow. The first term on the R.H.S. accounts for lateral pressure difference and second term of R.H.S. is a term for considering a lateral pressure loss. Also it can be seen that the missing terms from a fully three-dimensional system are the lateral cross products of velocity. The absence of these terms limits the application of COBRA-IV to those cases, in which complex three-dimensional circulation is negligible.

In COBRA-IV model, an attempt to preserve some of the identity of the cross-flow direction away from the gap was done by introducing the so-called G_s. This term shows the transverse momentum convected by transverse flow and it is modeled as follows:

$$G_s = C_s [D_c][D_c]^T \left\{ (N) \frac{s}{l} \langle \rho v^2 \rangle_s \cos \Delta\beta \right\},$$

where G_s is transverse momentum convected by the transverse flow, C_s is a coefficient to address the fact that coupling between the considering gaps is incomplete and should have a value less than unity, N is a binary value equal to -1 when the positive cross-flow

is out of the subchannel and +1 when the positive cross-flow is to the subchannel. The angle $\Delta\beta$ is the difference angle between the reference angle of the communicating gap and the gap of interest. This term is not used in the present work because the number of the subchannels is limited to two. Furthermore in the cases with the more than two subchannels the accuracy of this term has yet to be proven.

3.3 Numerical Solution

In order to solve the subchannel equations further assumptions have to be considered:

- The liquid and vapor are in thermal equilibrium.
- The phase velocities and volume fractions are uniformly distributed within the control volume.
- Quality of the axial and lateral flows are equal, allowing unique definition of flowing enthalpy and quality in both lateral and axially direction.

Since Δx is considered small enough that the volume and the area averages are equal. Thus:

$$m \equiv A\langle \rho\, u\rangle = A\,\langle\langle \rho\, u\rangle\rangle, \text{ and } W \equiv s\,\langle \rho\, v\rangle = s\langle\langle \rho\, v\rangle\rangle\ , \qquad (3\text{-}32)$$

with m is the axial mass flow rate and has dimension of $[kg/s]$ and W' is the net cross-flow mass per unit length flow between two interconnected subchannel and has dimension of $[kg/m.s]$.

The flowing enthalpy and flowing quality are defined as follows:

$$h^* = \frac{\langle \rho u h \rangle}{\langle \rho u \rangle} = \frac{\langle \rho v h \rangle}{\langle \rho v \rangle} \quad , \tag{3-33}$$

$$x^* = \frac{\langle \alpha \rho_v u_v \rangle}{\langle \rho u \rangle} = \frac{\langle \alpha \rho_v v_v \rangle}{\langle \rho v \rangle} \quad , \tag{3-34}$$

where u is the axial velocity, v is the lateral velocity and the subscript v indicates the vapor phase. The continuity equation (3-18) can be rewritten directly in terms of ρ and m, and W', which are the density [kg/m^3], mass flow rate [kg/s], and cross-flow mass per unit length [$kg/m.s$] respectively:

$$A\frac{\partial}{\partial t}\rho + \frac{\partial}{\partial x}m + [D_c]^T[W] = 0 \tag{3-35}$$

Using the definition of the flowing enthalpy (Eq. 3-33), the energy equation (3-24) can be written as:

$$A\frac{\partial}{\partial t}\rho h + \frac{\partial}{\partial x}m h^* + [D_c]^T[Wh^*] = Q, \tag{3-36}$$

where Q is heat transfer from all sources as they are modeled in the R.H.S of equation (3-24). Furthermore, multiplying continuity equation (3-35) by h^*:

$$Ah^*\frac{\partial}{\partial t}\rho + h^*\frac{\partial}{\partial x}m + h^*[D_C]^T[W] = 0,$$

and subtracting it from the energy equation (3-36), we can write:

$$A\left(\frac{\partial}{\partial t}\rho(h - h^*) + \rho\frac{\partial h}{\partial t}\right) + m\frac{\partial}{\partial x}h^* + [D_C]^T[Wh^*] - h^*[D_C]^T[W] = Q. \tag{3-37}$$

For the linear momentum equation, by using the definition of the momentum velocity, u^* as:

$$u^* = \frac{\langle \rho u^2 \rangle}{\langle \rho u \rangle} \quad ,$$

and considering a uniform phase distribution, the axial momentum balance equation (3-28) can be written as:

$$\frac{\partial m}{\partial t} + \frac{\partial m u^*}{\partial x} + [D_c]^T W u^* + A\frac{\partial p}{\partial x} = F \, , \tag{3-38}$$

where F is the sum of all forces acting on the control volume as they are modeled in the R.H.S of equation (3-28). Similarly the transverse momentum equation can be written as:

$$\frac{\partial}{\partial t} W + \frac{\partial (W u^*)}{\partial x} = C \, , \tag{3-39}$$

where C accounts for all lateral forces as they are modeled in the R.H.S of equation (3-31).

Finally, to rewrite the conservation equations in appropriate form as required for their discretization, two other definitions are necessary. The first is ψ [kg/m^3], for replacing the void fraction and flowing quality and consequently slip ratio by using the void and quality definitions:

$$\psi = \rho_l x^* (1-\alpha) - \rho_v \alpha (1-x^*) \, , \tag{3-40}$$

and the second is the momentum specific volume, v^* [m^3/kg], which is related to the void fraction and flowing quality, as follow:

$$v^* = \frac{(1-x^*)^2}{\rho_l(1-\alpha)} + \frac{(x^*)^2}{\rho_v \alpha} \,. \tag{3-41}$$

It should be noted that the function ψ permits us to relate the static enthalpy and the flowing enthalpy. The other way of defining Ψ is :

$$\psi = \frac{\rho\,(h^* - h)}{(h_v - h_l)} \,. \tag{3-42}$$

Using these definitions in equations (3-35), (3-37), (3-38), and (3-39), the desired form of the conservation equations becomes:

Mass:

$$A\frac{\partial}{\partial t}\rho + \frac{\partial}{\partial x}m + [D_c]^T[W] = 0 \,, \tag{3-43}$$

Energy:

$$A\left(\rho - h_{fg}\frac{\partial \psi}{\partial h}\right)\frac{\partial h}{\partial t} + m\frac{\partial h^*}{\partial x} + [D_c]^T\{Wh^*\} - h^*[D_c]^T\{W'\} = Q \,, \tag{3-44}$$

Axial Momentum:

$$\frac{\partial}{\partial t}m + 2m\frac{v^*}{A}\left(-A\frac{\partial \rho}{\partial t} - [D_c]^T[W]\right) + m^2\frac{(\partial v^*/\partial A)}{\partial x} + [D_c]^T\{u^*W\} = F \,, \tag{3-45}$$

Transverse Momentum:

$$\frac{\partial}{\partial t}W + \frac{\partial}{\partial x}(u^* W) = C \,, \tag{3-46}$$

Equation of state:

$$\rho = \rho(h, p^*) \quad , \tag{3-47}$$

where p^* is a reference pressure. Equations (3-44) to (3-47) are solved numerically in COBRA-IV.

3.3.1 Numerical Schemes

Two numerical solution techniques are used in COBRA-IV to solve the preceding system of subchannel equations. The first one consists of the implicit scheme very similar to that used in COBRA-IIIC [Rowe, 1973] and the second one is based on an explicit scheme specially designed for fast transient calculations. The implicit procedure provides a direct solution for steady state flow and therefore it has relatively limited capability. The implicit scheme can only be used to the cases with positive axial flow and very low cross-flows. The explicit solution removes the positive flow restriction however, it is limited to small time steps. It is used as an exclusive solution for transient problems and it can accept a steady state solution obtained from the implicit calculation as the initial conditions. In COBRA-IV two-phase slip ratio model, along with several options for the void-quality relation and two-phase friction multiplier in the axial direction are only available in implicit solution. In both numerical methods used by COBRA-IV the two following assumptions are considered: first, in both scheme, the reference pressure approach is used and second, the local fluid density is assumed to be

a function of the local enthalpy and a spatially uniform reference pressure. To solve subchannel equations, equations (3-43) through (3-47) must be recast in terms of five variables:

- m is axial mass flow rate,
- W is lateral mass flow rate per unit axial length (cross-flow),
- h is mixture static enthalpy or h^* as flowing enthalpy,
- ρ is mixture density and
- p is the pressure.

3.3.2 Implicit Solution

Figure 3.6 shows the spatial locations of the variables on the mesh. The superscript (*) is used to denote quantities which are convected by the flow; superscript (n) identify previous time step (no superscript implies in present time); (~) identifies values calculated at the actual time but previous iteration. Applying the following definitions and notations:

$\bar{A}_j = \frac{1}{2}(A_j + A_{j-1})$: average flow area,

$\bar{k}_{fj} = \frac{1}{2}(k_{fi} + k_{fl})$: average subchannel gap fluid thermal conductivity, where i and l are the adjacent subchannels,

$\bar{H}$: rod average heat transfer coefficient defined by $\frac{\sum_{i=1}^{n} H_i \Phi_i}{\sum_{i=1}^{n} \Phi_i}$,

n : the number of subchannels adjacent to rod,

T : subchannel temperature,

T_R : rod surface temperature,

T_w : temperature of conducting wall,

$\bar{m} = \frac{1}{2}(m_j + m_{j-1})$: average mass flow rate,

The discretized forms of subchannels equations are:

Continuity:

$$\frac{1}{\Delta t}\bar{A}_j\left(\rho_j - \rho_j^n\right) + \frac{m_j - m_{j-1}}{\Delta x} + [D_c]^T[W_j] = 0, \qquad (3\text{-}48)$$

Energy:

$$\frac{1}{\Delta t}A_j\left(\rho_j^n - h\overbrace{\frac{\partial \psi}{\partial h^*}}^{cte.}\right)\left(h_j^* - h_j^{*n}\right) + \frac{1}{\Delta x}m_{j-1}\left(h_j^* - h_{j-1}^*\right) + [D_c]^T\left\{h_j^*\,\tilde{W}_j\right\} - h_j^*\,[D_c]^T\left[\tilde{W}_j\right]$$

$$= [D_R]^T\left[P_r\,\Phi\bar{H}\right][D_r]\begin{Bmatrix} T \\ T_r \end{Bmatrix}_j + \frac{1}{(\Delta x)^2}\left(kA_j - \left(\bar{T}_{j+1} - \tilde{T}_j\right) - kA_{j-1}\left(\bar{T}_j - \tilde{T}_{j-1}\right)\right) +$$

$$[D_w]^T\left[L_w\bar{H}_w\right][D_w]\begin{Bmatrix} T \\ T_w \end{Bmatrix}_j - [D_c]^T\left[\frac{C\bar{s}k}{L_c}\right][D_c]\{T_j\} - [D_c]^T[W'][D_c]\{h'_j\}, \qquad (3\text{-}49)$$

Axial Momentum:

$$\frac{m_j - m_j^n}{\Delta t} - 2\bar{m}\frac{v_j^*}{A_j}\left[A_j\left(\frac{\rho_j - \rho_j^n}{\Delta t}\right) + [D_c]^T[W_j]\right] + m_{j-1}^2\frac{\left(\frac{v^*}{A}\right)_j - \left(\frac{v^*}{A}\right)_{j-1}}{\Delta x} + [D_c]^T\{u_j^*\,W_j\}$$

$$= -\bar{A}\left(\frac{p_j - p_{j-1}}{\Delta x}\right) - \bar{A}\,k_L\,m_j^2 - [D_c]^T[W'][D_c]\{u'_j\} - \bar{A}\,\rho_j\cos\theta, \qquad (3\text{-}50)$$

Transverse Momentum:

$$\frac{W_j - W_j^n}{\Delta t} + \frac{(u^* W)_j - (u^* W)_{j-1}}{\Delta x} = \frac{s}{l}[D_c]\{p_{j-1}\} - \frac{s}{l} C_j W_j \,, \tag{3-51}$$

with :

$$k_l = 0 \cdot 5 \frac{v_l f \phi}{2 D_h A_j^2} + \frac{k v^*}{2(\Delta x) A_j^2} \quad \text{and} \quad C_j = \left\{ \begin{array}{lll} 0.5 \frac{K_G}{\rho^* s^2} & \text{if} & |W| \geq 0.001 \\ 0.001 & \text{if} & |W| < 0.001 \end{array} \right\}. \tag{3-52}$$

The following comments can be made regarding on the equations (3-48) through (3-50):

1- The time derivatives are approximated by first order backward differences.

2- All major variables except, those actually forming the time difference are assumed to be at the current time level and must be solved simultaneously.

3- The spatial derivatives are approximated by first order backward differences.

4- Donor cell differencing is used for convected quantities such as h_j^*, v_j^* and u_j^*.

5- Donor cell difference is simplified in the axial direction by assuming a positive flow.

6- The total pressure difference is derived by integrating the axial pressure gradient which allows any pressure disturbance, such as those caused by non-uniform voiding to be propagated in the "upstream direction". This procedure requires an additional external iteration which makes the conditions be fully implicit.

7- The energy equation for the fluid is solved simultaneously with the energy equation for conducting wall.

The momentum equations (3-50) and (3-51) are coupled to form an expression that is solved for cross-flow at j in terms of the lateral pressure difference and the axial flows at j-1 position. Then the new axial flows at j can be found via the continuity equation. The axial momentum can be rewritten as:

$$\{p_{j-1}\} = \{p_j\} - \{F_j\}(\Delta x) - [R_j]\{W_j\}(\Delta x) \quad , \tag{3-53}$$

where $[R_j]$ contains all the coefficients of $\{W_j\}$ in equation (3-50) and $\{F_j\}$ consists all the remainder terms in equation (3-50).

The lateral momentum equation can be written in the following form:

$$[D_c]\{p_{j-1}\} = [Rp]\{W\} + \{Fp\} \tag{3-54}$$

where [Rp] and [Fp] are defined as:

$$[Rp] = \left[\frac{1}{(s/l)}\left(\frac{1}{\Delta t} + \frac{\{u_j^*\}}{\Delta x}\right) + C_j\right],$$

$$[Fp] = -\frac{s}{l}\frac{W_j^n}{\Delta t} + \frac{[u^* W]_{j-1}}{\Delta x} .$$

Multiplying equation (3-53) by $[D_c]$ and combining it with the equation (3-54) results in a set of simultaneous linear equations which are solved for the lateral flow distribution W at each axial location as:

$$[AAA]\,[W_j] = \{b_j\}, \tag{3-55}$$

where:

$$[AAA] = [D_c][R_j]\,\Delta x + [Rp] \ , \tag{3-56}$$

and

$$\{b_j\} = [D_c]\,\{p_j - F\Delta x\} - [Fp] \ . \tag{3-57}$$

It should be mentioned that the solution is considered to be converged when the maximum change in cross-flow, axial flow and enthalpy are simultaneously less than specified input values between successive iterations. The overall solution scheme consists of an external iterative sweep of the computational mesh from inlet to exit in which local values of h, ρ, W, m and p are updated at each axial level in turn. This involves two additional internal iterative solutions for the enthalpies in all subchannels and the cross-flows in all gaps at each axial level. The boundary conditions are a specified inlet flow and enthalpy distribution, inlet cross-flow equal to zero and uniform pressure (no lateral pressure difference) at the exit of the subchannel. A uniform overall pressure drop may be specified instead of the inlet flow.

The solution algorithm for the implicit procedure can be described as follows:

1) In steady state, the initial values of h, W and m at axial level j are defined as the values resulting the solution at j-1 when j>2 and as the specified inlet boundary values when j=2.

2) The subchannel pressures are then calculated. Only the pressure differences between subchannels is taken into account during the iteration and its initial value is defined as $[D_c]\{p_i\}=0$ (no pressure difference).

3) The fuel rod model is solved over the entire mesh using surface heat transfer coefficients and subchannel temperatures from the preceding iteration. Before the first iteration, these quantities are not available so the fuel model is bypassed and the input value of heat flux is supplied directly to the energy equation. After the first external iteration, the fuel model supplies fuel surface temperatures that are used with the surface heat transfer coefficients to calculate the energy input to the fluid.

4) The first operation at each axial level during the external channel iteration is the

solution of the temperature of the flow field.

5) The new enthalpies provide new densities in each subchannel via the equation of state.

6) The updated densities are used to evaluate the coefficients of equation (3-55). At this step, new heat transfer coefficients are also calculated for use in the fuel model before the next external iteration.

7) The cross-flows which resulted from the iterative solution of equation (3-55) are used in the continuity equation (3-48) with the new densities and the axial flows at the preceding level to compute the new axial flows. This completes the update of the flow field at axial level j.

8) Equation (3-57) is solved using the new cross-flows to provide a new estimate of the pressure difference between the subchannels at level j-1. This step acts to propagate the flow disturbance upstream because the change in j-1 will cause a corresponding change at the level j-2 in the next external iteration.

9) After all axial levels have been calculated, the convergence criteria are checked to determine if another external iteration is still required. If another iteration is necessary, and the inlet flow is specified, the solution proceeds directly to the fuel model and the external channel iteration is repeated.

10) If the overall pressure drop is used as the boundary condition, the inlet flows are then adjusted after each iteration, to satisfy this boundary condition.

3.3.3 Explicit Solution

The primary objective of the explicit solution scheme is to provide a numerical solution for transient thermalhydraulic analysis. For this propose the ACE (Advanced Continuous-fluid Eulerian) method which is an extension of the ICE (Implicit

Continuous Eulerian) technique [Harlow and Amsden, 1971] is used. The traditional use of ICE and its successors employs on an explicit energy equation where flows and energies from the previous time step are used to form the convective terms. In many low-speed two-phase flow applications, where density gradients exist, the explicit treatment of the convective terms can lead to severe computational difficulties, such as steam water oscillations in reflood phenomenon. The ACE method eliminates this problems by combining the energy equation implicitly with the continuity equation through the equation of state. The resulting expression for the flow divergence is solved simultaneously with the explicit momentum equations.

Since the explicit solution scheme is not going to be used in the present work, only an abbreviated form of the discretized equations are presented. Figure 3.7 shows the location of the major variables in the computational cell.

Mass conservation equation:

$$\bar{A}_j \frac{\Delta x}{\Delta t}(\rho_j - \bar{\rho}_j) + m_{j+\frac{1}{2}} - m_{j-\frac{1}{2}} + \Delta x [D_c]^T W_j = 0, \tag{3-58}$$

Energy conservation equation:

$$\bar{A}_j \frac{\Delta x}{\Delta t}\left(\rho h_j - \rho h_j^n\right) + m h^*_{j+\frac{1}{2}} - m h^*_{j-\frac{1}{2}} + \Delta x [D_c]^T W h_j^* = Q_j^n, \tag{3-59}$$

Axial momentum conservation equation:

$$m_{j+\frac{1}{2}} = m^n_{j+\frac{1}{2}} - \Delta t \frac{\bar{A}_{j+\frac{1}{2}}}{\Delta x}\left(p_{j+\frac{1}{2}} - p_j\right) - \Delta t F^n_{j+\frac{1}{2}}, \tag{3-60}$$

Lateral momentum conservation equation:

$$W_j = W_j^n + \Delta t \frac{S}{l}[D_c]p_j - \Delta t\, G_j^n \ . \tag{3-61}$$

All terms explicit in time have been combined into the variables Q^n, F^n and G^n respectively. All other not specifically supercripted by the symbol n, i.e., $m_{j+1/2}$, W_j and h_j^* are assumed to be new implicit values in time but explicit in space.

Also, an equation of state is necessary for assuming a uniform reference pressure, p^*, over the entire computational mesh, however the reference pressure may be a function of time. The reference pressure concept is justified only if the spatial pressure changes are small compared to the reference pressure in each cell. Hence:

$$\rho = \rho(h, p^*) \tag{3-62}$$

By inverting the state equation, all the enthalpies in equation of energy (3.59) and (3.49) can be expressed in terms of the specific volume, v;

$$h_j^* = h_o + \left(\frac{\partial h}{\partial v}\right)_p (v_j - v_o) \tag{3-63}$$

Where h_o and v_o can be considered constant. Using (3-63) in (3-60) yields the following result:

$$m v_{j+\frac{1}{2}}^* - m v_{j-\frac{1}{2}}^* + \Delta x [D_c]^T W v_j^* - \left(\frac{\partial v}{\partial h}\right)_p Q_j^n = \left(v_o - \left(\frac{\partial v}{\partial h}\right)_p\right) \cdot [M] \ , \tag{3-64}$$

where M is the left side of equation (3-58). Therefore, the right side of equation (3-64) is reduces to zero. The left side of equation (3-64) is the basis of the ACE method. It simply relates the divergence of the velocity field to the volumetric expansion caused by heat transfer. The solution scheme begins a time step by evaluating the source terms Q, F and G and obtaining initial estimates for the next flows m and W', based on pressure and flows from the previous time step. These tentative flows will not in general satisfy equation (3-64) but will yield a residual error, E_j, as follows:

$$mv^*_{j+\frac{1}{2}} - mv^*_{j-\frac{1}{2}} + \Delta x\,[D_c]^T W v^*_j - \left(\frac{\partial v}{\partial h}\right)_p Q^n_j = E_j \ . \tag{3-65}$$

The objective is to reduce this residual error to zero in all the computational cells. This is done by adjusting the pressures and flows in each cell sequentially in an iterative procedure developed by Hirt and Cook [1972]. The pressure change necessary to reduce E_j to zero in any computational cell is computed by using the total derivative of E with respect to pressure.

After calculating all necessary pressure changes, the remaining steps serve to update the flows, density and enthalpy in the cell. The new flows are found via the momentum equations. These new flows are then used in the continuity equation to find the new density (and specific volume) and, finally, a new enthalpy is found from the equation of state using the new density and the reference pressure. This procedure is repeated over all computational cells until the maximum error in the mesh is less than a specified error criterion. The solution is then considered converged and the calculations for the time step are completed.

3.4 Constitutive Equations

Since, the character of the final solution depends on the accuracy of the constitutive relations, a variety of empirical relations are available in COBRA-IV. Among them are equation of state of the fluid, i.e., a relation between fluid density and enthalpy, subcooled and saturated liquid property tables, void-quality relationship, superheated steam properties, heat transfer correlations for rod to coolant and coolant to wall connections and critical heat flux correlations. Since, studying the mixing phenomena between the interconnected subchannels is the objective of the present work, a detailed review of mixing modeling in COBRA-IV will be presented.

3.4.1 Turbulent Mixing Modeling

The model used for lateral turbulent energy and momentum exchange is based on a fluctuating equal mass exchange between adjacent subchannels. This is expressed on a fluctuating cross-flow per unit length, W', which is assumed to be proportional to the gap width, s, and the average axial mass flux according to the following form:

$$W' = \beta s \bar{G}, \tag{3-65}$$

where:

$$\bar{G} = \frac{G_i A_i + G_j A_j}{A_i + A_j}, \tag{3-66}$$

and A_i and A_j are the axial flow areas of the two adjacent subchannels and β is a turbulent mixing factor. This turbulent mixing model is based on an equal mass exchange

between two adjacent subchannels. This approach cannot produce a net flow change in either subchannel. However, if the enthalpies and velocities of two subchannels are different, a net exchange of energy and momentum will occur, hence:

$$F_h = \frac{W'}{s}\left(h_i^* - h_j^*\right), \tag{3-67}$$

$$F_m = F_t \frac{W'}{s}(U_i - U_j), \tag{3-68}$$

where F_h is the net turbulent diffusion of enthalpy, F_m is turbulent diffusion of momentum and F_t is a correction factor to take into account the difference between energy and momentum turbulent transport.

The Diffusive energy flux from channel i to j can be written as:

$$F_h = \frac{\varepsilon_t}{l}\rho\,(h_i - h_j), \tag{3-69}$$

where ε_t is the eddy diffusivity coefficient and l is an appropriate mixing length usually considered to be the centroid-to-centroid distance. By equating (3-69) and (3-67), the following relationship can be obtained:

$$W' = \varepsilon_t \rho \frac{s}{l}. \tag{3-70}$$

Also, by using equation (3-65) the following relation can be obtained:

$$\beta = \frac{\varepsilon_t}{l}\frac{\bar{\rho}}{\bar{G}}, \tag{3-71}$$

where $\bar{\rho}$ is the average density in the two adjacent subchannels.

The turbulent mixing coefficient, β, can be introduced as a constant parameter or can be calculated by using one of the following relationships:

$$\beta = a\,(Re)^{b},$$

$$\beta = a\,(Re)^{b}\,\frac{\bar{D}_h}{s} \text{ and}$$

$$\beta = a\,(Re)^{b}\,\frac{\bar{D}_h}{l}, \tag{3-72}$$

where a and b are input constants and $\bar{D}_h$ is the hydraulic diameter based on the sum of cross-sectional flow area and wetted perimeters of the adjacent subchannels and the Reynolds number, *Re, is* defined as:

$$Re = \frac{\bar{G}\,\bar{D}_h}{\bar{\mu}}, \tag{3-73}$$

where $\bar{\mu}$ as the average viscosity.

It is also possible to introduce β in a tabular form as a function of the flow quality evaluated from the mixed mean enthalpy of the two subchannels. This tabular form permits the dependence of the turbulent mixing coefficient, β, on the flow regime to be considered.

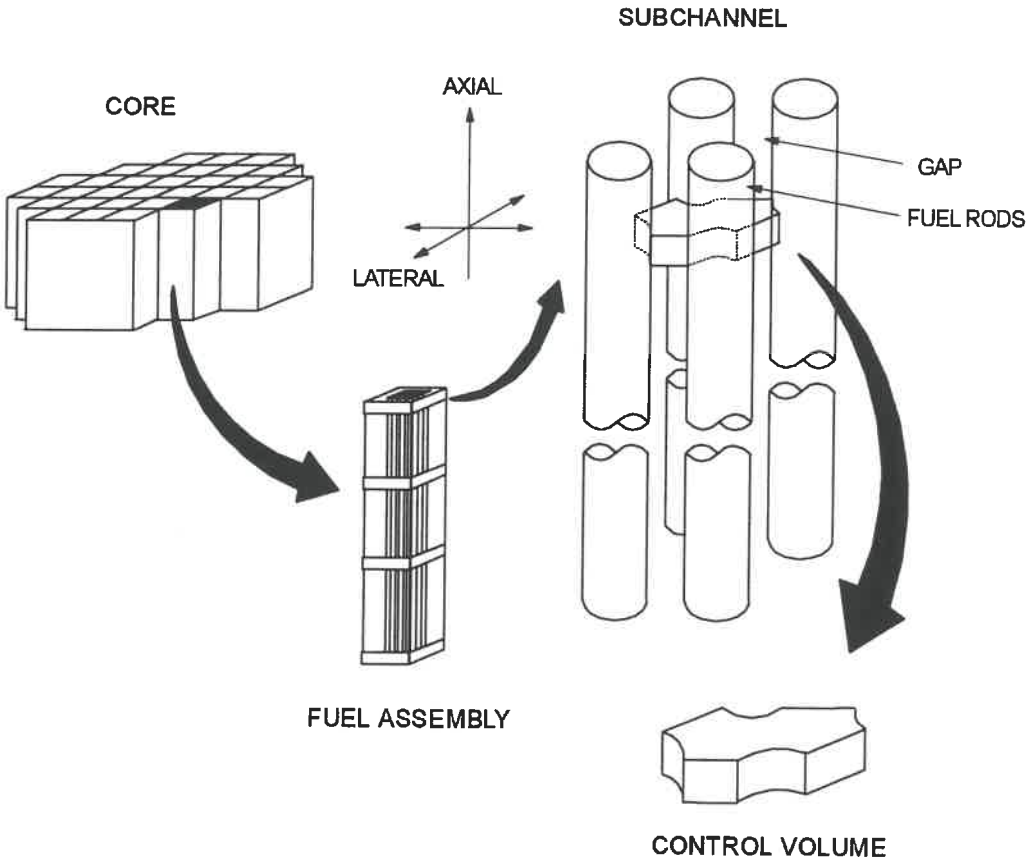


Figure 3.1: Relation of Subchannel Control Volume to Reactor Core

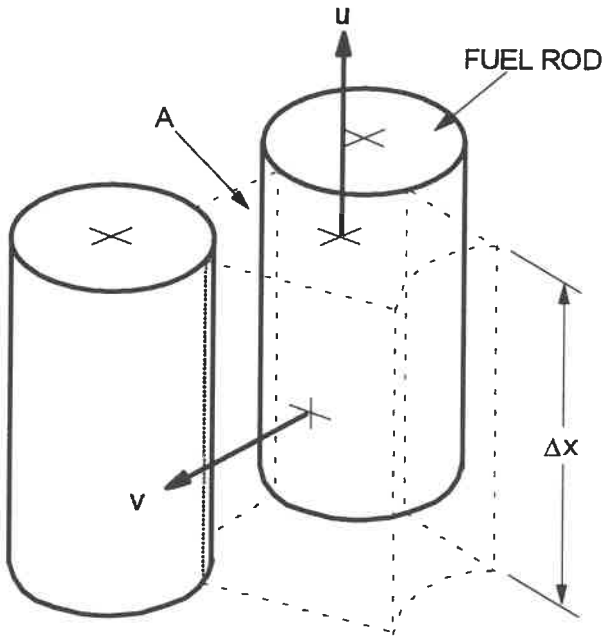


Figure 3.2: Subchannel Control Volume

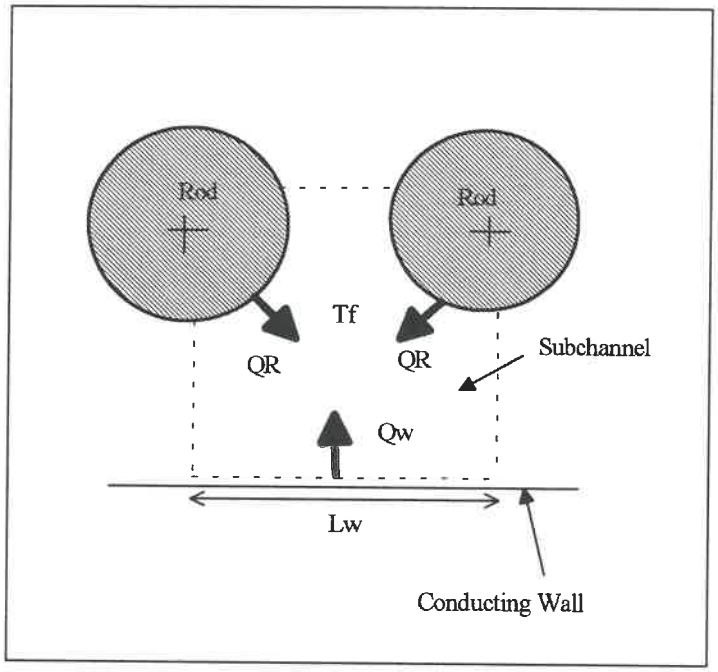


Figure 3.3: Rod and Wall Surface Heat Transfer Geometry

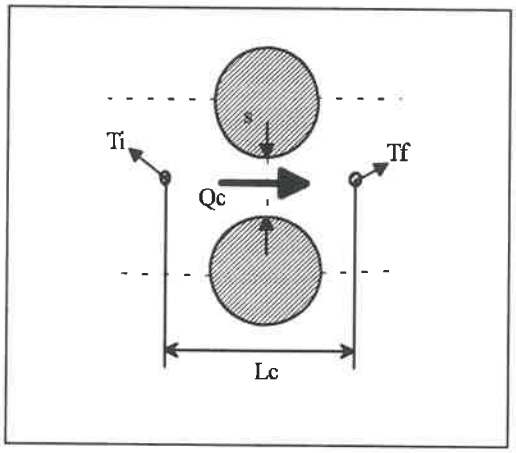


Figure 3.4: Lateral Heat Conduction Geometry

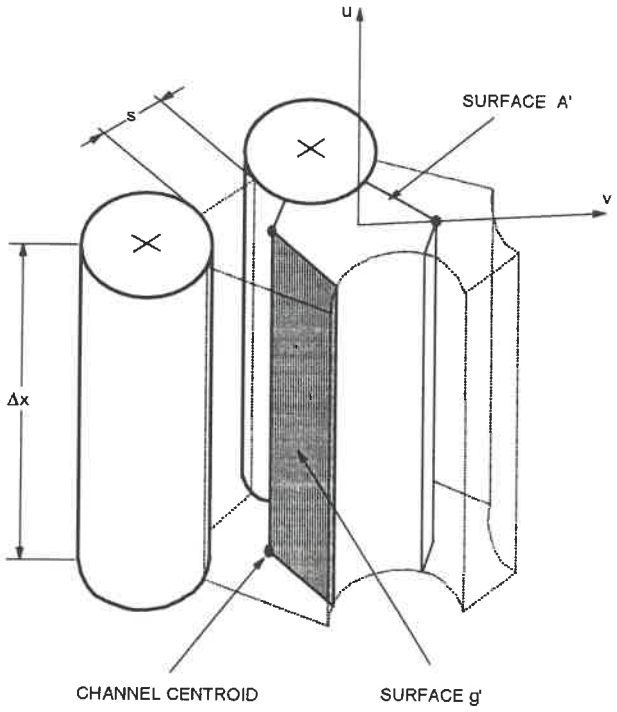


Figure 3.5: Control Volume for Lateral Momentum

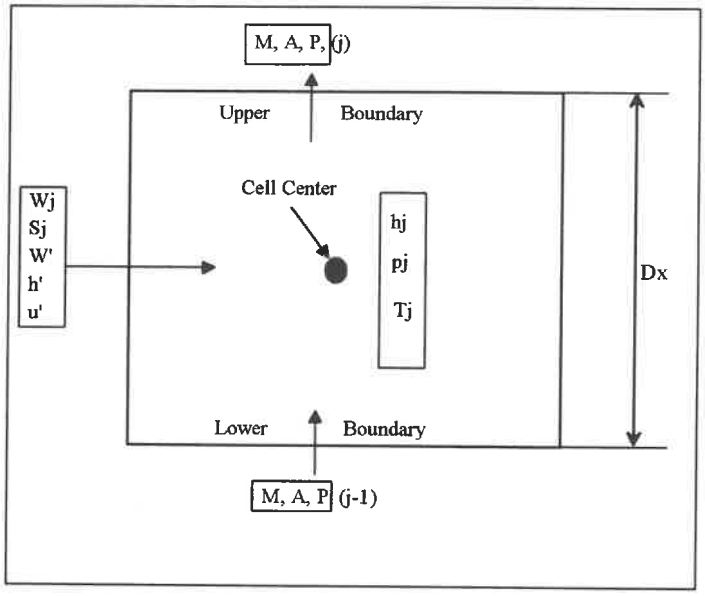


Figure 3.6: Placement of the Variables for Implicit Solution

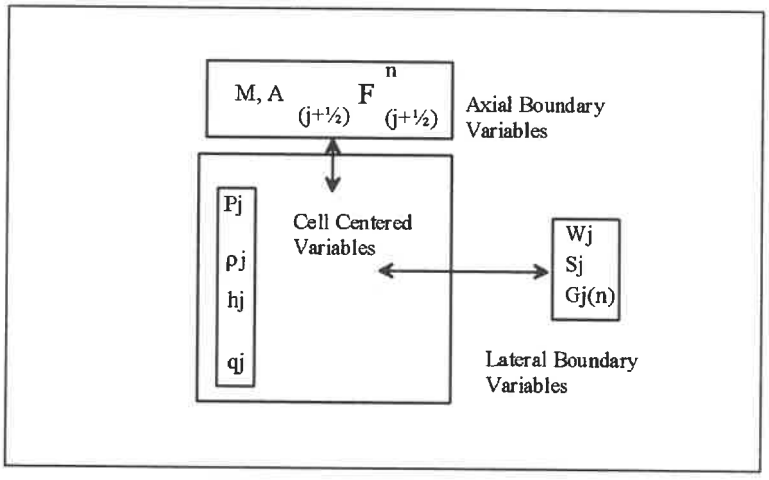


Figure 3.7: Placement of Major Variables on the Computation Mesh

CHAPTER 4

EXPERIMENTAL APPARATUS AND PROCEDURES

The objective of this chapter is to describe the experimental apparatus and procedures used to obtain the data which will be used to compare against the predictions of the COBRA-IV-I subchannel code. The experimental apparatus and procedures presented here, are based on the previous work carried out by Tapucu et al. [1990].

4.1 Experimental Apparatus

The apparatus used to perform experiments on two interconnected subchannel under two-phase flow conditions is shown in the Figure 4.1. A cross sectional view of the test section, representing the two interconnected subchannel is shown in Figure 4.2. Each half of the test section is machined from an acrylic block with a specially designed cutter to obtain the desired profile with very high accuracy. The gap clearance between the rods can be varied at will. For the experiments analyzed the gap clearance is 1.6 *mm*. The relevant geometrical parameters for the test section are given in the Table 4.1.

The water is supplied to the test section by a pump connected to a constant head water tank. The flow rate in each subchannel of the test section is adjusted with valves in each branch and a corresponding bypass circuits. The air is supplied from the mains of the laboratory and regulated by a relieving type regulator.

TABLE 4.1 Geometric Parameters of the test section

Rod radius	8.8 ± 0.1 *mm*
Gap clearance	1.66 ± 0.05 *mm*
CROSS-SECTIONAL AREA	
Subchannel A	116.9 ± 2 mm^2
Subchannel B	115.6 ± 2 mm^2
HYDRAULIC DIAMETERS	
Subchannel A	7.62 ± 0.2 *mm*
Subchannel B	7.62 ± 0.2 *mm*
Centroid-to-centroid distance	18.7 ± 0.1 *mm*
Interconnection length	1320.8 ± 5 *mm*

The air-water mixture at a pressure close to atmospheric is used as the working fluid. The mixing of the liquid and the gas is achieved in two phase mixers placed at the inlet of each subchannel. A cross sectional view of the phase mixer is given in Figure 4.3. The incoming water is gradually accelerated by reducing the flow area with a solid cone mounted in the water line right at the inlet of the mixer. The conical element is followed by a cylindrical one to keep the velocity of the water high over a distance of 25.4 *mm*. The injection of the air through the sintered brass wall of the air chamber is done mainly in this high water velocity region. This set-up ensures an adequate mixing of the air and the water. Each branch of the supply system is equipped with its own phase mixer. At the outlet of the test section, the two-phase mixtures flow into an air-water separator tank which consists of two compartments: one for each subchannel.

The compartments are open to the atmosphere and their water levels are kept constant.

4.2 Instrumentation

The flow parameters which have been measured during the experiments are: the liquid and gas flow rates at the inlet to the test section, the void fraction and the pressure drop along the test section. This section is devoted to detailed explanation of the instruments used to measure these parameters.

4.2.1 Liquid and Gas Flow Rates

The water flow rates at the inlet of each of the subchannels are measured with "Flow Technology" turbine flowmeters. According to the manufacturer's specifications, the accuracy of the flowmeters is better than ±1% of the reading. This feature is also confirmed by our own verifications tests performed by weighing the water collected in a tank over a predetermined time interval. The flow rate of the air is measured with "Brooks" rotameters. To cover a wide range of flow rates, a set of three rotameters is used for each subchannel. For a given test, the pressure of the air at the outlet of the rotameter is kept constant. The accuracy of the rotameters is ±1% of full scale.

4.2.2 Void Fraction Measurement

In the past 30 years, several techniques have been developed for the measurement of the void fraction. However, the application of each technique is usually limited to a specific problem. All of the existing methods can be classified as providing either local or spatially averaged measurements.

The local methods, such as conductivity probes, film anemometers and optical fiber probes can give detailed information on the phase distribution. However, these probes have the drawback of introducing substantial perturbations in the flow patterns, especially when they are used in channels having a small flow area.

The average void fraction on a line or a surface is generally obtained by absorption of X- or γ-rays. The volume averaged void fraction is usually measured by quick closing valves and by impedance gauges. The neutron absorption or scattering technique becomes a sensitive and powerful means of measuring the volume averaged void fraction when two-phase flow is in a steel pipe with thick walls.

One of the objectives of the present work is to obtain detailed information on the axial distribution of the average void fractions in the subchannels along the interconnected region. To fulfill this requirement, the void fraction at several axial locations should be measured quickly and simultaneously. Because of the simultaneous nature of the measurement, none of the above void fraction measuring techniques, with the exception of the impedance technique, is suitable for this research. Besides the advantage of simultaneous measurement, direct reading and relatively low degree of uncertainty in the void fraction determination, the impedance technique has some disadvantages. It requires lengthy and complex calibration of the gauges, and has rather poor accuracy at high void fractions (of 70% or more) and finally, the response depends quite strongly on the temperature of the water and on the amount of dissolved chemicals in the water supply.

As has already been pointed out, the impedance technique is quite suitable for the purpose of this research. With this technique, the values of the void fraction are

obtained by measuring the admittance between two parallel silver electrodes (void gauges). The electrodes, cylindrical in shape and 4.75 *mm* in diameter, were embedded in the acrylic blocks which form the test section and machined at the same time as the blocks to give the subchannel profile (Figure 4.4). The sealing of the electrodes was ensured by gluing them to the acrylic block. Set-crews were also used to ensure that the electrodes to be firmly held in the block when flow pressure was applied on the wall of the subchannels. There were 10 pairs of electrodes in each subchannel: two pairs before the beginning of the interconnected region and eight pairs in the interconnected region. The position of the electrodes are given in Figure 4.5. The electrodes are wired to a void monitor and a data acquisition system (Figure 4.6). A detailed block diagram of the electronic circuit associated with each electrode is given in Figure 4.7. Since the electrodes are immersed in the same conductive media, special care should be taken to ensure that no cross conduction (resistive or reactive) occurs between measuring subchannels. The electric isolation of each measuring subchannel is achieved by coupling transformers excited from a common low impedance 5 kHz oscillator. Also, in order to avoid possible current flow through the common power supply, differential input stages with high common mode rejection rates and a very high input impedance are used. Since the voltage across the resistance R mounted between the secondaries of the coupling transformer, Figure 4.7, is a direct function of the current through it, it may be assumed that this voltage is also proportional to the admittance between the electrodes, i.e., a function of the liquid fraction between them. To correct for variations in the conductivity of the water due to temperature changes a separate reference subchannel is used to continuously monitor the admittance of the inlet water (Figure 4.6 and 4.7). The response of the main channels is then divided by the response of the reference and the errors introduced by the changes mentioned above are substantially reduced.

The void monitor is connected directly to a data acquisition system (Figure 4.6). It shows the block diagram of the void fraction measurement system and its data acquisition unit. A software package has also been developed to handle all the void channels simultaneously. The final results, which consist of a large amount of data (300 points per subchannel obtained with a sampling of time 5 *ms*), were averaged and processed as output files.

4.2.3 Pressures

The pressure along subchannel "A" and pressure differences between the subchannels are measured with "Sensotec" pressure transducers. The location of the pressure taps during the calibration and experiments with interconnected subchannels are given in table 4.2.

Table 4.2 Location of the Pressure Taps During the Calibration and Experiments

Distance from P1 (*cm*)	P1	P30	P5	P7	P11	P15	P20	P27
Calibration experiments	not used	not used	not used	45.765	66.105	86.439	not used	not used
interconnected subchannel experiments	0	25.422	35.595	45.765	66.105	86.439	111.85	147.44

Figure 4.5 shows the locations at which the pressures where measured. After conditioning, the electrical signals from the pressure transducers are sent to the data acquisition system. This allows the measurement of the pressure over a predetermined

time interval (usually 50 seconds) and the determination of its mean value.

To prevent gas penetration into the connection line between the pressure taps and the pressure transducers, small bubble separation pots were installed on the lines as is shown in the Figure 4.8. The line coming from the pressure tap is connected to the top of the pot and the one going to the main pressure line is connected to the bottom of the same pot. This system limits the penetration of the bubbles to only the top of the pot when the toggle valve is opened to connect a given pressure tap to the main pressure line. The accumulation of air bubbles lowered the level of the water in the pot slightly. However, this level stabilized itself very quickly and an accurate measurement of the pressure was then possible. The pressure in the subchannel "A", 254.22 *mm* upstream of the beginning of the interconnection, is measured relative to the atmospheric pressure with a pressure transducer. Therefore, the absolute pressure along the subchannels can be determined.

4.2.4 Liquid Mass Exchange Between Subchannels

Since the prediction of COBRA-IV will be compared with data obtained on blocked subchannels which include the liquid mass exchange between the subchannels a brief description of the method used to determine this exchange will be given. The liquid exchange between the subchannels is determined by injecting salt into one of the channels upstream of the air-water mixer and determining the variation of salt concentration in both channels by sampling the liquid phase.

The sampling is carried out at a number of axial locations along the subchannels: for example, two samplings before the beginning of the interconnection, 9 samplings in

the interconnected region, and 1 sampling after the end of interconnection. In order to get a good idea of the average concentration at given location, the sampling is also done at five different points in the transverse direction.

The sampling needles are fully retractable, therefore they may be completely removed from the flow field when they are not in use. The salt concentration in the samples is determined by conductivity meter with an accuracy of ±1%. The average tracer concentration is usually less than 500 *mg/l* and it is assumed that the physical properties of the water, except its conductivity, are not affected.

4.3 Data Acquisition System

A software package has been developed to automate the data collection and processing. This software has been developed and modified at the Institute Génie Nucléaire. This package includes different modules that permit the collection and subsequent calculations of all necessary parameters for the calibration experiments as well as the experiments in two interconnected subchannels. Table 4.3 shows the configuration of the data acquisition system. All the collected signals are converted to the appropriate physical quantities, i.e., local void fraction, axial pressure drop, radial pressure difference between two subchannels and liquid flow rate. Based on these quantities, the necessary calculations for calibration and experiments in two interconnected subchannels are carried out.

Table 4.3 Configuration of Data Acquisition System

Single-phase measurements			Two-phase measurements							
			Calibration				Subchannel experiments			
	pressure	liquid flow rate	pressure	liquid flow rate	void fraction	absolute pressure	Radial [2] and axial pressure	liquid [2] flow rate	void fraction	absolute pressure
N[1]	675	675	300	300	300	300	500	500	100	500
M[1]	50	50	50	50	50	50	50	50	50	50
S[1]	1	1	1	1	2	2	2	2	3	2

1) S= number of sampling; N= number of signal readings during each sampling; M= time interval of readings (*ms*)

2) The pressure and the flow rate have been measured, simultaneously.

4.4 Experimental Procedures

The interconnected subchannel experiments were carried out in two stages. The first consisted of single subchannel experiments where the impedance void gauges were calibrated. Also in this stage of the experiments the relationships between :

1. the average volumetric flux of the gas phase,
2. the volumetric flow quality of the mixture,
3. the flow mass dryness fraction and
4. the frictional pressure loss,

with flow variables such as average void fractions and liquid phase mass fluxes have been determined. The second stage involved the two interconnected subchannel experiments, where the information from the first stage has been used to determine the

average void fraction and the gas mass flow rates in the interconnected subchannels. Knowledge of the frictional pressure losses is particularly important when the data is to be compared with the predictions of subchannel codes such as COBRA-IV.

This section will be devoted to the presentation of the experimental data obtained on flow in a single subchannel and to the procedures followed to determine the void fraction and the pressure drop in the two interconnected subchannel experiments.

4.4.1 Single Subchannel Calibration Experiments

In this section the resulting calibration curves for void gauges as well as the results of measuring the frictional pressure loss, the volumetric flow quality, the volumetric flux of the gas and the dryness fraction will be presented.

4.4.1.1 Calibration of the Impedance Void Gauges

The impedance void gauges used in this research were calibrated by comparing their response to the two-phase mixture flowing through the subchannel with the average void fraction in the whole subchannel. The average void fraction was determined by measuring the volume of water after isolating the subchannel using quick closing valves installed at both ends. Because of the fluctuating nature of the flow and consequently the signals, the response of the ten impedance gauges were multiplexed for a sampling time of 50 *ms* and a total of 300 data points for each electrode were collected. The average of these values was taken as the mean value of the electrode response. At the end of each data acquisition run the average void fraction in the test section was determined with the aforementioned quick closing valve technique. Each

subchannel was individually calibrated; during the calibration the temperature of the water was kept constant at 20 ± 1 °C.

As typical examples, Figure 4.9 and 4.10 give the resulting calibration curves for void gauges A-6 and B-6. The liquid mass fluxes ranged from 1000 to 3500 kg/m^2s. From the calibration curves, it can be concluded that, for the subchannel geometry, void fractions up to 70% can be accurately measured. It should be pointed out that each void gauge was calibrated with its associated electronic circuit and connection cables. The main assumption made in the calibration of the void gauges was that the changes in the void fraction along the subchannel caused by the expansion of the gas with decreasing absolute pressure could be ignored. In other words, the void fraction obtained by the quick closing valve technique adequately represents the void fraction seen by all impedance void gauges. This assumption may not be completely true when the gauges are distributed over a long distance (1418 *mm* in the present study) and when the pressure drop over this distance is not negligible compared to operating pressure of the system. Therefore, the void fraction obtained from the calibration curve of each impedance gauge should be corrected to reflect the real void fraction at each axial location. The procedure with which the correction was carried out will be describe later.

4.4.1.2 Frictional Pressure Losses

Because of the uncertainty involved in the calculation of the frictional pressure losses in two-phase flow using correlations available in the open literature, it was believed that for a better analysis of the pressure drop data obtained in these experiments, the frictional loss characteristics of the test section should be determined experimentally. The experimental set-up used for the determination of the frictional

pressure losses is given in Figure 4.11. These pressure measurements were systematically taken between pressure taps 7 and 15. The total pressure drop can be written in terms of its frictional, acceleration and gravity components, as follows:

$$\Delta p_T = \Delta p_{friction} + \Delta p_{accelaration} + \Delta p_{gravity}. \tag{4-1}$$

Since the distance over which Δp is measured is small ($h_{7\text{-}15}$ = 406.74 *mm*), $\Delta p_{accelaration}$ can be neglected in the comparison with $\Delta p_{friction}$ and $\Delta p_{gravity}$. Therefore, the measured pressure drop was, equal to the frictional pressure loss. In vertical flow, the gravitational component was subtracted from the total pressure drop to yield the frictional pressure drop. Also, to obtain the real pressure drop, the measured pressure drop was then corrected for the water column contained in the pressure line between taps 7 and 15. Thus,

$$\Delta p_T = \Delta p_{measured} + \rho g h_{7-15} \text{ and}$$

$$\Delta p_{friction} = \Delta p_T - \Delta p_{gravity}, \tag{4-2}$$

where the gravitational component was given by :

$$\Delta p_{gravity} = h_{7-15}\,(\alpha\rho_g + (1-\alpha)\rho_l)g. \tag{4-3}$$

The frictional pressure gradient is then given by:

$$\left[\frac{dp}{dz}\right]_{friction} = \frac{\Delta p_{friction}}{h_{7-15}}. \tag{4-4}$$

The pressure loss experiments were performed by keeping the liquid phase mass

flow rate constant and by varying the void fraction. For each experiment, the pressures, the liquid flow rates, the void fractions, the absolute pressure of the two-phase flow (almost half-away between pressure taps 7 and 15), and gas flow rates have been measured. The data on frictional pressure losses are presented in terms of the two-phase friction factor multiplier, Φ_L^2, which is defined by:

$$\Phi_L^2 = \frac{\left[\frac{dp}{dz}\right]_{TP,friction}}{\left[\frac{dp}{dz}\right]_{fo,friction}}, \tag{4-5}$$

where $[dp/dz]_{fo,friction}$ is the pressure drop evaluated as if the entire two-phase mixture flows as liquid in the subchannel. This pressure drop is given by:

$$\left[\frac{dp}{dz}\right]_{fo,friction} = f\frac{G^2}{2\rho_1 D_H}. \tag{4-6}$$

where G for all practical purposes can be considered to be equal to G_l (since $G_g << G_l$).

For the friction factor, f, the following relations give the best results for the subchannel geometry used in this work and for Re numbers between 5000 and 32000:

$$\text{Channel A: } \left\{ \begin{array}{ll} 5000 < Re < 8174 & f = 0.6417\,Re^{-0.3465} \\ 8174 < Re < 32000 & f = 0.3000\,Re^{-0.2621} \end{array} \right\}$$

$$\text{Channel B: } \left\{ \begin{array}{ll} 5000 < Re < 8089 & f = 0.5904\,Re^{-0.3393} \\ 8089 < Re < 30000 & f = 0.2908\,Re^{0.2606} \end{array} \right\} \tag{4-7}$$

Figures 4.12 and 4.13 show the variation of the two-phase multiplier, Φ_L^2, with the mass fluxes between 1000 and 3500 kg/m^2s for subchannel A and B respectively.

These figures include the data on mass flux of 3500 kg/m^2s at low void fractions, however they are not used in present work.

4.4.1.3 Volumetric Flow Quality and Flux of the Gas, and Dryness Fraction

Figures 4.14 and 4.15 show the relationship between the volumetric flow quality, β, and the volume averaged void fraction, $<< \alpha >>$, for liquid mass fluxes from 1000 to 3500 kg/m^2s for subchannels A and B respectively. All the data are on or above the line $y=x$. Thus this shows that the slip ratio is greater than unity. The relationship between β and $<<\alpha>>$ seems to be independent of the mass flux for void fractions up to 40%. Beyond this limit, for a given void fraction, the volumetric flow quality decreases with increasing liquid mass flux.

Figures 4.16 through 4.21 give the relationship between the volumetric flux of the gas, $< j_g >$ and the void fraction, the relationship between the void fraction and the dryness fraction and the relationship between the void fraction and volumetric flux $< j >$ for both channels, respectively.

4.4.2 Interconnected Subchannels

The calibration curves for the response of the electrodes and the $\{\beta$ vs. $<<\alpha>>\}$ relationship presented in the preceding section have been used during the two interconnected subchannel experiments to determine parameters such as void fraction and gas flow rates along the interconnected region.

4.4.2.1 Void Fraction

The average responses of the void gauges located at ten points in the high and low void subchannels have been simultaneously measured. Subsequently, the void fraction corresponding to each gauge was determined by using its calibration curve which has a behavior similar to those given in Figures 4.9 and 4.10. Each calibration curve was fitted by using polynomials sixth order and used the void fraction module of the acquisition and processing software presented earlier.

As has already been pointed out, the calibration of the void gauges was carried out by comparing their response to the two-phase mixture flowing through the subchannel with the average void fraction in the whole subchannel as given by quick closing valves (QCV). In this procedure, the main assumption was that the variation of the void fraction along the subchannels due to the expansion of the gas could be ignored and a single value of the void fraction could be assigned to all gauges. This assumption is not true, when the probes are distributed over a long distance and the pressure drop is substantial when compared to the absolute pressure of the system. Therefore, the void fractions read from the calibration curves should be corrected with the procedure detailed below to take into account the expansion of the gas phase.

As can be seen from Figure 4.5, in both subchannels, void gauges A-5 and B-5 are located almost in the middle of the test section. Since the pressure variation along the subchannel is nearly linear (observed experimentally), it can be expected that the average void fraction determined by the QCV system in the whole subchannel closely reflects the void fraction existing at the level of these gauges and, their calibration curve is reasonably accurate. In addition, the relationship between the volumetric flux of the

gas, $< j_g >$, the liquid mass flux, the void fraction (Figure 4.16 and 4.17), and the absolute pressure at the level of these void gauges have been determined. Because of the expansion of the gas, the calibration curves for the gauges upstream of gauge #5 will overestimate the void fraction and those downstream of the gauge #5 underestimate the void fraction. The degree of overestimation and underestimation increases with increasing distance from gauge #5.

Using the relationship $< j_g > = j_g (< \alpha > , m_l)$, the void fractions obtained from the response of the electrodes and the calibration curves of the gauges upstream and downstream of gauges A-5 and B-5 can be corrected to obtain the real void fraction. This correction has been calculated as follows.

1. Under single subchannel flow conditions using the void fraction measured by gauge #5, determine the total pressure drop gradient.
2. Assuming a linear pressure variation along the subchannel and knowing the absolute pressure at the level of the fifth void gauge determine the absolute pressure at the level of void gauge #1 and #10.
3. Knowing the volumetric flux density of the gas at the level of void gauge #5, determine this flux density at the level of void gauges #1 and #10
4. Using the relationship $< j_g >$ - $< \alpha >$ for liquid mass fluxes of 1000, 2000, 2500, 3000 kg/m^2 s (Figures 4.16 and 4.17), determine the void fraction at the level of gauges #1 and #10.

Figures 4.22 through 4.25 give the plot of $\varepsilon_{10} = \frac{\alpha'_{10}}{\alpha_{10}}$ and $\varepsilon_1 = \frac{\alpha'_1}{\alpha_1}$ (α is the void fraction obtained from the calibration curve and α' is the true void fraction) as a function of α_n and mass flux. It should be pointed out that according to the void gauge calibration procedures, under single subchannel flow conditions, for a given mixture in

the subchannel all gauges yield the same void fraction, i.e., $\alpha_1 = ... = \alpha_n = ... = \alpha_{10} = \alpha_{QCV}$. For gauges #1 and #5, and gauges #5 and #10, $\varepsilon_n = \frac{\alpha'_n}{\alpha_n}$ is assumed to be given by:

$$\varepsilon_n = \frac{\alpha'_n}{\alpha_n} = 1 + (\varepsilon_1 - 1)\frac{z_{5-n}}{z_{5-1}} \qquad n = 1, 2, 3, 4, 5 \ , \tag{4-8}$$

for gauges between gauge #1 and #5, by:

$$\varepsilon_n = \frac{\alpha'_n}{\alpha_a} = 1 + (\varepsilon_{10} - 1)\frac{z_{5-n}}{z_{5-10}} \qquad n = 5, 6, 7, 8, 9, 10 \ , \tag{4-9}$$

for gauges between #5 and #10; where $z_{5\text{-}n}$ is the distance of nth gauge from the fifth gauge. In interconnected subchannels, the value of the void fraction determined using the calibration curve of the nth gauge (α_n) is therefore corrected by multiplying this by ε_n determined from the relationships 4.8 and 4.9. The values of ε_1 or ε_{10} are determined from the correction curves (Figures 4.22 through 4.25) by using the void α determined by the calibration curve.

4.4.2.2 Liquid Phase Mass Exchange

Section 4.2.4 outlined the method with which the liquid mass exchanges between the subchannels were determined. Because the experimental results which will be used in the blockage case include the liquid mass exchange, the basis of this method will be explained now. This method consists of injecting a salt solution into the blocked subchannel and determining the variation of salt concentrations in both subchannels. This allows the liquid masses exchanged between the subchannels to be determined when the tracer concentration variation in both of them are known.

In order to derive the mass and tracer conservation equations, let us consider Figure 4.26 which shows the liquid mass flows entering and leaving the control volume as well as the tracer influx and efflux. Applying the mass conservation principle to the control volumes and denoting the mass transferred from blocked subchannel to unblocked subchannel and vice versa by δw and $\delta w'$ respectively, the following equations can be written:

Blocked subchannel (i):

$$\delta w - \delta w' = -\frac{m_i}{\Delta z} dz, \tag{4-10}$$

Unblocked subchannel (j):

$$\delta w - \delta w' = \frac{m_j}{\Delta z} dz. \tag{4-11}$$

In turn the mass conservation principle applied to the tracer yields:

Blocked subchannel (i):

$$C_i \delta w - C_j \delta w' = -\frac{C_i m_i}{\Delta z} dz, \tag{4-12}$$

Unblocked subchannel (j):

$$C_i \delta w - C_j \delta w' = \frac{C_j m_j}{\Delta z} dz. \tag{4-13}$$

where m and C are the mass flow rate and the cross sectional average of the tracer

concentration in the subchannel respectively.

Mass Conservation:

Blocked subchannel (i):

$$m_{i,n+1} - m_{i,n} - \Delta w'_{n+\frac{1}{2}} + \Delta w_{n+\frac{1}{2}} = 0, \qquad (4\text{-}14)$$

Unblocked subchannel (j):

$$m_{j,n+1} - m_{j,n} - \Delta w_{n+\frac{1}{2}} + \Delta w'_{n+\frac{1}{2}} = 0\,, \qquad (4\text{-}15)$$

The addition of the equations 4-20 and 4-21 gives:

$$m_{i,n} + m_{j,n} - m_{i,n+1} - m_{j,n+1} = 0 \qquad (4\text{-}16)$$

Tracer Conservation

Blocked subchannel (i):

$$m_{i,n+1}C_{i,n+1} - m_{i,n}C_{i,n} + C_{i,n+\frac{1}{2}}\Delta w_{n+\frac{1}{2}} - C_{j,n+\frac{1}{2}}\Delta w'_{n+\frac{1}{2}} = 0\,, \qquad (4\text{-}17)$$

Unblocked subchannel (j):

$$m_{j,n+1}C_{j,n+1} - m_{j,n}C_{j,n} - C_{i,n+\frac{1}{2}}\Delta w_{n+\frac{1}{2}} + C_{j,n+\frac{1}{2}}\Delta w'_{n+\frac{1}{2}} = 0\,, \qquad (4\text{-}18)$$

Combining equations 4-14, 4-15, 4-17 and 4-18 the values of $\Delta w_{n+\frac{1}{2}}$ and $\Delta w'_{n+\frac{1}{2}}$

can be written as:

$$\Delta w'_{n+\frac{1}{2}} = \frac{m_{i,n}\left(C_{i,n+\frac{1}{2}} + C_{i,n}\right)}{C_{j,n+\frac{1}{2}} - C_{i,n+\frac{1}{2}}} + \frac{m_{i,n+1}\left(C_{i,n+1} - C_{i,n+\frac{1}{2}}\right)}{C_{j,n+\frac{1}{2}} - C_{i,n+\frac{1}{2}}} \tag{4-19}$$

$$\Delta w_{n+\frac{1}{2}} = \frac{m_{j,n}\left(C_{j,n+\frac{1}{2}} - C_{j,n}\right)}{C_{i,n+\frac{1}{2}} - C_{j,n+\frac{1}{2}}} + \frac{m_{j,n+\frac{1}{2}}\left(C_{j,n+1} - C_{j,n+\frac{1}{2}}\right)}{C_{i,n+\frac{1}{2}} - C_{j,n+\frac{1}{2}}} \tag{4-20}$$

Substituting 4-19 and 4-20 into Equation 4-14 and taking into account Equation 4-16 for the mass flow rates in the blocked subchannel (*i*), the following relationship results:

$$m_{i,n+1} = m_{i,n}\frac{C_{i,n} - C_{j,n+1}}{C_{i,n+1} - C_{j,n+1}} - m_{j,n}\frac{C_{j,n+1} - C_{j,n}}{C_{i,n+1} - C_{j,n+1}} \tag{4-21}$$

The above equation is only valid from the beginning of the interconnected region up to blockage. For sampling in the regions upstream of the blockage, the tracer is injected before phase mixer. All concentrations appearing in equation (4-21) have been determined experimentally. The tracer concentration at the inlet of the blocked subchannel ($C_{j,0}$) as well as the flow rates to the channels have also been measured.

For sampling in the downstream region, the tracer injection was done in the recirculation zone which develops behind the blockage. In this case, the exit conditions of both channels (flow rates and tracer concentrations) have been measured. The equation which applies to the regions downstream of the blockage can be easily derived and has the following form:

$$m_{i,n} = m_{i,n+1}\frac{C_{i,n+1} - C_{j,n}}{C_{j,n} - C_{j,n}} + m_{j,n+1}\frac{C_{j,n+1} - C_{j,n}}{C_{j,n} - C_{j,n}}. \qquad (4\text{-}22)$$

All concentrations appearing in the above equation have also been determined experimentally.

4.4.2.3 Net Gas Mass Transfer

The net gas mass transfer from the blocked subchannel to the unblocked subchannel and vice versa is determined by using the information on liquid phase volume flow rates (as determined by tracer technique) and void fractions along the interconnected region in conjunction with the volumetric flow quality curve, $\beta=\beta(<\alpha>,m_1)$, obtained under single subchannel flow conditions and given in Figure 4-14. The volumetric flow quality is defined as:

$$\beta = \frac{Q_g}{Q_g + Q_l} \quad , \qquad (4\text{-}23)$$

where Q_g and Q_l are the volume flow rates of the gas and liquid phases respectively. From equation 4-23, Q_g can be written as follows:

$$Q_g = \frac{\beta Q_l}{1 - \beta} \quad . \qquad (4\text{-}24)$$

Since the variation of the void fraction and liquid mass flow rate is known, the value of β in the high and low void subchannels can be determined from Figure 4-14. Equation 4-24 is then used to determine the gas flow rates in the subchannels.

It should be pointed out that the flow pressure in the single subchannel calibration experiments, where the relationship $\beta=\beta(<\alpha>,m_l)$ is determined, may differ from the flow pressure in the interconnected subchannels. A set of experiments were conducted by Tapucu et al. [1988] to determine the effect of varying pressure on the volumetric quality for a given liquid flow rate and void fraction. It is observed that, for liquid mass fluxes higher than 1800 kg/m^2s and for the pressure range from 120 kPa to 240 kPa, the volumetric quality is independent of the flow pressure. Some effect of the pressure on the volumetric flow quality has been reported in the above reference for liquid mass fluxes less than 1400 kg/m^2s and for void fractions higher than 55%.

An error analysis done by Teyssedou [1987] showed that the uncertainty in this method depends on the void fraction and it is evaluated to be 6% and 12% for void fractions of 10% and 60% respectively. Therefore, for better accuracy, the gas mass flow rates were determined in the low void subchannel. The flow rates in the neighboring subchannel were obtained by taking the difference between the total gas mass flow to the test section and the gas mass flow rates determined in the low void subchannel.

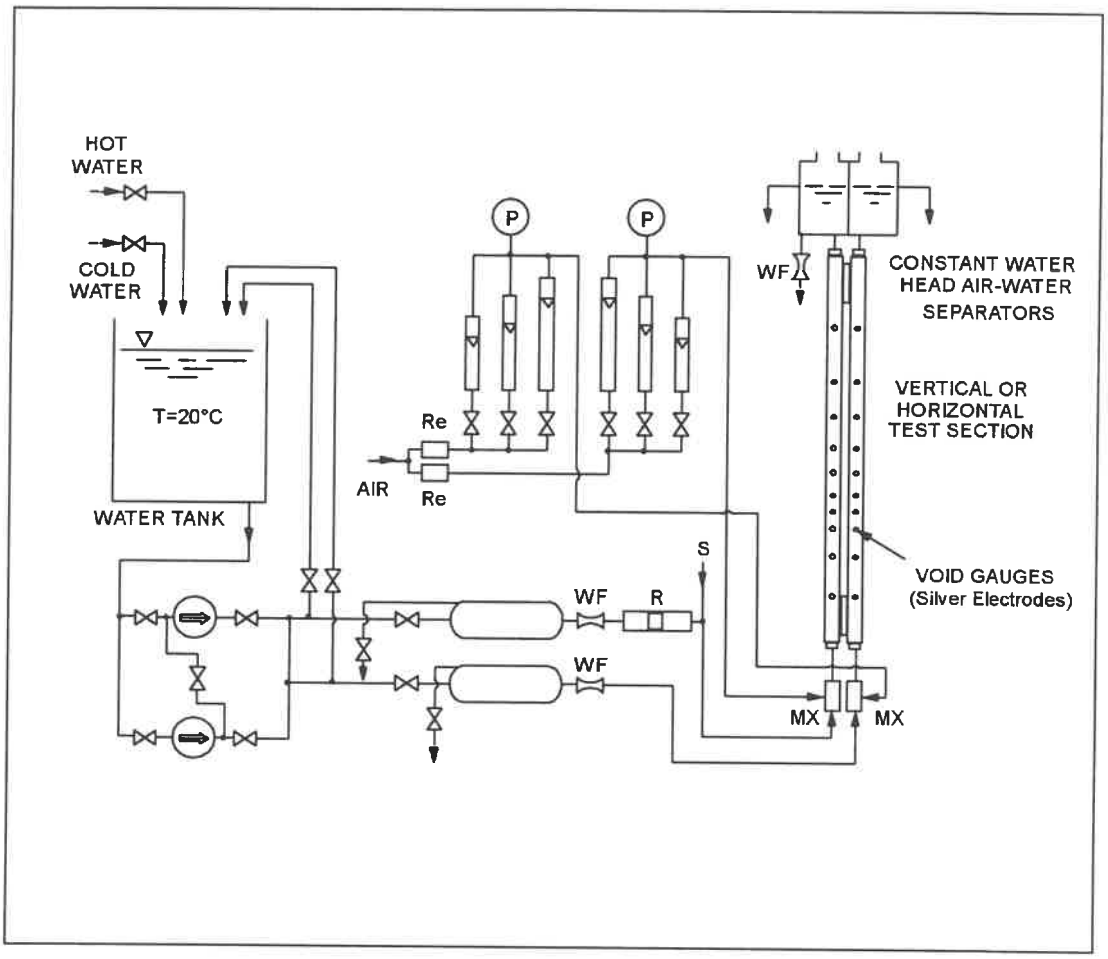


Figure 4.1: Two-Phase Flow Experimental Apparatus

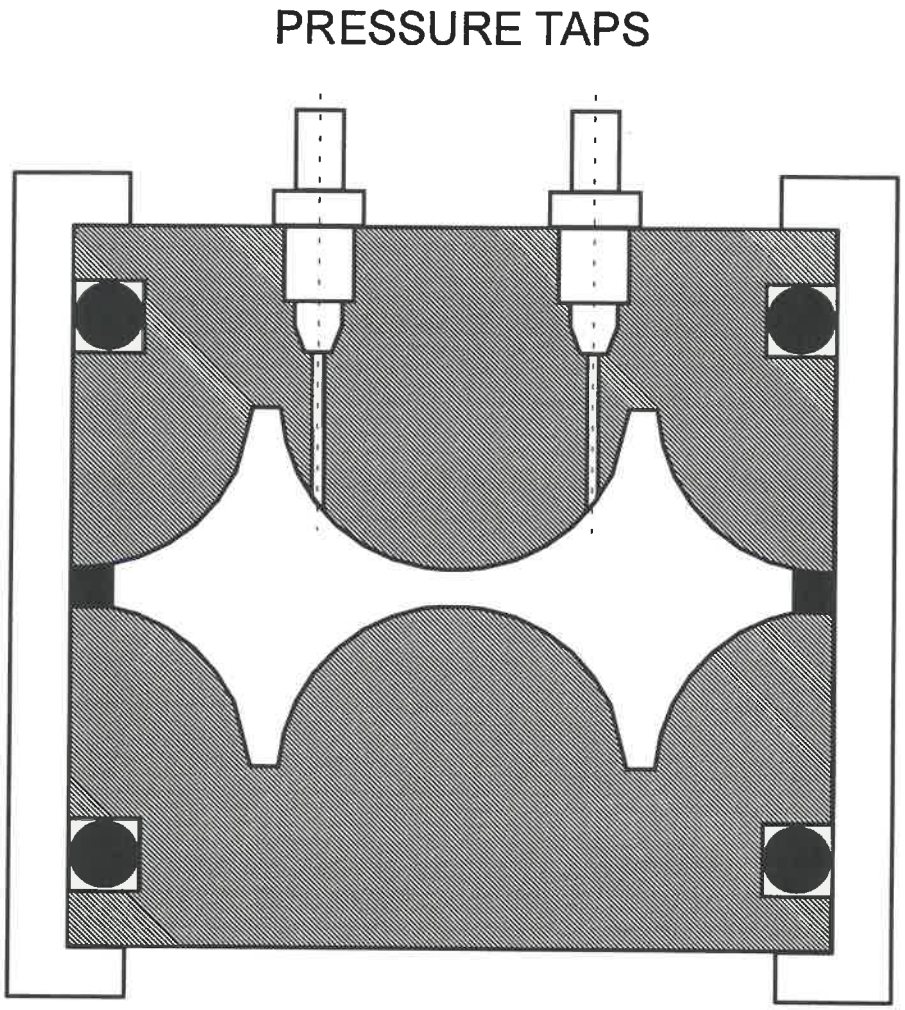


Figure 4.2: Cross-Sectional View of the Test Section

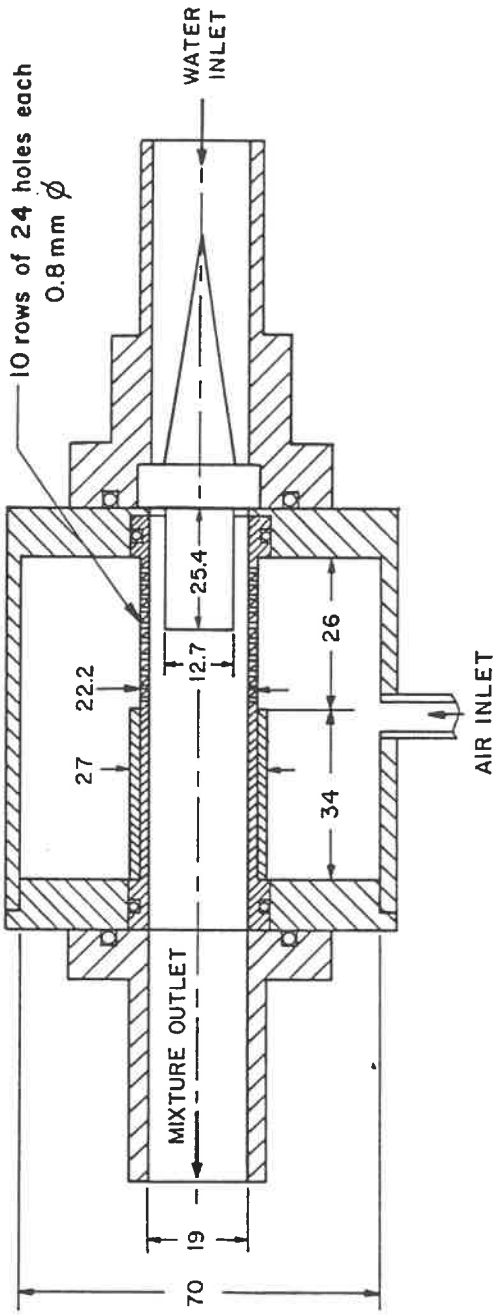


Figure 4.3: Air-Water Mixer

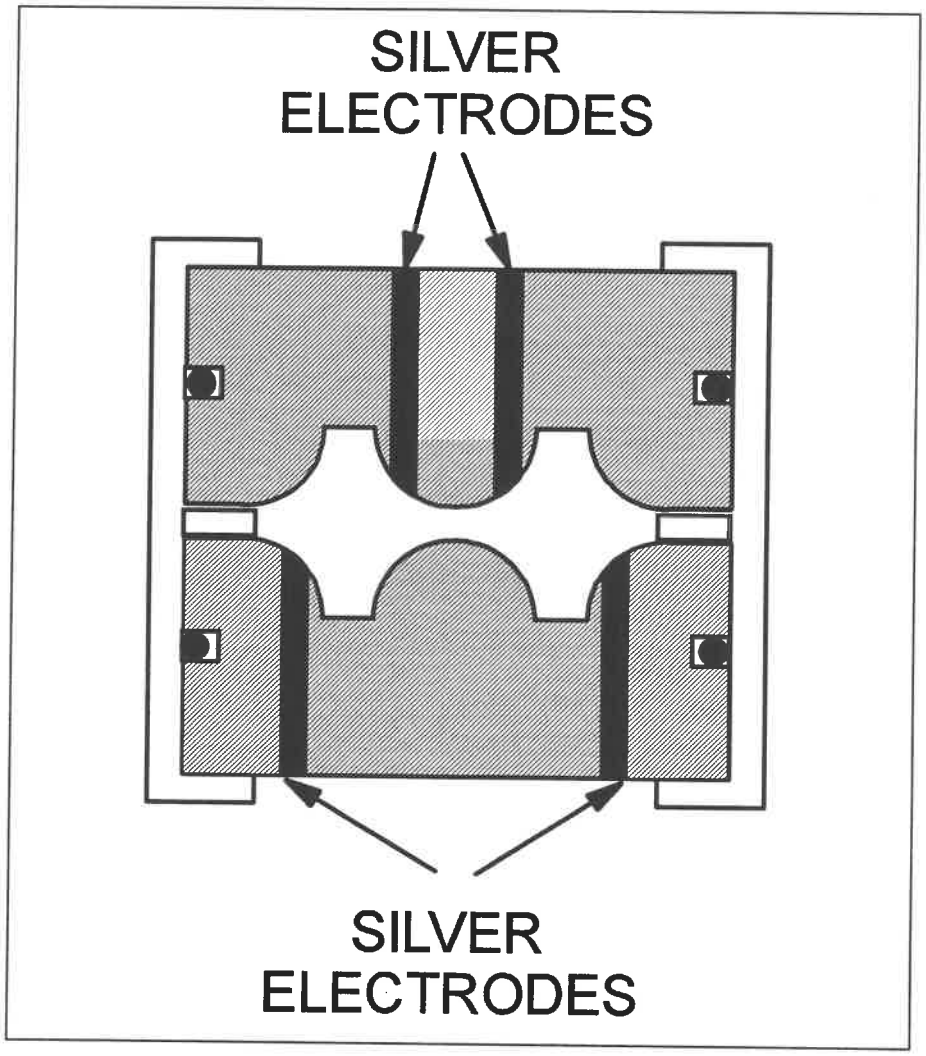


Figure 4.4: Impedence Gauge

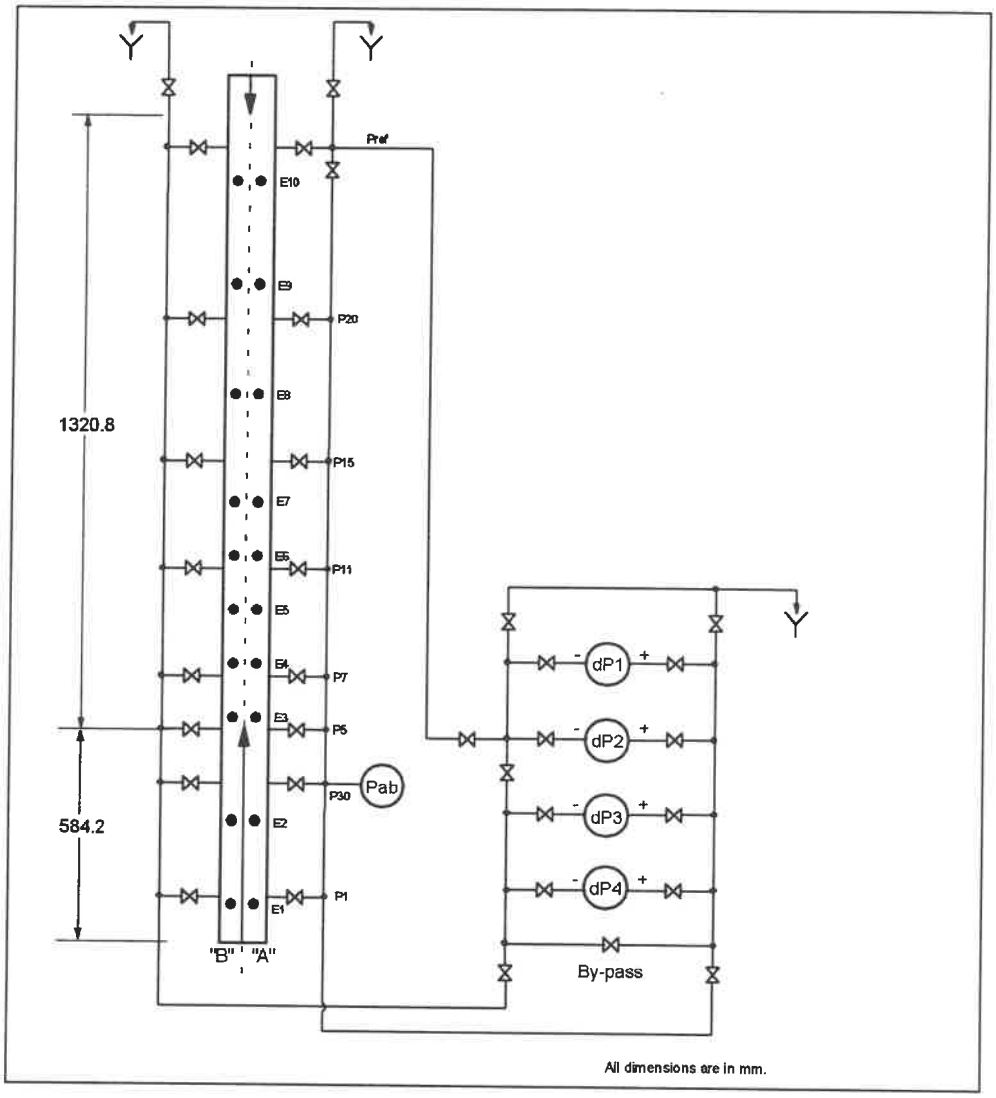


Figure 4.5: Location of the Void Gauges and Pressure Taps

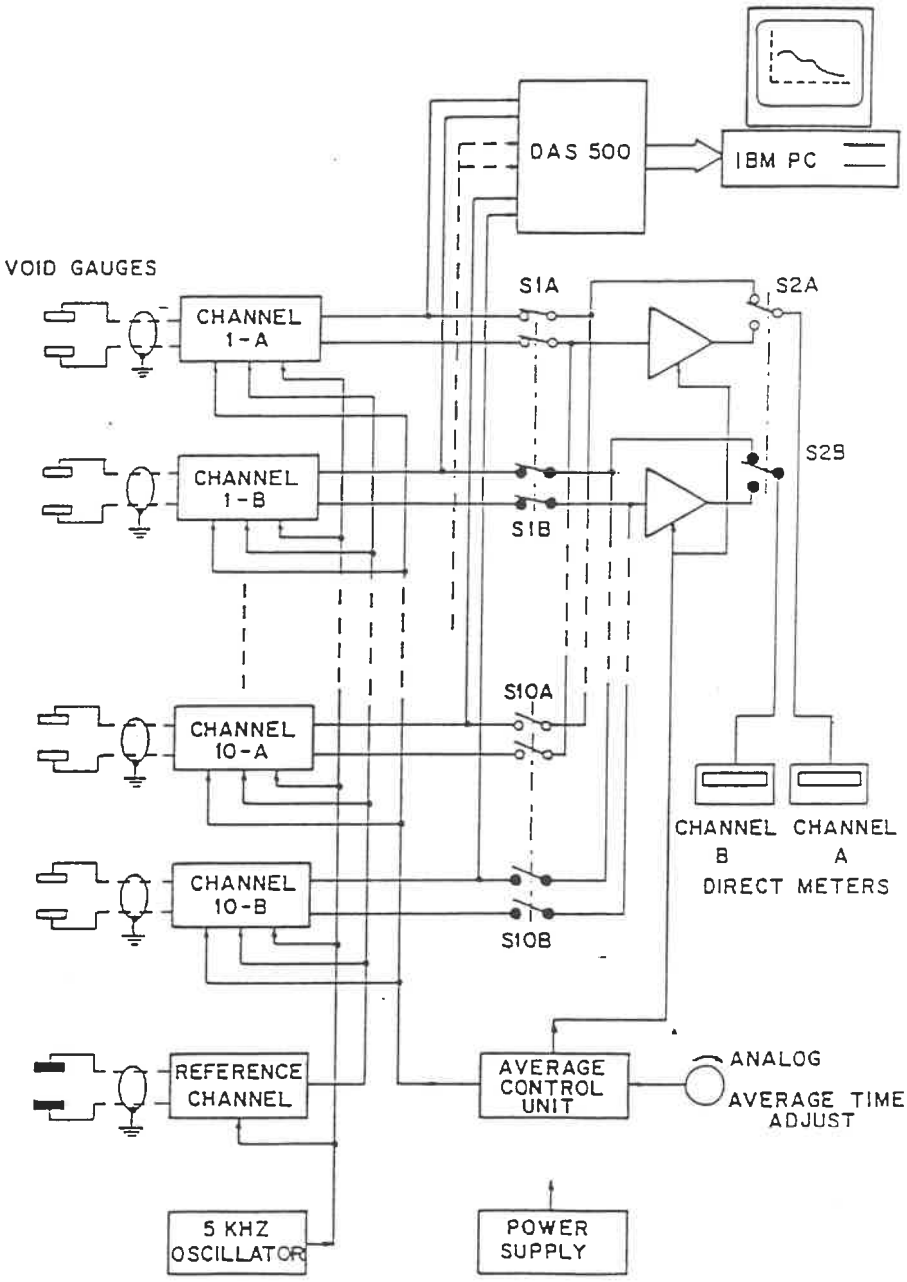


Figure 4.6: Block Diagram of the Void Fraction Measurment System

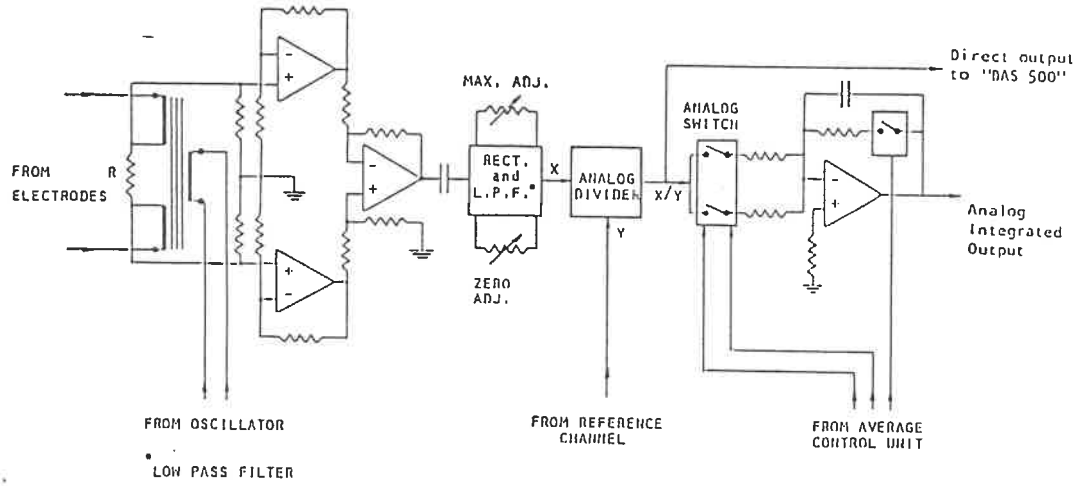


Figure 4.7: Electronic Circuit Associated with the Void Gauges

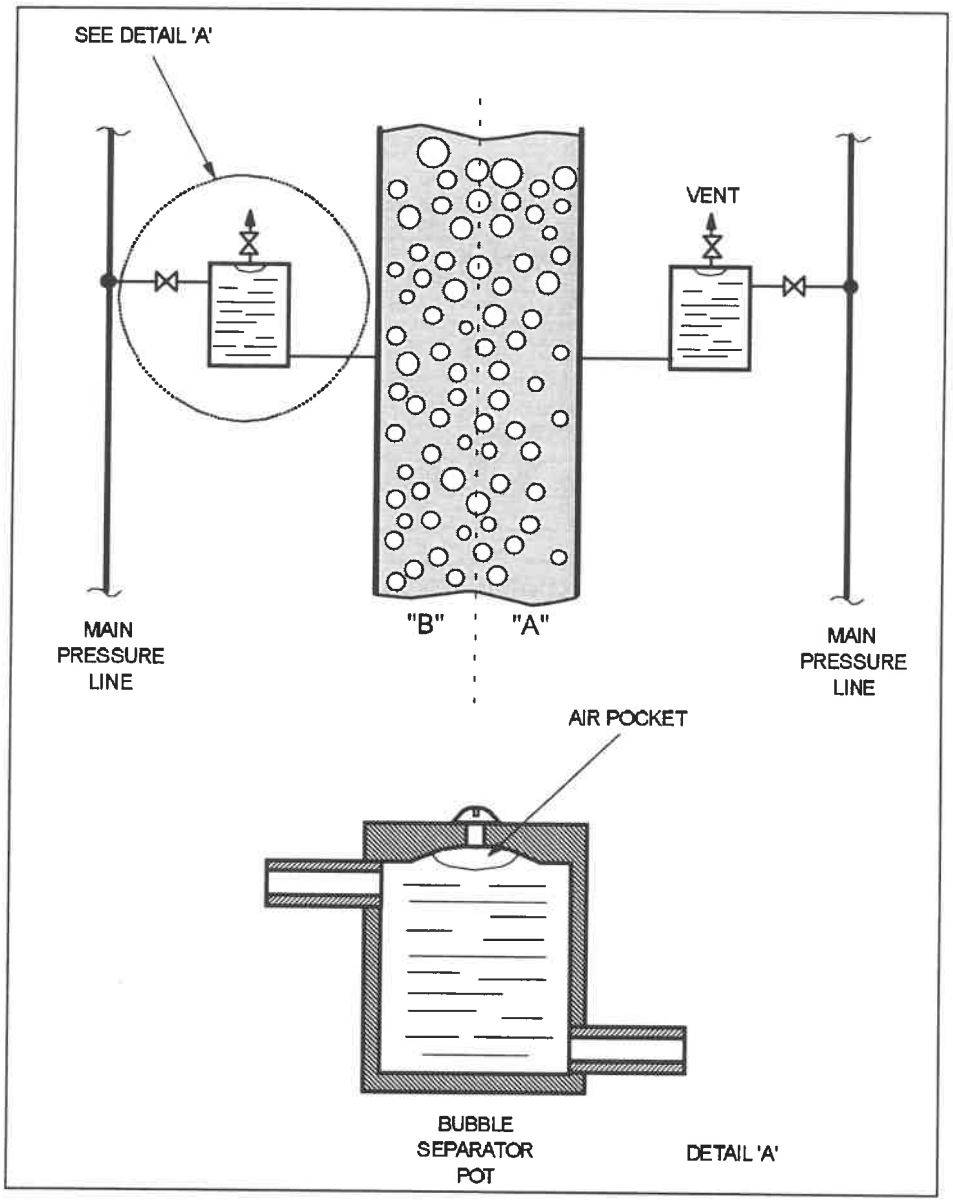


Figure 4.8: Gas Phase Separation Pots.

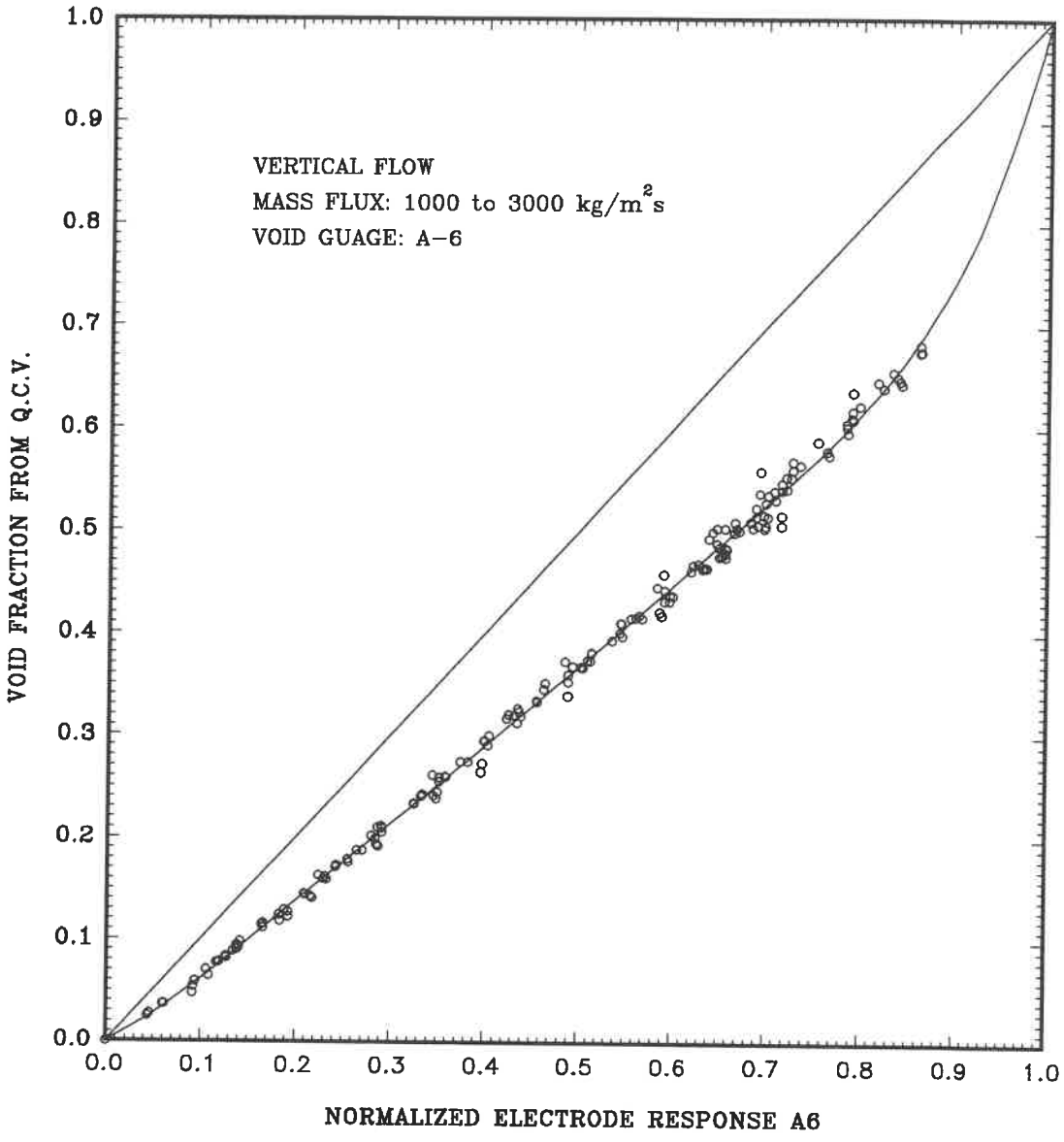


Figure 4.9: Typical Calibration Curve of a Void Gauge

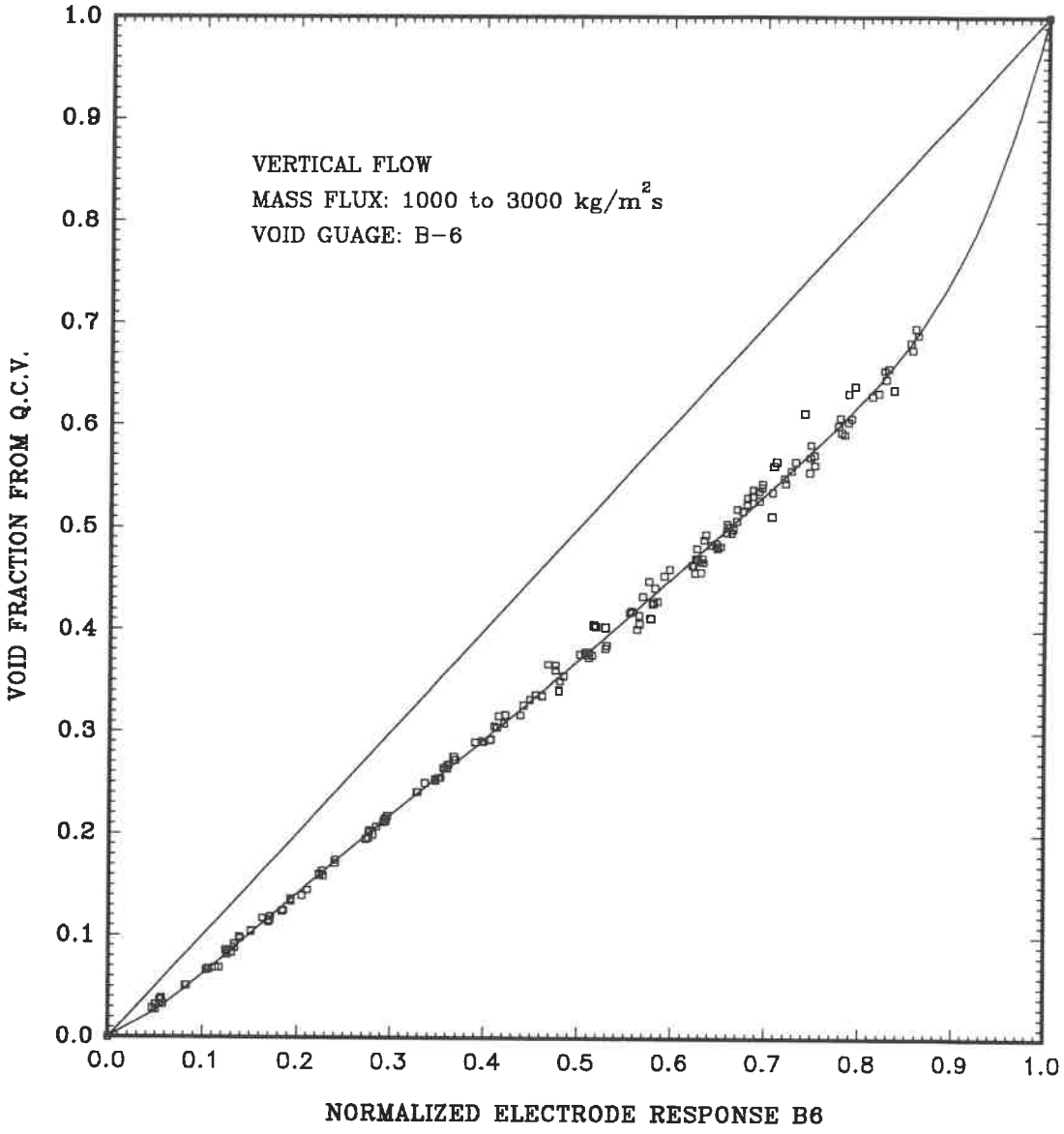


Figure 4.10: Typical Calibration Curve of Void Fraction

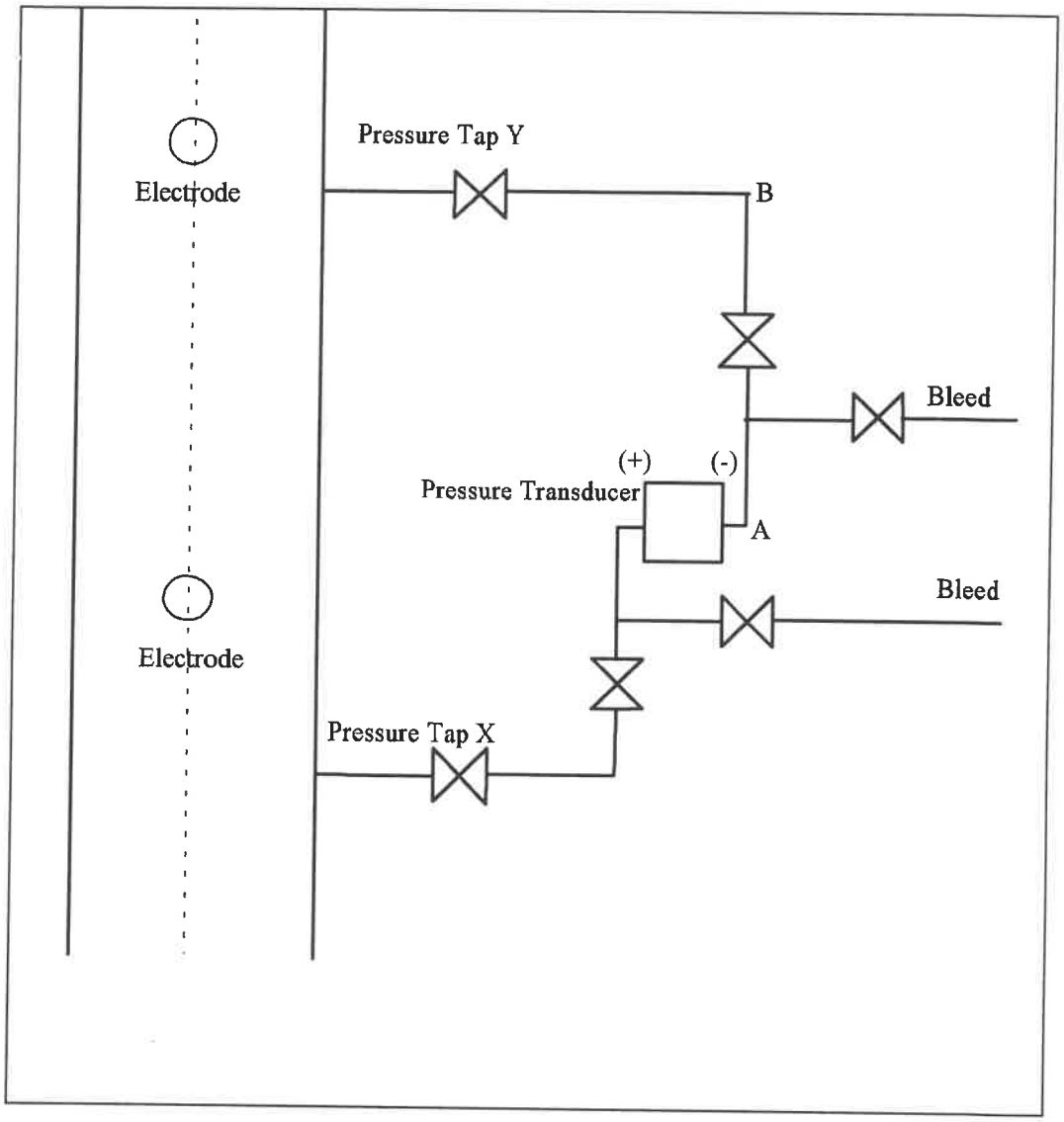


Figure 4.11: Set-up for Frictional Pressure Loss

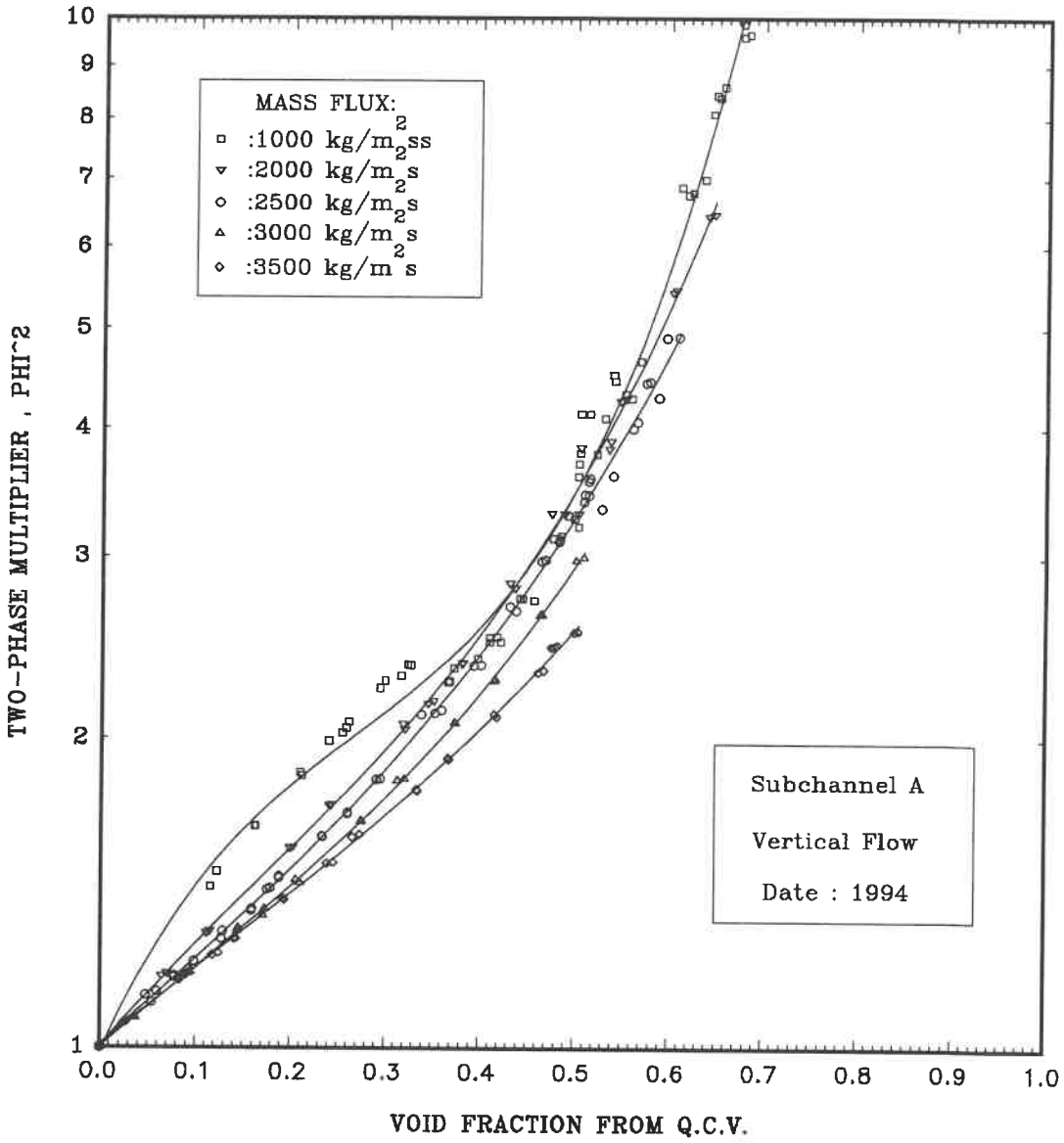


Figure 4.12: Variation of the Two-Phase Multiplier, Φ_L^2, with void fraction, Channel A

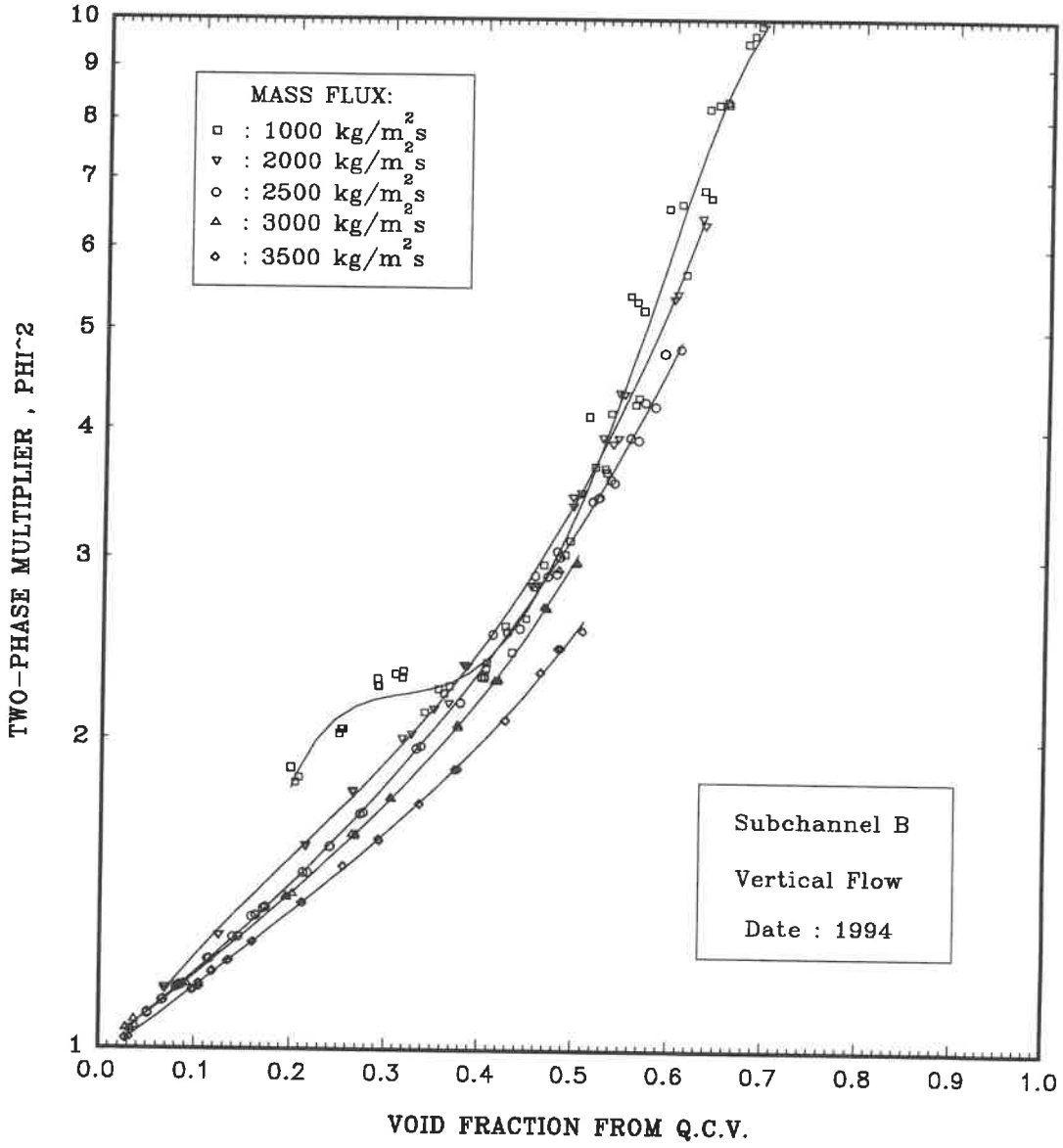


Figure 4.13: Variation of the Two-Phase Multiplier, Φ_L^2, with Void Fraction, Channel B

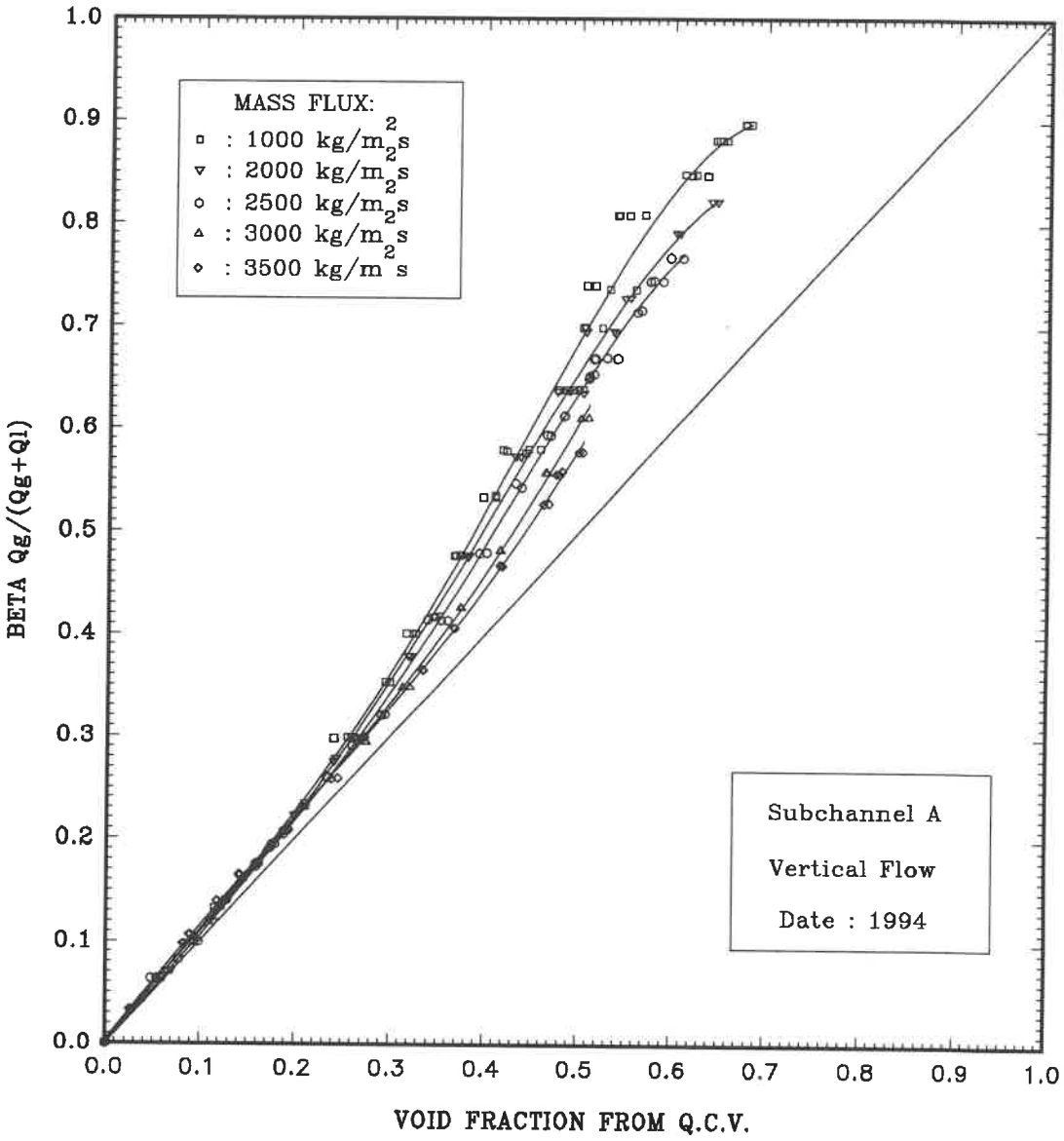


Figure 4.14: Relationship between Volumetric Flow Quality and Void Fraction Channel A

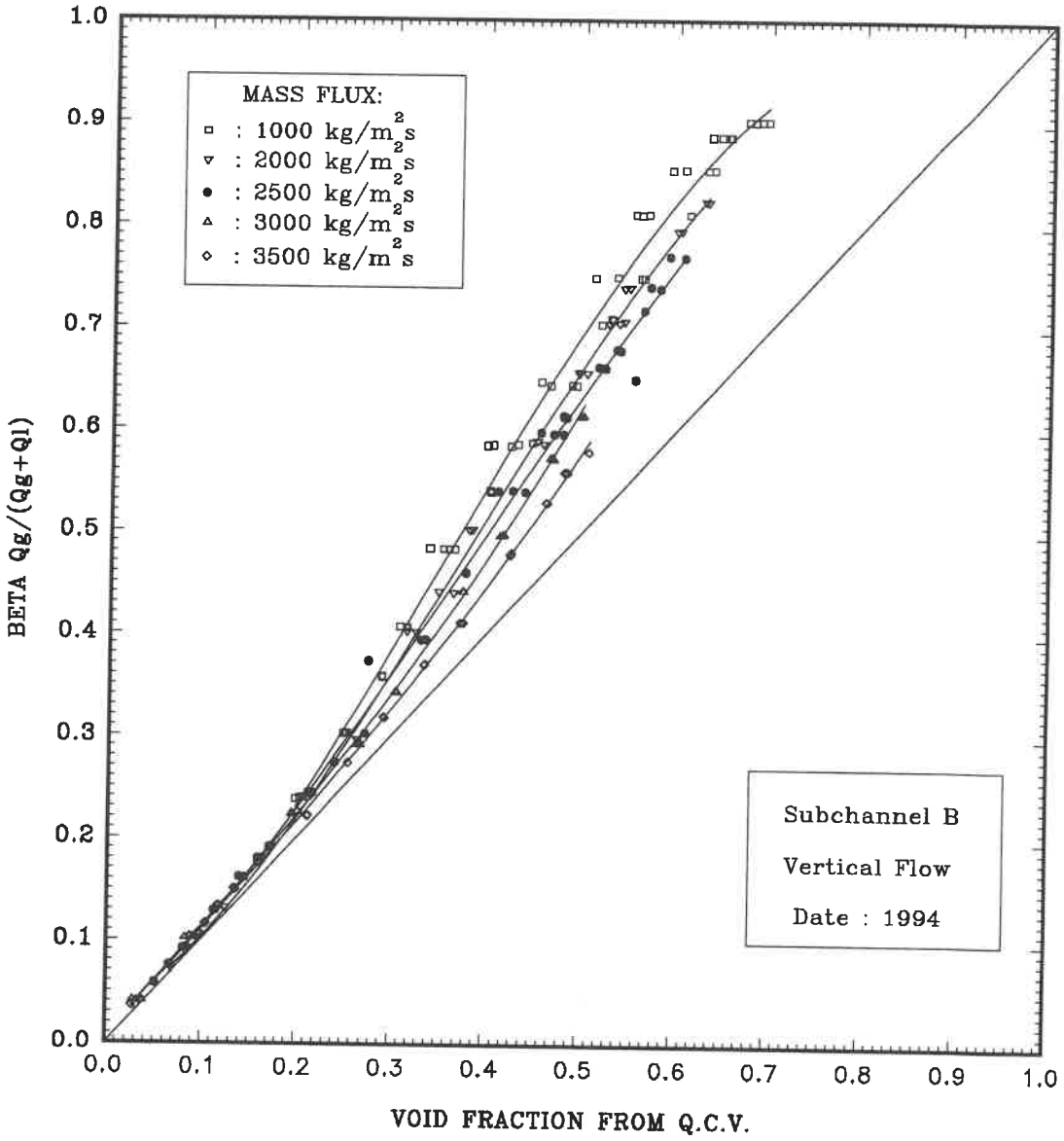


Figure 4.15: Relationship between Volumetric Flow Quality and Void Fraction Channel B

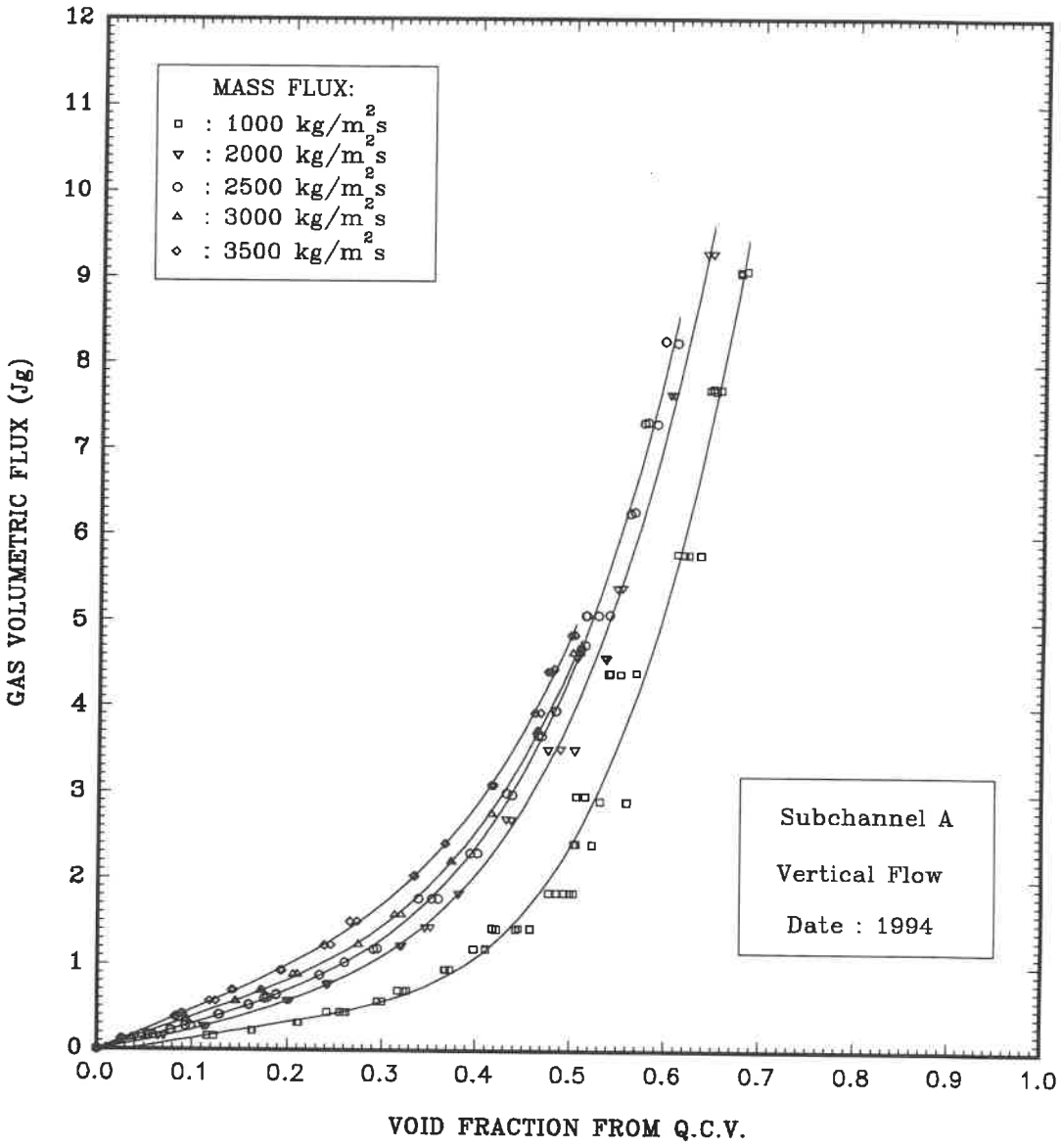


Figure 4.16: Relationship between Volumetric Flux of the Gas and Void Fraction, Channel A

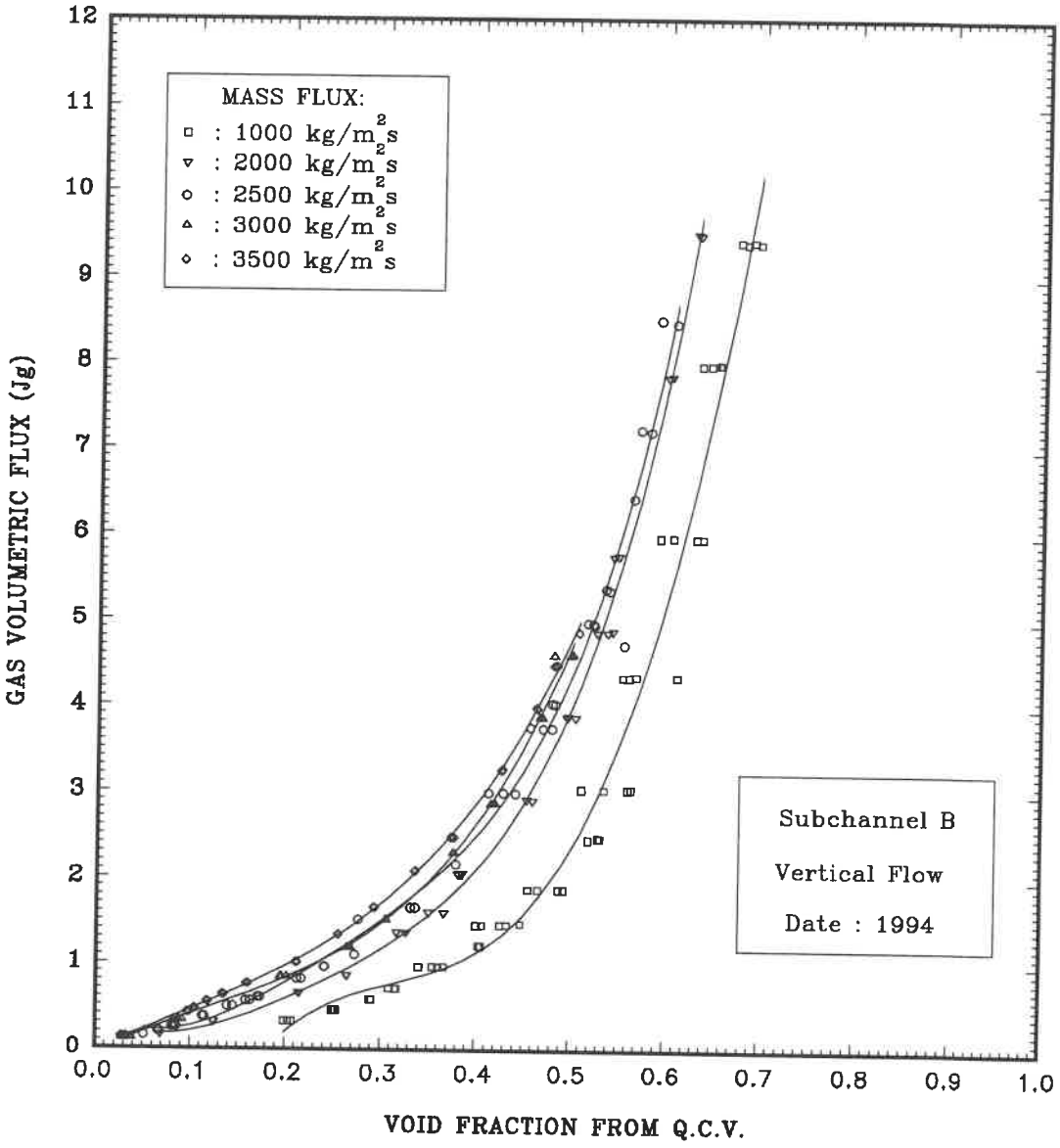


Figure 4.17: Relationship between Volumetric Flux of the Gas and Void Fraction, Channel B

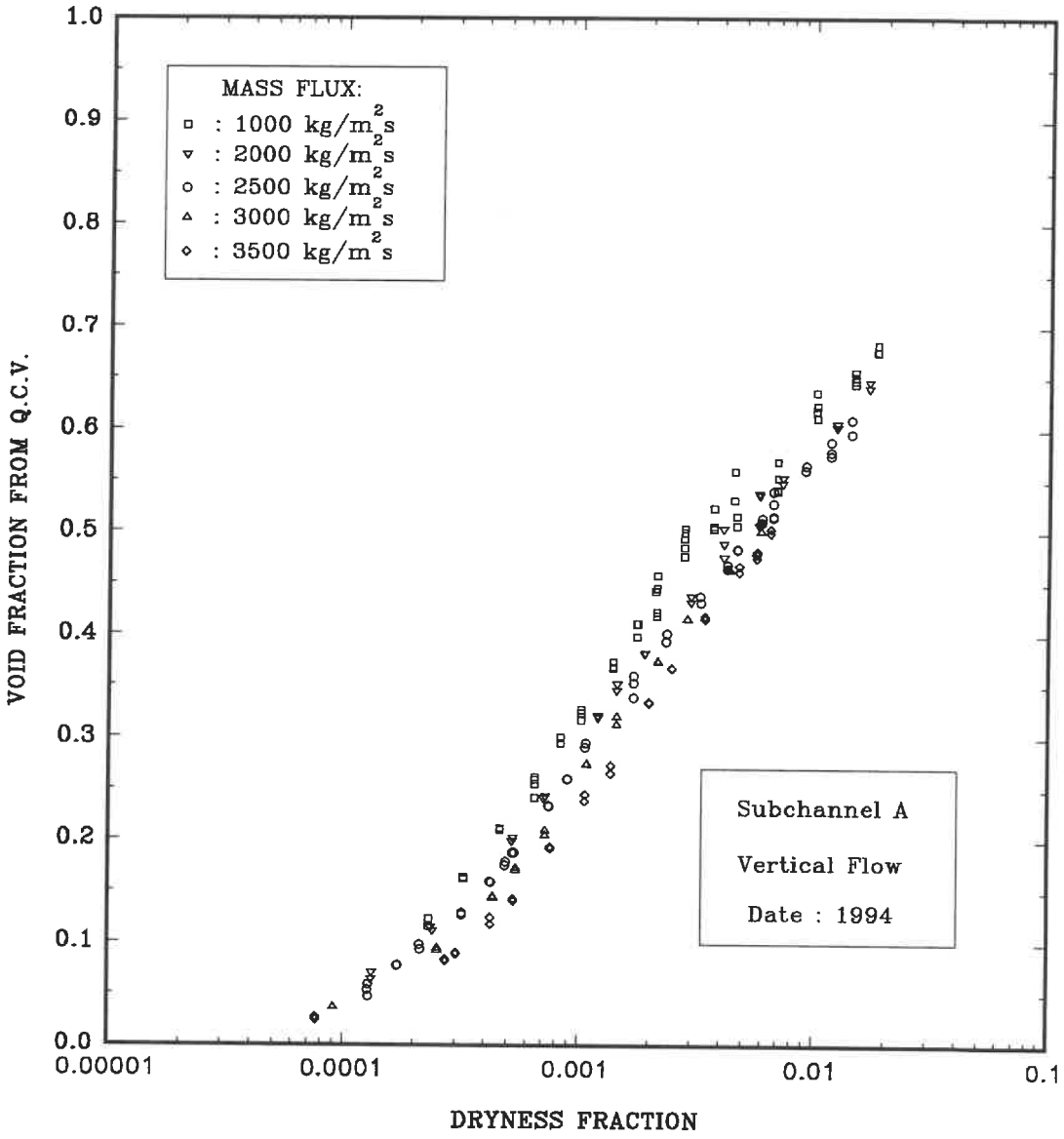


Figure 4.18: Relationship between the Void Fraction and the Dryness Fraction, Channel A

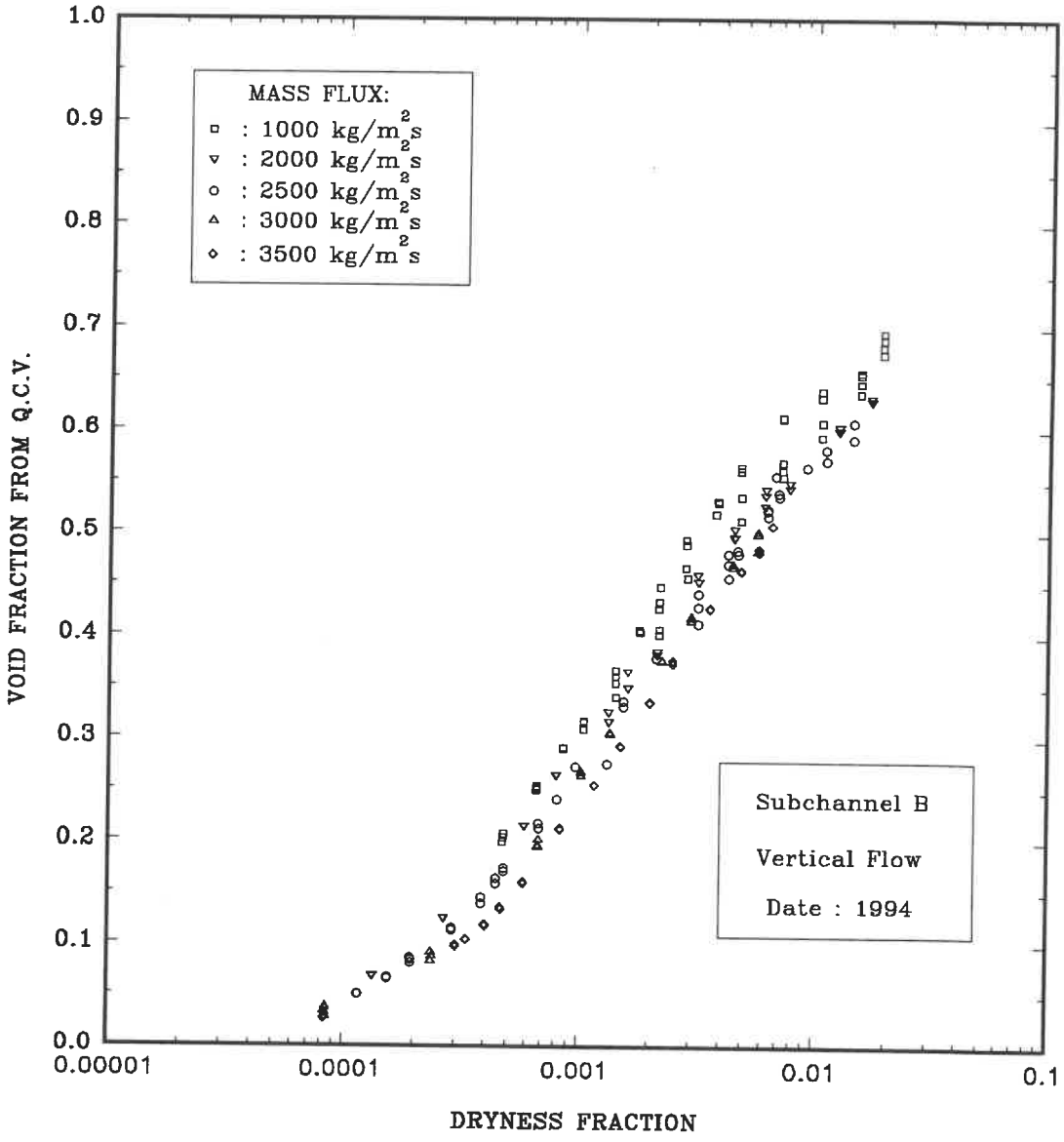


Figure 4.19: Relationship between the Void Fraction and the Dryness Fraction, Channel B

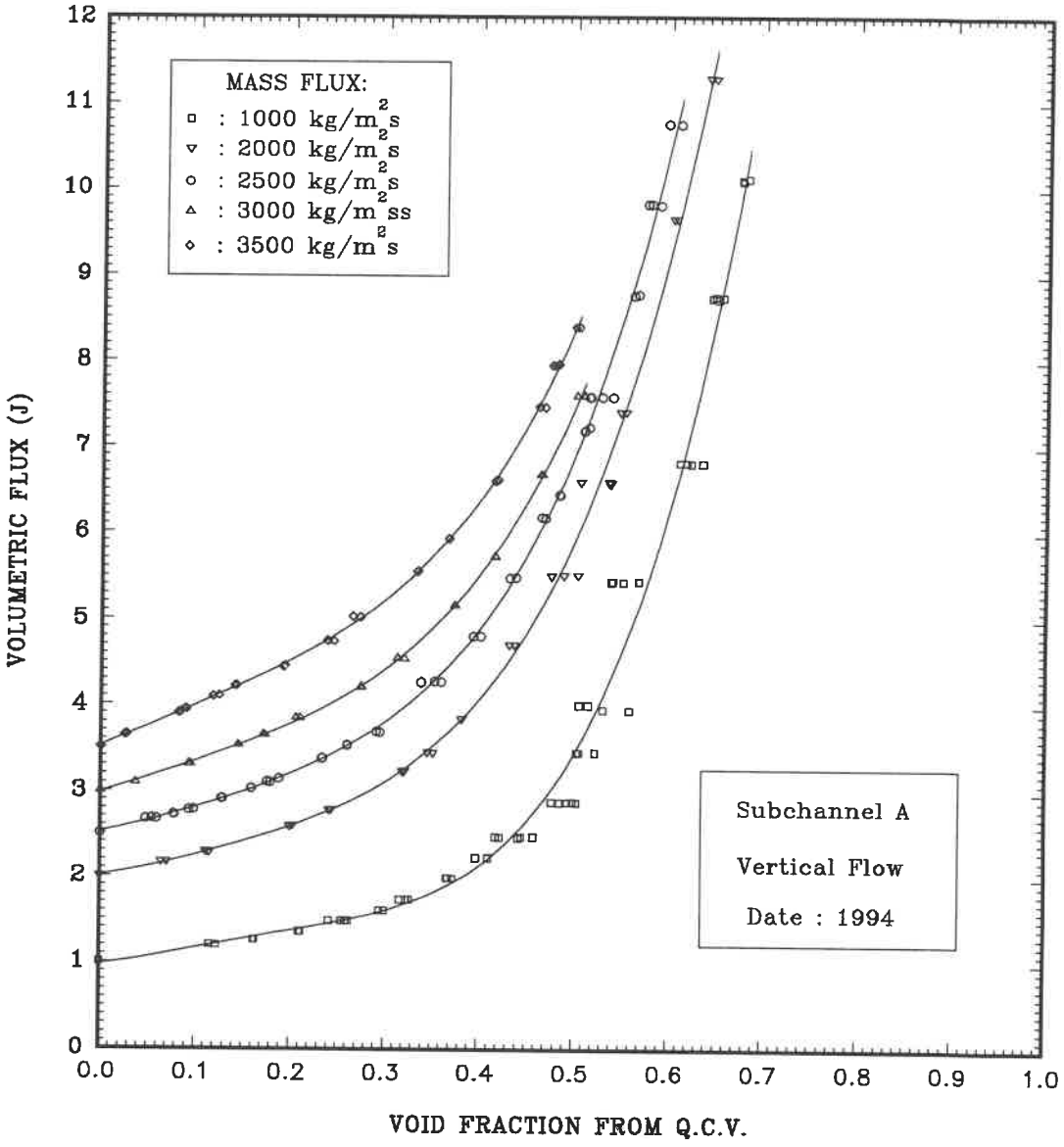


Figure 4.20: Relationship between the Volumetric flux of liquid and void Fraction, Channel A

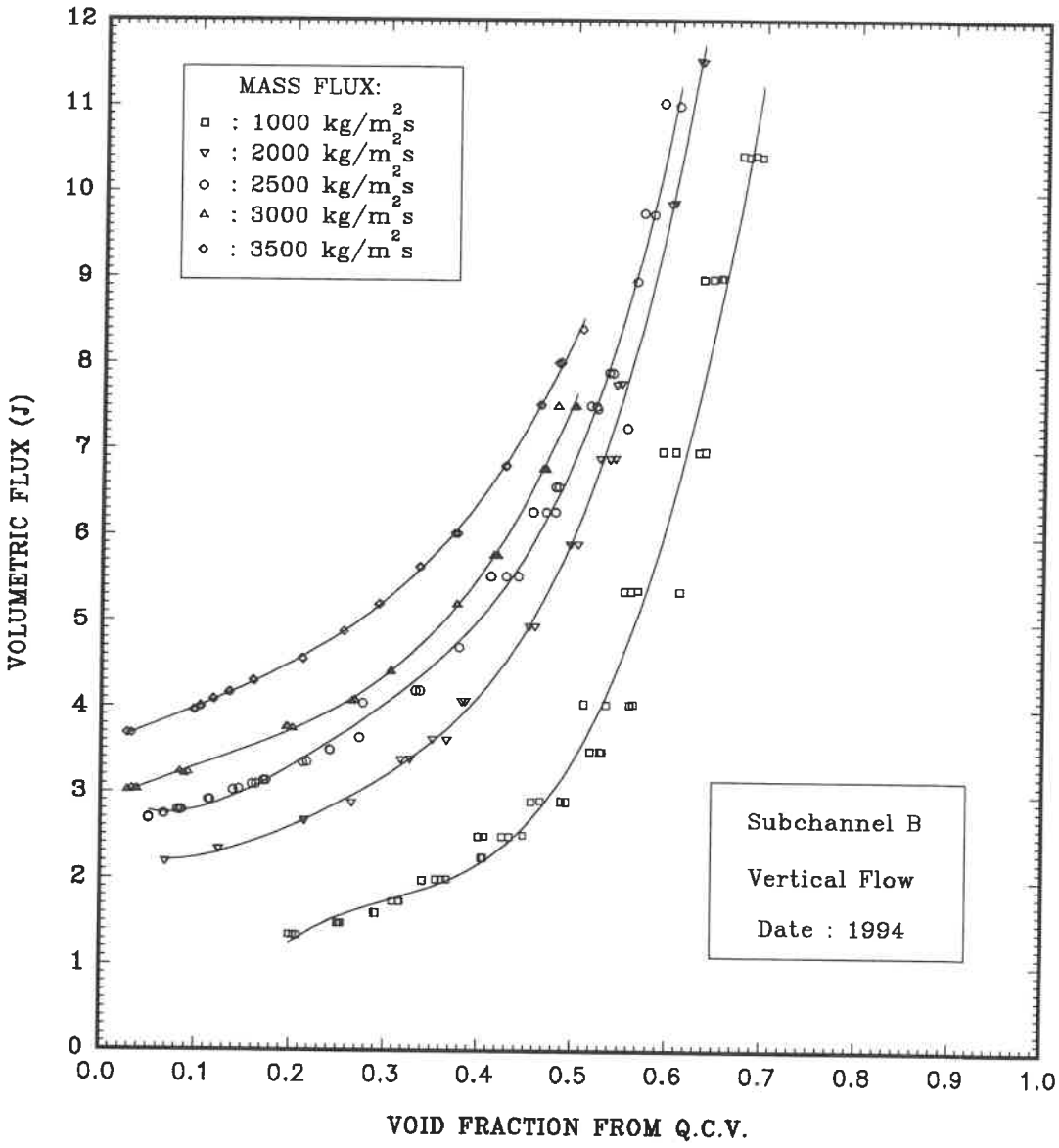


Figure 4.21: Relationship between the Volumetric flux of liquid and void Fraction, Channel B

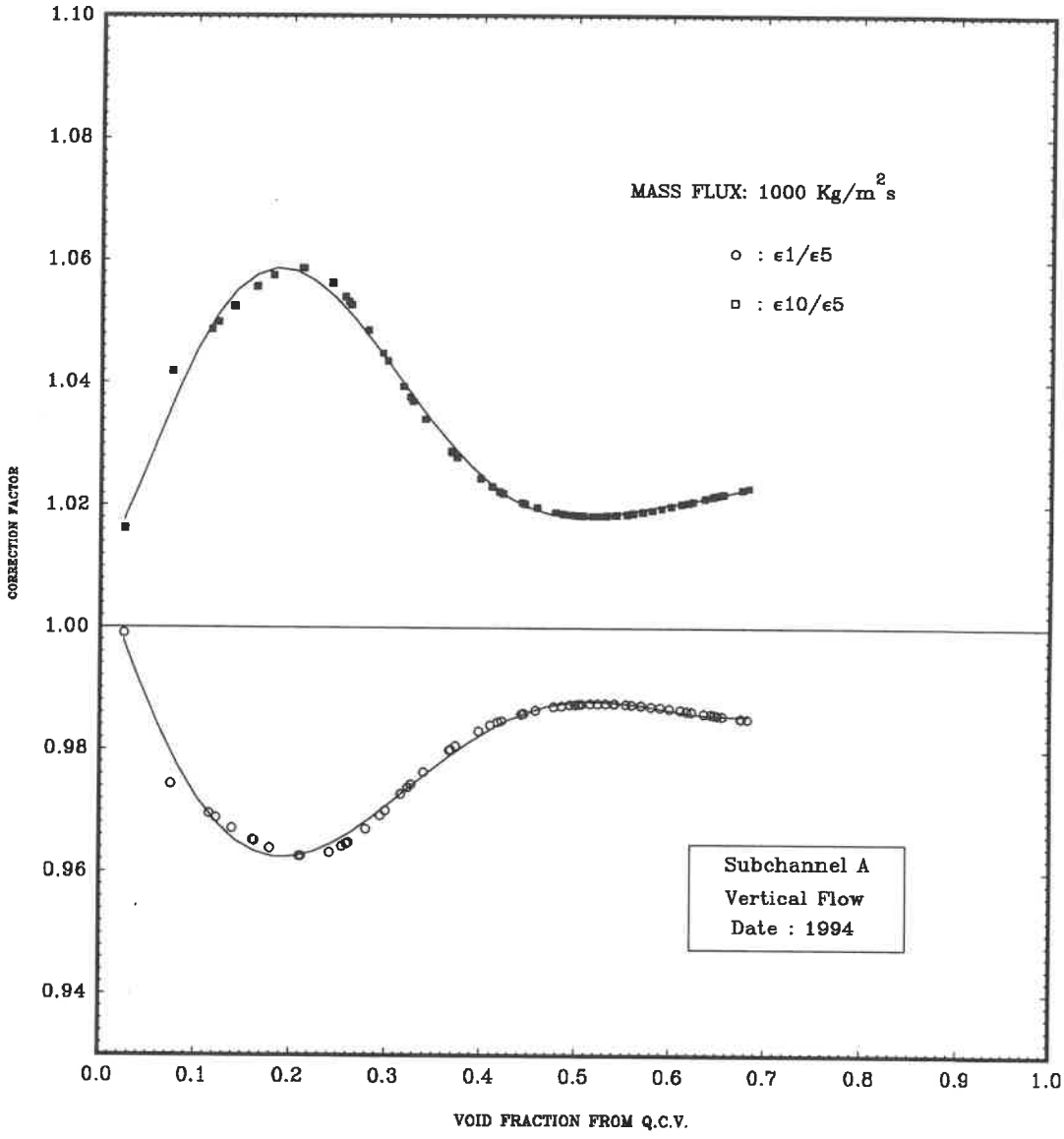


Figure 4.22: Void Fraction Correction Curve, 1000 kg/m^{2}s

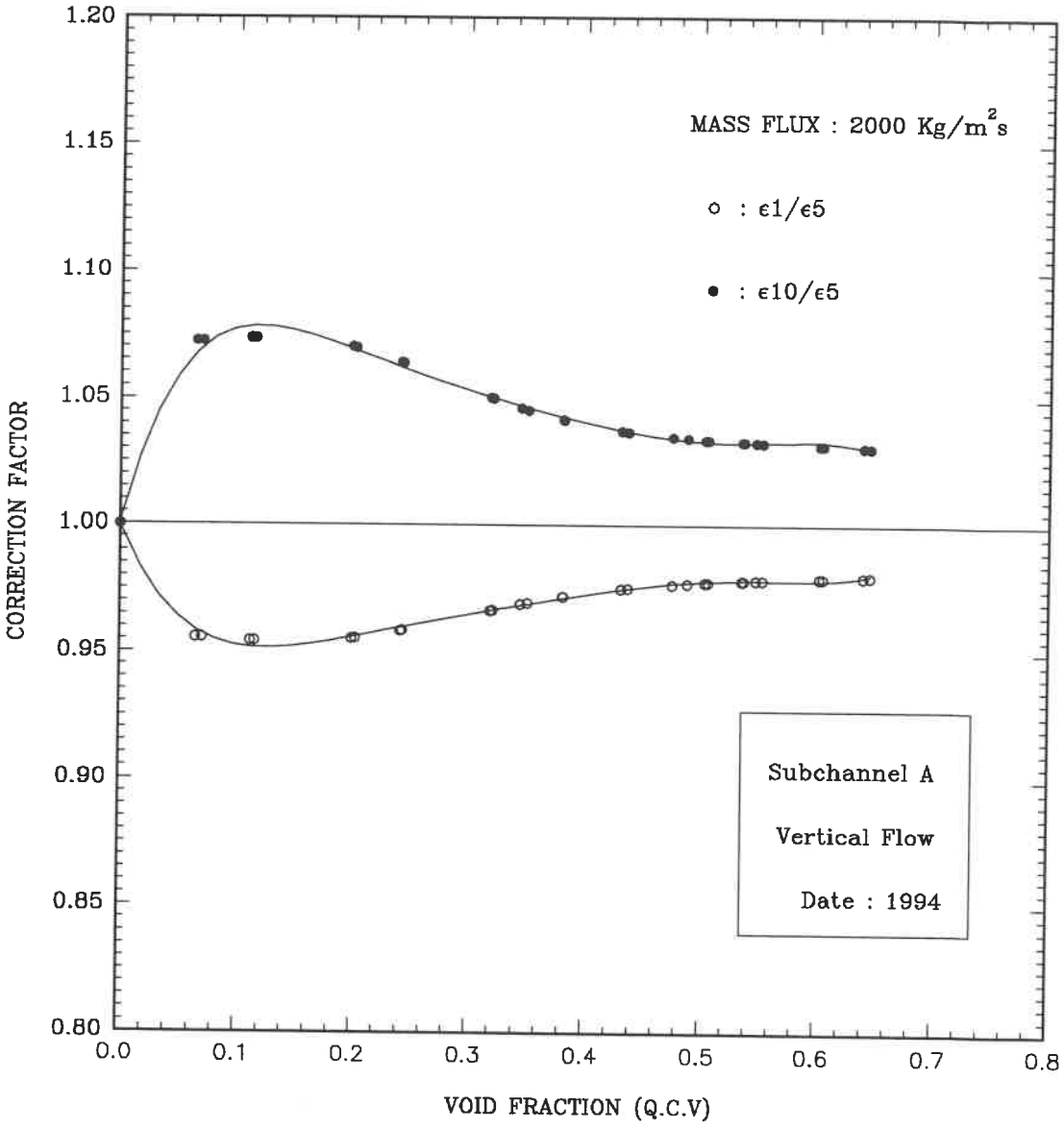


Figure 4.23: Void Fraction Correction Curve, 2000 kg/m^{2}s

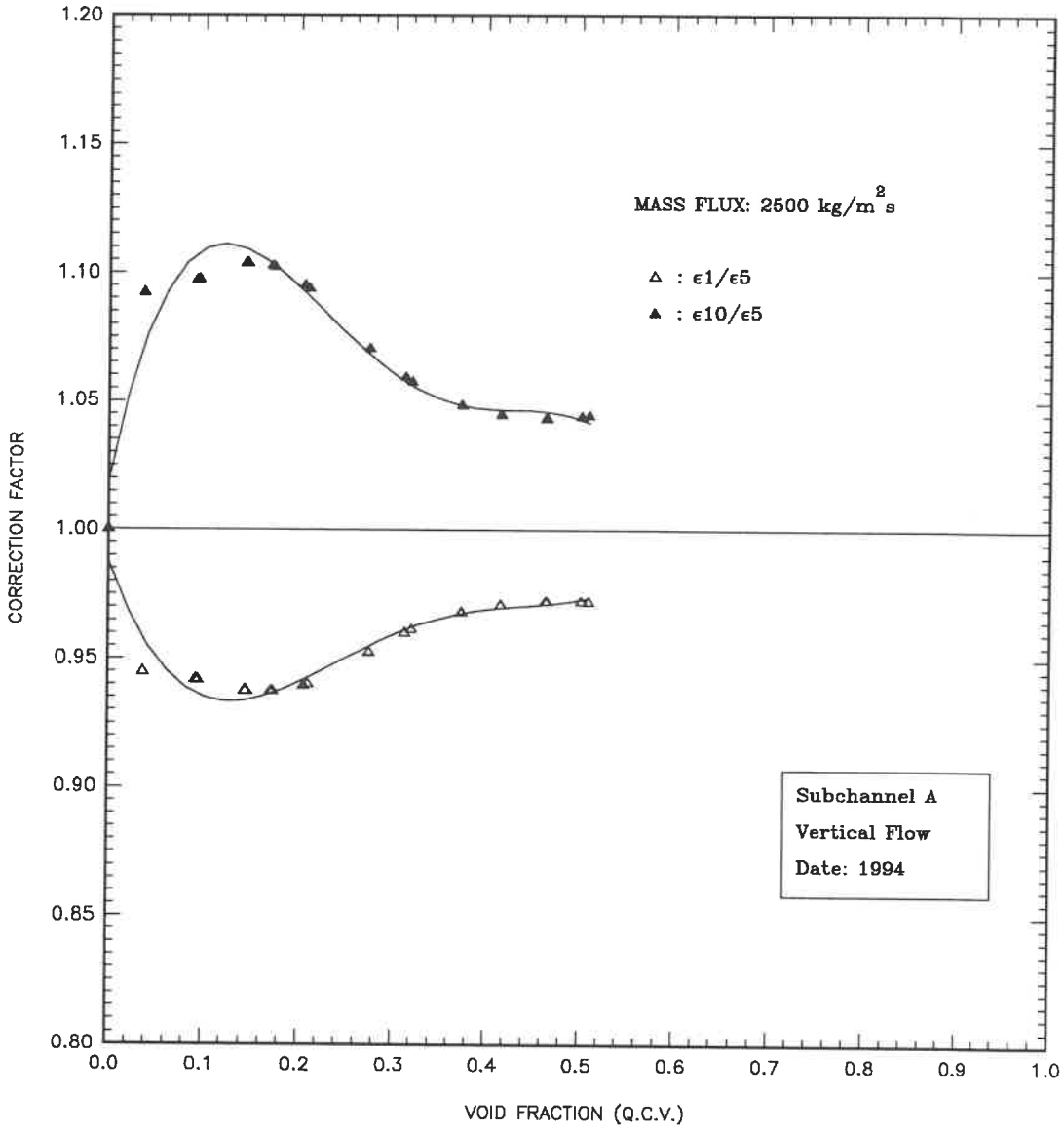


Figure 4.24: Void Fraction Correction Curve, 2500 kg/m^{2}s

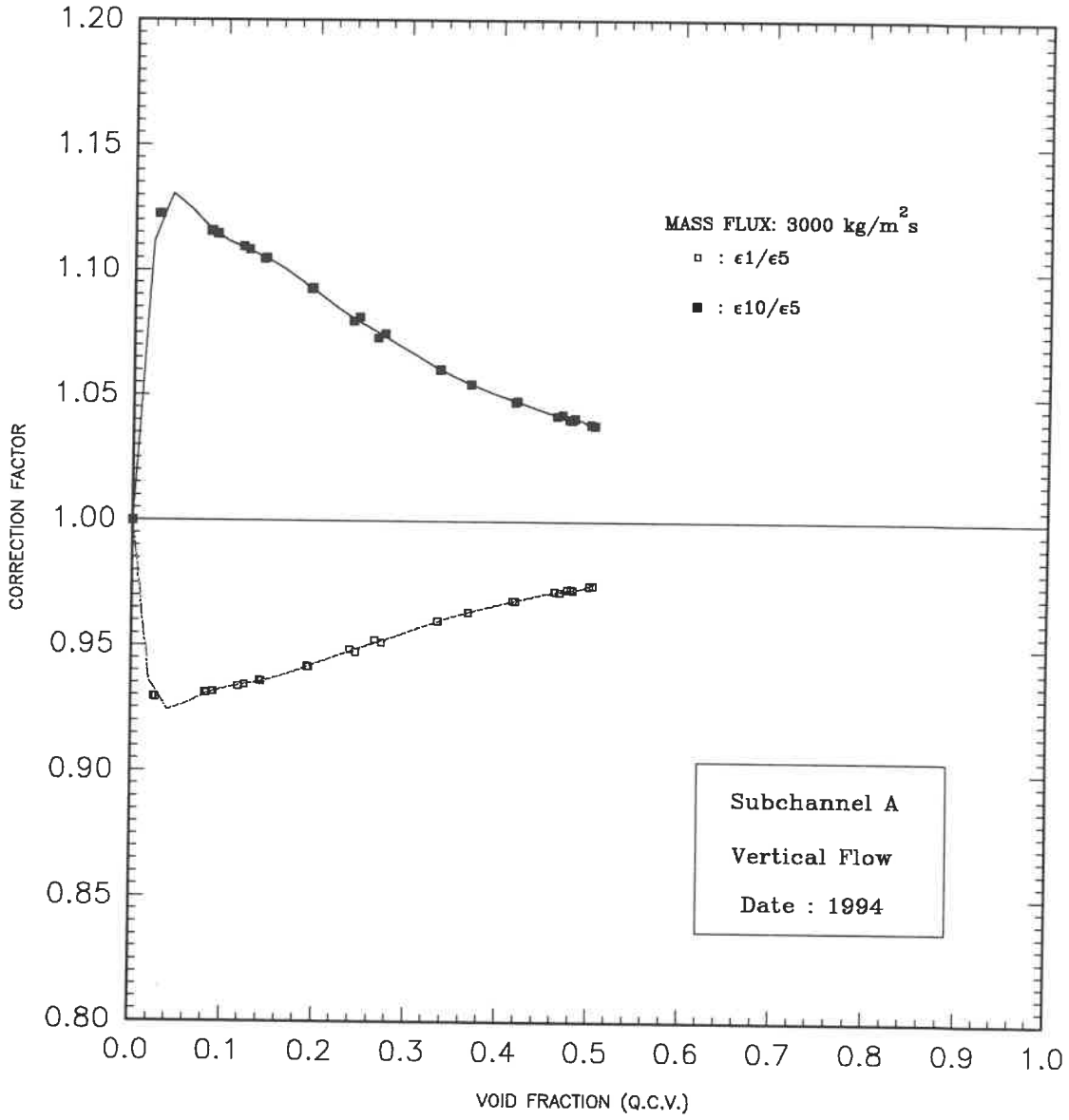


Figure 4.25: Void Fraction Correction Curve, 3000 kg/m^{2}s

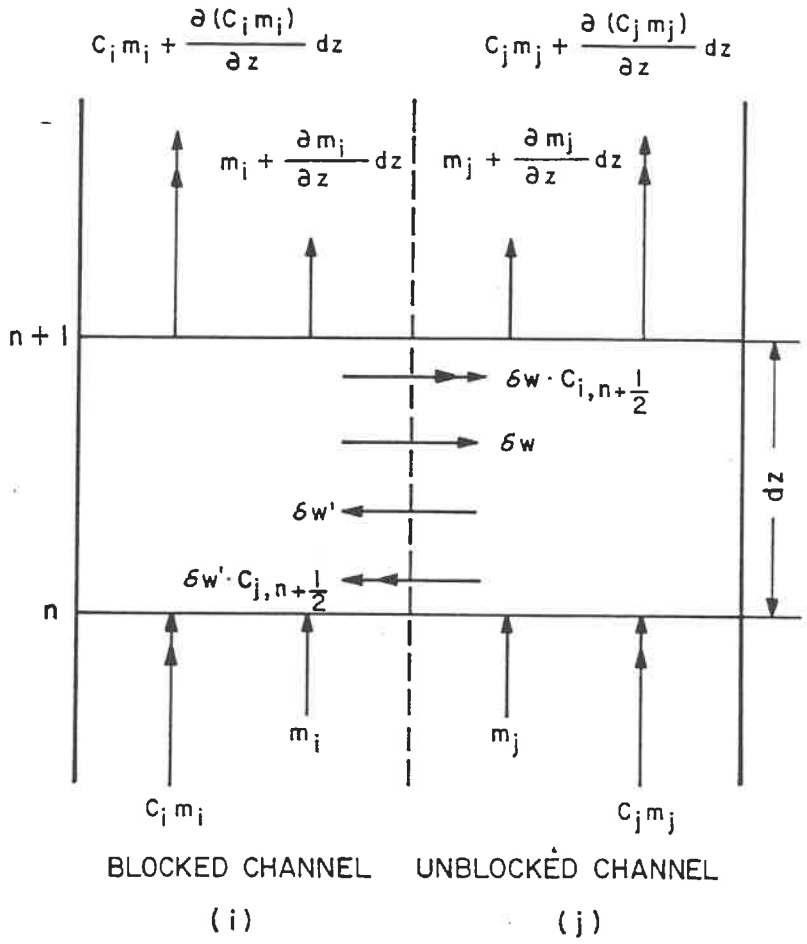


Figure 4.26: Mass Conservation: Liquid and Tracer

CHAPTER 5

COMPARISON OF MEASURED AND PREDICTED RESULTS-NO BLOCKAGE CASES

In this chapter, the experimental data obtained on two laterally interconnected subchannels without blockage will be compared with the prediction of the COBRA-IV subchannel code. In this series of experiments detailed measurements were only taken on pressure and void fraction. The liquid mass transfer across the interconnection were not measured during the experiments. This means that the optimization of the mixing coefficient is not complete, since the performance of the mixing model is evaluated based on both the void fraction and the liquid mass exchange prediction. The inlet flow conditions for the experiments identified as run SV94-01 to run SV94-21 are summarised in Table 5.1.

5.1 Constitutive Equations and Input Data for COBRA-IV

As has been mentioned in the previous chapters, to solve the system of basic equations, several constitutive equations based on experiments should be provided to obtain a closed form of the conservation equations which can then be solved numerically. In this section, all constitutive relationships developed based on the experiments and the form of the input data for the simulations are presented. Since, in the present experiments, an adiabatic two component mixture has been considered, the only needed constitutive equations to carry out the simulations with COBRA-IV are the axial friction factor, the two-phase multiplier, the void/dryness relationship, and the turbulent mixing coefficient.

5.1.1 Constitutive Equations

I) Axial Friction Factor:

As mentioned in Chapter 4, special experiments were carried out to determine the friction factor for the subchannel geometry used in this investigation. The global friction factor relation which is valid for both subchannel A and B is then calculated using the following relationship (Figure 5.1):

$$f = a(Re)^b + c, \tag{5-1}$$

with: $a = 1.973478633$,

$b = -0.532671232$,

$c = 0.011847571$.

This relationship is valid for: $5000 < Re < 30000$.

It should be mentioned that in the statistical process the experimental points, which are measured between tap 7 and tap 15 in channel B, are weighted five times more than all other points to adjust the performance of the relation for the Reynolds number greater than 15000 .

II) Two-Phase Multiplier:

Using the results of the data presented in Chapter 4, a relationship between the two-phase multiplier and the dryness fraction, which is valid for both subchannel A and B, is calculated as follows (Figure 5.2):

$$\Phi^2(x) = a_0 + a_1 x + a_2 x^2 + a_3 x^3 + a_4 x^4 + a_5 x^5 + a_6 x^6, \qquad (5\text{-}2)$$

with : $a_0 = 1.00$,

$a_1 = 1087.173297$,

$a_2 = -300395$,

$a_3 = 52084481$,

$a_4 = -4206104611$,

$a_5 = 153884825026$,

$a_6 = -1.988159\ E{+}12.$

This relationship is valid for: $x \leq 0.02$.

III) Void Fraction / Dryness fraction Relationship:

The experiments performed on single channel flow, show that the relationship between the void fraction and the dryness fraction is nearly independent of the liquid mass flow rates. The relation for void fraction and dryness fraction which is valid for both subchannels is (Figure 5.3):

$$\alpha(x) = b_0 + b_1 x + b_2 x^2 + b_3 x^3 + b_4 x^4 + b_5 x^5 + b_6 x^6, \qquad (5\text{-}3)$$

with: $b_0 = 0.018368$,

$b_1 = 347.036094$,

$b_2 = -105965$,

$b_3 = 16724953$,

$b_4 = -1364355779$,

$b_5 = 54932166059$,

$b_6 = -8.632631E{+}11.$

This relationship is valid for: $0.00002 \leq x \leq 0.02$.

IV) Turbulent Mixing Coefficient (β):

COBRA-IV uses the lateral turbulent energy and momentum exchange model based on a fluctuating equal mass exchanges between adjacent subchannels (Section 3.4.1). In this model the mixing coefficient, besides a direct input as a constant, could also be given by an appropriate expression or could be specified as a function of quality in tabular form. In the present work, β is considered to be constant and it will be optimized by using the experimental data on axial void fraction profile.

5.1.2 Configuration of the Input Data

The following input data have been specified for COBRA-IV: (Following the order as they appear in the input file)

1) Property table of water and steam (Table 5.2):
   - A pseudo property table is used for air-water mixture.
2) Friction factor and two phase flow correlations:
   - No subcooled void correlation is considered.
   - The void fraction is expressed as a function of dryness fraction by Equation (5-3).
   - Two-phase multiplier is expressed as a function of quality by Equation (5-2).
   - No wall viscosity correlation is used (adiabatic experiments).
   - No laminar friction factor is considered.
3) No axial heat flux is added but a uniform axial heat profile is defined.
4) Subchannels layout dimensions:
   - Flow area, wet perimeter, heated perimeter, adjacent subchannel connection information and gap spacing are introduced. No thermal connection or directed cross-flow are considered.

5) No subchannel area variation is considered.

6) No gap size variation is considered.

7) No wire wrap or anyother type of apacer is introduced.

8) The layout for the rod is introduced but no thermal model is applied.

9) Options for the numerical calculations:

- Since the experiments are all in steady-state conditions, the implicit steady-state scheme is chosen.
- Only the interconnected region is introduced as the total axial length.
- The external cross-flow convergence limit is fixed as 0.1. (Numerous tests show that external cross-flow convergence limits smaller than 0.1 do not improve the predictions of COBRA-IV and increase the number of iteration and CPU time).
- The internal cross-flow convergence limit for the iterative Gauss-Seidel solution scheme at axial level j is set to 0.001.
- The external axial flow convergence limit, defined for the implicit axial momentum equation as the maximum allowable error for iterative axial flows is considered equal to 0.001.
- The cross-flow resistance factor K_{ij}, is taken to be 1.0 (Numerous runs have shown that the predictions of COBRA-IV, in the case of laterally interconnected subchannels without blockage are practically independent of K_{ij}.)
- The transverse momentum parameter is taken as s/l=0.088 (l is the centroid to centroid distance and s is the gap distance). The numerous tests show that the value of transverse momentum parameter has no influence in the predictions of the COBRA-IV.
- The turbulent momentum factor is considered to be zero.
- The effective axial velocity component of the cross-flow (u^*) is taken equal to the arithmetic average of the velocities in the interconnected subchannels,

$$u^* = \frac{(u_i + u_j)}{2}.$$

- No cross-flow solution accelerator is used.
- The number of axial nodes is fixed to 120 (Previous tests have shown that increasing the number of nodes beyond this does not improve the prediction of COBRA).
- The turbulent mixing correlation is used in the form given by Equation (3-72) and β is optimised on the basis of the experimental results.

11) The inlet enthalpy, mass flux and the system pressure at the exit are specified.

In each simulation, the inlet enthalpy is chosen in such way that the calculated quality (dryness fraction) corresponds to the actual void fraction at the inlet of the subchannel. All fluid property calculations in COBRA use the concept of a reference pressure (operating pressure in the present work) which is uniformly applied over the entire computational mesh. The reference pressure is specified in the input and determines the saturation properties from the property table. When the concept of a reference pressure is used, the fluid density is unaffected by the local pressure head. It should be mentioned that the approach of considering a reference pressure is justifiable, whenever the maximum spatial pressure change is small compared to the reference pressure.

5.2 Results of the Comparison

The experiments can be divided into two series: first, the experiments with equal inlet mass fluxes and second, those with unequal inlet mass fluxes. For each series of the experiments, equal and unequal inlet void fraction were examined. In this section, the results of the comparison are presented based on the inlet flow conditions.

5.2.1 Equal Inlet Mass Fluxes

In this series of experiments three different inlet mass fluxes are examined.The first is 3000 kg/m^2s identified by runs SV94-01 through SV94-05. The second is an inlet mass flux equal to 2000 kg/m^2s identified by runs SV94-18 and SV94-19 and the third is inlet mass flux which is equal to 1000 kg/m^2s identified by runs SV94-20 and SV94-21.

I) <u>Unequal Inlet Void Fraction</u>

A) HVS 60% - LVS 00%

Figures 5.4 through 5.9 show the experimental results on the pressure and the void fraction when the inlet mass fluxes to both subchannels are equal to 3000 kg/m^2s (run SV94-01). Figures 5.4 and 5.5 show that the prediction of the total pressure drop in both subchannels at the beginning of interconnection are slightly overestimated and they are slightly influenced when β is varied from 0.01 to 0.1. Figures 5.6 and 5.7 show that the COBRA-IV subchannel code with the adjustable coefficient β is not able to follow the void fraction profile in the low void fraction subchannel very well. However, COBRA-IV predicts the void fractions in both subchannel reasonably well when β is taken to be 0.05. Figures 5.8 and 5.9 show the predictions of COBRA for liquid flow rate. Since no data have been collected on liquid mass flow rates in the subchannels, no comparison could be done. Figures 5.10 and 5.11 show the total pressure drop for the case SV94-03 in which all the inlet flow conditions are the same as for the run SV94-01 except that subchannel B is now the high void fraction subchannel (60%). It can be observed that prediction of COBRA-IV are in good agreement with the experiments. A weak dependence of total pressure on β at the beginning of interconnection is again

observed. Figure 5.12 and 5.13 show that the predictions of COBRA-IV for void fraction profile when β is taken equal to 0.05, produce the best predictions. Figures 5.14 and 5.15 show the prediction of COBRA-IV for liquid flow rate in both subchannels. Figures 5.16 and 5.17 show the prediction of the total pressure drop against experimental data for the run SV94-18 with equal inlet mass fluxes 2000 kg/m^2s. In this case, the predictions of COBRA-IV for the total pressure drop are in good agreement with experimental data, however, a slight underestimation can be observed. Figures 5.18 and 5.19 show that β=0.05 give the best prediction of the void fraction profile for both subchannels. Figures 5.20 and 5.21 show the prediction of COBRA-IV for the liquid flow rate in both subchannels. Figure 5.22 through 5.27 compare the predictions of COBRA-IV for the case SV94-20 with inlet mass fluxes in both subchannels equal to 1000 kg/m^2s against the experimental data. It can be observed that the value of β equal to 0.05 again gives the best agreement between the COBRA-IV predictions and experimental results.

B) HVS 40% - LVS 00%

Figures 5.28 and 5.29 show the predictions of the total pressure drop against experimental data for run SV94-02 with equal inlet mass flux 3000 kg/m^2s. In this case, the predictions of COBRA-IV follows the experimental trends. Figures 5.30 and 5.31 show that β=0.01 gives the best prediction of the void profile for both subchannels. Figures 5.32 and 5.33 show the liquid flow rate predicted by COBRA-IV for both subchannels. Figures 5.34 through 5.39 show the predictions of COBRA-IV for the total pressure drop, the void fraction profile and the liquid flow rate for the case SV94-04 with the subchannel B identified as high void subchannel. Excellent predictions of the total pressure drop (Figures 5.34 and 5.35) and the void fraction profile with

β=0.01 (Figures 5.36 and 5.37), resulted. Figures 5.40 through 5.51 show the predictions of COBRA-IV for the cases SV94-19 and SV94-21 with inlet mass flux equal to 2000 kg/m^2s and 1000 kg/m^2s respectively. An excellent agreement between the predictions of COBRA-IV for β equal to 0.05 and the experimental data in both the total pressure drop and the void fraction profile can be observed.

II) Equal Inlet Void Fraction

In the run SV94-05 equal inlet mass fluxes (3000 kg/m^2s) and equal inlet void fractions into the subchannels (40%) are considered. Figures 5.52 and 5.53 show that COBRA-IV underestimates the total pressure drop in both subchannels. Since the flow conditions of the subchannels are identical, no void migration is observed (Figures 5.54 and 5.55), however, the slight increase in the void fraction experimentally is observed in both subchannels is probably due to expansion of the gas phase with the pressure drop. Since COBRA-IV uses a reference pressure to calculate the properties of the gas it should not be able to see any expansions in the gas phase.

5.2.2 Unequal Inlet Mass Fluxes

Two series of experiments with the unequal inlet mass fluxes were carried out:
- 3000 kg/m^2s for subchannel A and 1000 kg/m^2s for subchannel B, and
- 3000 kg/m^2s for subchannel A and 2000 kg/m^2s for subchannel B.

I) The experiments with G_A=3000 kg/m²s and G_B=1000 kg/m²s:

In run SV94-06 the inlet voids were set to 60% in subchannel A and 0% in

subchannel B. Figures 5.58 and 5.59 show the predictions of total pressure with a slight overestimation in the beginning of the interconnection. Figures 5.60 and 5.61 show that the void fractions are well predicted in both subchannels. A fast increase of void fraction in the receiver subchannel is correctly predicted in all cases, however the best agreement is obtained by using β=0.01. In the donor subchannel, β=0.05 gives the best prediction. Figures 5.62 and 5.63 show the predictions of COBRA-IV for the liquid flow rates in each subchannel for the values of β between 0.01 and 0.1. In run SV94-08 the subchannel with the low inlet mass flux has an inlet void fraction of 60%. Figures 5.64 and 5.65 show that the total pressure drop can be correctly predicted with both β=0.05 or 0.1. Figures 5.66 and 5.67 show that the value of β between 0.01 and 0.05 will give reasonable results for the void fraction. Figures 5.68 and 5.69 show that the prediction of COBRA-IV for liquid flow rate strongly depends on the values of β.

In run SV94-07 the inlet void of subchannel A is set to about 40%. Figures 5.70 and 5.71 show the predictions of COBRA-IV for total pressure drop follow the experimental trends very well. Figures 5.72 and 5.73 show that in both subchannel the best predictions for the void fraction are obtained with β=0.05. Figures 5.74 and 5.75 show the predictions of COBRA-IV for the liquid flow rate in both subchannels. Run SV94-09 is the same as run SV94-08 except that the inlet void fraction for the low inlet mass flux subchannel is 40%. Figures 5.76 through 5.81 give the predictions of the total pressure drops, he void fractions and the liquid flow rates in both subchannel. It can be concluded that in general, the β=0.05 gives the best results for both subchannels.

Runs SV94-10 and SV94-11 have equal inlet void fraction in both subchannels (60% and 40% respectively). The results are given in figures 5.82 through 5.93. Figures 5.82, 5.83, 5.88 and 5.89 show the slight underestimation of total pressure drop in both

experiments by COBRA-IV. Figures 5.84, 5.85, 5.90 and 5.91 show that the predictions of COBRA-IV for the void fractions are not affected by the β. Dispersion in the data points could be due to instrumental uncertainty or local void fraction profile in the flow section. It seems also that the liquid flow rate predictions of COBRA-IV is not affected by the choice of β (Figures 5.86, 5.87, 5.92 and 5.93).

II) The experiments with G_A=3000 kg/m²s and G_B=2000 kg/m²s:

Figures 5.94 through 5.129 show the predictions of COBRA-IV against experimental data for these series of runs identified by SV94-12 through SV94-17.

In run SV94-12 unequal void fraction at the inlet of the subchannels with high mass subchannel as the high void subchannel (60%) was tested. Figures 5.94 and 5.95 show that the predictions of the COBRA-IV for the total pressure drops are slightly affected by the values of the β. The best result for total pressure drop predictions are obtained by both β=0.05 or 0.1. Figures 5.96 and 5.97 show that β equal to 0.05 gives the best predictions for the void fraction, however, the difference between the experimental data and code's predictions exist. Figures 5.98 and 5.99 show the predictions of the COBRA-IV for the liquid flow rates in both subchannels. In run SV94-14 the low mass flux subchannel has the inlet void fraction equal to 60%. Once again, the predictions of the COBRA-IV for the pressure drop are slightly affected by the values of β (Figures 5.100 and 5101). The void fractions are satisfactorily predicted by some values of β between 0.01 and 0.05 (Figures 5.102 and 5.103). Figures 5.104 and 5.105 show that the predictions of the COBRA-IV for the liquid flow rate strongly depend on the values of β. In run SV94-13 inlet void fraction equal to 40% in high mass flux subchannel tested. Figures 5.106 and 5.107 show that COBRA-IV with some value

of β between 0.01 and 0.1 correctly predict the experimental data. Figures 5.108 and 5.109 show that the predictions of the COBRA-IV for the void fraction with the value of β equal to 0.01 are in good agreement with experimental data. The liquid flow rate predictions for run SV94-13 are shown in the figures 5.110 and 5.111. In run SV94-15 the inlet void fraction of low mass flux subchannel was set to 40%. Figures 5.112 through 5.117 show the predictions of the COBRA-IV for the total pressure drops, the void fractions, and the liquid flow rates for run SV94-15. A value of β equal to 0.01 can be considered as the best value of mixing coefficient parameter in this case. Runs SV94-16 and SV94-17 have equal inlet void fractions in both subchannels (60% and 40% respectively). The results are given in the Figures 5.118 through 5.117. In both runs slight underestimation of the total pressure drop can be observed (figures 5.118, 5.119, 5.124, and 5.125). The predictions of the COBRA-IV for the void fraction are not affected by the values of β (Figures 5.120, 5.121, 5.126, 5.127). Figures 5.122, 5.123, 5.128, and 5.129 show that the predictions of the COBRA-IV for the liquid flow rates are also not affected by the changes in the values of β.

5.3 General Conclusions

Table 5.3 summarizes the obtained results for the experiments presented in section 5.2. Different tests show that finding a relationship between the best value of the mixing factor β as a function of the average inlet flow conditions, i.e., average inlet dryness fraction (X_{av}), average inlet mass flux (G_{av}) and average inlet void fraction (α_{av}) is not possible. Also, an attempt to develop a relationship between the best values of β and the inlet average flow conditions of donor subchannel has also failed. This leads us to divide the results into two categories: equal inlet mass fluxes and unequal inlet mass fluxes.

5.3.1 Equal Inlet Mass Fluxes

Tables 5.4 and 5.7 show the results for equal inlet mass fluxes category. From Table 5.4 it can be concluded that for $G_A=G_B=G_{Av.}=3000\ kg/m^2s$ the best value for β depends on the inlet void fraction of the donor subchannel. For the inlet void fraction about 60% the value of **β=0.05** produces the best results. And for the inlet void fraction around 40% the value of **β=0.01** produces the best results. A comparison between SV94-03 and SV94-05 shows that average inlet void fraction can not be used as a parameter to describe the appropriate values of β. In turn, the average inlet dryness fraction for the same cases seems to be the most appropriate criterion. Table 5.7 shows that, for the lower values of the inlet mass fluxes the β-values which gives the best results are higher than those with high mass fluxes. This observation can be explained by the fact that for higher inlet mass flux, the ratio of the dynamic forces acting on the bubbles in the axial direction to the forces acting in the lateral direction is much greater and this does not permit the bubbles to easily migrate in the lateral direction. Also, for the lower mass flux cases, it can be observed that for the average inlet values of dryness fraction less than 0.005 (inlet void fraction less than 60%), essentially a unique value of **β=0.05**, independent of the inlet void fraction allows good predictions to be obtained. It is obvious that additional experiments with the liquid mass exchange measurements are still necessary to better understand the mixing phenomenon.

5.3.2 Unequal Inlet Mass Fluxes

Tables 5.5 and 5.6 show that the degree of intersubchannel mixing, when there is substantial difference between inlet mass fluxes, strongly depends on the subchannel in which the higher void fraction is introduced. When the high mass flux subchannel is

the high void subchannel (cases SV94-06, SV94-07, SV94-12 and SV94-13), the degree of mixing is independent of the inlet void fraction and in most cases a value of **β=0.05** gives the best results. On the other hand, when the low mass flux subchannel corresponds to the high void subchannel (SV94-08, SV94-09, SV94-14, SV94-15), the degree of intersubchannel mixing depends on the inlet void fraction and mass flux of this subchannel. When the difference between the inlet mass flux are great (SV94-08 and SV94-09) higher inlet void fraction causes a lower degree of intersubchannel mixing (β=0.025 for SV94-08 and β=0.050 for SV94-09) and when the difference between inlet mass fluxes are small (SV94-14 and SV94-15) the higher inlet void fractions causes a higher degree of intersubchannel mixing (β=0.025 for SV94-14 and β=0.010 for SV94-15). This means that with increasing the difference between inlet mass fluxes, the effect of increasing the void fraction in the low mass flux subchannel is to decrease the intersubchannel mixing. Therefore, finding a relationship between the best values of β as a function of the inlet average conditions, is impossible, however, for each special run an appropriate value of β exsits. This means that a single value of β cannot correctly predict the behaviour of the cases in which the inlet mass fluxes in the subchannels are different. In the other words, neither a tabular form of β (as a function of dryness fraction) nor a constant values of β can be used in such cases. Consequently, a more complete model that allows different mixing effects to be separated should be introduced (void drift, turbulent mixing,...). Finally, the best values of β for those cases with different mass fluxes in the subchannels but equal inlet void fractions (SV94-10, SV94-11, SV94-16 and SV94-17) depends essentially on the liquid mass transfer between subchannels, which in the present work are not available. However, for these cases, the values of β which gives the best results decrease with increasing average inlet void fraction.

Table 5.1: Inlet Flow Conditions used for the Experiments

Experiment	Channel A		Channel B	
	Liquid Mass Flux (kg/m^2s)	Inlet Void Fraction (%)	Liquid Mass Flux (kg/m^2s)	Inlet Void Fraction (%)
SV94-01	3000	61.4	3000	0.00
SV94-02	3000	42.1	3000	0.00
SV94-03	3000	0.00	3000	61.2
SV94-04	3000	0.00	3000	40.00
SV94-05	3000	40.00	3000	38.80
SV94-06	3020	61.40	1037	0.00
SV94-07	2997	40.70	1026	0.00
SV94-08	3028	0.00	1042	60.40
SV94-09	3025	0.00	1037	40.10
SV94-10	3001	60.10	1024	59.40
SV94-11	3029	39.30	1026	38.64
SV94-12	3004	60.70	2009	0.00
SV94-13	3000	40.70	2020	0.00
SV94-14	3003	0.00	2006	60.20
SV94-15	3016	0.00	2001	39.60
SV94-16	3000	60.40	2010	58.80
SV94-17	3017	40.10	2023	39.70

Table 5.1 (Continued)

Experiment	Channel A		Channel B	
	Liquid Mass Flux (kg/m^2s)	Inlet Void Fraction (%)	Liquid Mass Flux (kg/m^2s)	Inlet Void Fraction (%)
SV94-18	2019	60.30	2004	0.00
SV94-19	2017	40.30	2012	0.00
SV94-20	1011	59.90	1024	0.00
SV94-21	1013	39.20	1019	0.00

Table 5.2: Pseudo-property Table for the Air-Water Mixture

Pressure (*psia*)	Tempreature (*F*)	Specific Volume of Liq. (ft^3/lb_m)	Specific Volume of Air (ft^3/lb_m)	Enthalpy of Liquid (Btu/lb_m)	Enthalpy of Gas (Btu/lb_m)	Viscosity of Liq. ($lb_m/ft\ hr$)
12.00	48.00	0.01605	8.98	30.00	850.00	2.42400
13.00	58.00	0.01605	8.98	40.00	850.00	2.42400
14.00	68.00	0.01605	8.98	50.00	850.00	2.42400
15.00	78.00	0.01605	8.98	60.00	850.00	2.42400
16.00	88.00	0.01605	8.98	70.00	850.00	2.42400

Table 5.3: General Results obtained for the experiments SV94-01 to SV94-21

RUN	G_A (kg/m^2s)	G_B (kg/m^2s)	α_A (%)	α_B (%)	$G_{AV.}$ (kg/m^2s)	$\alpha_{AV.}$ (%)	$X_{Av.}$ (Inlet)	β_A	β_B	$\beta_{opt.}$
SV94-01	3000	3000	61.40	0.00	3000.00	30.700	0.005	0.050	0.050	0.050
SV94-02	3000	3000	42.10	0.00	3000.00	21.050	0.001	0.010	0.010	0.010
SV94-03	3000	3000	0.00	61.20	3000.00	30.600	0.005	0.050	0.050	0.050
SV94-04	3000	3000	0.00	40.00	3000.00	20.000	0.001	0.010	0.010	0.010
SV94-05	3000	3000	40.00	38.80	3000.00	39.400	0.002	0.010	0.010	0.010
SV94-06	3020	1037	61.40	0.00	2028.50	30.700	0.008	0.050	0.050	0.050
SV94-07	2997	1026	40.70	0.00	2011.50	20.350	0.001	0.050	0.100	0.075
SV94-08	3028	1042	0.00	60.40	2035.00	30.200	0.003	0.025	0.010	0.010
SV94-09	3025	1037	0.00	40.10	2031.00	20.050	0.001	0.050	0.050	0.050
SV94-10	3001	1024	60.10	59.40	2012.50	59.750	0.010	0.050	0.050	0.050
SV94-11	3029	1026	39.30	38.64	2027.50	38.970	0.002	0.010	0.010	0.010
SV94-12	3004	2009	60.70	0.00	2506.50	30.350	0.006	0.050	0.050	0.050
SV94-13	3000	2020	40.70	0.00	2510.00	20.350	0.001	0.050	0.050	0.050
SV94-14	3003	2006	0.00	60.20	2504.50	30.100	0.004	0.025	0.010	0.025
SV94-15	3016	2001	0.00	39.60	2508.50	19.800	0.001	0.010	0.010	0.010
SV94-16	3000	2010	60.40	58.80	2505.00	59.600	0.010	0.050	0.050	0.050
SV94-17	3017	2023	40.10	39.70	2520.00	39.900	0.002	0.010	0.010	0.010
SV94-18	2019	2004	60.30	0.00	2011.50	30.150	0.005	0.050	0.050	0.050
SV94-19	2017	2012	40.30	0.00	2014.50	20.150	0.001	0.050	0.050	0.050
SV94-20	1011	1024	59.90	0.00	1017.50	29.950	0.005	0.050	0.050	0.050
SV94-21	1013	1019	39.20	0.00	1016.00	19.600	0.001	0.100	0.050	0.075

Table 5.4: Result obtained for the Case with $G_A=G_B=3000$ *kg/m²s*

Run	G_A	G_B	α_A	α_B	X_A	X_B	$G_{Av.}$	$\alpha_{Av.}$	$X_{Av.}$	β_A	β_B	$\beta_{Optimum}$
SV94-01	3000	3000	61.40	0.00	0.011	0.000	3000	30.70	0.005	0.050	0.050	0.050
SV94-02	3000	3000	42.10	0.00	0.002	0.000	3000	21.05	0.001	0.010	0.010	0.010
SV94-03	3000	3000	0.00	61.20	0.000	0.011	3000	30.60	0.005	0.050	0.050	0.050
SV94-04	3000	3000	0.00	40.00	0.000	0.002	3000	20.00	0.001	0.010	0.010	0.010
SV94-05	3000	3000	40.00	38.80	0.002	0.002	3000	39.40	0.002	0.010	0.010	0.010

Table 5.5 Result obtained for the Cases with $G_A=3000$ and $G_B=1000$ (kg/m²s)

Run	G_A	G_B	α_A	α_B	X_A	X_B	$G_{Av.}$	$\alpha_{Av.}$	$X_{Av.}$	β_A	β_B	$\beta_{Optimum}$
SV94-06	3020	1037	61.40	0.00	0.011	0.000	2028	30.70	0.008	0.050	0.050	0.050
SV94-07	2997	1026	40.70	0.00	0.002	0.000	2011	20.35	0.001	0.010	0.100	0.075

Run	G_A	G_B	α_A	α_B	X_A	X_B	$G_{Av.}$	$\alpha_{Av.}$	$X_{Av.}$	β_A	β_B	$\beta_{Optimum}$
SV94-08	3028	1042	0.00	60.40	0.000	0.010	2035	30.20	0.003	0.025	0.010	0.025
SV94-09	3025	1037	0.00	40.10	0.000	0.002	2031	20.05	0.001	0.050	0.050	0.050

Run	G_A	G_B	α_A	α_B	X_A	X_B	$G_{Av.}$	$\alpha_{Av.}$	$X_{Av.}$	β_A	β_B	$\beta_{Optimum}$
SV94-10	3001	1024	60.10	59.40	0.010	0.010	2012	59.75	0.010	0.050	0.050	0.050
SV94-11	3029	1026	39.30	38.64	0.002	0.002	2027	38.97	0.002	0.010	0.010	0.010

Table 5.6: Result obtained for the Cases with G_A=3000 and G_B=2000 (kg/m^2s)

Run	G_A	G_B	α_A	α_B	X_A	X_B	$G_{Av.}$	$\alpha_{Av.}$	$X_{Av.}$	β_A	β_B	$\beta_{Optimum}$
SV94-12	3004	2009	60.70	0.00	0.010	0.000	2506	30.35	0.006	0.050	0.050	0.050
SV94-13	3000	2020	40.70	0.00	0.002	0.000	2510	20.35	0.001	0.050	0.050	0.050

Run	G_A	G_B	α_A	α_B	X_A	X_B	$G_{Av.}$	$\alpha_{Av.}$	$X_{Av.}$	β_A	β_B	$\beta_{Optimum}$
SV94-14	3003	2006	0.00	60.20	0.000	0.010	2504	30.10	0.004	0.025	0.010	0.025
SV94-15	3016	2001	0.00	39.60	0.000	0.001	2508	19.80	0.000	0.010	0.010	0.010

Run	G_A	G_B	α_A	α_B	X_A	X_B	$G_{Av.}$	$\alpha_{Av.}$	$X_{Av.}$	β_A	β_B	$\beta_{Optimum}$
SV94-16	3000	2010	60.40	58.80	0.010	0.010	2505	59.60	0.010	0.050	0.050	0.050
SV94-17	3017	2023	40.10	39.70	0.002	0.002	2520	39.90	0.002	0.010	0.010	0.010

Table 5.7: Results obtained for the cases with G_A=G_B=2000 and G_A=G_B=1000 (kg/m^2s)

Run	G_A	G_B	α_A	α_B	X_A	X_B	$G_{Av.}$	$\alpha_{Av.}$	$X_{Av.}$	β_A	β_B	$\beta_{Optimum}$
SV94-18	2019	2004	60.30	0.00	0.010	0.000	2011	30.15	0.005	0.050	0.050	0.050
SV94-19	2017	2012	40.30	0.00	0.002	0.000	2014	20.15	0.001	0.050	0.050	0.050
SV94-20	1011	1024	59.90	0.00	0.010	0.000	1017	29.95	0.005	0.010	0.050	0.050
SV94-21	1013	1019	39.20	0.00	0.002	0.000	1016	19.60	0.001	0.100	0.050	0.075

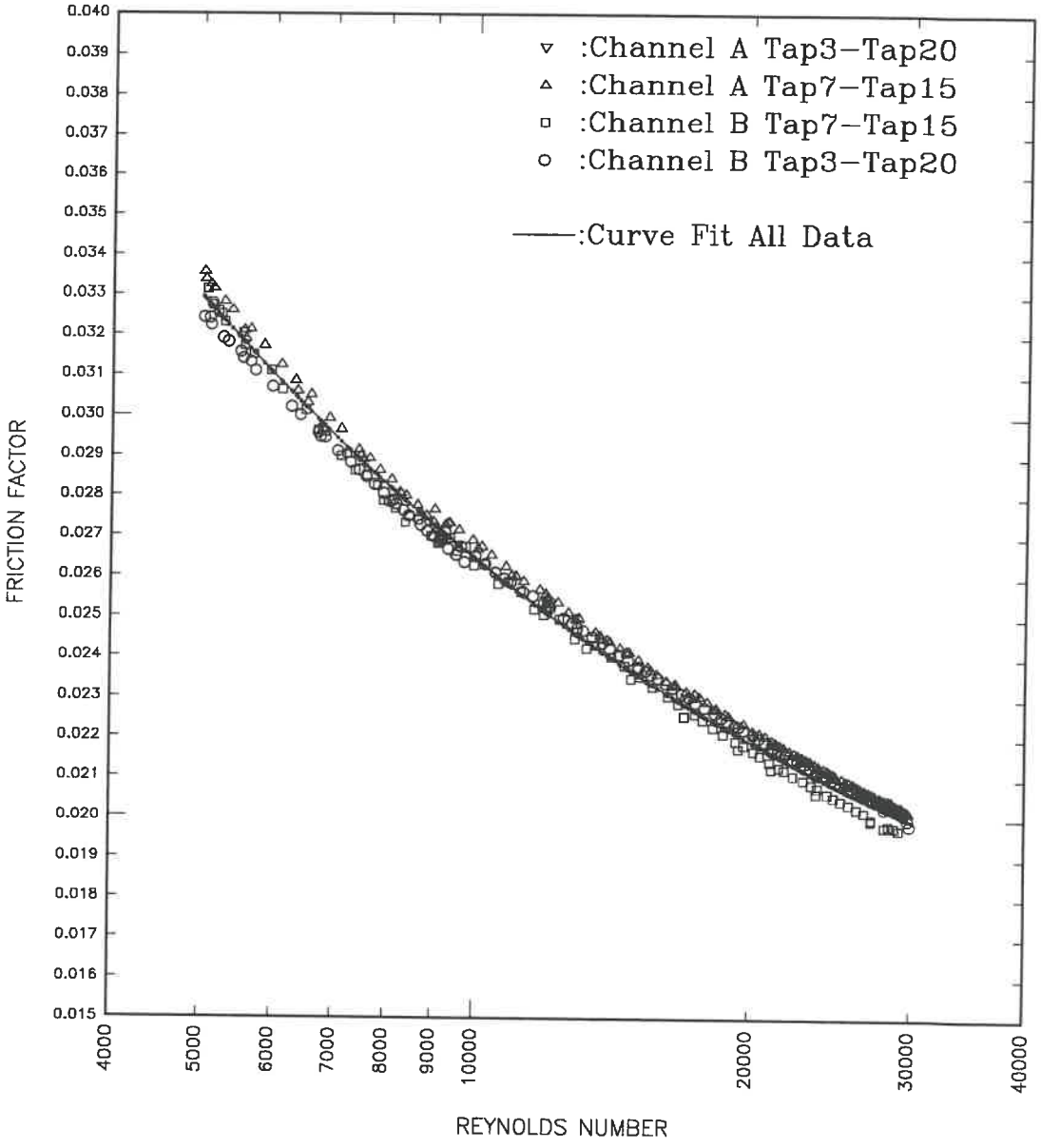


Figure 5.1: Friction factor vs. Reynolds number valid for both channel A, B

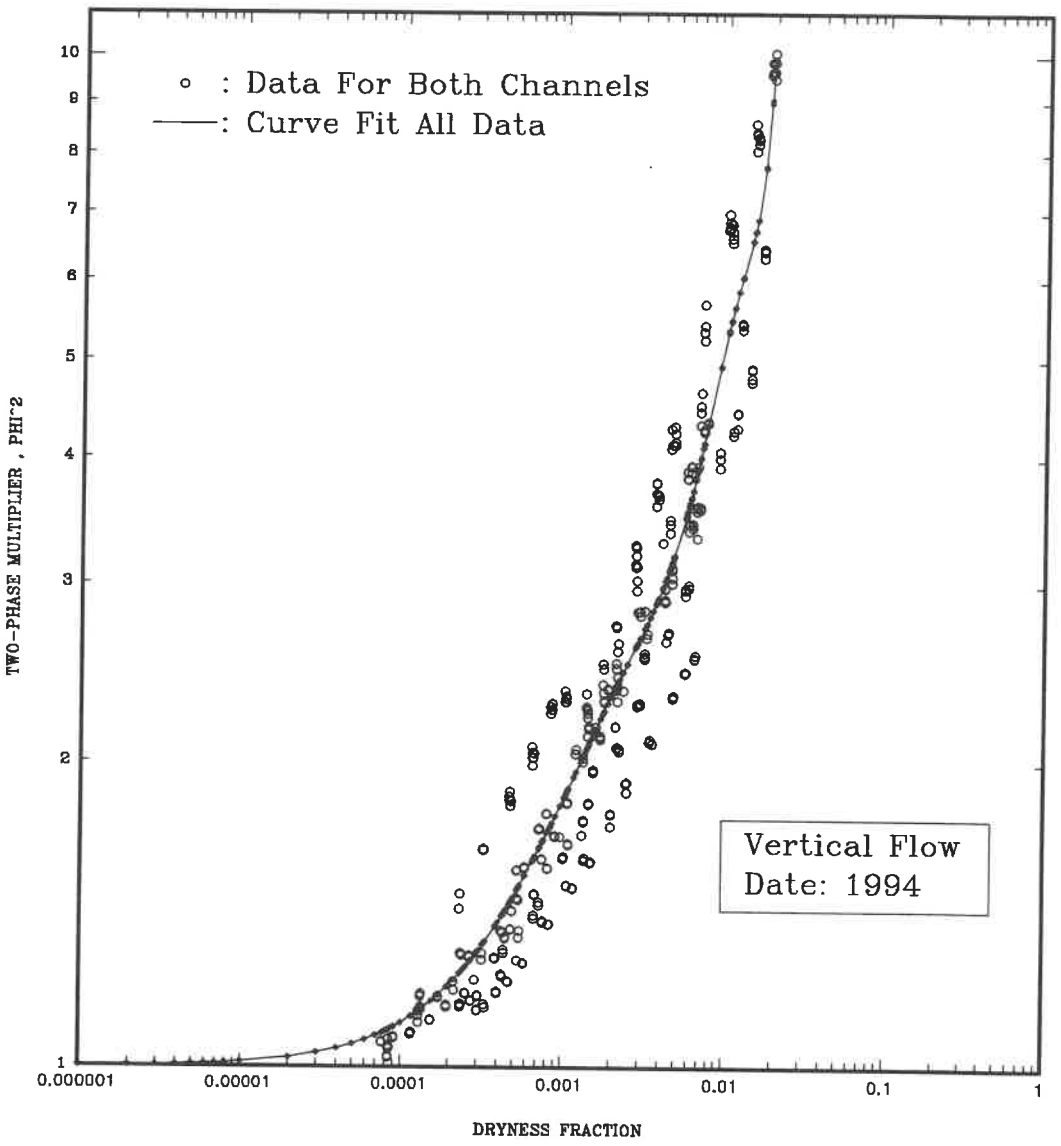


Figure 5.2: Two-phase Multiplier vs. Dryness Fraction Valid for both channel

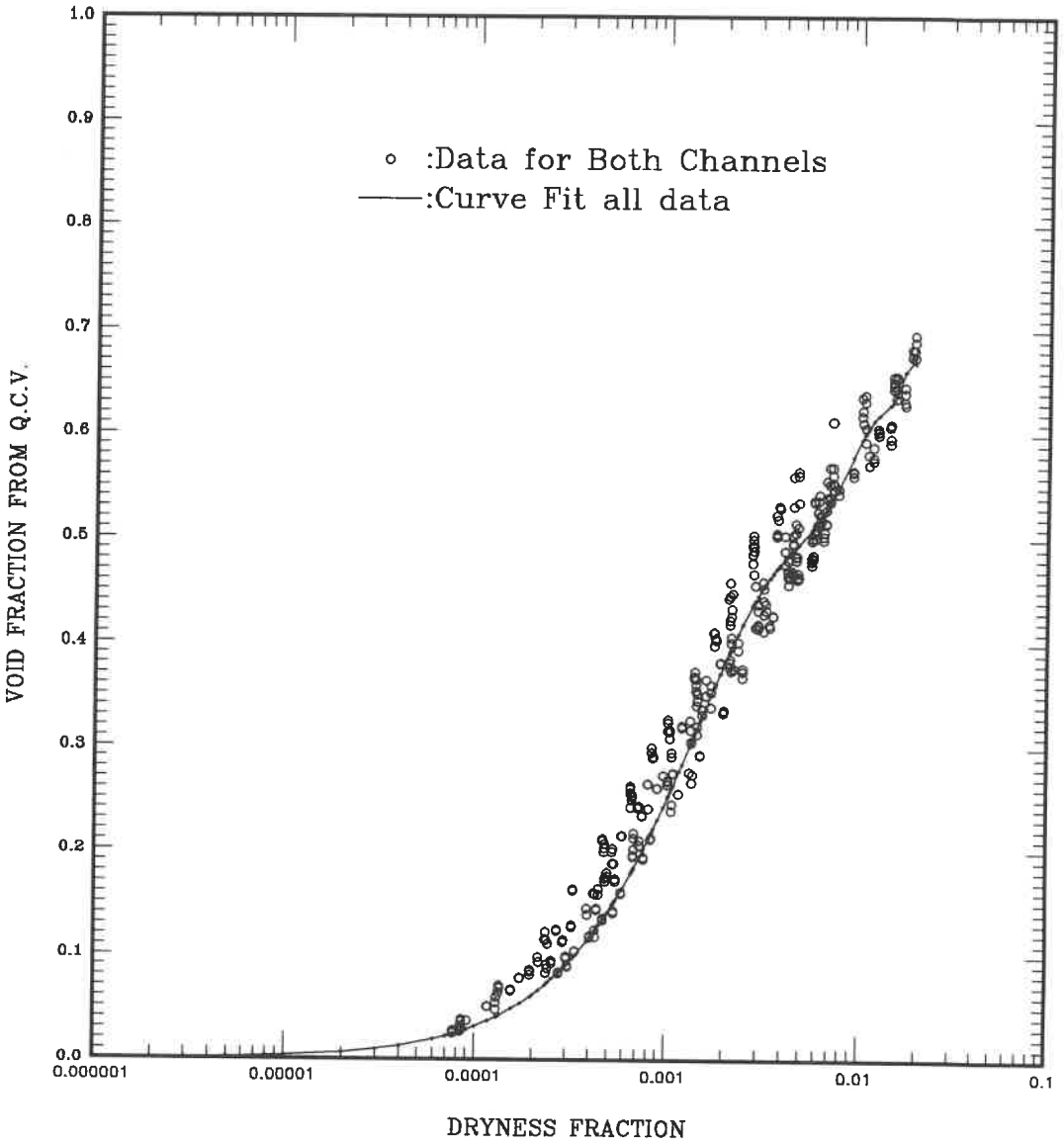


Figure 5.3: Void Fraction vs. Dryness Fraction Valid for both channel

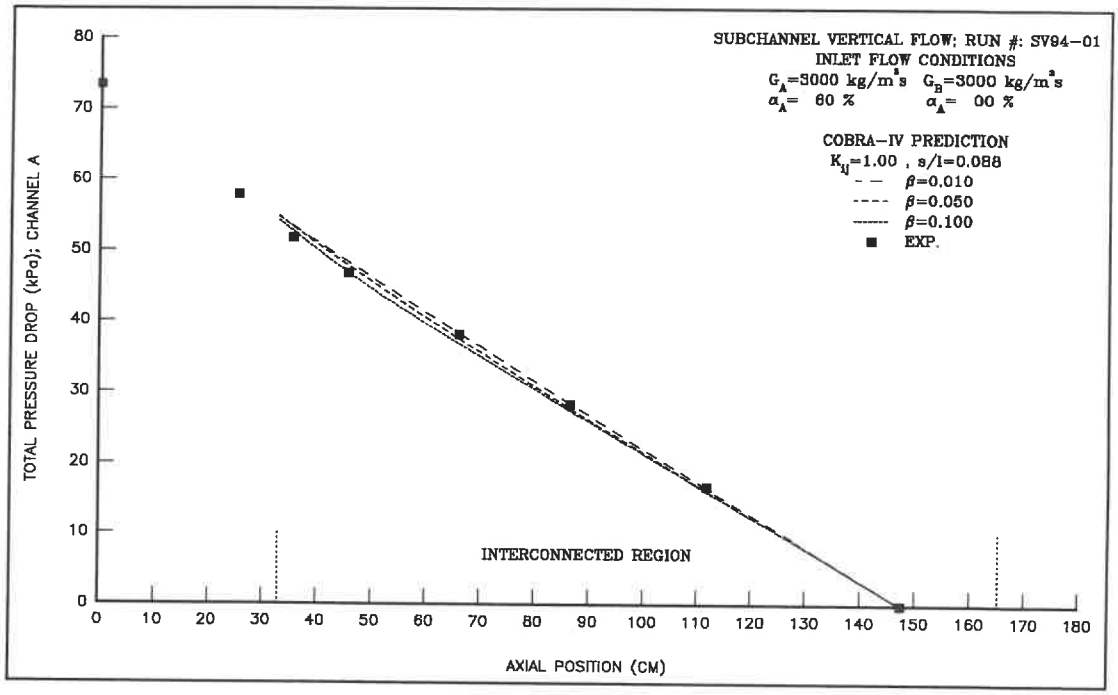


Figure 5.4: Total Pressure Drop Profile, Run SV94-01, Channel A

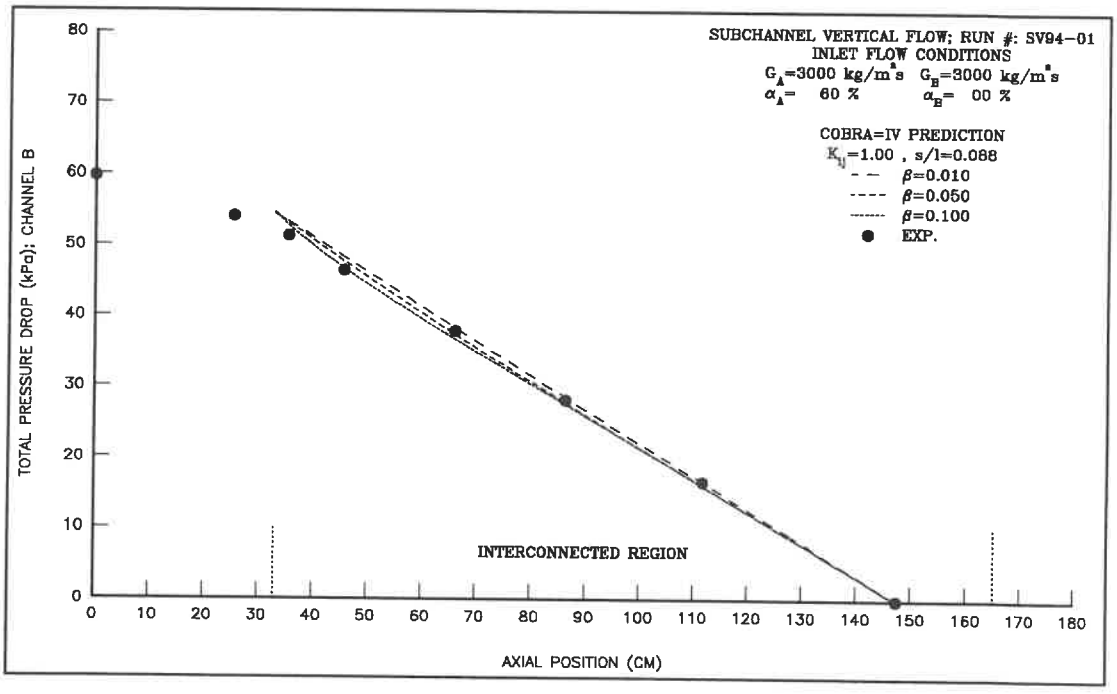


Figure 5.5: Total Pressure Drop Profile, Run SV94-01, Channel B

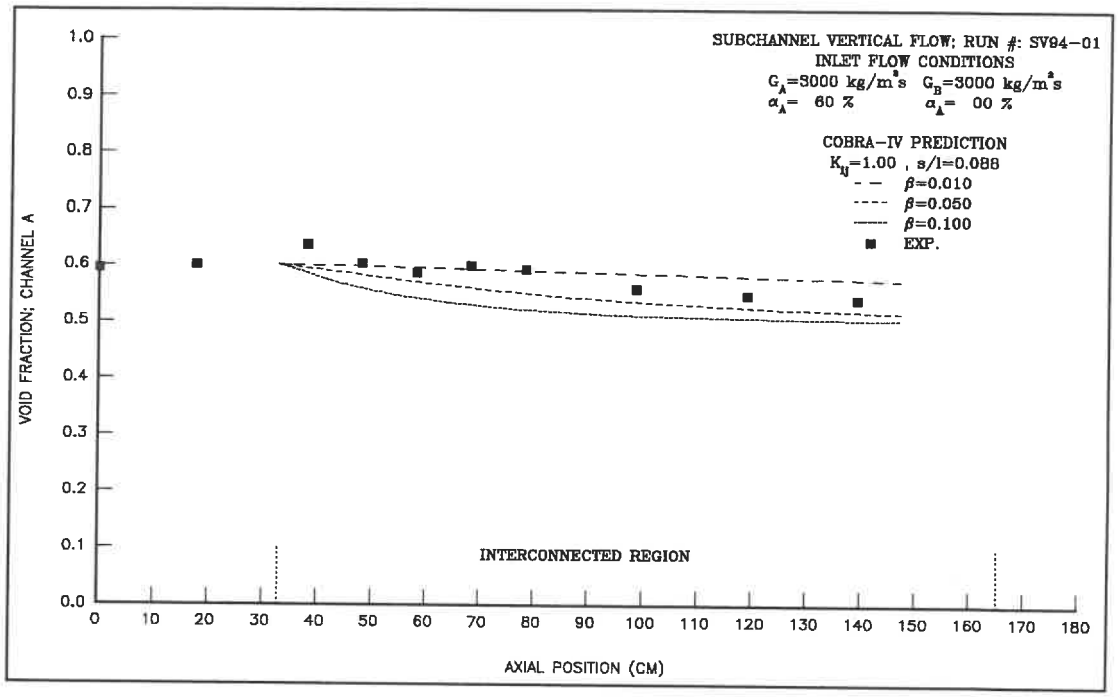


Figure 5.6: Void Fraction Profile, Run SV94-01, Channel A

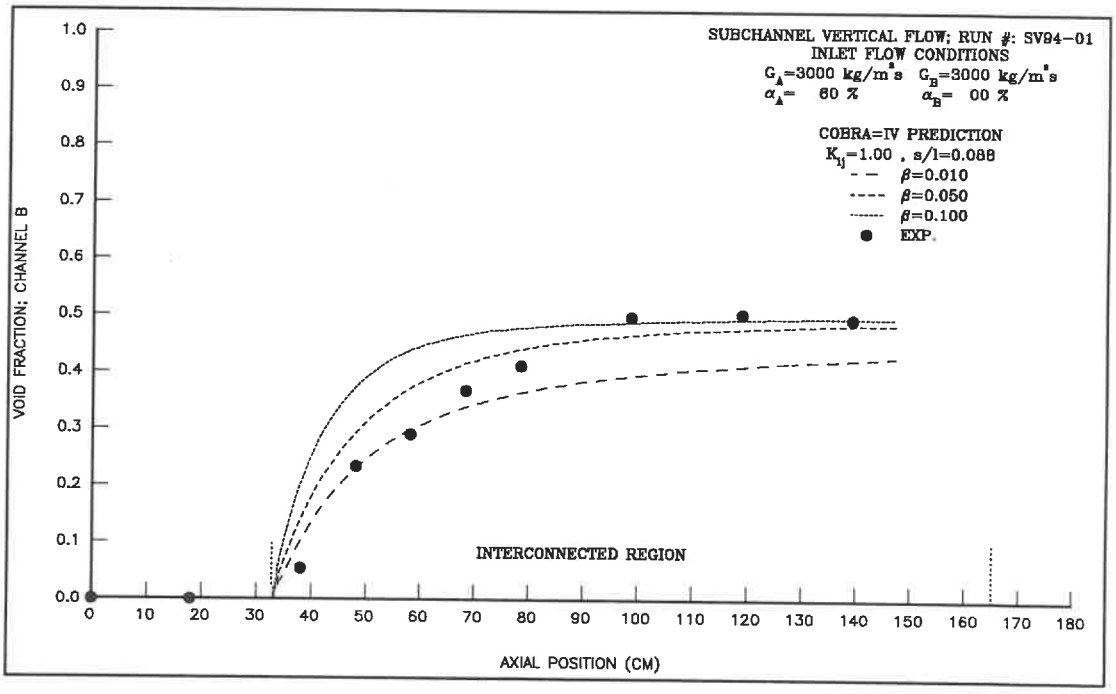


Figure 5.7: Void Fraction Profile, Run SV94-01, Channel B

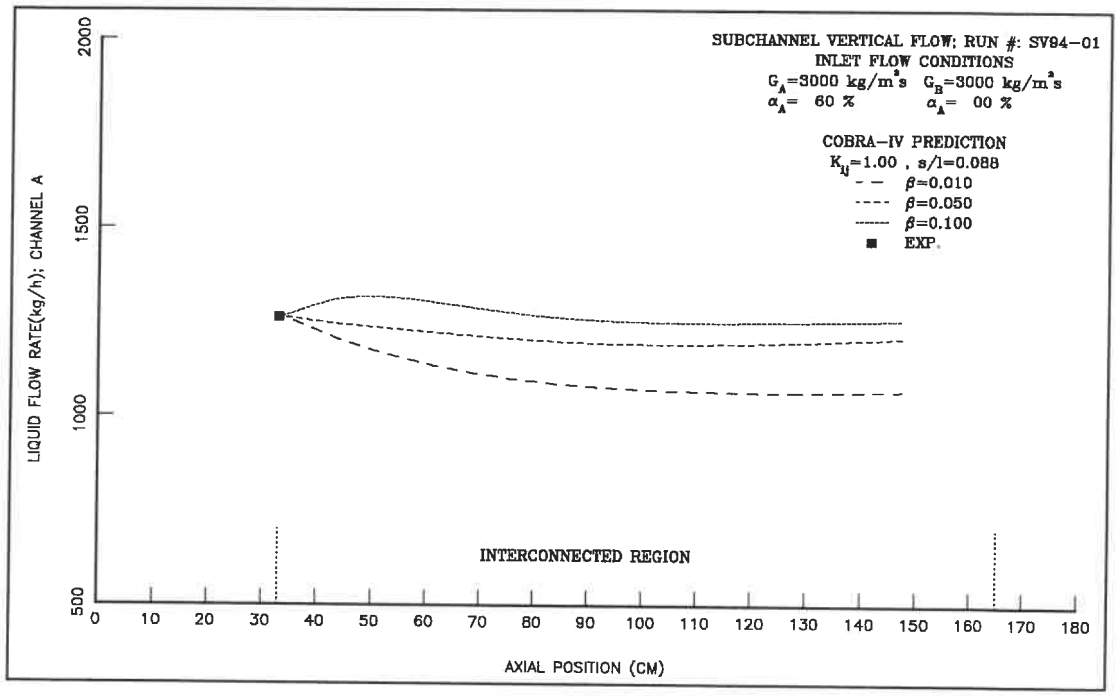


Figure 5.8: Mass Flow Rate Profile, Run SV94-01, Channel A

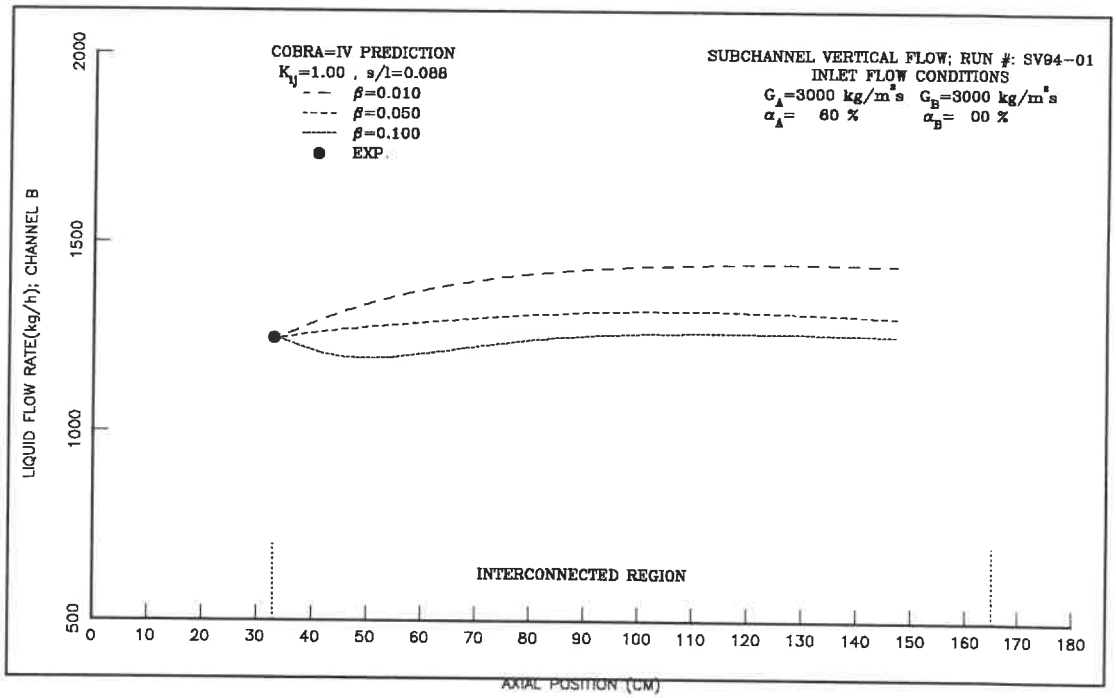


Figure 5.9: Mass Flow Rate Profile, Run SV94-01, Channel B

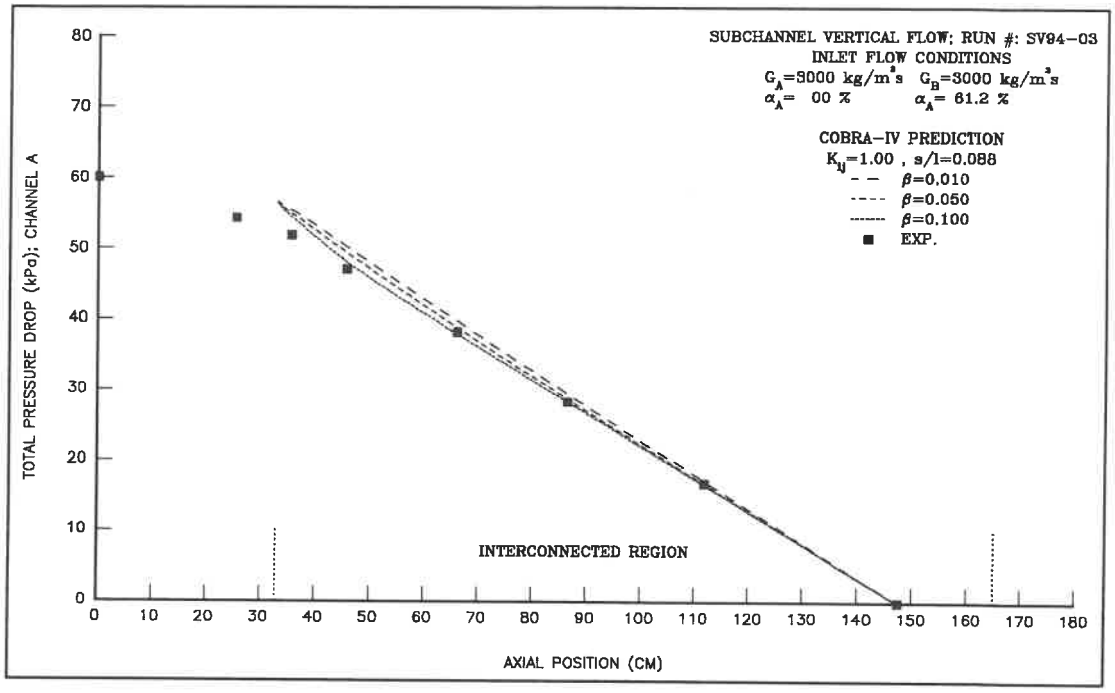


Figure 5.10: Total Pressure Drop Profile, Run SV94-03, Channel A

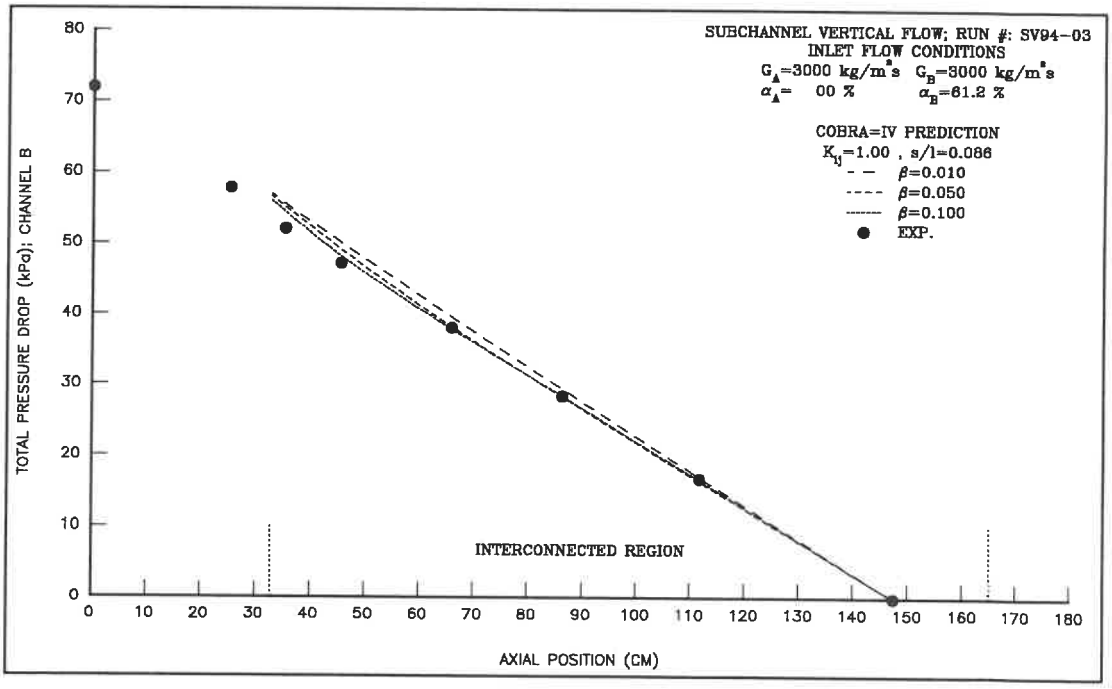


Figure 5.11: Total Pressure Drop Profile, Run SV94-03, Channel B

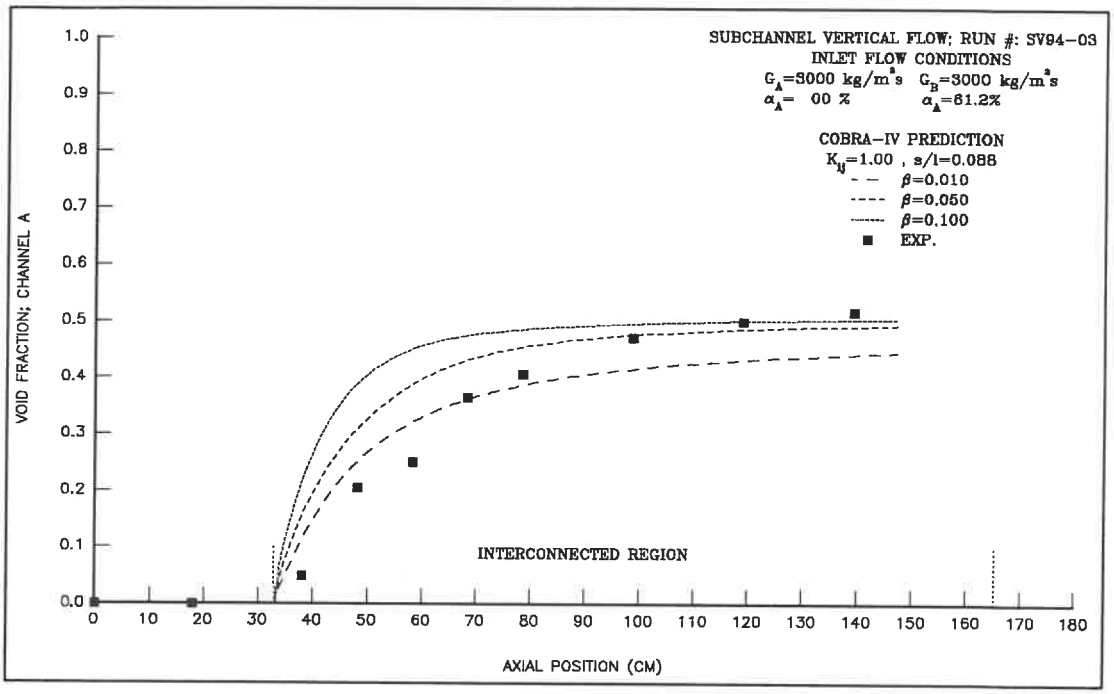


Figure 5.12: Void Fraction Profile, Run SV94-03, Channel A

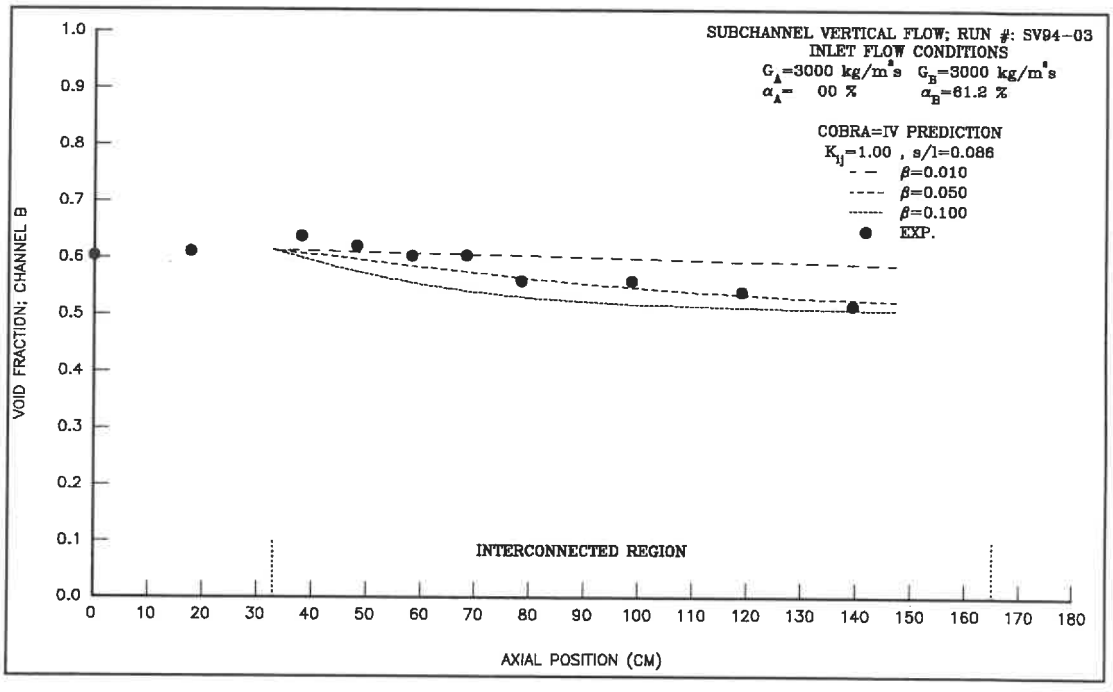


Figure 5.13: Void Fraction Profile, Run SV94-03, Channel B

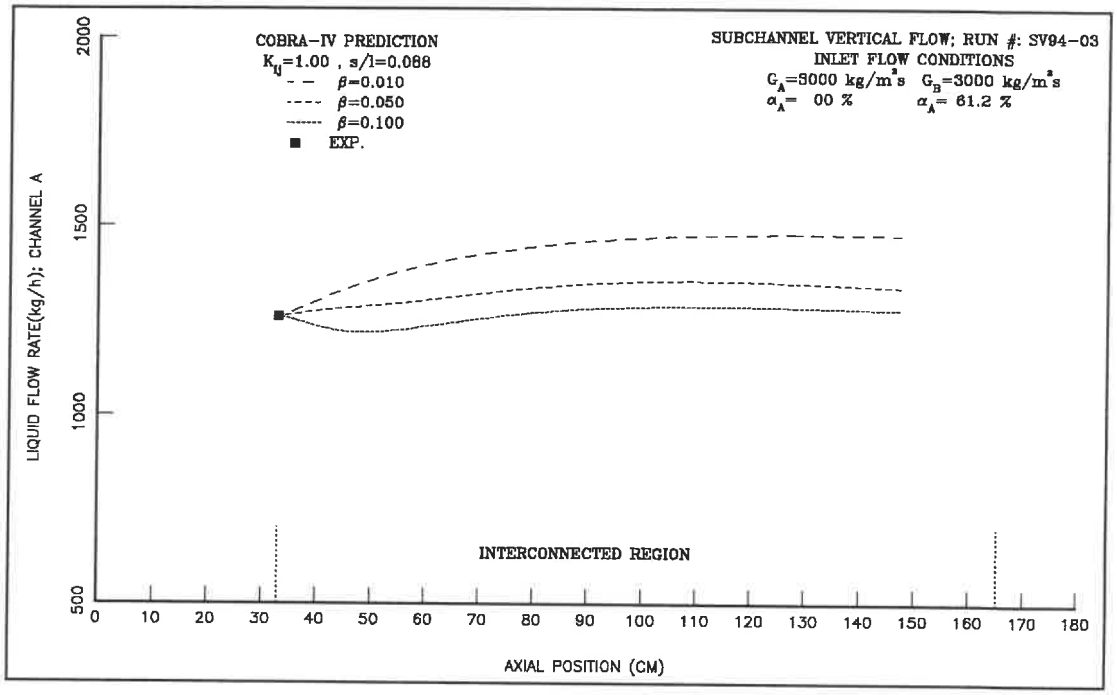


Figure 5.14: Mass Flow Rate Profile, Run SV94-03, Channel A

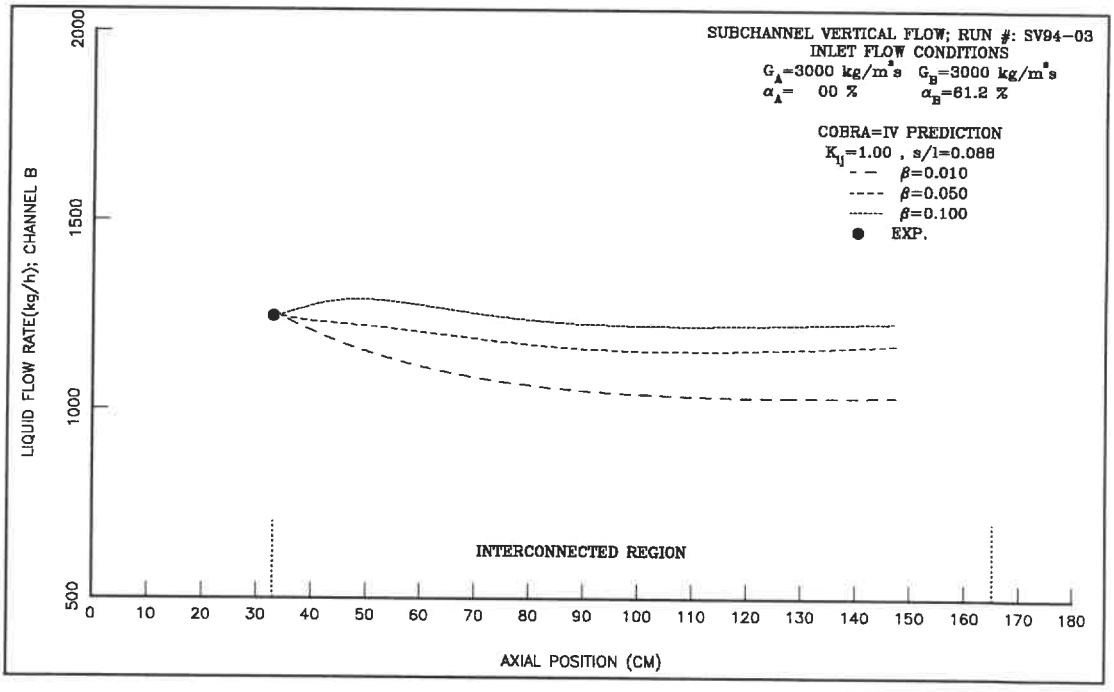


Figure 5.15: Mass Flow Rate Profile, Run SV94-03, Channel B

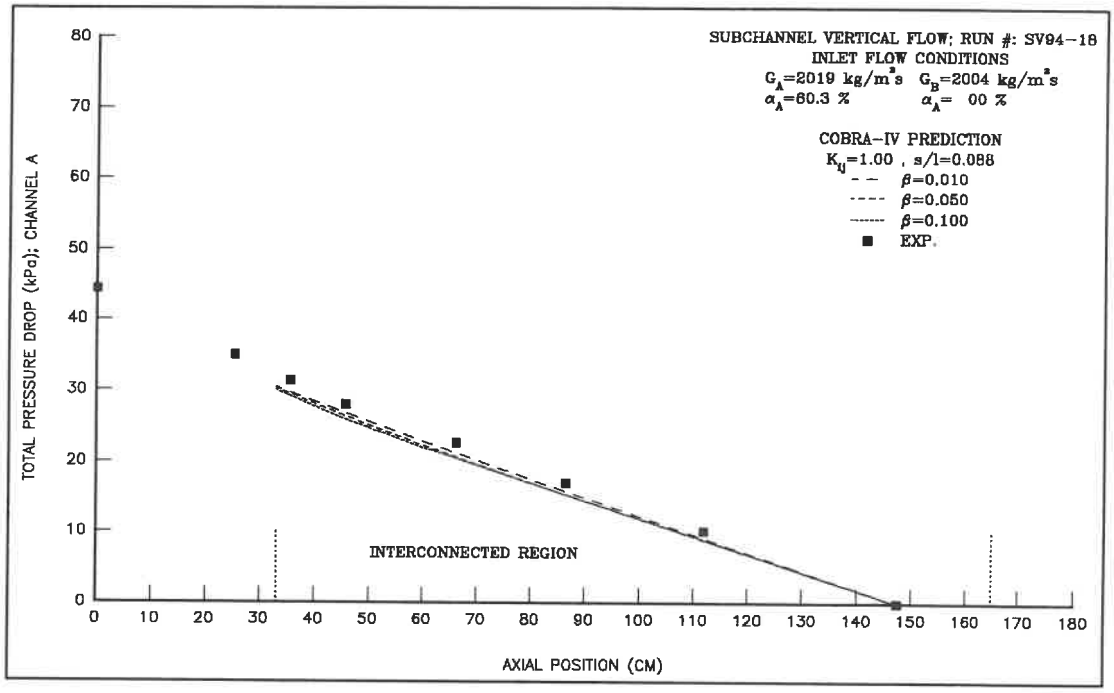


Figure 5.16: Total Pressure Drop Profile, Run SV94-18, Channel A

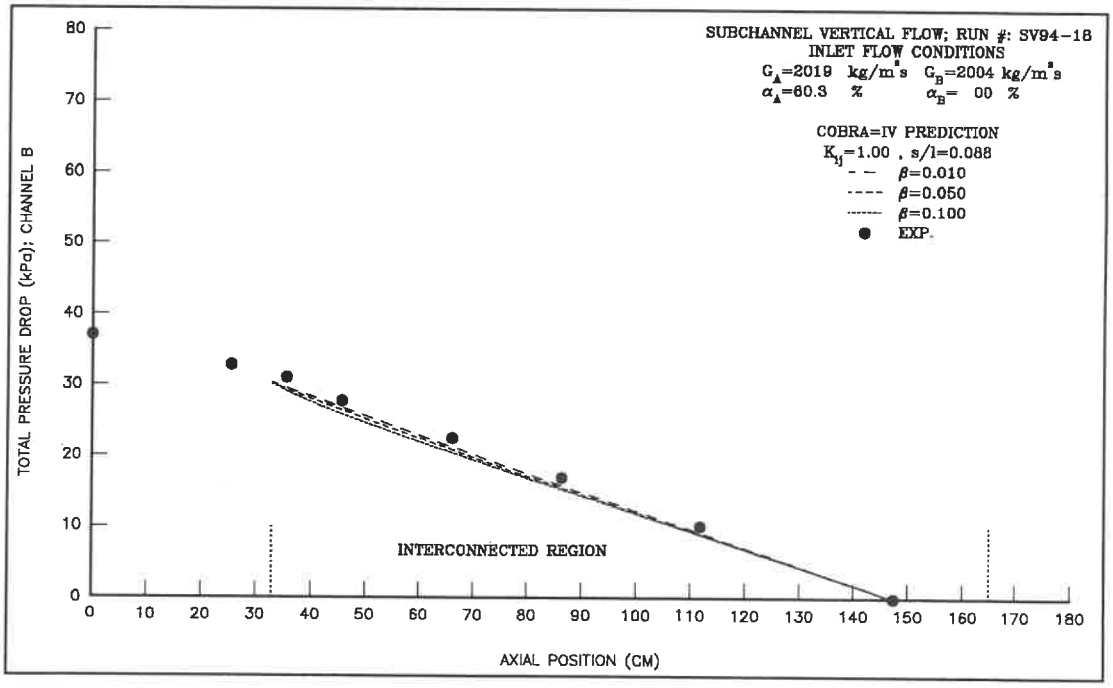


Figure 5.17: Total Pressure Drop Profile, Run SV94-18, Channel B

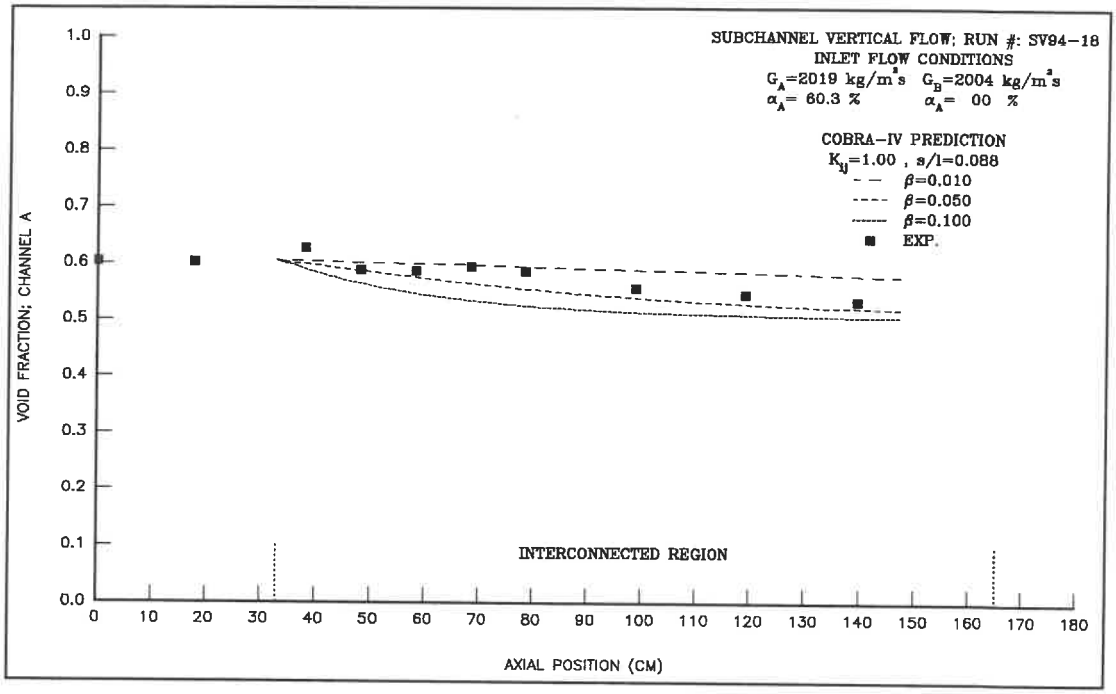


Figure 5.18: Void Fraction Profile, Run SV94-18, Channel A

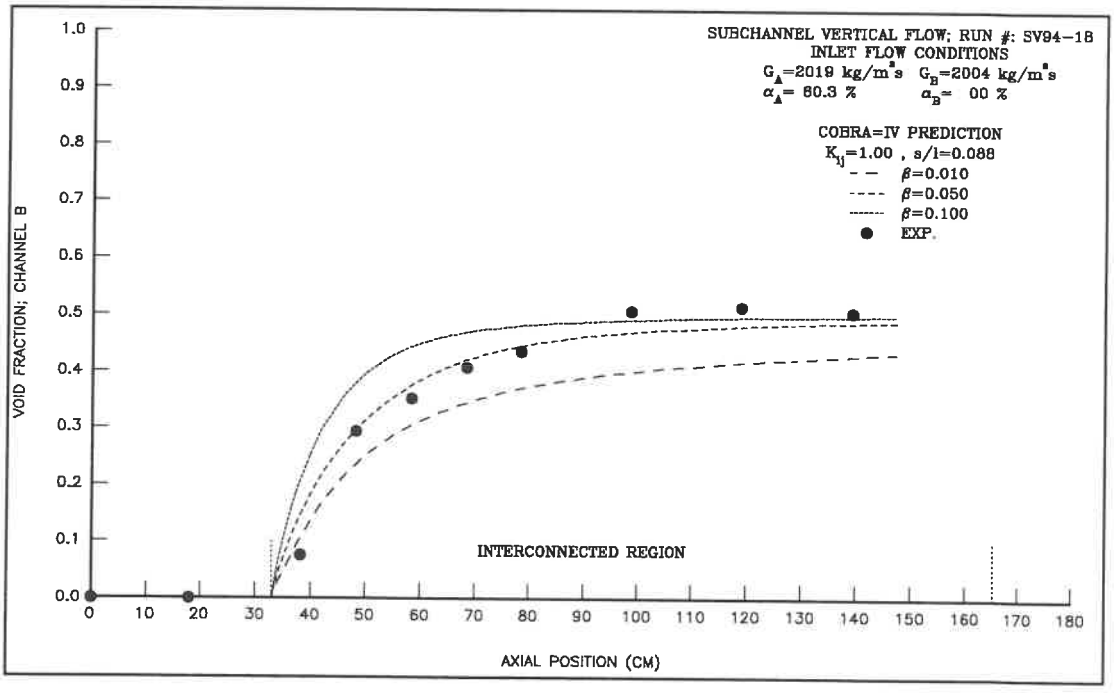


Figure 5.19: Void Fraction Profile, Run SV94-18, Channel B

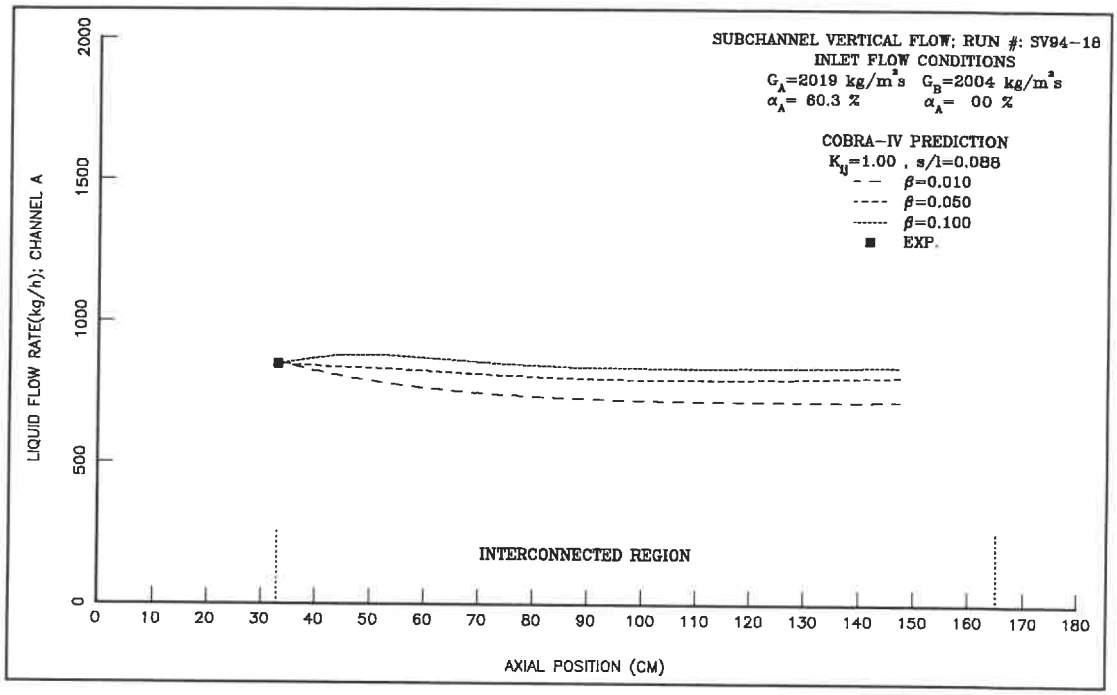


Figure 5.20: Mass Flow Rate Profile, Run SV94-18, Channel A

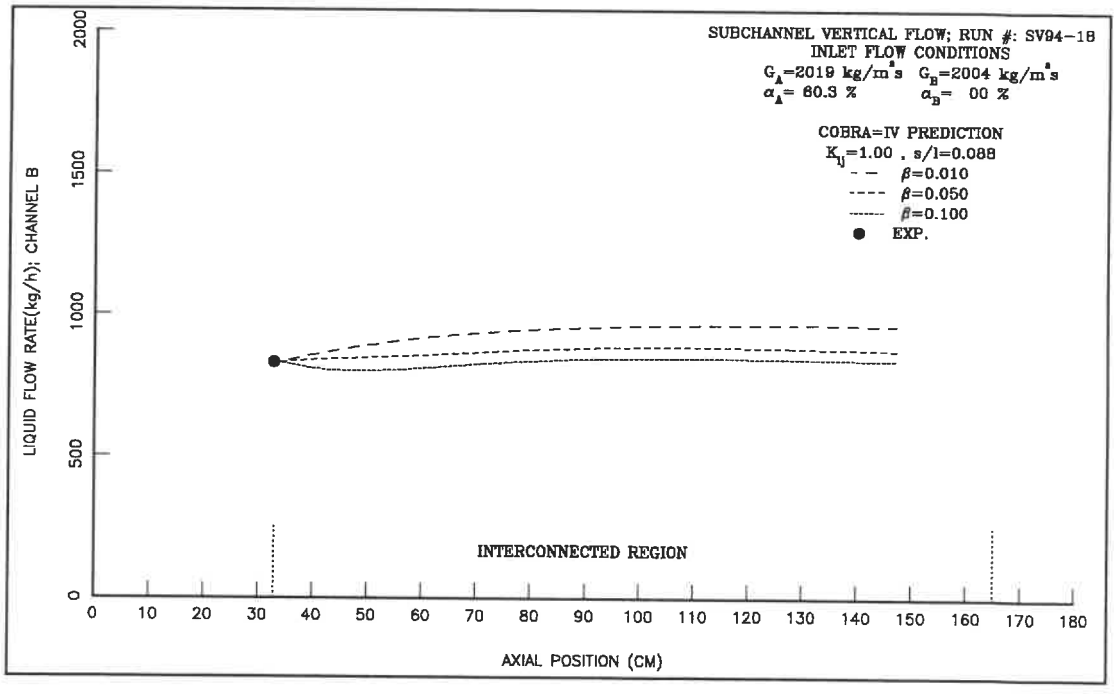


Figure 5.21: Mass Flow Rate Profile, Run SV94-18, Channel B

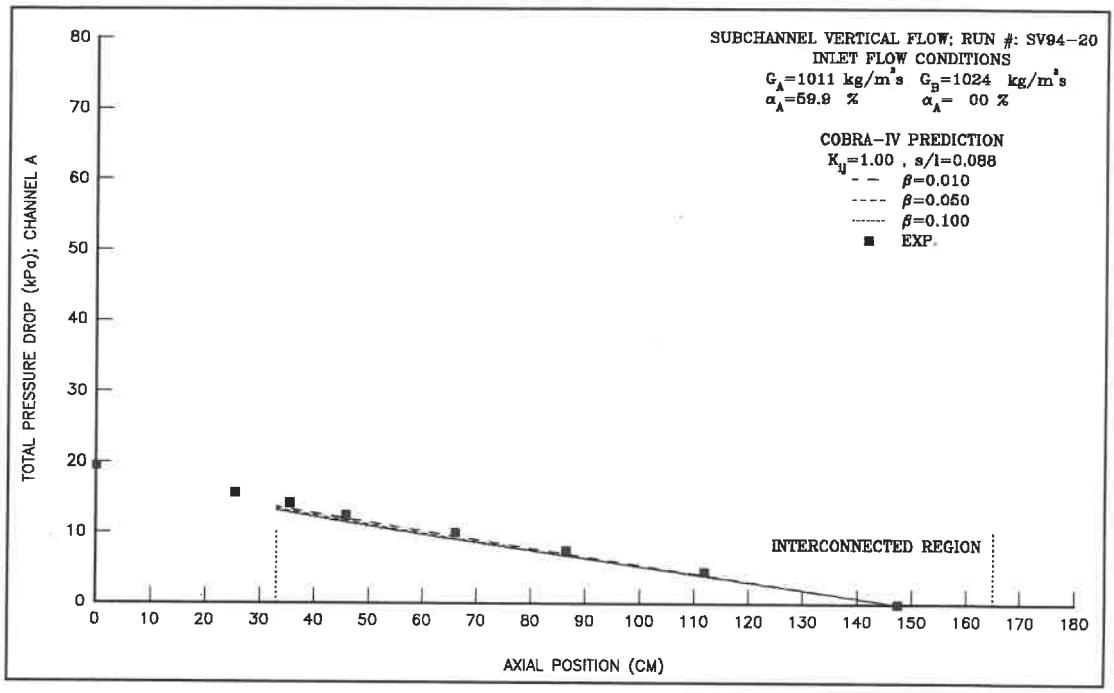


Figure 5.22: Total Pressure Drop Profile, Run SV94-20, Channel A

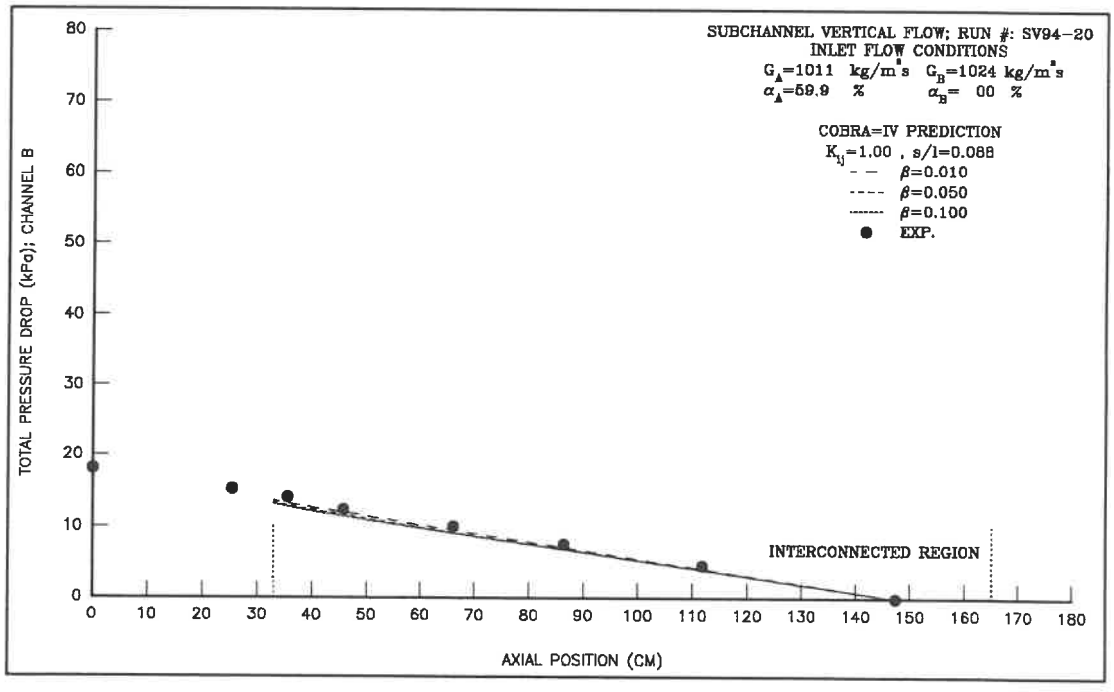


Figure 5.23: Total Pressure Drop Profile, Run SV94-20, Channel B

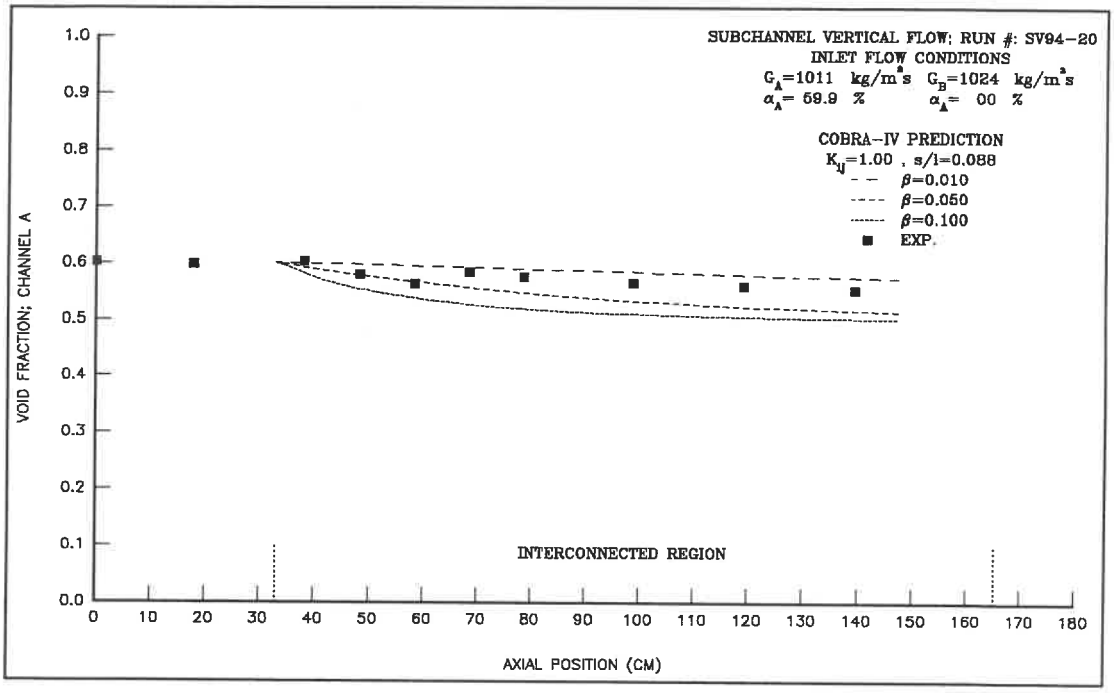


Figure 5.24: Void Fraction Profile, Run SV94-20, Channel A

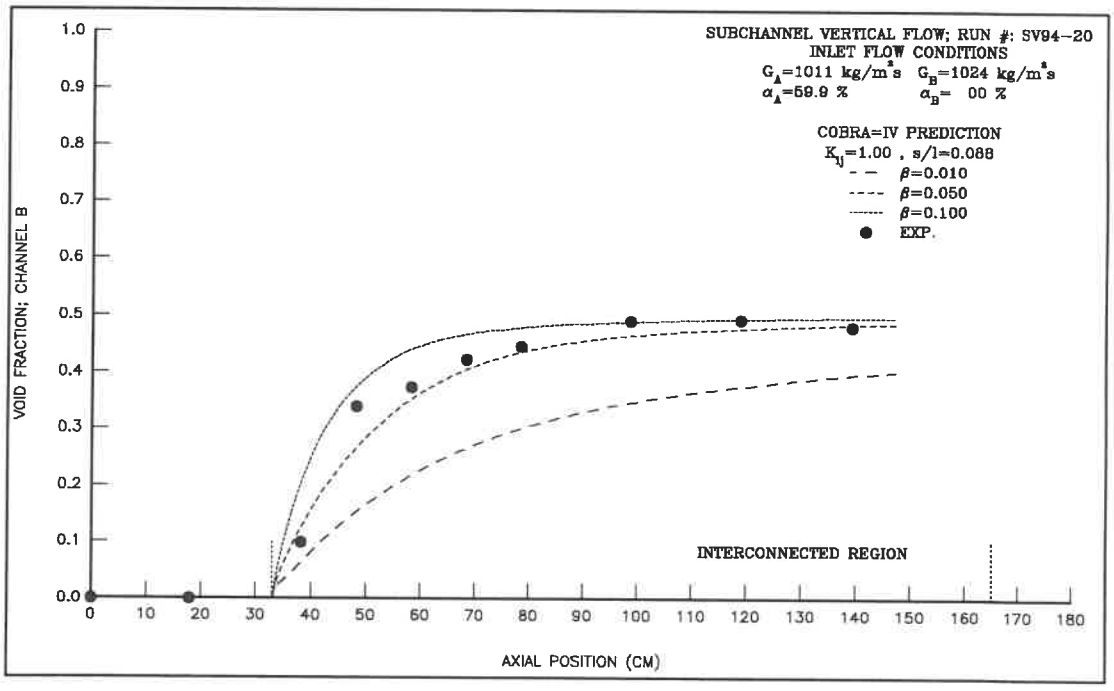


Figure 5.25: Void Fraction Profile, Run SV94-20, Channel B

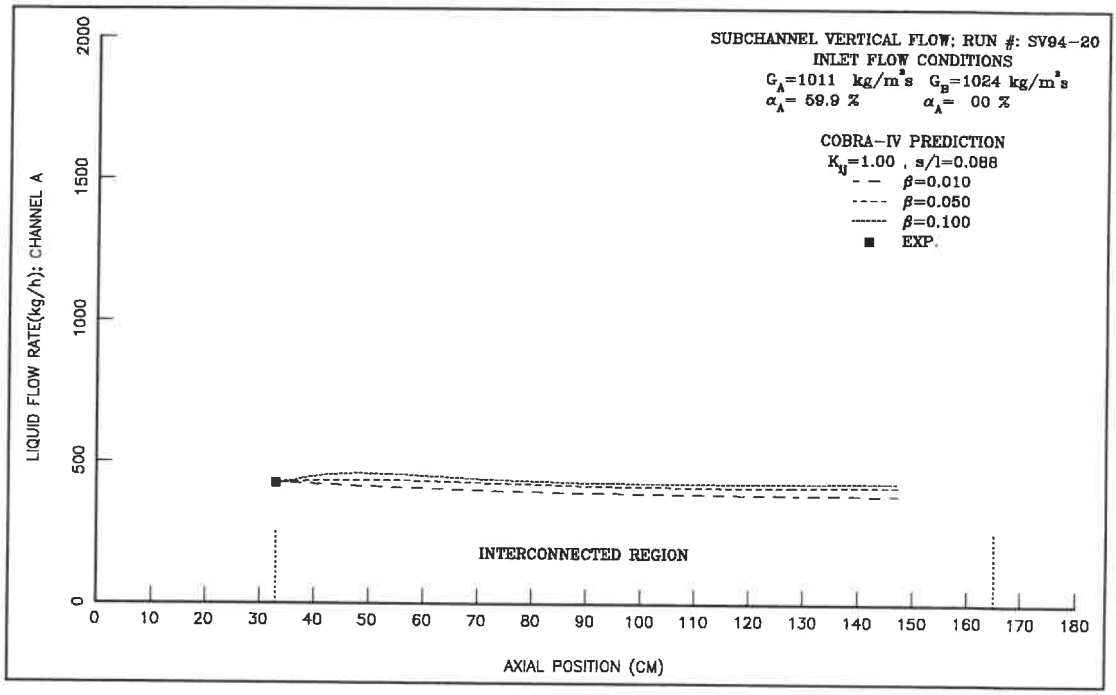


Figure 5.26: Mass Flow Rate Profile, Run SV94-20, Channel A

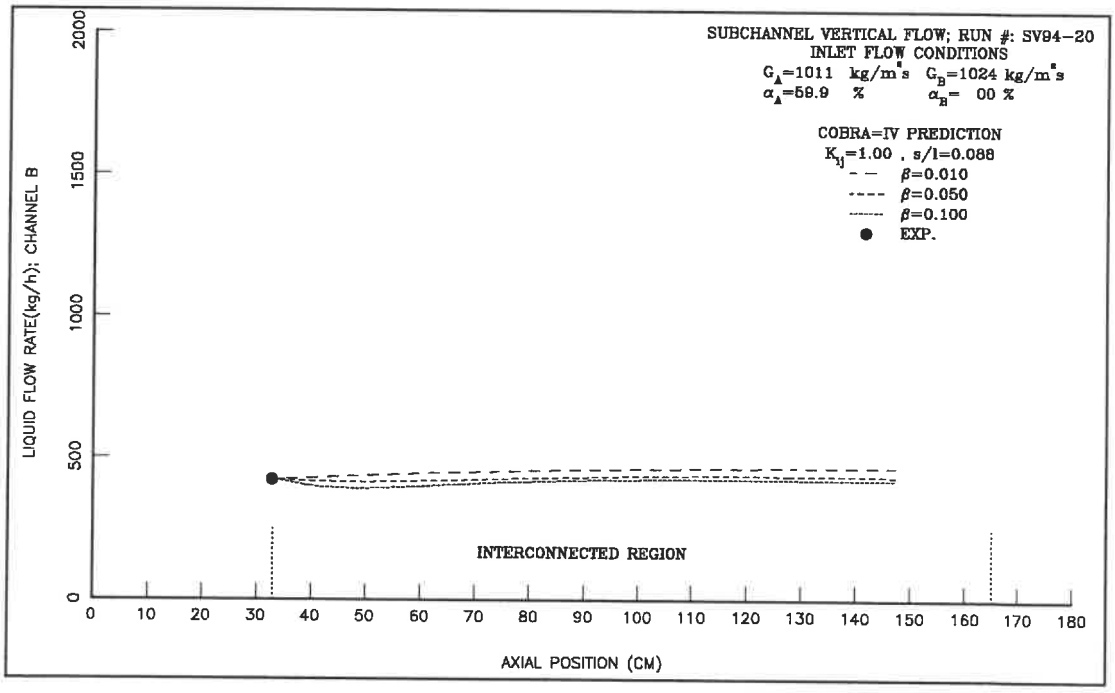


Figure 5.27: Mass Flow Rate Profile, Run SV94-20, Channel B

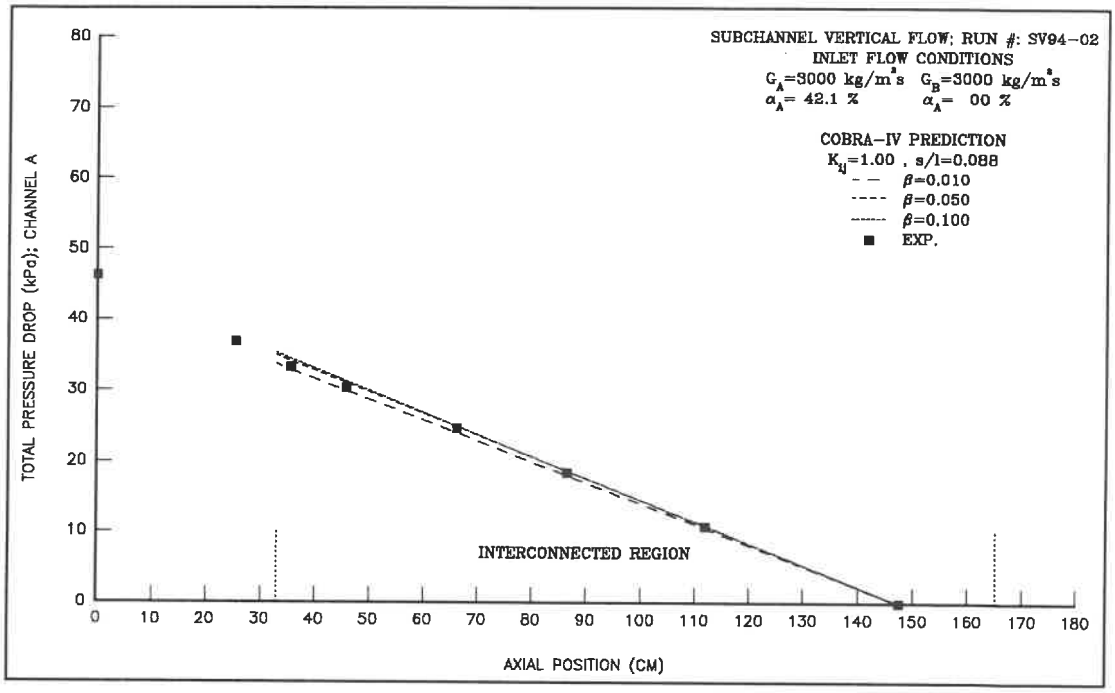


Figure 5.28: Total Pressure Drop Profile, Run SV94-02, Channel A

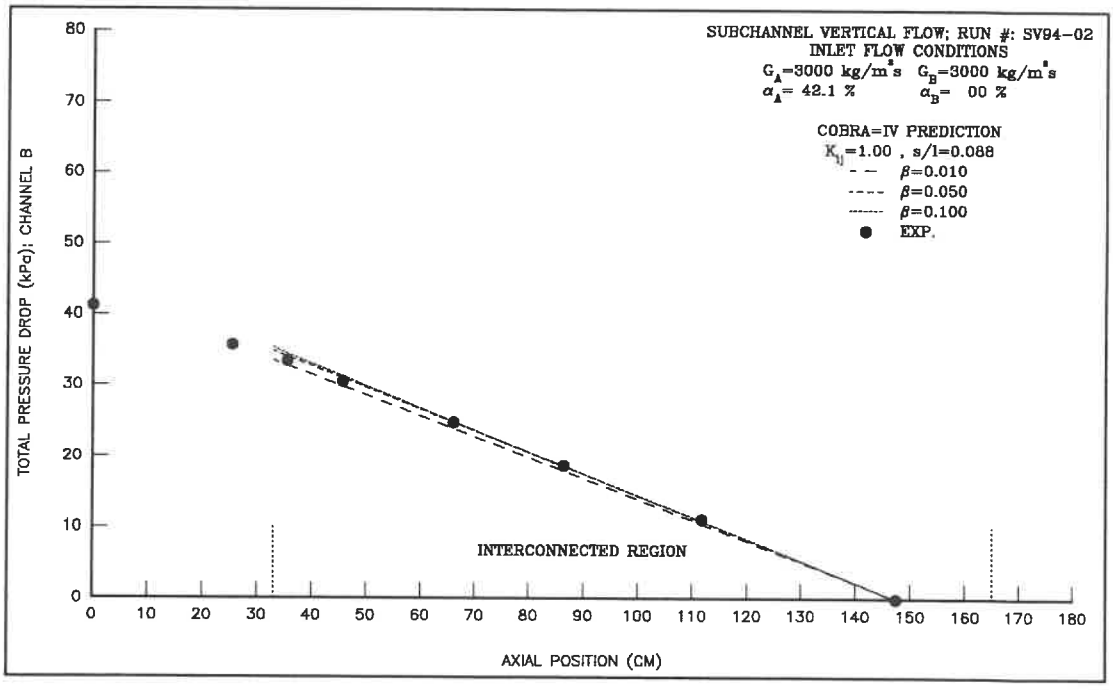


Figure 5.29: Total Pressure Drop Profile, Run SV94-02, Channel B

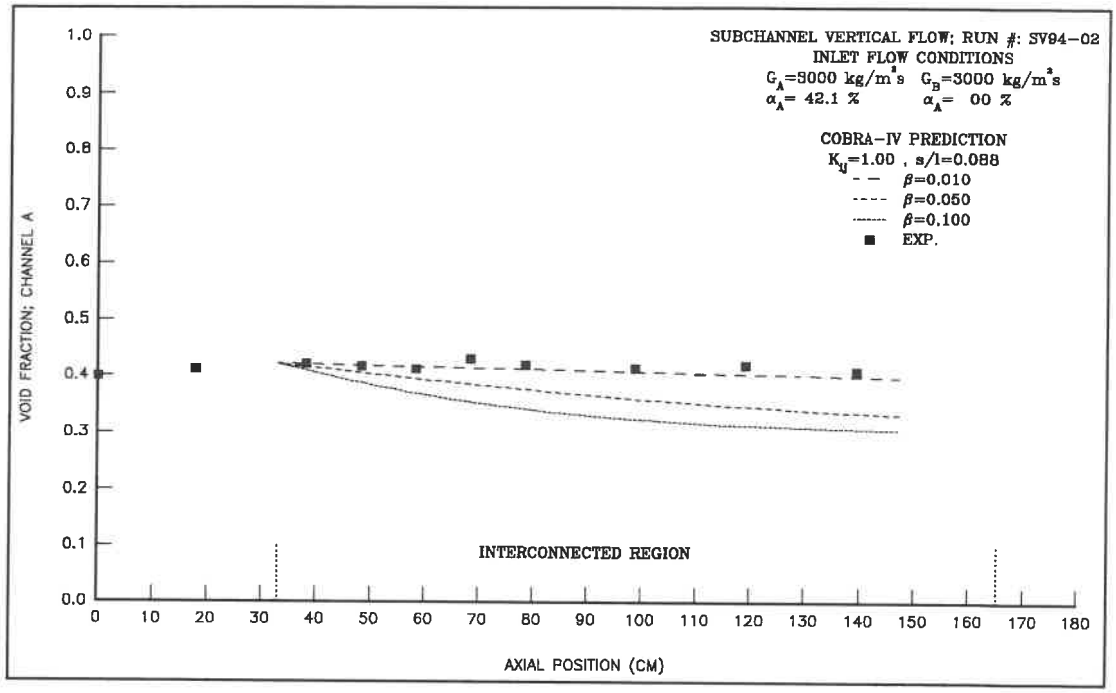


Figure 5.30: Void Fraction Profile, Run SV94-02, Channel A

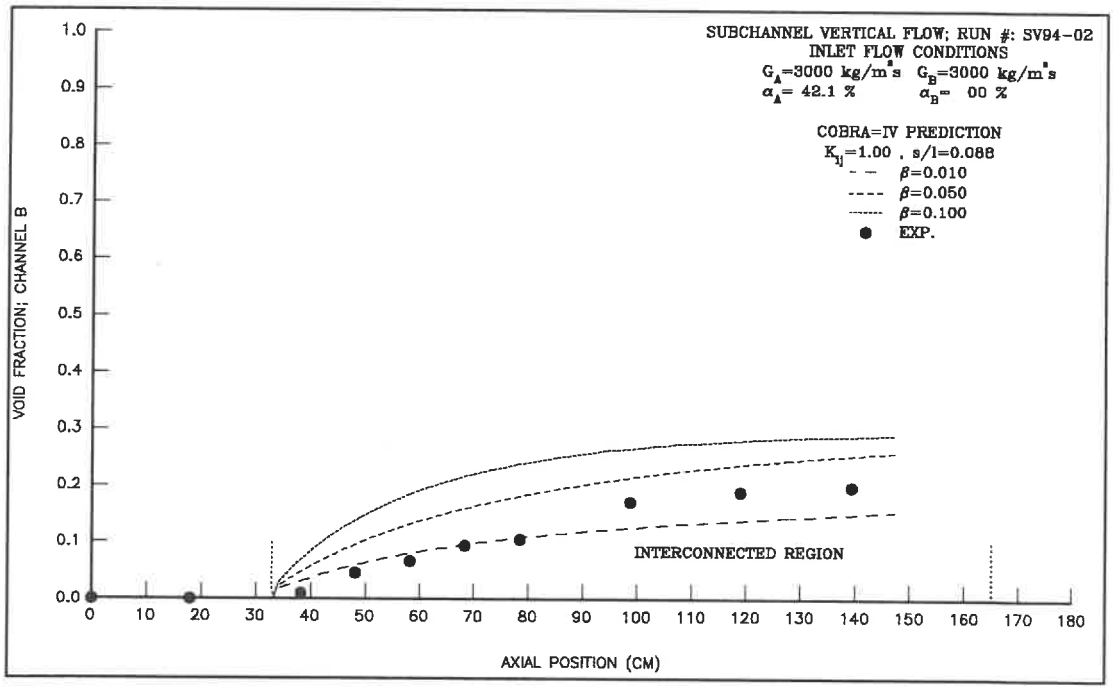


Figure 5.31: Void Fraction Profile, Run SV94-02, Channel B

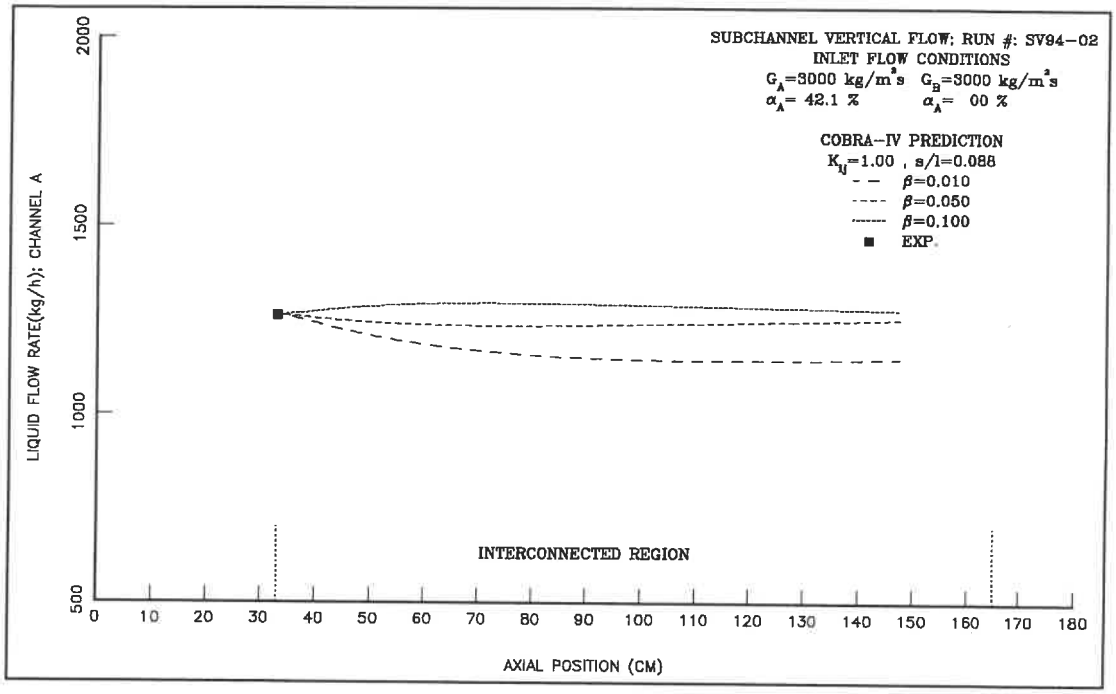


Figure 5.32: Mass Flow Rate Profile, Run SV94-02, Channel A

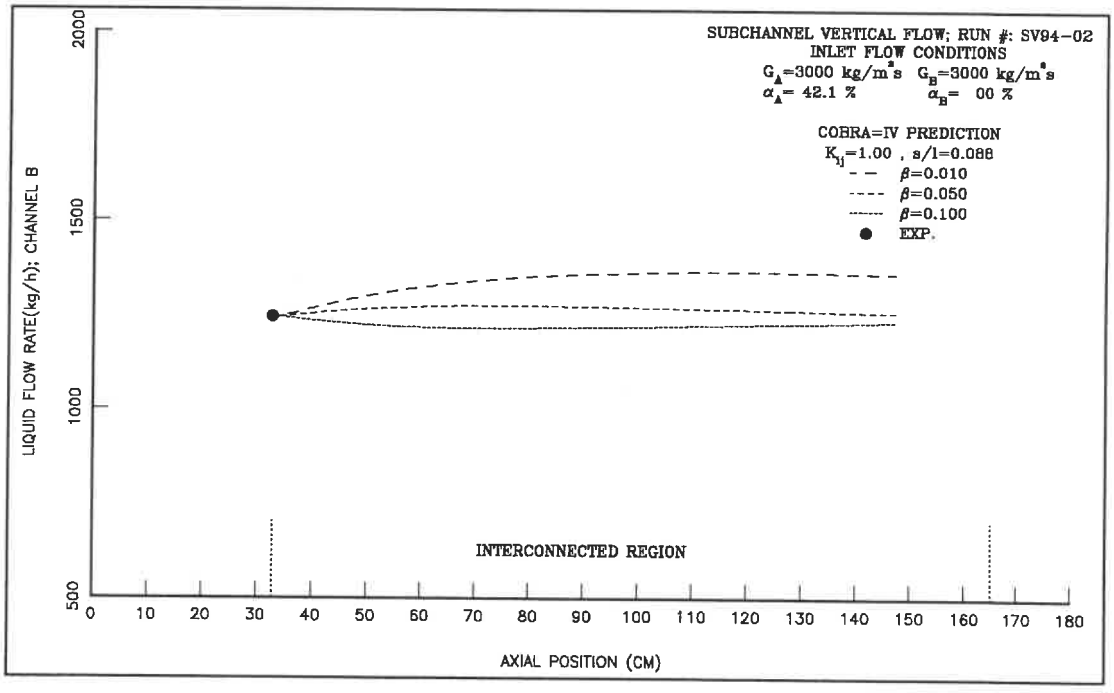


Figure 5.33: Mass Flow Rate Profile, Run SV94-02, Channel B

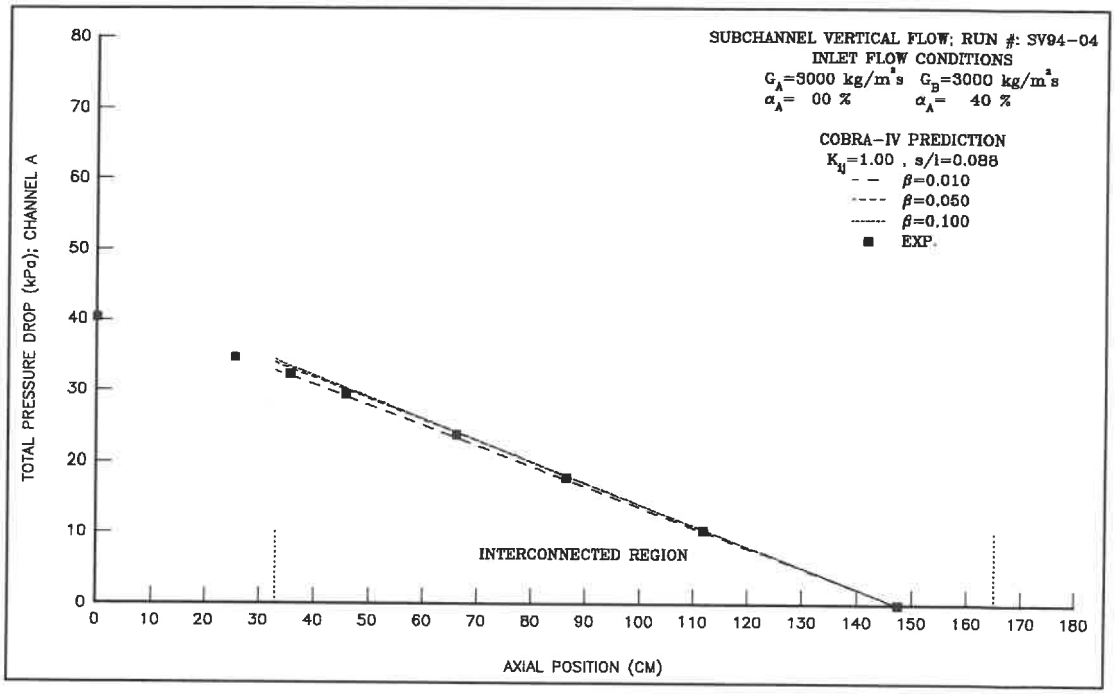


Figure 5.34: Total Pressure Drop Profile, Run SV94-04, Channel A

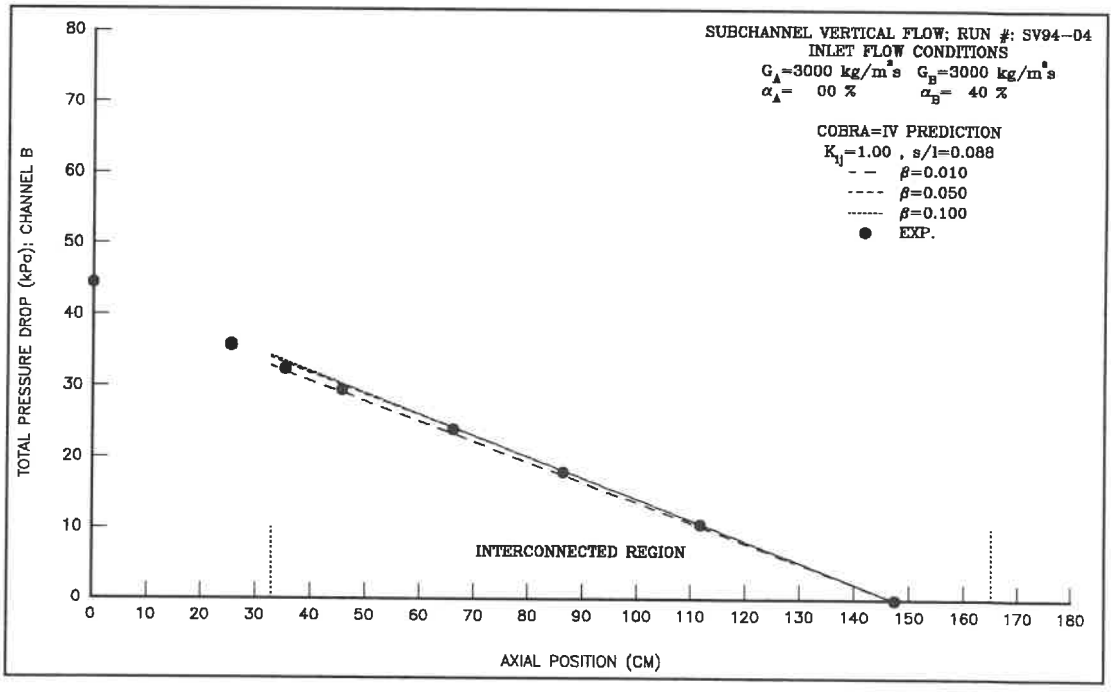


Figure 5.35: Total Pressure Drop Profile, Run SV94-04, Channel B

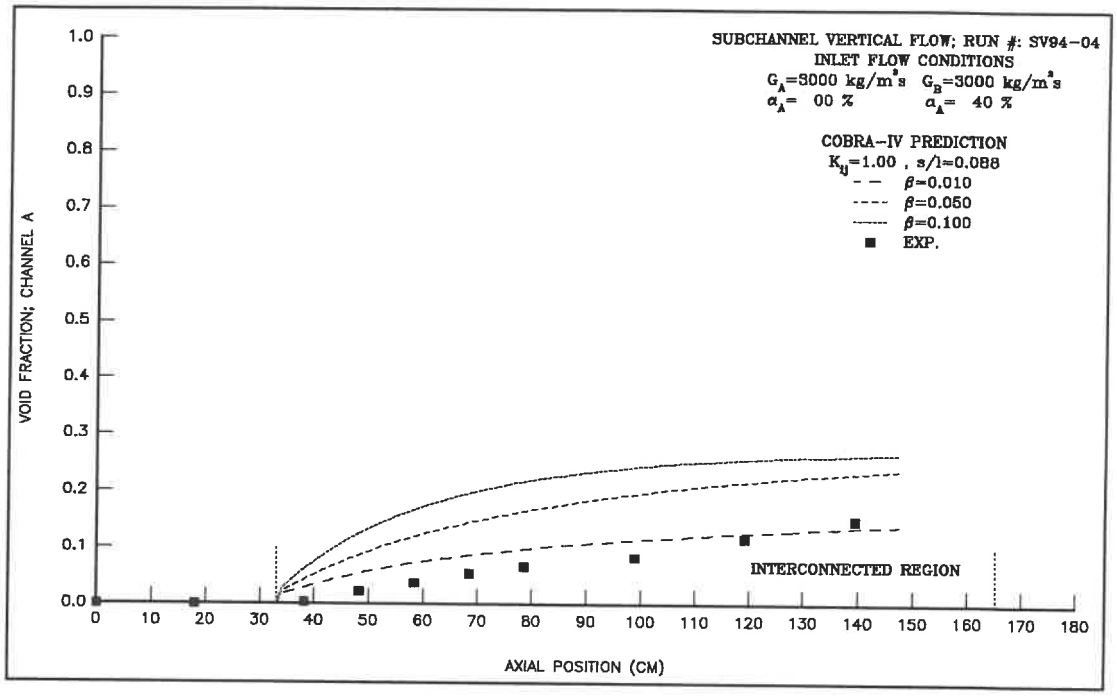


Figure 5.36: Void Fraction Profile, Run SV94-04, Channel A

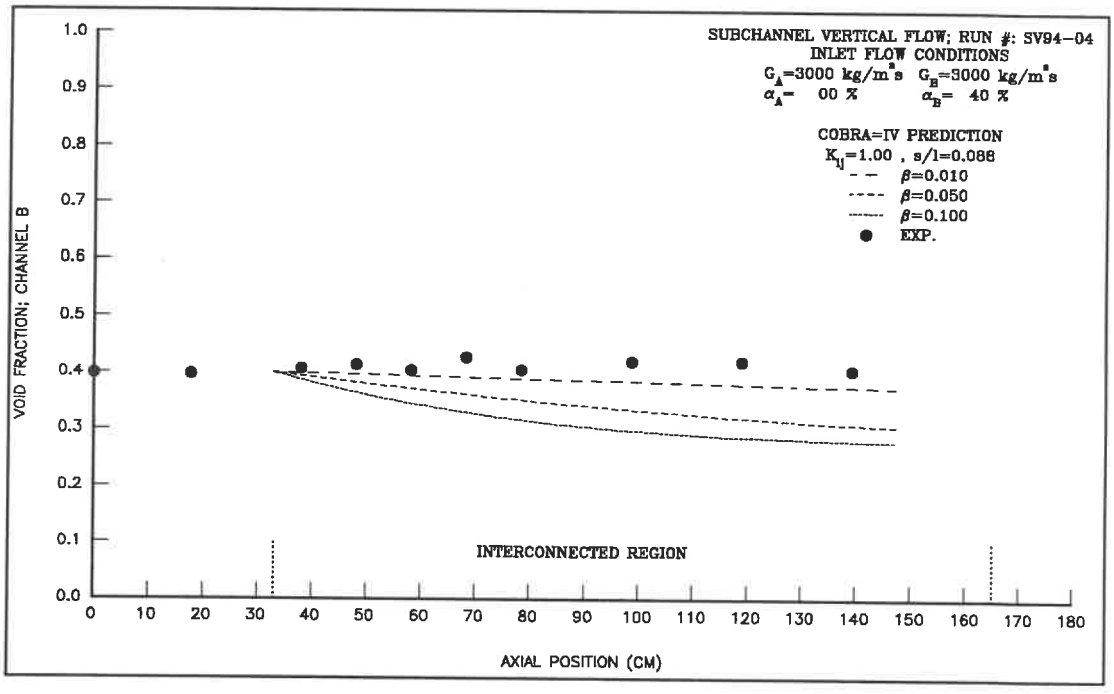


Figure 5.37: Void Fraction Profile, Run SV94-04, Channel B

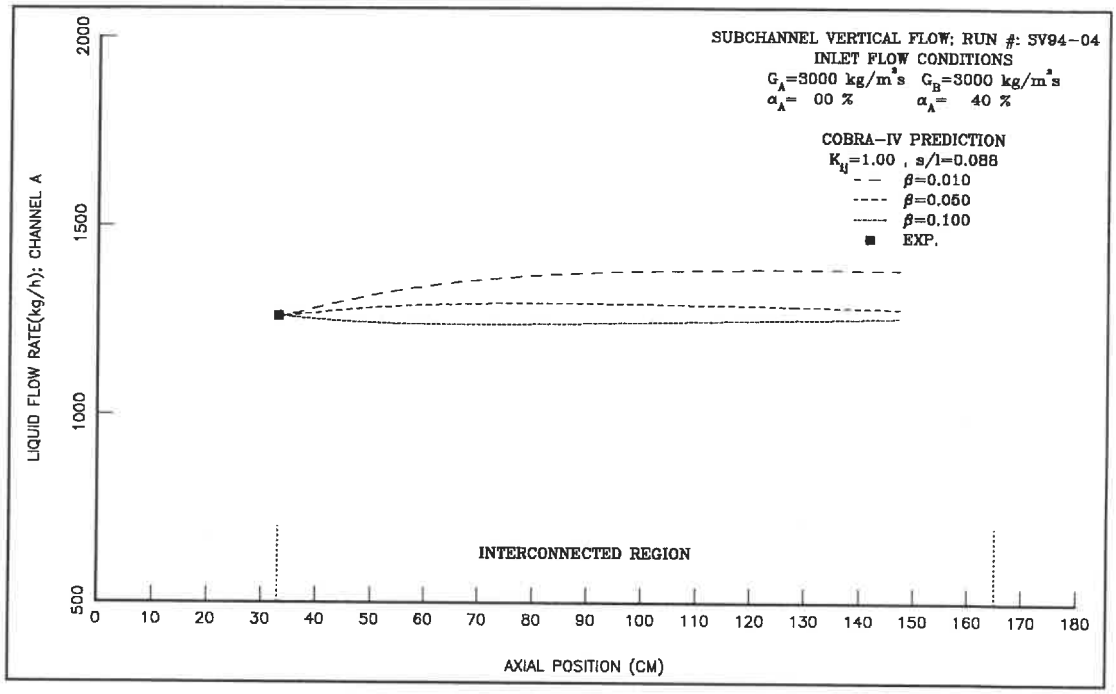


Figure 5.38: Mass Flow Rate Profile, Run SV94-04, Channel A

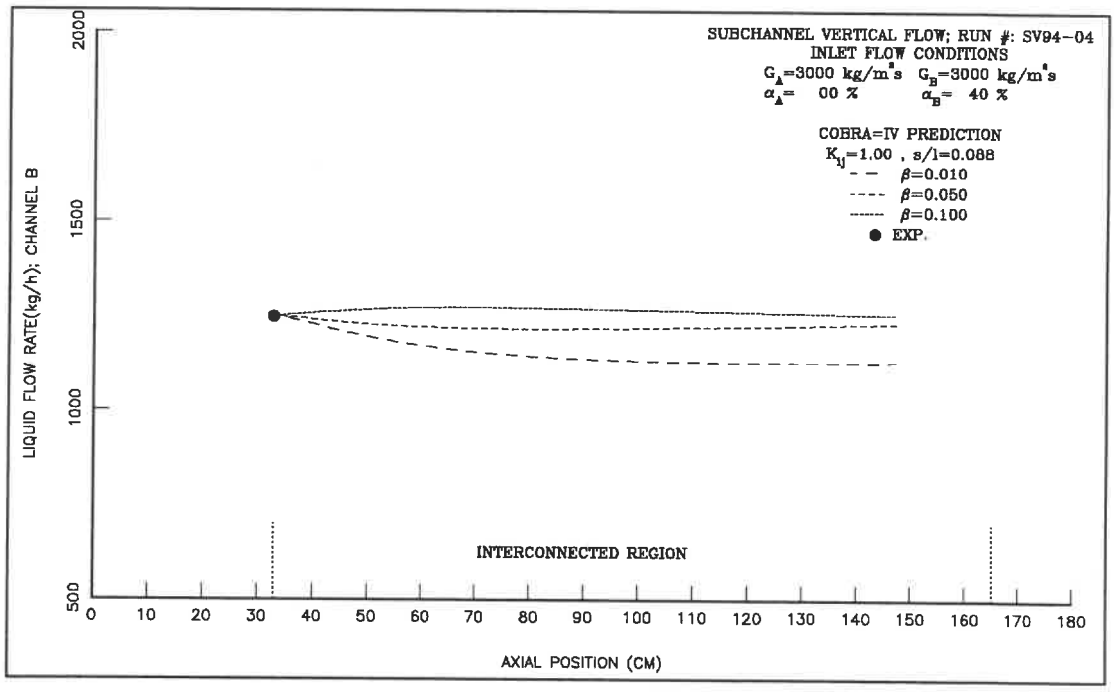


Figure 5.39: Mass Flow Rate Profile, Run SV94-04, Channel B

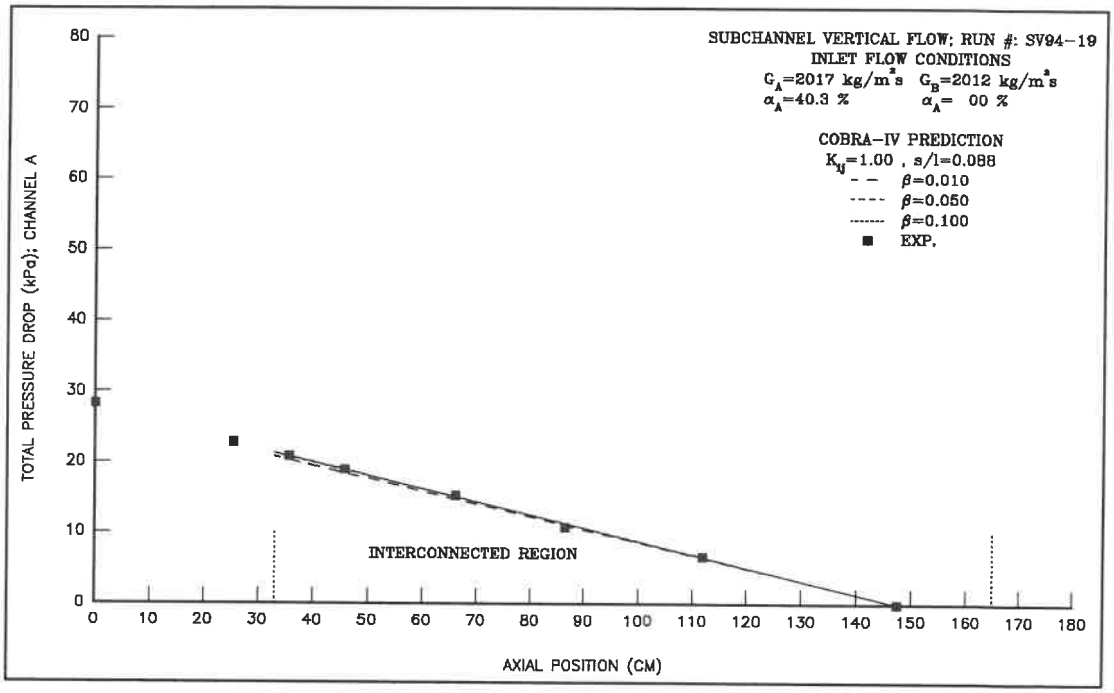


Figure 5.40: Total Pressure Drop Profile, Run SV94-19, Channel A

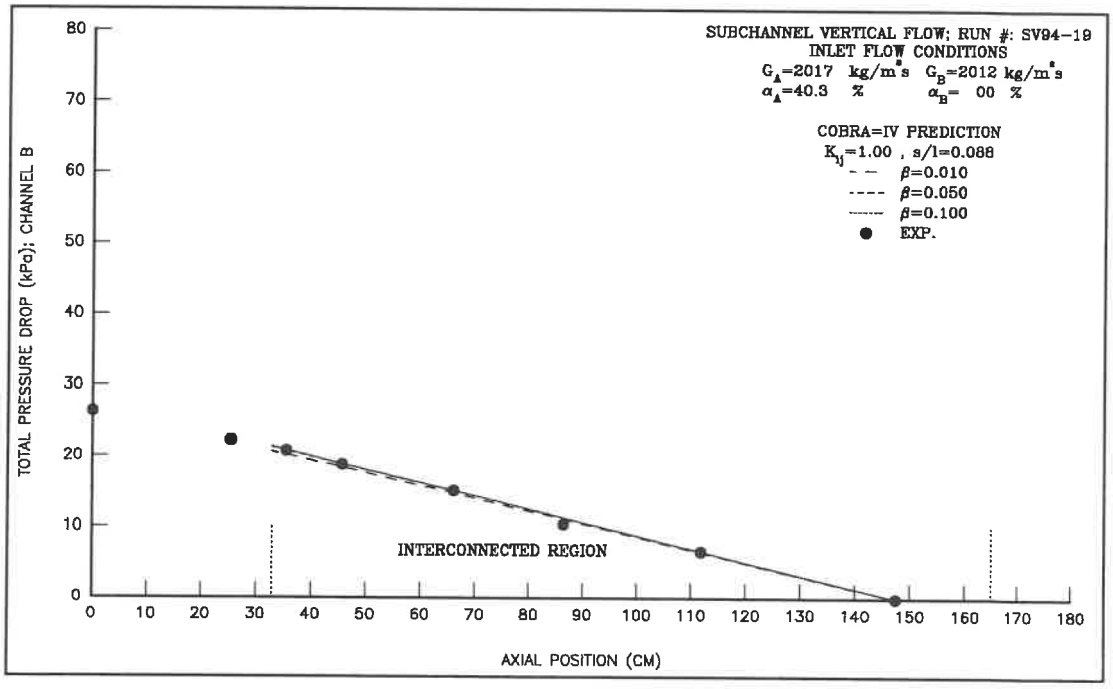


Figure 5.41: Total Pressure Drop Profile, Run SV94-19, Channel B

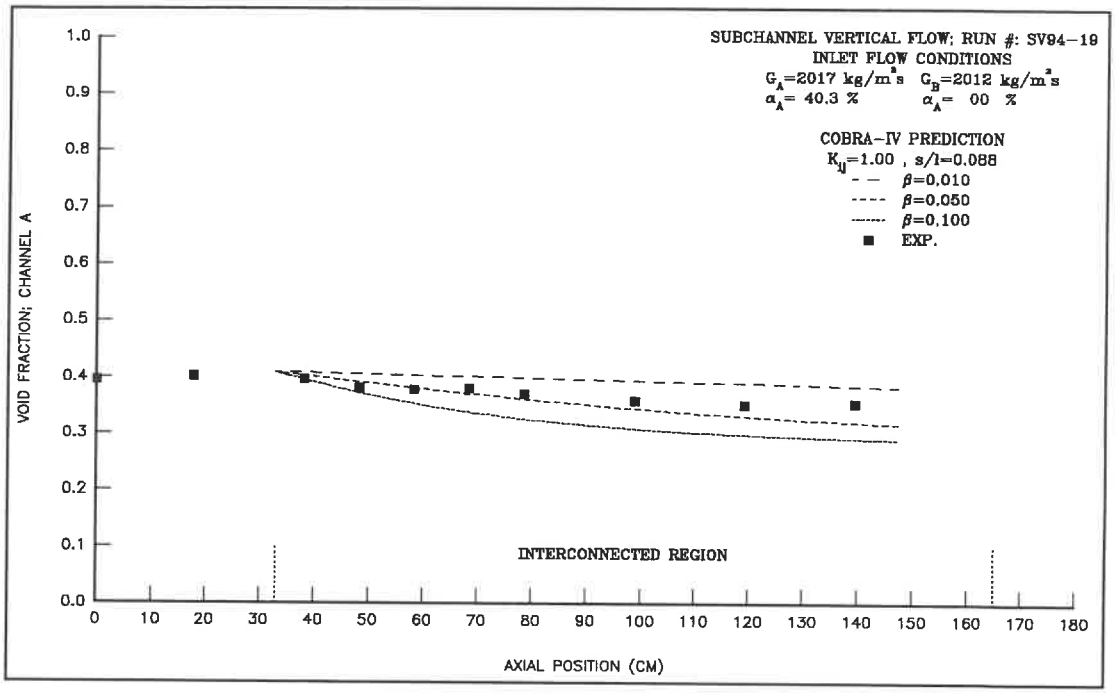


Figure 5.42: Void Fraction Profile, Run SV94-19, Channel A

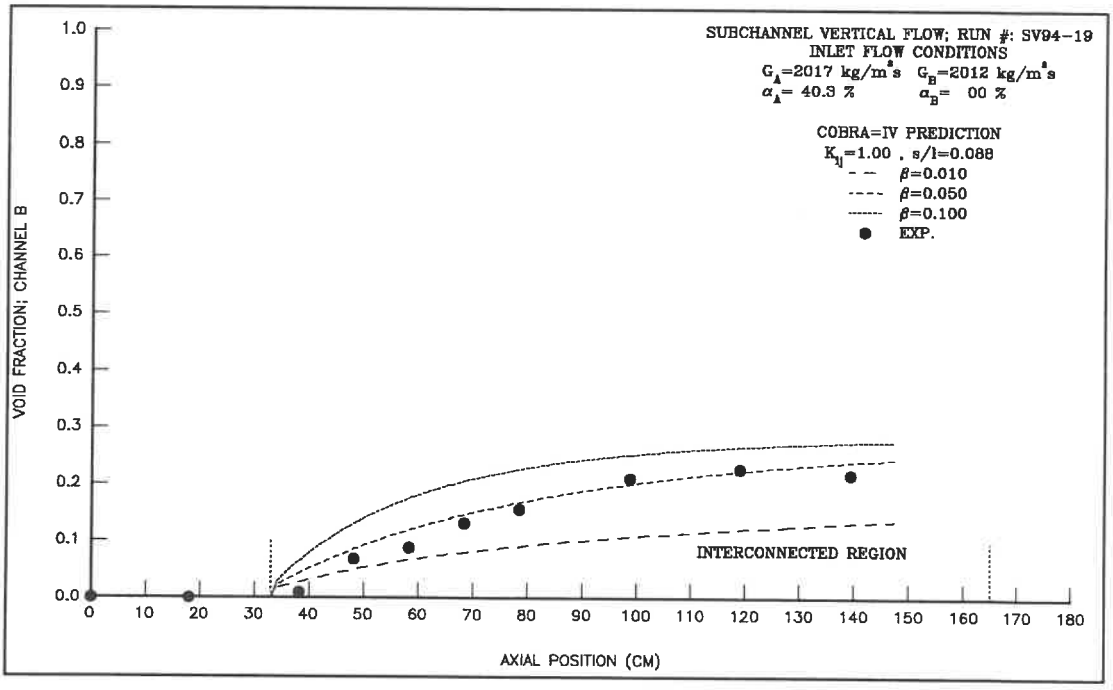


Figure 5.43: Void Fraction Profile, Run SV94-19, Channel B

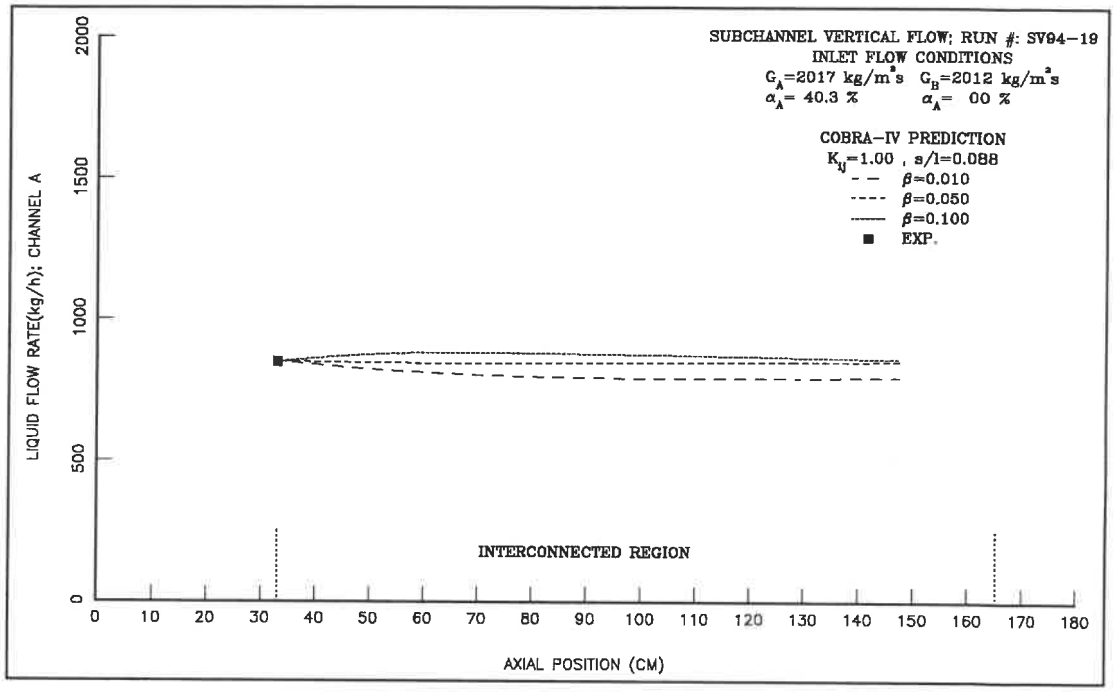


Figure 5.44: Mass Flow Rate Profile, Run SV94-19, Channel A

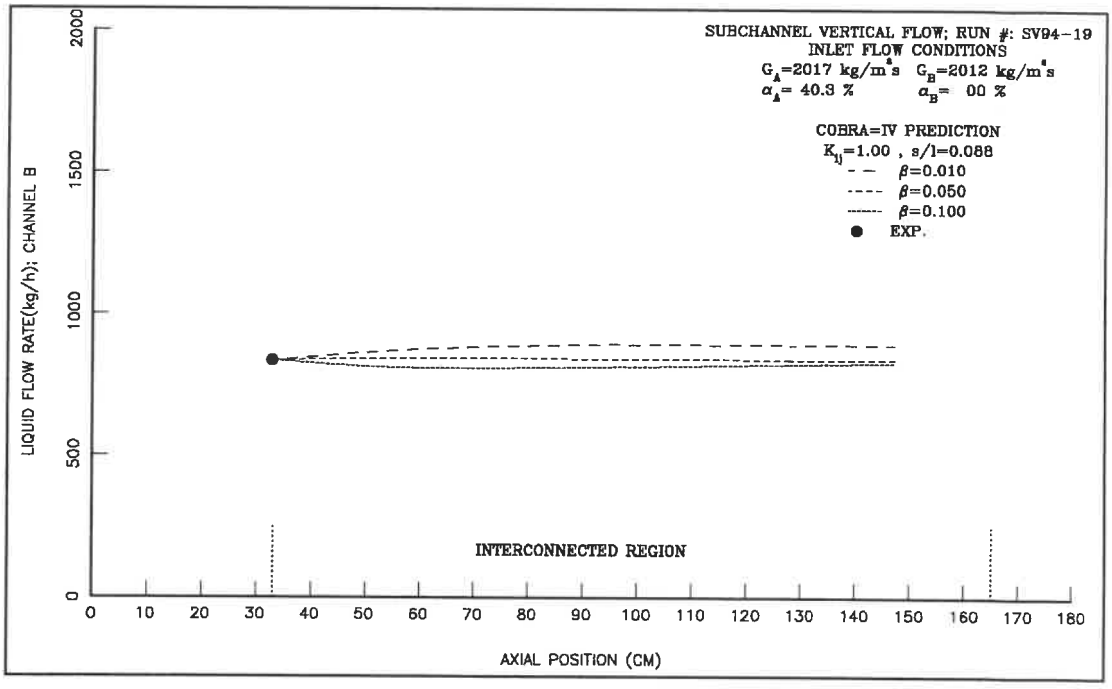


Figure 5.45: Mass Flow Rate Profile, Run SV94-19, Channel B

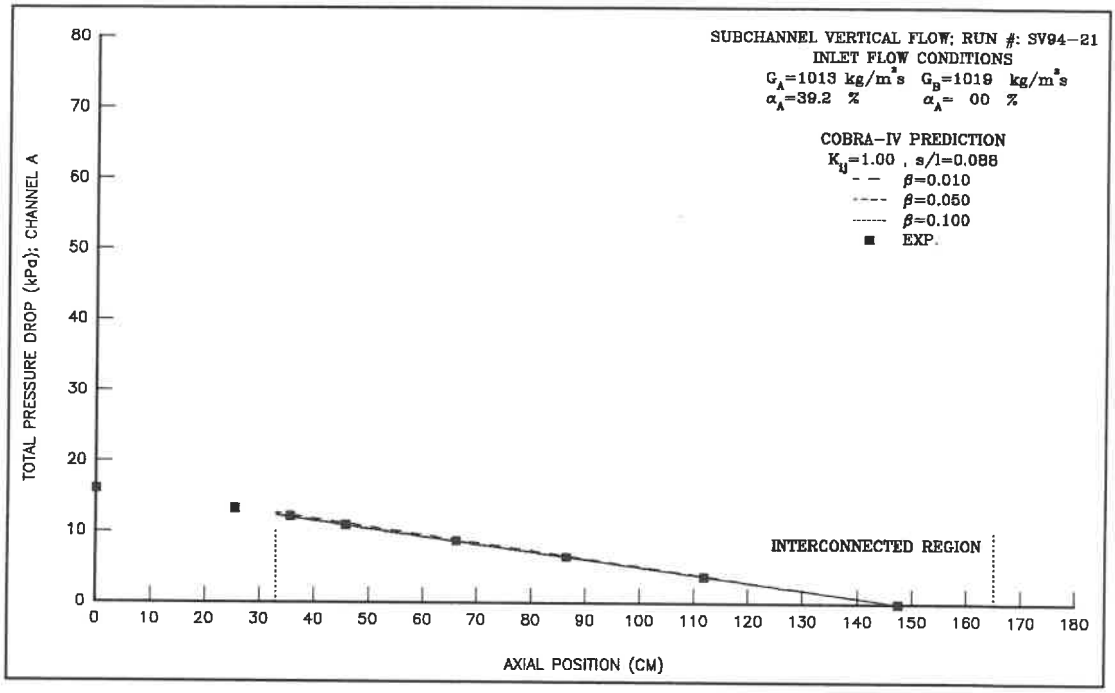


Figure 5.46: Total Pressure Drop Profile, Run SV94-21, Channel A

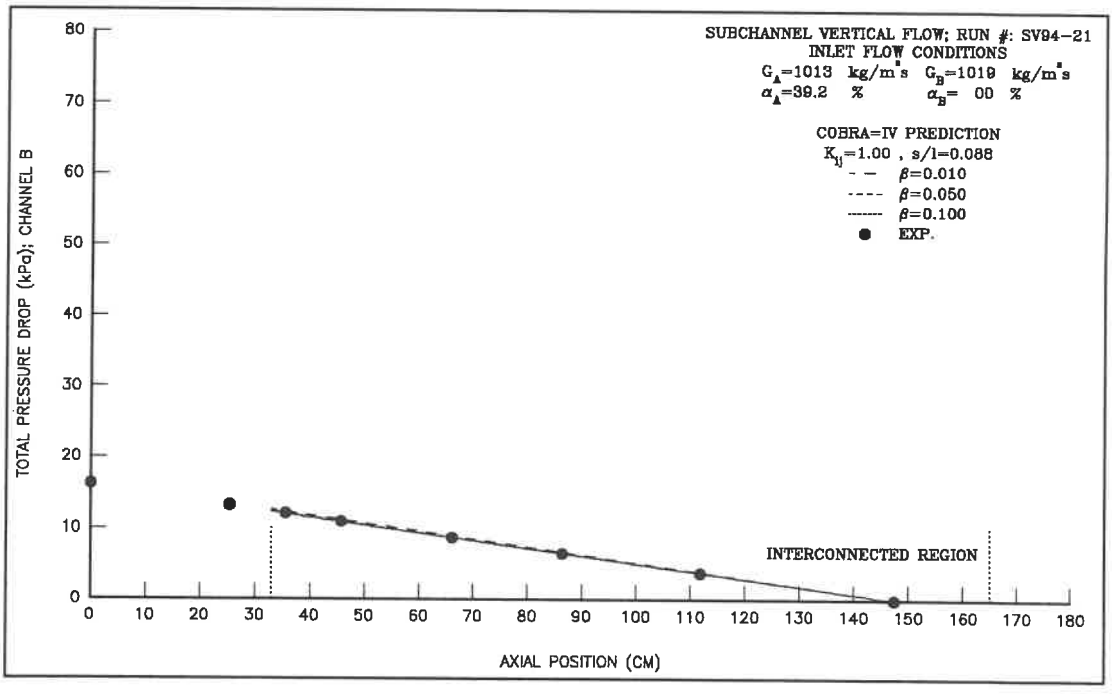


Figure 5.47: Total Pressure Drop Profile, Run SV94-21, Channel B

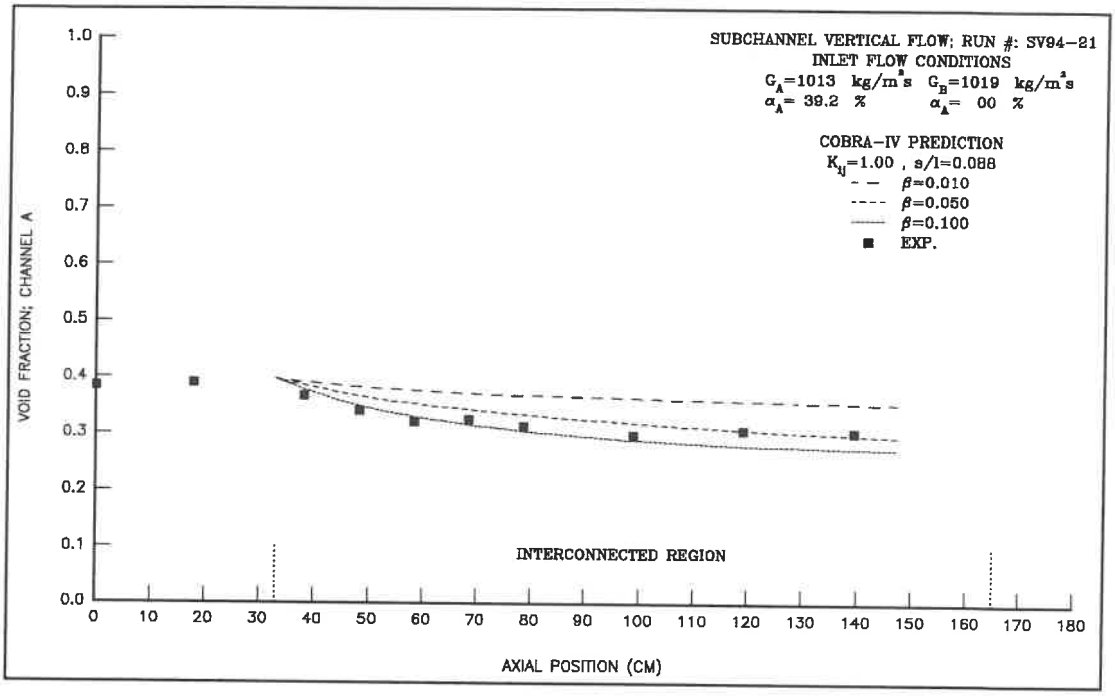


Figure 5.48: Void Fraction Profile, Run SV94-21, Channel A

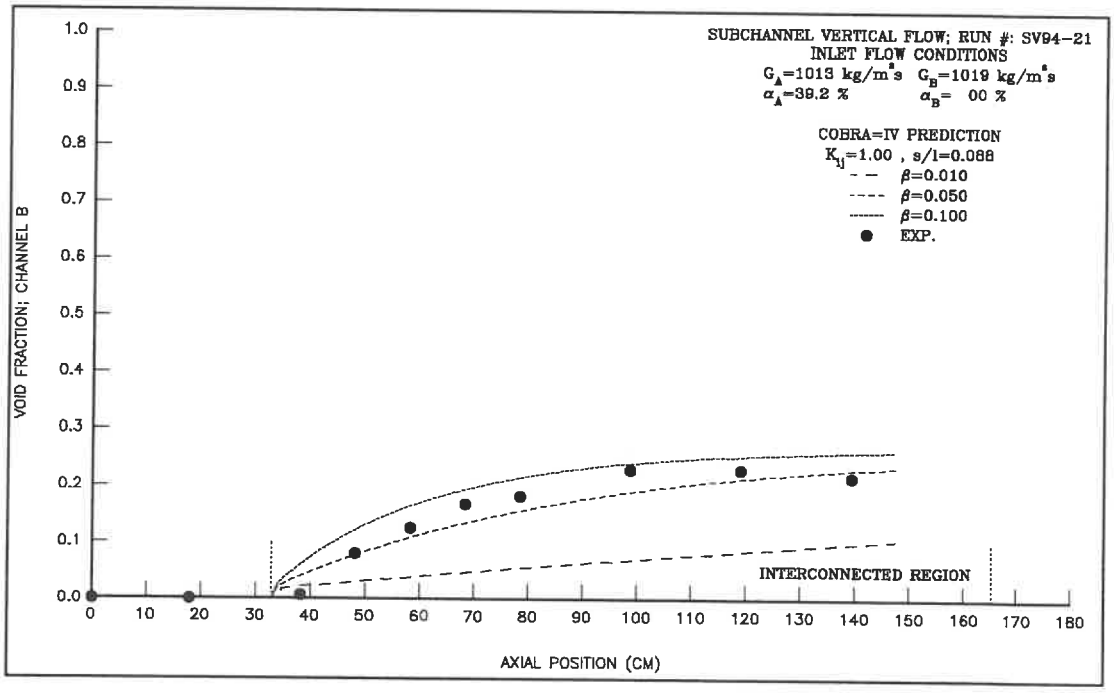


Figure 5.49: Void Fraction Profile, Run SV94-21, Channel B

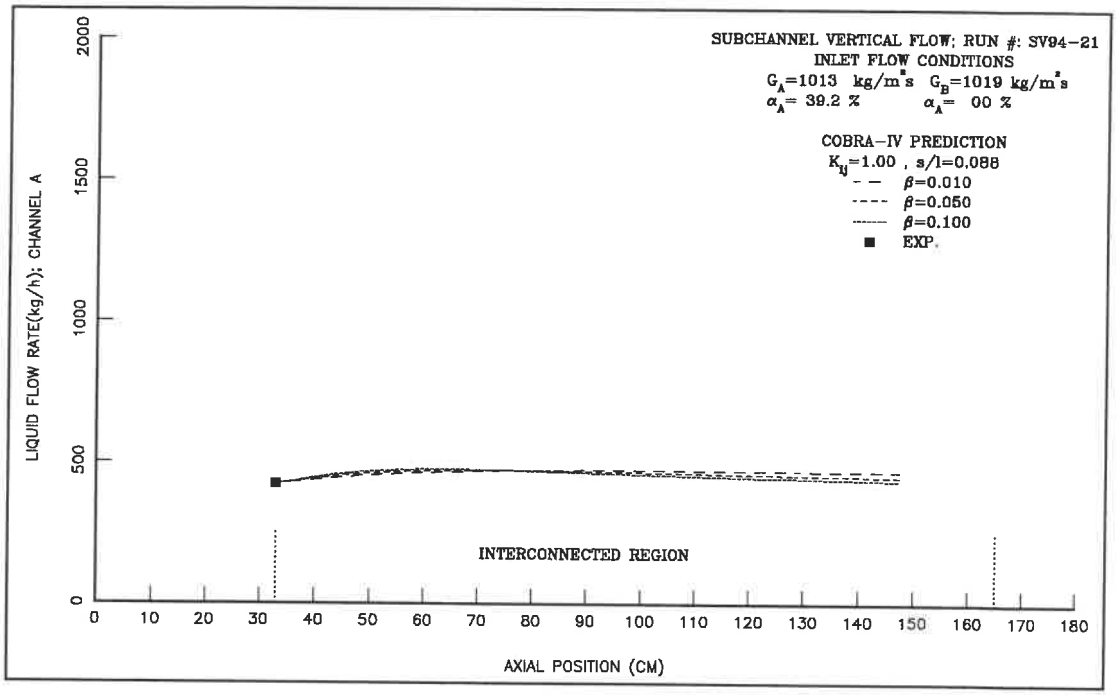


Figure 5.50: Mass Flow Rate Profile, Run SV94-21, Channel A

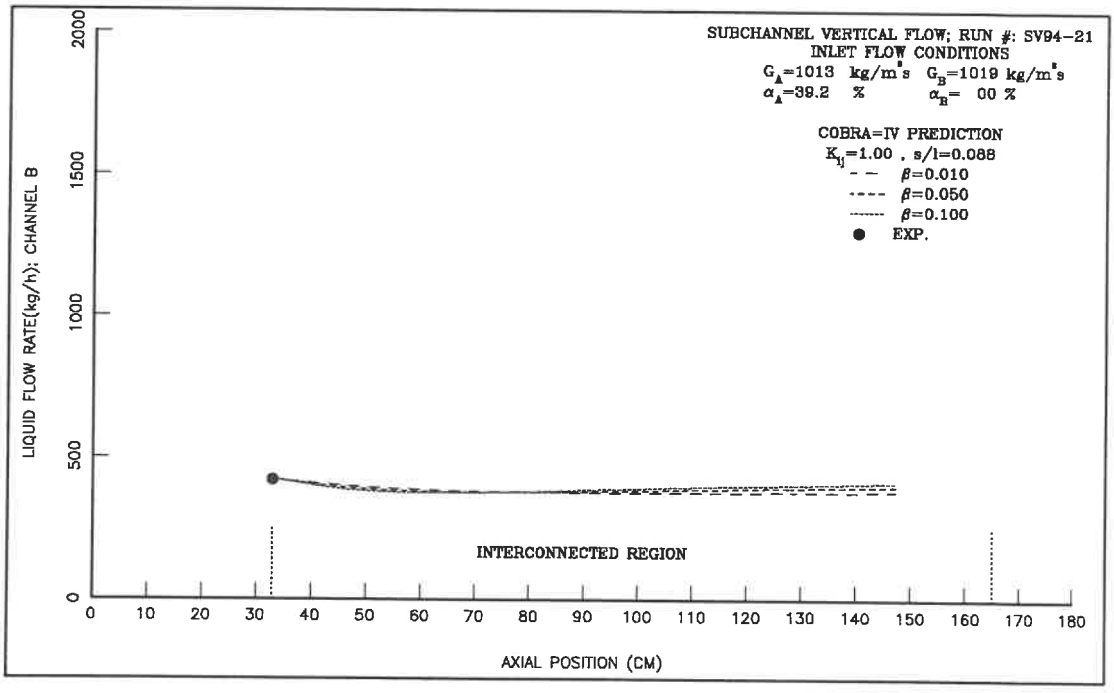


Figure 5.51: Mass Flow Rate Profile, Run SV94-21, Channel B

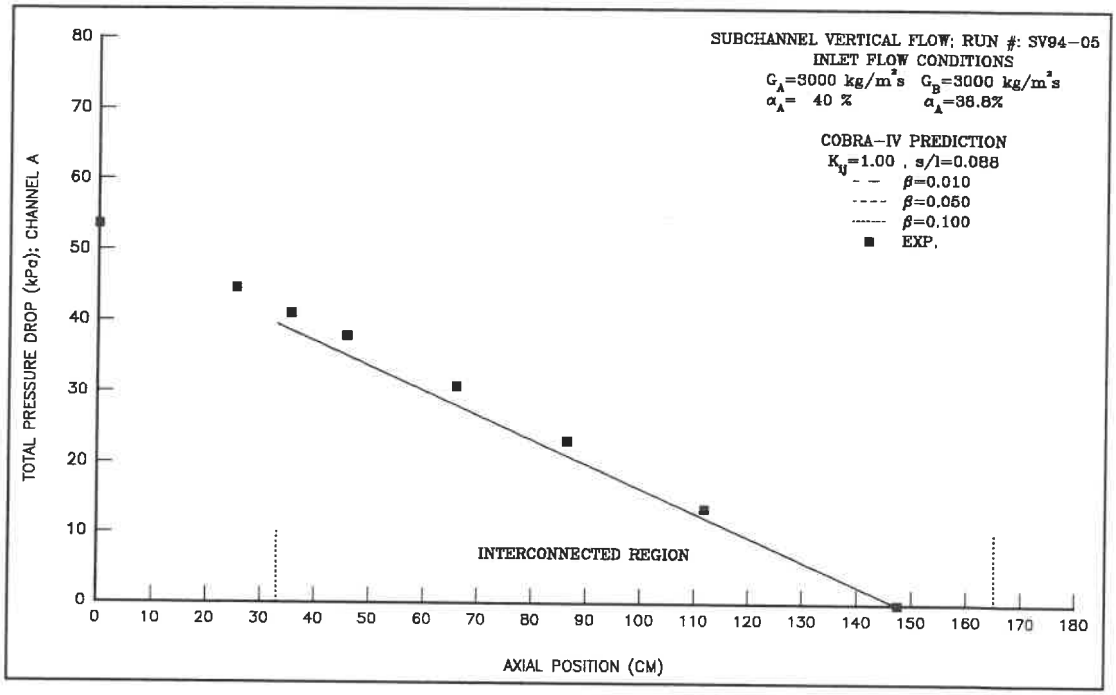


Figure 5.52: Total Pressure Drop Profile, Run SV94-05, Channel A

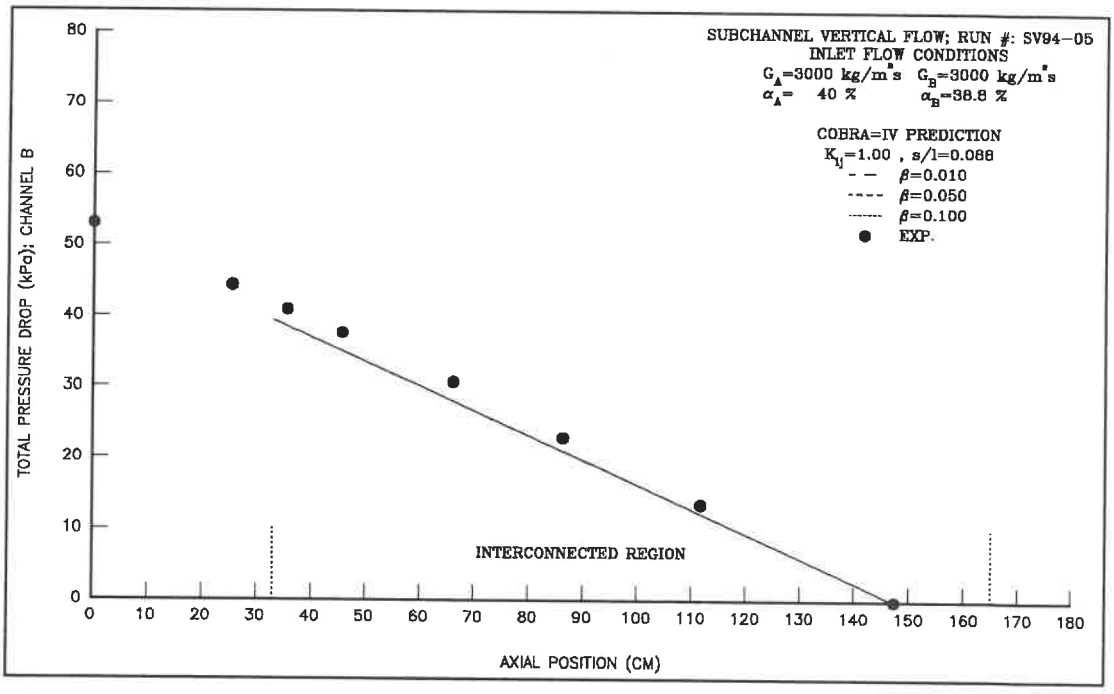


Figure 5.53: Total Pressure Drop Profile, Run SV94-05, Channel B

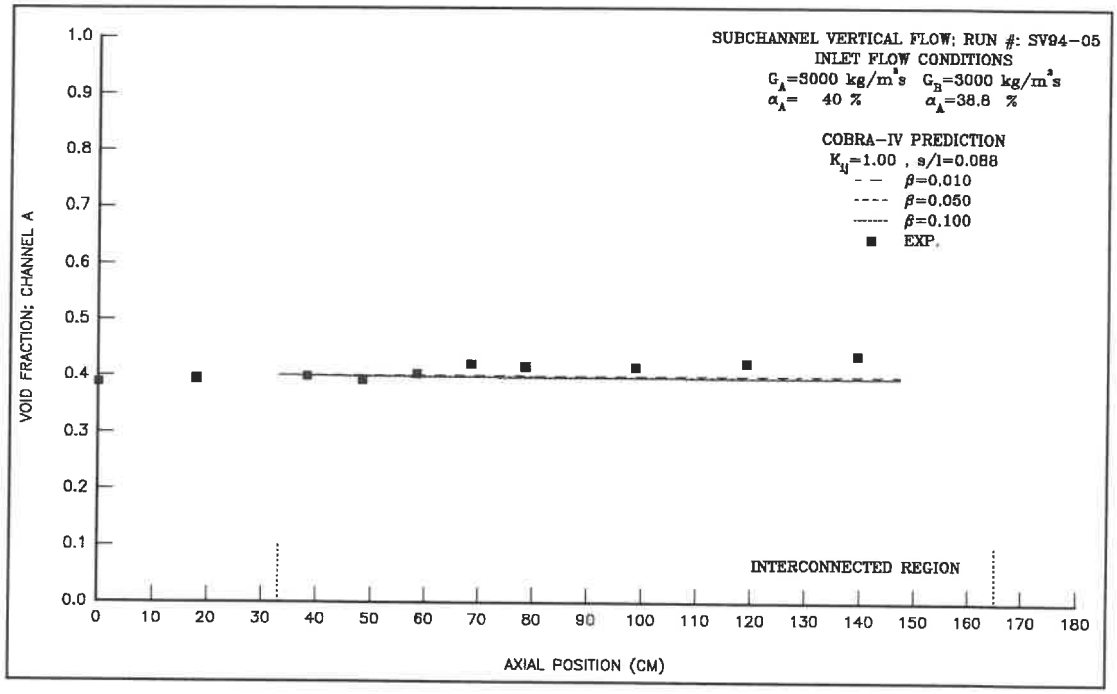


Figure 5.54: Void Fraction Profile, Run SV94-05, Channel A

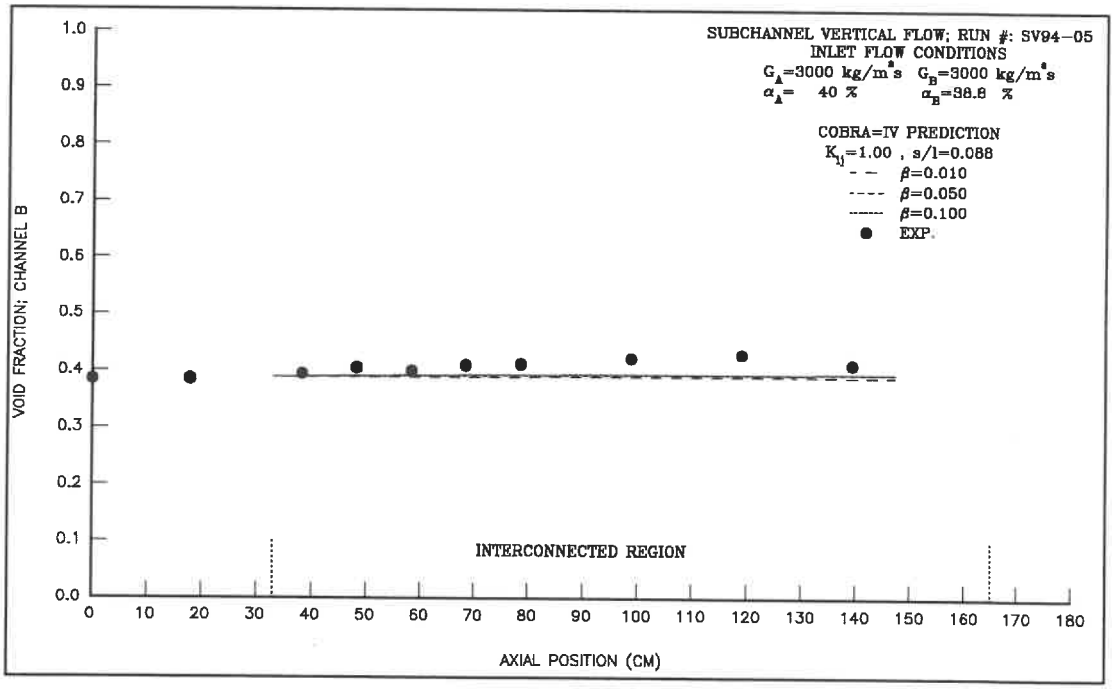


Figure 5.55: Void Fraction Profile, Run SV94-05, Channel B

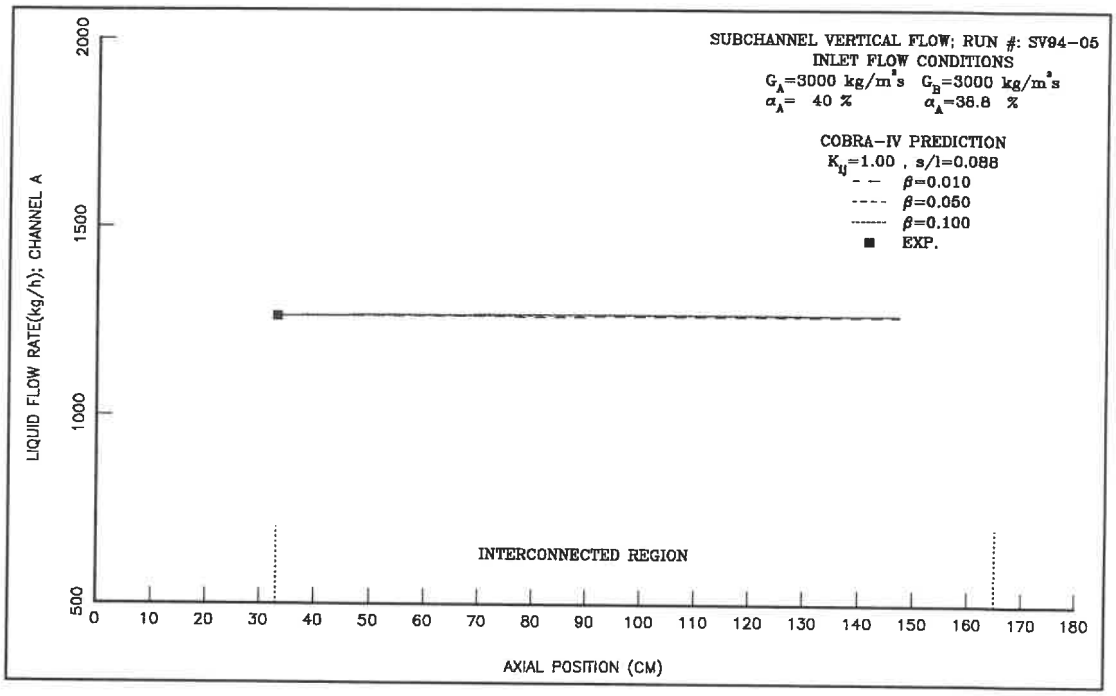


Figure 5.56: Mass Flow Rate Profile, Run SV94-05, Channel A

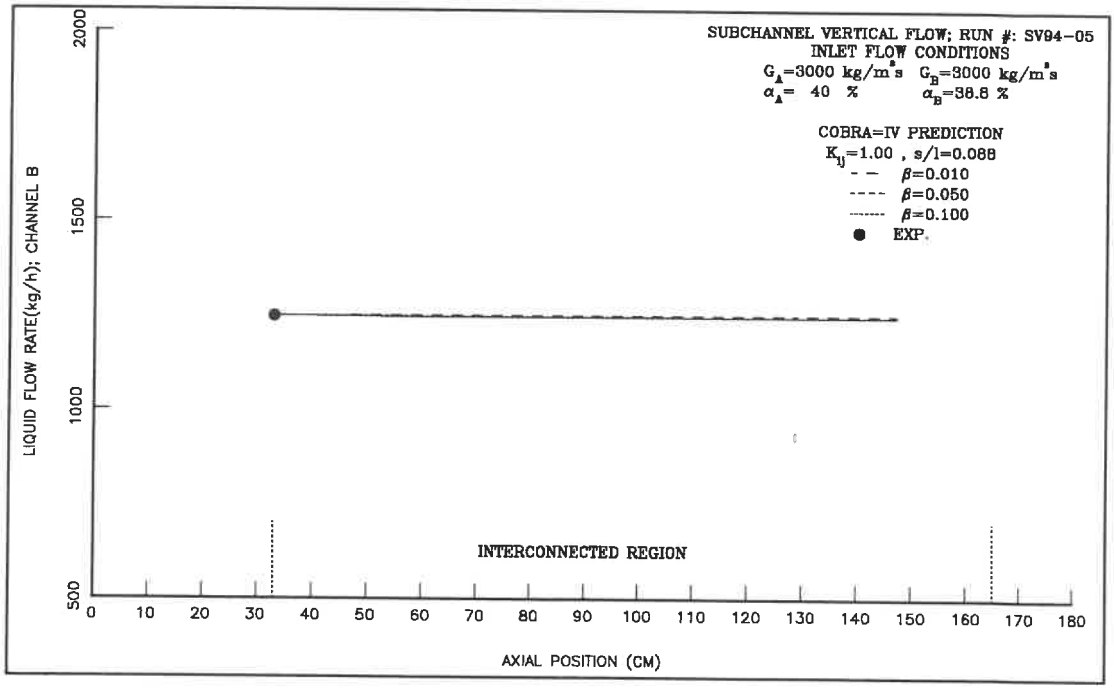


Figure 5.57: Mass Flow Rate Profile, Run SV94-05, Channel B

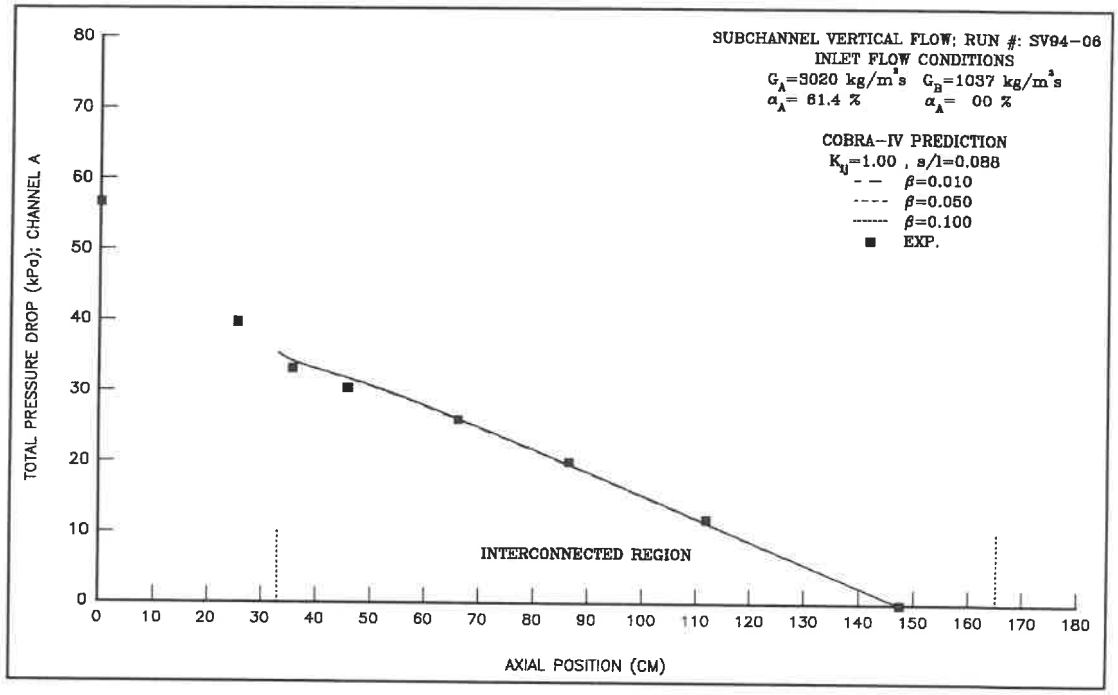


Figure 5.58: Total Pressure Drop Profile, Run SV94-06, Channel A

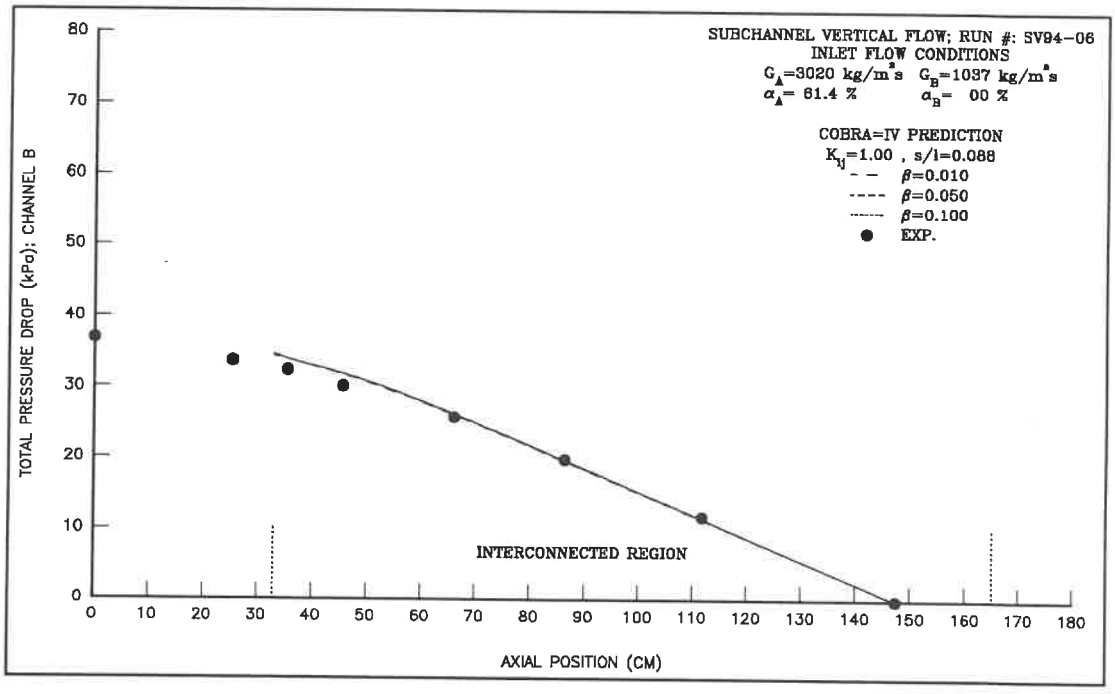


Figure 5.59: Total Pressure Drop Profile, Run SV94-06, Channel B

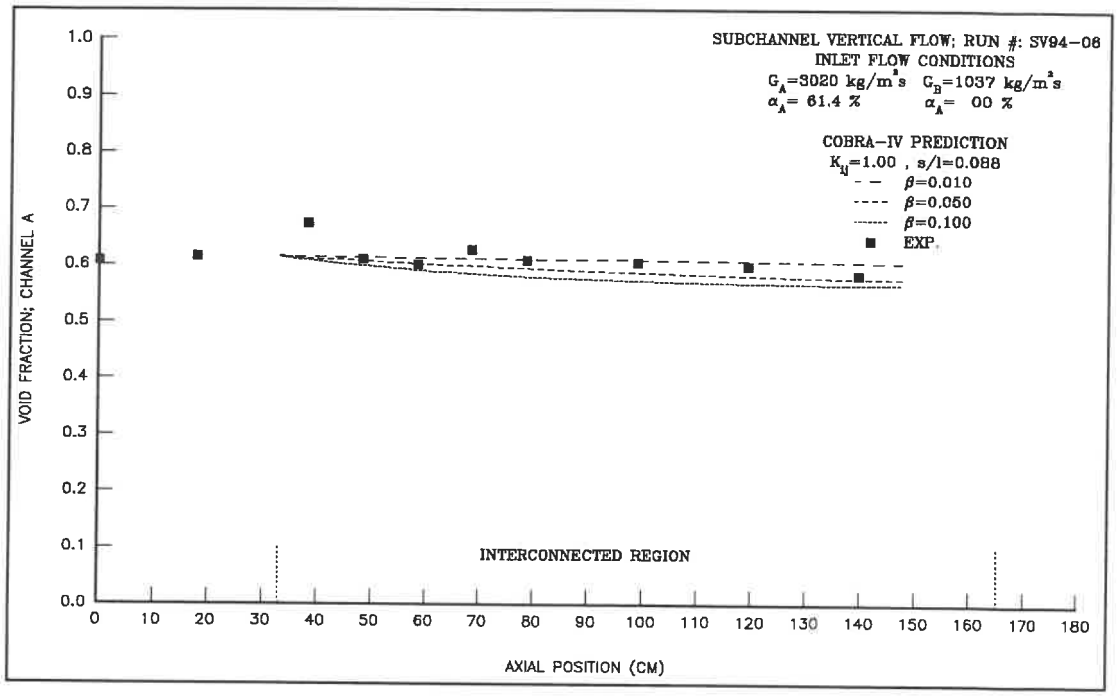


Figure 5.60: Void Fraction Profile, Run SV94-06, Channel A

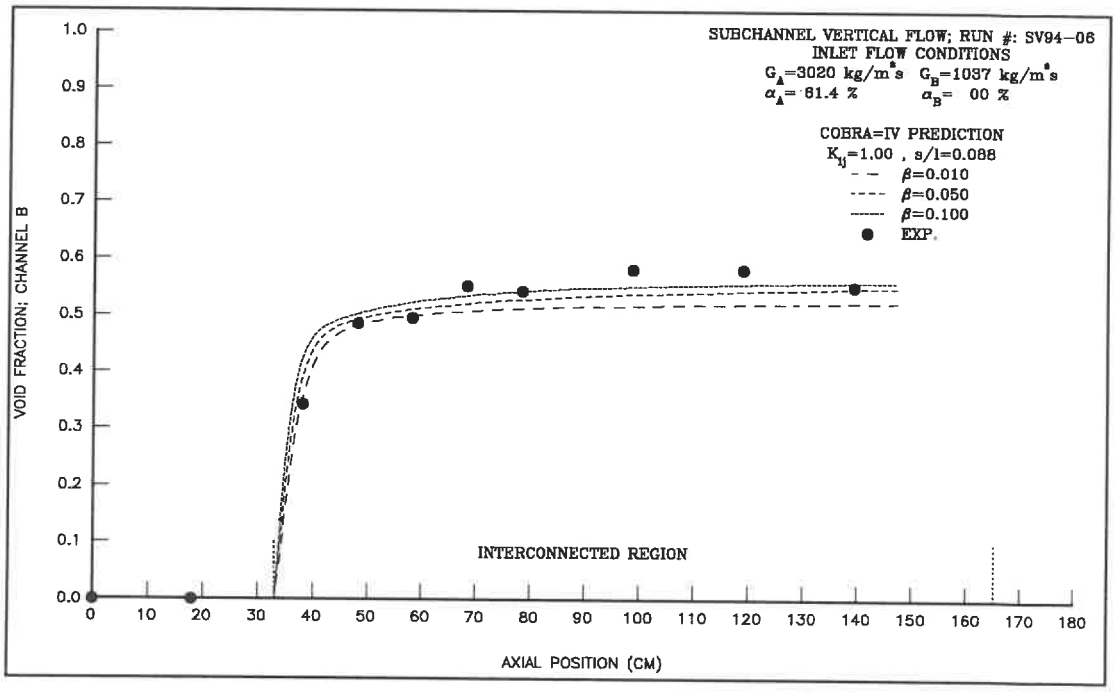


Figure 5.61: Void Fraction Profile, Run SV94-06, Channel B

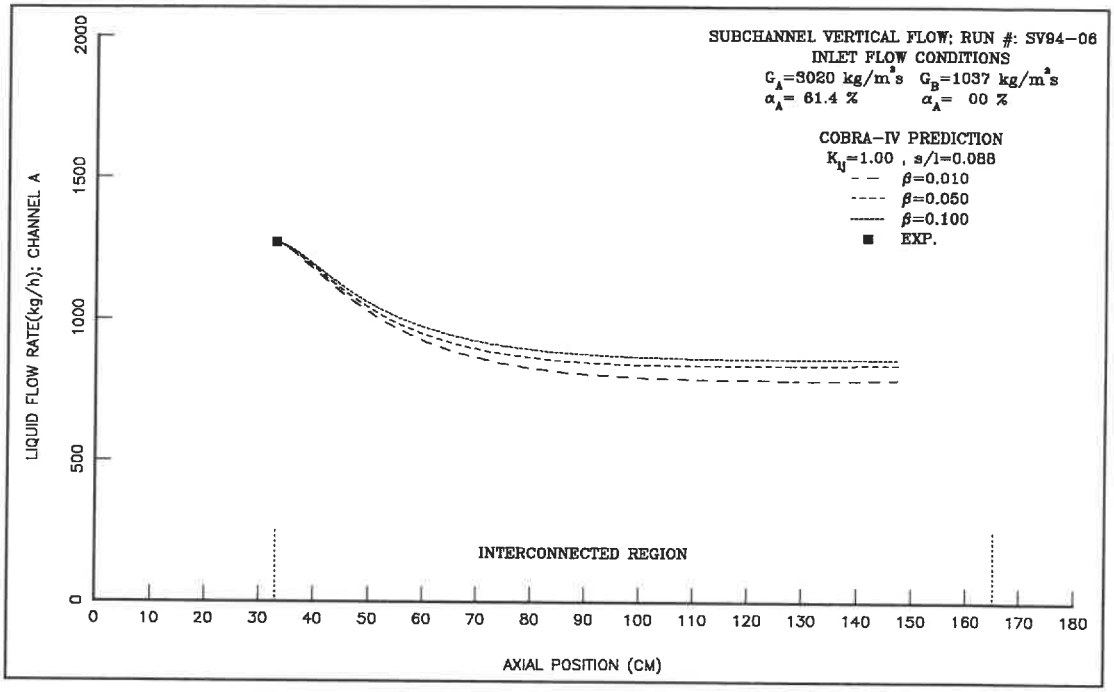


Figure 5.62: Mass Flow Rate Profile, Run SV94-06, Channel A

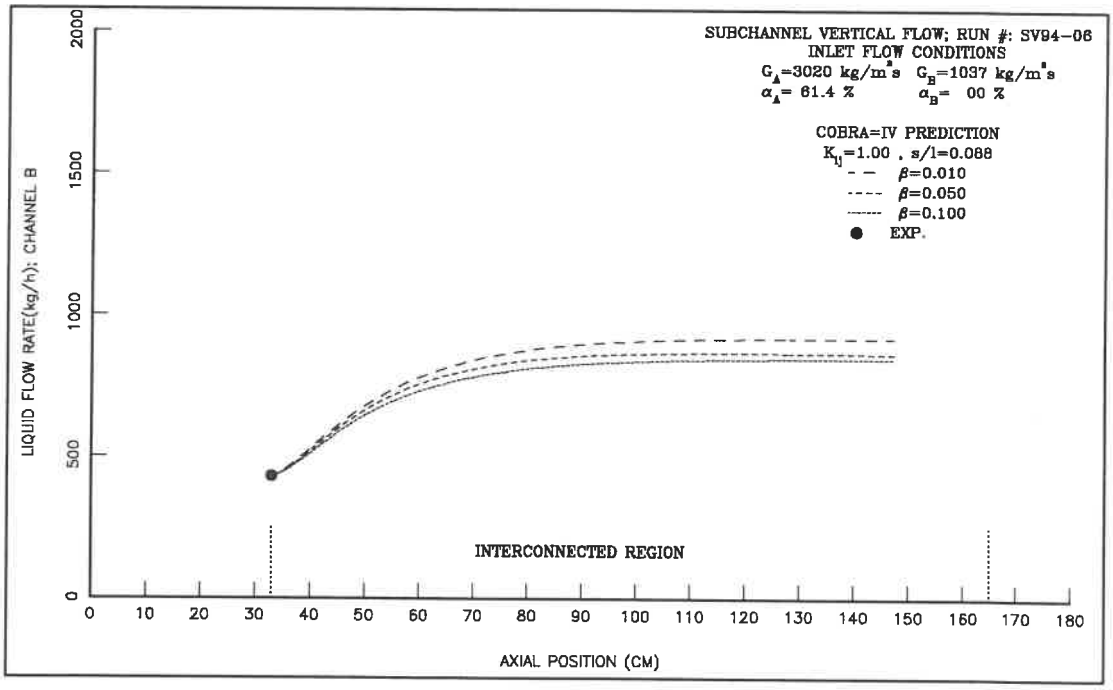


Figure 5.63: Mass Flow Rate Profile, Run SV94-06, Channel B

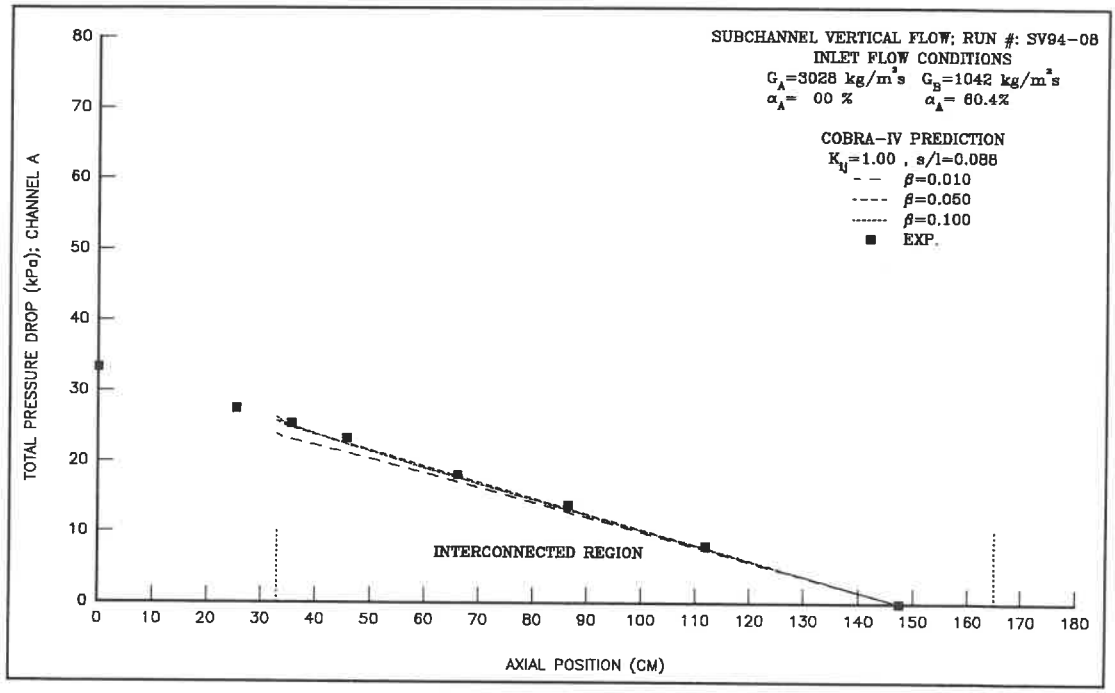


Figure 5.64: Total Pressure Drop Profile, Run SV94-08, Channel A

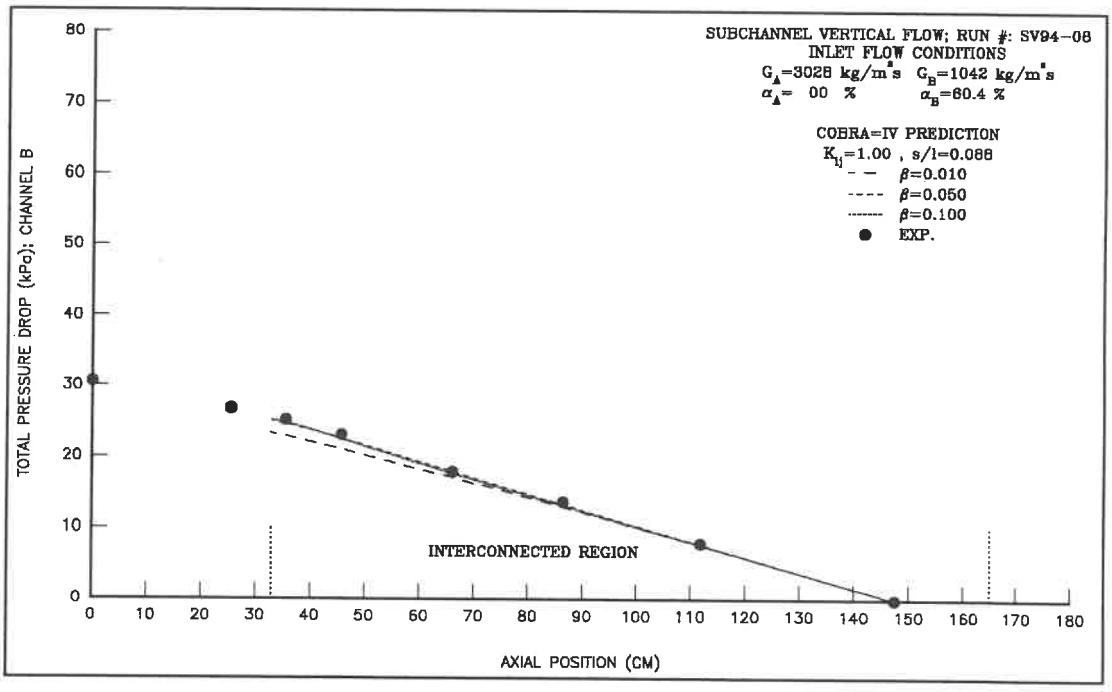


Figure 5.65: Total Pressure Drop Profile, Run SV94-08, Channel B

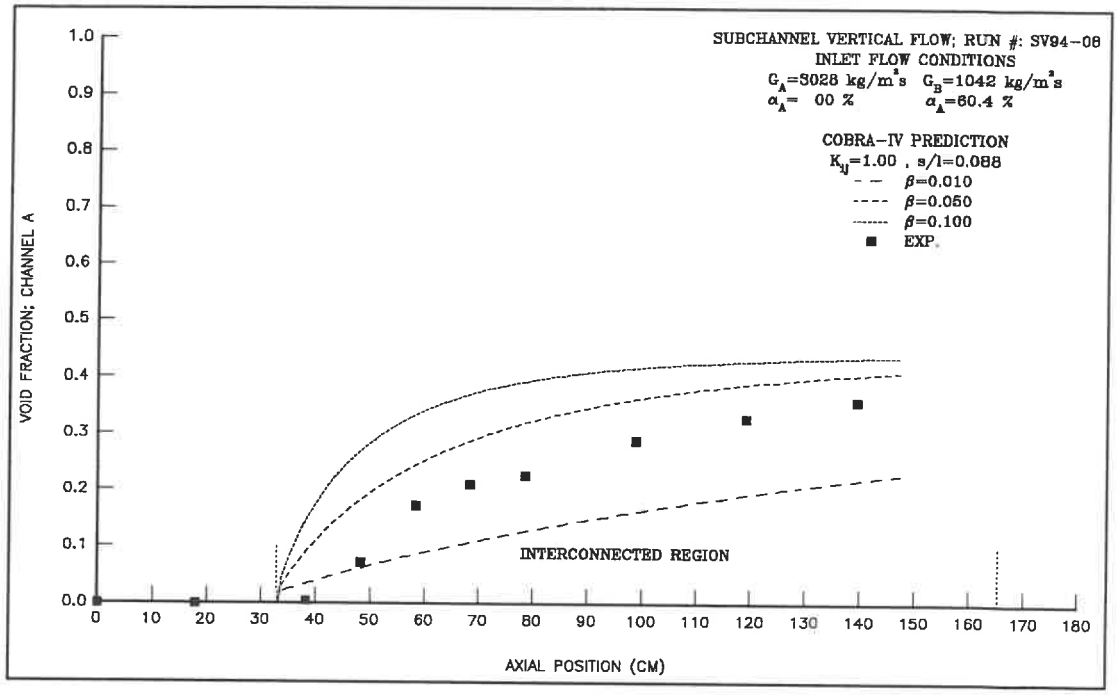


Figure 5.66: Void Fraction Profile, Run SV94-08, Channel A

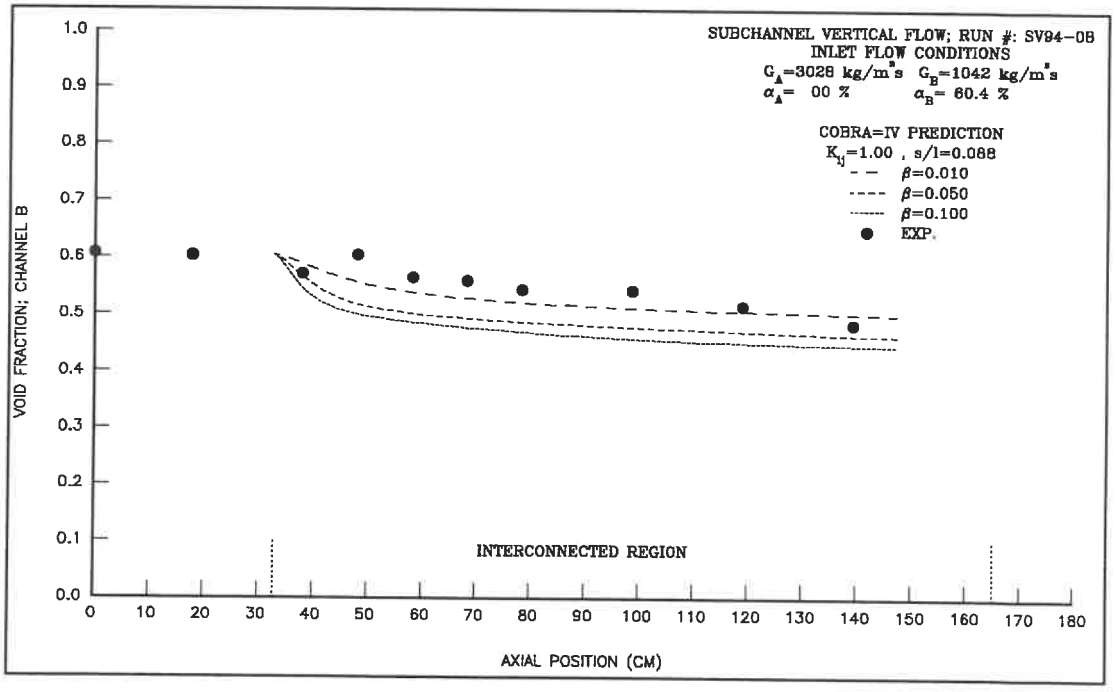


Figure 5.67: Void Fraction Profile, Run SV94-08, Channel B

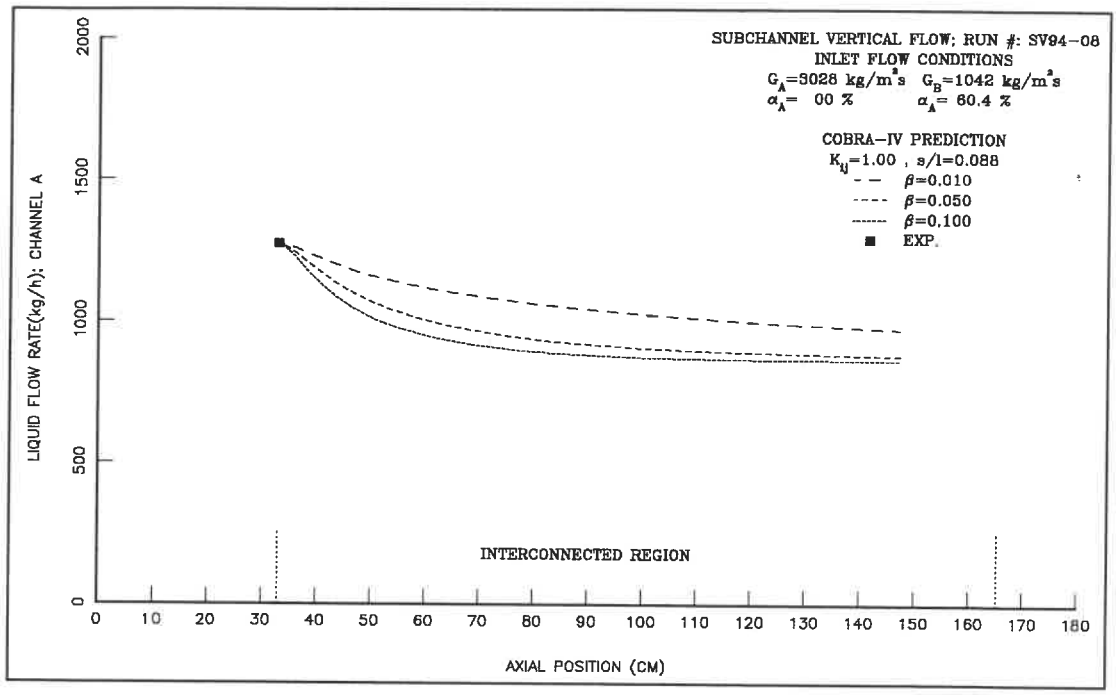


Figure 5.68: Mass Flow Rate Profile, Run SV94-08, Channel A

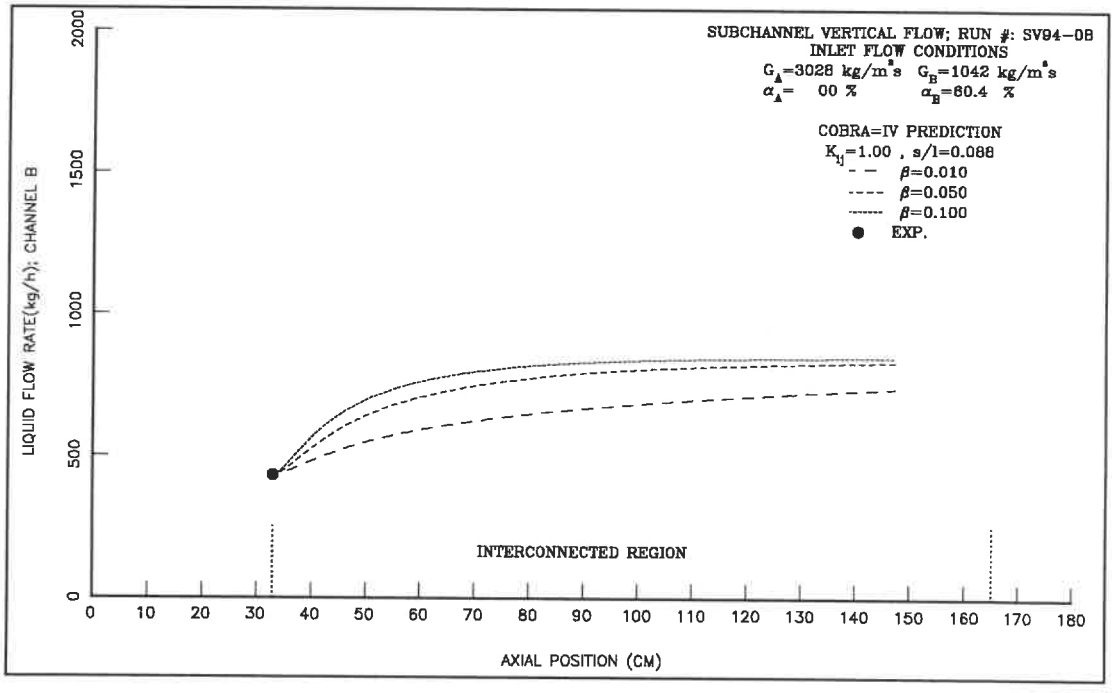


Figure 5.69: Mass Flow Rate Profile, Run SV94-08, Channel B

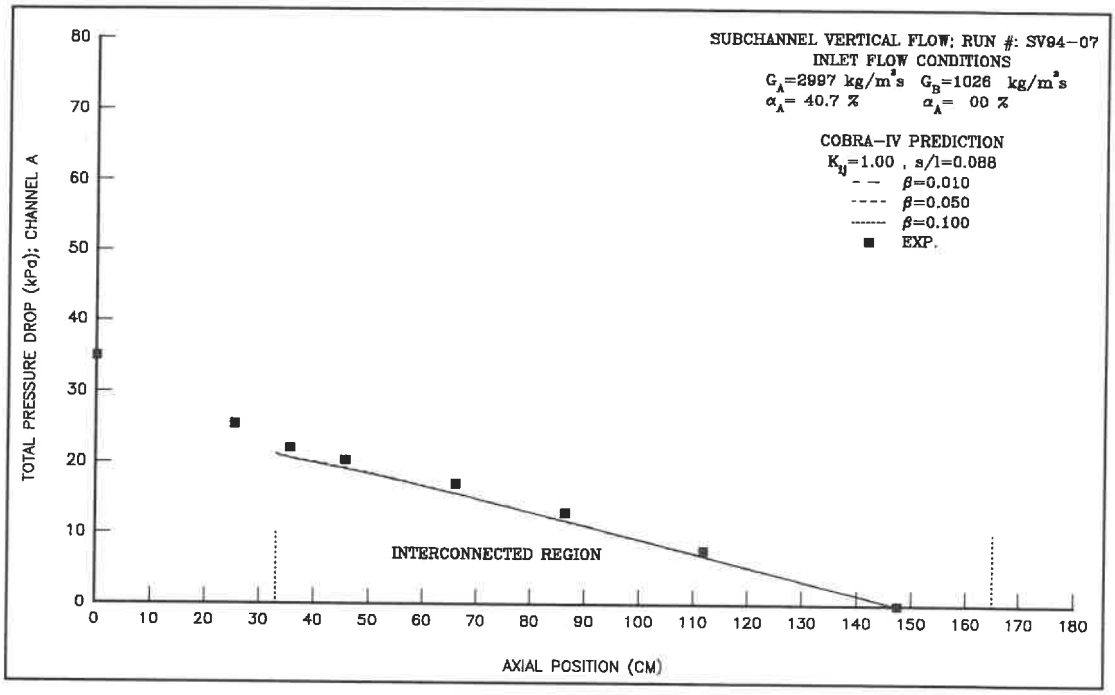


Figure 5.70: Total Pressure Drop Profile, Run SV94-07, Channel A

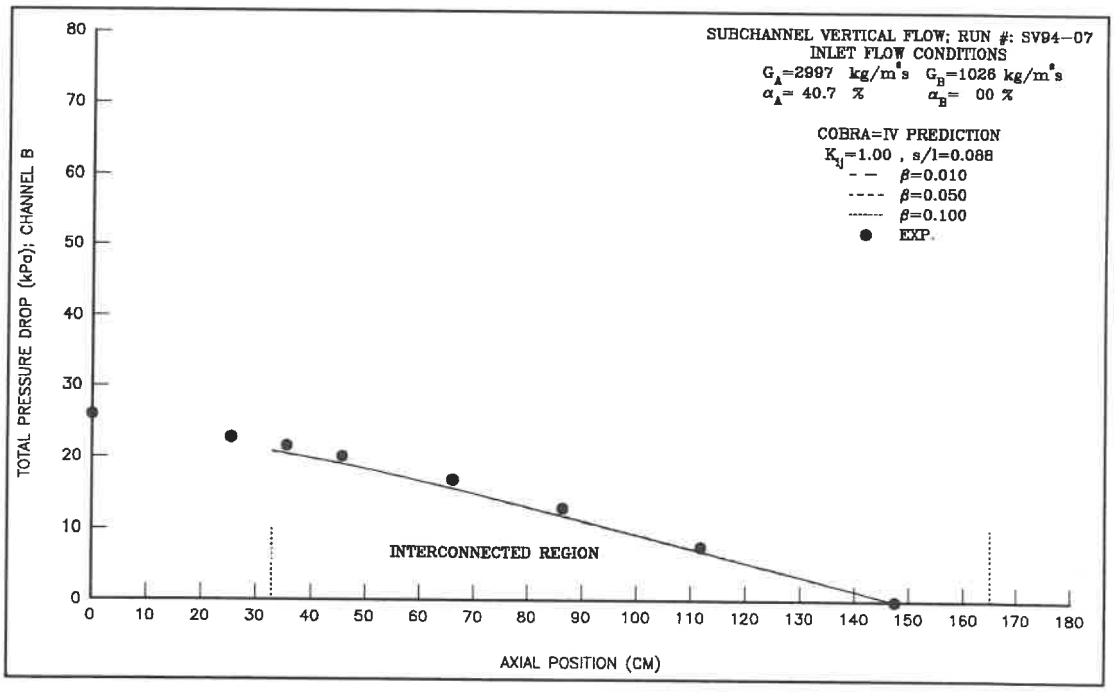


Figure 5.71: Total Pressure Drop Profile, Run SV94-07, Channel B

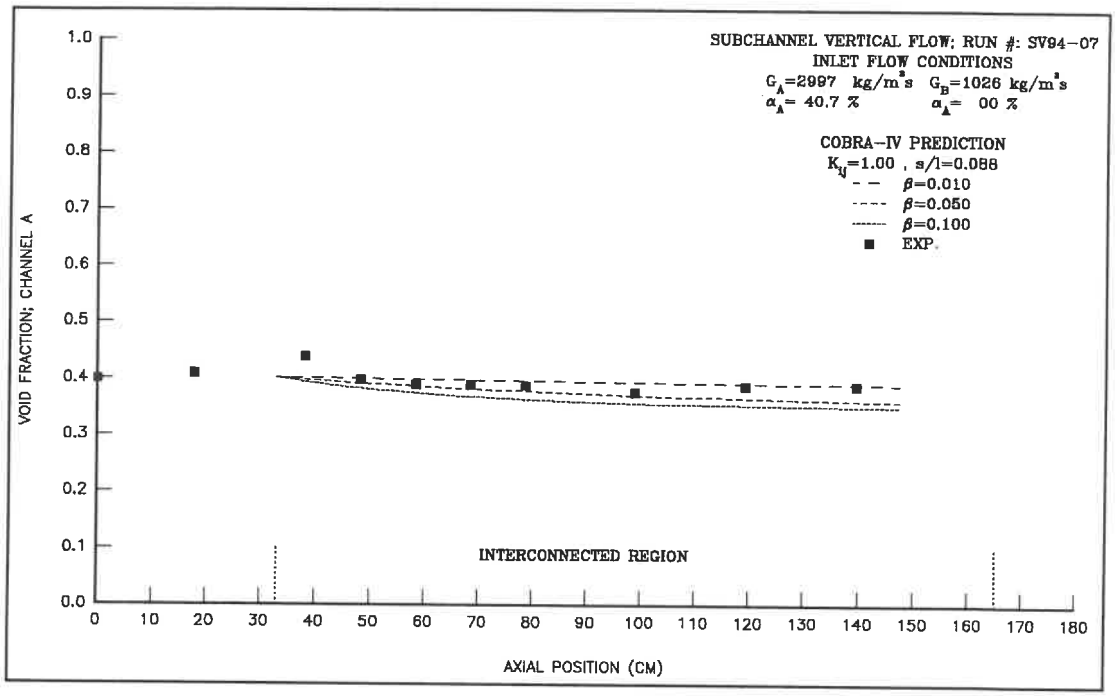


Figure 5.72: Void Fraction Profile, Run SV94-07, Channel A

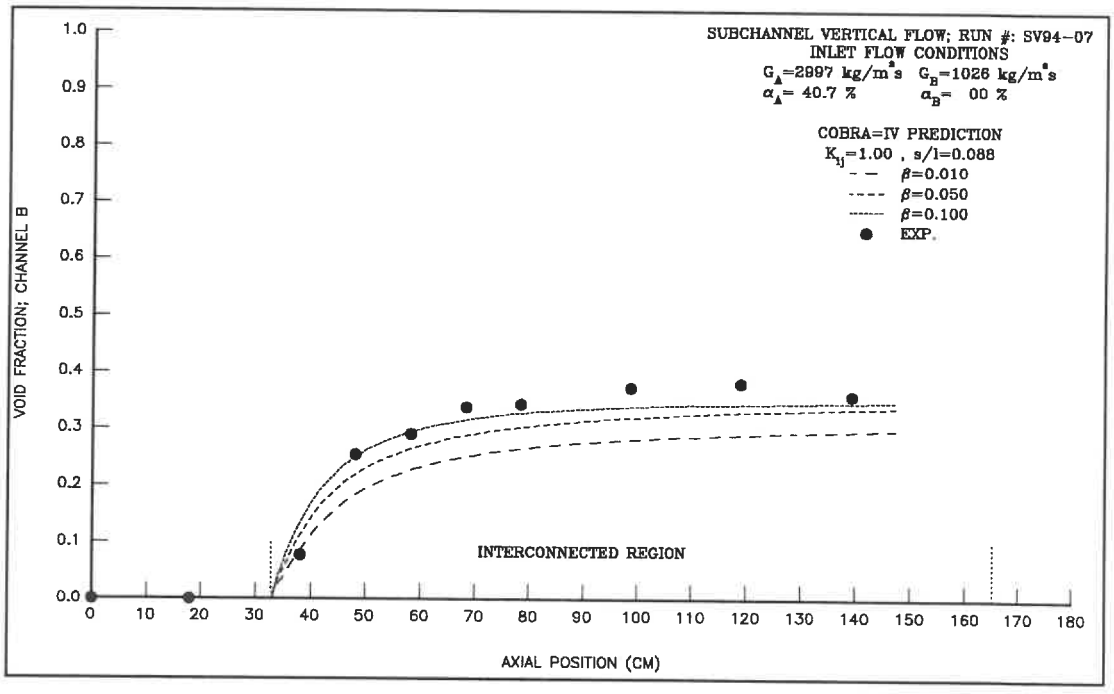


Figure 5.73: Void Fraction Profile, Run SV94-07, Channel B

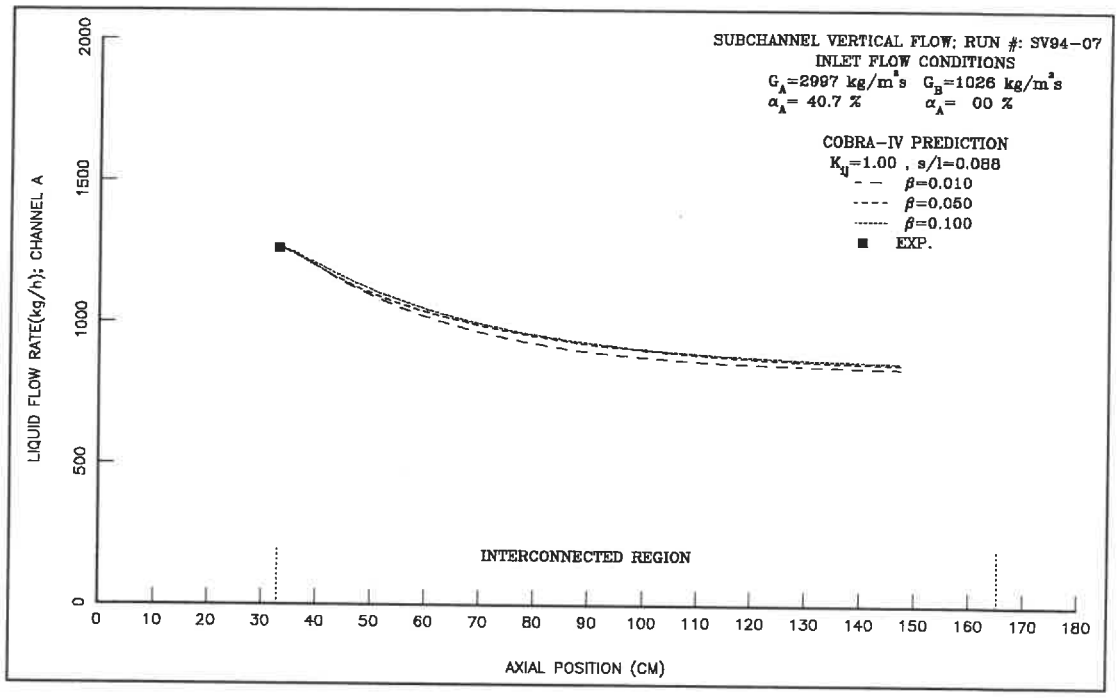


Figure 5.74: Mass Flow Rate Profile, Run SV94-07, Channel A

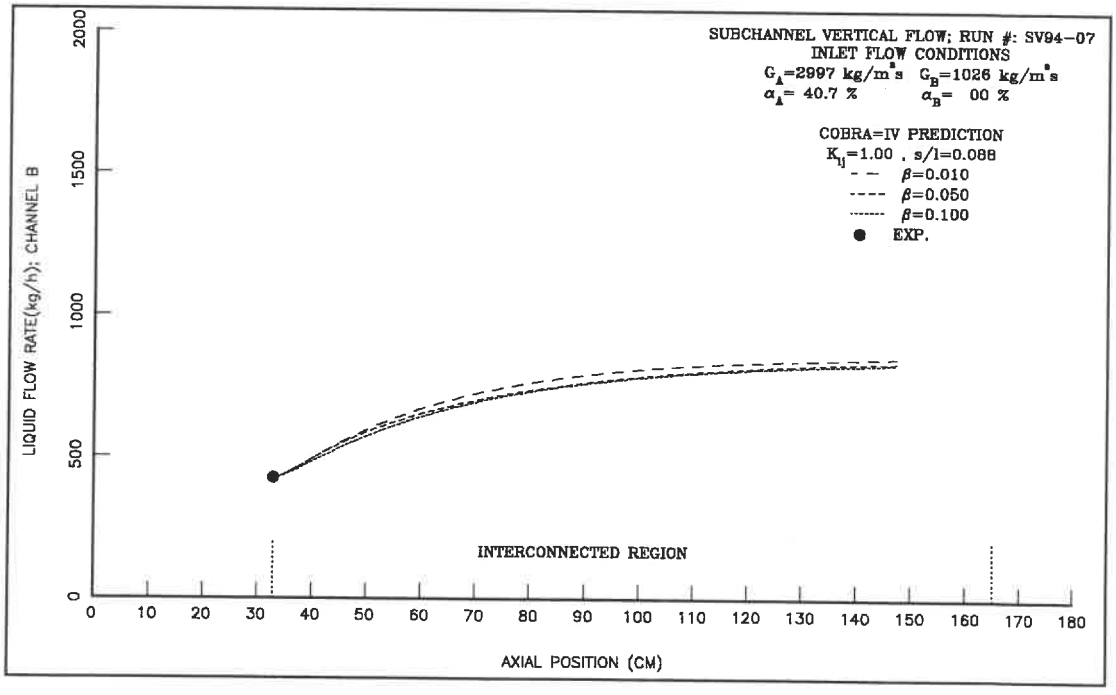


Figure 5.75: Mass Flow Rate Profile, Run SV94-07, Channel B

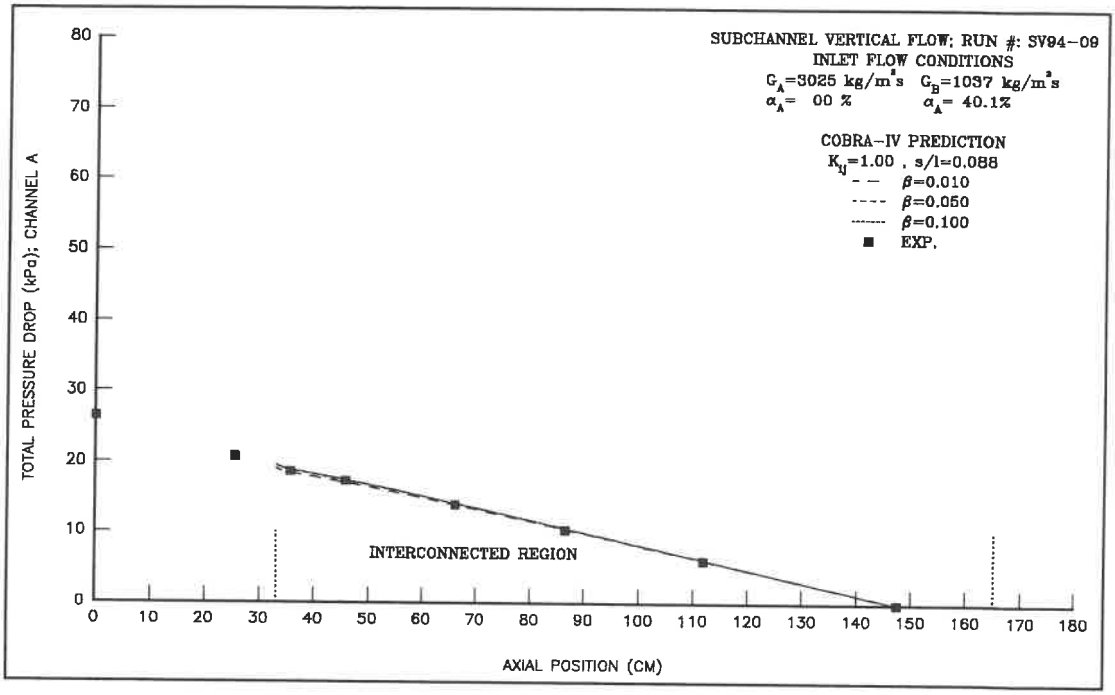


Figure 5.76: Total Pressure Drop Profile, Run SV94-09, Channel A

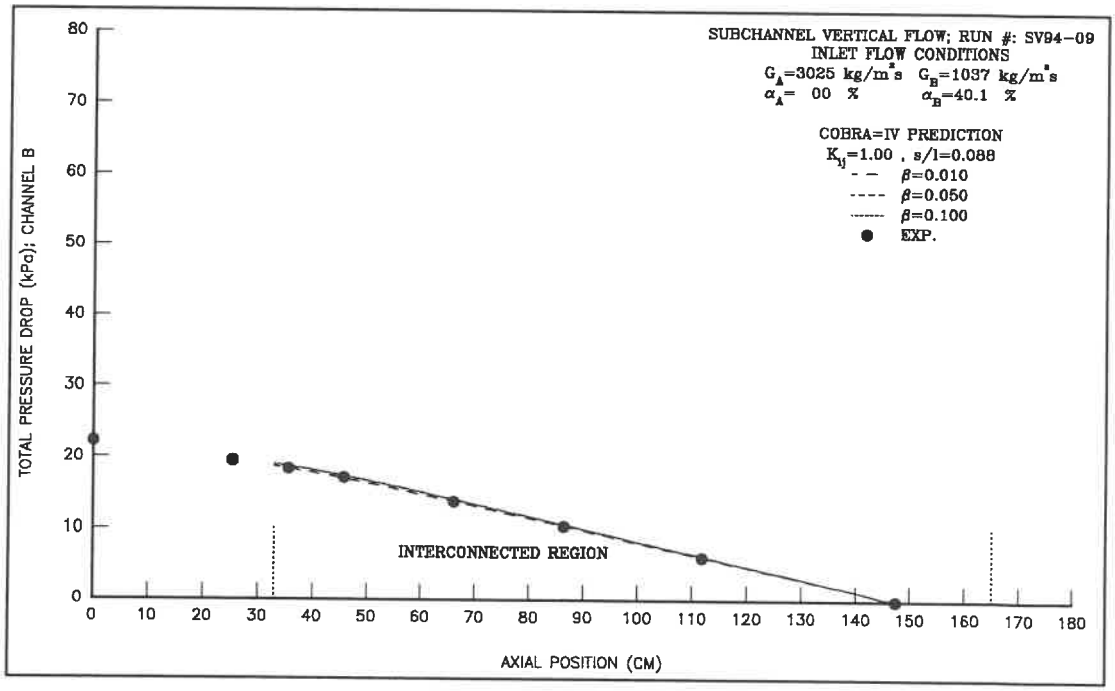


Figure 5.77: Total Pressure Drop Profile, Run SV94-09, Channel B

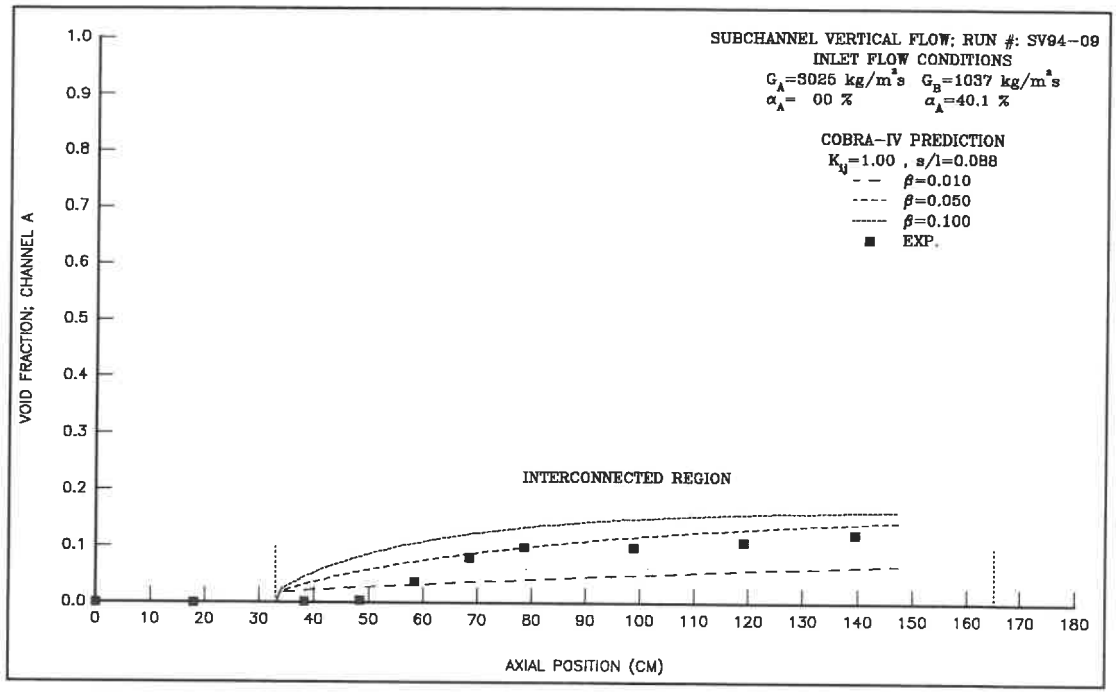


Figure 5.78: Void Fraction Profile, Run SV94-09, Channel A

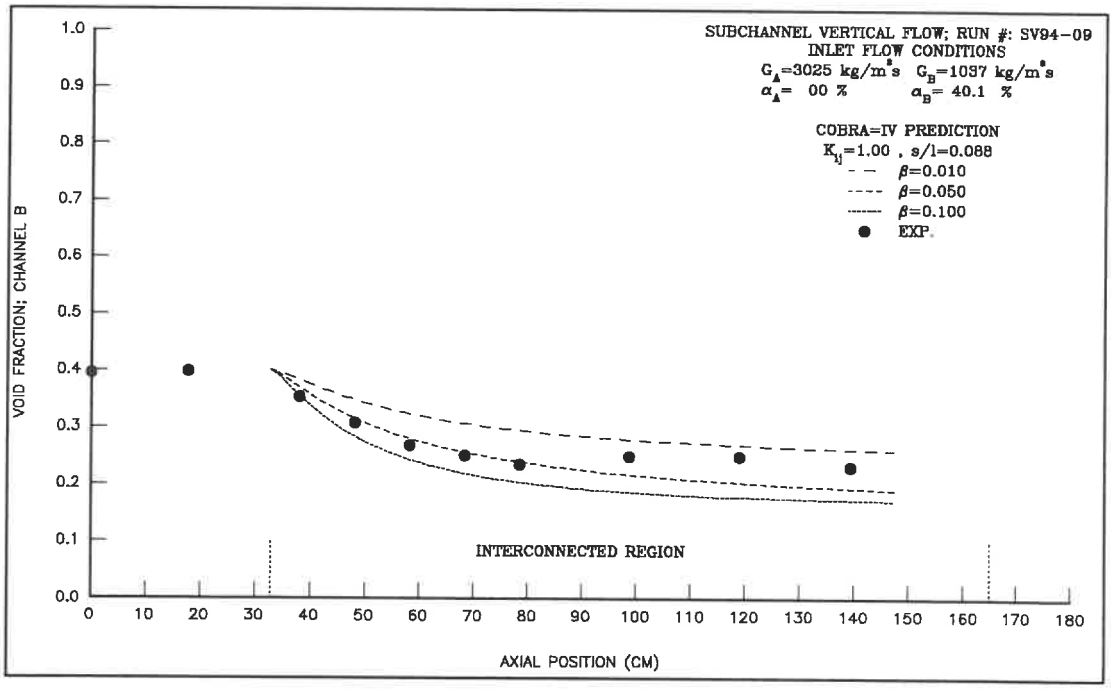


Figure 5.79: Void Fraction Profile, Run SV94-09, Channel B

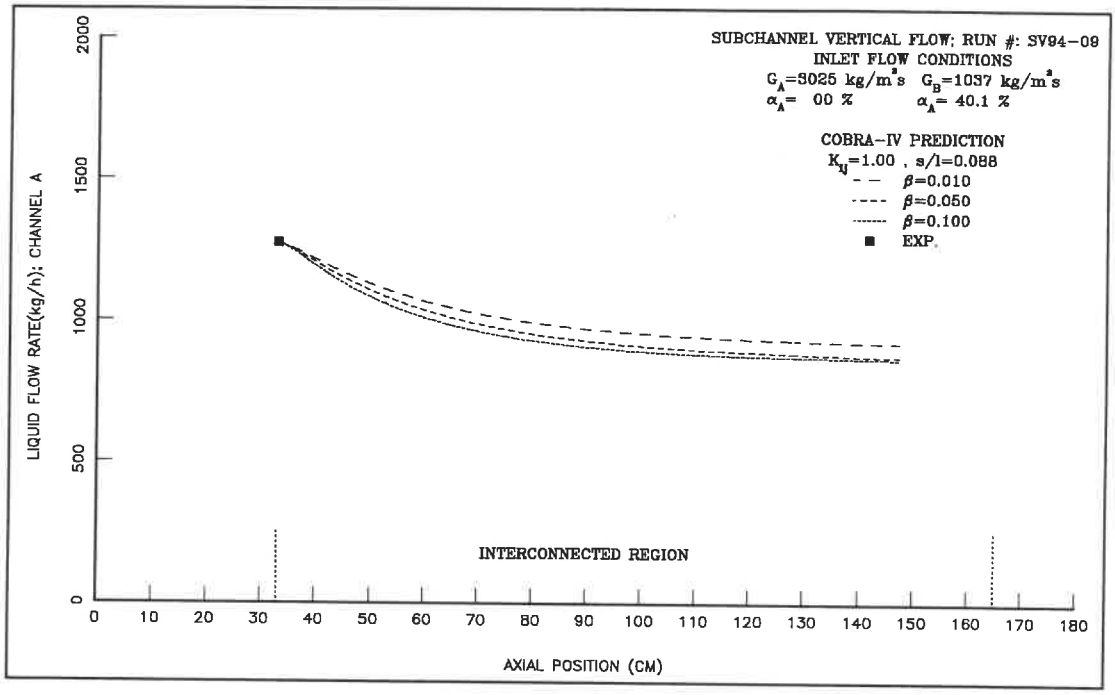


Figure 5.80: Mass Flow Rate Profile, Run SV94-09, Channel A

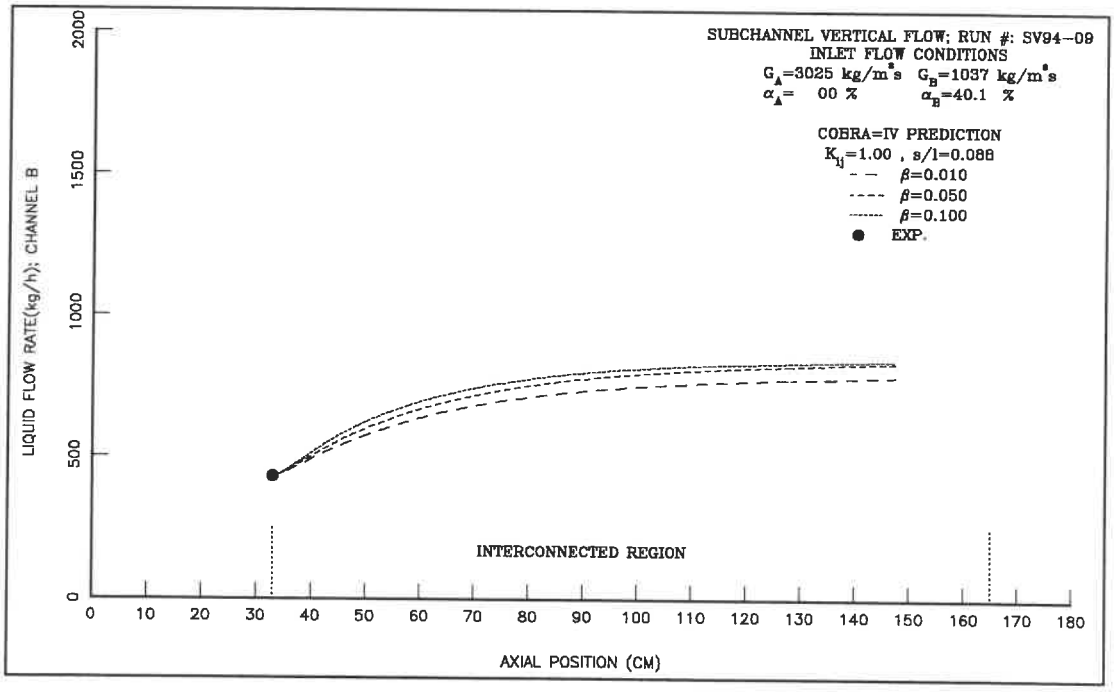


Figure 5.81: Mass Flow Rate Profile, Run SV94-09, Channel B

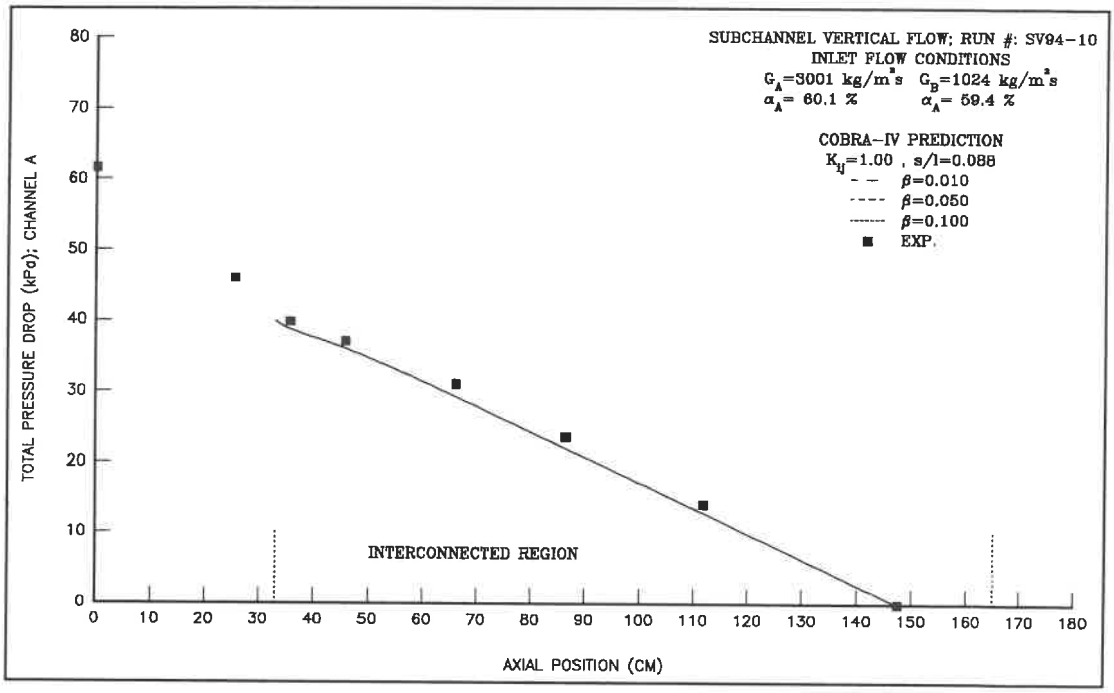


Figure 5.82: Total Pressure Drop Profile, Run SV94-10, Channel A

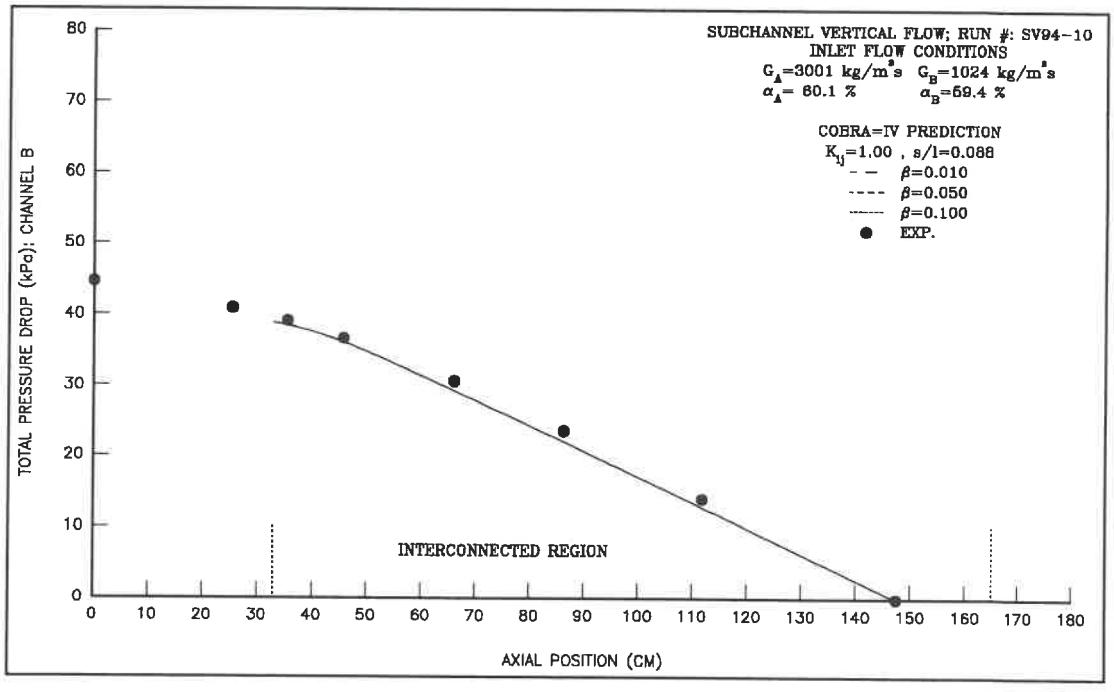


Figure 5.83: Total Pressure Drop Profile, Run SV94-10, Channel B

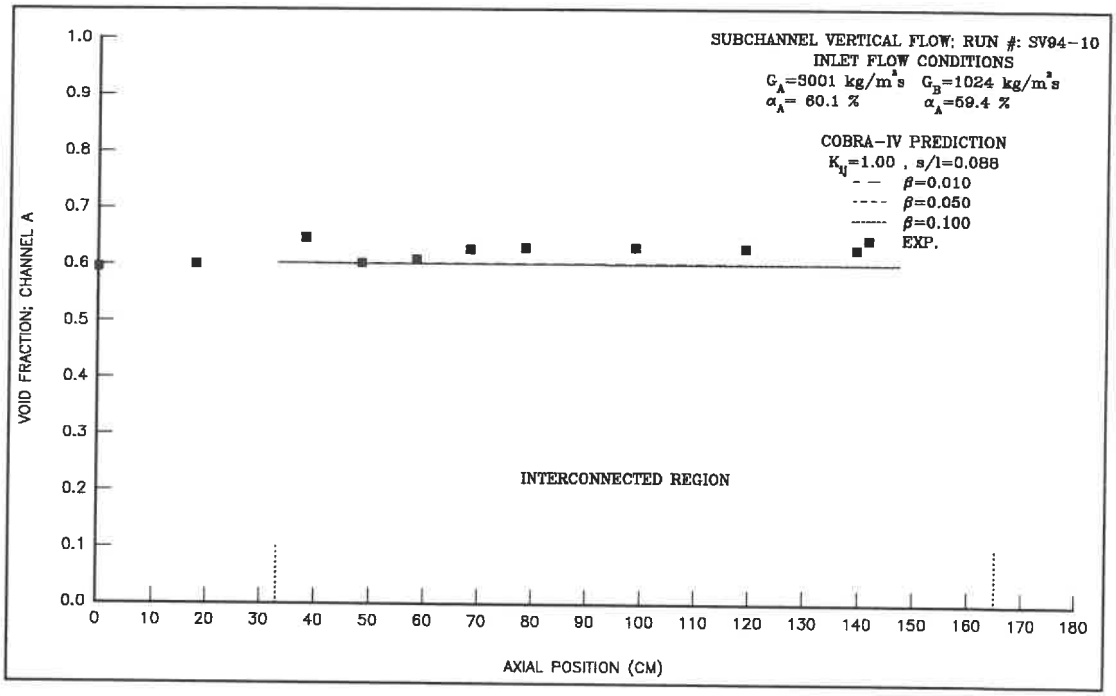


Figure 5.84: Void Fraction Profile, Run SV94-10, Channel A

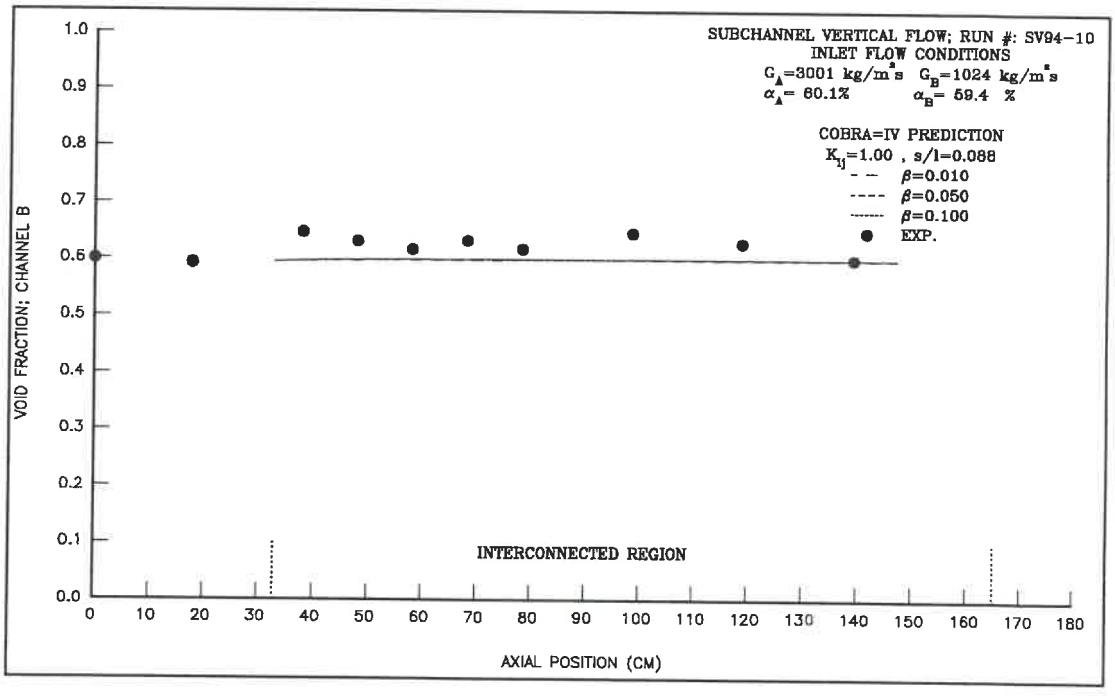


Figure 5.85: Void Fraction Profile, Run SV94-10, Channel B

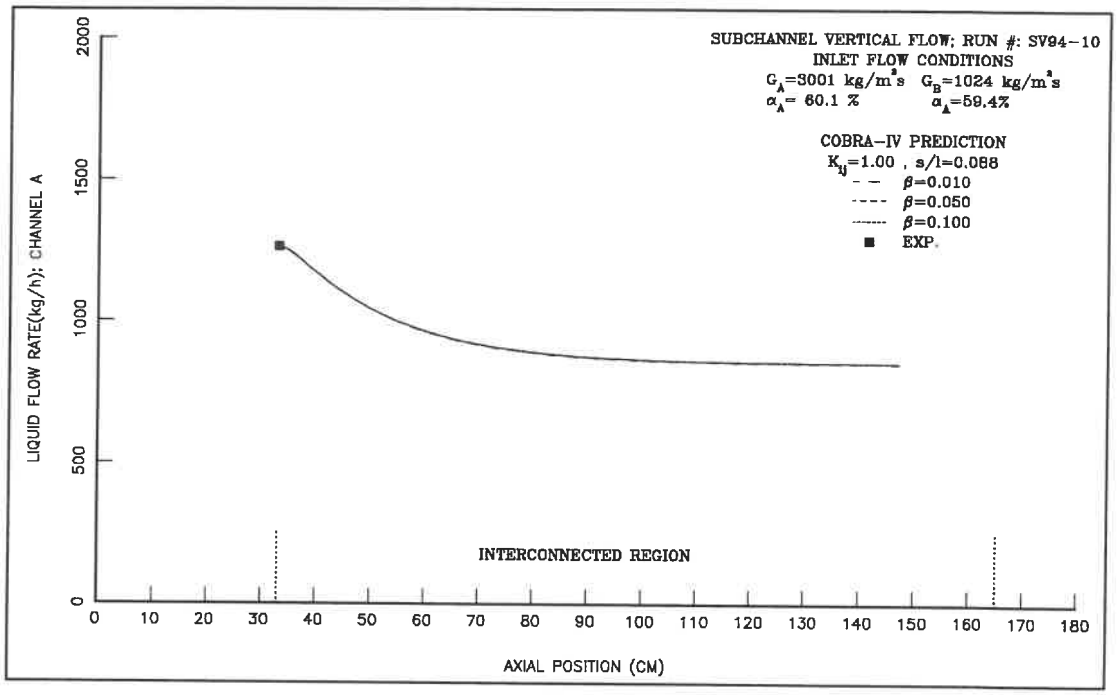


Figure 5.86: Mass Flow Rate Profile, Run SV94-10, Channel A

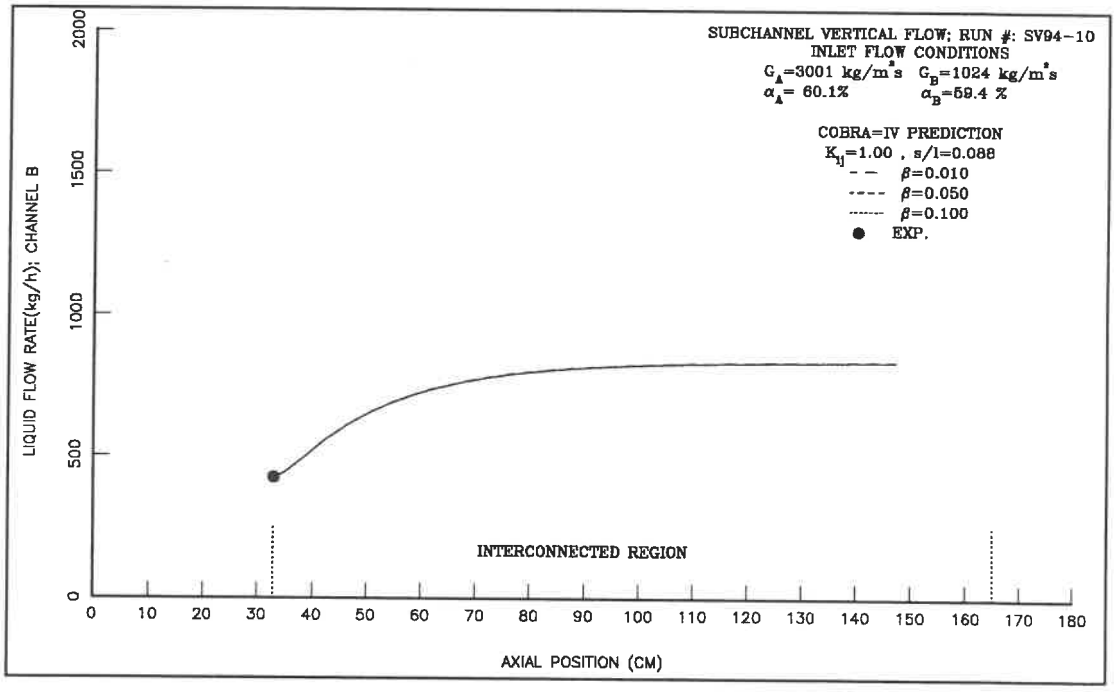


Figure 5.87: Mass Flow Rate Profile, Run SV94-10, Channel B

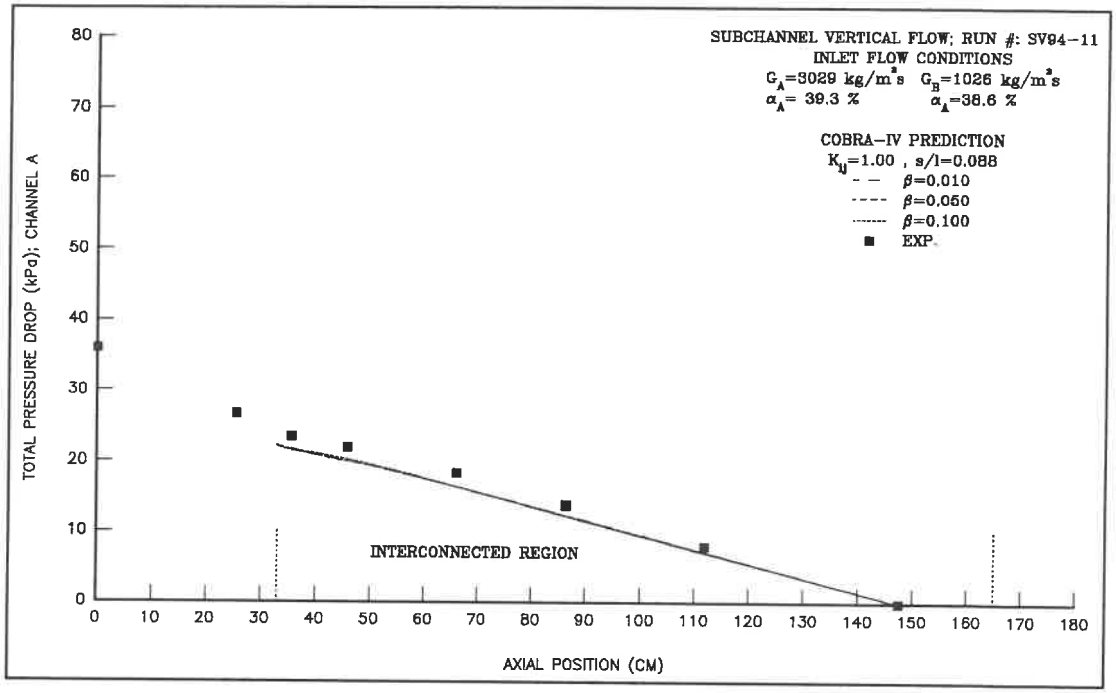


Figure 5.88: Total Pressure Drop Profile, Run SV94-11, Channel A

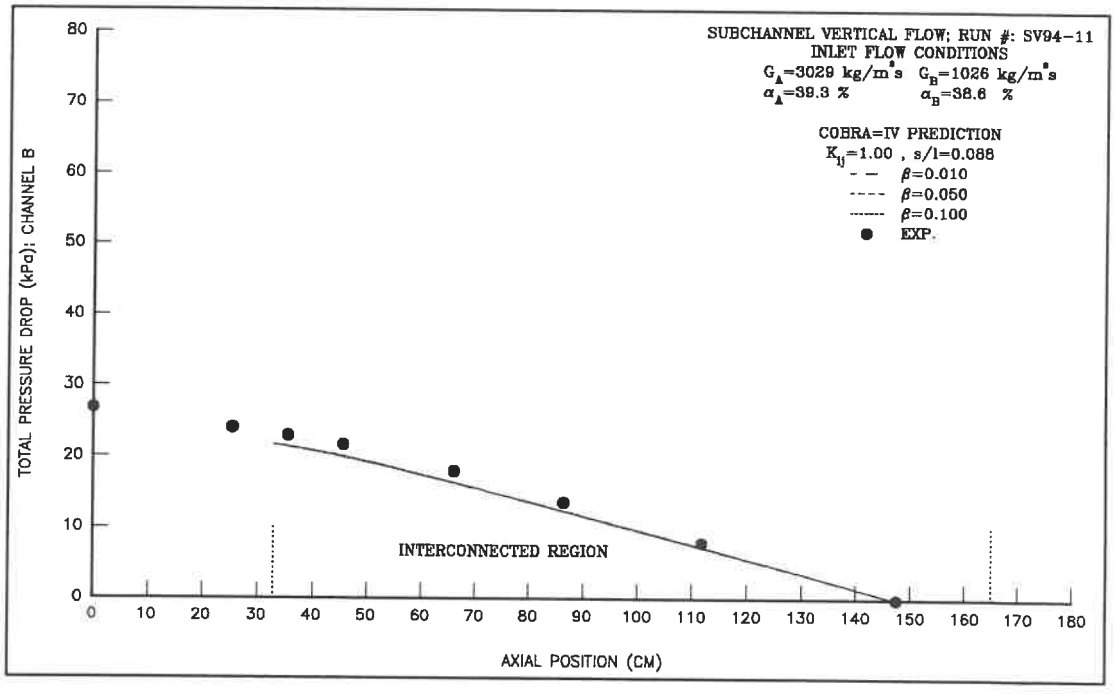


Figure 5.89: Total Pressure Drop Profile, Run SV94-11, Channel B

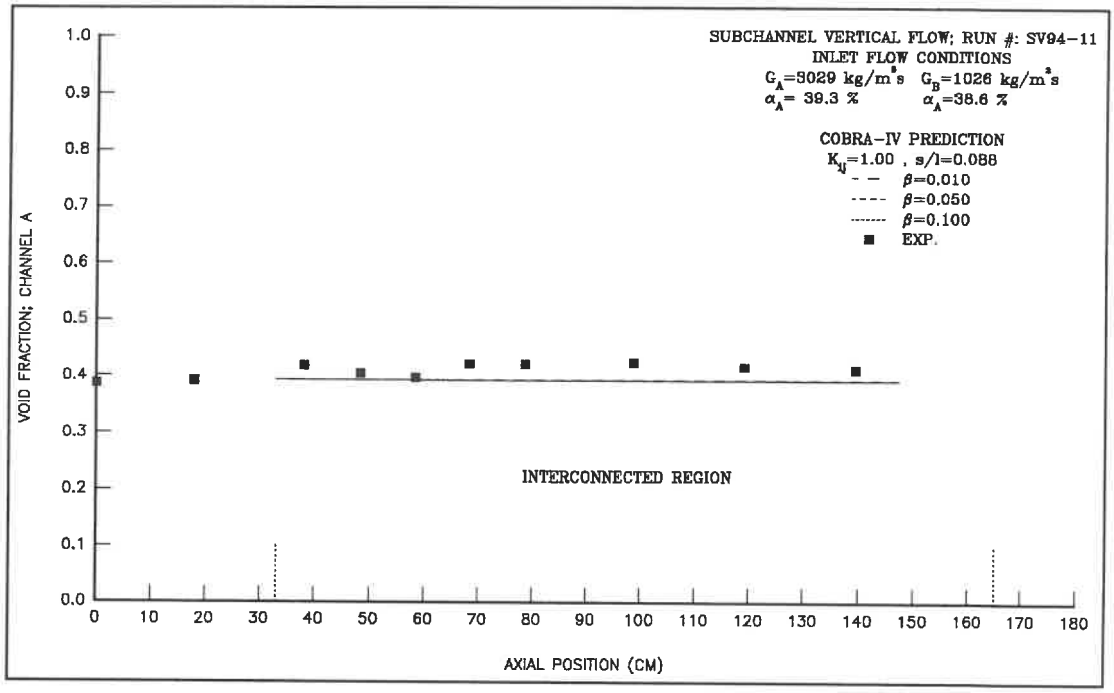


Figure 5.90: Void Fraction Profile, Run SV94-11, Channel A

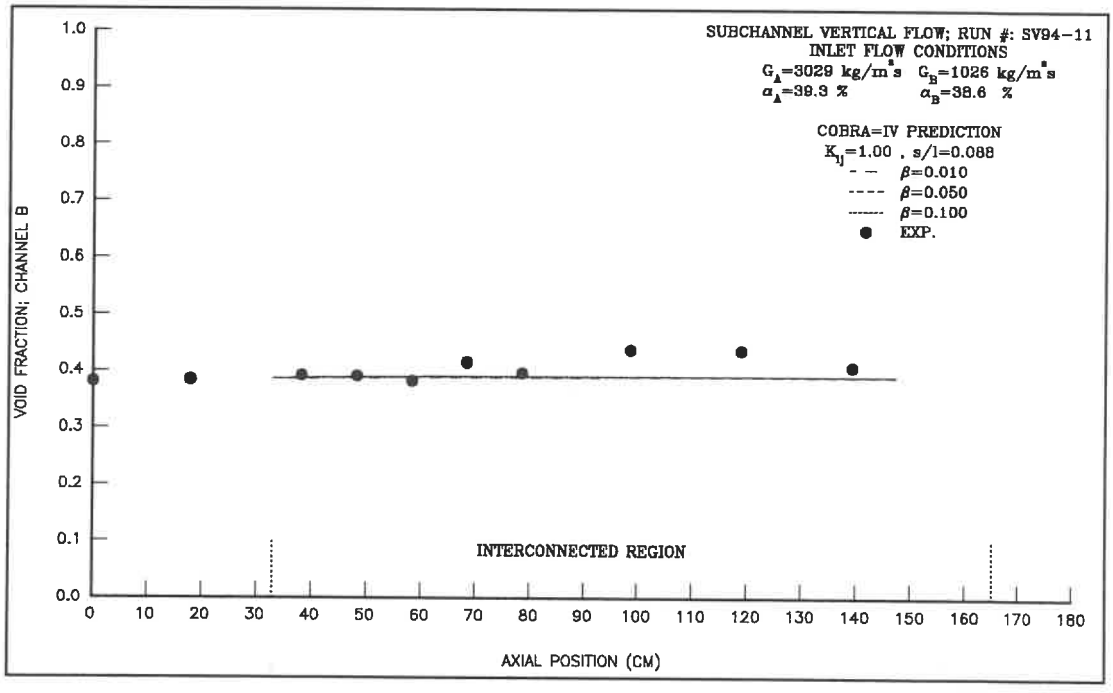


Figure 5.91: Void Fraction Profile, Run SV94-11, Channel B

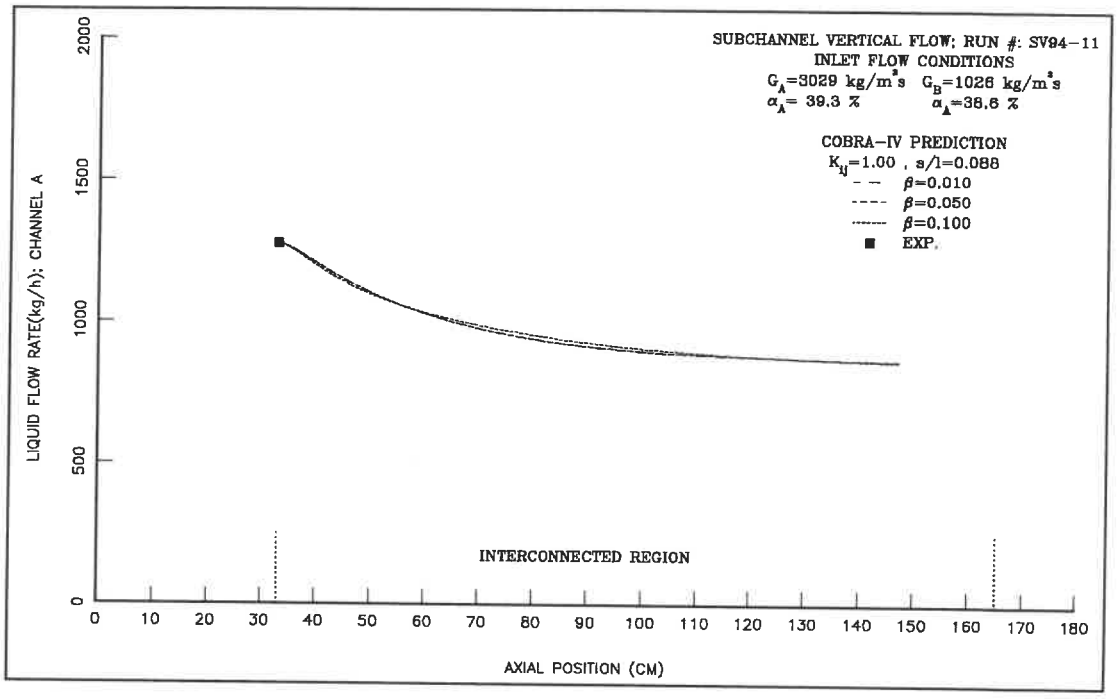


Figure 5.92: Mass Flow Rate Profile, Run SV94-11, Channel A

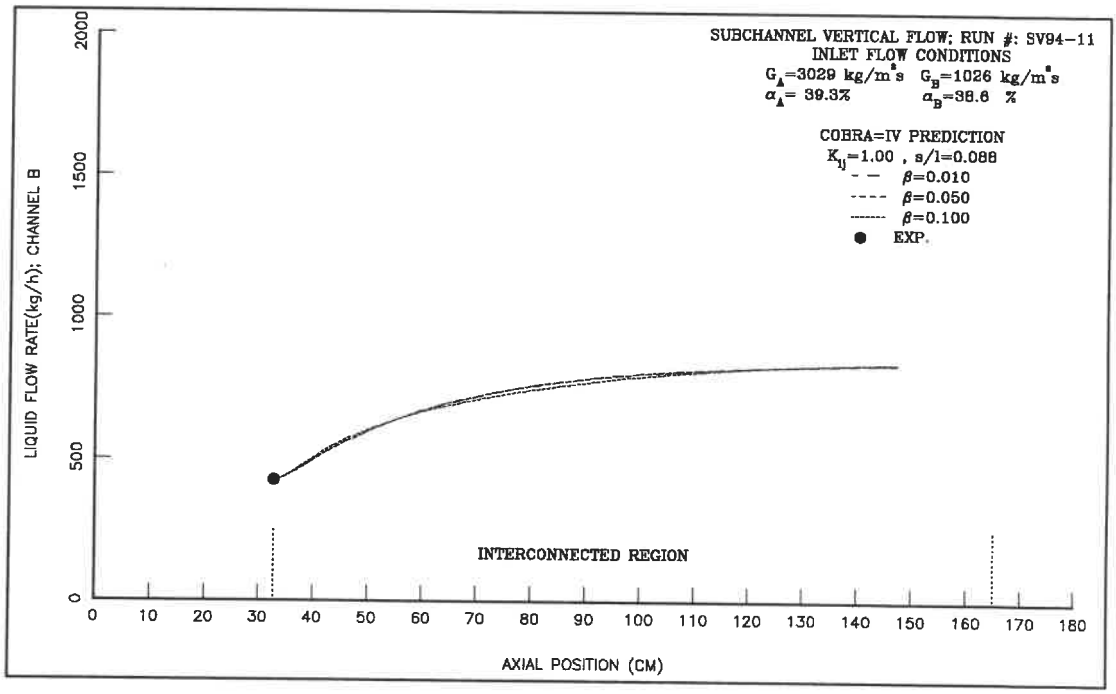


Figure 5.93: Mass Flow Rate Profile, Run SV94-11, Channel B

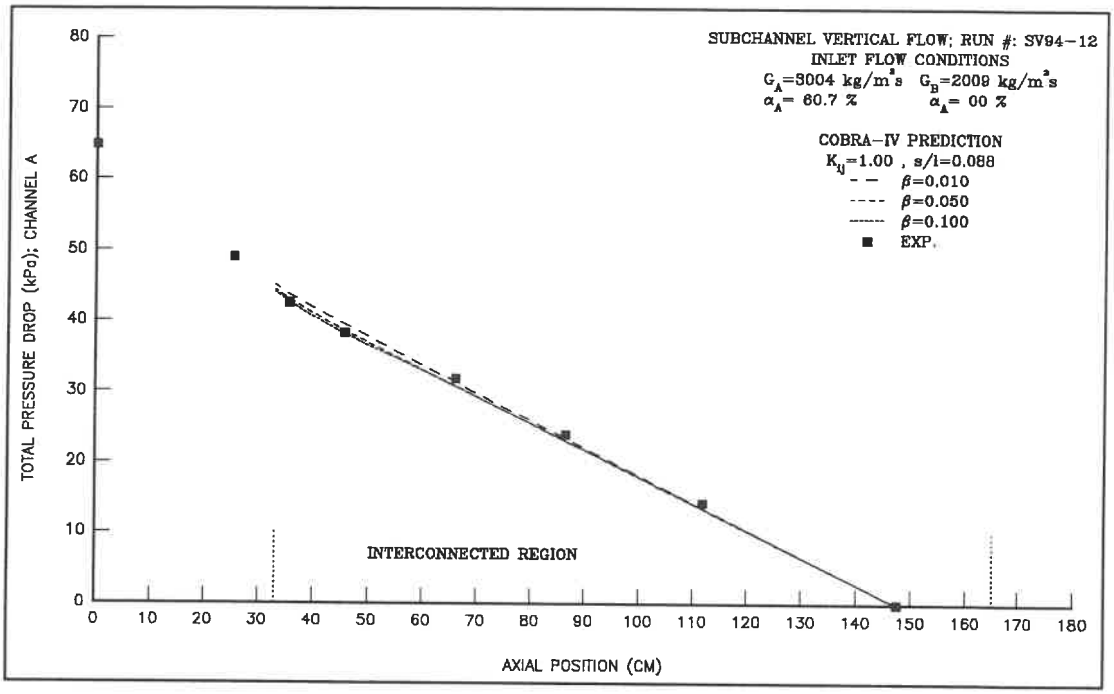


Figure 5.94: Total Pressure Drop Profile, Run SV94-12, Channel A

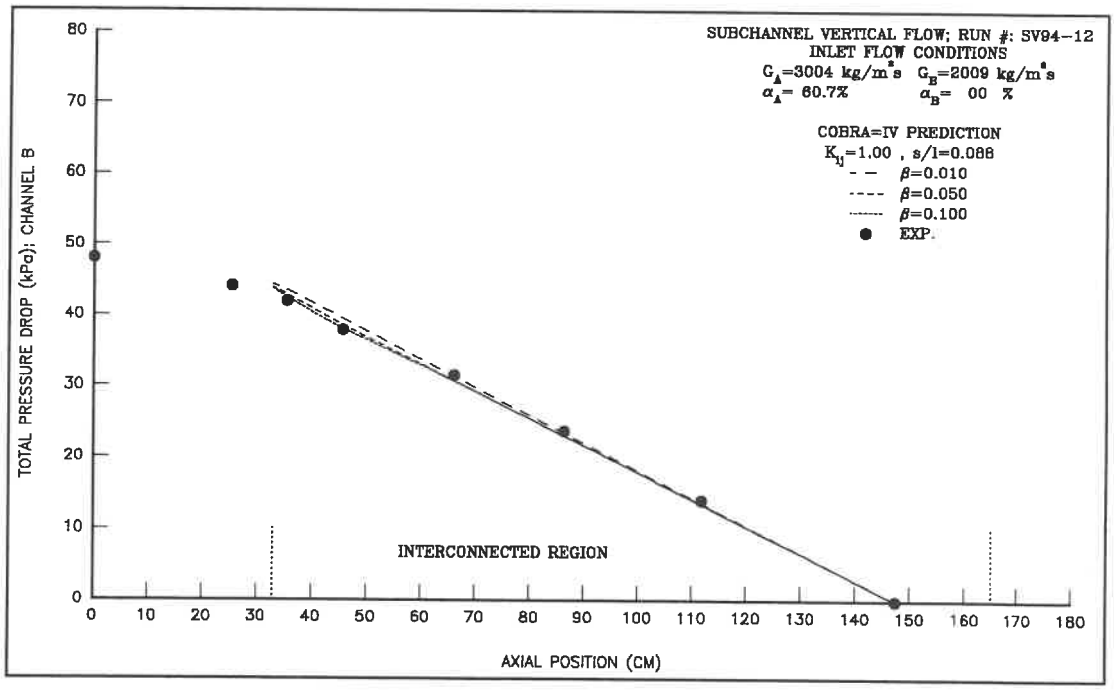


Figure 5.95: Total Pressure Drop Profile, Run SV94-12, Channel B

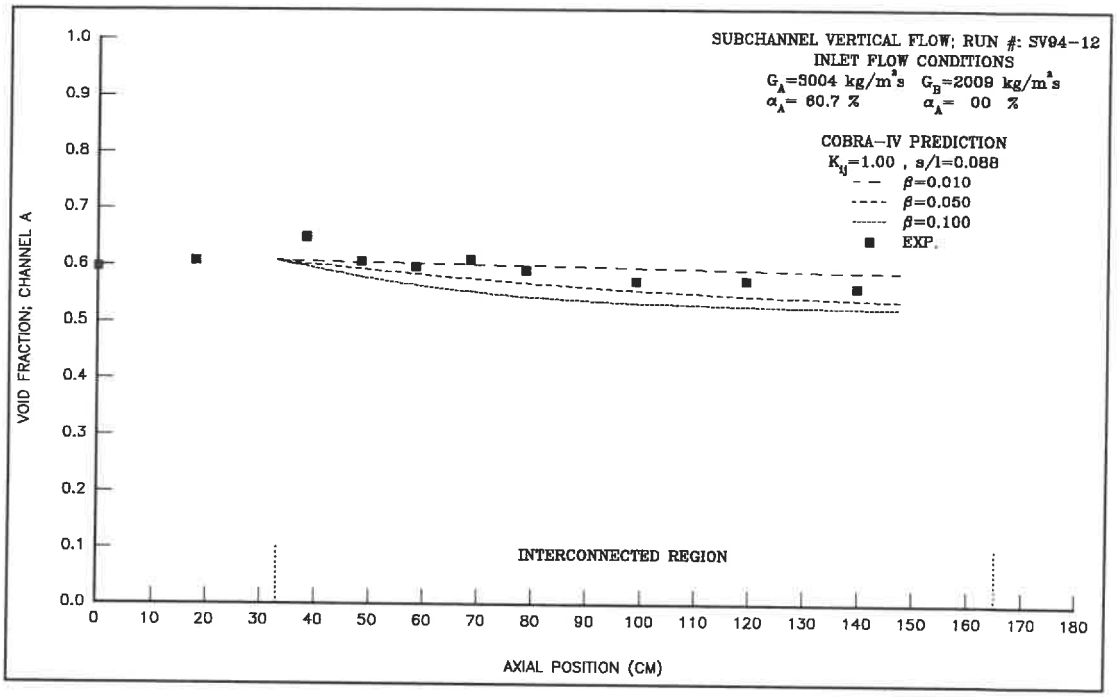


Figure 5.96: Void Fraction Profile, Run SV94-12, Channel A

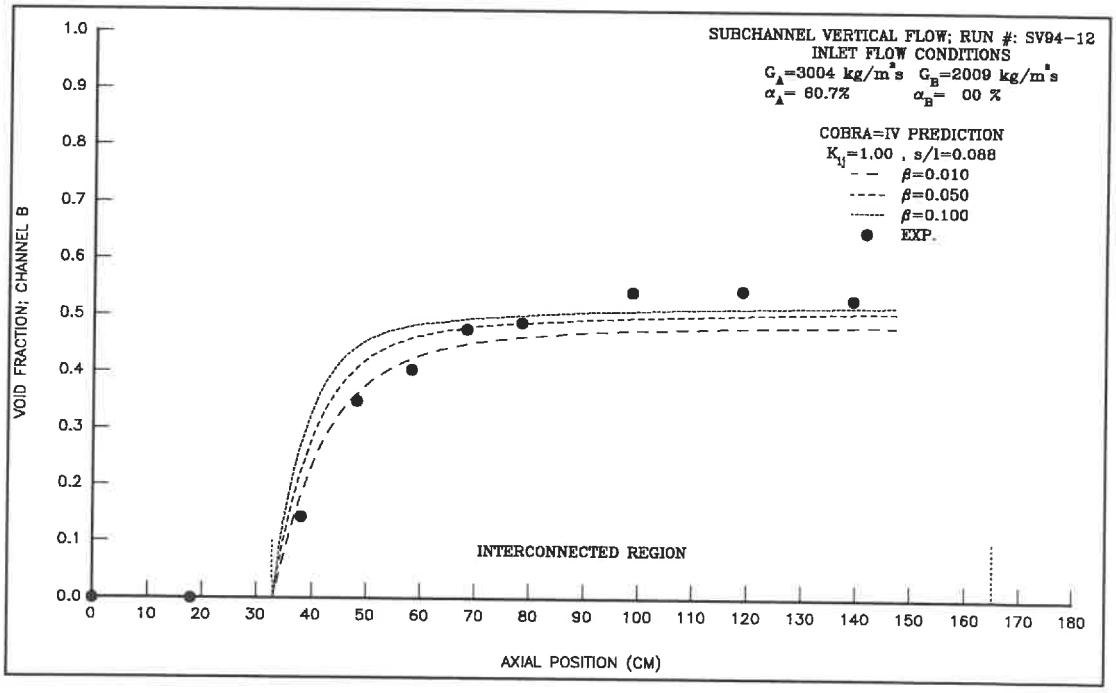


Figure 5.97: Void Fraction Profile, Run SV94-12, Channel B

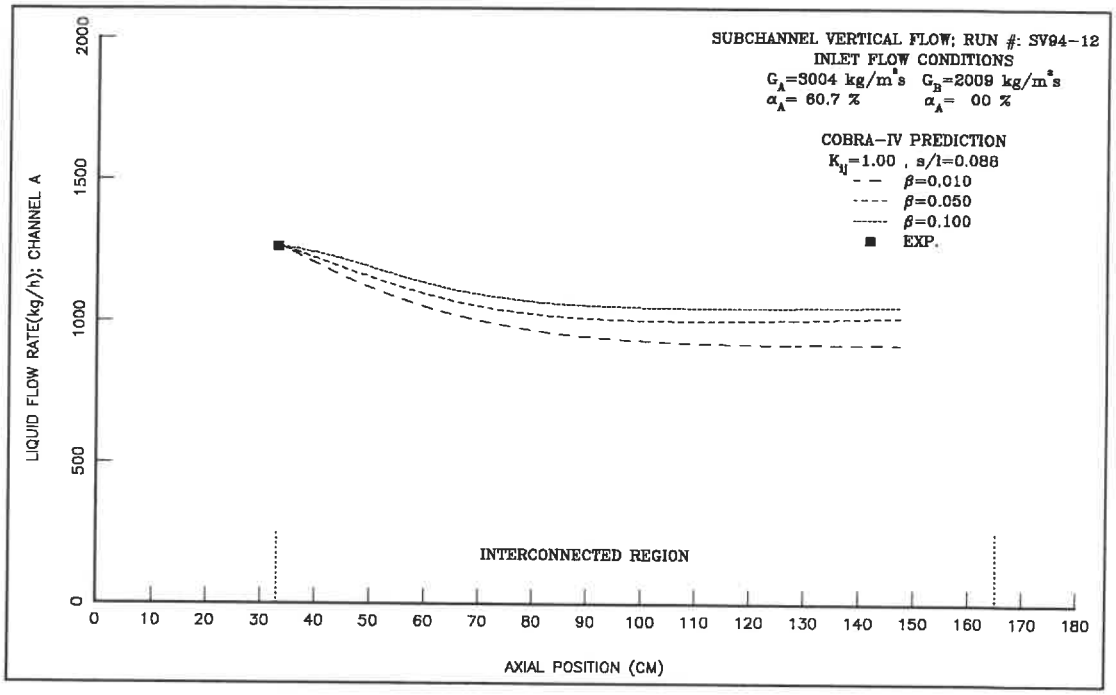


Figure 5.98: Mass Flow Rate Profile, Run SV94-12, Channel A

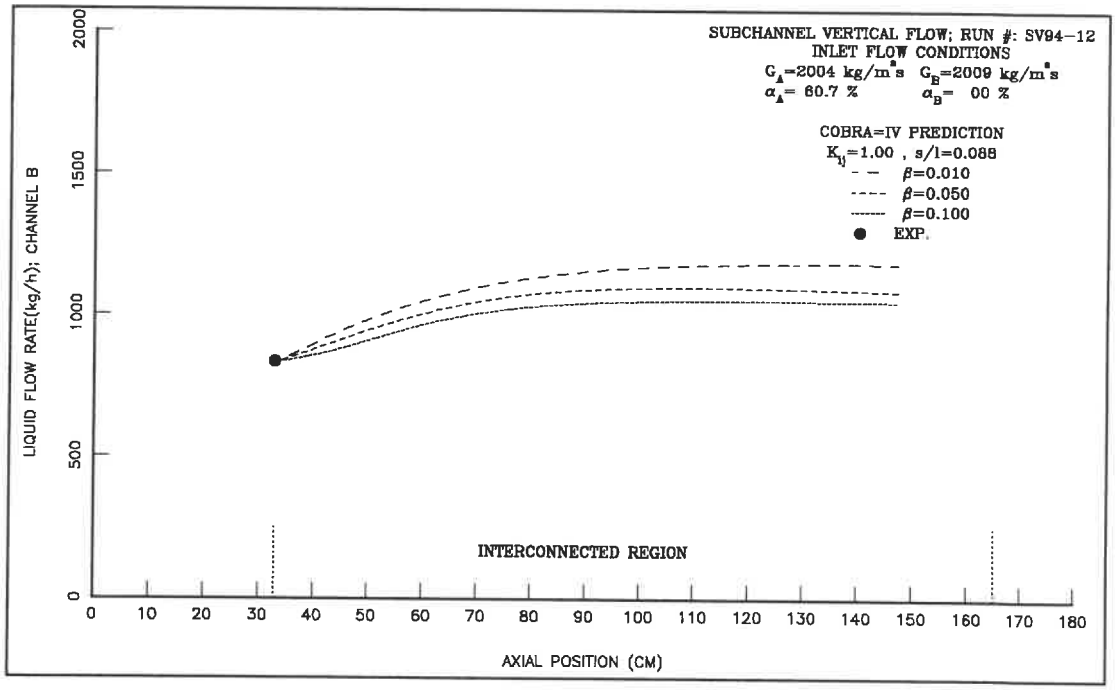


Figure 5.99: Mass Flow Rate Profile, Run SV94-12, Channel B

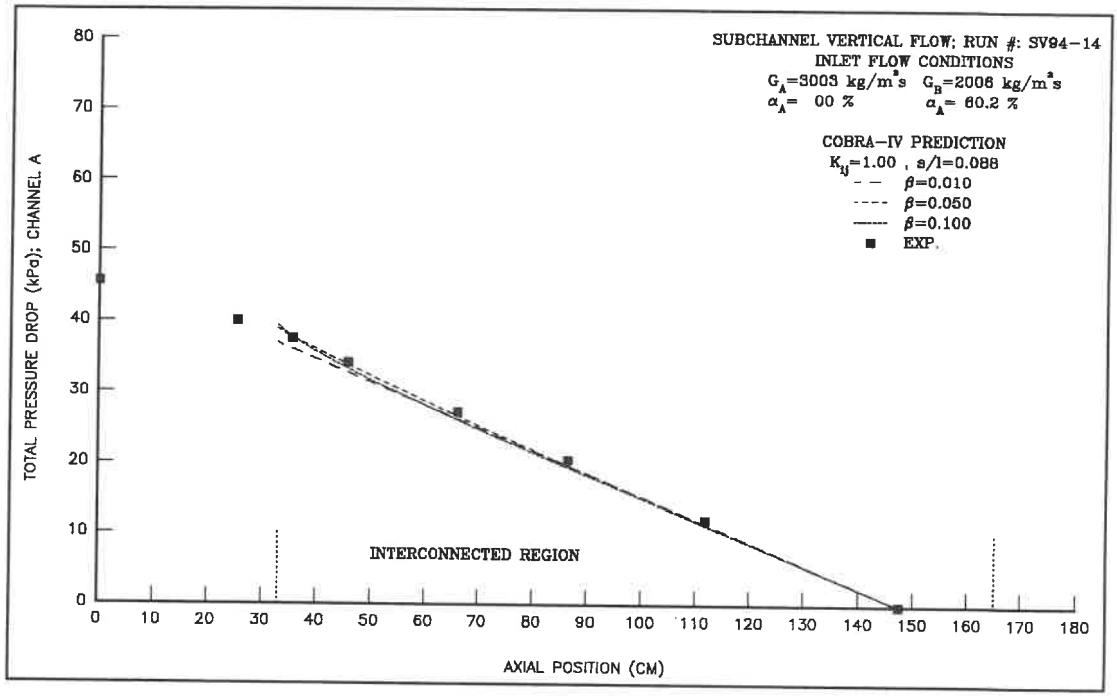


Figure 5.100: Total Pressure Drop Profile, Run SV94-14, Channel A

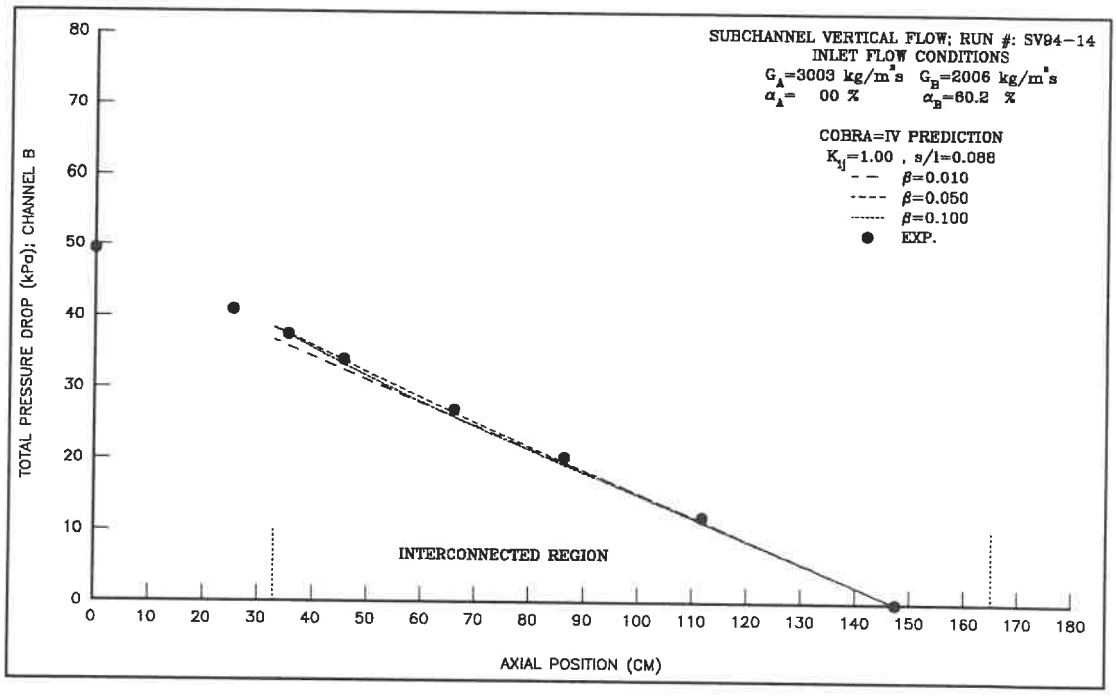


Figure 5.101: Total Pressure Drop Profile, Run SV94-14, Channel B

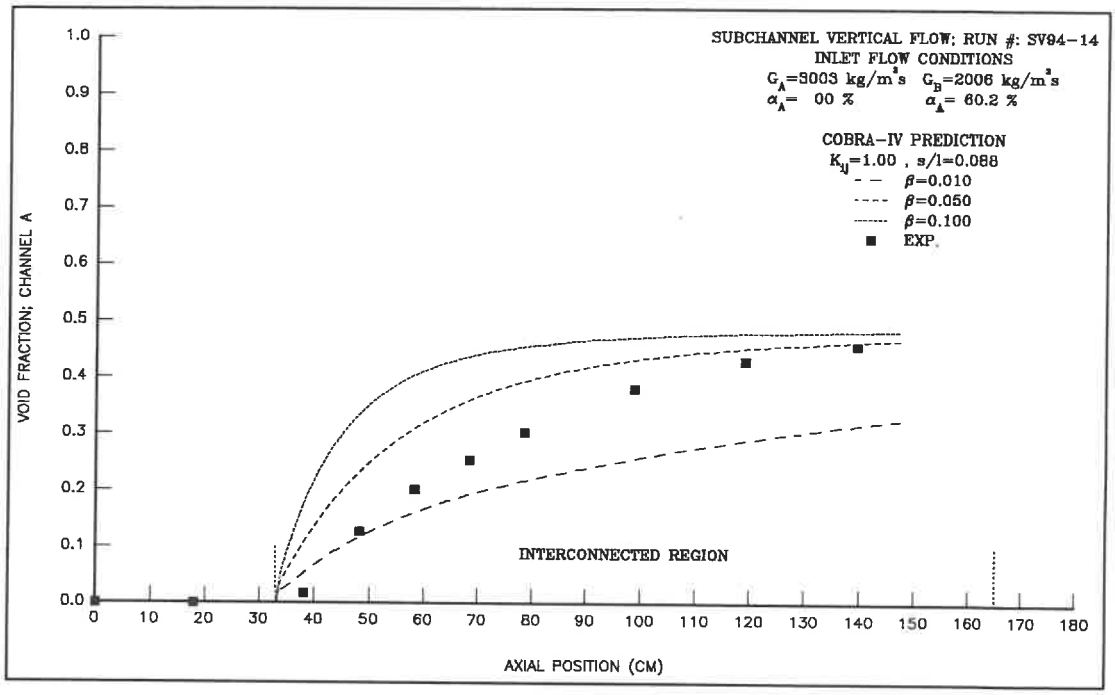


Figure 5.102: Void Fraction Profile, Run SV94-14, Channel A

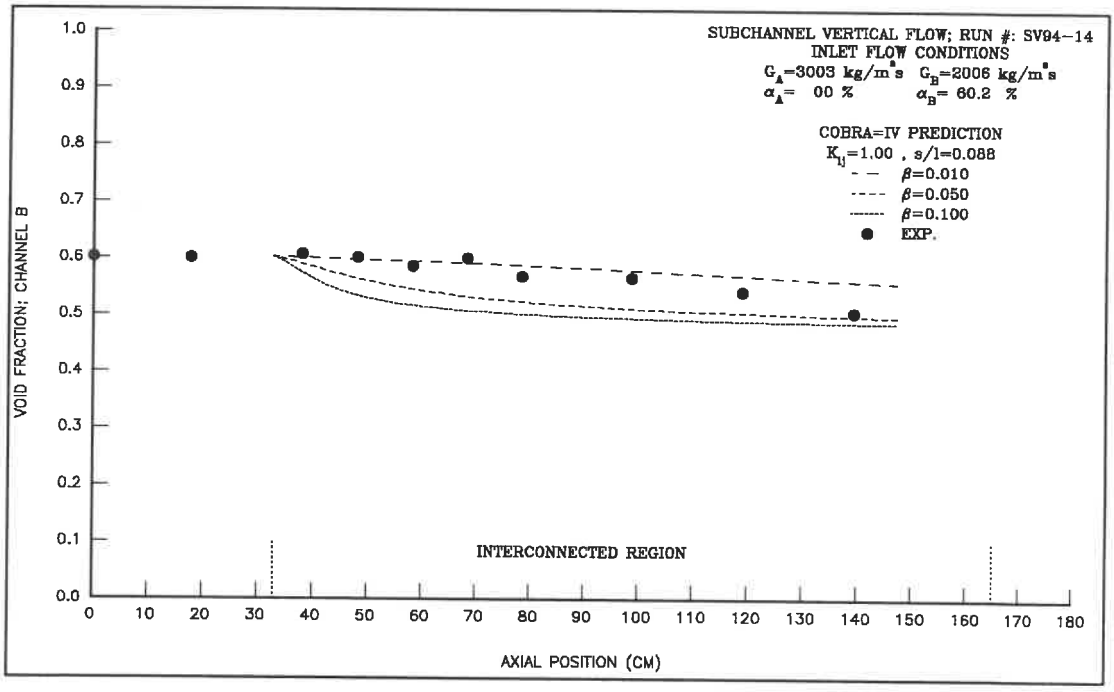


Figure 5.103: Void Fraction Profile, Run SV94-14, Channel B

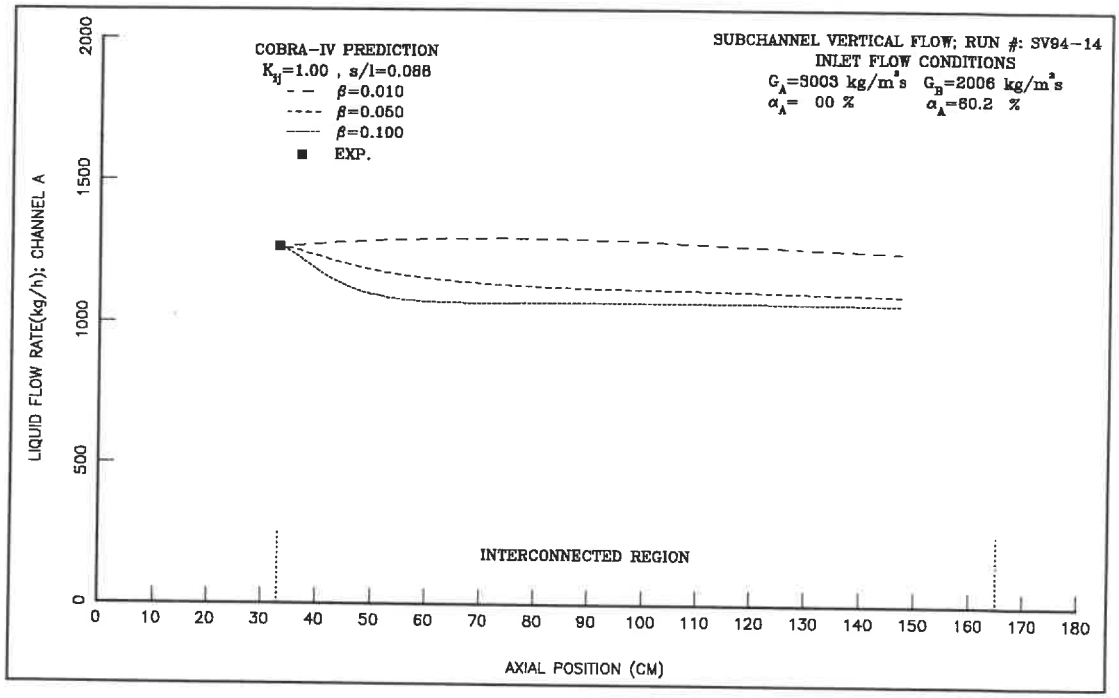


Figure 5.104: Mass Flow Rate Profile, Run SV94-14, Channel A

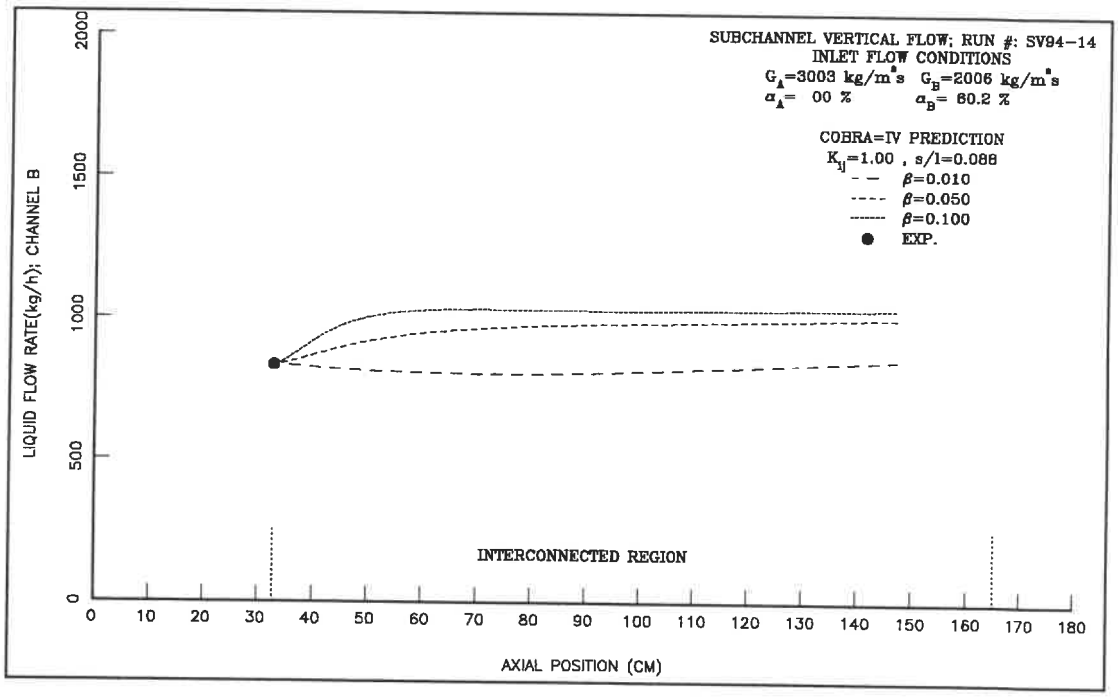


Figure 5.105: Mass Flow Rate Profile, Run SV94-14, Channel B

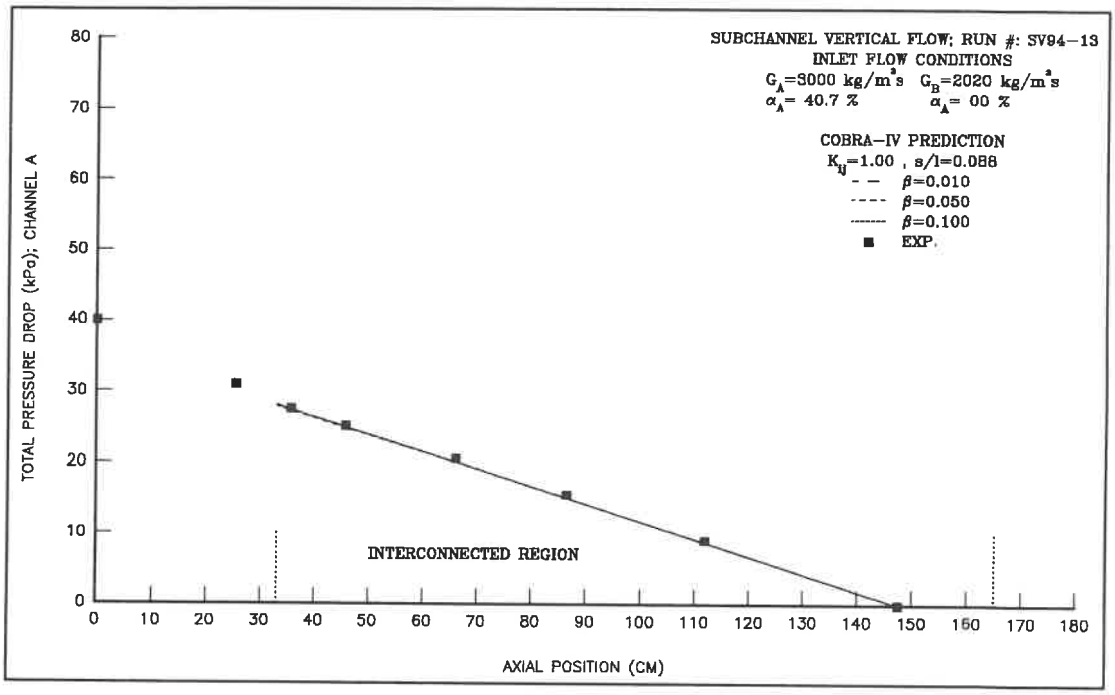


Figure 5.106: Total Pressure Drop Profile, Run SV94-13, Channel A

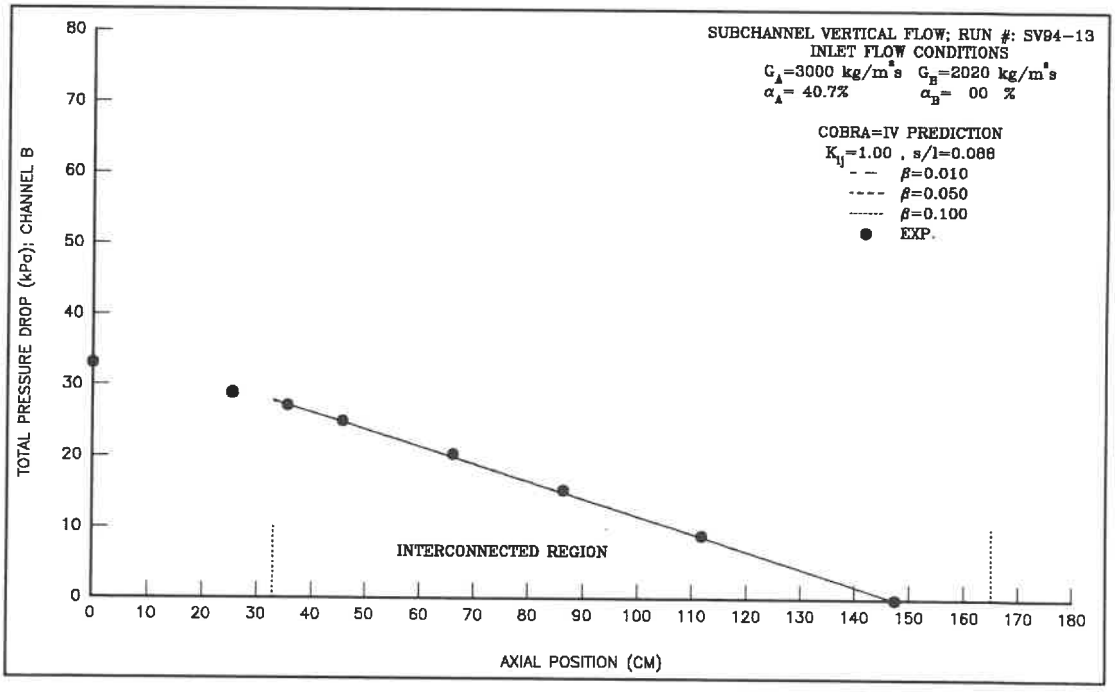


Figure 5.107: Total Pressure Drop Profile, Run SV94-13, Channel B

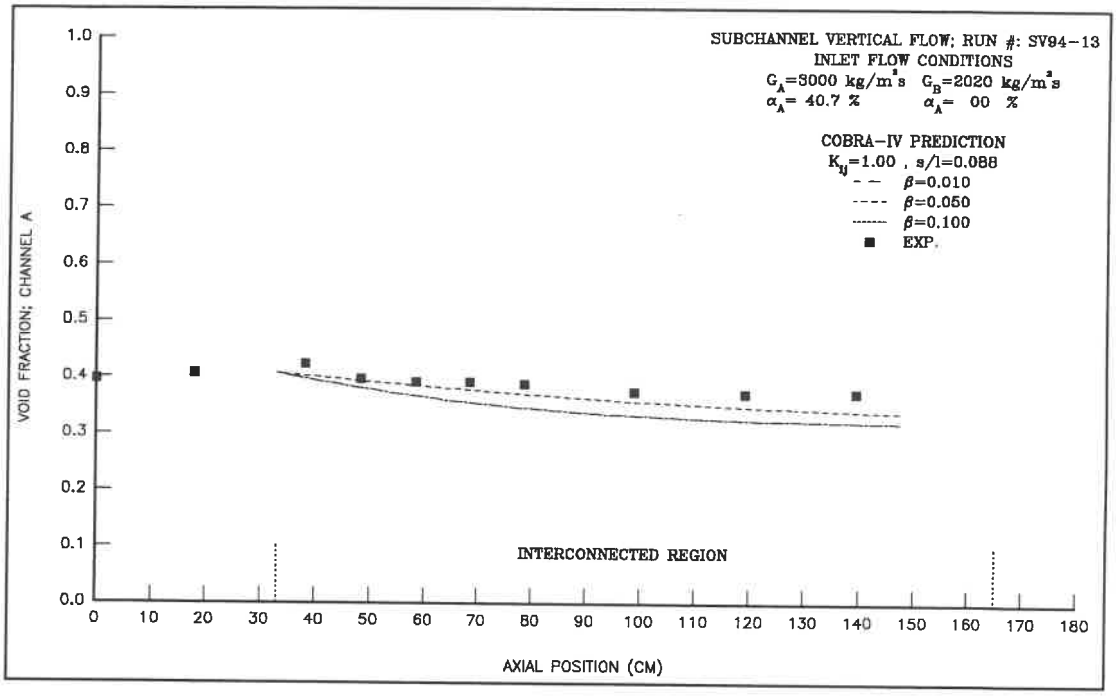


Figure 5.108: Void Fraction Profile, Run SV94-13, Channel A

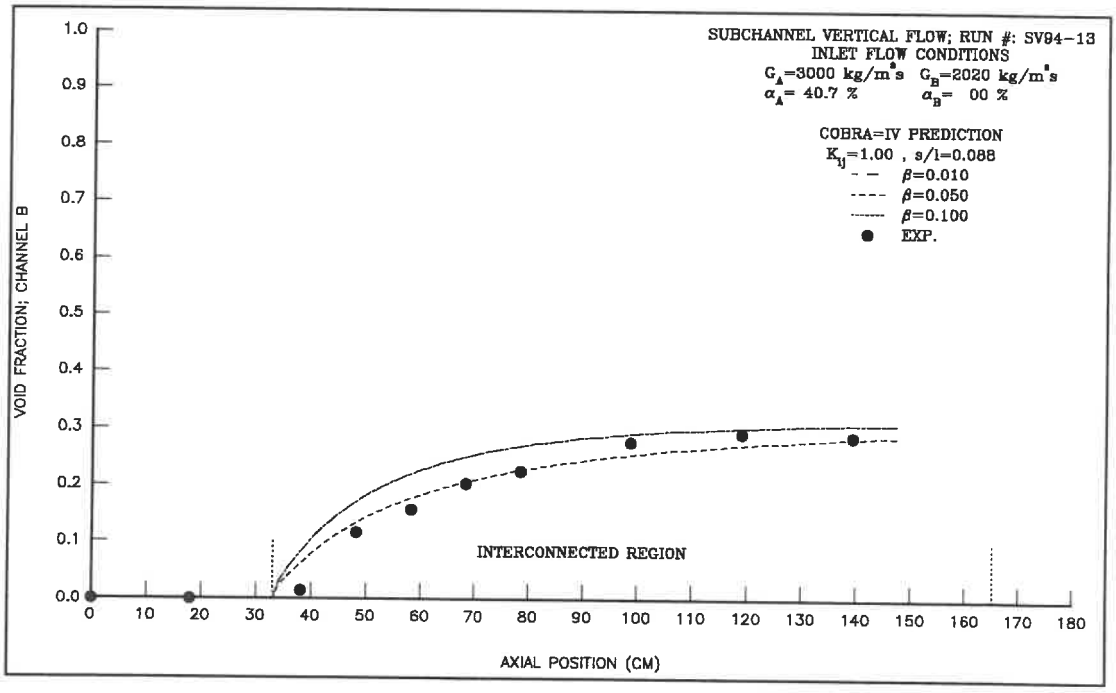


Figure 5.109: Void Fraction Profile, Run SV94-13, Channel B

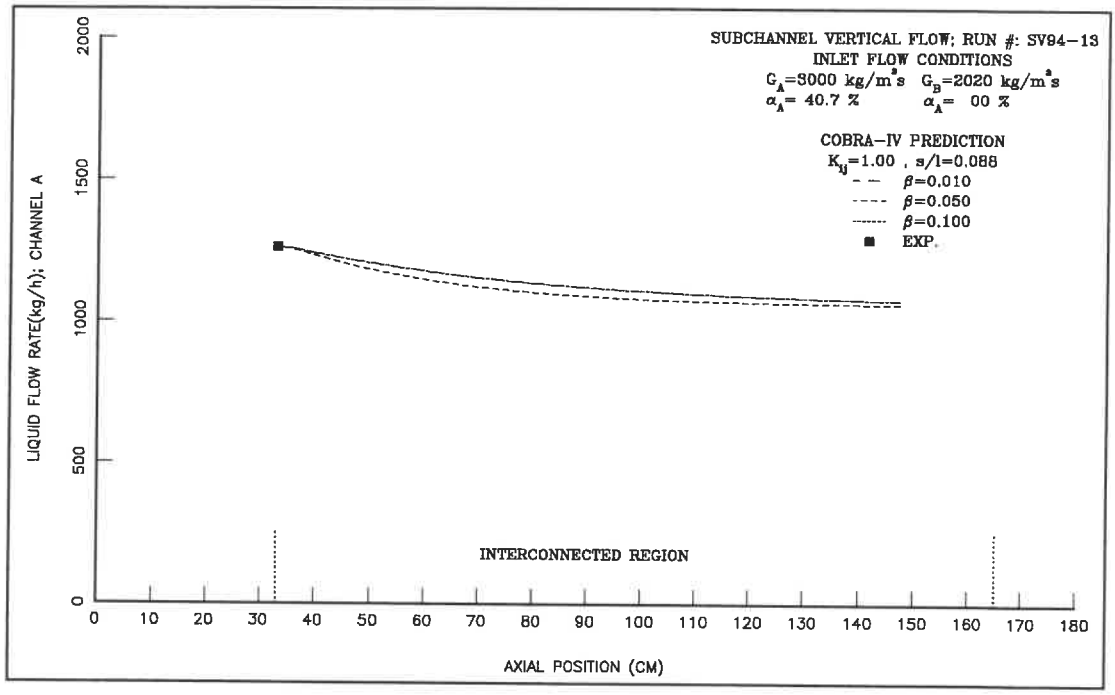


Figure 5.110: Mass Flow Rate Profile, Run SV94-13, Channel A

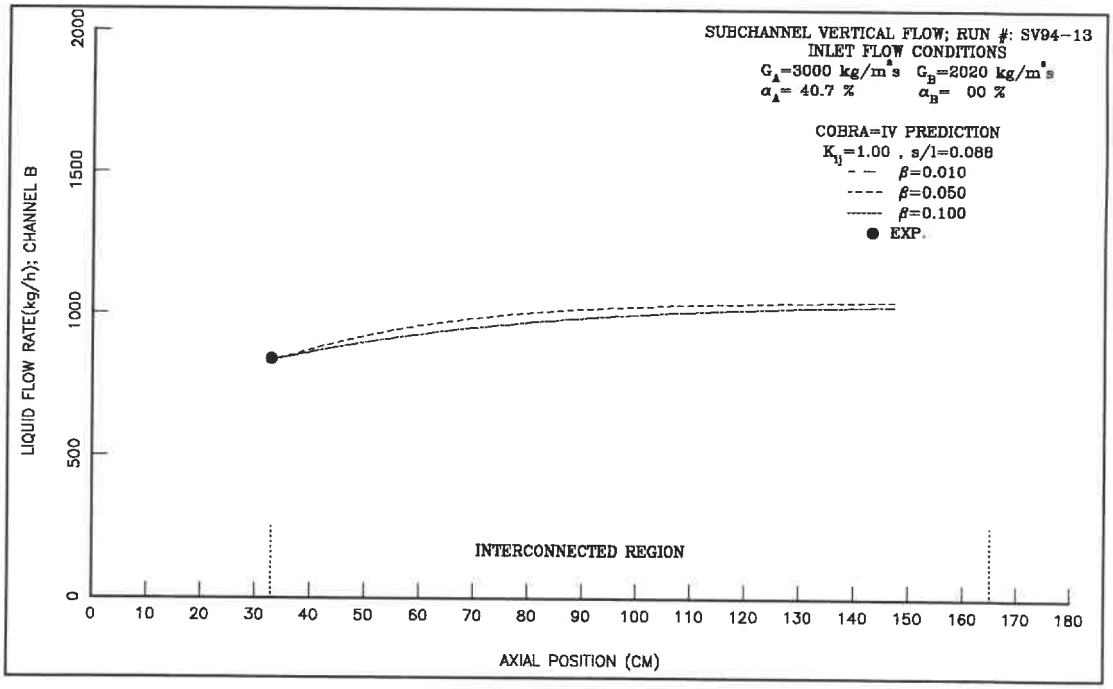


Figure 5.111: Mass Flow Rate Profile, Run SV94-13, Channel B

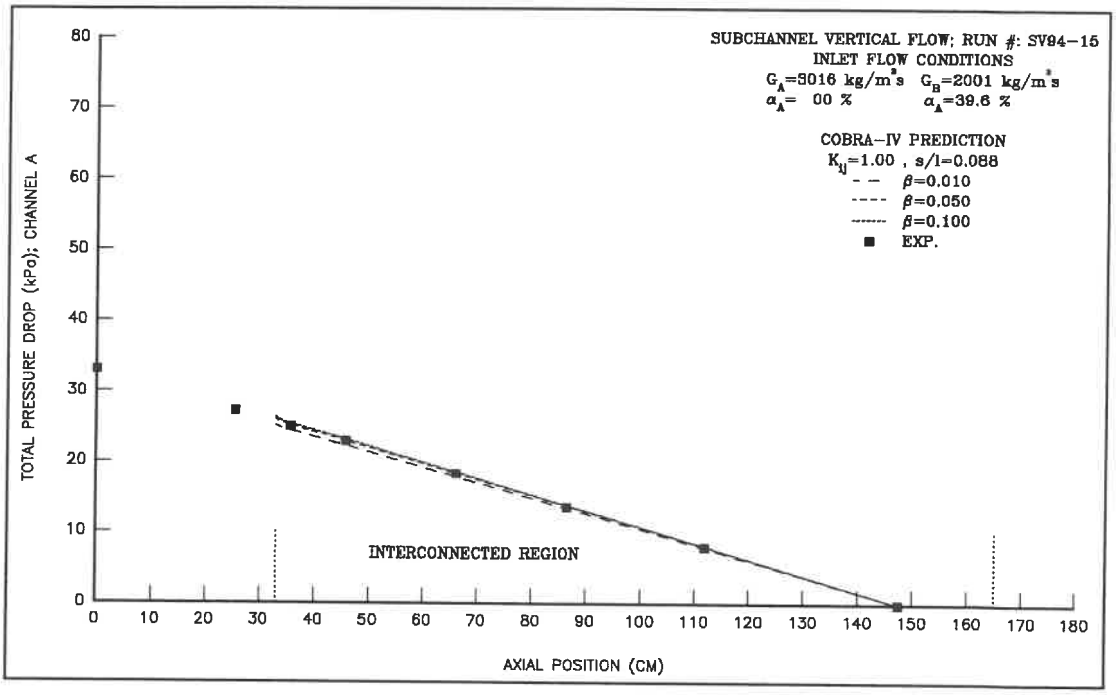


Figure 5.112: Total Pressure Drop Profile, Run SV94-15, Channel A

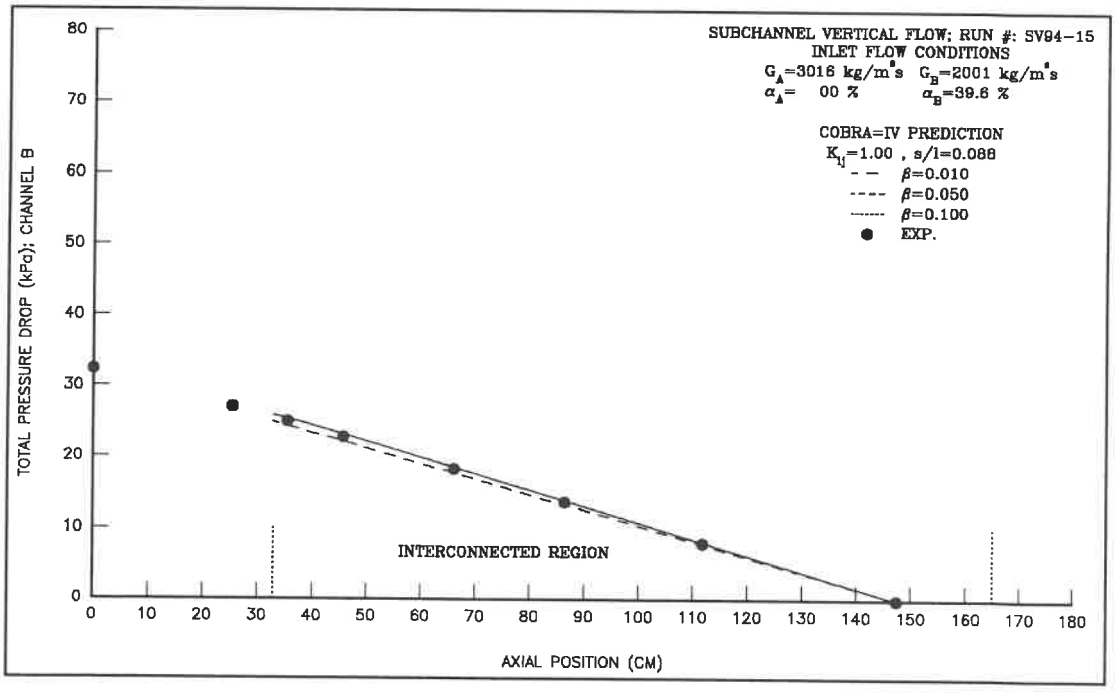


Figure 5.113: Total Pressure Drop Profile, Run SV94-15, Channel B

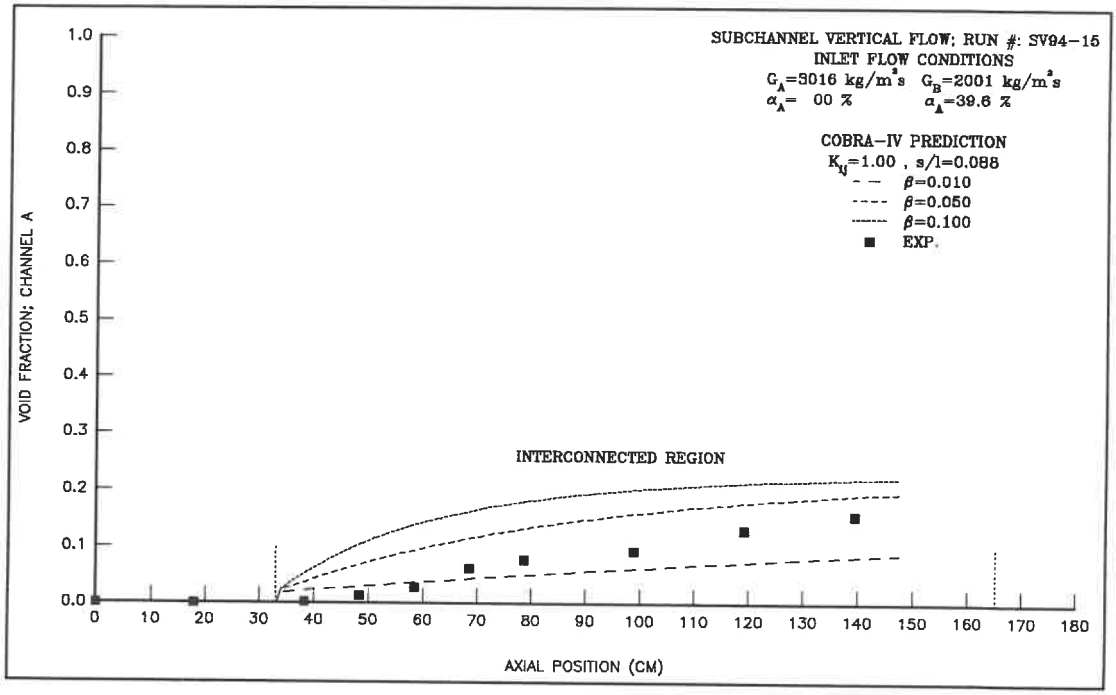


Figure 5.114: Void Fraction Profile, Run SV94-15, Channel A

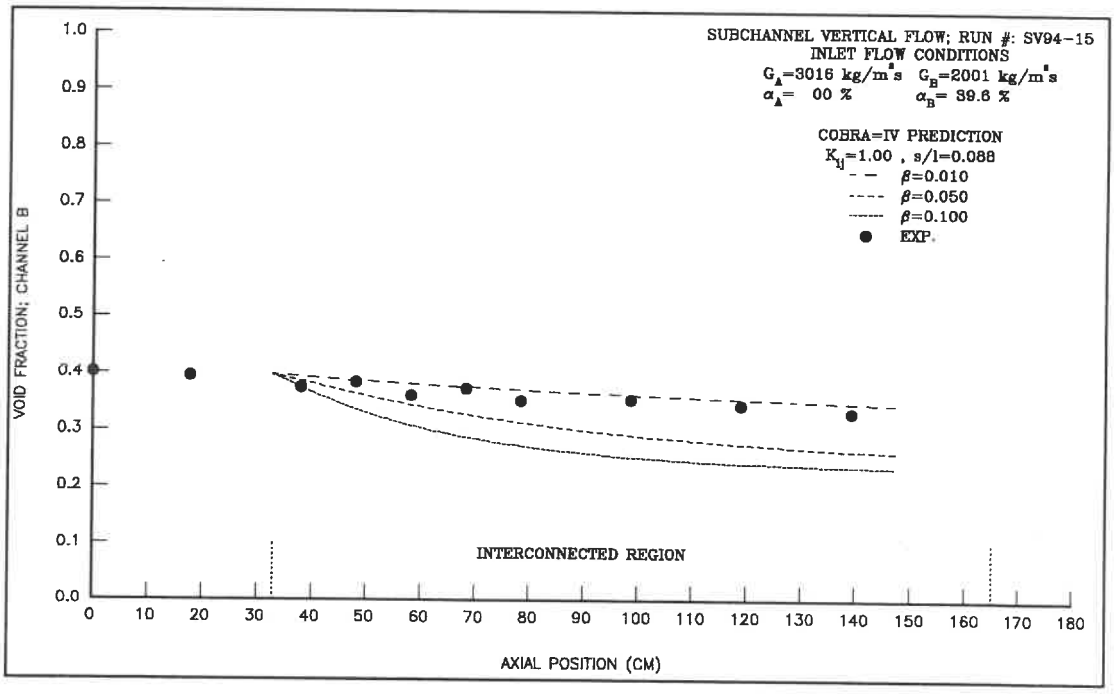


Figure 5.115: Void Fraction Profile, Run SV94-15, Channel B

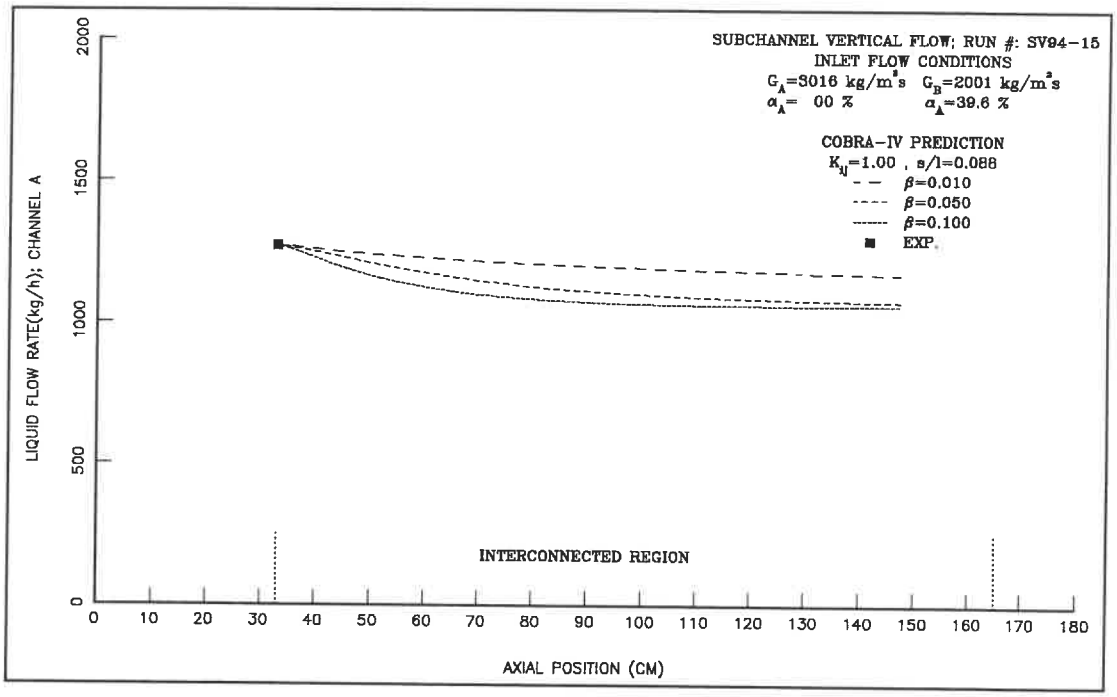


Figure 5.116: Mass Flow Rate Profile, Run SV94-15, Channel A

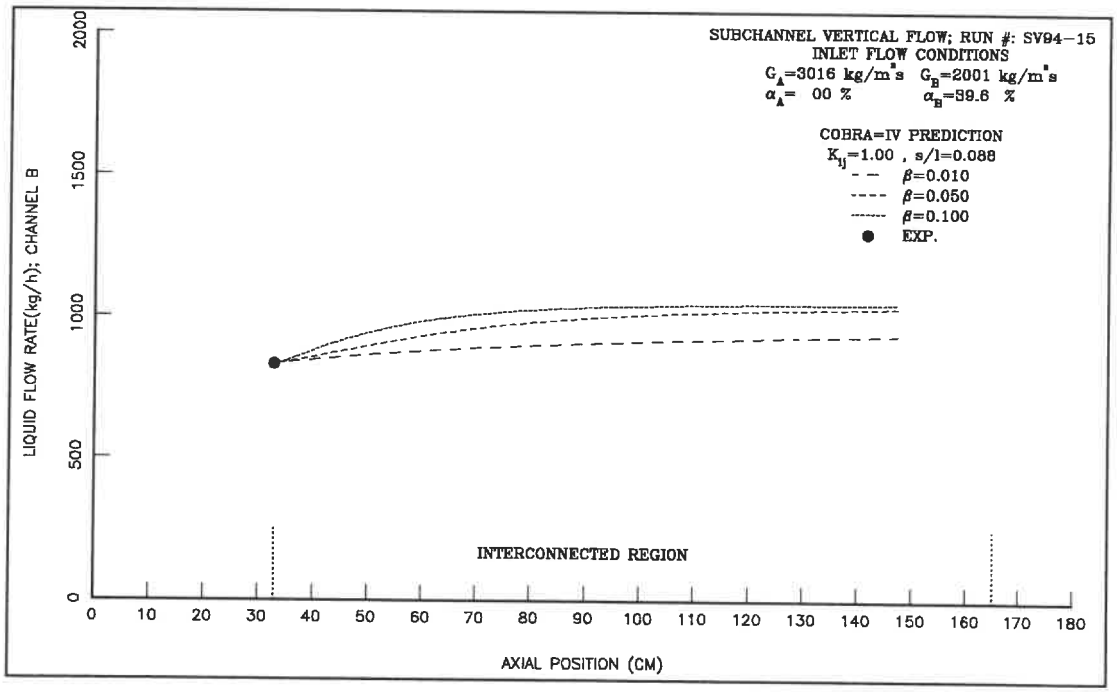


Figure 5.117: Mass Flow Rate Profile, Run SV94-15, Channel B

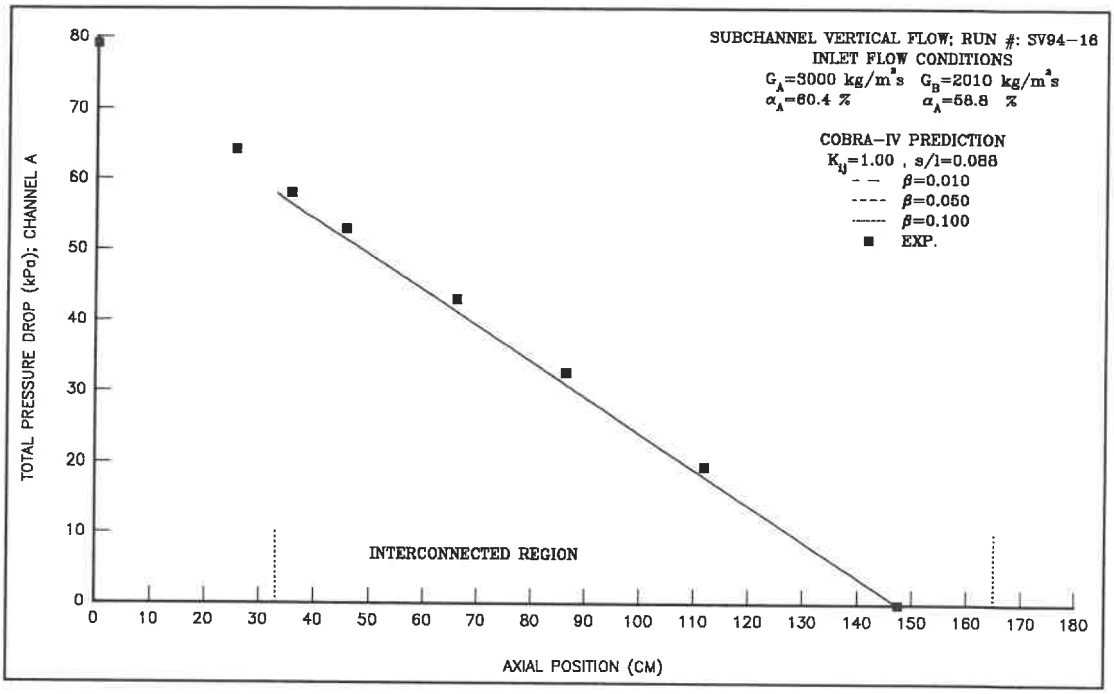


Figure 5.118: Total Pressure Drop Profile, Run SV94-16, Channel A

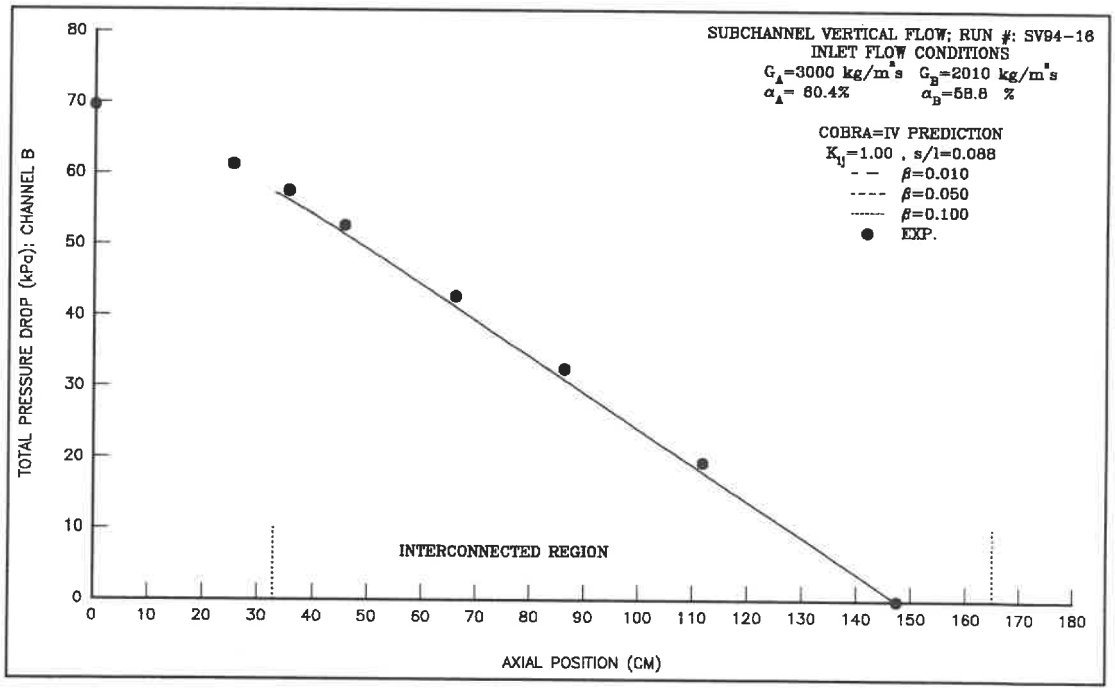


Figure 5.119: Total Pressure Drop Profile, Run SV94-16, Channel B

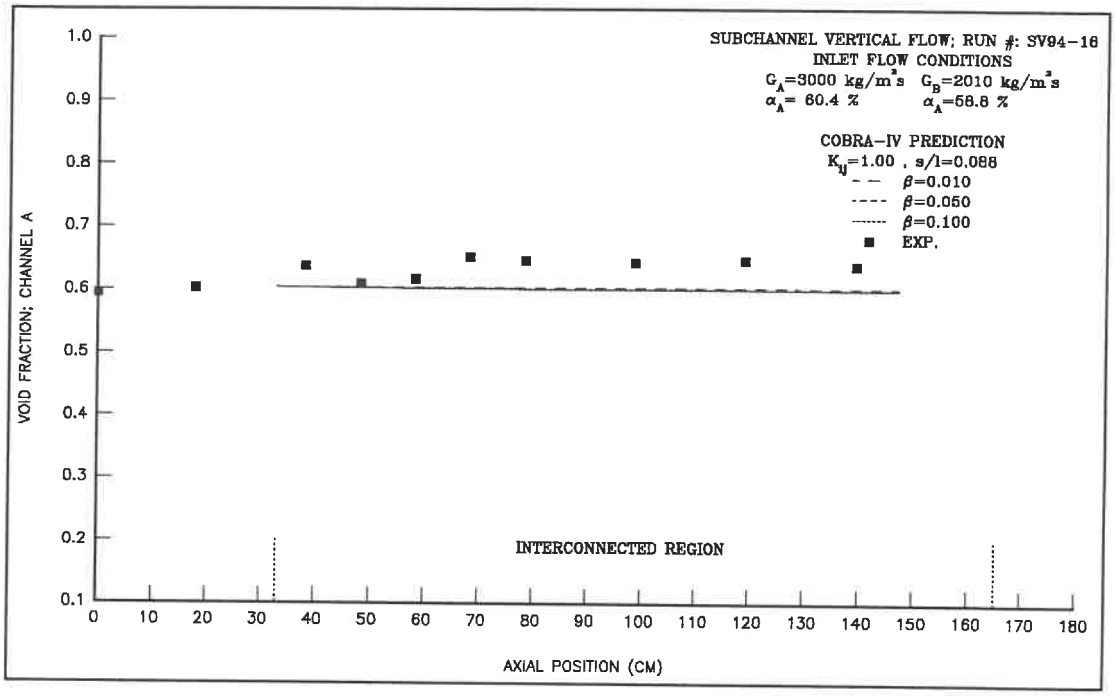


Figure 5.120: Void Fraction Profile, Run SV94-16, Channel A

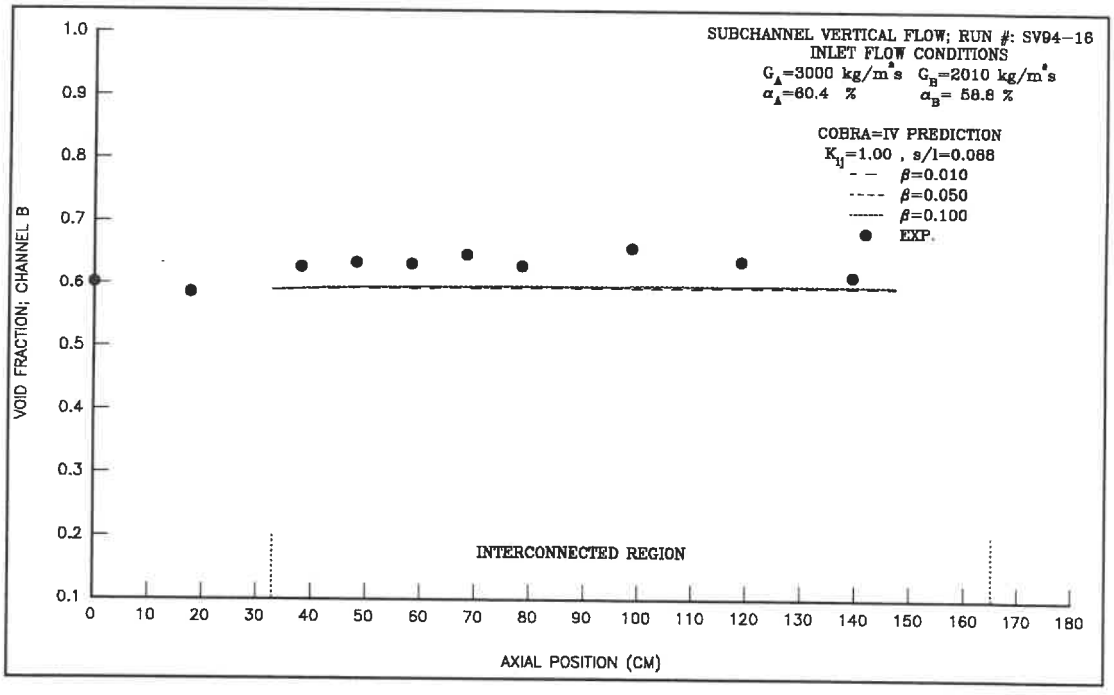


Figure 5.121: Void Fraction Profile, Run SV94-16, Channel B

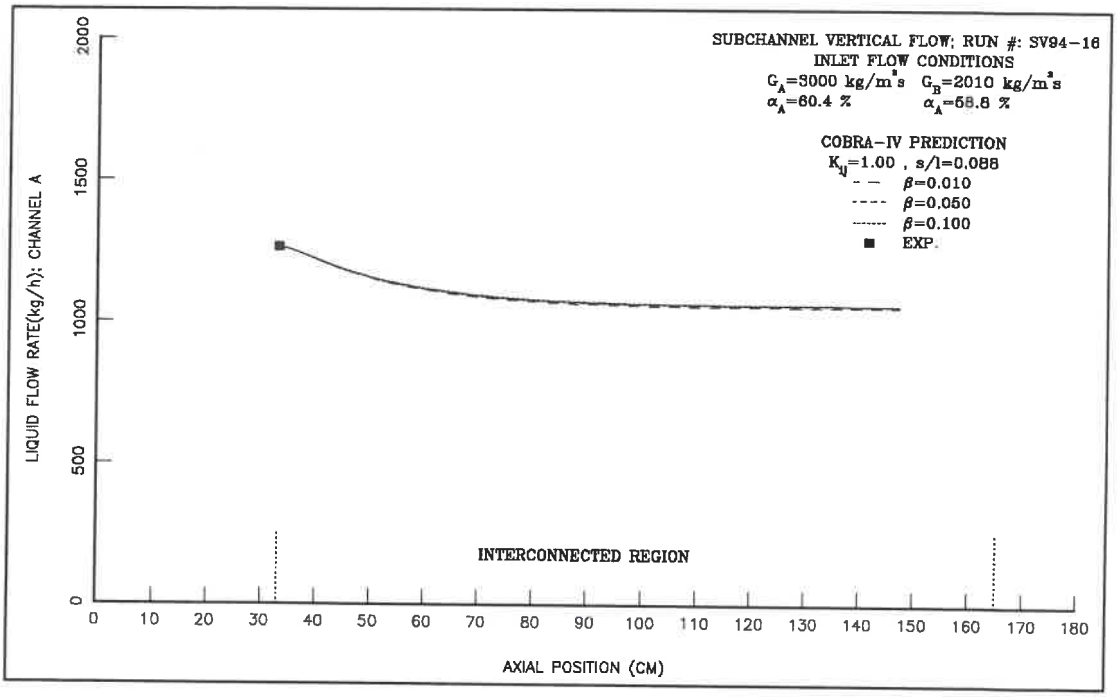


Figure 5.122: Mass Flow Rate Profile, Run SV94-16, Channel A

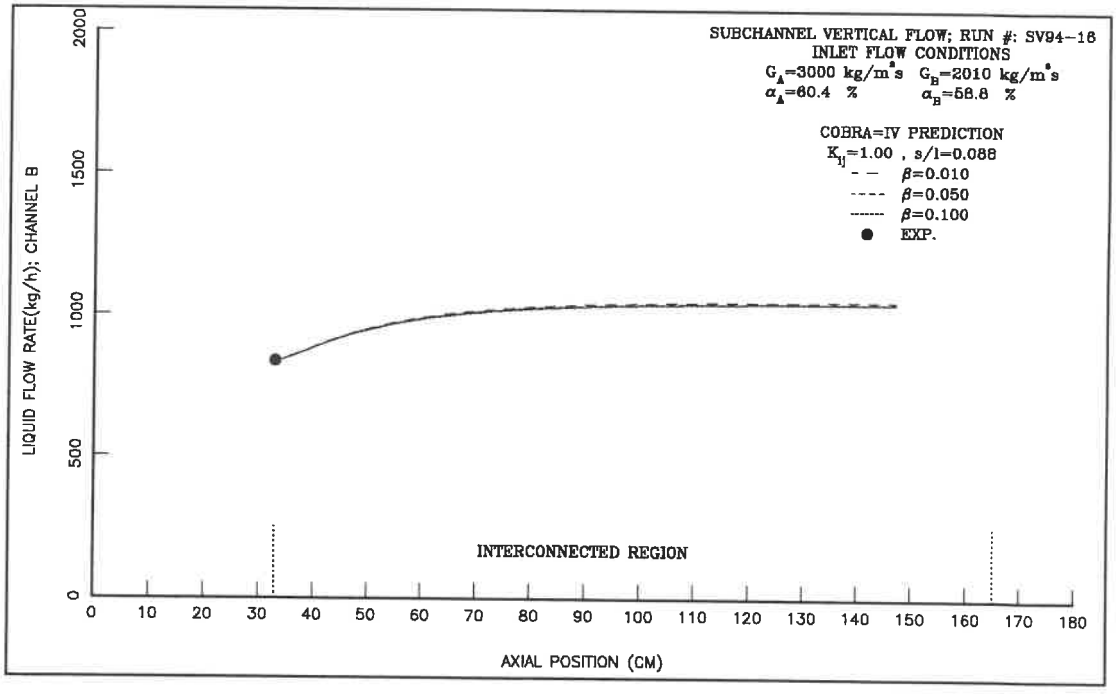


Figure 5.123: Mass Flow Rate Profile, Run SV94-16, Channel B

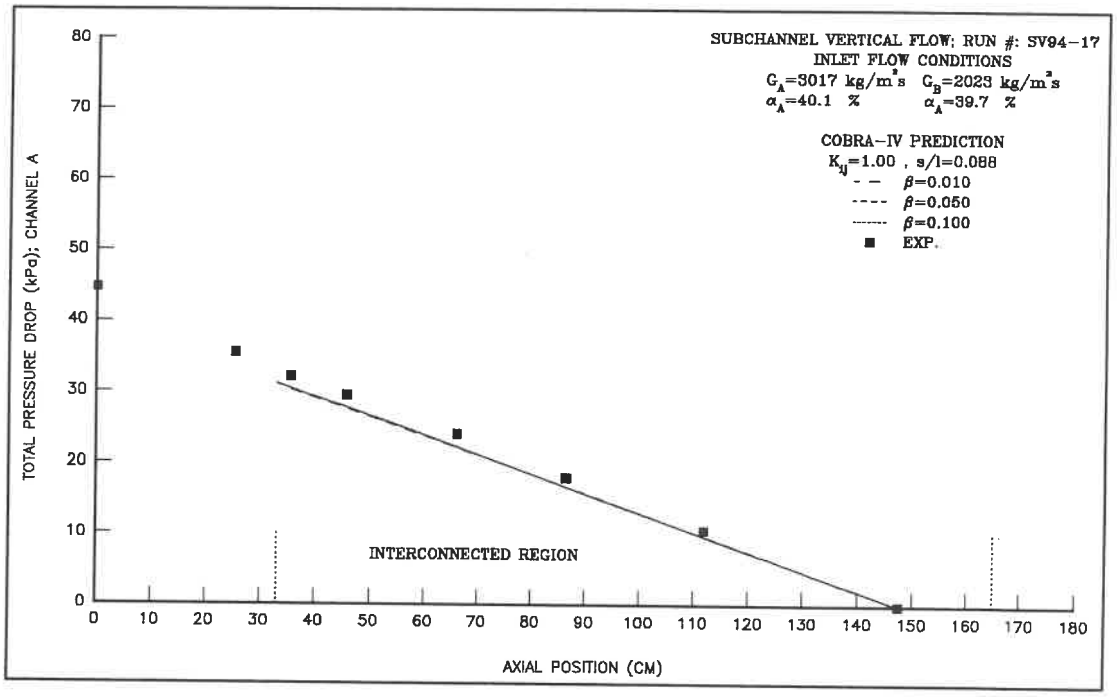


Figure 5.124: Total Pressure Drop Profile, Run SV94-17, Channel A

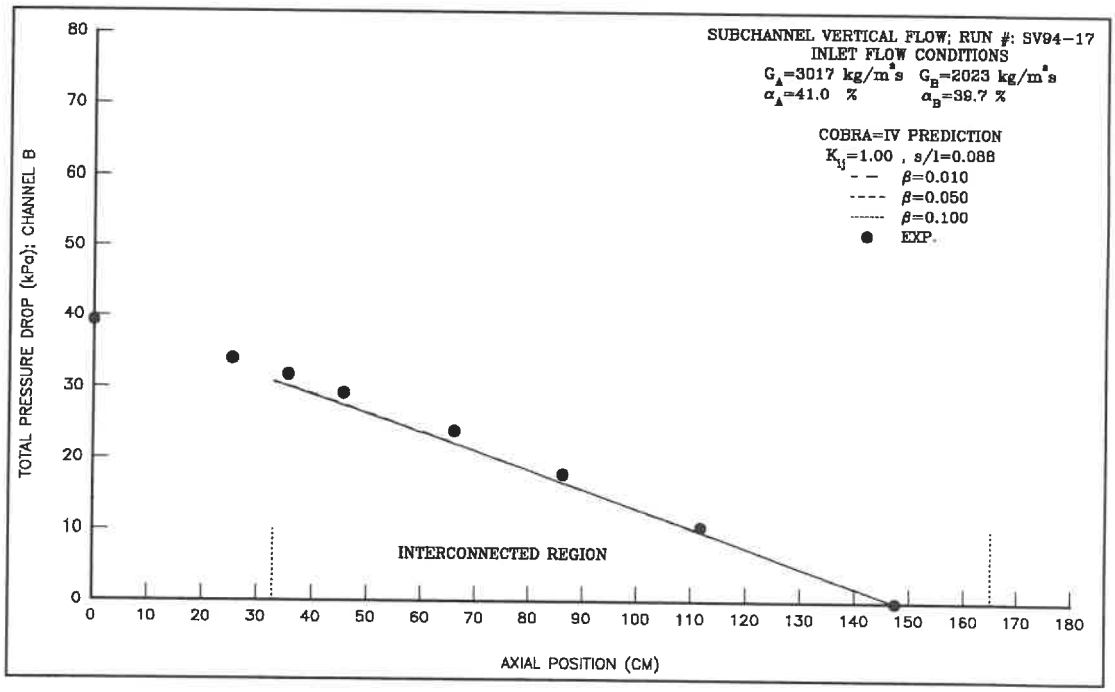


Figure 5.125: Total Pressure Drop Profile, Run SV94-17, Channel B

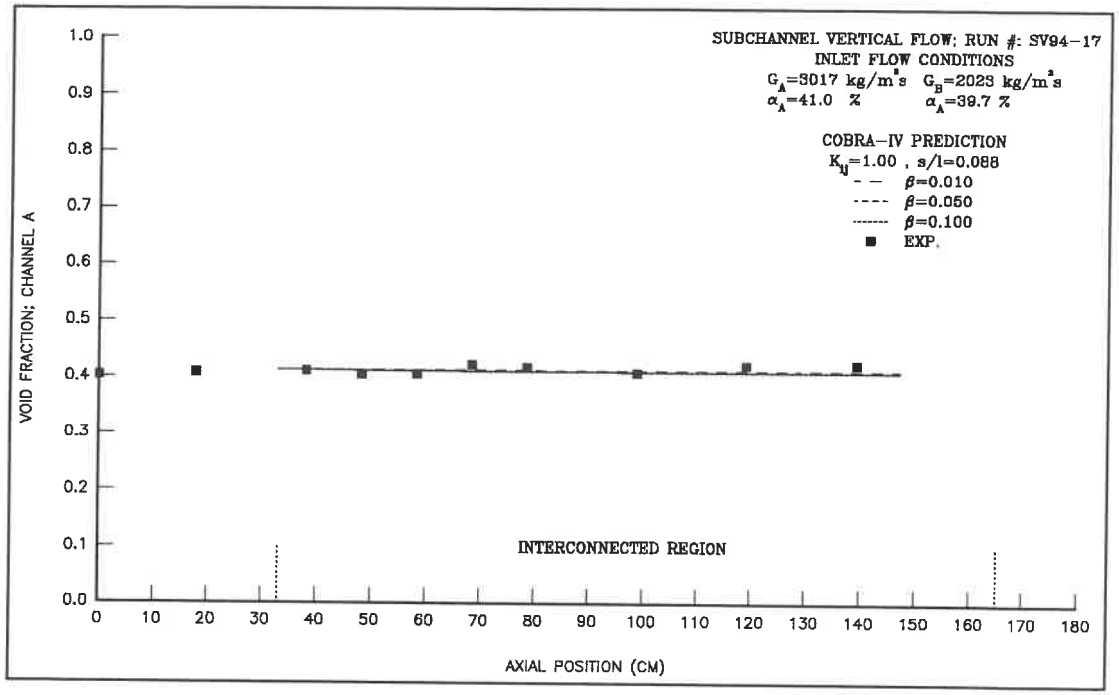


Figure 5.126: Void Fraction Profile, Run SV94-17, Channel A

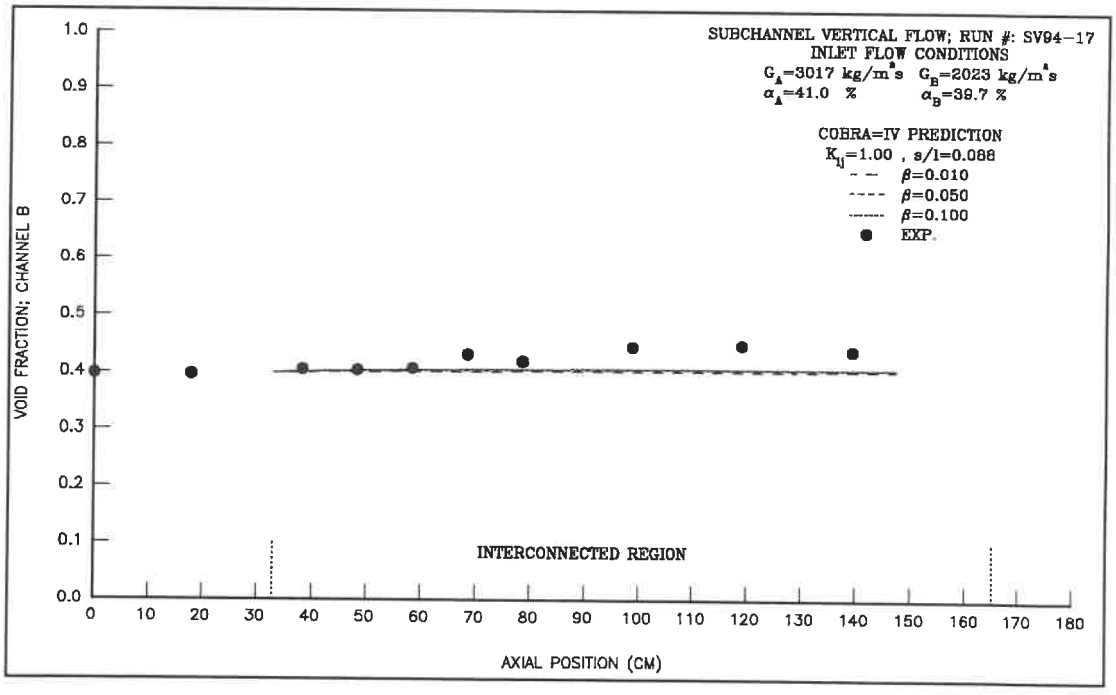


Figure 5.127: Void Fraction Profile, Run SV94-17, Channel B

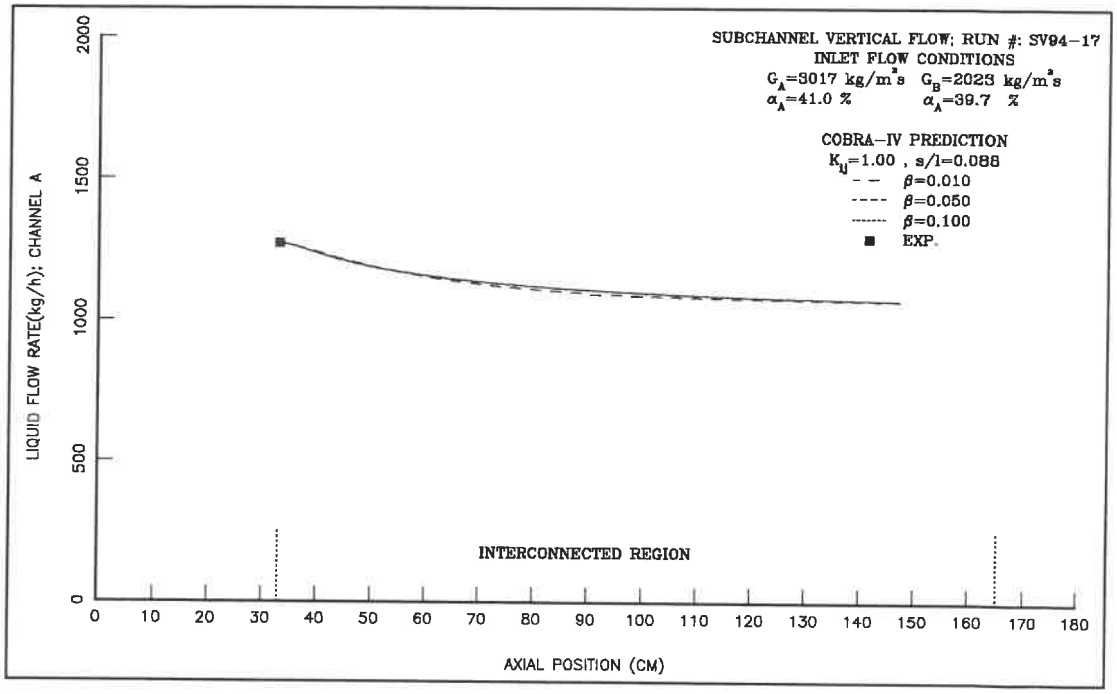


Figure 5.128: Mass Flow Rate Profile, Run SV94-17, Channel A

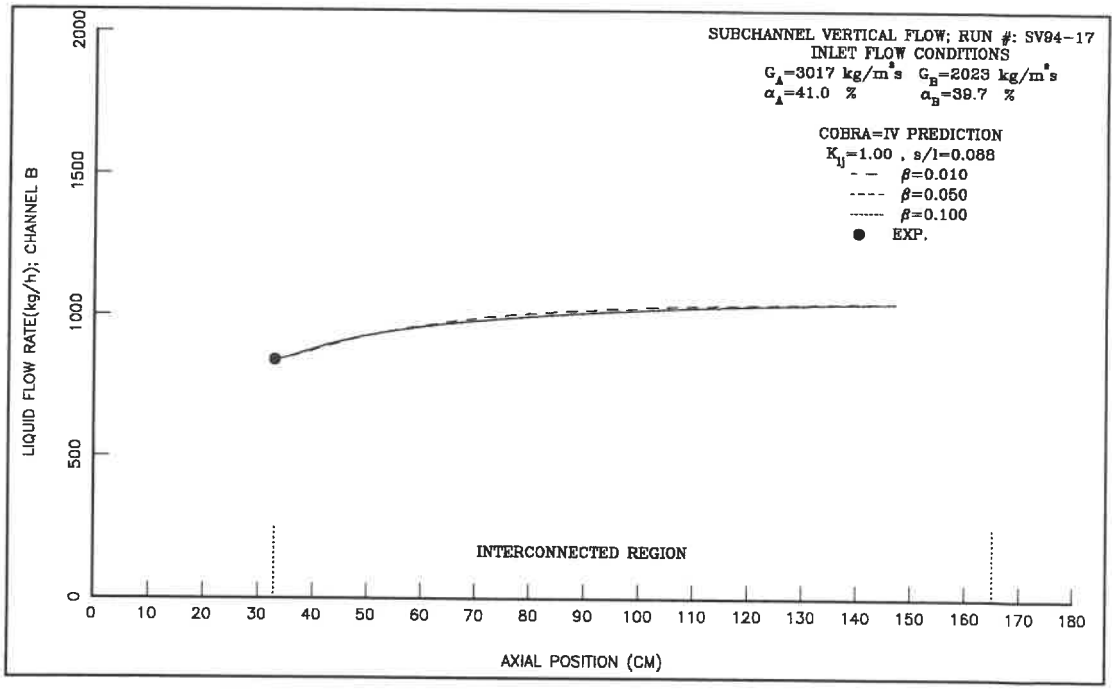


Figure 5.129: Mass Flow Rate Profile, Run SV94-17, Channel B

CHAPTER 6

COMPARISON OF MEASURED AND PREDICTED RESULTS-BLOCKAGE CASES

Improving the capability of the subchannel codes to accurately predict the consequences of coolant flow area restrictions in nuclear fuel assemblies, is one of the most important considerations during the development of the subchannel codes. In this case, the predictions of the total pressure drop across the flow area singularities and the flow distribution in the subchannels are of prime importance. One of the consequences of the blockage of a subchannel or a group of subchannels is to divert, depending on the severity of the blockage, some or all of the flow into neighboring unblocked subchannels. The flow recovery downstream of the blockage is in general a slow process and it may take many hydraulic diameters before the flow is restored to its far upstream value. Therefore, immediately downstream of the blockage, higher enthalpies will prevail in the blocked subchannel than in the unblocked subchannels, and the heat transfer in this region may be impaired or intensified due to enhancement of the turbulence caused by the blockage. In this section, the ability of COBRA-IV to predict the hydrodynamic behavior of two laterally interconnected subchannels with a blockage will be examined. For this purpose, the predictions of the COBRA-IV subchannel code will be compared with the experimental results obtained from the experiments carried out at École Polythechnique by Tapucu et al. [1984, 1988] and Teyssedou [1987]. These experiments have already been compared against the predictions of COBRA-IIIC [Tapucu et al. 1984, 1988, Teyssedou, 1987]. The first section will present a review of the modelling concepts used for this kind of problem and the second section will be devoted to the comparison of the prediction of COBRA-IV with the experimental data

under both single-phase and two-phase flow conditions.

6.1 Basic Definitions and Considerations

The blockage, is a reduction in the cross sectional area available for the coolant flow at some axial location in a subchannel reactor fuel assembly due to the ballooning of the fuel rods or by the presence of grid spacers, end plates, etc. There are two kinds of blockages: smooth and plate. The ballooning of the cladding induces a smooth blockage but grid spacers and end plates are plate types blockage. The study of blocked subchannels can be separated into two classes. The first treat the flow conditions and heat transfer mechanisms in the neighbourhood of the blockage, i.e., the recirculating zone which develops immediately after the blockage and the second deals with the redistribution of the coolant flow between the blocked and unblocked subchannel. Also, when a blockage occurs in a rod bundle, its local and long range effects on the coolant flow and heat transfer processes should be determined. The local effects include the separation of the flow from the fuel surface, the reattachment of the flow to the surface in the downstream region and the recirculating zones which develop both upstream and, mainly, downstream of the blockage. Long range effects include the flow diversion out of the blocked subchannel and the recovery of this diverted flow downstream of the blockage. Irrecoverable or irreversible pressure losses caused by flow blockages are also important in the determination of hydraulic behaviour of blocked subchannels. These pressure losses are generally deduced from the variation of the static pressure upstream and downstream of the blockages. A complete review of the influence of blockage on the flow in the interconnected subchannels has been presented by Teyssedou [1987]. This work is the main source for the following section.

6.2 Basic Relations

Theoretical models for partially blocked flows have been developed for simple flow area changes. These area changes can be classified as follows:

- Sudden expansion,
- Sudden contractions,
- Sharp inserts (short or long),
- Nozzle-diffuser and venturies.

The total two-phase pressure drop is usually calculated by using the momentum or energy balance equations. However, the evaluation of irreversible pressure losses caused by flow area changes (blockage) requires the use of an additional equation. The theoretical results of irreversible pressure losses are presented by Teyssedou [1987].

The irreversible pressure drop coefficient caused by inserts can be written as (Tapucu et al. [1984]):

$$\Delta p_{form,TP} = -K_{TP}\frac{G_1^2}{2\rho'} \quad , \tag{6-1}$$

where $\Delta p_{form,\,TP}$ is the irreversible pressure loss and ρ' is the momentum density. An alternate model to calculate this pressure drop is:

$$\Delta p_{form,TP} = -K'_{TP}\frac{G_1^2}{2\rho_l} \quad , \tag{6-2}$$

where ρ_l is the density of liquid phase. Based on the theoretical models explained by Teyssedou [1987], K'_{TP} (the so-called k in COBRA-IV input), the irreversible pressure

drop coefficient and the contraction coefficient C, are related as:

Janseen - Kervinen model:

$$K_{TP} = \left(\frac{1}{\sigma C} - 1\right)^2, \quad \sigma = \frac{A_2}{A_1}, \quad C = \frac{A_c}{A_2} \quad , \tag{6-3}$$

where: A_1 , A_2 and A_c are the flow section of the channel, the free flow section of the blocked region and the flow area of the vena contracta respectively.

Momentum-Energy model (Separated flow):

$$K_{TP} = \left[2\left(\frac{1}{\sigma C} - 1\right) - \frac{\rho' \rho_H}{\rho''^2}\left(\frac{1}{\sigma^2 C^2} - 1\right)\right], \tag{6-4}$$

where ρ_H is the homogeneous two-phase density, ρ' is the momentum density ρ'' is defined by:

$$\rho''^2 = \left(\frac{x^3}{\alpha^2 \rho_g^2} + \frac{(1-x)^3}{(1-\alpha)^2 \rho_l^2}\right)^{-1}, \tag{6-5}$$

where x is the dryness fraction and α is the void fraction.

Momentum-Energy model (Homogeneous flow):

$$K_{TP} = \left[\frac{\rho'}{\rho_m}\left(\frac{1}{\sigma C} - 1\right)^2\right]. \tag{6-6}$$

Using the irreversible (form) pressure loss and void fraction data [Tapucu et al. 1988], the irreversible pressure loss coefficient (K_{TP}) has been calculated for plate and smooth blockages. The variation of this coefficient for both types of blockages as a function of the void fraction for a given blockage fraction and as a function of the blockage fraction for a given void fraction were given by Teyssedou [1987]. The author concluded that for the plate blockage, at a given blockage fraction, the irreversible pressure loss coefficient first decreases with increasing void fraction and then increases. However, the overall changes, within the range of void fraction studied, were rather small. Therefore, the dependency of this coefficient on void fraction can be considered weak. On the other hand, K_{TP} increases rapidly with increasing blockage fraction.

For smooth blockages, the irreversible pressure loss coefficient increases with increasing the void and the blockage fractions. Futhermore, comparing the K_{TP} obtained for plate and smooth blockages, it is observed that smooth blockages give considerably lower K_{TP}.

6.3 Comparison of COBRA-IV Predictions with the Experimental Results

In this section, all the constitutive relationships developed based on the experiments and the form of the input data for the simulations will be presented. Since, these input data are essentially the same as those presented in Section 5.1.2, only the differences will be presented.

6.3.1 Input Data Configuration

All the input data are the same as those used in Section 5.1.2 except:

- The void fraction as a function of dryness fraction is given by:

$$\alpha = 6.67 * 10^2 x - 4.18 * 10^5 x^2 + 1.43 * 10^8 x^3 + 2.24 * 10^{12} x^4 - 7.86 * 10^{13} x^5 \quad (6\text{-}7)$$

- The two-phase multiplier versus quality is:

$$\Phi_l^2(x) = 1. + 1.186 * 10^3 x - 1.002 * 10^5 x^2 + 3.374 * 10^6 x^3 \quad (6\text{-}8)$$

- The turbulent friction factor is considered as: f=0.0032+0.221$(Re)^{-0.237}$
- The area reduction and axial location for both smooth and plate blockages are introduced in the same manner as given by Tapucu et al. [1984, 1988] (Figures 6-1 and 6-2).
- In order to introduce the loss coefficients a quasi-spacer is defined in the location of the area reduction

The following additional computational options are used:

- The implicit steady-state scheme is chosen.
- Only the region from the beginning of the interconnection up to the location of the last pressure tap is considered as the total axial length.
- The convergence limits for the external cross-flow are 0.1 and 0.01 for the two-phase and single-phase cases, respectively.
- The internal cross-flow convergence criterion for the Gauss-Seidel iterative scheme at axial level j is considered equal to 0.001.
- The external axial flow convergence criterion, defined for the axial momentum equation as the allowable error for the iterative axial flows is considered equal to 0.001.
- The cross-flow resistance factor, K_{ij}, has been varied.
- Transverse-momentum parameter, s/l, is considered to be 0.096.
- For the single-phase flow cases β is considered equal to zero while for the

two-phase flow cases it is given as an appropriate input value.

6.3.2 Comparison of COBRA Predictions with Single-Phase Data

Table (6.1) shows the experimental conditions of the runs. Three code parameters, the transverse momentum parameter factor (s/l), the diversion cross-flow factor (K_{ij}) and the irreversible pressure loss coefficient (k) or (K'_{TP}) are adjustable before starting each run. Numerous test show that the predictions of COBRA-IV are insensitive to variation of s/l. Therefore a single value of s/l equal to 0.096 is used for all runs. In all cases, the sensivity analysis for K_{ij} is carried out. In general the predictions of code are not dependent on the values of K_{ij}. Therefore a single value of K_{ij} equal to 1.0 is used. Since the axial pressures have been measured with a differential pressure transducer, the gravitational pressure loss component is automatically subtracted from the total pressure loss. Therefore, the following relation has been used for comparison of the predictions of COBRA with the experimental data:

$$\Delta p_{friction} + \Delta p_{acc.} = \underbrace{\Delta p_{Total}}_{\text{Predicted by COBRA}} - h_{n-Ref}\rho_l g \quad , \qquad (6\text{-}8)$$

where $h_{n\text{-}Ref}$ is the distance between the nth pressure tap and the reference pressure tap.

I. Plate Blockage, 59.2% Area Reduction:

In RUN#08, a plate blockage having a flow area reduction of 59.2% was placed in one the subchannels. The subchannels had equal inlet mass fluxes of about 1800 kg/m^2s. Figures 6.3 and 6.4 show the predictions of the friction and acceleration pressure drop by COBRA-IV against the experimental data. The blocked subchannel

interconnected region can be divided into three parts: upstream of the blockage, downstream of the blockage and vicinity of the blockage. It seems that a value of k equal to 0.5 produce the best predictions both downstream and upstream of the blockage. The incapability of COBRA-IV to accurately predict the pressures immediately after the blockage is quite understandable: the one-dimensional model which is used in COBRA-IV is not able to predict the recirculating zone behaviour. Figures 6.5 and 6.6 show the comparisons of the predicted liquid flow rate against the experimental data. Figure 6.6 shows that the k=0.5 gives quiet satisfactory predictions upstream and downstream of the blockage, however, 5 cm downstream of the blockage a slight overestimation of liquid flow rate is observed. This means that once the recirculation zone is ended the experimental liquid transfer to the blocked subchannel is faster than the predicted values.

II. Plate Blockage, 29.8% Area Reduction :

In two runs identified as RUN#10 and RUN#11 a plate blockage having a flow area reduction of 29.8% was placed in the one of the subchannels. Figures 6.7 and 6.8 show the COBRA-IV predictions for friction and acceleration pressure drop in both subchannels against the experimental data (RUN#10 with equal inlet mass fluxes of about 1800 kg/m^2s). Reasonable predictions are obtained with the value of k equal to 0.18 or 0.3. Figures 6.9 and 6.10 show that the predictions of COBRA-IV for liquid flow rate in the unblocked subchannel is quite satisfactory however, in the vicinity of the blockage where the liquid flow rates are slightly underestimated. In RUN #11 the same plate blockage with higher inlet mass flux (around 2650 kg/m^2s) has been tested. Figures 6.11 and 6.12 show that k=0.3 gives the best predictions for the pressure drop upstream and downstream of the blockage in both subchannels. However, in the vicinity of the

blockage an underestimation of the pressure drop due to flow area restriction in subchannels. this may be due to the limitations of the one-dimensional modelling. Figure 6.14 also confirms that the value k=0.3 can be considered as the best value for the irreversible pressure loss coefficient.

III. Smooth Blockage, 58.6% Area Reduction :

In two series of the runs identified as RUN #18 and RUN #19, a smooth blockage having an area reduction of 58.6% has been used. In RUN #18 the inlet mass fluxes were set to about 1850 kg/m^2s and in RUN #19 they were about 2650 kg/m^2s. Figures 6.15 through 6.22 show the COBRA-IV predictions against the experimental data for these cases. Since in both cases the experimental values for irreversible pressure loss coefficient in single and two subchannel experiments are 0.03 and 0.08 respectively [Tapucu et al. 1984], k has been taken equal zero. In the other words, the irreversible pressure loss for the smooth blocked cases is practically due to friction. Figure 6.15 through 6.22 prove the validity of choosing k=0. With this value of k, COBRA-IV predicts the pressure drop and the liquid low rate quite well. However, in the vicinity of the blockage, particularly in the blocked subchannel an underestimation of the pressure drop can be observed. Moreover, in both cases, the influence of the K_{ij} in the predictions of COBRA-IV can be seen. Downstream of the blockage the variation of the K_{ij} does not affect the predictions of COBRA-IV. But, in the vicinity and upstream of the blockage, the predictions of code in both pressure drop and liquid flow rate are affected by the values of K_{ij}. Also, it can be observed that K_{ij}=1.0 gives better result than K_{ij}=10.0 or 0.1.

6.3.3 Conclusions for Single-Phase Flow Cases

From the comparison presented above the following conclusions, summarised in the Table 6.2 can be made:

- The value of *s/l* does not affect the code predictions,
- The value of K_{ij} has a limited influence on the predictions of the code. K_{ij}=1.0 seems to produce the best results.
- The prediction of partially blocked flows with COBRA-IV depends on the value of the irreversible pressure loss coefficient, *k*.
- Because of the one-dimensional modelling the flow redistribution near the blockage cannot be accurately predicted.
- For smooth blockage cases COBRA-IV can safely be used for flow area reduction of up to 60%.
- For plate blockage cases, the use of COBRA-IV can be extended to 60% of the flow area reduction. The experimental values of irreversible pressure drop coefficient *k*, can be used without any major error. Table 6.2 shows the experimental values of *k* [Tapucu et. al. 1984] as well as the best values for the simulation with COBRA-IV and COBRA-IIIC.

6.3.4 Comparison of COBRA Predictions With Two-Phase Flow Data

Table 6.3 shows the experimental conditions used in the experiments selected to be compared with the predictions of the COBRA-IV. The effect of four main parameter have been verified: the transverse-momentum parameter, *s/l*, the cross-flow resistance factor, K_{ij}, the loss pressure coefficient, *k*, and the turbulent mixing factor, β. Different tests have shown that the value of *s/l* has no effect on the predictions of COBRA-IV and it can be considered as a constant equal to 0.096. Also, different tests show that

increasing the numbers of nodes, does not improve COBRA's predictions.

I. Equal Inlet Void Fraction

-Plate Blockage, 31.90% Area Reduction:

In RUN #01 a plate blockage having a flow area reduction of 31.90% was placed in one of the subchannels. The subchannels had equal inlet void fraction of about 60% and equal inlet mass fluxes of about 2000 kg/m^2s. Figures 6.23 through 6.28 show the comparison between the predictions of COBRA-IV for total pressure drop, void fraction and liquid flow rates in both the blocked and unblocked subchannels with experimental data. The best agreement between the predicted and the experimental data is obtained for K_{ij}=10.00, β=0.068 and k=0.7. As can be observed the predicted pressure is lower than the experimental data (Figures 6.23 and 6.24). It seems that the error in the prediction of the slope of the pressure gradient is due to an error in the frictional pressure calculation, i.e., f or Φ_l^2. Also, the use of the constant reference pressure in each node to determine the fluid properties, i.e., specific volume of the gas can cause errors in the calculations of the acceleration pressure losses for each node. Therefore, this method losses its validity when the pressure losses are important. Figures 6.25 and 6.26 shows the void fraction predictions against experimental data. Good agreement between the predictions of COBRA-IV and the experimental data can be observed, however, a slight underestimation in the void fraction downstream of the blockage in the unblocked subchannel is observed. Figures 6.27 and 6.28 show the inability of the COBRA-IV code to correctly predict the liquid mass flow rate in both subchannels. However, in the region upstream of the blockage the agreement between the predictions and the experimental data is quite good. In the region downstream of the

blockage, COBRA-IV does not predict the rapid changes of the flow rates in both subchannels. During the different numerical tests, it has been observed that the convergence of the numerical calculations depends on the values of K_{ij} and β in such a way that for K_{ij} less than 3.75 the calculations diverge. When K_{ij} is higher than 3.75, the number of external iterations decreases without any appreciable effect on the predictions of the code. The predictions of the pressure drop are insensitive to changes of β. However, for the liquid flow rate increasing β strongly affects the predictions of COBRA in regions downstream of the blockage. The effect of β on the void fraction will be further discussed in the next experiments.

-Plate Blockage, 61.00% Area Reduction:

In RUN #04 a plate blockage having a flow area reduction of 61% in one the subchannels was placed in one of the subchannels. The subchannels had equal inlet void fractions of about 60% and equal inlet mass fluxes 2000 kg/m^2s. Figures 6.29 and 6.30 show that the predictions of COBRA-IV underestimate the experimental values of the pressure drop in both subchannels. It seems that this underestimation is due to errors in frictional pressure drop calculation. Figures 6.31 and 6.32 show that k does not affect the void fraction profile and the code is not able to see the experimental trend downstream of the blockage. Figures 6.33 and 6.34 show that COBRA is not able to correctly predict flow rate. Bigger values of k gives better result for the maximum value of the flow rate but fast recovery of liquid flow rate observed just downstream of the blockage is not predicted. Sensitivity studies show that the minimum value for K_{ij} (>3.75) is necessary to obtain converged solution. Furthermore, the maximum value of the β required by the code to converge is 0.12.

-Smooth Blockage, 58.00% Area Reduction:

In RUN #10 a smooth blockage having a flow area reduction of 58% was placed in of the subchannels. The subchannels had equal inlet mass fluxes of bout 2000 kg/m^2s. The experimental values of k in single and two channel experiments are 0.60 and 1.25, respectively [Tapucu et al. 1988]. Figures 6.35 and 6.36 show that the use of experimental values of k overestimate the pressure drop in the blocked subchannel. Also it can be observed that the gradient of the pressure drop is not correctly predicted in both subchannels. Furthermore, the trend of the data at the vicinity of the blockage is well predicted due to weakness of the recirculation zone. Figures 6.37 and 6.38 show the void fraction predictions for RUN #10. These predictions are completely independent of the values of k. Figures 6.39 and 6.40 show that the liquid flow rate is well predicted in the region upstream of the blockages. In the region downstream of the blockage an important difference between the predicted values and the experimental results is observed.

In RUN #13, a smooth blockage (60% flow area reduction) was placed in one of the subchannels. the subchannels had equal inlet void fractions of about 30% and equal inlet mass fluxes about 2000 kg/m^2s. Figures 6.41 through 6.46 show the predictions of the code against the experimental data. Two values of k (0.10 and 0.50) have been examined. The void fraction profiles are not affected by the values of k. The values of K_{ij} have almost no influence in the predictions of COBRA, however, increasing the value of K_{ij}, allows number of iteration to decrease.

II. Blocked Subchannel (H.V.) and Unblocked Subchannel (L.V.)

-Plate Blockage, 31.90% Area Reduction:

In RUN #02 a plate blockage having a flow area reduction of 31.90% was placed in of the subchannels. The blocked subchannel had an inlet void fraction of 60% and both subchannel had equal inlet mass flux of around 2000 kg/m^2s. Figures 6.47 through 6.52 show the effect of β and Figure 6.53 through 6.58 show the effect of *k*-coefficient in the predictions of the code. Numerous tests have shown that the change of K_{ij} does not affect COBRA's predictions. The variations of β from 0.010 to 0.080 practically has no major influence in the predictions of the pressures (Figures 6.47 and 6.48). The best prediction of the void fraction profile in both the blocked and the unblocked subchannls are obtained by using β=0.080. Only a slight underestimation at the region upstream of the blockage in the unblocked subchannel is observed (Figure 6.50). Figures 6.51 and 6.52 show the influence of β in the prediction of the liquid flow rate. As can be observed, the predictions of the liquid flow rate are sensitive to the value of β. However, the changes in β did not improve the liquid flow rate predictions. Figures 6.53 and 6.54 show that the change of the values of *k*-coefficient affect the pressure drop predictions in the region upstream of the blockage. The value of *k* equal to 0.8 allows the best predictions of the pressure drop to be obtained. Figure 6.55 and 6.56 show that different values of *k* have practically no affect on the predictions of the void fraction profiles in both subchannels. Figures 6.57 and 6.58 show that in the region upstream of the blockage the agreement between the predictions of the liquid flow rates and the experimental data is satisfactory, but in the region downstream of the blockage the code does not pick up the trend of experimental data except for regions far from the blockage. The effect of changing *k* is mainly felt in the downstream region close to

blockage where a lower value of k causes a lower flow rate in unblocked subchannel.

-Plate Blockage, 61.00% Area Reduction:

In RUN #05, a plate blockage having a flow area reduction of 61% was placed in one of the subchannels. The blocked subchannel had an inlet void fraction of about 60% and both subchannel had equal inlet mass flux of around 2000 kg/m^2s. The experimental values of k, for single and two channel experiments are 1.10 and 1.67 respectively [Tapucu et. al. 1988]. Figure 6.59 and 6.60 show that the value k=1.1 gives good agreement between the code predictions and the experimental data. Figures 6.61 and 6.62 show that the code predicts void fraction in the blocked subchannel quiet well. But in the unblocked subchannel, downstream of the blockage, an underestimation of void fraction can be observed. Also, from the same Figures it can be concluded that the value of k has no major influence in the predictions of the void fraction. Figures 6.63 and 6.64 show that the predictions of the code for liquid flow rates are strongly influenced by the values of k, however, the predictions of the data are rather poor.

-Smooth Blockage, 58.00% Area Reduction:

In RUN #11, a smooth blockage having a flow area reduction of 58% was placed in one of the subchannels. The blocked subchannel had an inlet void fraction of about 60% and both subchannel had equal inlet mass flux of around 2000 kg/m^2s. Figures 6.65 and 6.66 show that the code is able to correctly predict the pressure drop by using k=0.3 and β=0.096. Also, Figures 6.67 and 6.68 show that for the same values of k and β a good agreement between the experimental data on void fraction and code predictions is obtained. Figure 6.69 and 6.70 show that the trend in the liquid flow rate

are reasonably well followed but the values are different.

II. Blocked Subchannel (L.V.) and Unblocked Subchannel (H.V.)

-Plate Blockage, 31.90% Area Reduction:

In RUN #03, a plate blockage having a flow area reduction of 31.9% was placed in one of the subchannels. The unblocked subchannel had an inlet void fraction of about 60% and both subchannel had equal inlet mass flux of around 2000 kg/m^2s. Figures 6.71 through 6.76 compare the predictions of the COBRA-IV code against the experimental data. It can be observed that the pressure drops (Figures 6.71 and 6.72) and the void fraction profiles (Figures 6.73 and 6.74) are in a good agreement with data when k=0.30 and β=0.080 are used. Again COBRA-IV was not able to pick up the experimental trends for the liquid flow rates observed in the region downstream of the blockage. The effect of the K_{ij} in the predictions of the code have also been studied. It is observed that a minimum value of K_{ij} is necessary to obtain a converged solution (K_{ij}>0.22). The values larger than 0.22 gives no substantial change in the prediction of the code and the number of the external iteration rapidly decreases. It is also observed that the values of β larger than 0.12 do not allow the iterative solution to be converged

-Plate Blockage, 61.00% Area Reduction:

In RUN #06, a plate blockage having a flow area reduction of 61% was placed in one of the subchannels. The unblocked subchannel had an inlet void fraction of about 60% and both subchannel had equal inlet mass flux of around 2000 kg/m^2s. Figures 6.77 and 6.78 show that β=0.080 and k=1.00 produce a prediction that is in good agreement

with the experimental data. The values which were used in COBRA-IIIC were 0.061 and 0.1 respectively [Tapucu et al. 1988]. Figures 6.79 and 6.80 show that the prediction of COBRA-IV for the void fractions except in the vicinity of the blockage are satisfactory. Figures 6.81 and 6.82 show that, the predictions of COBRA-IV for liquid flow rates do not follow the experimental trends especially in the region downstream of the blockage. The increase in k and β increase the liquid flow rates in the unblocked subchannel and decrease the liquid flow rate in the blocked subchannel without properly picking up the experimental trend. The value of K_{ij}=5.00 guaranties the convergence of the numerical solution.

-Smooth Blockage, 58.00% Area Reduction:

In RUN #12, a smooth blockage having a flow area reduction of 58% was placed in one of the subchannels. The unblocked subchannel had an inlet void fraction of about 60% and both subchannel had equal inlet mass flux of around 2000 kg/m^2s. Figures 6.83 and 6.84 show that the value of k=0.1 produce the best prediction of the pressure drops. Figures 6.85 and 6.86 show that the prediction of the void fraction profile in both subchannels are satisfactory, however, the experimental trends close to the blockage in the blocked subchannel are not picked up. Figures 6.87 and 6.88 show that the code predicts the liquid flow rate quite well. A better prediction of the flow close to the blockages, can be achieved by increasing k. However, greater values of k cause the prediction of the pressure drop to be deteriorate. Sensitivity test have shown that increasing the value of the K_{ij} does not affect the predictions and allows the number of iteration to be reduced

6.3.5 Conclusions for Two-Phase Flow Cases

The following conclusions can be made:

- The value of *s/l* has no influence in the code predictions.
- It is observed that the convergence of the code depends on the values of K_{ij} and β, in such a way that for the values less than a minimum value of the K_{ij} and for values greater than a value of β the code will not be convergent. This could be due this fact that the implicit scheme used in COBRA-IV is designed for the cases when the axial flow is much more important than the lateral flow. Thus, increasing K_{ij} decrease the cross-flow which stabilise the numerical scheme.
- It is observed that the predictions depend on the values of β and *k*. The variation of *k* affects the predictions of total pressure loss and liquid mass flow rate in both subchannels, while changing β has practically no influence on the prediction of total pressure drop but it changes the predictions of the void fraction and liquid flow rate.
- Table 6.4 shows the summary of the comparison between the experimental *k*-coefficient and the best values of β and *k* used in simulations by COBRA-IIIC and COBRA-IV [Tapucu et. al. 1988]. It can be observed that the *k*-coefficient used in COBRA-IV are not very far from experimental *k*-coefficients, however, in the cases with 60% plate blockage, the best value of *k* is slightly less than the experimental value (Runs #04 and #05). Therefore, the experimental values of *k* can be safely used in all cases.
- It can be concluded that the COBRA-IV can be used in smooth blockage up to 60% of the flow area reduction.
- In the case of the plate blockages, the code can also be used up to 60% flow area reduction. In this cases, COBRA-IV cannot produce the acceptable predictions for

liquid flow rate but the predictions of the void fraction and the pressure drop are in good agreement with the experimental data.

- The predictions of the code strongly depend on the validity of the constitutive relations. For example it seems that the error calculations in the pressure drop in RUN #01 and RUN #04 are due to inaccuracies in constitutive relations for f and Φ_l^2.

Table 6.1: Inlet Flow Conditions Used in Single-Phase flow Experiments

Experiment	Shape of the Blockage	Flow Area Reduction (%)	Channel A Mass Flux (kg/m^2s)	Channel B Mass Flux (kg/m^2s)
RUN #08	PLATE	59.2	1,859	1,761
RUN #10	PLATE	29.8	1,854	1,717
RUN #11	PLATE	29.8	2,633	2,393
RUN #18	SMOOTH 1-piece	58.6	1,816	1,862
RUN #19	SMOOTH 1-piece	58.6	2,640	2,665

Table 6.2: Summary of the Comparison of the code predictions with Experimental Data (Single-Phase)

Run	*k*-coefficient from single channel experiments	*k*-coefficient from two channel experiments	COBRA-III C K_{ij}	COBRA-III C k	COBRA-IV K_{ij}	COBRA-IV k
#08	1.00	1.00	1.00	0.10	1.00	0.50-0.80
#10	0.18	0.30	1.00	0.20-0.30	1.00	0.18-0.30
#11	0.18	0.30	1.00	0.20-0.30	1.00	0.30-0.40
#18	0.03	0.08	1.00	0.00	1.00	0.00
#19	0.03	0.08	1.00	0.00	1.00	0.00

Table 6.3: Inlet Flow Conditions Used in the Two-Phase flow Experiments

Run	Shape of Blockage	Flow Area Reduction (%)	Blocked channel		Unblocked Channel	
			Mass Flux (kg/m^2s)	Void Fraction (%)	Mass Flux (kg/m^2s)	Void Fraction (%)
#01	Plate	31.90	2,006	58.90	1,969	60.00
#02	Plate	31.90	2,020	59.50	1,994	0.00
#03	Plate	31.90	2,008	0.00	1,964	60.20
#04	Plate	61.00	2,016	59.70	1,983	61.20
#05	Plate	61.00	2,020	59.70	1,956	0.00
#06	Plate	61.00	2,002	0.00	1,969	59.50
#10	Smooth	58.00	2,009	59.70	1,973	60.50
#11	Smooth	58.00	2,006	60.30	1,962	0.00
#12	Smooth	58.00	2,009	0.00	1,988	60.70
#13	Smooth	58.00	2,004	28.80	1,979	28.90

Table 6.4: Summary of the Comparison of the Code Predictions with Experimental Data (Two-Phase)

Run	k-coefficeient from single channel experiments	k-coefficient from two channel experiments	COBRA-III C			COBRA-IV		
			K_{ij}	β	k	K_{ij}	β	k
#01	0.32	0.78	1.00	0.30-0.58	0.70	Min. 3.75	0.068	0.7-0.8
#02	0.30	0.54	1.00	0.034	0.40	1.00	0.068	0.80
#03	0.30	0.48	1.00	0.078	0.30	Min. 0.22	0.080	0.30
#04	1.21	1.64	1.00	0.635	0.50	Min. 3.75	0.068	1.70
#05	1.10	1.67	1.00	0.080	0.30	1.00	0.080	1.10
#06	1.10	1.63	1.00	0.061	0.10	5.00	0.086	1.00
#10	0.60	1.25	1.00	0.600	0.30	1.00	0.200	0.60
#11	0.35	1.22	1.00	0.096	0.25	1.00	0.096	0.30
#12	0.34	0.89	1.00	0.075	0.10	1.00	0.096	0.10
#13	0.15	0.88	1.00	0.017	0.10	5.00	0.068	0.10-0.50

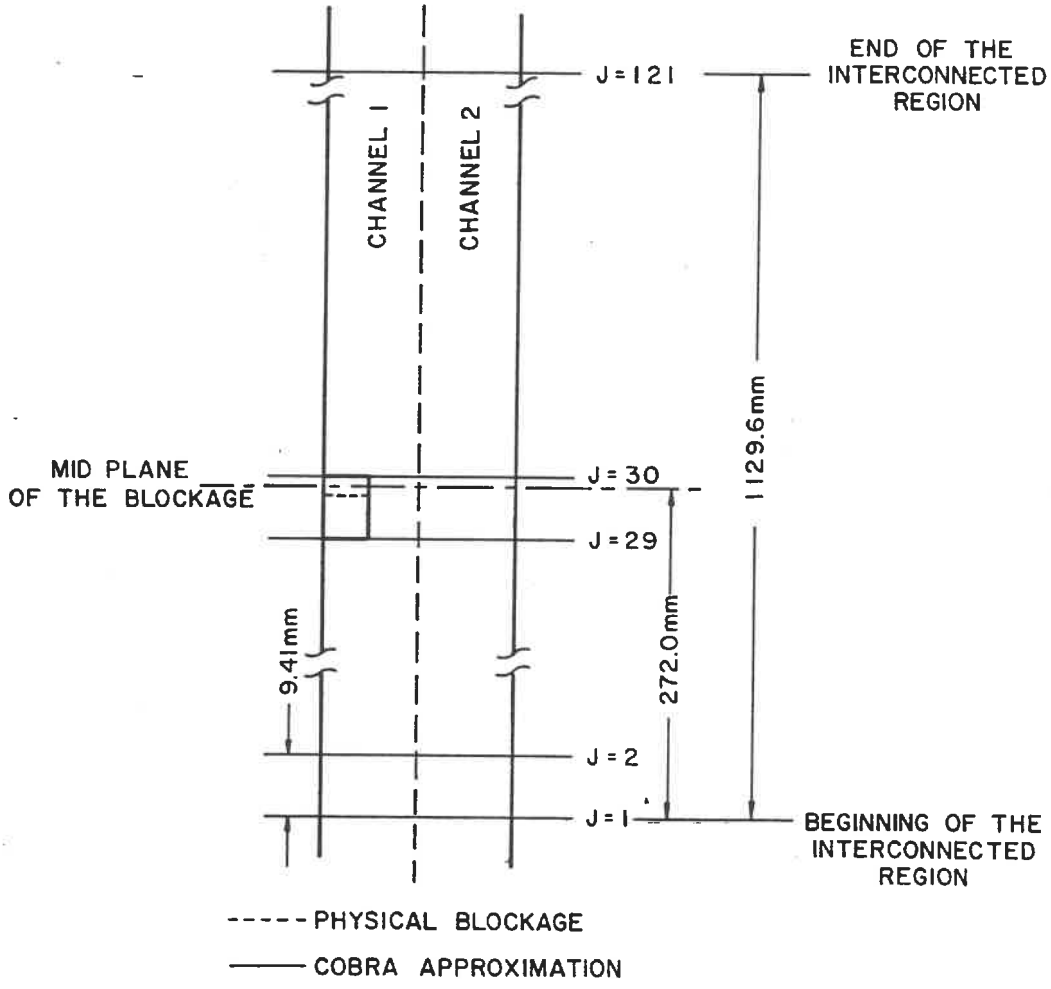


Figure 6-1: Simulation of a Plate Blockage

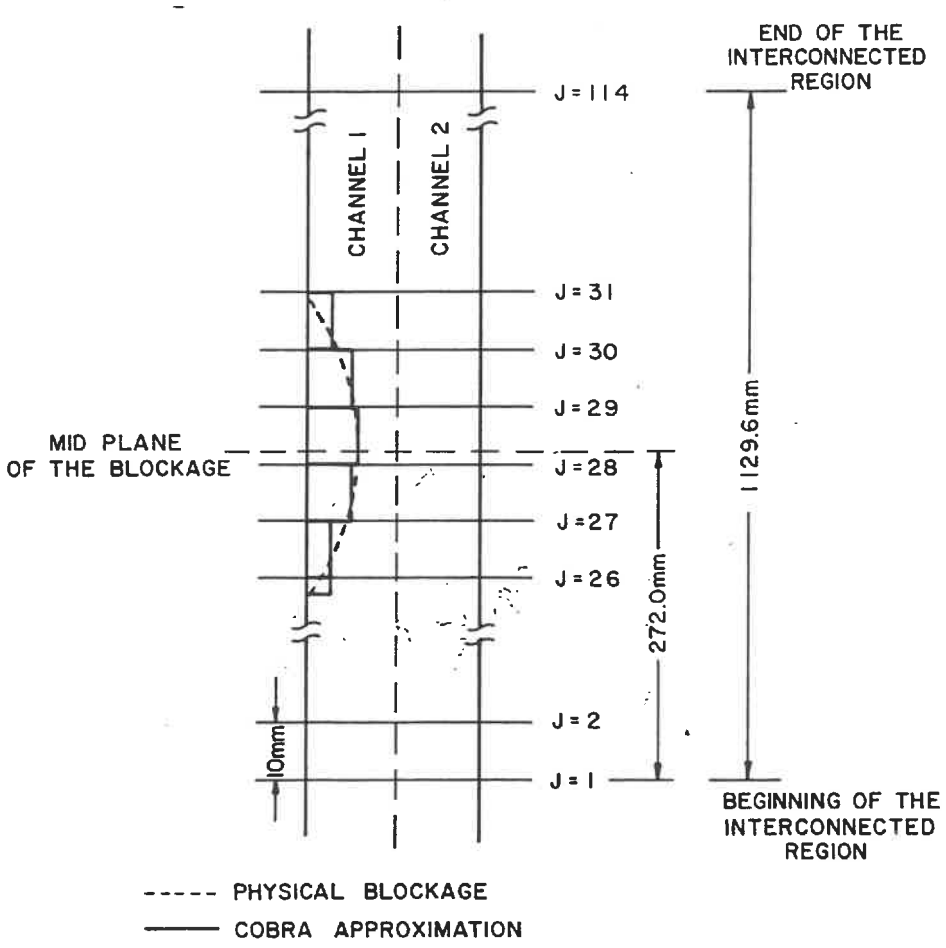


Figure 6-2: Simulation of a Smooth Blockage

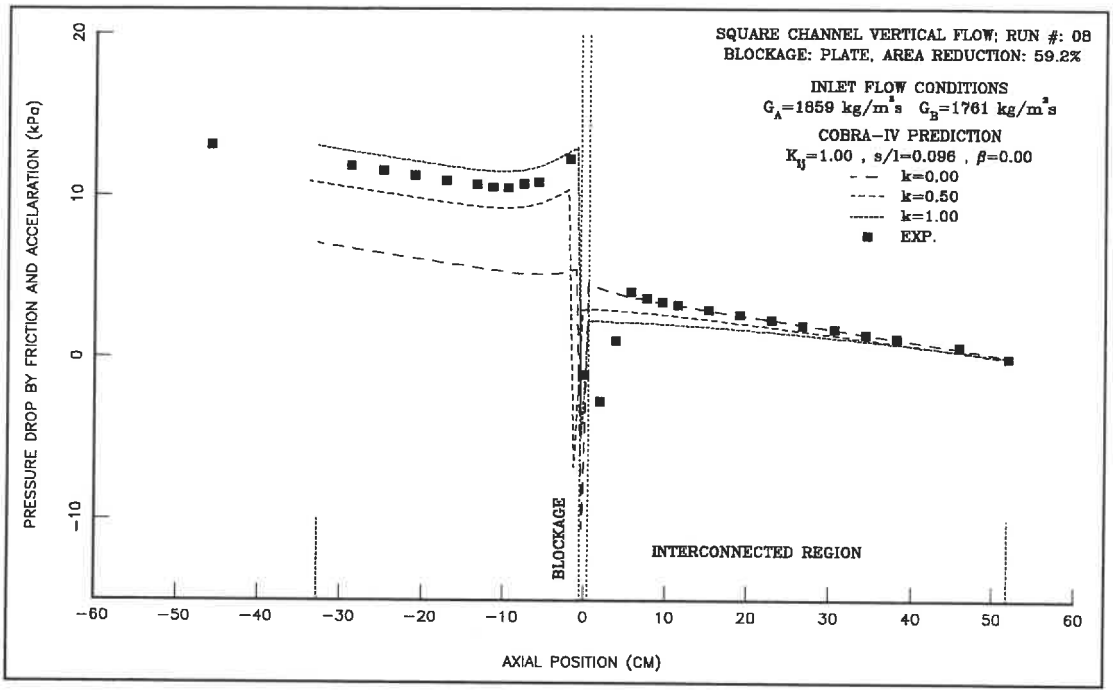


Figure 6.3: Pressure Drop profile, Single-Phase, Blocked Channel, RUN #08

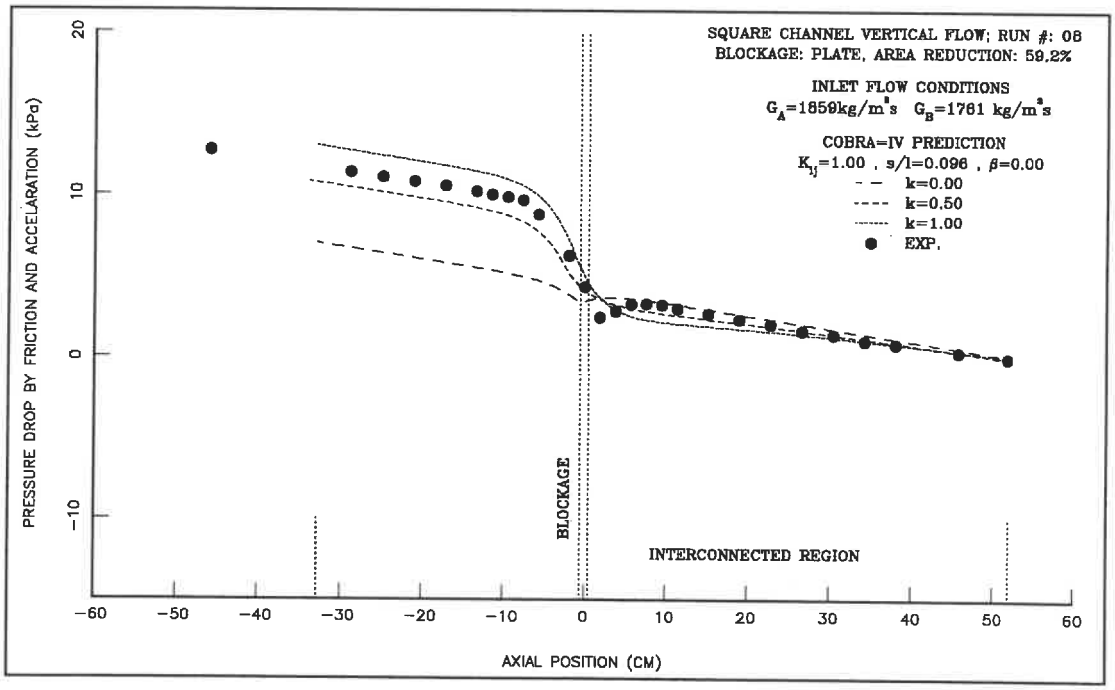


Figure 6.4: Pressure Drop profile, Single-Phase, Unblocked Channel, RUN #08

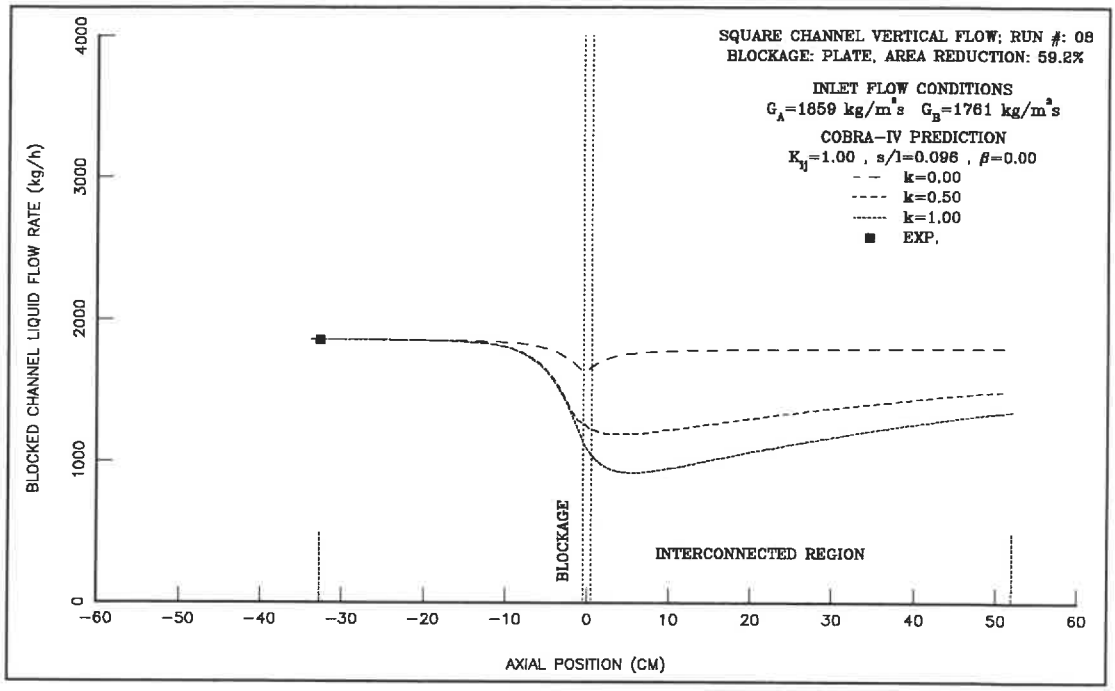


Figure 6.5: Liquid Flow Rate Profile, Single-Phase, Blocked Channel, RUN #08

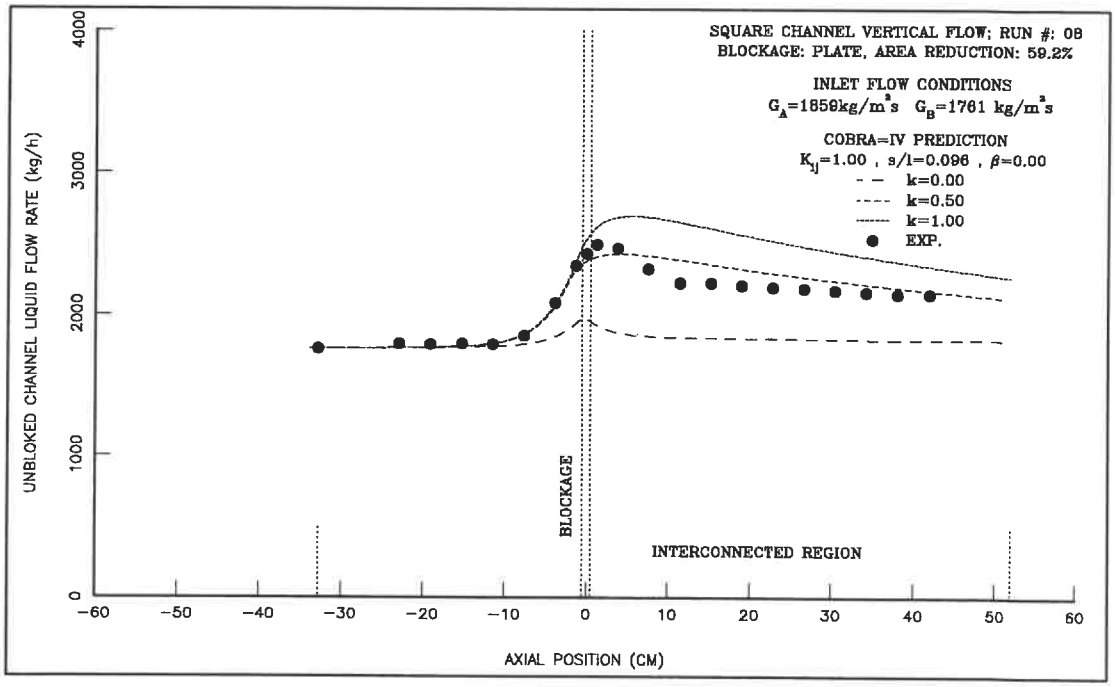


Figure 6.6: Liquid Flow Rate Profile, Single-Phase, Unblocked Channel, RUN #08

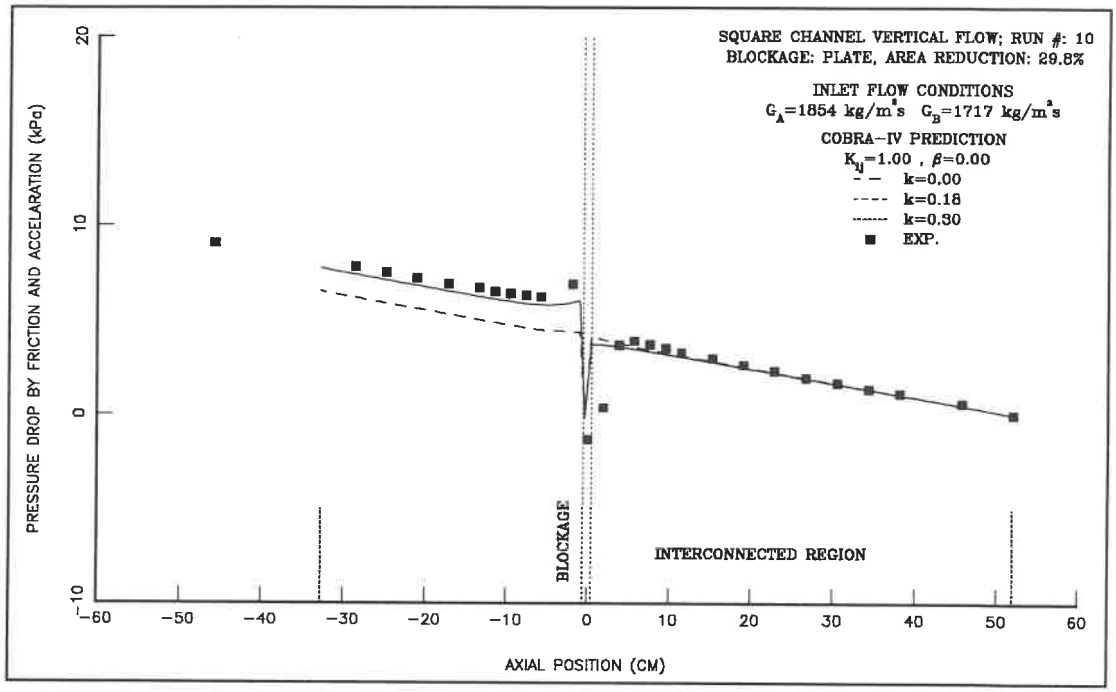


Figure 6.7: Pressure Drop profile, Single-Phase, Blocked Channel, RUN #10

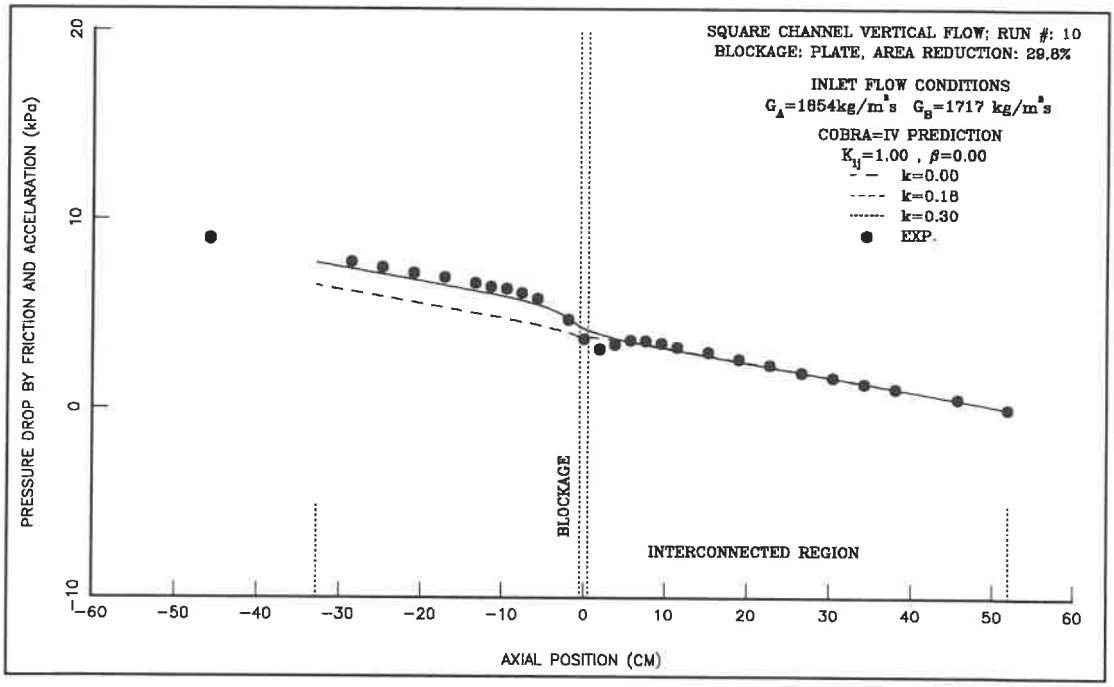


Figure 6.8: Pressure Drop profile, Single-Phase, Unblocked Channel, RUN #10

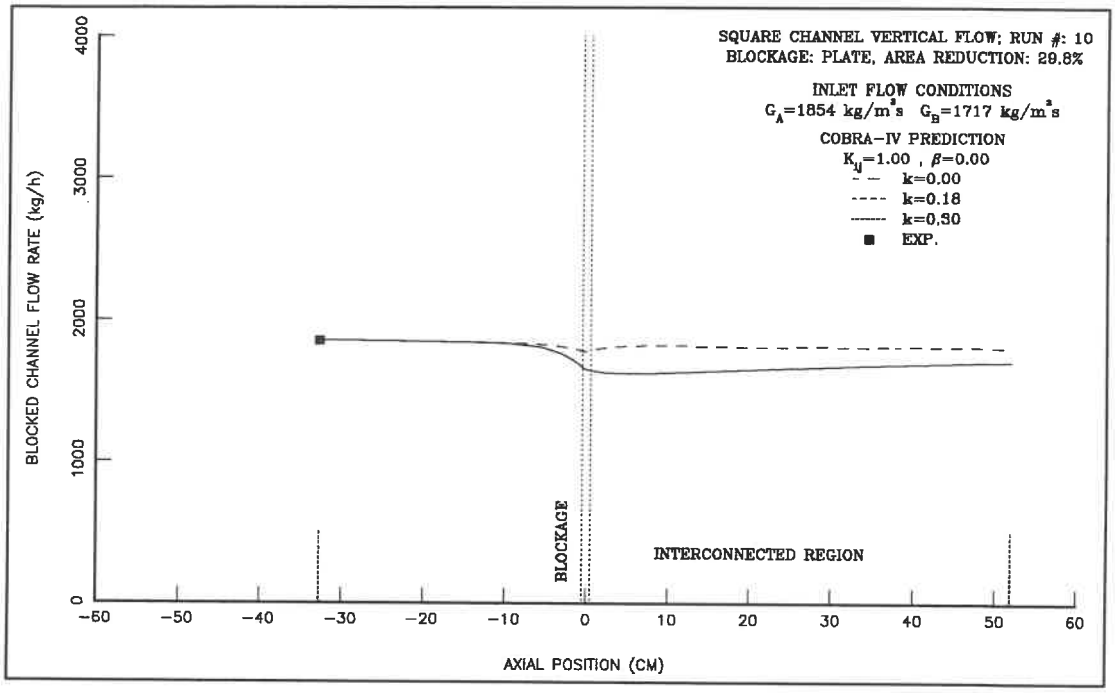


Figure 6.9: Liquid Flow Rate Profile, Single-Phase, Blocked Channel, RUN #10

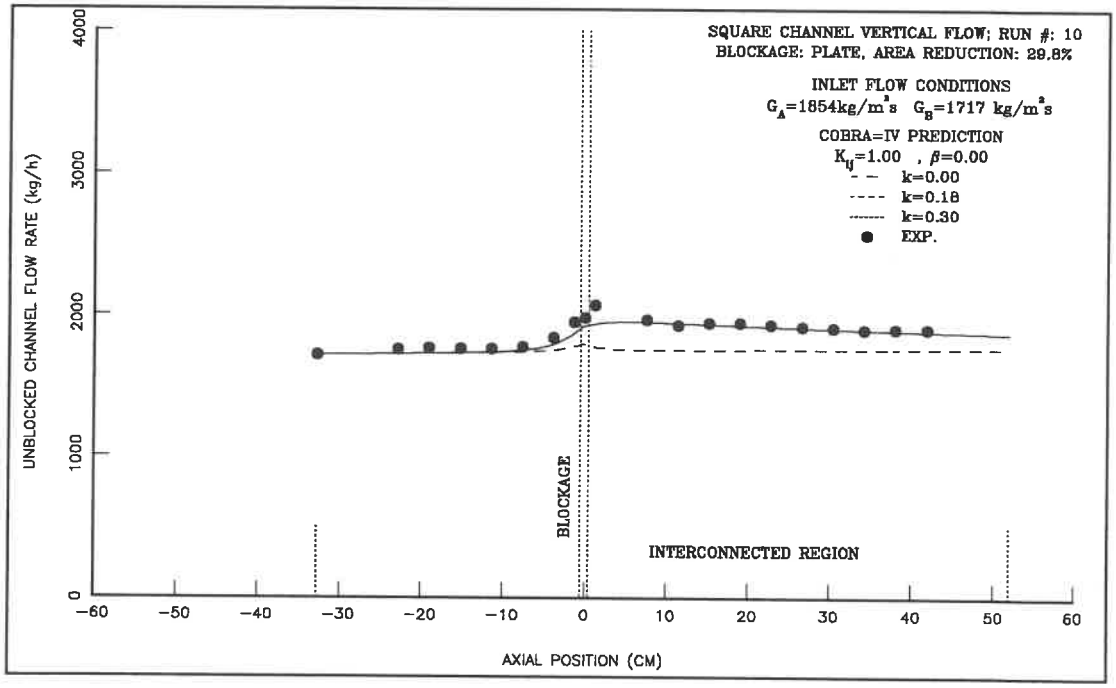


Figure 6.10: Liquid Flow Rate Profile, Single-Phase, Unblocked Channel, RUN #10

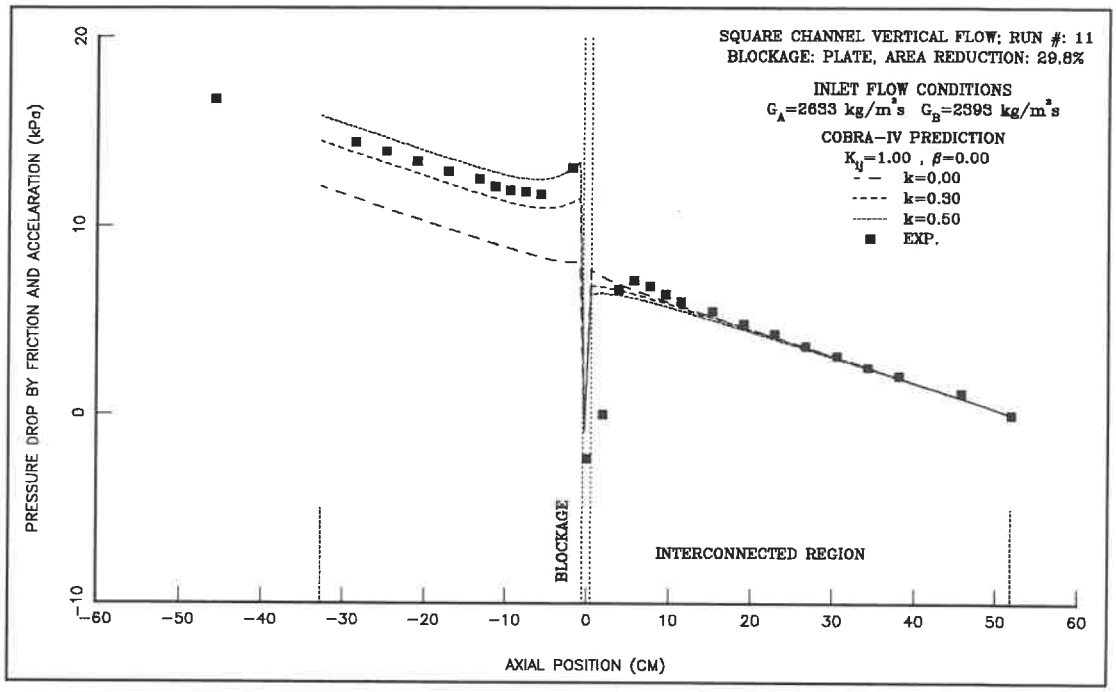


Figure 6.11: Pressure Drop profile, Single-Phase, Blocked Channel, RUN #11

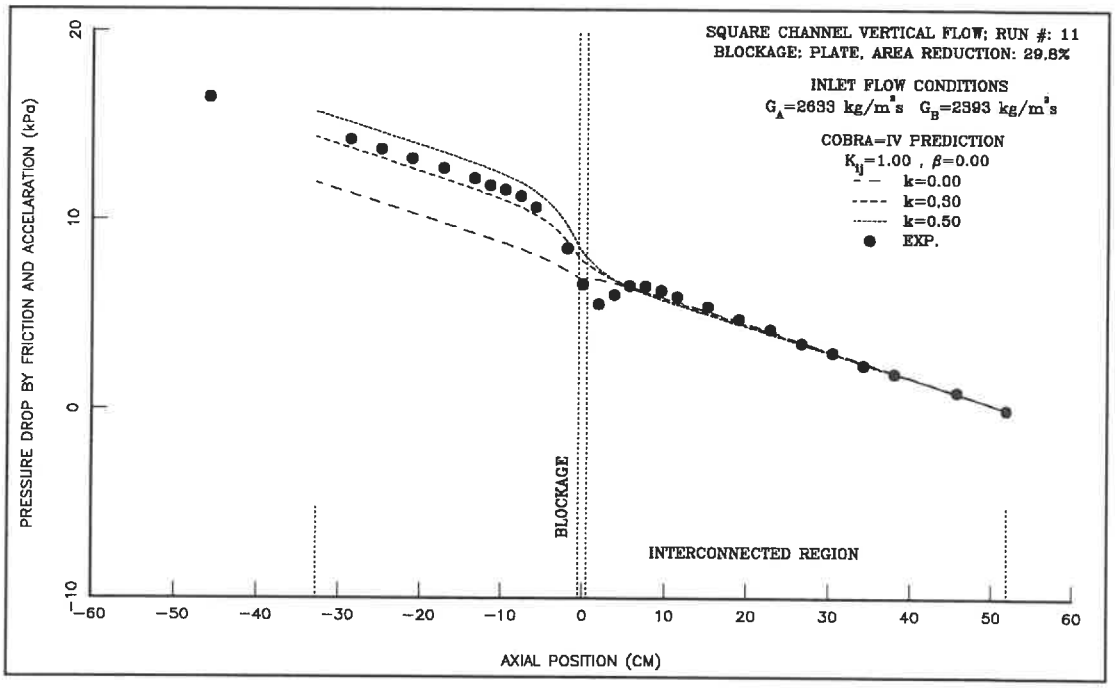


Figure 6.12: Pressure Drop profile, Single-Phase, Unblocked Channel, RUN #11

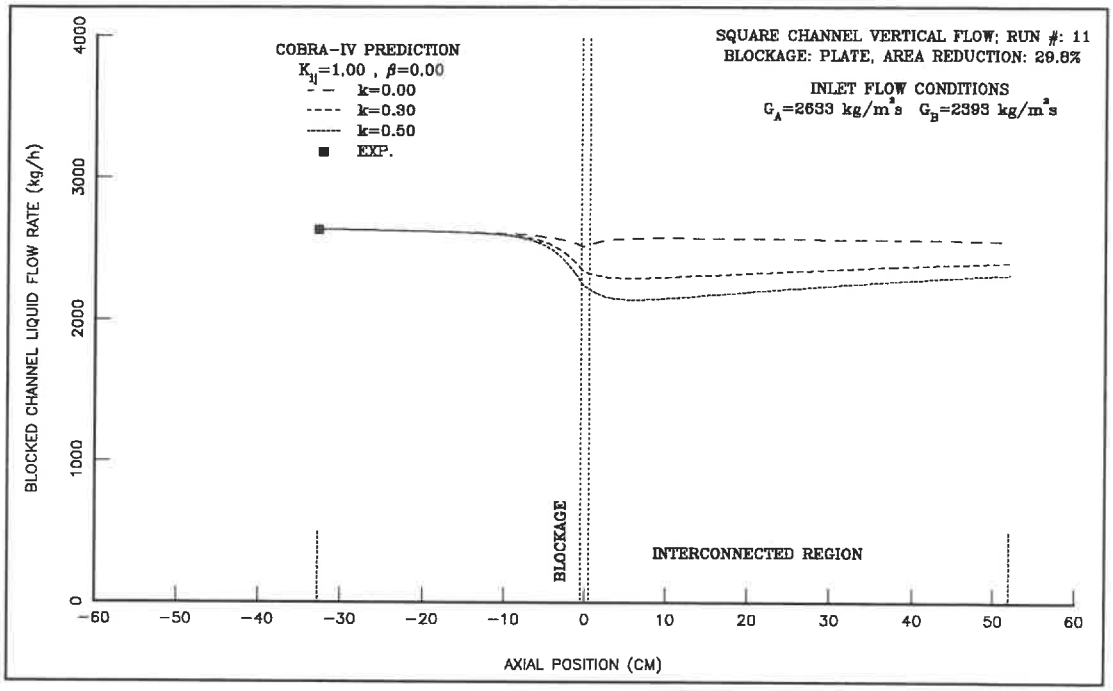


Figure 6.13: Liquid Flow Rate Profile, Single-Phase, Blocked Channel, RUN #11

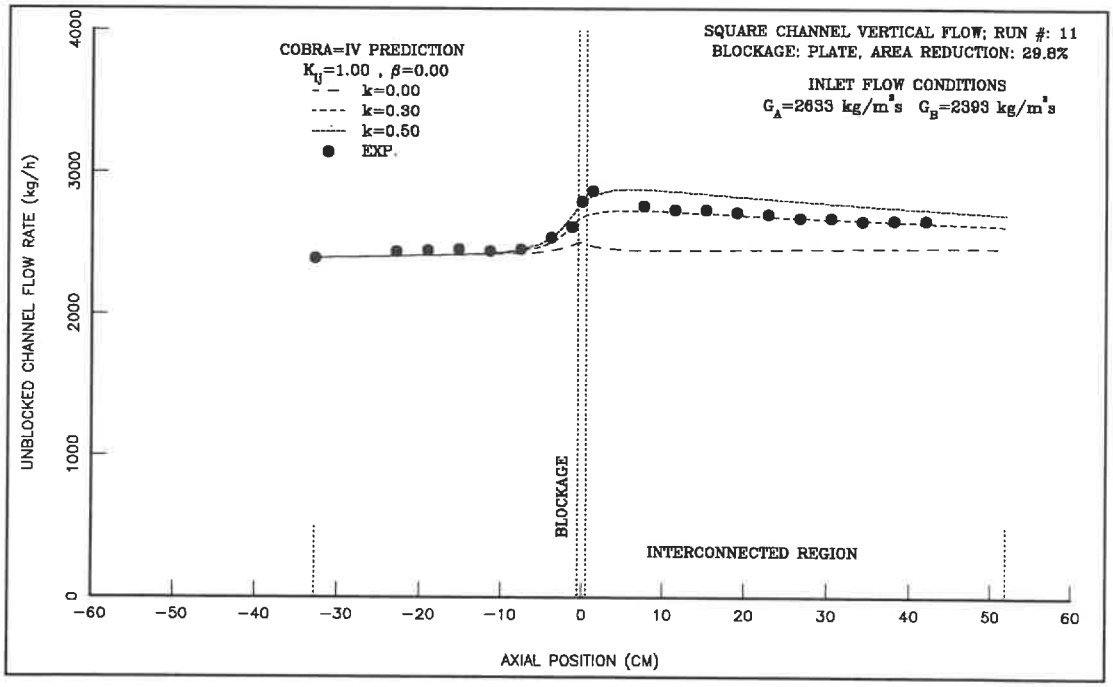


Figure 6.14: Liquid Flow Rate Profile, Single-Phase, Unblocked Channel, RUN #11

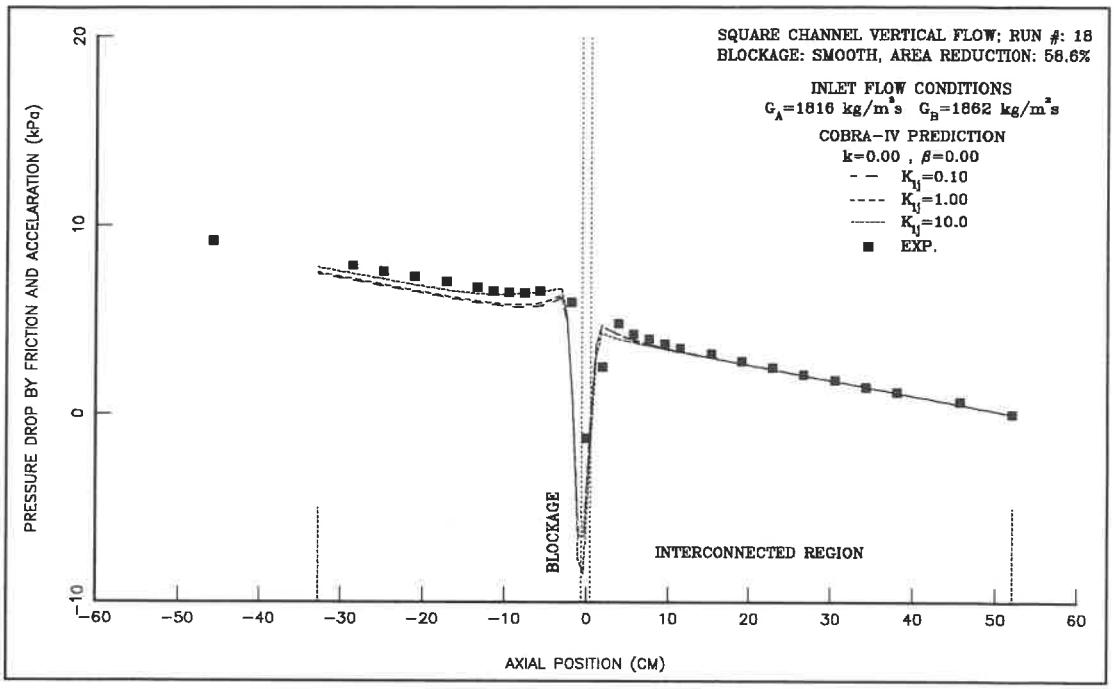


Figure 6.15: Pressure Drop profile, Single-Phase, Blocked Channel, RUN #18

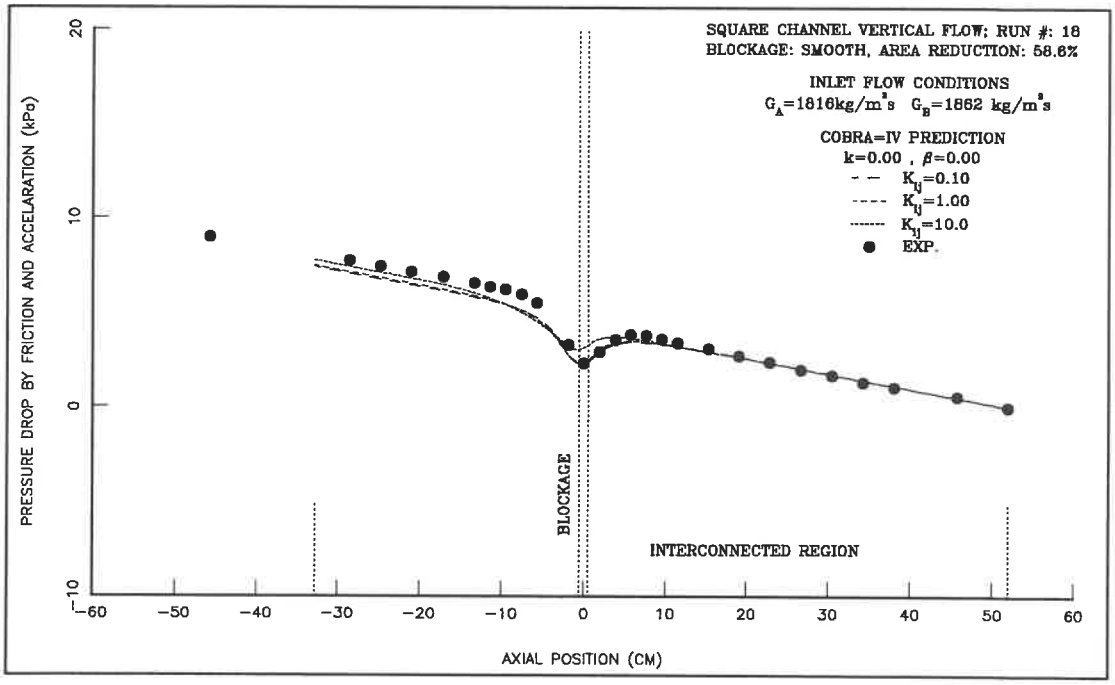


Figure 6.16: Pressure Drop profile, Single-Phase, Unblocked Channel, RUN #18

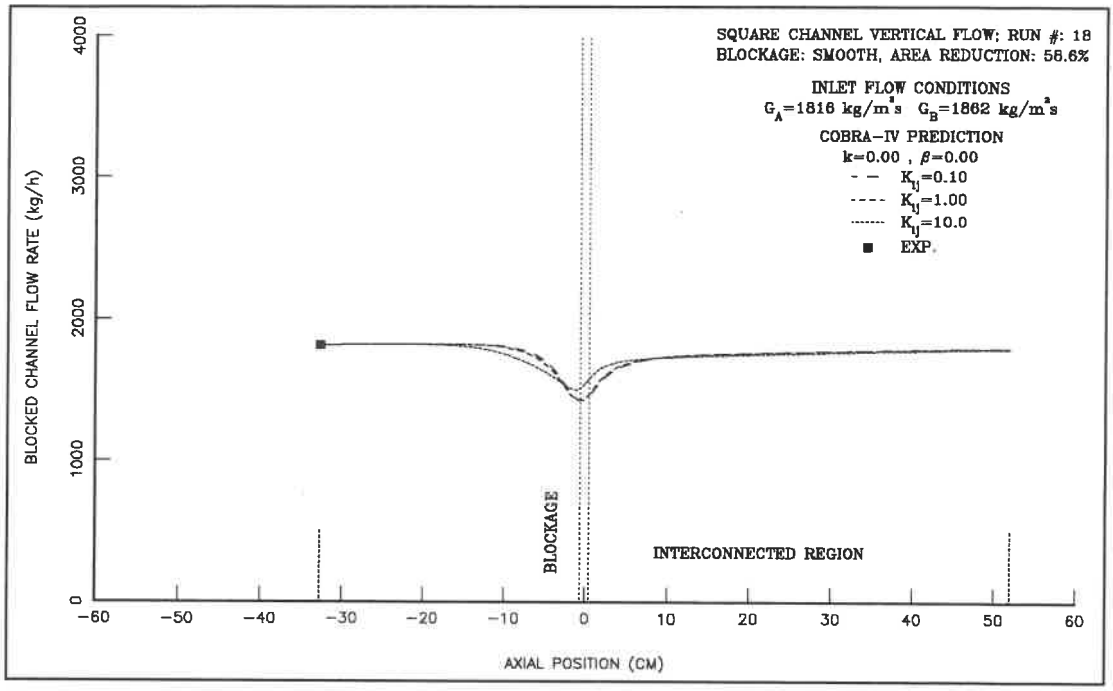


Figure 6.17: Liquid Flow Rate Profile, Single-Phase, Blocked Channel, RUN #18

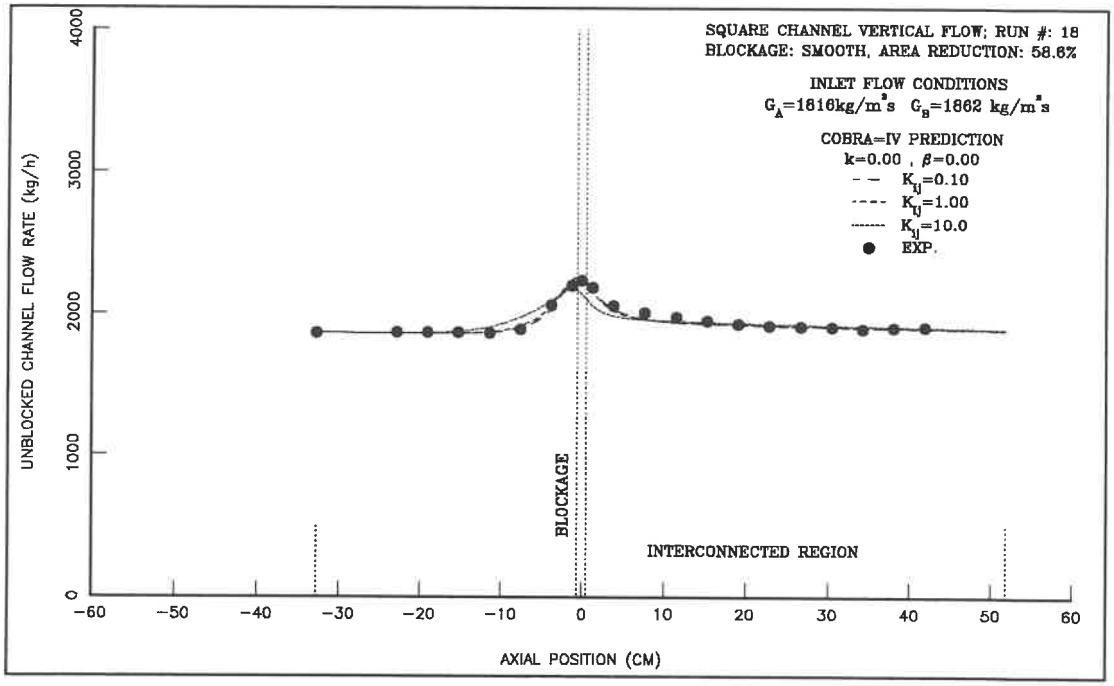


Figure 6.18: Liquid Flow Rate Profile, Single-Phase, Unblocked Channel, RUN #18

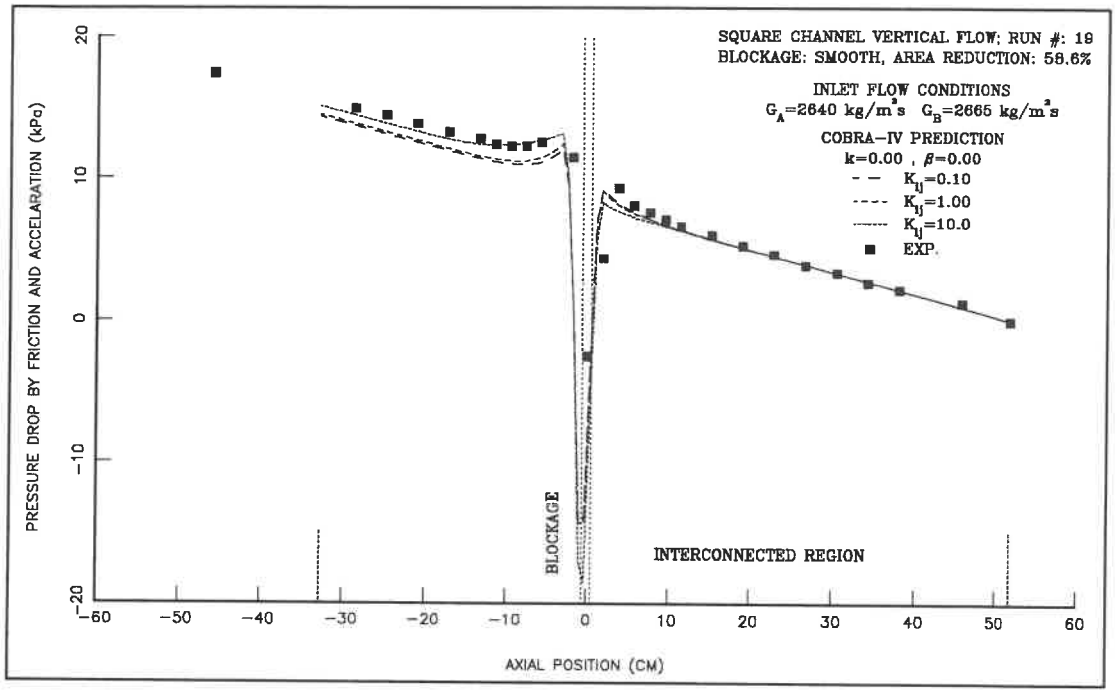


Figure 6.19: Pressure Drop profile, Single-Phase, Blocked Channel, RUN #19

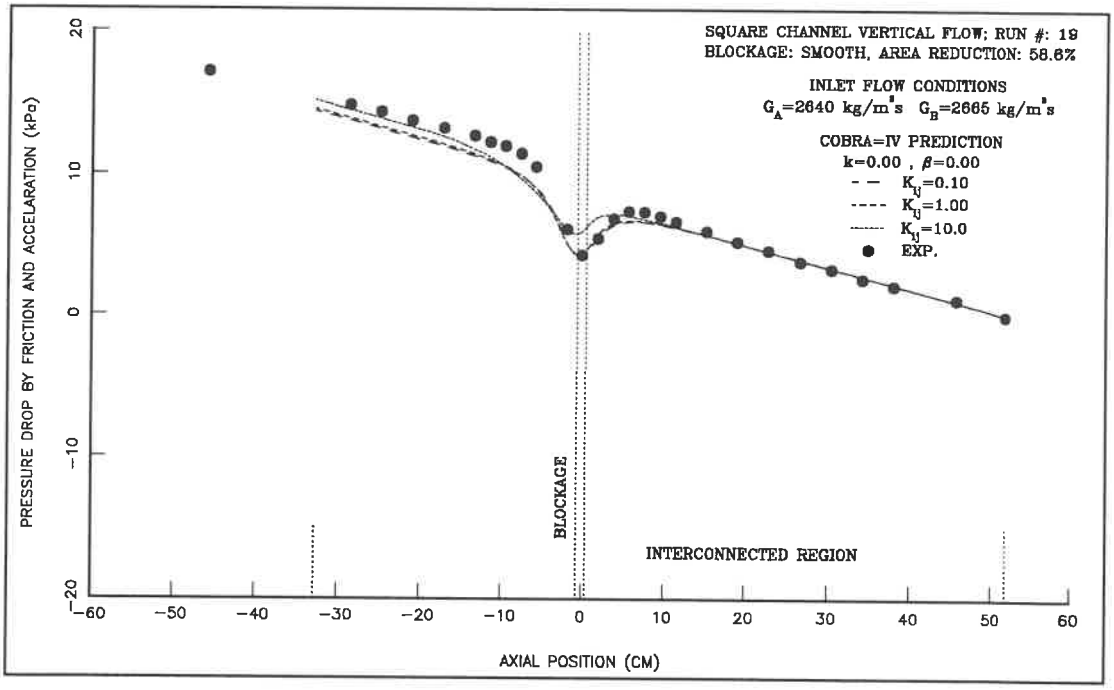


Figure 6.20: Pressure Drop profile, Single-Phase, Unblocked Channel, RUN #19

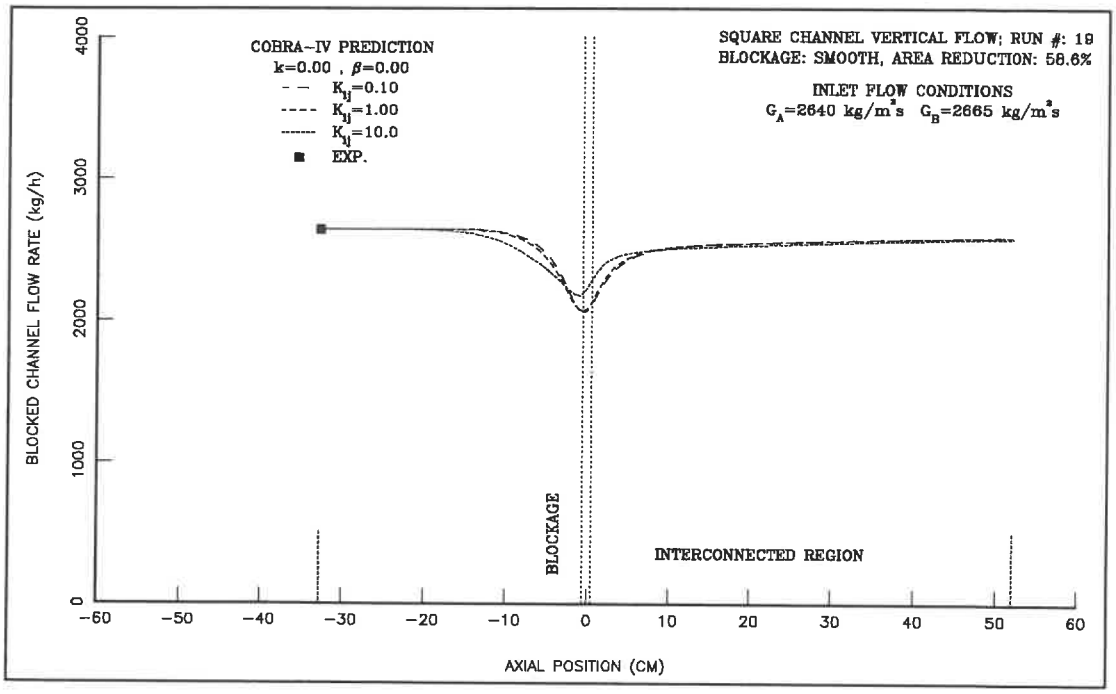


Figure 6.21: Liquid Flow Rate Profile, Single-Phase, Blocked Channel, RUN #19

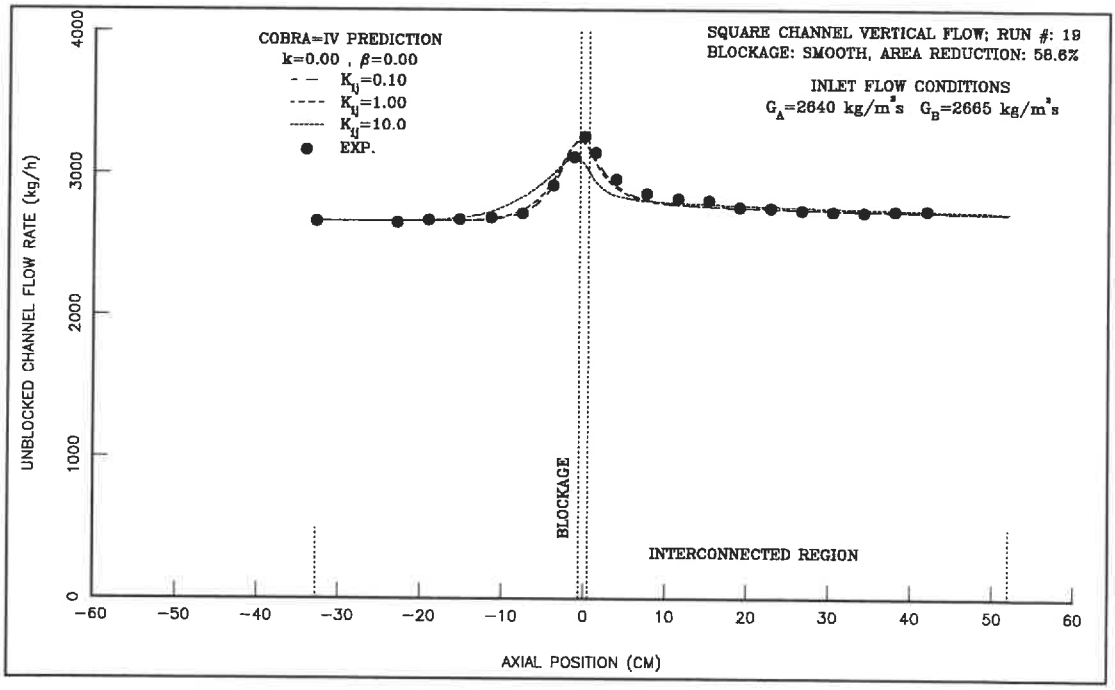


Figure 6.22: Liquid Flow Rate Profile, Single-Phase, Unblocked Channel, RUN #19

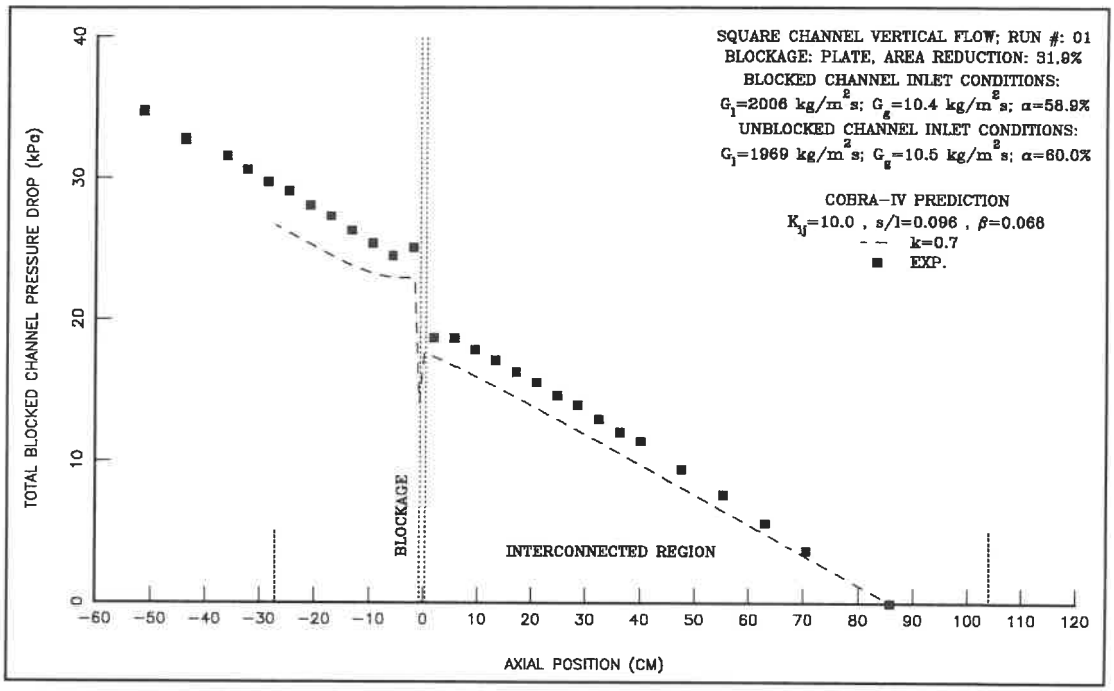


Figure 6.23: Pressure Drop profile, Two-Phase Case, Blocked Channel, RUN #01

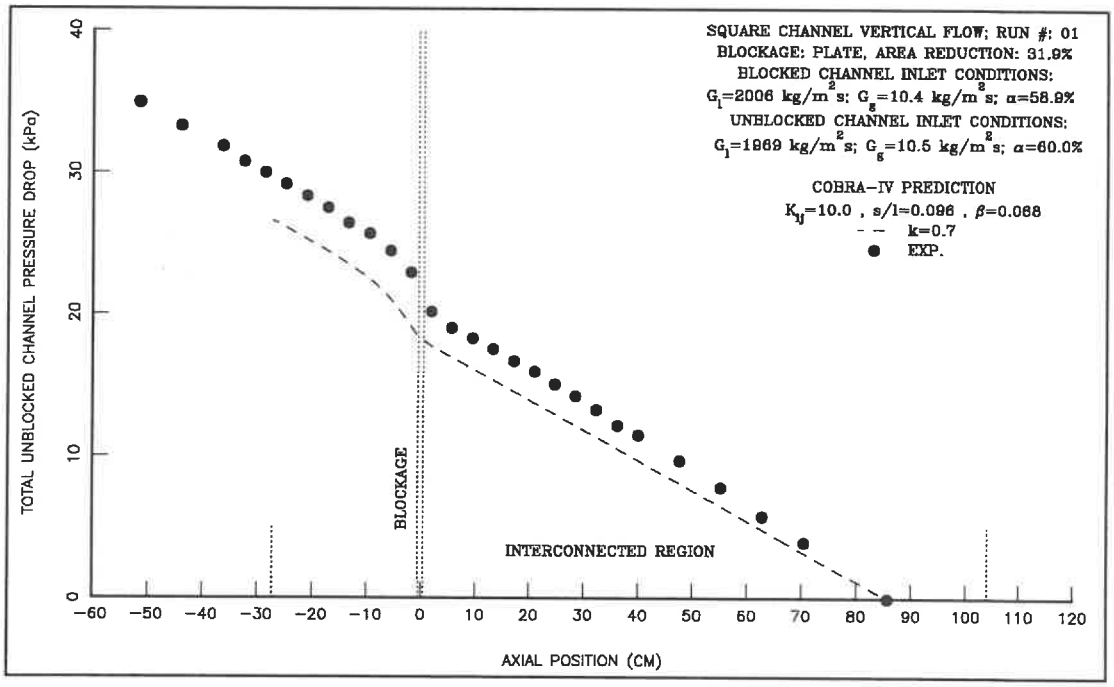


Figure 6.24: Pressure Drop profile, Two-Phase Case, Unblocked Channel, RUN #01

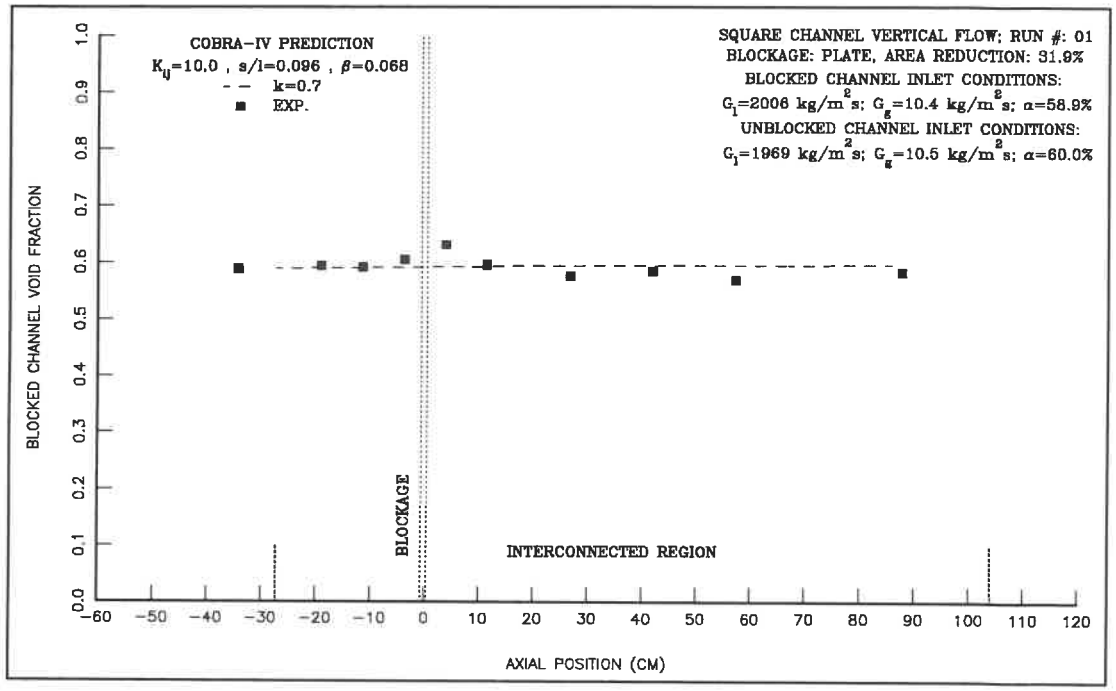


Figure 6.25: Void Fraction profile, Two-Phase Case, Blocked Channel, RUN #01

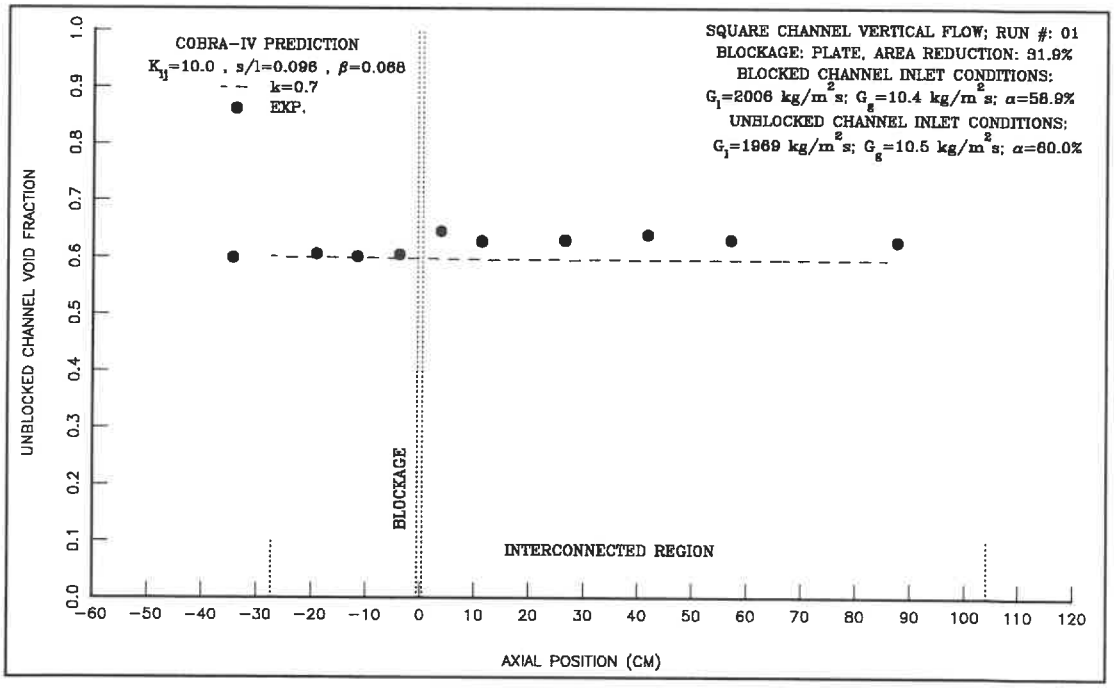


Figure 6.26: Void Fraction profile, Two-Phase Case, Unblocked Channel, RUN #01

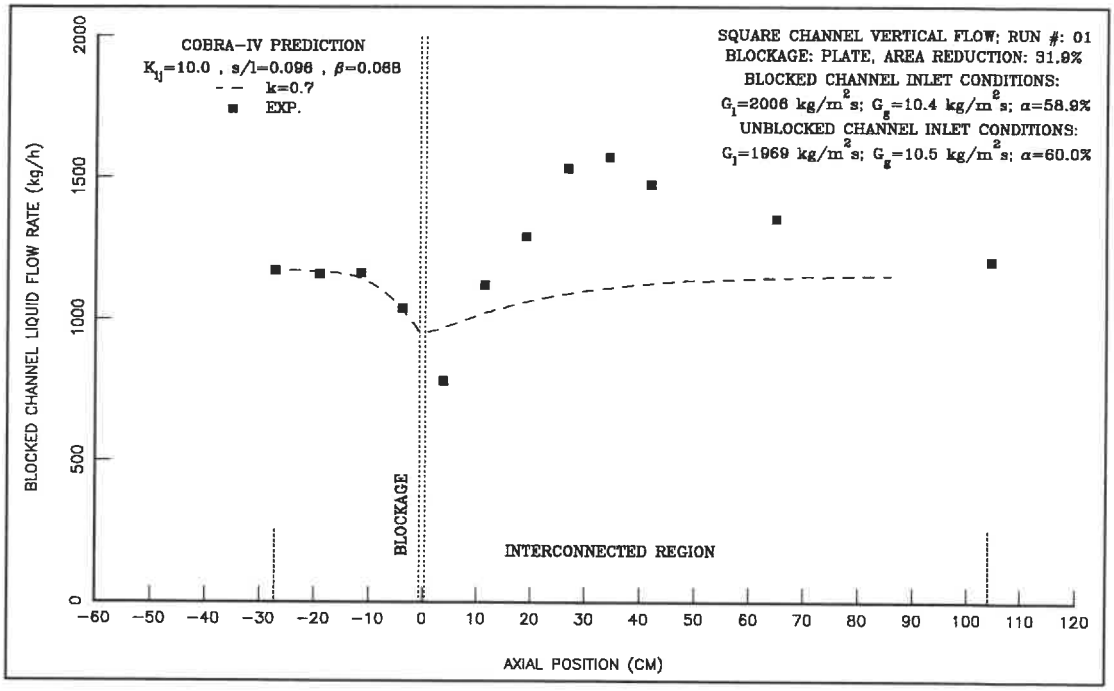


Figure 6.27: Liquid Flow Rate, Two-phase Case, Blocked Channel, RUN #01

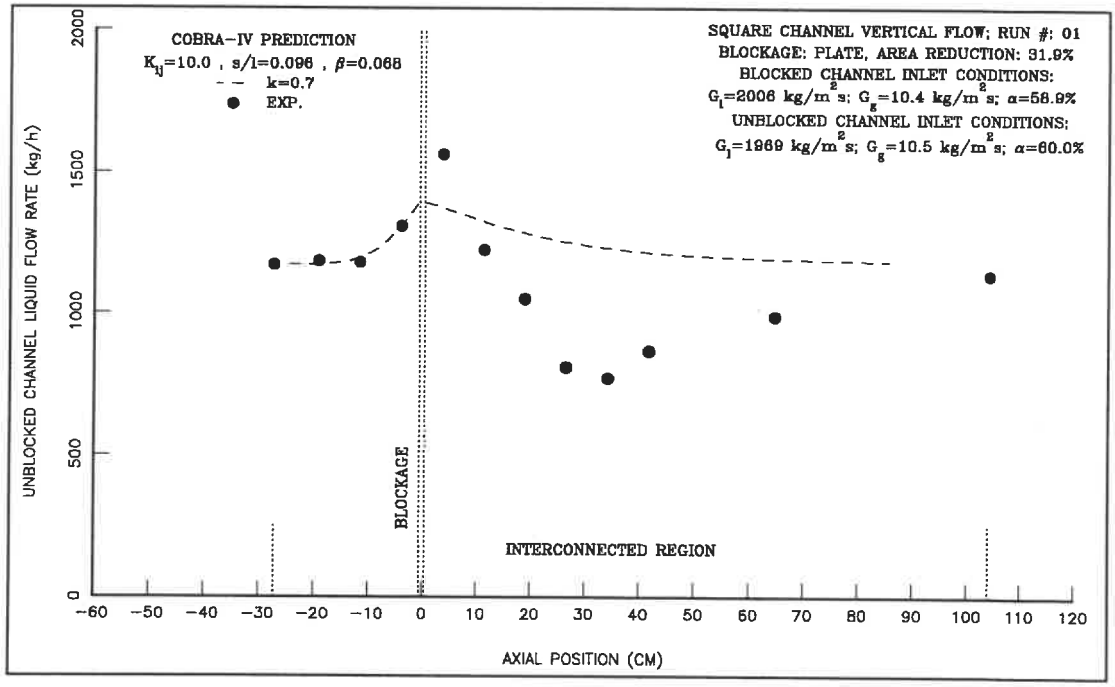


Figure 6.28: Liquid Flow Rate, Two-Phase Case, Unblocked Channel, RUN #01

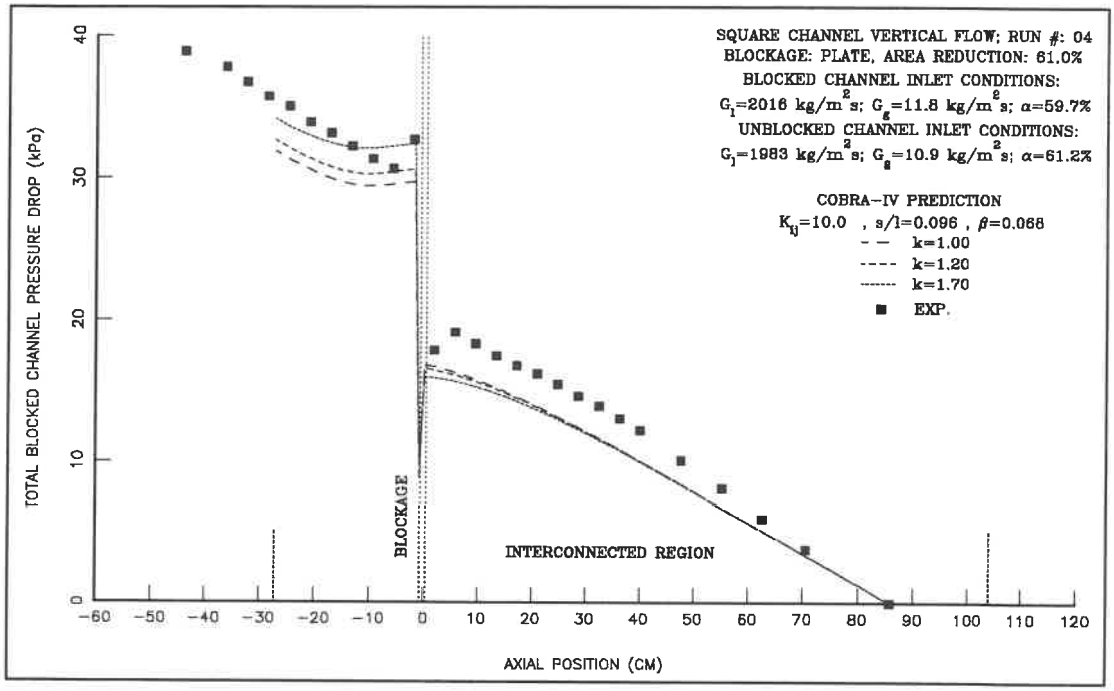


Figure 6.29: Pressure Drop profile, Two-Phase Case, Blocked Channel, RUN #04

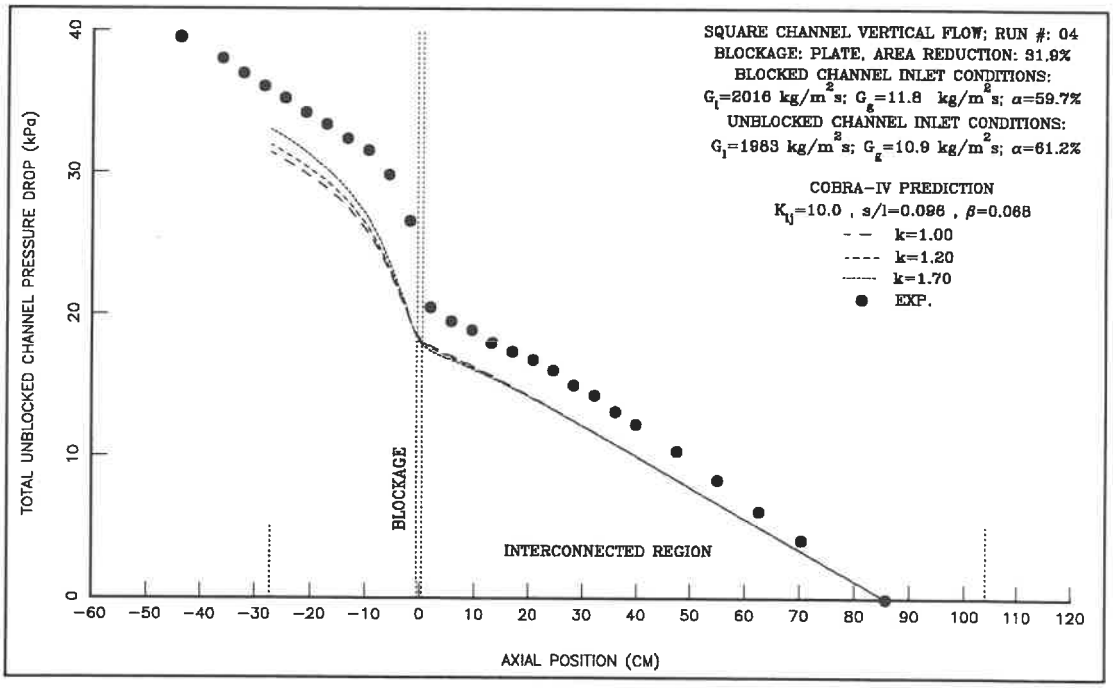


Figure 6.30: Pressure Drop profile, Two-Phase Case, Unblocked Channel, RUN #04

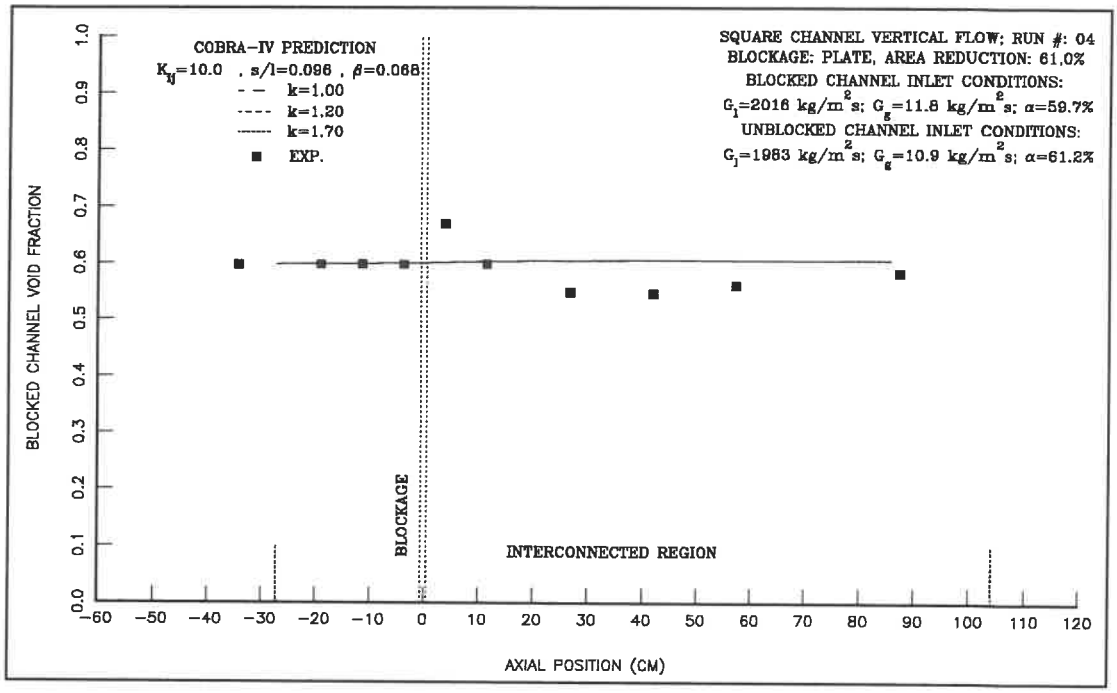


Figure 6.31: Void Fraction profile, Two-Phase Case, Blocked Channel, RUN #04

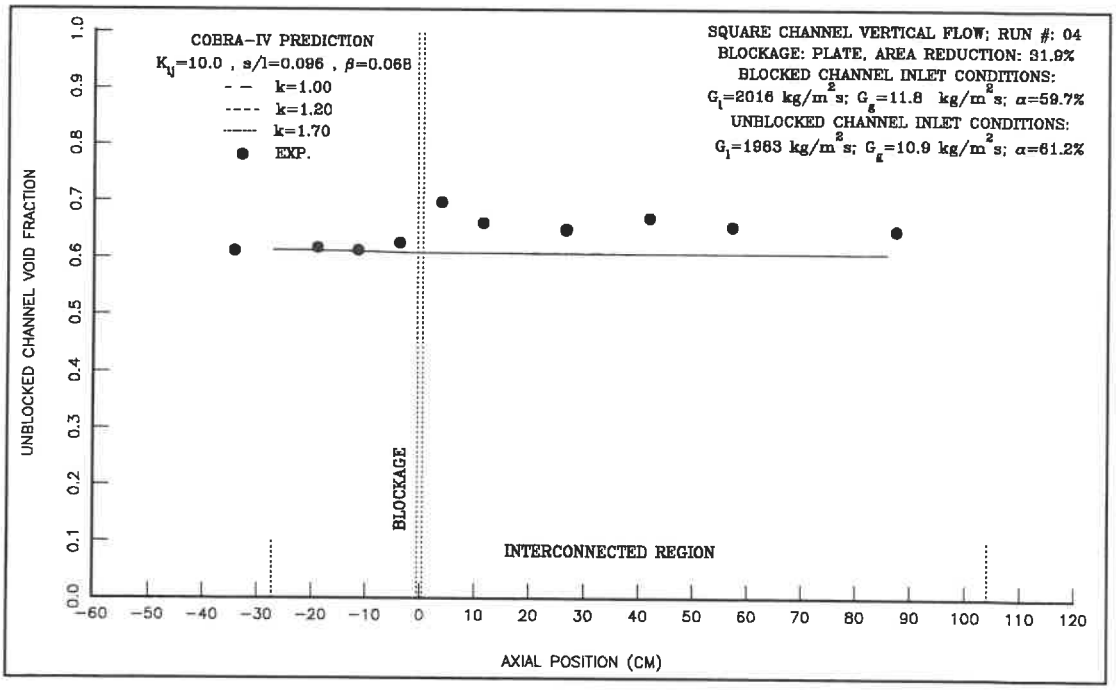


Figure 6.32: Void Fraction profile, Two-Phase Case, Unblocked Channel, RUN #04

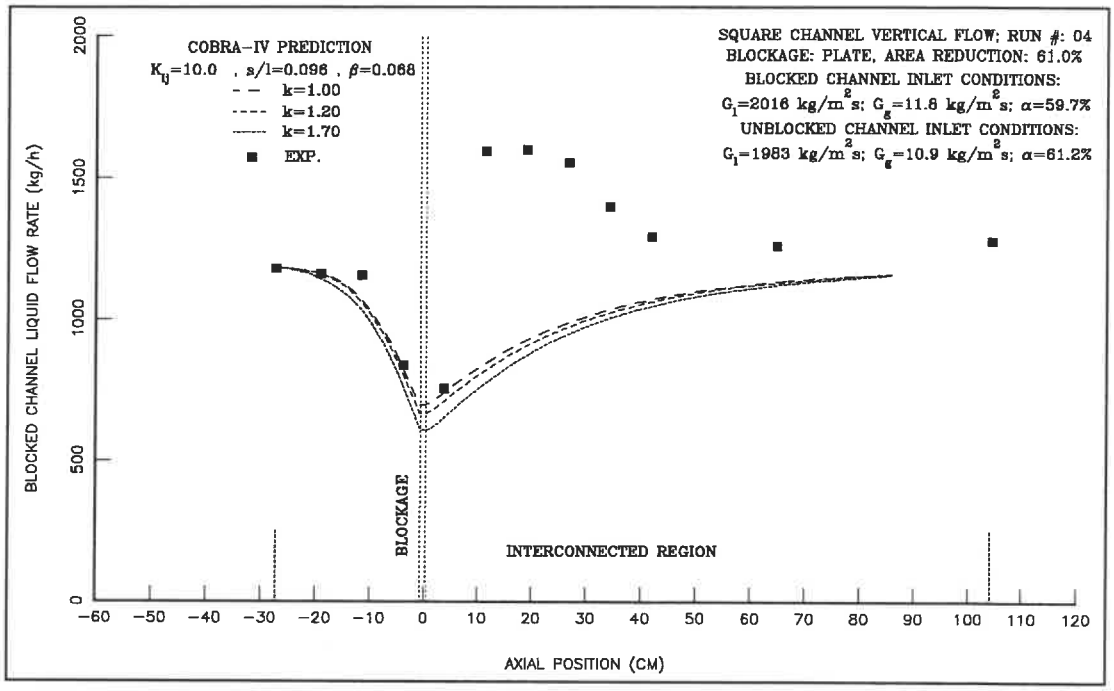


Figure 6.33: Liquid Flow Rate, Two-phase Case, Blocked Channel, RUN #04

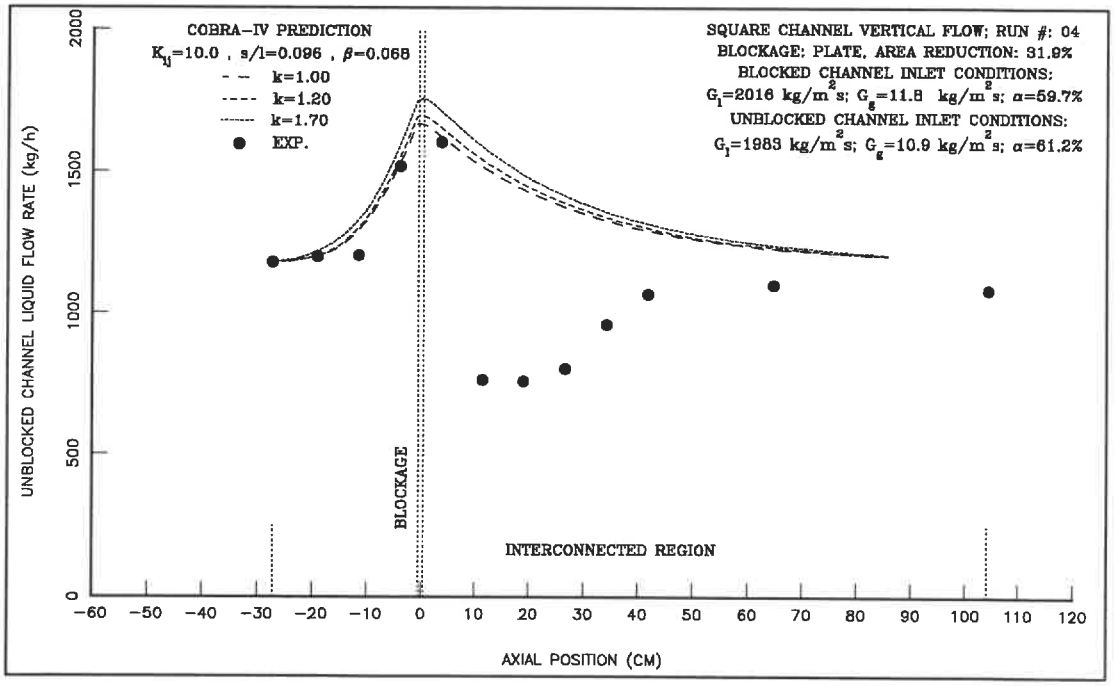


Figure 6.34: Liquid Flow Rate, Two-Phase Case, Unblocked Channel, RUN #04

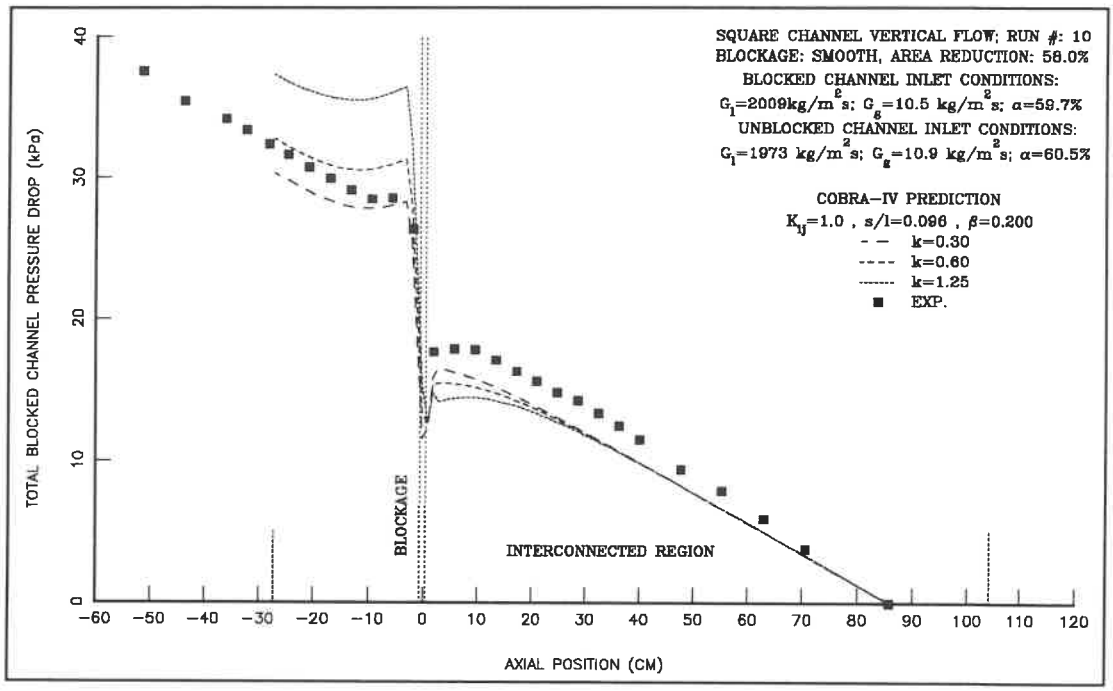


Figure 6.35: Pressure Drop profile, Two-Phase Case, Blocked Channel, RUN #10

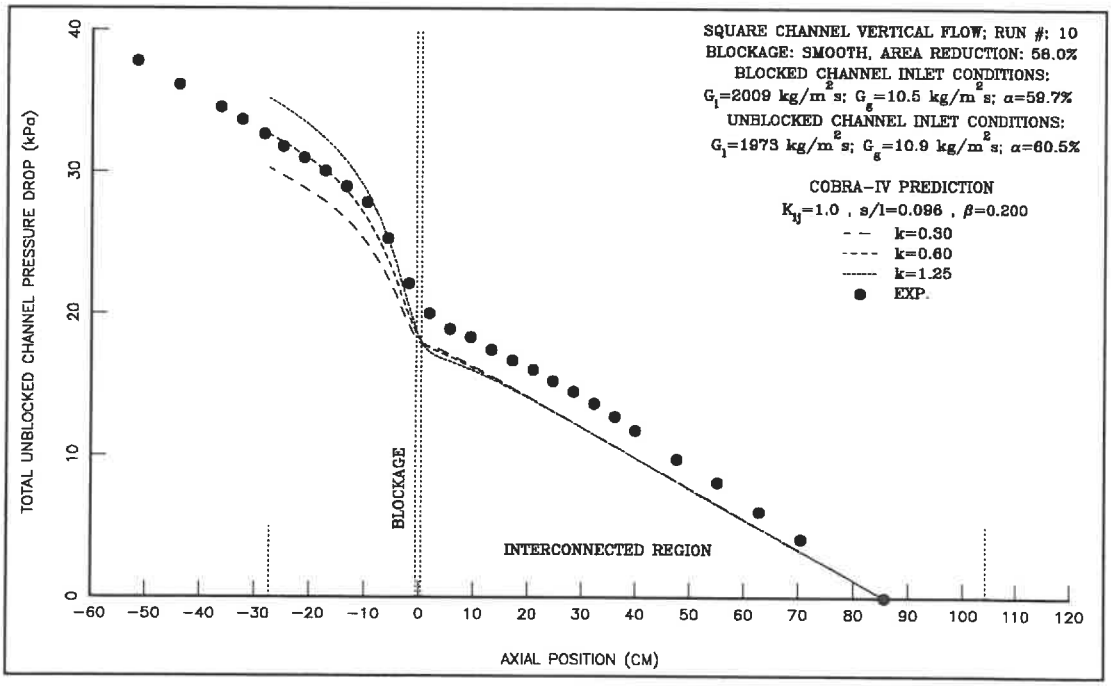


Figure 6.36: Pressure Drop profile, Two-Phase Case, Unblocked Channel, RUN #10

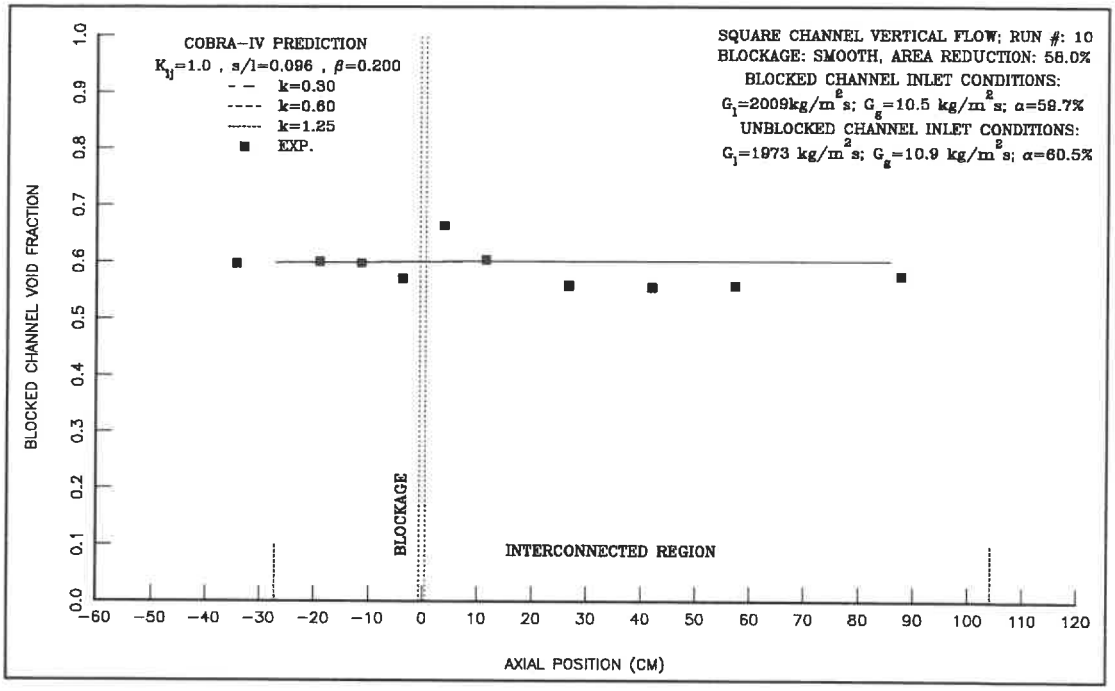


Figure 6.37: Void Fraction profile, Two-Phase Case, Blocked Channel, RUN #10

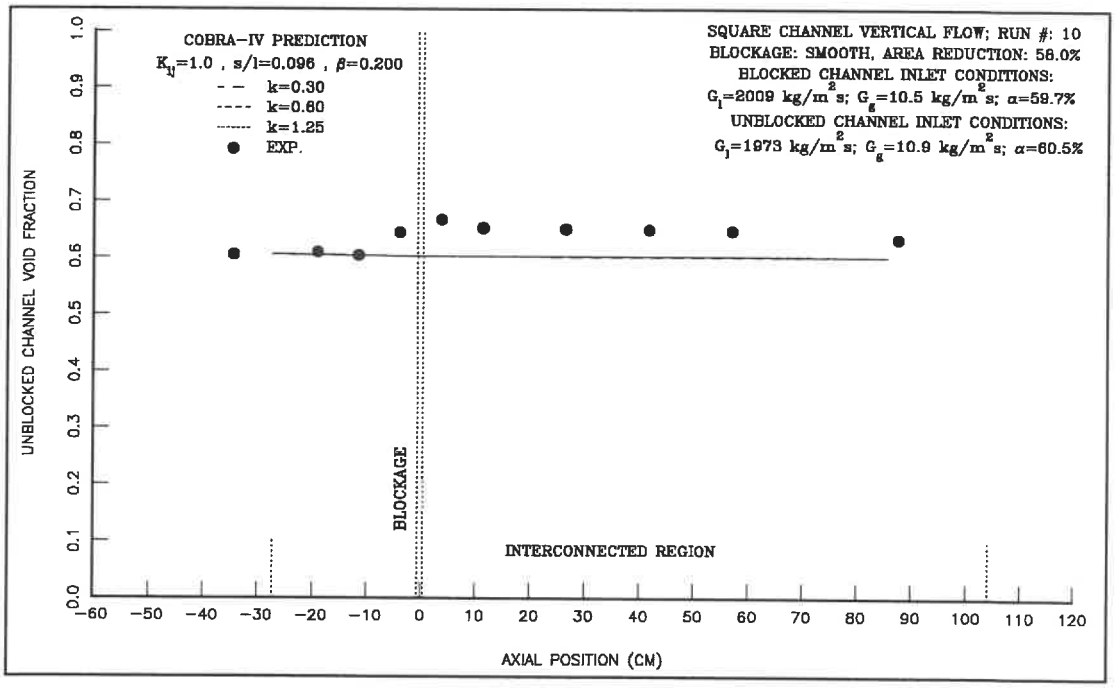


Figure 6.38: Void Fraction profile, Two-Phase Case, Unblocked Channel, RUN #10

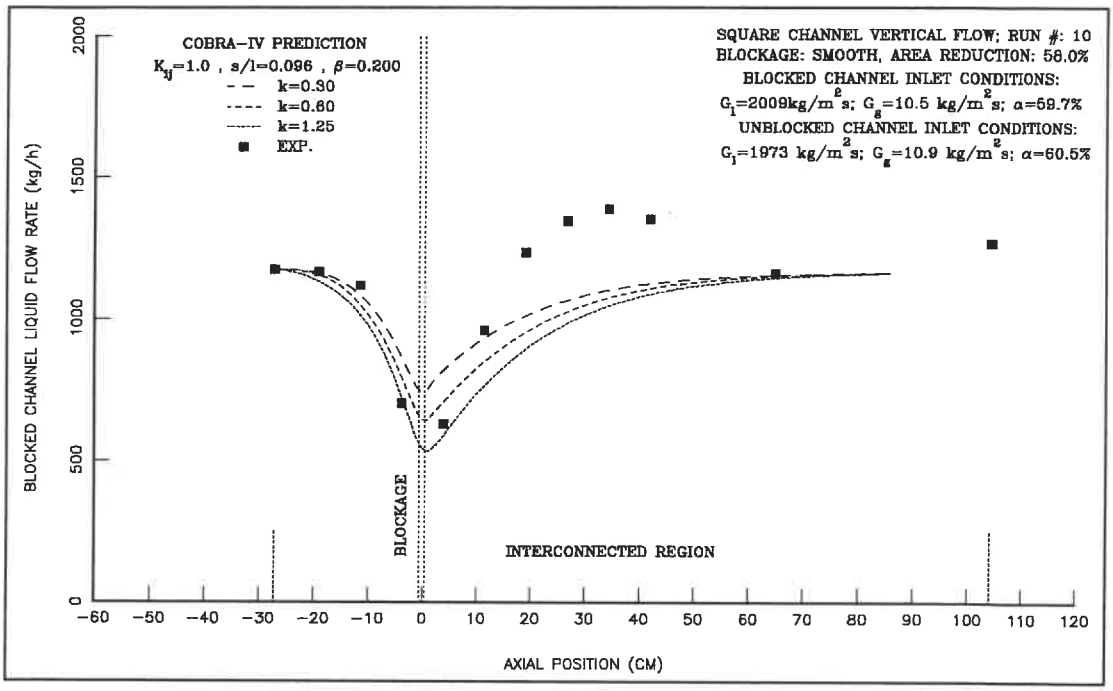


Figure 6.39: Liquid Flow Rate, Two-phase Case, Blocked Channel, RUN #10

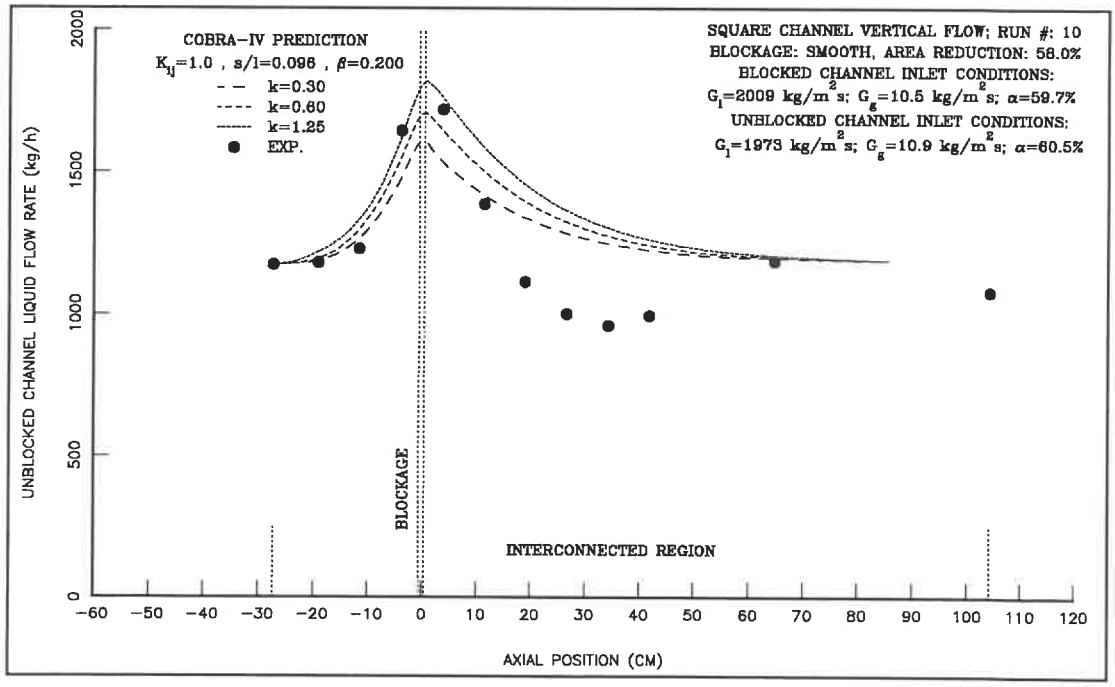


Figure 6.40: Liquid Flow Rate, Two-Phase Case, Unblocked Channel, RUN #10

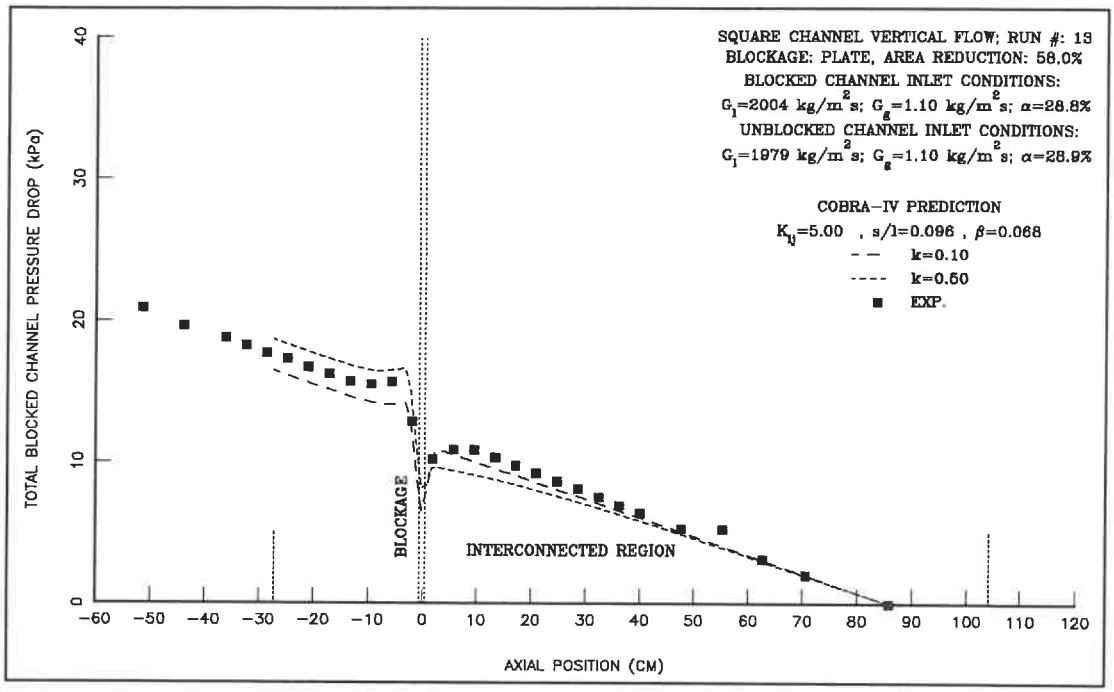


Figure 6.41: Pressure Drop profile, Two-Phase Case, Blocked Channel, RUN #13

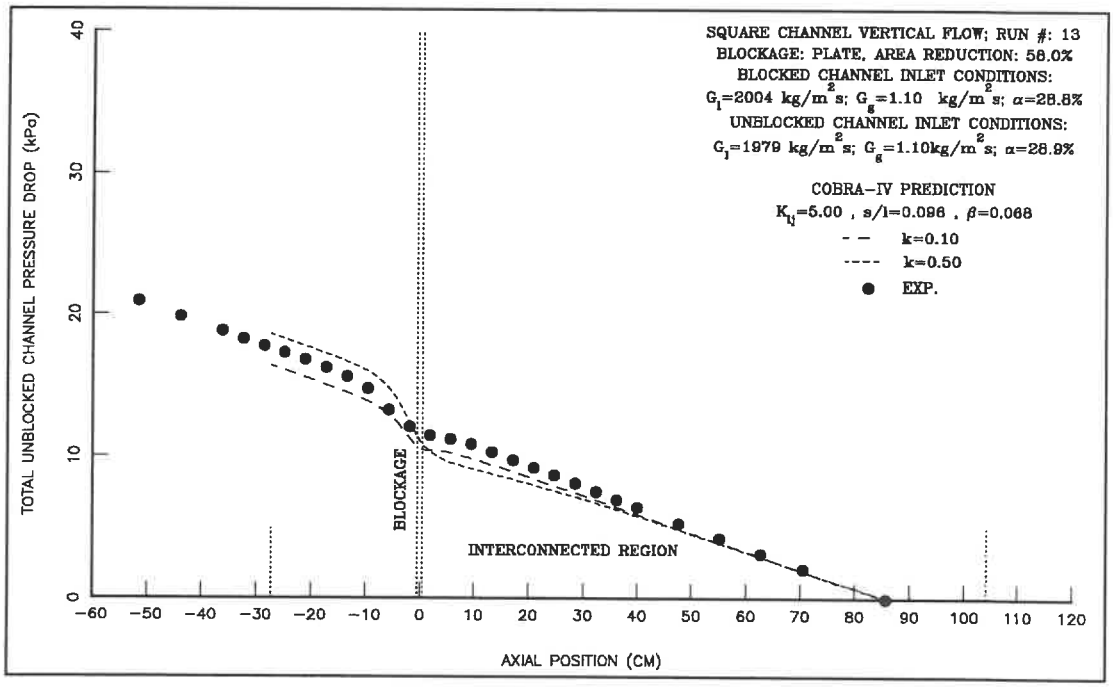


Figure 6.42: Pressure Drop profile, Two-Phase Case, Unblocked Channel, RUN #13

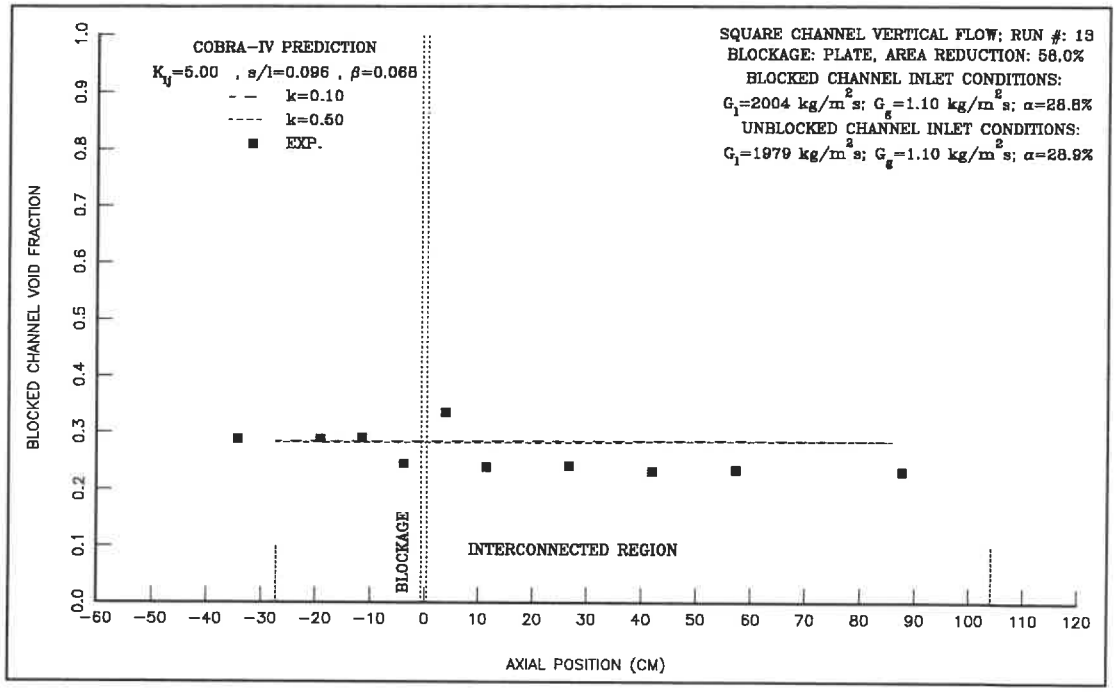


Figure 6.43: Void Fraction profile, Two-Phase Case, Blocked Channel, RUN #13

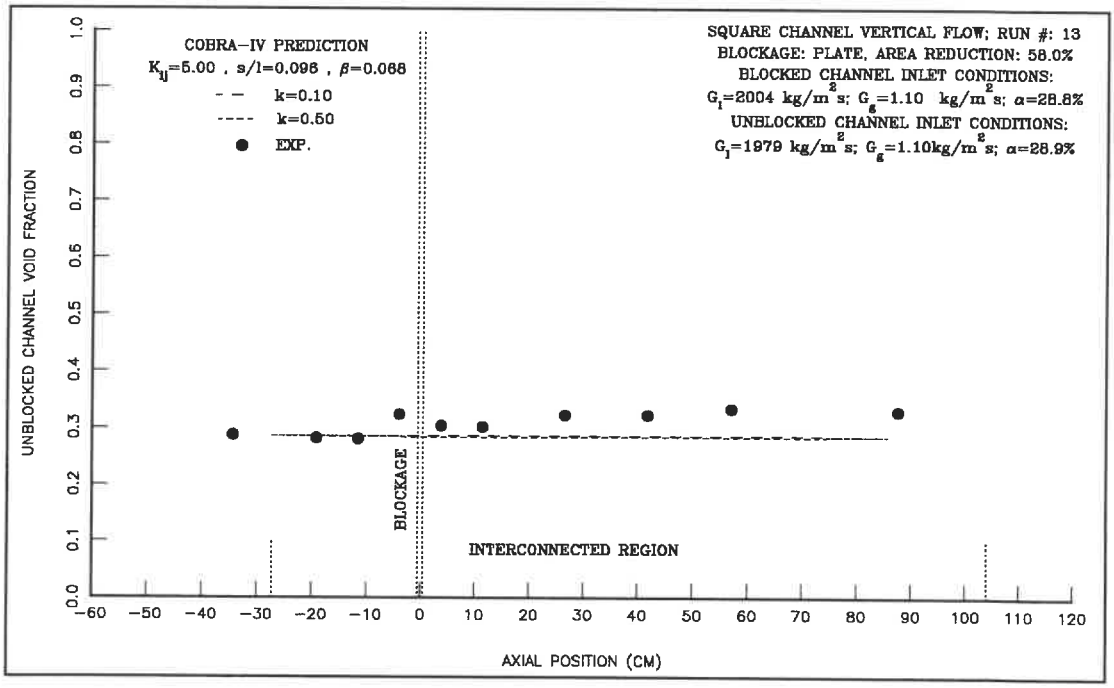


Figure 6.44: Void Fraction profile, Two-Phase Case, Unblocked Channel, RUN #13

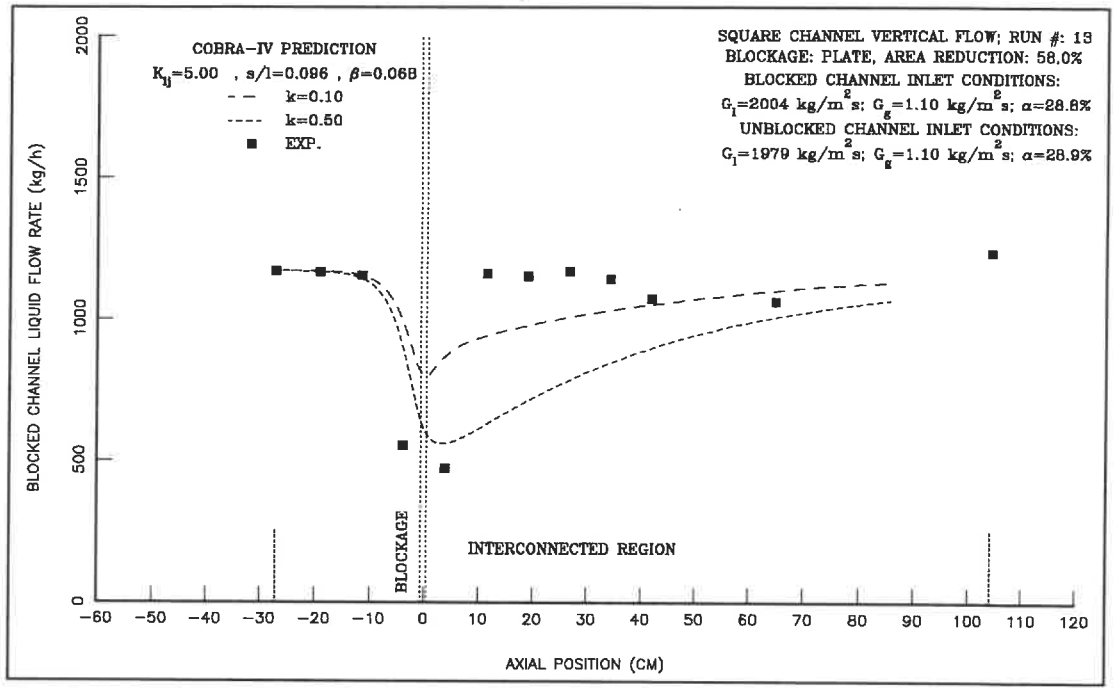


Figure 6.45: Liquid Flow Rate, Two-phase Case, Blocked Channel, RUN #13

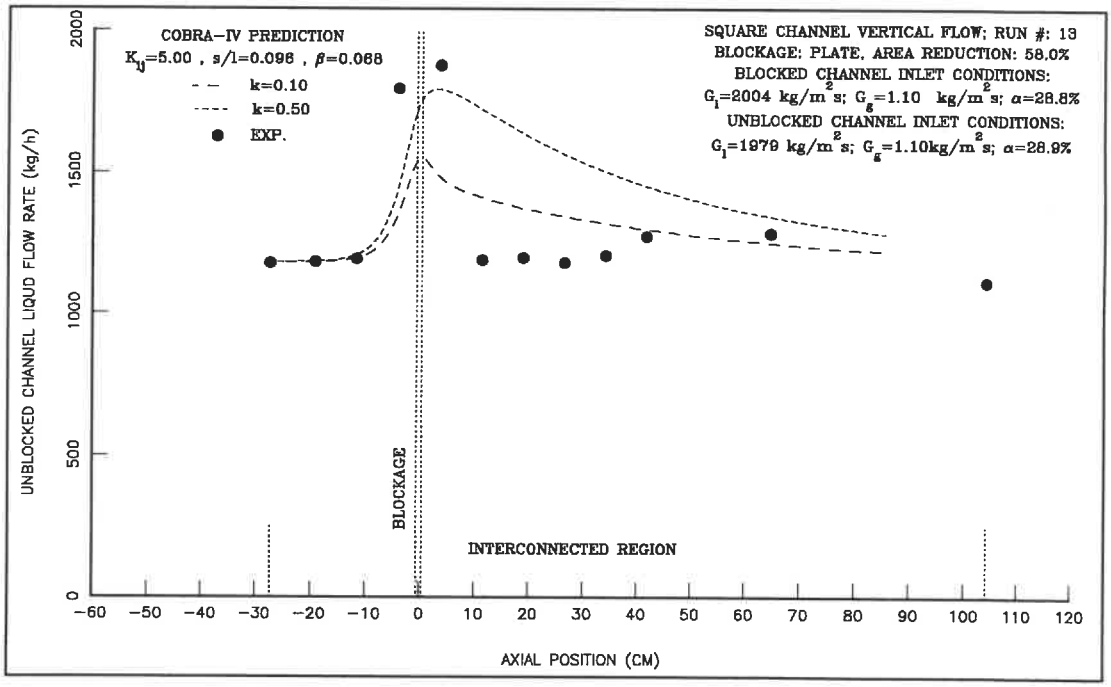


Figure 6.46: Liquid Flow Rate, Two-Phase Case, Unblocked Channel, RUN #13

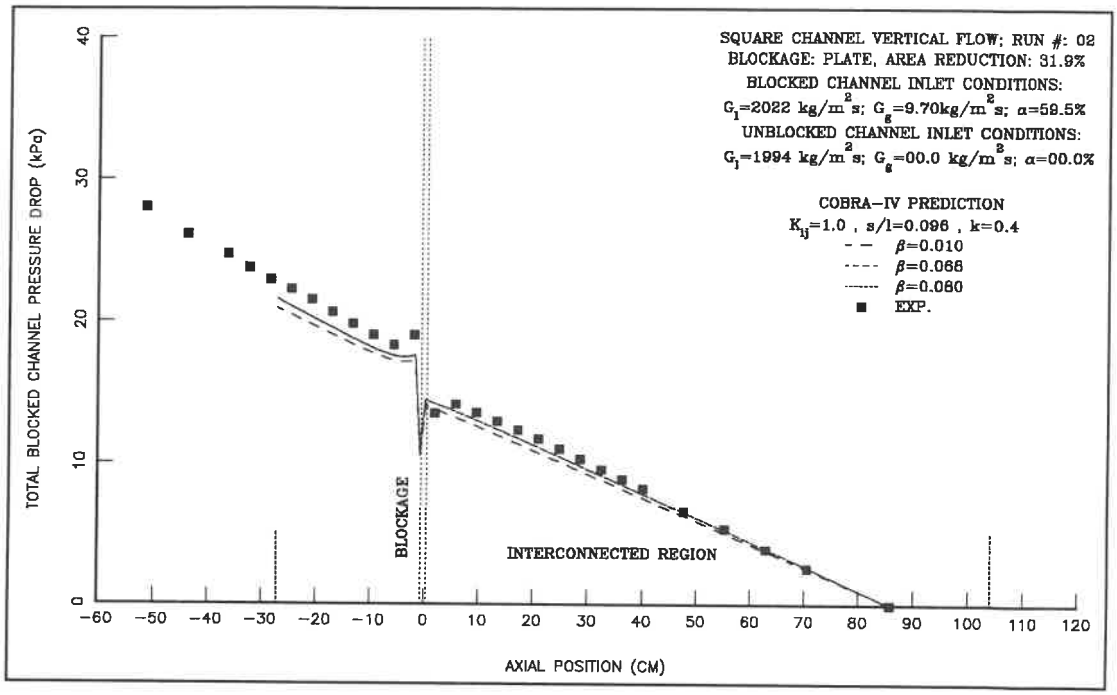


Figure 6.47: Pressure Drop profile, Two-Phase Case, Blocked Channel, RUN #02

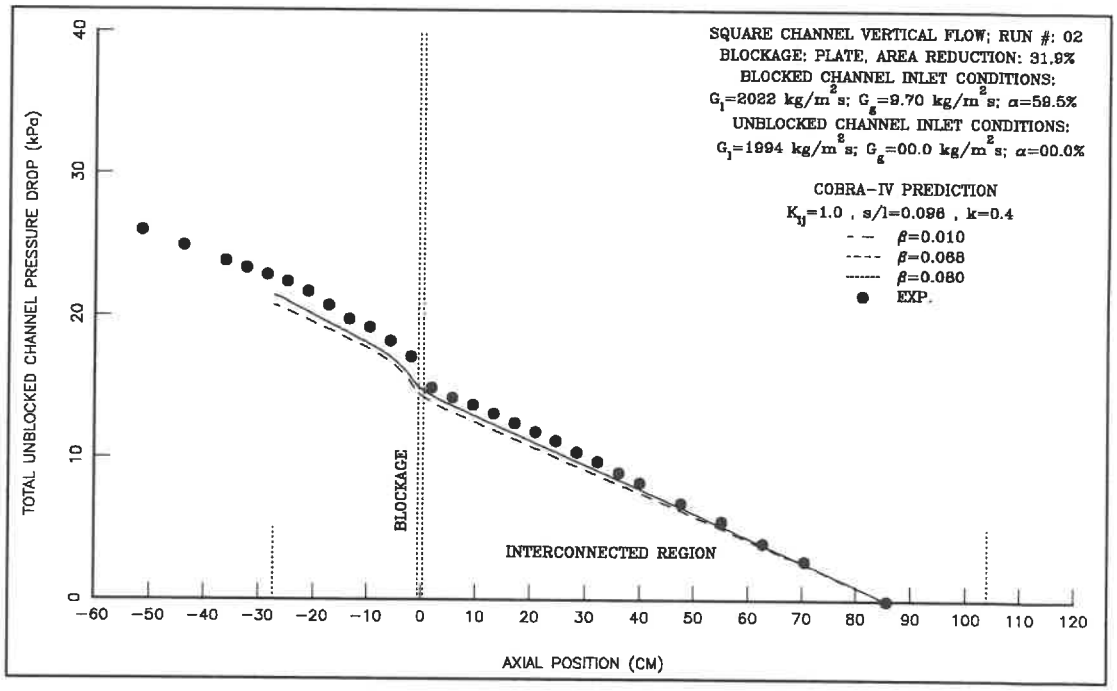


Figure 6.48: Pressure Drop profile, Two-Phase Case, Unblocked Channel, RUN #02

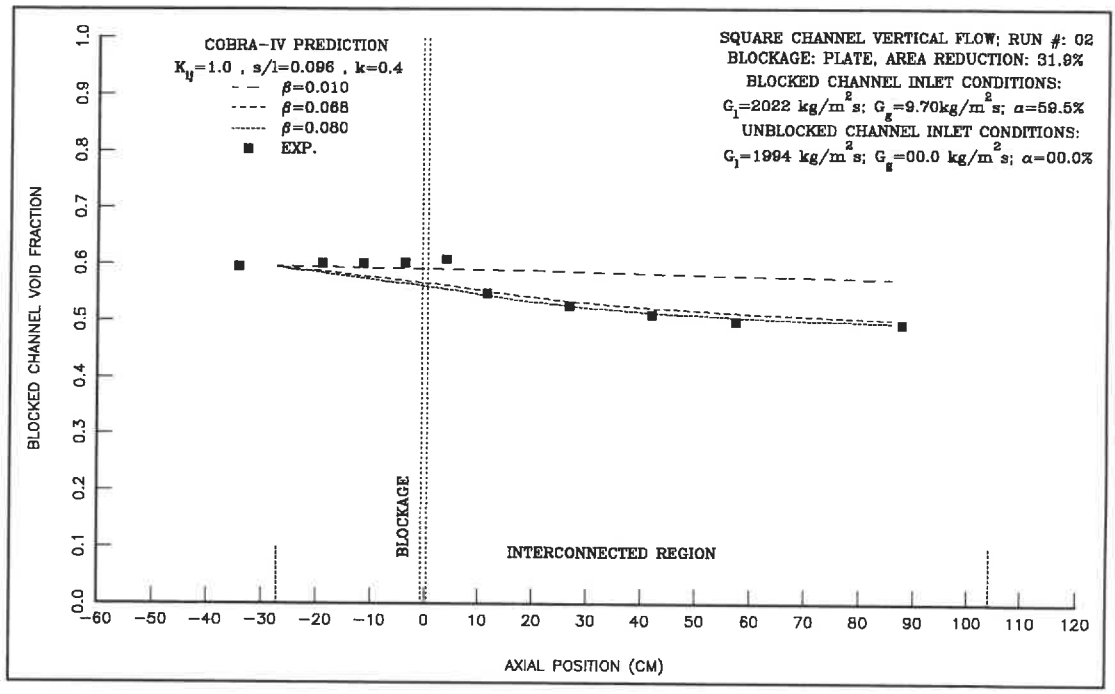


Figure 6.49: Void Fraction profile, Two-Phase Case, Blocked Channel, RUN #02

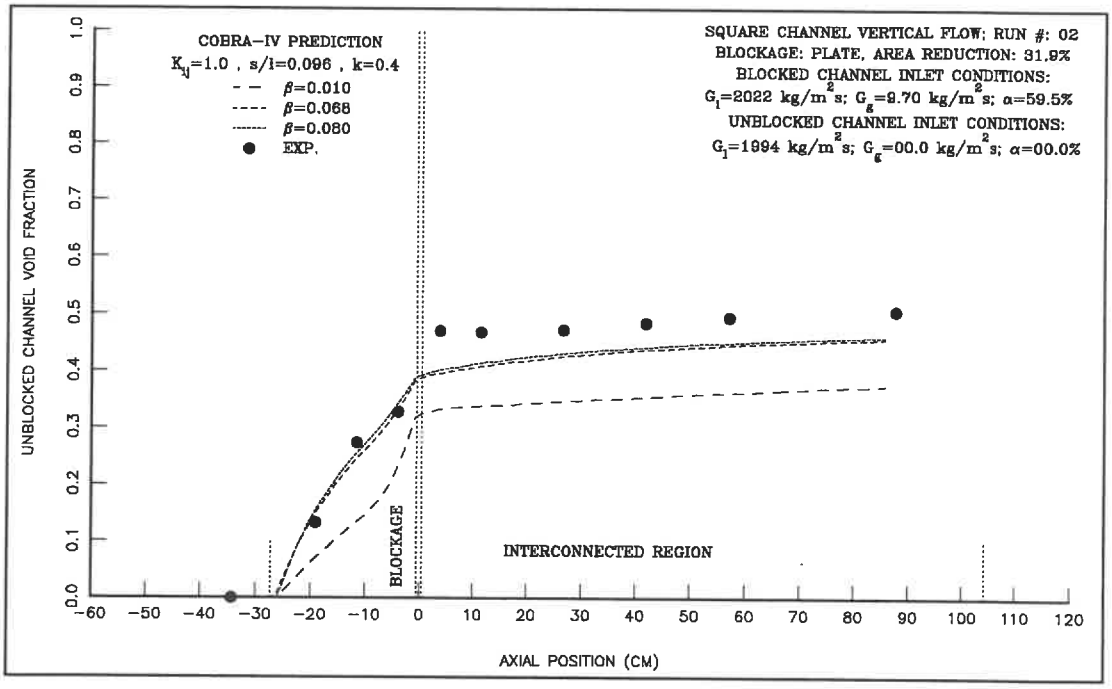


Figure 6.50: Void Fraction profile, Two-Phase Case, Unblocked Channel, RUN #02

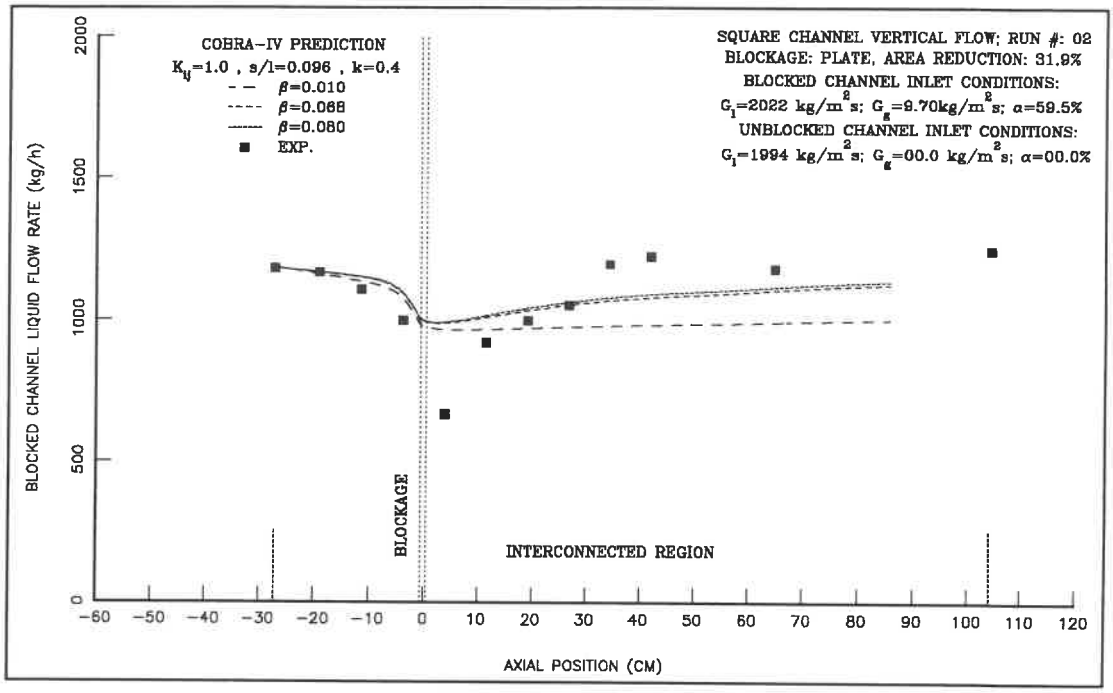


Figure 6.51: Liquid Flow Rate, Two-phase Case, Blocked Channel, RUN #02

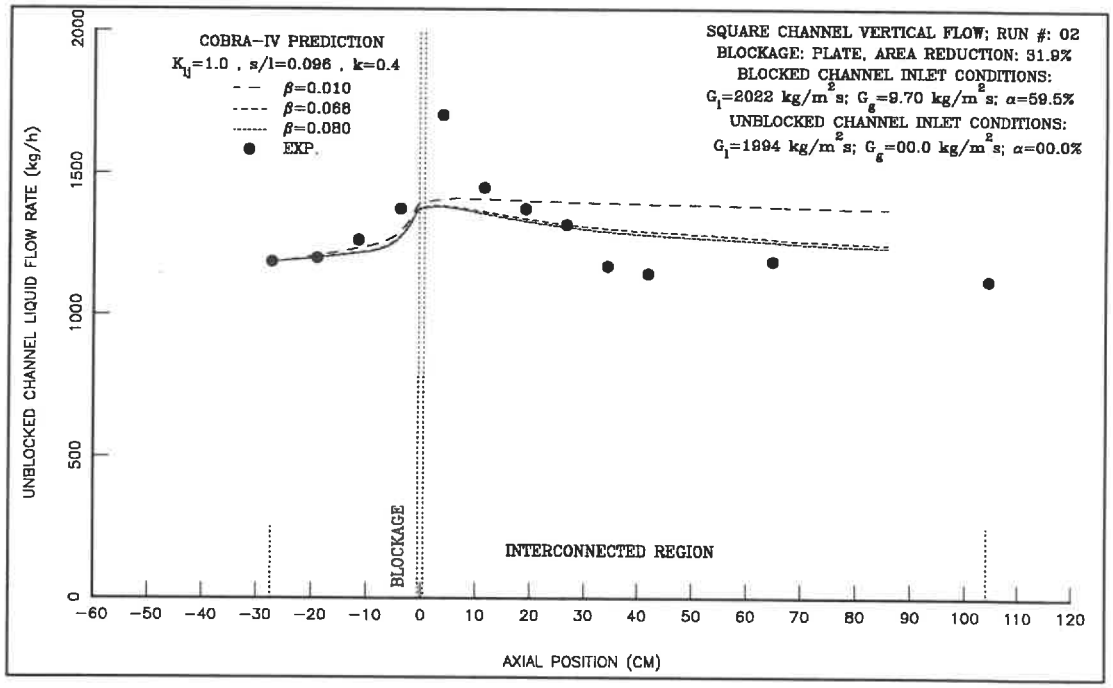


Figure 6.52: Liquid Flow Rate, Two-Phase Case, Unblocked Channel, RUN #02

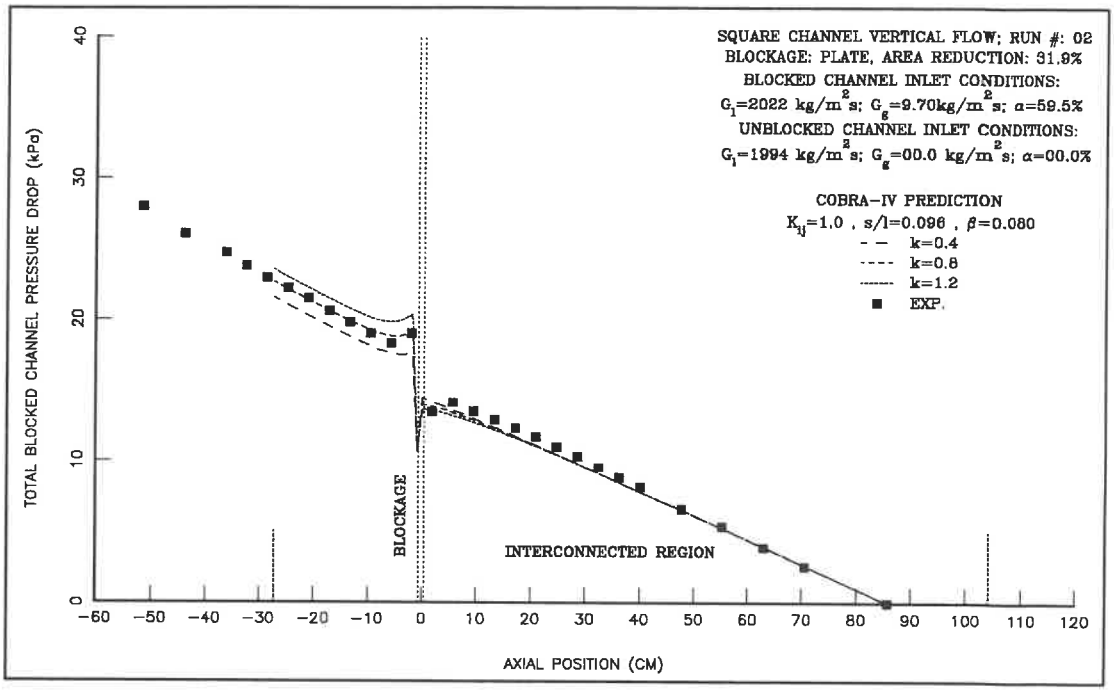


Figure 6.53: Pressure Drop profile, Two-Phase Case, Blocked Channel, RUN #02

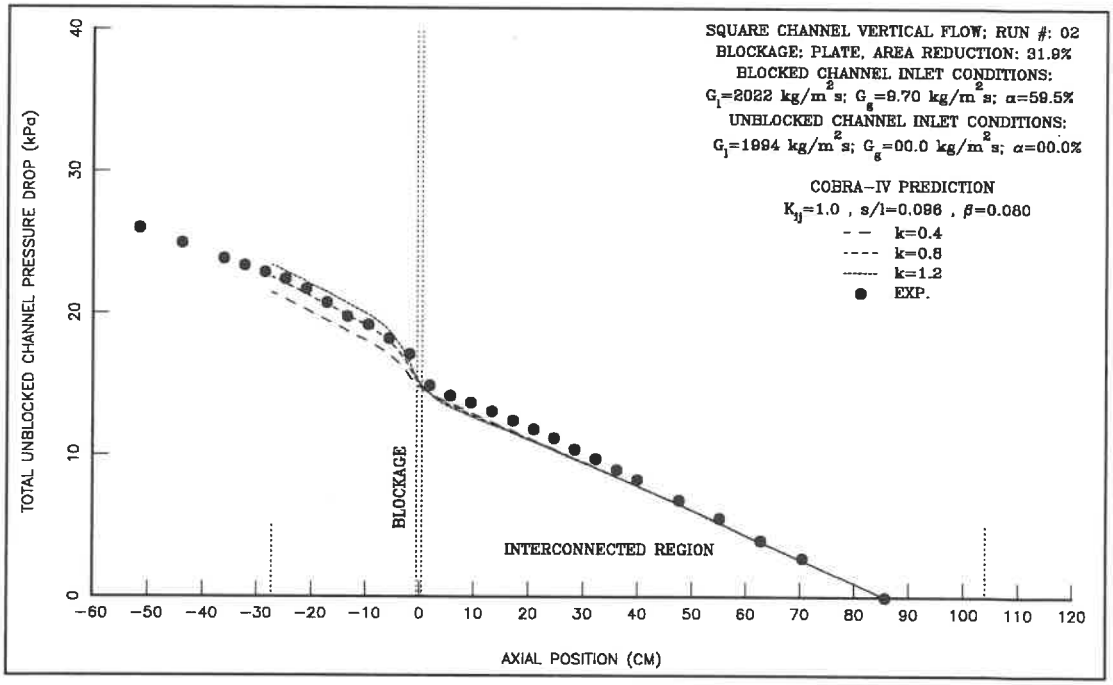


Figure 6.54: Pressure Drop profile, Two-Phase Case, Unblocked Channel, RUN #02

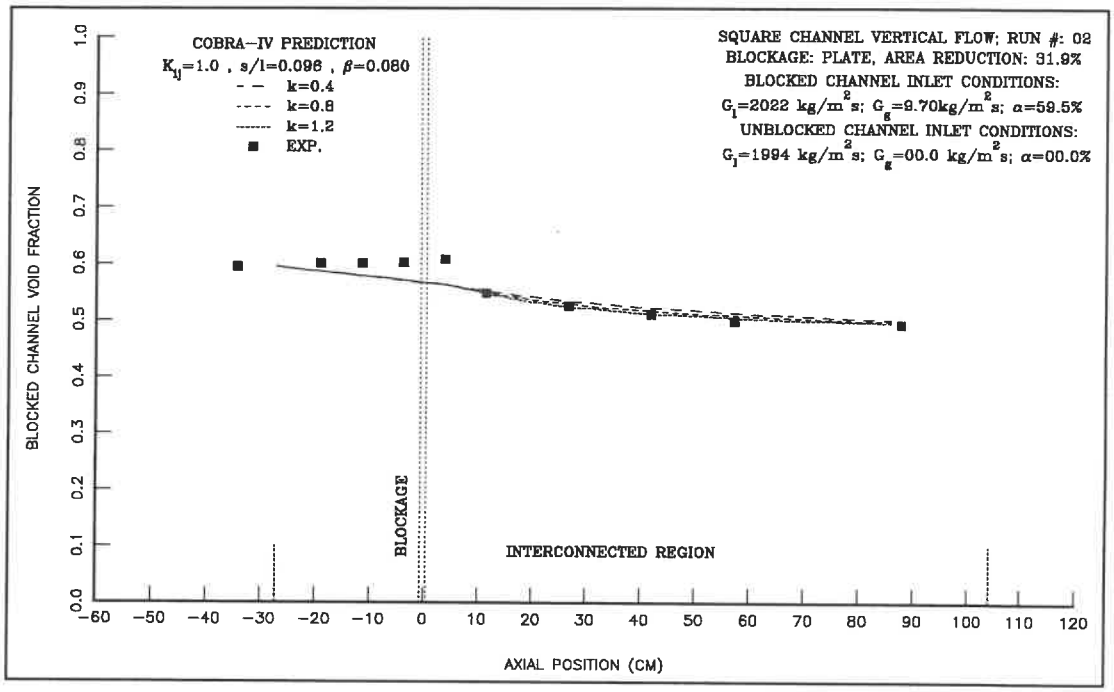


Figure 6.55: Void Fraction profile, Two-Phase Case, Blocked Channel, RUN #02

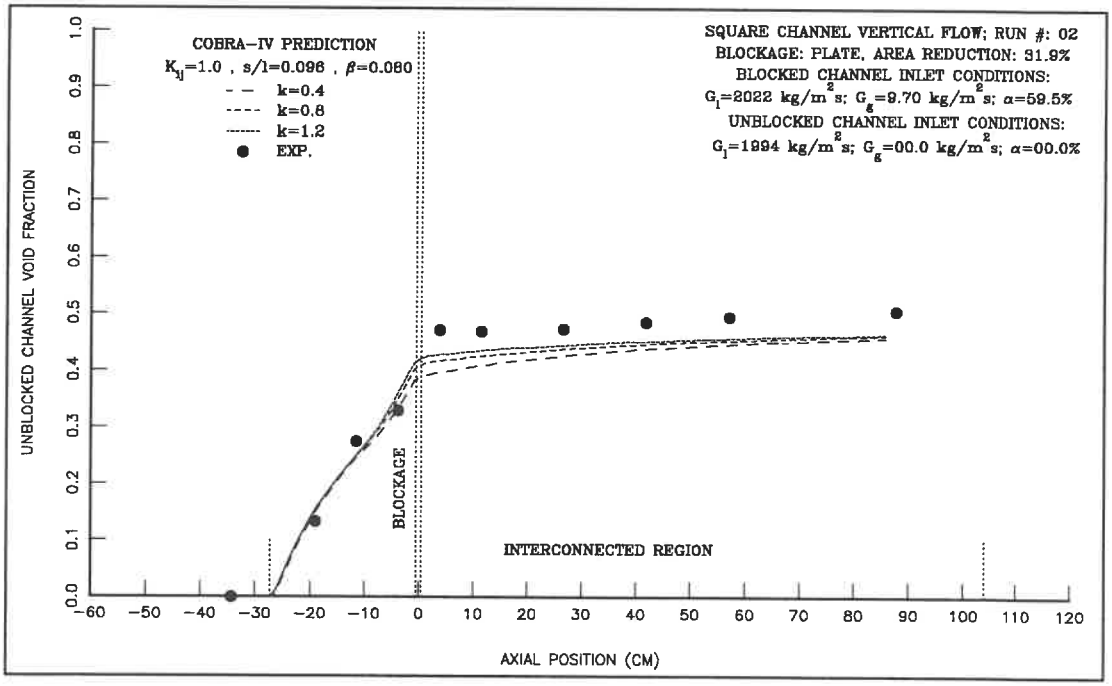


Figure 6.56: Void Fraction profile, Two-Phase Case, Unblocked Channel, RUN #02

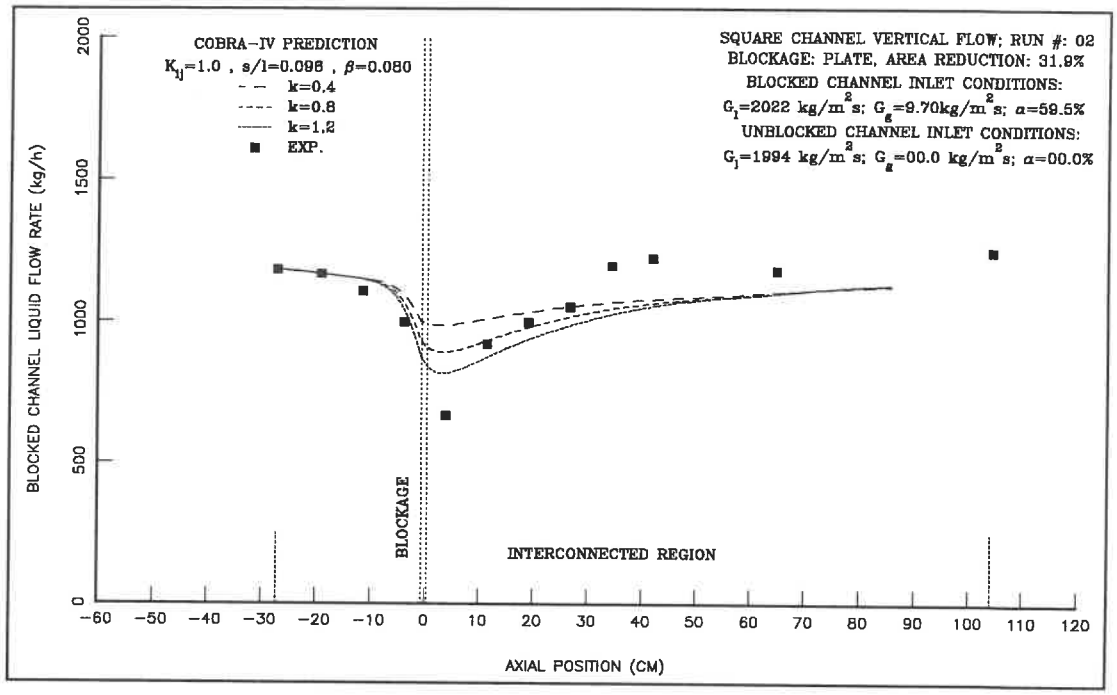


Figure 6.57: Liquid Flow Rate, Two-phase Case, Blocked Channel, RUN #02

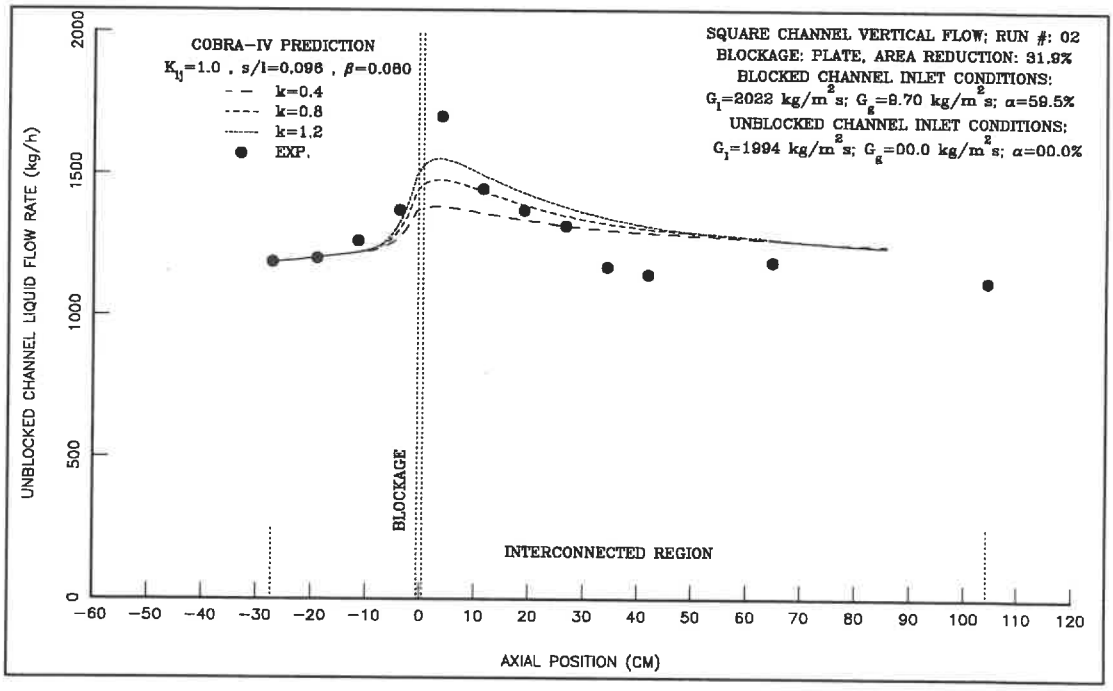


Figure 6.58: Liquid Flow Rate, Two-Phase Case, Unblocked Channel, RUN #02

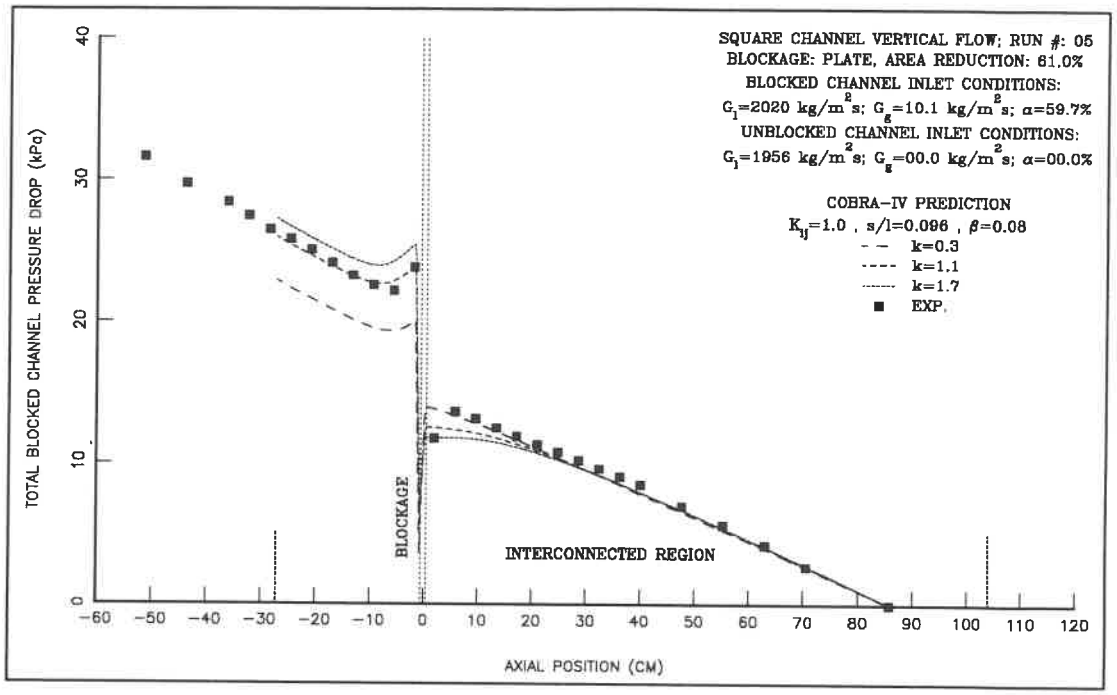


Figure 6.59: Pressure Drop profile, Two-Phase Case, Blocked Channel, RUN #05

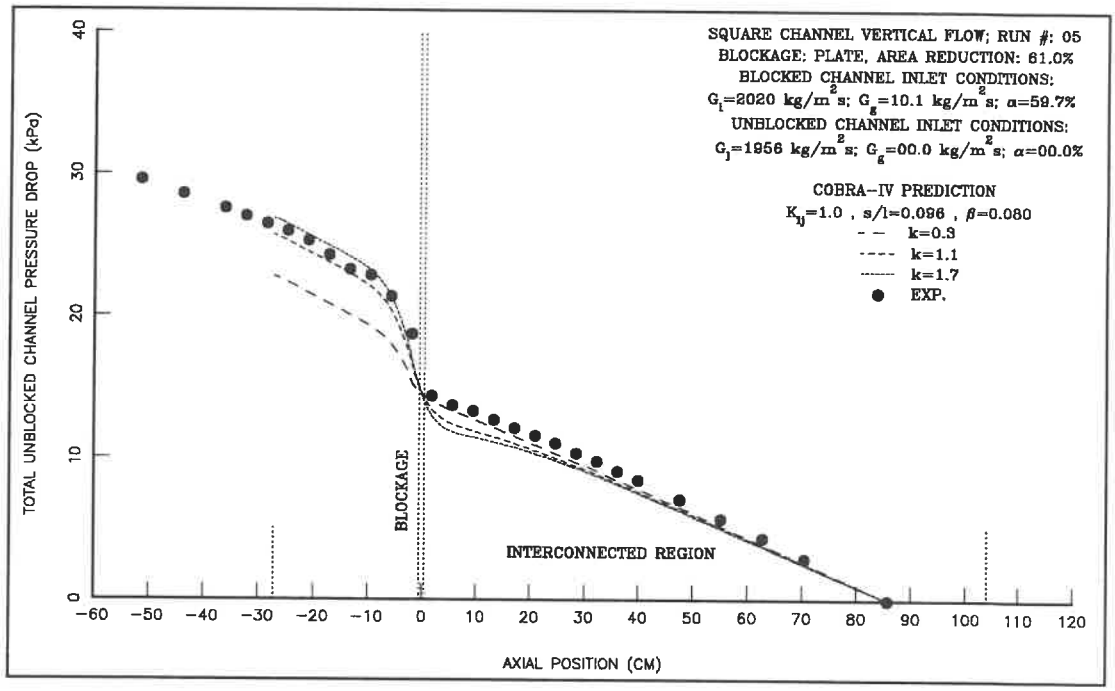


Figure 6.60: Pressure Drop profile, Two-Phase Case, Unblocked Channel, RUN #05

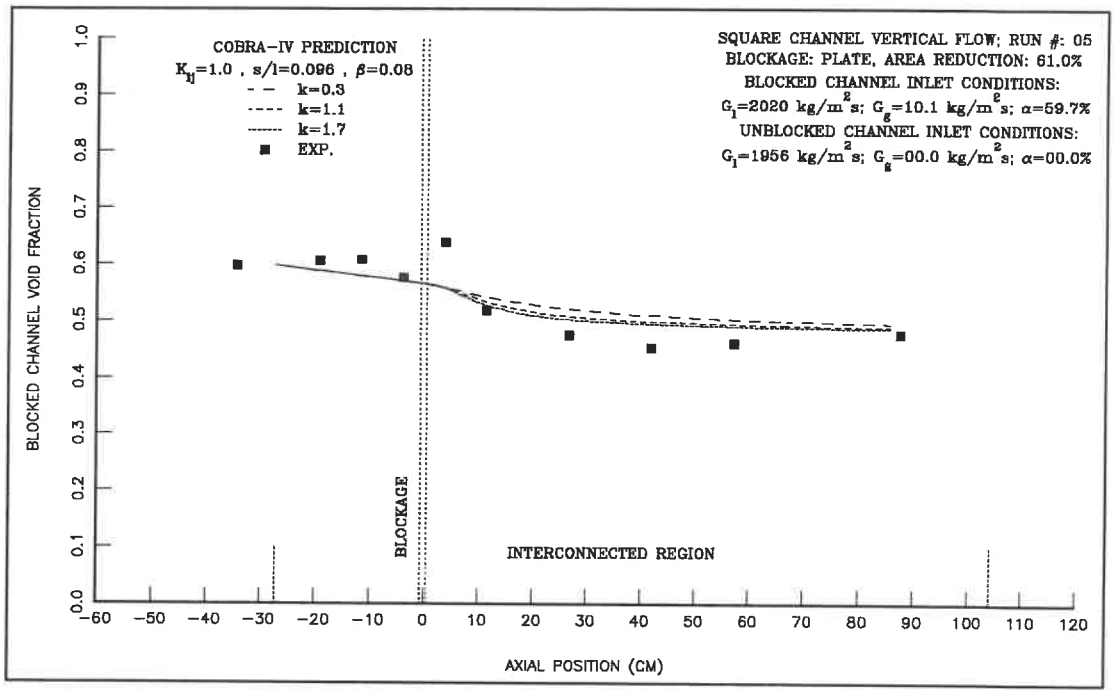


Figure 6.61: Void Fraction profile, Two-Phase Case, Blocked Channel, RUN #05

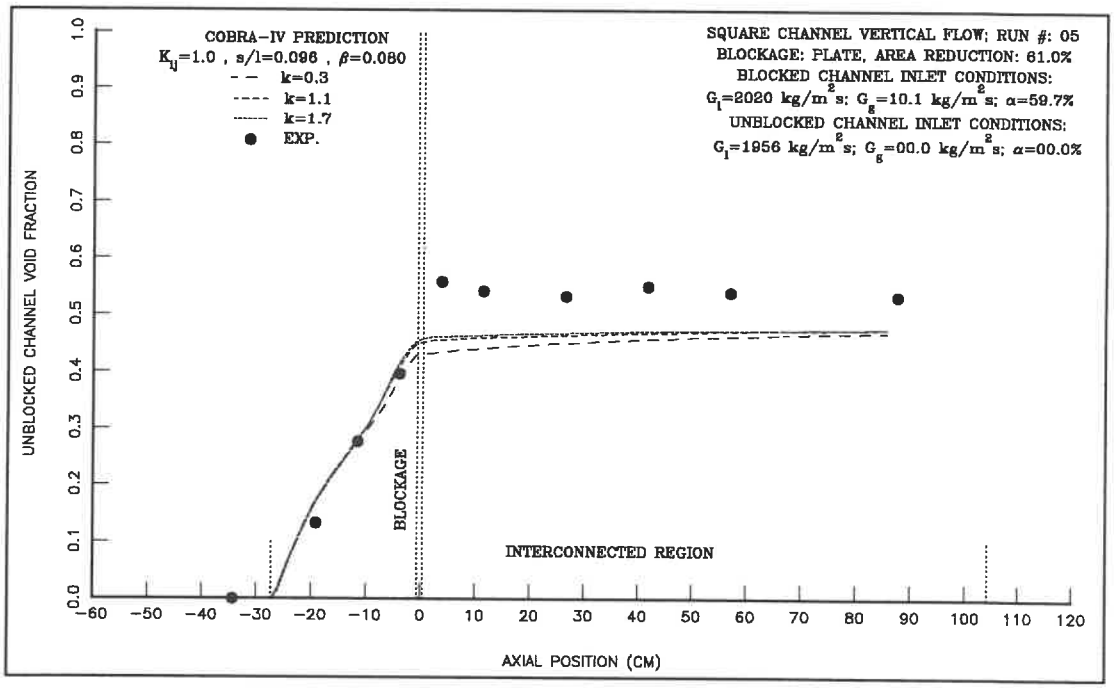


Figure 6.62: Void Fraction profile, Two-Phase Case, Unblocked Channel, RUN #05

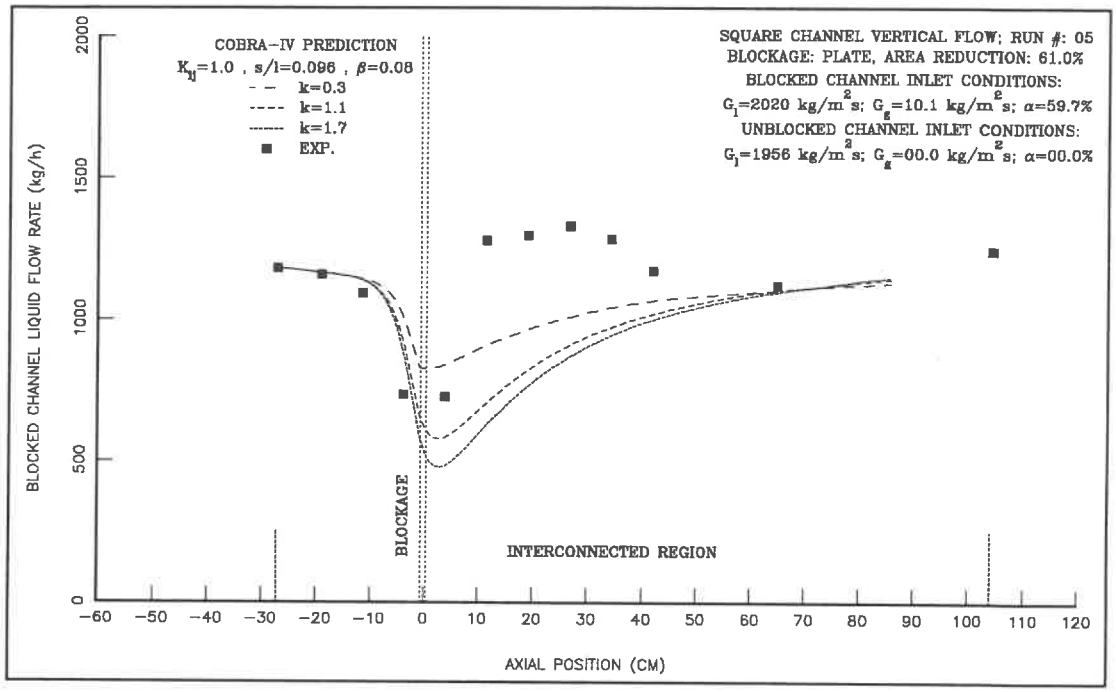


Figure 6.63: Liquid Flow Rate, Two-phase Case, Blocked Channel, RUN #05

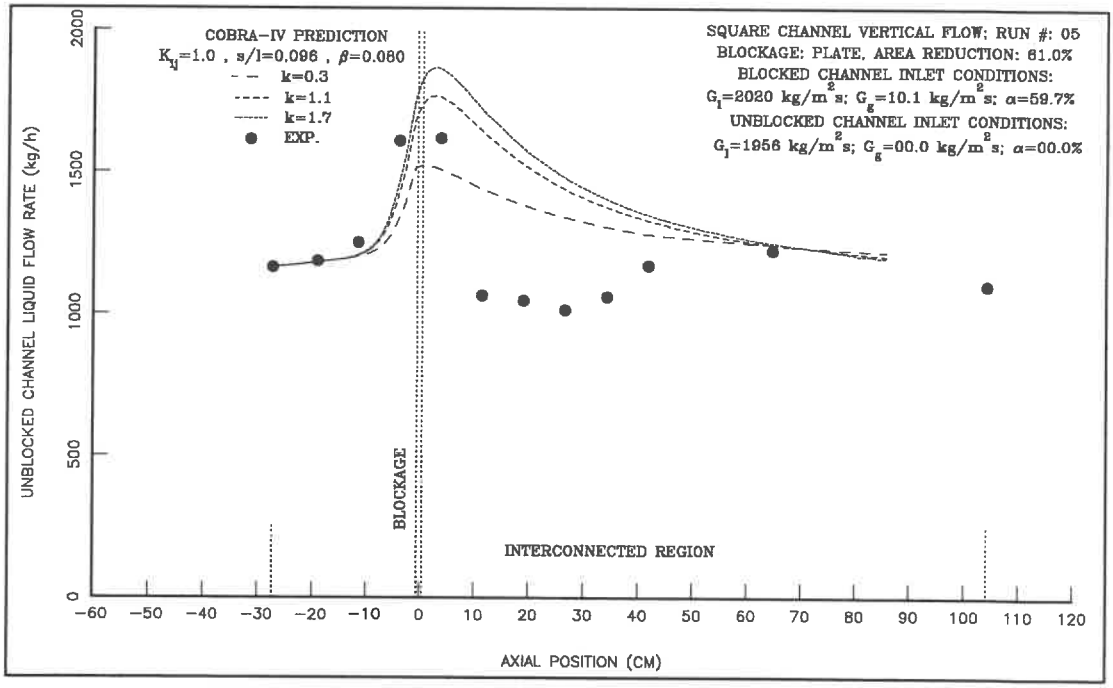


Figure 6.64: Liquid Flow Rate, Two-Phase Case, Unblocked Channel, RUN #05

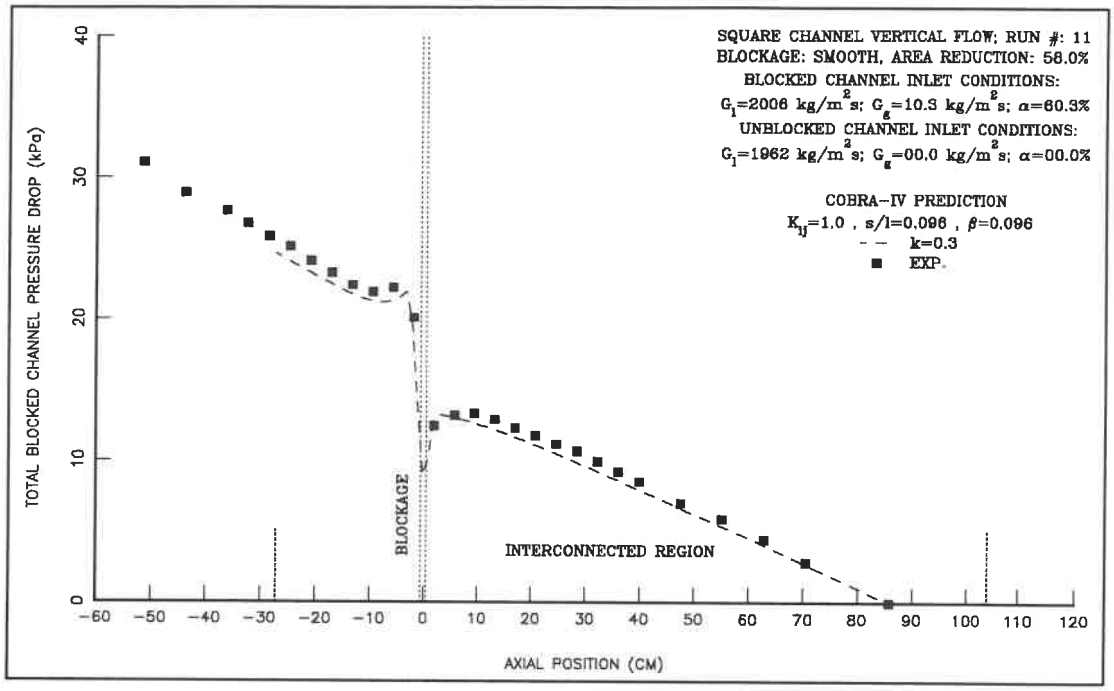


Figure 6.65: Pressure Drop profile, Two-Phase Case, Blocked Channel, RUN #11

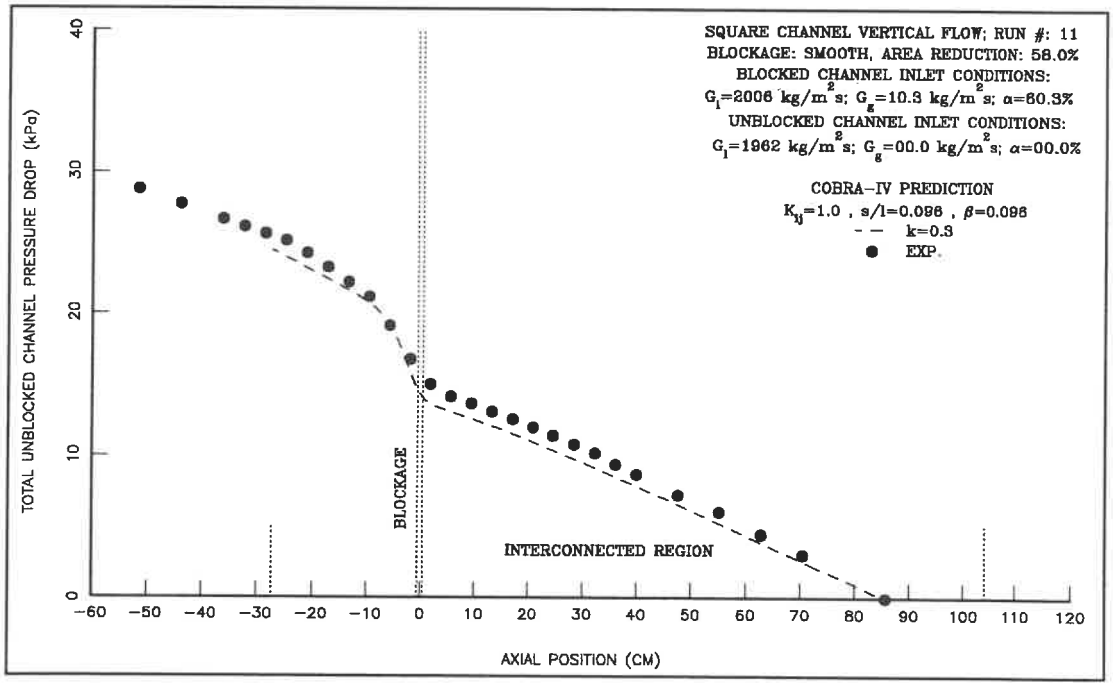


Figure 6.66: Pressure Drop profile, Two-Phase Case, Unblocked Channel, RUN #11

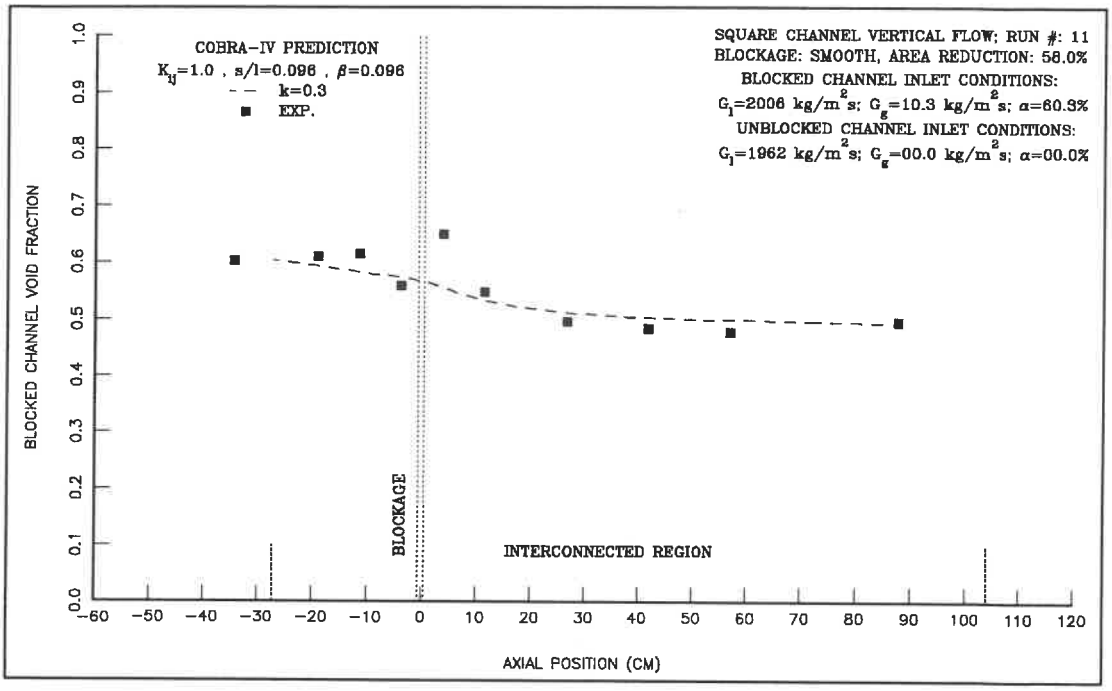


Figure 6.67: Void Fraction profile, Two-Phase Case, Blocked Channel, RUN #11

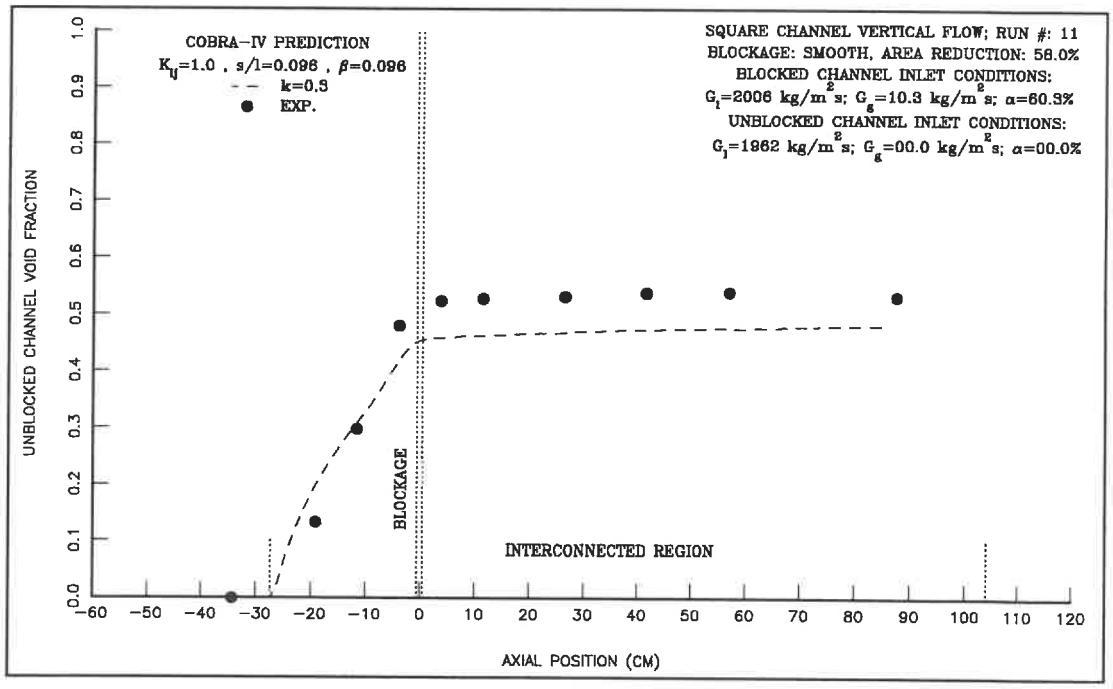


Figure 6.68: Void Fraction profile, Two-Phase Case, Unblocked Channel, RUN #11

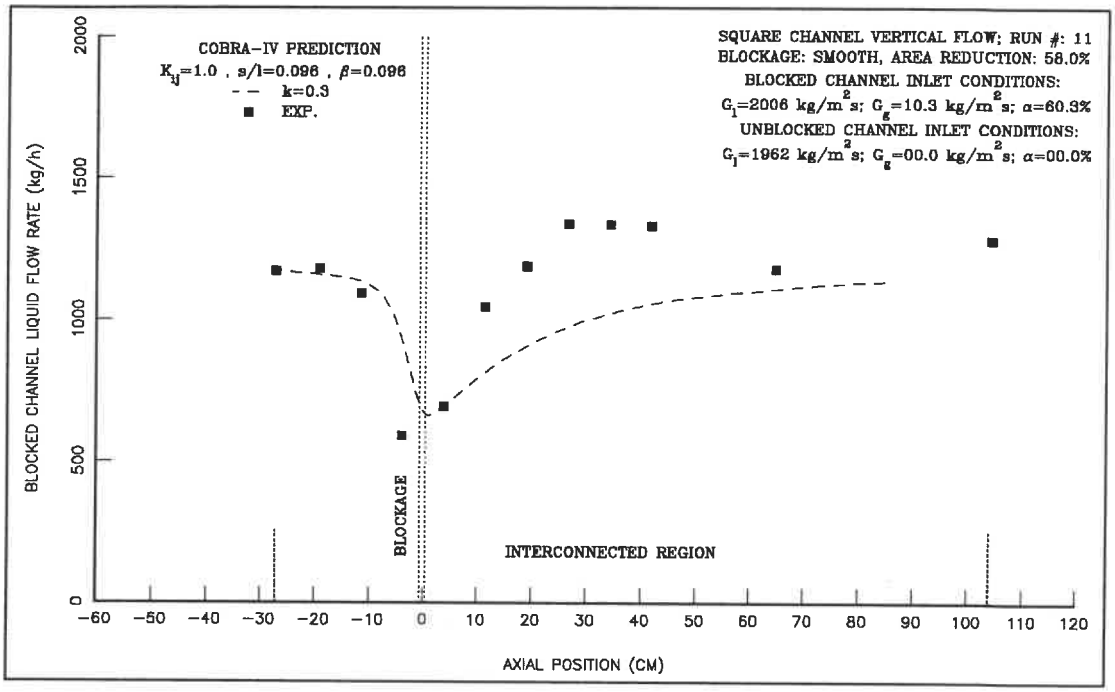


Figure 6.69: Liquid Flow Rate, Two-phase Case, Blocked Channel, RUN #11

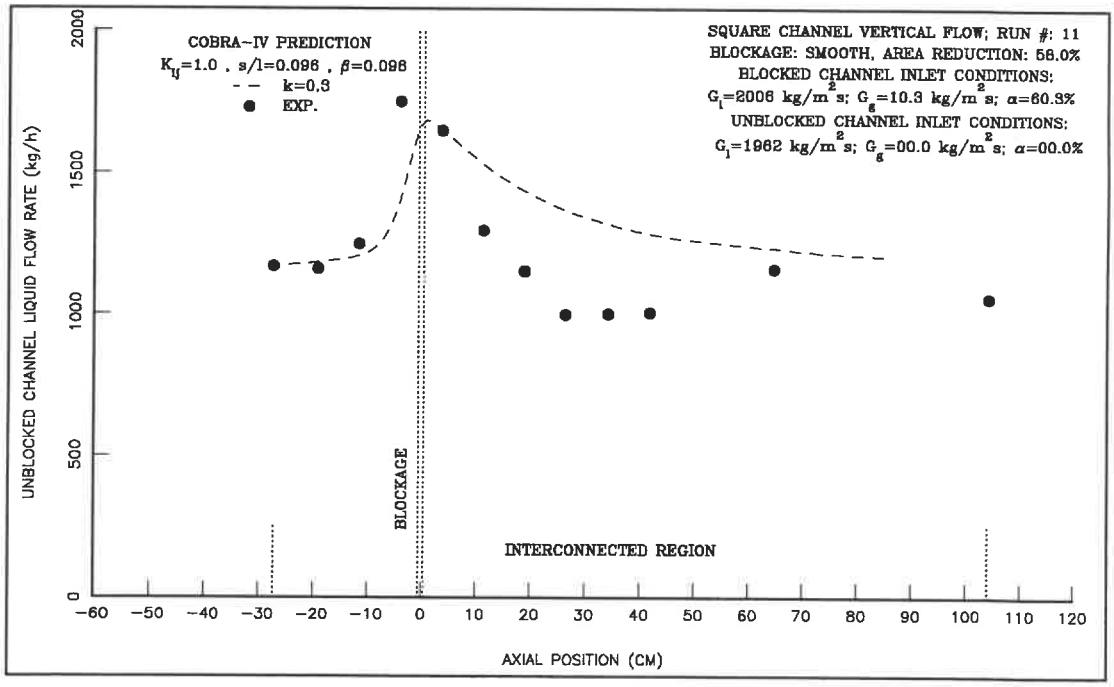


Figure 6.70: Liquid Flow Rate, Two-Phase Case, Unblocked Channel, RUN #11

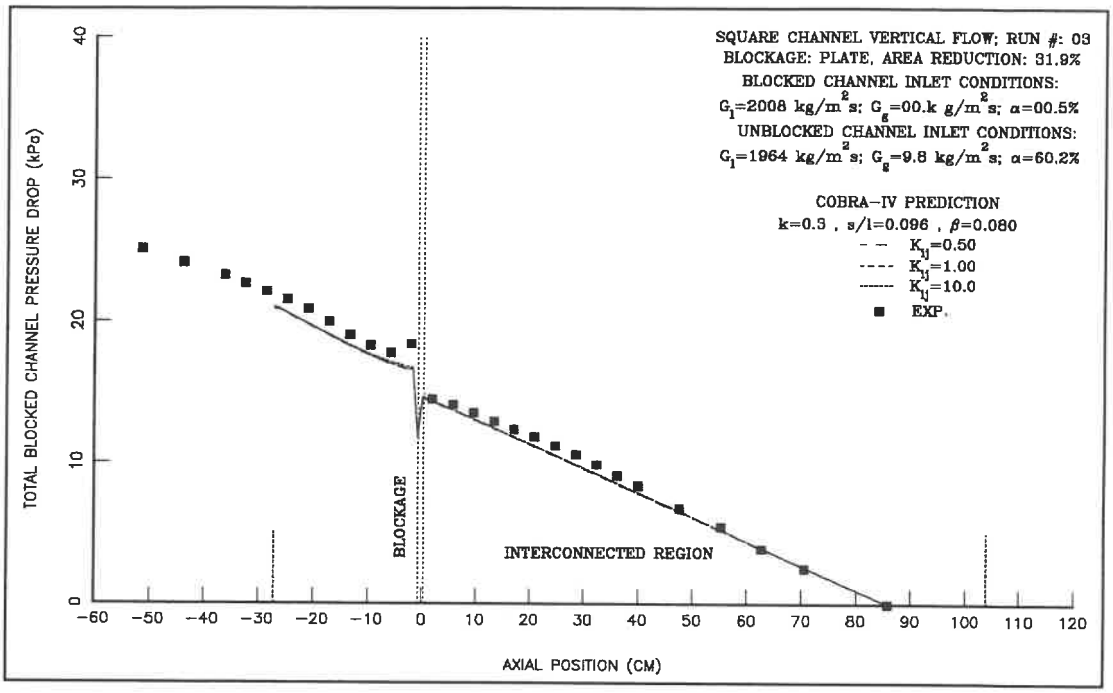


Figure 6.71: Pressure Drop profile, Two-Phase Case, Blocked Channel, RUN #03

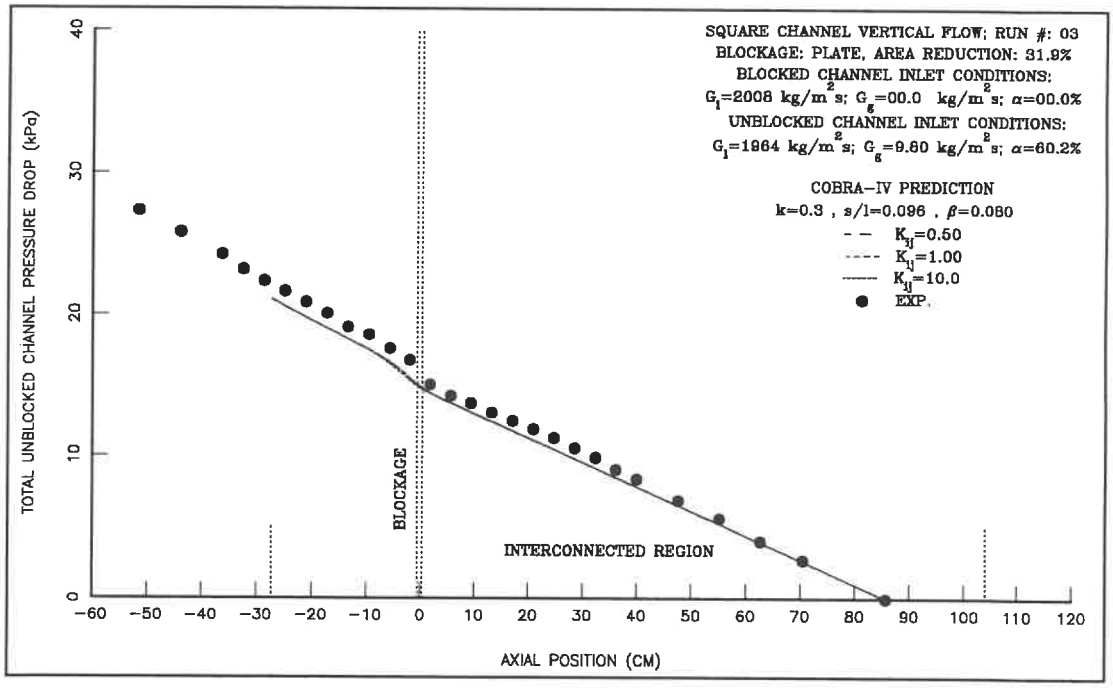


Figure 6.72: Pressure Drop profile, Two-Phase Case, Unblocked Channel, RUN #03

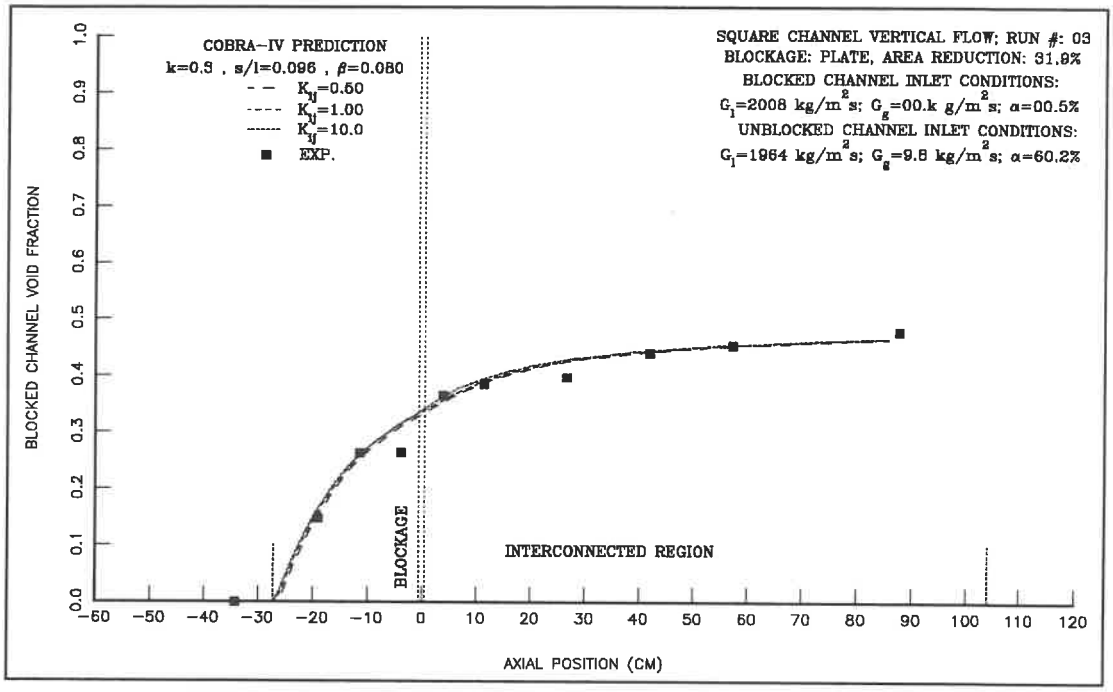


Figure 6.73: Void Fraction profile, Two-Phase Case, Blocked Channel, RUN #03

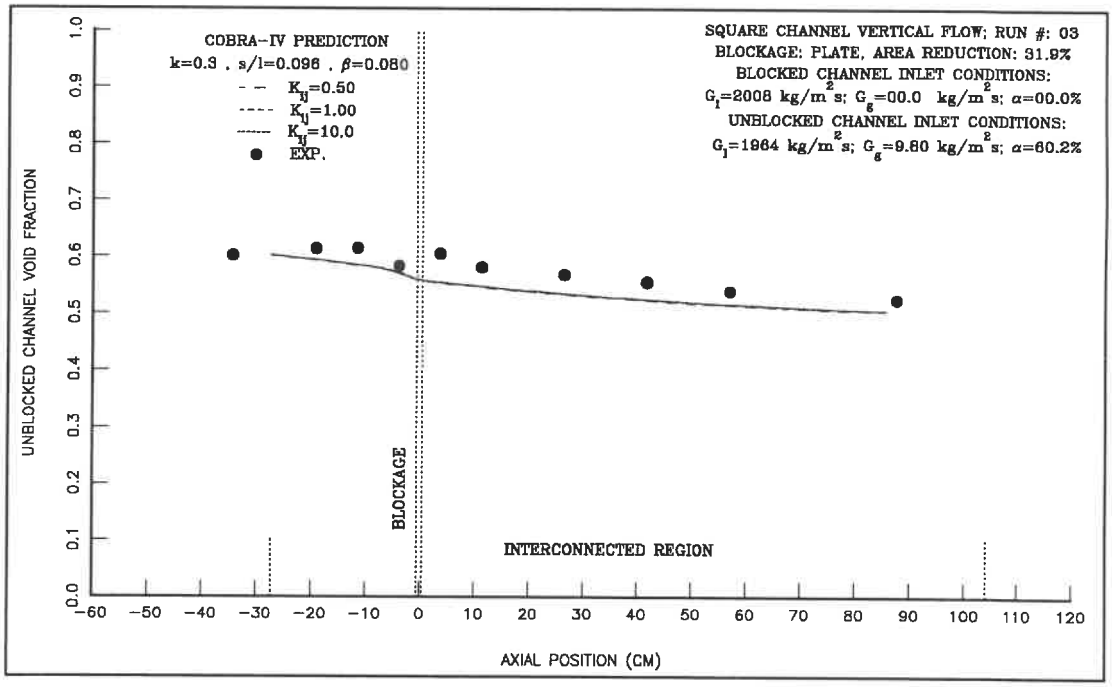


Figure 6.74: Void Fraction profile, Two-Phase Case, Unblocked Channel, RUN #03

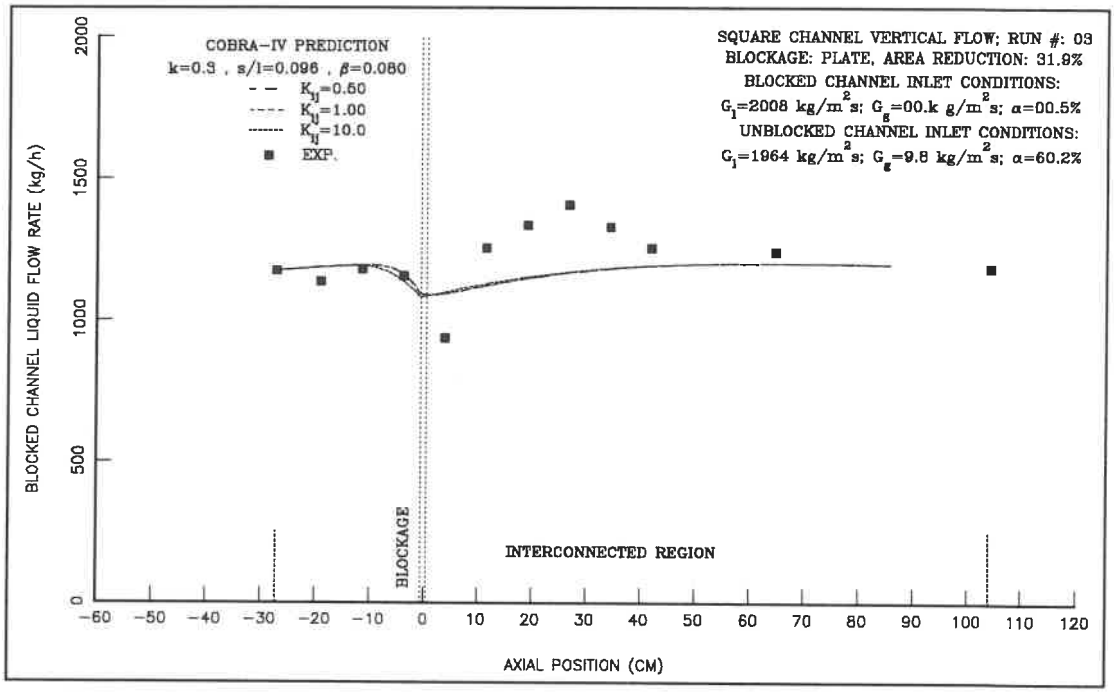


Figure 6.75: Liquid Flow Rate, Two-phase Case, Blocked Channel, RUN #03

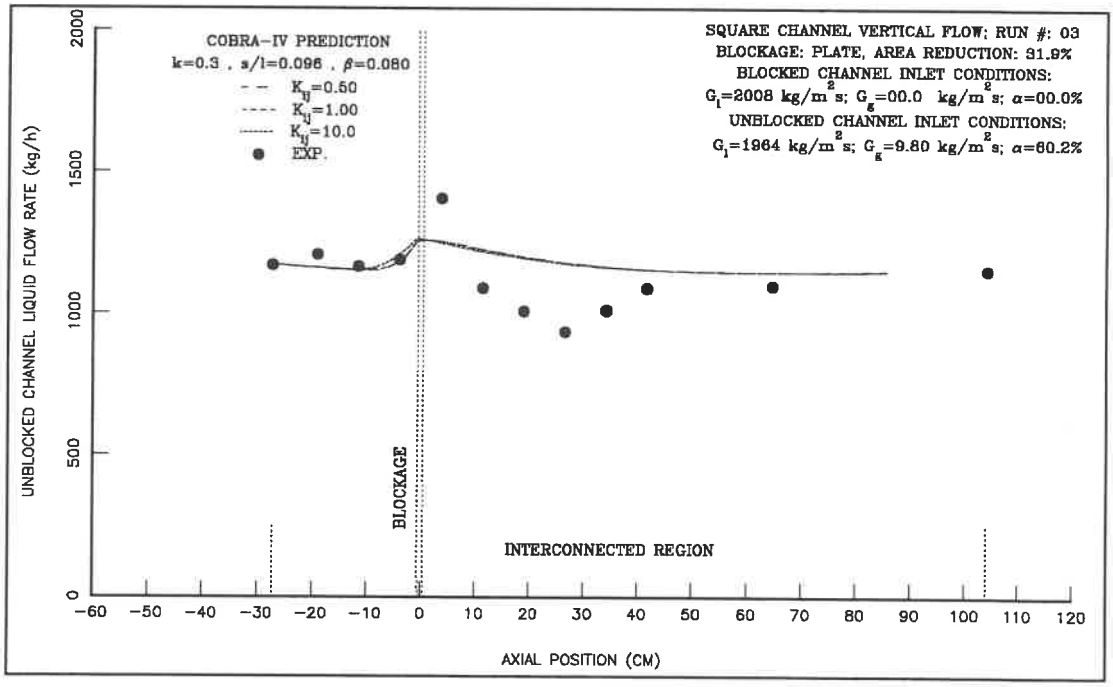


Figure 6.76: Liquid Flow Rate, Two-Phase Case, Unblocked Channel, RUN #03

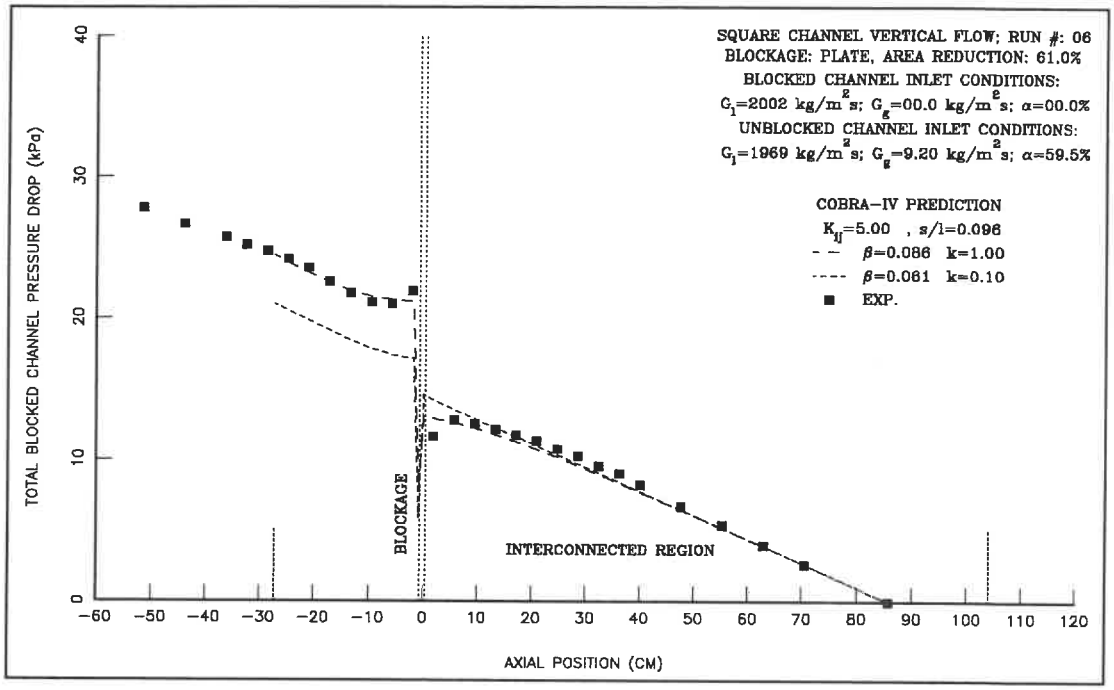


Figure 6.77: Pressure Drop profile, Two-Phase Case, Blocked Channel, RUN #06

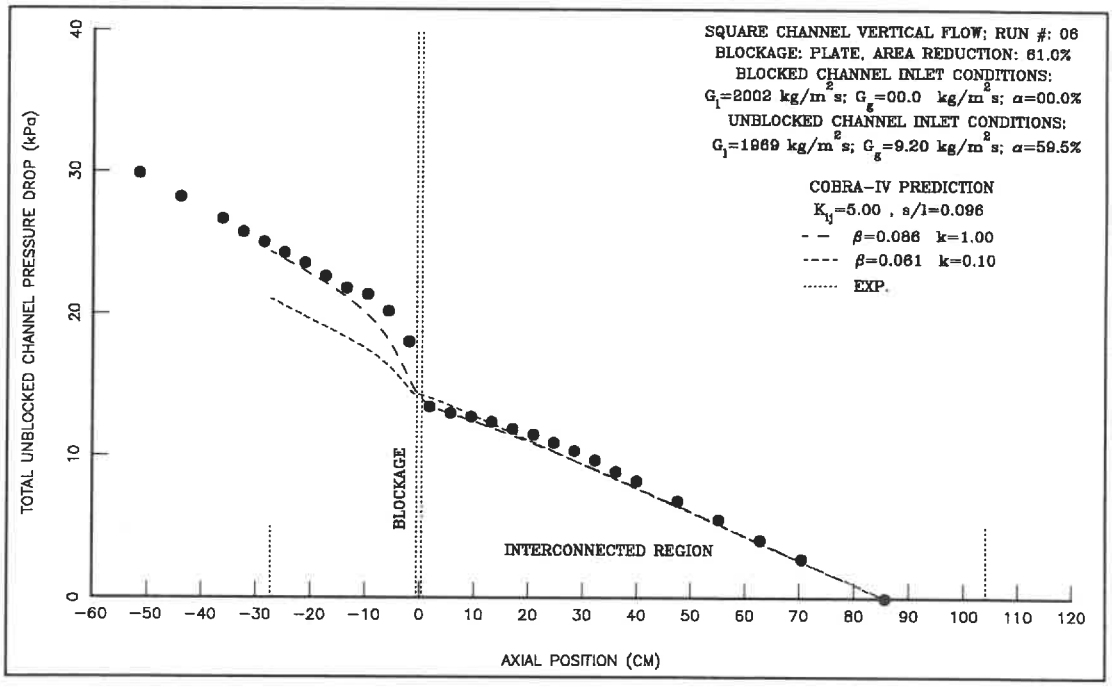


Figure 6.78: Pressure Drop profile, Two-Phase Case, Unblocked Channel, RUN #06

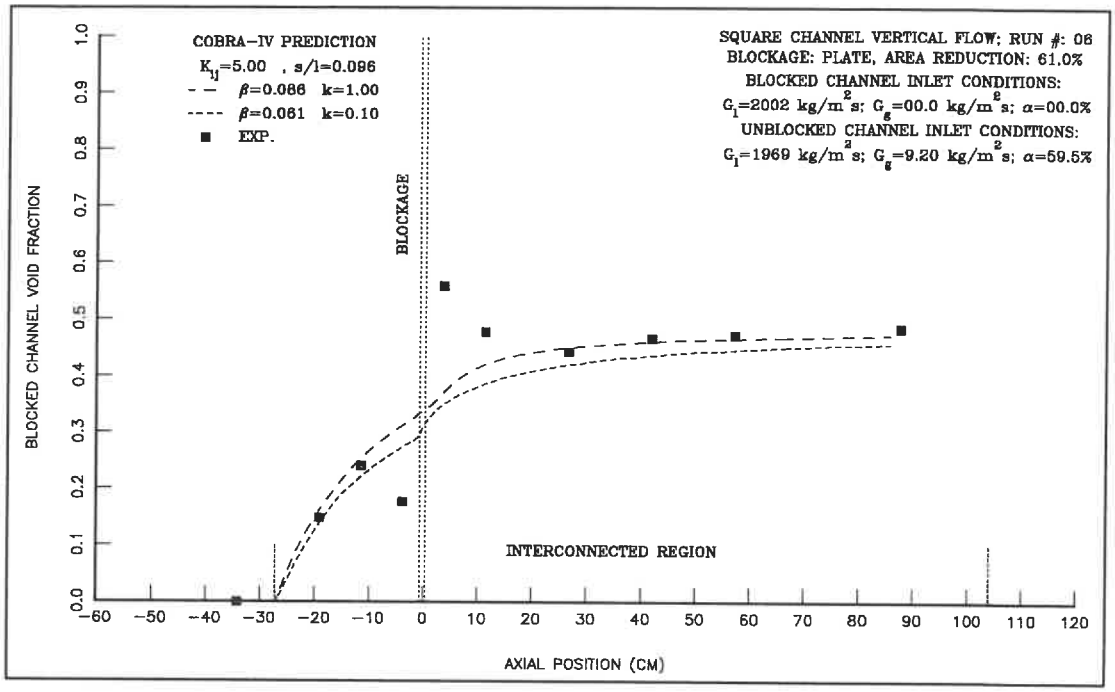


Figure 6.79: Void Fraction profile, Two-Phase Case, Blocked Channel, RUN #06

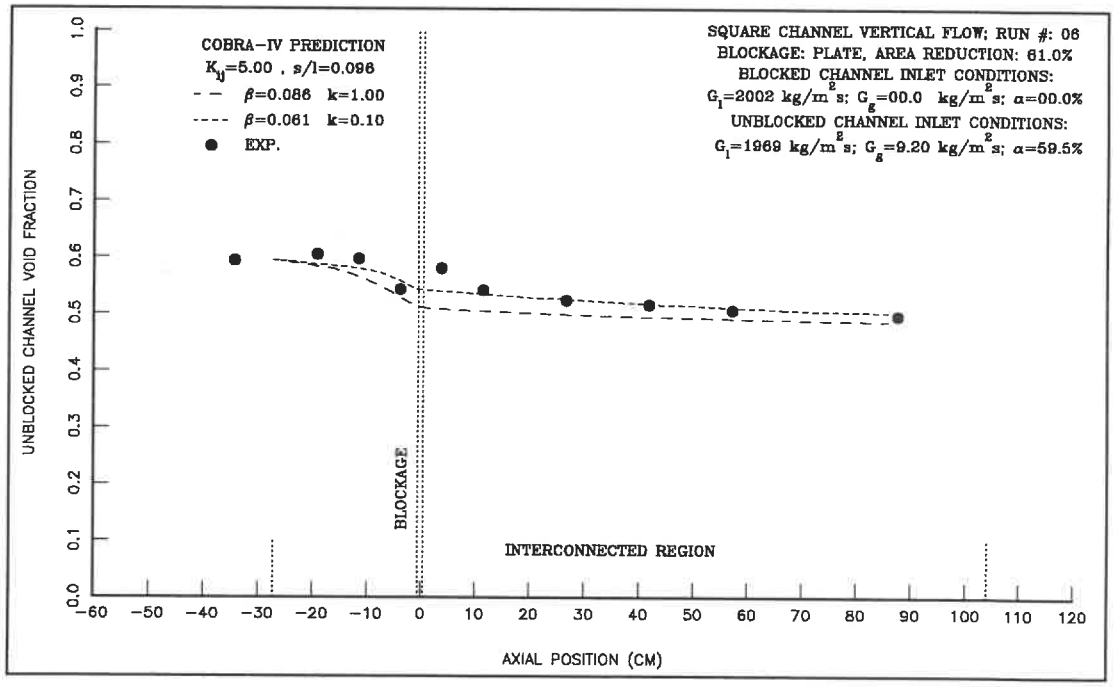


Figure 6.80: Void Fraction profile, Two-Phase Case, Unblocked Channel, RUN #06

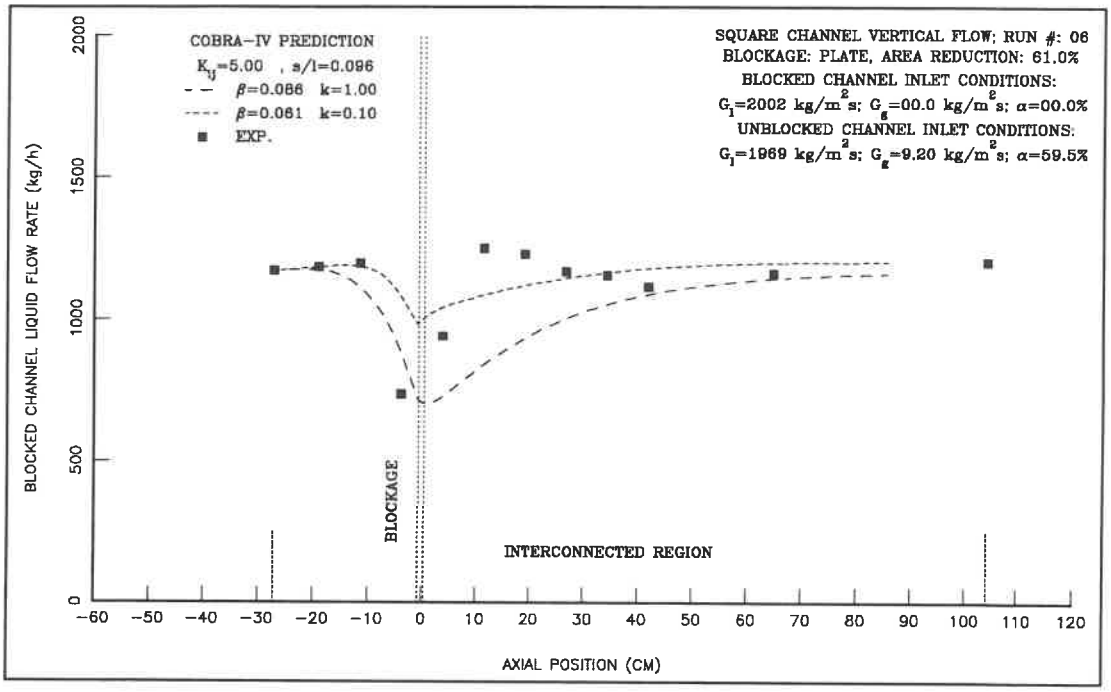


Figure 6.81: Liquid Flow Rate, Two-phase Case, Blocked Channel, RUN #06

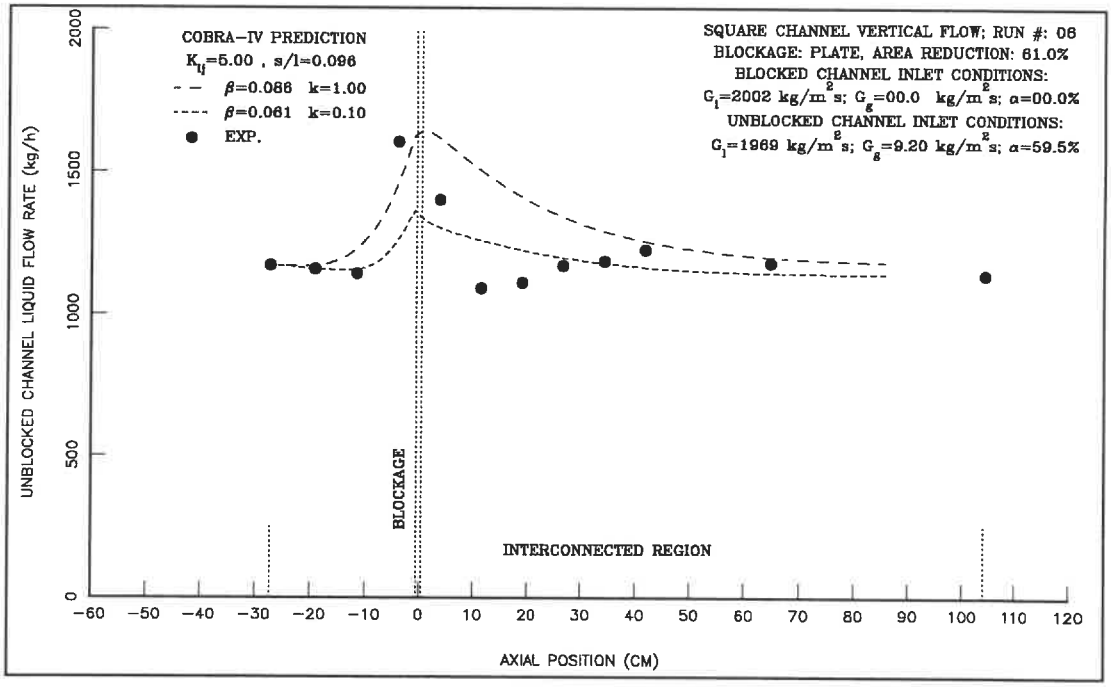


Figure 6.82: Liquid Flow Rate, Two-Phase Case, Unblocked Channel, RUN #06

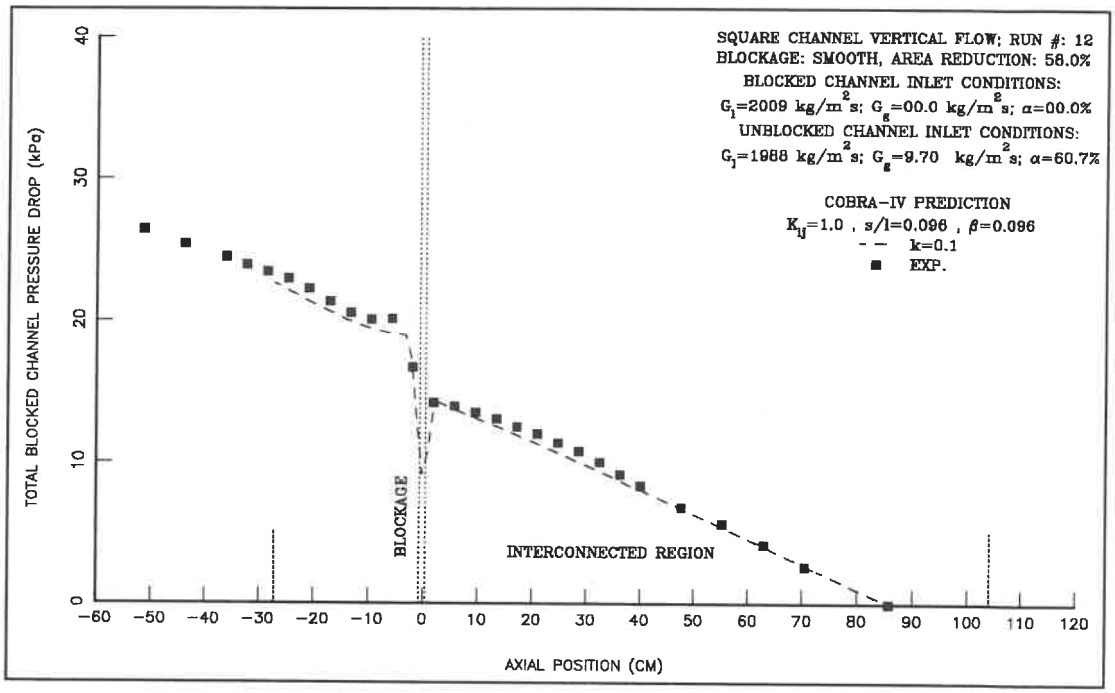


Figure 6.83: Pressure Drop profile, Two-Phase Case, Blocked Channel, RUN #12

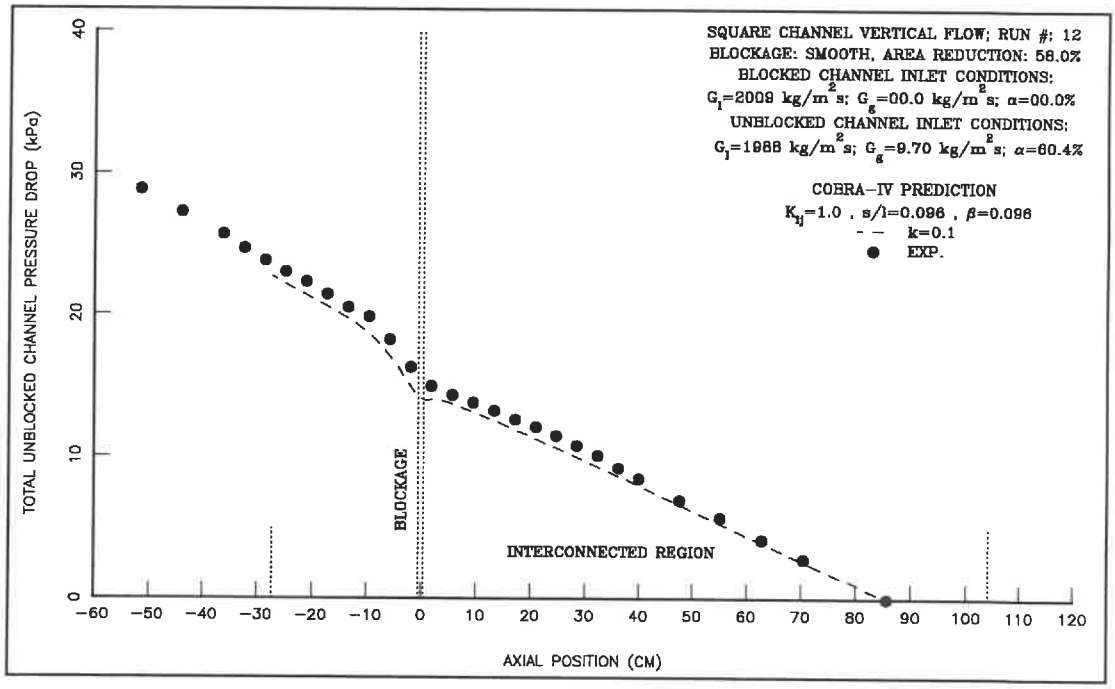


Figure 6.84: Pressure Drop profile, Two-Phase Case, Unblocked Channel, RUN #12

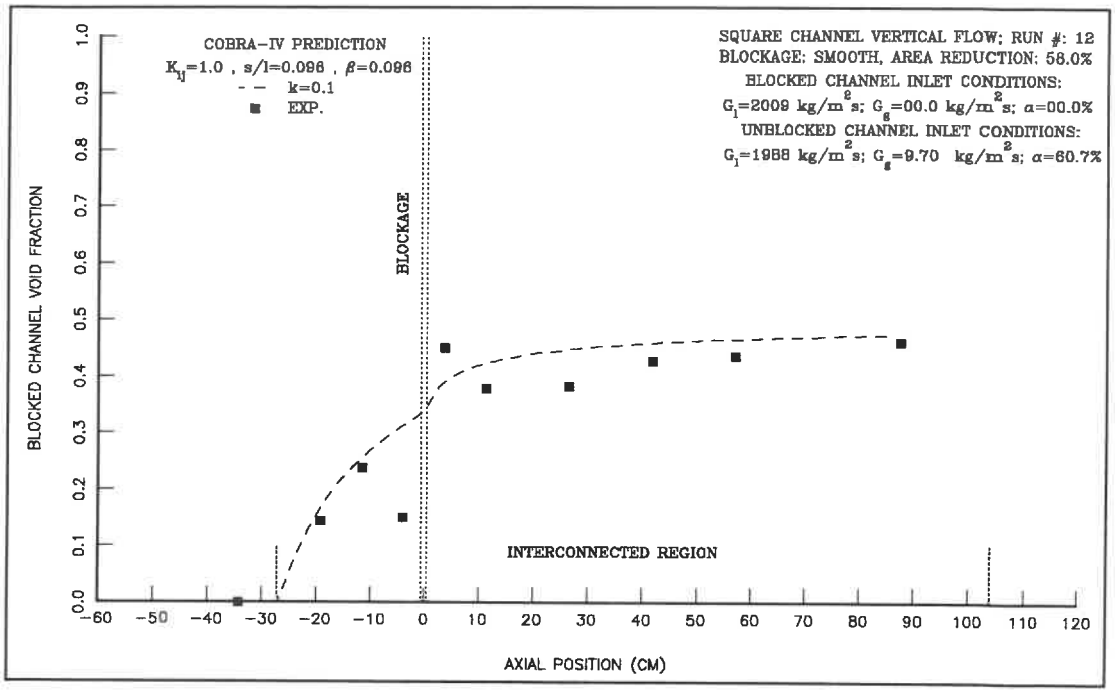


Figure 6.85: Void Fraction profile, Two-Phase Case, Blocked Channel, RUN #12

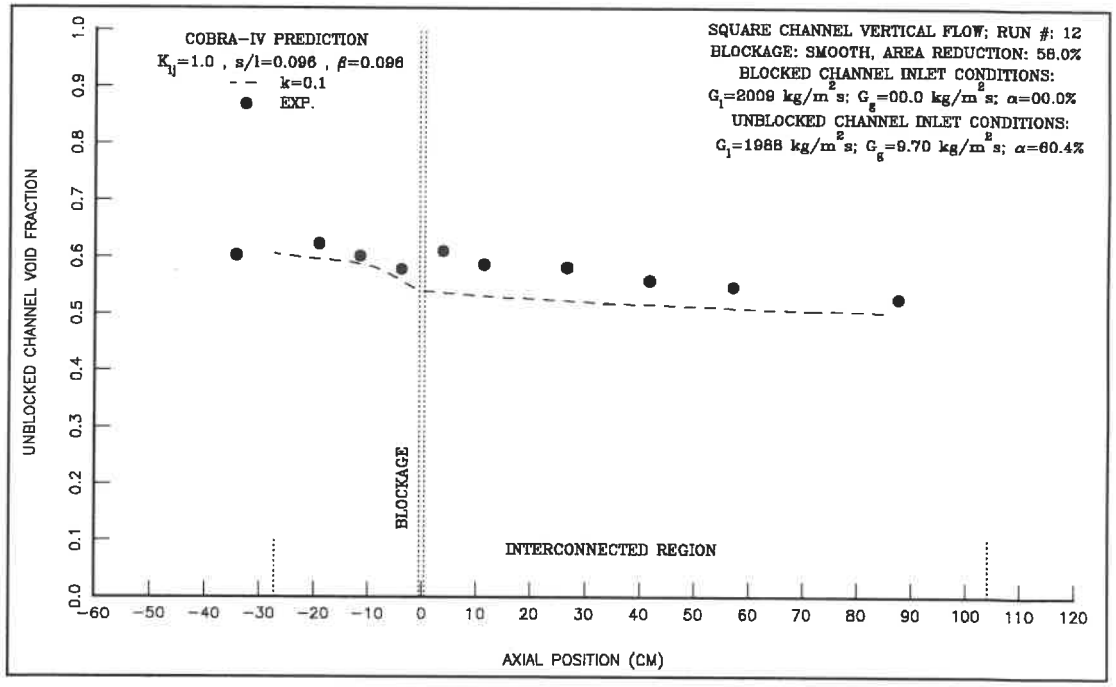


Figure 6.86: Void Fraction profile, Two-Phase Case, Unblocked Channel, RUN #12

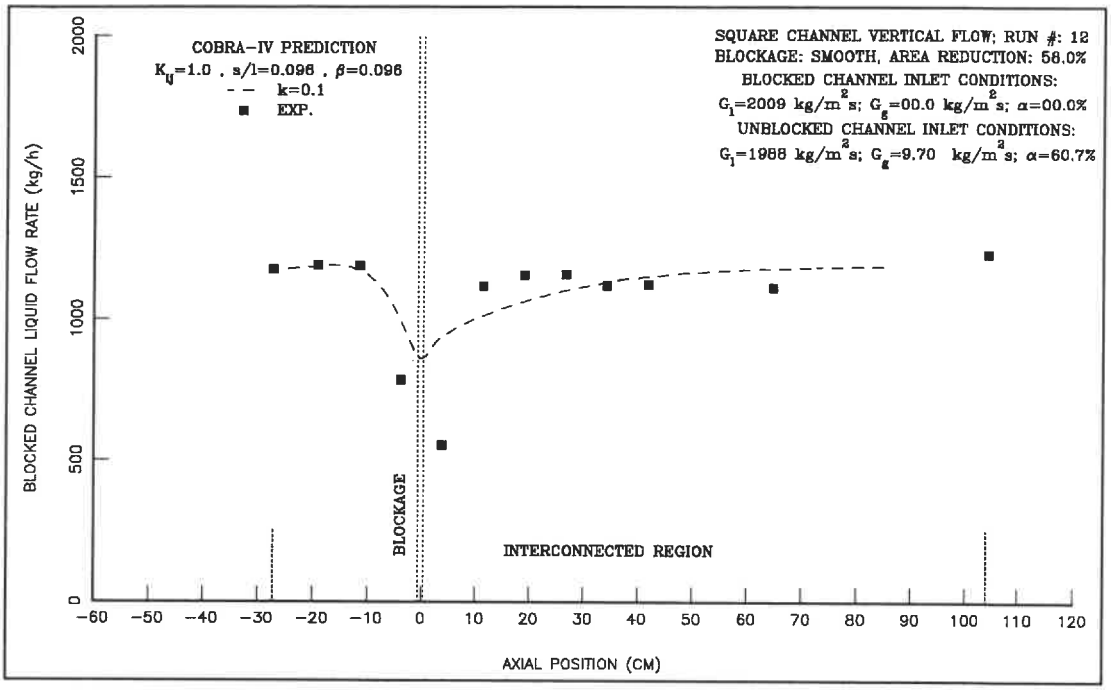


Figure 6.87: Liquid Flow Rate, Two-phase Case, Blocked Channel, RUN #12

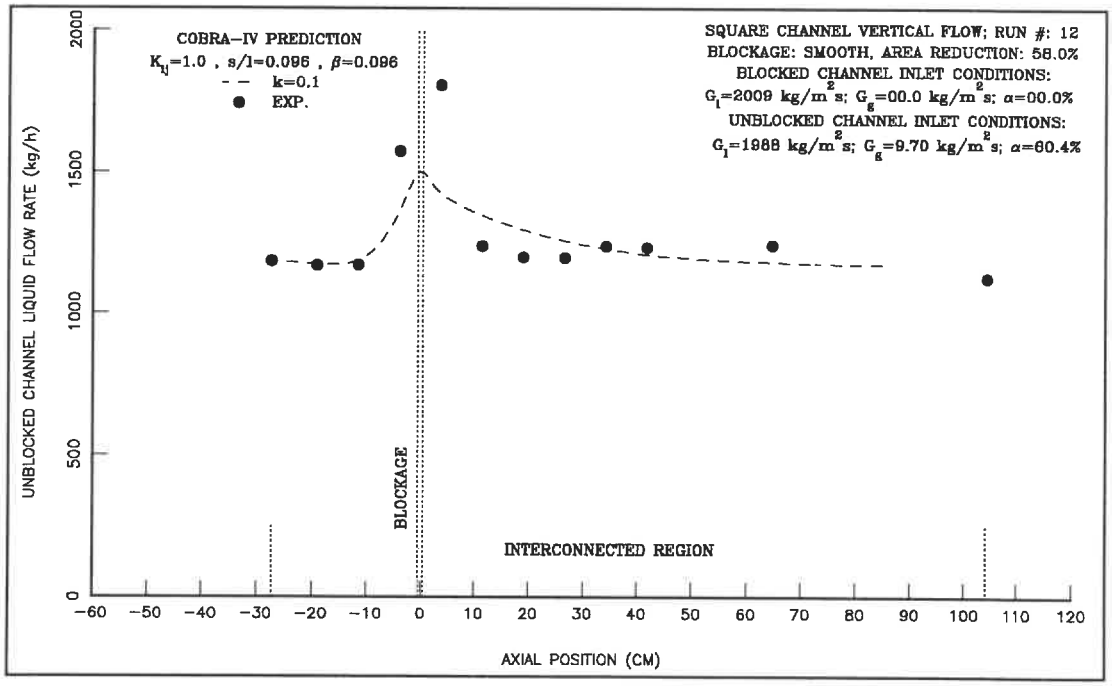


Figure 6.88: Liquid Flow Rate, Two-Phase Case, Unblocked Channel, RUN #12

CHAPTER 7

CONCLUSIONS AND RECOMMENDATIONS

This chapter will review the principal conclusions of this research and will present the recommendations for the future work that could be done in order to study the hydraulic behavior of interconnected subchannels.

Briefly, Chapter 1 was an introductory chapter where the importance of rod bundle thermalhydraulic analysis was presented. The literature survey in Chapter 2 showed that the three essential steps to develop a subchannel computer codes are: two-phase flow modeling, intersubchannel mixing phenomena and numerical procedure. In Chapter 3 the governing equations and the numerical procedure in the forms used by COBRA-IV were presented. In Chapter 4 all experimental instrumentation and experimental procedure used in the present and previous works were explained. In Chapter 5, all the measured data on the pressure drop and the void fraction obtained from two laterally interconnected subchannels as well as the predictions of COBRA-IV for the same conditions were presented. The value of mixing coefficient, β, considered to be the main parameter and the changes of the code's prediction due to variations of β were studied. In Chapter 6, the predictive capability of COBRA-IV for blockage cases was studied. This predictive capability was tested by a sensitivity analysis over the code's main parameters. Therefore, the content of this chapter will be divided into two parts. The first one will be devoted to the conclusions obtained from comparison between experimental data without the blockage against the predictions of COBRA-IV. In the second part the ability of COBRA-IV to handle blockage cases will be discussed.

I. Conclusions from Comparison: No-blockage Cases:

The conclusions can be divided into two categories: equal inlet mass fluxes and unequal inlet mass fluxes:

a) Equal inlet mass fluxes:

It was concluded that for the experiments in which inlet mass fluxes were equal, the value of β as a global mixing coefficient, depends on the inlet flow conditions. For the cases with inlet mass fluxes equal to **3000** kg/m^2s in the subchannels, the best value for β depends on the inlet void fraction of the donor subchannel. For the inlet void fraction about **60%** the value of **β=0.05** produces the best results in COBRA-IV. And for the inlet void fraction around **40%** the value of **β=0.01** produces the best results. This means that the intersubchannel mixing increase when the inlet void fraction increases. For the inlet void fraction between **40%** to **60%** no tested value of β could be suggested, however, a logarithmic interpolation between the best values of β for these two inlet void fraction, can be applied. For the inlet void fraction lower than **40%** the value of **β=0.01** may be considered to be the best. Also, it has been concluded that the average inlet void fraction can not be used as a parameter to obtain the appropriate values of β. Furthermore, it was concluded that for the lower values of the inlet mass fluxes the mixing effects are more important than those with high mass fluxes. It was observed that for the lower mass flux cases and average inlet values of the dryness fraction less than **0.005** (inlet void fraction less than **60%**), essentially a unique value of **β=0.05**, independent of the inlet void fraction, allows good predictions to be obtained.

b) Unequal inlet mass fluxes:

It was observed that the degree of intersubchannel mixing, when there is substantial difference between inlet mass fluxes, depends on the subchannel in which the higher void fraction is introduced.

1- When the high mass flux subchannel is the high void subchannel the degree of mixing is independent of the inlet void fraction and in most cases with inlet void fraction less than **60%**, a value of β**=0.05** gives the best result.

2- When the low mass flux subchannel corresponds to the high void subchannel, the degree of intersubchannel mixing depends on the inlet void fraction of the lower mass flux subchannel and mass flux difference between the two subchannels. It was observed that, when the difference between the inlet mass fluxes increased, higher inlet void fraction in the low mass flux subchannel causes a lower degree of intersubchannel mixing. On the other hand, when the difference between inlet mass fluxes decreased the higher inlet void fractions cause a higher degree of intersubchannel mixing. This means that probably, a critical inlet mass flux difference exists where the rate of intersubchannel mixing changes its behavior.

3- Because of the above observed behavior, finding a relationship between the values of β as a function of the *inlet average conditions* for the cases with unequal inlet mass fluxes was impossible. In addition, it was concluded that a simple model of intersubchannel mixing can adequately predict the behavior of the cases in which the inlet mass fluxes in the subchannels are different, *if a good knowledge of the β-values for that case exists*. However, neither a tabular or functional form of β (as a function of

dryness fraction) nor a constant values of β can be considered as a proper form of the input β-values in such cases.

4- Finally, the best values of the β for those cases with different mass fluxes in the subchannels but equal inlet void fractions depend essentially on the liquid mass transfer between subchannels, which in the present work were not available.

II. Conclusions from Comparison; Blockage Cases:

a) Single-Phase Cases:

- The value of K_{ij} has a limited influence on the predictions of code. K_{ij}=1.0 seems to produce the best results.
- The prediction of partially blocked flows with COBRA-IV depends on the value of the irreversible pressure loss coefficient, *k*.
- Because of the one-dimensional modeling the flow redistribution near the blockage cannot be accurately predicted.
- For smooth blockage cases COBRA-IV can safely be used up to 60% of flow area reduction.
- For plate blockage cases, the use of COBRA-IV can be extended to 60% of the flow area reduction. The experimental values of *k*-coefficient can be used without any major error.

b) Two-Phase Cases:

- It is observed that the convergence of the code depends on the values of K_{ij} and β, in such a way that for the values less than a minimum value of the K_{ij} and for values greater than a maximum value of β the code is not convergent.

- It is observed that the predictions depend on the values of β and *k*. The variation of *k* affects the predictions of the total pressure loss and liquid mass flow rate in both subchannels, while changing β has practically no influence in the prediction of the total pressure drop but it changes the predictions of the void fraction and liquid flow rate.
- It was observed that the coefficient *k* used in COBRA-IV are not very far from experimental *k*-coefficients, however, in the cases with 60% plate blockage, the best value of *k* is slightly less than the experimental value. Therefore, the experimental values of *k* can be safely used in all cases.
- It was concluded that the COBRA-IV can be used in smooth blockage up to 60% of the flow area reduction. In the case of the plate blockages, the code can also be used up to 60% flow area reduction. In these cases, COBRA-IV cannot produce the acceptable predictions for liquid flow rate but the predictions of the void fraction and the pressure drop are in good agreement with the experimental data.
- Compared to COBRA-IIIC, it can be concluded that COBRA-IV can handle almost any type of the blockages less than 60% without introducing unrealistic values of irreversible pressure loss.

Recommendations:

- The first recommendation is to perform a series of experiments covering a wider range of equal and unequal inlet mass fluxes, void fractions and of void fraction differences between the subchannel. Since the best β-values must be chosen based on both the void fraction and the liquid mass flow rate, the liquid flow rate also has to be measured. Later, based on the results, the attempt to correlate the mixing coefficient to void fractions, inlet mass flux of each subchannel or/and their difference, subchannel geometry, should be repeated. Also, the possibility of the existence of a critical inlet mass flux difference where the rate of the intersubchannel mixing changes its behavior,

should be studied.

- From the experimental observations in the present work, it can be concluded that, adding a model based on the dynamic interfacial forces acting on the bubbles, to describe the mixing phenomena could be useful. Perhaps, improving the mixing models depends on the modeling of the dynamic forces acting on the bubbles rather than on the improvement of empirical relations for existing models.
- The influence of K_{ij} and β on the convergence of the numerical scheme used by COBRA-IV must be studied. Based on the inlet flow conditions, the minimum necessary value of K_{ij} for the convergence of the numerical scheme may be determined. Consequently, the effect where an increase of K_{ij} causes the decrease in the number of external iterations, may be precisely studied.
- A relationship between the best values of K_{ij}, β, k, blockage area reduction and inlet flow conditions could be investigated. This can be done by carrying out more simulations of blockage cases.

BIBLIOGRAPHY

BANERJEE, S., (1980). Separated Flow Models-II: Higher Order Dispersion Effects in Averaged Formulation, Int. J. Multiphase Flow, Vol. 6, pp. 241-248.

BANERJEE, S. & CHAN, A.M.C. (1980). Separated Flow Models-I: Analysis of Averaged and Local Instantaneous Formulation, Int. J. Multiphase Flow, Vol. 6, pp. 1-24.

BARNE F., ET AL. (1990). The CATHARE strategy and assessment, Nucl. Eng. Design, Vol. 124, pp. 257-284.

BERGLES, A.E. (1969). Two-phase Flow Observations for High Pressure Water in a Rod Bundle, Proc. Two-Phase Flow and Heat Transfer in Rod Bundles, ASME Winter Ann. Meet., New York, pp. 47-56.

BOURÈ, J. (1973). Dynamique des ecoulements diphasiques: propagation des petites perturbation, Report CEA-R-4456.

BOWRING, R.W. (1968). HAMBO, A Computer Program Used for the Subchannel Analysis of the Hydraulic and Burnout Characteristics of Rod Clusters, pt. 2, Equations, AEEW-R 582.

CARVER, M.B., JUDD, R.A., KITELEY, J.C. AND TAHIR, A. (1987). The Drift Flux Model in ASSERT Subchannel Code, Nuclear Journal of Canada, 1, No. 2, pp.153-156.

CHIU, C. (1981). Three-dimensional Transport Coefficient Model and Prediction-Correction Numerical Method for Thermal Margin Analysis of PWR Cores, Nucl. Eng. Design, Vol. 64, pp. 103-195.

DELHAYE, J.M. (1968). Equation fondamentales des èçoulement diphasiques, I, II, Report CEA-R-3429.

DELHAYE, J.M., GIOT M. & RIETHMULLER, M.L. (1981). Thermalhydraulic of Two-Phase Flow, Hemisphere Publishing Corporation, McGraw-Hill Book Company.

DU BOUSQUET, J.L., BOURÈ, J. (1969). Mélange par diffusion turbulente entre deux sous-cannaux d'un rèacteur à grappe, Rèunion du groupe Europeen de ecoulement diphasique, Karlsure, June 2-5.

GONZALEZ-SANTALO, J.M. (1972). Two-Phase flow Mixing in Rod Bundles Subchannels, ASME Paper 72-WA/NE-19, pp. 1-13.

GOSMAN, A.D., ET AL. (1973) The SABRE Code for Prediction of Coolant Flows and Temperature in Pin Bundles Containing Blockages, UKAEA, AEEW-R905.

GRAY, W. G. & LEE, P.C.Y. 1977 On the Theorems for Local Volume Averaging of Multiphase Systems, Int. J. Multiphase Flow, Vol. 3, pp. 333-340.

GUIDO-LAVALLE, G., CARRICA, P., CLAUSSE, A., QAZI, M.K. (1994). A Bubble Number Density Constitutive Equation, Nucl. Eng. Design, Vol. 152, pp. 213-224.

HARLOW, F. H., AMSDEN, A. A. (1971). A Numerical Fluid Dynamics Calculation Method for All Flow Speeds, Journal of Computational Physics, Vol. 8, pp. 197-213.

HIRT, C. W., COOK, J. L. (1972). Calculating Three-dimensional Flows Around Structure and Over Rough Terrain, Journal of Computational Physics, Vol. 10, pp. 324-340.

ISHII, M. (1975) Thermo-Fluid Dynamic Theory of Two-phase Flow, Eyrolles, Paris.

ISHII, M. (1977). One-Dimensional Drift Flux Model and Constitutive Equations For Relative Motion between Phases in Various Two-Phase Flow Regimes, Report ANL 77-47.

ISHII, M., CHAWALA, F.C. (1978). Equations of Motion for Two-phase Flow in a Pin Bundle of Nuclear Reactor, Int. J. Heat Mass Transfer, Vol. 21, pp. 1057-1068.

ISHII, M., & ZUBER, N. (1979) Drag Coefficient and Relative Velocity in Bubbly, Droplet or Particulate Flows, AICh E Jl, Vol. 25, pp. 843-855.

KATAOKA, I., ISHII, M. & SERIZAWA, A. (1984). Local Formulation of Interfacial Area Concentration and its Measurements in Two-phase Flow, Report ANL. 84-86.

KATAOKA, I. (1986). Local Instant Formulation of Two-phase Flow, Int. J. Multiphase Flow, Vol. 12, No. 5, pp. 745-756.

KELLY, J.E., KAO S.P., KAZIMI, M.S. (1981). THERMIT-II: A Two Fluid Model For Light Water Reactor Subchannel Transient Analysis, MIT-EL-81-041.

KOCAMUSTAFAOGULLARI, G. (1971). Thermo-fluid Dynamic Theory of Separated Flow, Ph.D. Thesis, Georgia Institute of Technology, Atlanta, Ga.

LAHEY Jr, R.T. , SCHRAUB, F.A. (1969) Mixing, Flow Regime and Void Fraction for Two-phase Flow in Rod Bundles, Proc. Two-phase Flow and Heat Transfer, in Rod Bundles, ASME Winter Ann. Meet., ASME, New York, pp. 1-14.

LAHEY Jr, R.T., MOODY, F.J. (1977) The Thermalhydraulics of a Boiling Water Nuclear Reactor, American Nuclear Society, USA

LAHEY, R.T. JR (1986). Subchannel Measurement of the Equilibrium Quality and Mass Flux Distribution in a Rod Bundle, Proc. 8th Int. Heat Transfer Conf., San Francisco, pp. 2399-2404.

MASTERSON, R.E., WOLF, L. (1978) COBRA-IIIP: An improved Version of COBRA for Full-core Light Water Reactor Analysis, Nucl. Eng. Design, Vol. 48, pp. 293-310.

MAHAFFY, J.H. (1982). A Stability Enhancing Two-step Method for Fluid Flow Calculations, J. of Computational Physics, Vol. 46, pp. 329-341.

ROUHANI, S.Z. (1978). Two-Phase flows and Heat Transfer with Application to Nuclear Reactor Design Problem, Edited by Ginoux, J.J., McGraw-Hill Book Company, pp. 301-327.

ROWE, D.S. (1967) Cross-Flow Mixing Between Parallel Flow Channels During Boiling ; COBRA: Computer Program for Coolant Boiling in Rod Arrays, BNWL 371.

ROWE, D.S. (1970). COBRA-II, A Digital Computer Program for Thermal Hydraulic Subchannel Analysis of Rod Bundle Nuclear Fuel Elements, BNWL 1229.

ROWE, D.S. (1973). COBRA-IIIC: A Digital Computer Program for Steady State and Transient Theraml-Hydraulic Analysis of Rod Bundle Nuclear Fuel Elements, BNWL-1229.

SADATOMI, M., KAWAHARA, A., SATO, Y. (1994). Flow Redistribution Due to Void Drift In Two-phase Flow in a Multiple Channel Consisting of Two Subchannels, Nucl. Eng. Design, Vol. 148, pp. 463-474.

SATO, Y., SADATOMI, M. (1988). Two-Phase Gas-liquid Flow Distribution in Multiple Channels, Proc. Japan-US Seminar on Two-phase Flow Dynamic, Ohtso, 1988, pp. E41-10.

SCHAWRTZ, L. (1950), Theorie des Distribution, Vol. I & II, Hermann Paris.

SCHAWRTZ, L. (1961). Mèthodes Mathèmatiques pour Les Sciences Physiques, Hermann, Paris.

SCHLISHTING , H. (1979) Boundary Layer Theory, McGraw-Hill Book Company, 7th Edt..

SHA, W.T. (1980). An Overview of Rod-Bundle Thermelhydraulic Analysis, Nucl. Eng. Design, Vol. 62, pp 1-24.

SHOUKRI, M., TAWFIK, H., CHAN A.M.C. (1984). Two-phase Redistribution in Horizontal Subchannel; Flow Turbulent Mixing and Gravity Separation, Int. J. Multiphase Flow, Vol.10, pp. 357-369.

STEWART, C.W., WHEELER, C.L., CENA, R.J., MCMONAGLE, C.A., CUTA, J.M., TRENT, D.S (1977). COBRA IV: The Model and the Method, BNWL-2214, NRC-4.

SUGAWARA, S., SAKAI, T., WATANABE, K., RUMMENS, H.E.C. (1991) Subchannel Analysis by the FIDAS Code based on the Three-fluid Model, Vol. 132, pp. 253-264.

TAPUCU, A., GENCAY, S., TROCHE, N. (1984) Experimental Study of the Diversion Cross-Flow Caused by Subchannel Blockages. Volume 1: One-Phase Flow, Electrical Power Research Institute NP-3459, Research Project 1378-1.

TAPUCU, A., TEYSSEDOU, A., GECKINLI, M., TROCHE, N. (1988). Experimental Study of the Diversion Cross-Flow Caused by Subchannel Blockages, Volume 2: Two-Phase Flow, Electric Power research Institute NP-3459, Research Project 1378-1.

TAPUCU, A., GEÇKINLI, M., TROCH, N., GIRARD, R. (1988). Experimental Investigation of Mass Exchange Between Two Laterally Interconnected Subchannels, Nucl. Eng. Design, Vol. 105, pp. 295-312.

TAPUCU, A., TEYSSEDOU, A.J., DAVIDSON, M. AND JOUHRI, H. (1990) Experimental Study of Mass Exchange Between Two laterally Interconnected Two-phase Flows: Effect of Gap Clearance, École polytechnique de Montréal, Report IGE-85.

TEYSSEDOU, A.J. (1987). Thermalhydraulic Behavior of Interconnected Subchannels with Blockage, Ph.D. Thesis, Ècole polytechnoque de Montrèal.

TAPUCU, A., TEYSSEDOU, A., TYE, P., TROCHE, N. (1994). The Effect of Turbulent Mixing Models on the Predictions of Subchannel Codes, Nucl. Eng. design, Vol. 149, pp.221-231.

THURGOOD, M.J., KELLY, J.M., GUIDOTTI, T.E., KOHRT, R.J., CROWELL, K.R. (1983). COBRA-TRAC A Thermalhyraulic Code for Transient Analysis of Nuclear Reactor Vessels and Primary Coolant System, NUREG/CR-3046.

TRAPP, J.A. & REIMKE, R.A. (1986). A Nearly Implicit Hydrodynamics Numerical Scheme for Two-phase Flows, J. of Computational Physics., Vol. 66, pp. 62-82.

TSUGE A., SAKATA K., HIRAO Y. (1979). Abnormal Characteristic of Two-phase Flow in Vertical Tube Banks, in S.C. Yao and P.A. Pffund (eds.), Fluid Flow and Heat Transfer over Rod Tube Bundles, ASME, New York, pp. 129-142.

TYE, P.F. (1991). An Investigation of the Model for Mass, Momentum and Energy Interchange Between Interconnected Subchannels as Applied in the ASSERT-4 Subchannel Code, Mémoire de Mâtrise, École Polytechnique de Montrèal.

VAN DER ROS, T. (1970). On Two-phse Flow Exchange Between Interacting Hydraulic Channels, Doctorate Thesis, Eindhoven Univ. of Technology, The Netherlands.

VAN DOORMAL, J.P. (1980) A Review of Pertinent Methods Used in Multi-Dimensional Rod-Bundle Thermalhydraulic Analysis, W.N.R.E report, 907-16

WALLIS, G.B. (1969) One-dimensional Two-phase Flow, McGraw-Hill Book Company.

WHITAKER, S. (1982). Handbook of Multiphase System, pp. 1-5 to 1-35, Edited by Hetseroni, G., Hemisphere Publishing Corporation, McGraw-Hill Company.

WOLF, L., FISCHER, K. (1987). Comprehensive Assessment of the ISPRA BWR and PWR Subchannel Experiments and Code Analysis with Different Two-phase Models and Solution Scheme, Nucl. Eng. Design, Vol. 99, pp. 329-350.

ZERNIK, W., CURRIN, H.B., ELYASH, E. AND PREVITI, G. (1962) THINC, A Thermal Hydrodynamic Interaction Code for a Semi-open or Closed Channel Core, WCAP-3704, Westinghouse Electric Corp..

ZUBER, N. & FINDLAY, J.A. (1965). Average Volumetric Concentration in Two-phase Flow Systems, J. Heat Transfer, Vol. 87, pp. 453-468.

ÉCOLE POLYTECHNIQUE DE MONTRÉAL
3 9334 00285772 8